TESIS DE LA UNIVERSIDAD DE ZARAGOZA

2023 125

Alba Peiró Chamarro

Fallas activas de la cordillera Ibérica Centro-Oriental

http://zaguan.unizar.es/collection/Tesis

Director/es
Simón Gómez, José Luis

ISSN 2254-7606

Prensas de la Universidad
Universidad Zaragoza

© Universidad de Zaragoza
Servicio de Publicaciones

ISSN 2254-7606

Universidad Zaragoza
1542

Tesis Doctoral

FALLAS ACTIVAS DE LA CORDILLERA IBÉRICA CENTRO-ORIENTAL

Autor

Alba Peiró Chamarro

Director/es

Simón Gómez, José Luis

UNIVERSIDAD DE ZARAGOZA
Escuela de Doctorado

Programa de Doctorado en Geología

2023

Repositorio de la Universidad de Zaragoza – Zaguan http://zaguan.unizar.es

FALLAS ACTIVAS DE LA CORDILLERA IBÉRICA CENTRO-ORIENTAL

Alba Peiro Chamarro

Tesis Doctoral en Geología
Director: José Luis Simón Gómez

Departamento de
Ciencias de la Tierra
Universidad Zaragoza

Tesis Doctoral

FALLAS ACTIVAS DE LA CORDILLERA IBÉRICA CENTRO-ORIENTAL

Alba Peiro Chamarro

Departamento de Ciencias de la Tierra
Facultad de Ciencias
Universidad de Zaragoza

Director:
José Luis Simón Gómez

Departamento de Ciencias de la Tierra
Universidad Zaragoza

Grupo de Investigación
Geología para la Ciencia y la Sociedad
GEOtransfer
Universidad Zaragoza

Instituto Universitario de Investigación en Ciencias Ambientales de Aragón
Universidad Zaragoza

GOBIERNO DE ESPAÑA
MINISTERIO DE EDUCACIÓN, CULTURA Y DEPORTE

Universidad Zaragoza
1542

Esta memoria, presentada por Dña. **Alba Peiro Chamarro** para optar al título de Doctora en Ciencias Geológicas, ha sido realizada bajo la dirección del Dr. **José Luis Simón Gómez** en el Área de Geodinámica Interna del Departamento de Ciencias de la Tierra de la Universidad de Zaragoza.

Zaragoza, 2022

José Luis Simón Gómez
Director de Tesis

FALLAS ACTIVAS DE LA CORDILLERA IBÉRICA CENTRO-ORIENTAL

Tesis doctoral presentada bajo la modalidad de compendio de publicaciones:

Peiro, A., Simón, J.L., Román-Berdiel, M.T. (2020). Fault relay zones evolving through distributed longitudinal fractures: the case of the Teruel graben system (Iberian Chain, Spain). *Journal of Structural Geology* 131, 103942. doi: 10.1016/j.jsg.2019.103942

Peiro, A., Simón, J.L. (2021). The Río Grío-Pancrudo Fault Zone (central Iberian Chain, Spain): recent extensional activity revealed by drainage reversal. *Geological Magazine* 159(1), 21-36. doi: 10.1017/S0016756821000790

Peiro, A., Simón, J.L., Arlegui, L.E., Ezquerro, L., García-Lacosta, A.I., Lamelas, T., Liesa, C.L., Luzón, A., Martín-Bello, L., Pueyo-Anchuela, O., Russo, N. (2022). Hanging-wall deformation at the active Sierra Palomera extensional fault (Jiloca basin, Spain) from structural, morphotectonic, geophysical and trench analysis. *Tectonophysics* 828, 229274. doi: 10.1016/j.tecto.2022.229274

Peiro, A., Simón, J.L., Martín-Bello, L., Arlegui, L.E., Ezquerro, L., Luzón, A., Medialdea, A., Corral, B., Liesa, C.L. (2022). Recent activity and paleoseismicity of an intraplate extensional fault: the Calamocha fault (Jiloca graben, central Iberian Chain). *International Journal of Earth Sciences*, online. doi: 10.1007/s00531-022-02265-3

Simón, J.L., Simón-Porcar, G., **Peiro, A.**, (2022). *Memory of the Earth* and human memory on natural disasters: the 1953 earthquake in western Aragón (Spain). *Geoheritage*, online. doi: 10.1007/s12371-022-00758-w

Otras publicaciones relacionadas con esta tesis:

Peiro, A., Simón, J.L., Liesa, C.L (2017). New evidence of recent fracturing at the relay zone between the Concud and Teruel faults (eastern Iberian Chain). *Geogaceta* 62, 31-34.

Simón, J.L., Arlegui, L.E., Liesa, C.L., Ezquerro, L., Lafuente, P., Luzón, M.A., **Peiro, A.** (2018): Paleosismicidad de la falla de Teruel y su relación con la falla de Concud (Cordillera Ibérica). *Resúmenes III Reunión Ibérica sobre Fallas Activas y Paleosismología*, Universidad de Alicante, 111-114.

Peiro, A., Simón, J.L., Román-Berdiel, T. (2019). Zonas de relevo de falla en el margen oriental de la fosa del Jiloca (Cordillera Ibérica): geometría, cinemática y modelización analógica. *Boletín Geológico y Minero* 130(3), 393-416. doi: 10.21701/bolgeomin.130.3.002.

Peiro, A., Simón, J.L. (2021). Caracterización preliminar de la zona de falla de Río Grío-Pancrudo: estructura extensional de primer orden en la evolución reciente de la Cordillera Ibérica. *Geo-Temas* 18, 846-849.

Simón, J.L., Simón-Porcar, G., **Peiro, A.** (2021). *El terremoto de Used: ciencia y memoria*. Universidad de Zaragoza y Centros de Estudios del Jiloca y Darocenses, Aragón, 78 p. ISBN: 978-84-949076-6-1.

Simón, J.L., **Peiro, A.**, Arlegui, L.E., Ezquerro, L., García-Lacosta, A.I., Lafuente, P., Liesa, C.L., Luzón, A., Martín-Bello, L., Pueyo, Ó., Soriano, M.A. (2022). Actividad plio-cuaternaria de fallas en el sistema extensional Teruel-Jiloca-Calatayud (Cordillera Ibérica central). *Resúmenes IV Reunión Ibérica sobre Fallas Activas y Paleosismología*, Teruel, Universidad de Zaragoza, 27-30.

AGRADECIMIENTOS

¡Ay, qué complicado concentrar tanto mis agradecimientos a todas las personas maravillosas que se han cruzado en mi camino personal y académico estos últimos años! Pero lo voy a intentar…

En primer lugar, se lo quiero agradecer a José Luis, mi maestro y mentor durante ocho años, que ha hecho de esta tesis, y de todos nuestros proyectos juntos, un trabajo que a mi parecer es impecable, completo y perfecto, casi como los de antes. Un *clásico*, en el buen sentido. Con una trayectoria digna de admiración y una capacidad asombrosa de sumergir a cualquiera en su pasión por la geología, mediante la buena enseñanza, la divulgación e incluso la música. Estoy orgullosa de haber sido tu doctoranda, y para mí ya es un éxito enorme, después de mucho esfuerzo, el haberme quedado con un cachico de todo eso. Gracias por la *transferencia* de conocimiento todos estos años.

Me alegro mucho de haber formado parte de un equipo, y un área, con personas magníficas y extraordinariamente capaces de todo. A Carlos y Luis, pilares fundamentales de nuestro *club* de estructural y paleosismología. Sin vuestras enseñanzas, ayuda, disponibilidad y colaboración tampoco habría salido adelante esta tesis. A los demás miembros: Antonio, Andrés, Ana Rosa… En este momento quiero acordarme de Arsenio. También en especial, a mis profesoras Arantxa, Teresa y Asunción, por vuestra calidez y vuestra capacidad de escuchar y enseñar. A Lope, Paloma y Leticia, por allanar tanto y tan amablemente mi camino. Los que sois de otras áreas siempre habéis sido un soplo de aire fresco, y todos, ya desde la carrera, fuisteis capaces de ir despertando en mí el interés en hacer buena ciencia.

No me olvido de mis supervisores durante la estancia en L'Università dell'Insubria (Como, Italia), Alessandro Michetti y Franz Livio, ni de mis compañeros Francesca, Emanuelle y Giorgio. Por todas las trincheras en Rieti y platos de pasta en La Selva (*ma che pasta*!). Qué buenos momentos con *i miei amici* de la residencia La Presentazione. Tampoco de todos los investigadores de otras universidades españolas que me acogieron y dieron buenos consejos en cada congreso. A Alicia Medialdea, Juanvi Cantavella, Sandra Ruiz, y muchas personas más, por la ayuda y los proyectos conjuntos.

A mi grupo de investigadores PIF, y todos los análogos españoles, por luchar con mucho esfuerzo para conseguir el reconocimiento de tantos de los derechos laborales de los que disfrutamos cada día, y encima estar formado por gente tan maja. Puedo asegurar que, sin todas estas pequeñas cosas, nuestro día a día no sería igual. Y no sé en qué párrafo nombrar a Alexandra Elbakyan, pero he creído conveniente éste ya que, sin su labor, desde luego también tendríamos muchas barreras para hacer ciencia.

Gracias también a mis geos, por todas las risas compartidas, andanzas vividas y cerves bebidas juntos. A Lucía, Manu, Álvaro, Francho, Pablo… Hemos aprendido y crecido tanto todos estos años… Lo que une hacer el cabra por el monte, y por todo lo que no sea el monte. A Marcos, Rosi y Ana por ser los mejores compas de despacho, y a muchos otros colegas de (he de admitir que no tantos como me gustaría) cafés en las rocas.

A todas mis chicas, que me han acompañado y animado hasta el infinito y más allá: Celia, Laura, Chiara (*Alla fine questa nonna è riuscita a finire la tesi*!), Julia… Especialmente a mis *consejeras sapias*, que lo son desde hace dieciséis increíbles años: Pilar, Lola, Mariajo, Alicia… Todas habéis creído en mí, me habéis aconsejado bien, sacado muchas sonrisas y achuchado cuando más lo necesitaba. Habéis sido, sois y seréis un pilar fundamental en mi vida.

A Jorge. Ay, Jorge, cuánto tengo que agradecerte… Empezando por todos los días desde que estamos juntos. Cada día que me has escuchado, hecho reír tanto, motivado, ayudado, aconsejado, comprendido y abrazado (también han colaborado un poquico tus croquetas y los vermús en nuestra terraza). Se dice rápido, pero tú y yo sabemos lo difícil que ha sido, y cuánto nos ha unido. Nos reencontramos cuando empezaba la tesis y ahora me ves acabarla, así que parte de ella también es tuya. Gracias por todo, y por haber querido formar el mejor equipo conmigo. *Yo seguiré cuidando de las olas, tú sigue vigilando la marea*.

Y por último, a mi familia. Gracias a mis hermanas, Ana y Maranta, y a mis padres, Jesús y Rosa (venga, también a las peludicas de la familia). Hoy estoy escribiendo esto y terminando la tesis gracias a vosotros, a vuestro esfuerzo, cariño, amor, ayuda y comprensión desde que era ese terremotillo. Vosotros me mostrasteis la naturaleza de verdad, en nuestro valle de Ordesa y en nuestro patio, y fomentasteis mi curiosidad ¡Y mirad cómo de lejos me ha llevado ese camino! Estoy muy orgullosa de mi familia, y gran parte de esta tesis también es vuestra. GRACIAS.

Gracias mamá, por tanto.

Quiero agradecer al Ministerio de Educación, Cultura y Deporte, y al Subprograma de Formación y Movilidad, la beca predoctoral FPU (FPU17/02470) que, junto con la partida económica de los proyectos LMP127_18 y PID2019-108705-GB-I00, me han permitido financiar los gastos de esta investigación.

Por último, y antes de que paséis a la tesis, he de admitir que mi amor por la ciencia y las artes me ha llevado a que, parafraseando a José Luis, "*la propia subjetividad del autor y el deseo más o menos consciente de imprimir un sello personal a la obra han hecho que el desarrollo del trabajo haya discurrido a veces por los mismos caminos de una búsqueda estética, en sentido amplio, además de puramente científica*". Así que ya seas geólogo o no, espero que disfrutes, en la medida de lo posible, del trabajo de mis últimos ocho años.

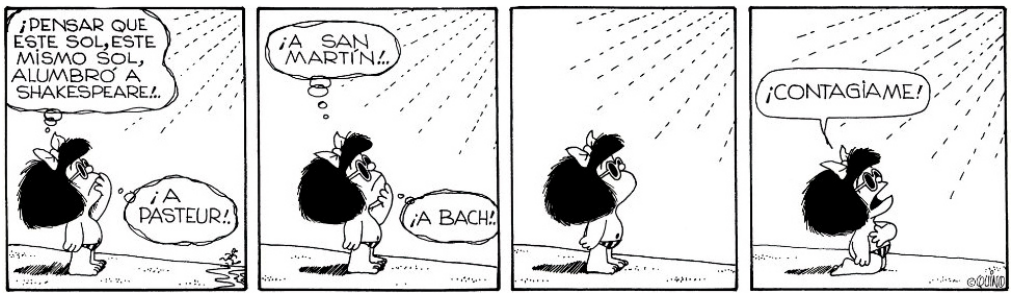
¡PENSAR QUE ESTE SOL, ESTE MISMO SOL, ALUMBRÓ A SHAKESPEARE!..
¡A PASTEUR!
¡A SAN MARTÍN!..
¡A BACH!
¡CONTAGIAME!
©QUINO


INDICE

CAPÍTULO I.
INTRODUCCIÓN

1. Planteamiento e interés del trabajo

Las fallas activas de la Cordillera Ibérica centro-oriental están localizadas en una zona intraplaca, es decir, en un contexto geodinámico normalmente caracterizado por una deformación lenta de la corteza terrestre (de entre 0,1 y 0,01 mm/a), actividad sísmica de intensidad baja a moderada y largos periodos de recurrencia de sus terremotos (del orden de entre 10^3 y 10^5 años; Villamor y Berryman, 1999; Meghraoui y Crone, 2001). A pesar de ello, el tamaño de los terremotos potenciales en este tipo de áreas puede ser grande (Slemmons y dePolo, 1986) y, en consecuencia, su posible peligrosidad sísmica. En estos contextos intraplaca, los catálogos sísmicos no pueden ser la única fuente de información de los estudios de tectónica activa, ya que los periodos de recurrencia tan largos se traducen en una falta de representatividad de terremotos destructivos. Es el caso de la Cordillera Ibérica centro-oriental, donde el catálogo sísmico no recoge una actividad significativa atribuible a sus fallas activas principales, ni en época histórica ni instrumental. En ello radica la importancia de su estudio en esta tesis, que pretende poner el foco en las evidencias de actividad cuaternaria de estas fallas para que se tengan en cuenta en las futuras evaluaciones del riesgo sísmico de la región.

En la actualidad no existe una definición unificada de "falla activa", ni ésta ha evolucionado mucho desde sus primeras formulaciones por Wood (1916) y Willis (1923). Estos autores le atribuyen cuatro condiciones esenciales: (a) la falla debe haber producido desplazamiento bajo el contexto tectónico vigente; (b) debe presentar evidencias de que dicha actividad es reciente; (c) debe existir probabilidad de que vuelvan a producir desplazamiento en el futuro, y (d) pueden tener asociada actividad sísmica. Slemmons y McKinney (1977), en su revisión y recopilación de las definiciones de "falla activa" planteadas, citan y defienden esta primera definición como una de las más usadas hasta esa fecha. Sin embargo, la mayoría de los trabajos difieren en cuál debería ser la edad del movimiento más reciente de una falla para que ésta pueda considerarse activa: 10 ka (Bonilla, 1967; Slemmons y McKinney, 1977), 100 ka (Allen *et al*., 1965), 500 ka (Nichols y Buchanan-Banks, 1974; Lensen, 1976), y 3 Ma (Wesson *et al*., 1975), entre otros. El Western States Seismic Policy Council (WSSPC) considera, desde 1997, que se puede diferenciar entre fallas activas durante el Holoceno (últimos 10 ka), activas durante el Cuaternario superior (últimos 130 ka), y fallas activas durante todo el Cuaternario (que en el año 1997 abarcaba los últimos 1,6 Ma). Cabría preguntarse si esta diferenciación se extendería hasta los 2,58 Ma hasta los que se considera que alcanza actualmente el Cuaternario (Cohen *et al*., 2022).

El estudio de fallas activas consiste en la caracterización detallada de estas estructuras y de su actividad, mediante una aproximación multidisciplinar que integra la geología estructural, morfotectónica y paleosismología, entre otras (McCalpin, 2009). Las dos primeras permiten inferir dos factores influyentes en el potencial sismogénico de las fallas: su geometría y cinemática generales (Wells y Coppersmith, 1994). Sin embargo, esa caracterización general debe ser completada con la visión más detallada que proporciona la paleosismología, que permite identificar y datar sus paleoterremotos individuales. Con todas estas disciplinas se accede, por tanto, al registro geológico de las fallas activas y puede preverse su comportamiento sismológico en el futuro.

Los resultados pueden aportar información científica muy variada. Su mayor utilidad es en la elaboración de mapas de peligrosidad sísmica, cuya fiabilidad depende de la precisión de los datos geológicos recogidos. Consecuentemente, los estudios de tectónica activa tienen repercusión a la hora de establecer normas de protección civil o en materia de edificación (en España, por ejemplo, en la Norma de Construcción Sismorresisente actual, NCSE-02, BOE nº244, del 11 de octubre de 2002, o en las futuras), de cara a mitigar posibles pérdidas económicas y sociales. Por último, también deben tenerse en cuenta a la hora de conocer el potencial de las formaciones geológicas presentes en sus bloques para el almacenaje de hidrocarburos o CO_2 extraído de la atmósfera, entre otros (e. g. Agosta *et al*., 2008; Manzocchi *et al*., 2010).

2. Objetivos

Los objetivos de esta tesis forman parte de una línea del grupo de investigación desarrollada desde hace casi dos décadas. Se realiza el estudio de algunas fallas, se completa el trabajo inacabado de otras y se complementa con el de aquellas ya estudiadas en profundidad. Los objetivos son los siguientes:

1. Completar el conocimiento general de la tectónica reciente extensional en la Cordillera Ibérica centro-oriental, especialmente de las fosas del Jiloca y Calatayud. Se caracterizan los aspectos estructurales, paleosismológicos y morfotectónicos de varias de las fallas activas que forman los márgenes del sistema de fosas: Río Grío-Pancrudo, Calamocha y Sierra Palomera. Para alcanzar este objetivo es necesario:
   - Identificar y describir las unidades litológicas neógenas y cuaternarias que afloran en las cercanías a las estructuras, y aquellas desplazadas por las mismas. Cuando sea posible, se correlacionan con las divisiones estratigráficas regionales propuestas en la literatura.
   - Llevar a cabo el análisis estructural de las fallas a diferentes escalas: de afloramiento, mesoestructural y cartográfico. Con ello se define su geometría (longitud, dirección y buzamiento, ramificaciones…), así como su cinemática (sentido de movimiento, dirección de transporte, salto vertical y desplazamiento neto).
   - Extender el análisis estructural a las zonas de relevo entre las fallas. Se contribuye a conocer los mecanismos de interacción de fallas extensionales en relevo, mediante el estudio de casos regionales, sismicidad instrumental y modelos analógicos. Asimismo, se profundiza en las condiciones genéticas bajo las cuales se desarrollan los patrones de fracturación.
   - Realizar la excavación de trincheras o el estudio de taludes artificiales en las fallas, para proceder a su análisis paleosismológico. También se datan sus depósitos por Luminiscencia Ópticamente Estimulada. De estos datos geológicos se obtiene información sobre modelos evolutivos de la fracturación, y se estiman sus eventos más recientes, periodos de recurrencia o saltos cosísmicos.
   - Contribuir a la caracterización morfotectónica de los alrededores de las fallas y combinarlo con la del sistema de fosas, mayormente mediante la cartografía de superficies de erosión.
   - Contrastar los datos estructurales y morfotectónicos para la realización de cartografías de detalle y, junto con los resultados paleosismológicos, para la evaluación del grado de actividad de las fallas (tasas de desplazamiento a corto y largo plazo).
2. Integrar estos resultados con la información disponible en la literatura sobre otras fallas activas, también localizadas en bordes de fosas de la Cordillera Ibérica centro-oriental: Munébrega, Daroca, Concud, Teruel, Valdecebro, El Pobo, Peralejos-Tortajada-Cabigordo, La Hita y las del Maestrat.
3. Caracterizar los efectos del terremoto de Used de 1953, profundizando en los datos geológicos e históricos asociados al mismo, y contextualizándolo tectónicamente. Divulgar la memoria social del mismo, como último seísmo destructivo ocurrido en el sistema extensional de Calatayud-Jiloca-Teruel.
4. Caracterizar todas las fallas estudiadas desde el punto de vista sismogénico, estimando a partir de modelos de correlación empírica las posibles magnitudes, saltos cosísmicos y periodos de recurrencia de los grandes terremotos asociados a ellas. Se contrastan con las estimaciones realizadas previamente por otros autores para algunas de las fallas.
5. Reflexionar sobre las posibles incertidumbres de las dataciones OSL propuestas en la literatura, realizadas en la región de estudio y en algunas de sus fallas, comparándolas con dataciones nuevas.
6. Proponer un modelo que represente el estado tectónico actual de la región dentro del contexto geodinámico de la Península Ibérica. Incorporará la caracterización de la cinemática de las macroestructuras y la información dinámica de paleoesfuerzos procedente de la literatura.
7. Contribuir con todo ello a completar y mejorar la información recogida en la *Quaternary Active Faults Database of Iberia* (QAFI) referente a las fallas activas de la Cordillera Ibérica centro-oriental, para la realización de futuros análisis de peligrosidad sísmica.

3. Antecedentes

El estado del conocimiento neotectónico de la Cordillera Ibérica centro-oriental es amplio, pero también disperso e incompleto, carencias que esta tesis pretende paliar. En los trabajos de Moissenet *et al.* (1974) o Adrover *et al.* (1976) ya se mencionan algunas de las fallas que limitan el sector norte de la cuenca de Teruel por el este. Sin embargo, no es hasta las recopilaciones de Moissenet (1980), Capote *et al.* (1981) y Peña *et al.* (1981) cuando comienzan a mencionar la existencia de estructuras recientes y actividad tectónica local que controlan los sedimentos cuaternarios del sistema de fosas de Teruel. Moissenet (1982, 1983, 1985) y Gutiérrez *et al.* (1983a) también continúan sus investigaciones en esta línea. Simón (1982, 1983) y Gutiérrez *et al.* (1983b) amplían esa caracterización extensional reciente a la fosa del Jiloca y, el primer autor, también al sistema de fosas del Maestrat. Colomer (1987) alude a ella en la cuenca de Calatayud y el semigraben de Daroca. Posteriormente, las hojas del Mapa Geológico Nacional 1:50.000 (MAGNA) incluyen muchas de las rupturas en sus cartografías de las fosas de Calatayud, Jiloca y Teruel, y describen en sus memorias "señales de una relativamente intensa actividad tectónica intracuaternaria" (del Olmo *et al.*, 1983a; Godoy *et al.*, 1983a, b; Hernández *et al.*, 1983a, b; Olivé *et al.*, 1983a, b; Ramírez *et al.*, 1983). Con la realización del Mapa Neotectónico y Sismotectónico Nacional (Gracia *et al.*, 1989; Gutiérrez *et al.*, 1989; Simón *et al.*, 1989) comienza la recopilación, ampliación y consolidación de la información recogida hasta entonces. Sin embargo, no es hasta la década siguiente cuando se comienza a analizar más en detalle el carácter neotectónico de fallas concretas. Gracia (1990; 1992) y Gutiérrez (1998) aluden a ella en la cuenca de Calatayud, y Simón y Soriano (1993), Simón *et al.*, (2005) y Gutiérrez *et al.*, (2008) profundizan en la del Jiloca y en el conjunto de fosas de Calatayud-Teruel. A partir de este momento y hasta día de hoy, se han estado estudiando exhaustivamente muchas de ellas, mayormente desde el punto de vista estructural y adoptando el enfoque paleosismológico, del que carecían los estudios previos. Algunos de estos trabajos son más generales y abarcan desde el área de Calatayud hasta las fosas de Teruel (Gutiérrez *et al.*, 2012; Simón *et al.*, 2012), y otros más específicos comienzan a profundizar en las fallas de la cuenca de Calatayud y fosas contiguas (Gutiérrez *et al.*, 2009, 2020a). Los estudios de Perea (2006), Perea *et al.* (2012) y Simón *et al.* (2013) atañen a las fallas de la zona del Maestrat. Las fallas que limitan las fosas del Jiloca y Teruel también se caracterizan en numerosos trabajos (Lafuente, 2011; Lafuente *et al.*, 2011a, 2014; Martín-Bello *et al.*, 2014; Simón *et al.*, 2013, 2014, 2016, 2017, 2019, Ezquerro *et al.*, 2020). Parte de esta información se ha ido incorporando parcialmente a la *Quaternary Active Faults Database of Iberia* (QAFI) hasta su última versión v. 4 (IGME, 2022).

Cabe reservar un párrafo concreto para los antecedentes de la zona de falla de Río Grío-Pancrudo, una estructura clave en esta tesis pero que ya había sido, en parte, objeto de estudio previo. Algunas características de su actividad extensional reciente las sugiere Moissenet (1980) y las exponen más detalladamente Gutiérrez *et al.* (2013). Sin embargo, los trabajos anteriormente mencionados se centran mayoritariamente en su segmento norte, el de Río Grío-Lanzuela, más en concreto en el sector entre los pueblos de Tobed y Codos, mientras que su segmento sur, el de Cucalón-Pancrudo, no se ha descrito con anterioridad a esta tesis y tan sólo aparece tentativamente cartografiado en varios mapas geológicos (Gracia *et al.*, 1989; Gabaldón *et al.*, 1991; Cortés-Gracia y Casas-Sainz, 1996; IGME y ENRESA, 1998; Cortés-Gracia, 1999).

Paralelamente al estudio de los procesos tectónicos, se ha tenido en cuenta la evolución del relieve, principalmente de superficies de erosión-colmatación. El modelo regional básico de niveles de superficies de erosión fue formulado inicialmente por Simón (1982) y Peña *et al.* (1984), y con ciertas diferencias por Pailhé (1984). Posteriormente, se pudieron identificar subniveles dentro de este modelo (Gutiérrez-Elorza y Gracia, 1997; Ezquerro, 2017; Simón-Porcar *et al.*, 2019; Ezquerro *et al.*, 2020), y son éstos los adoptados en esta tesis. Se han empleado de la misma manera que se ha hecho clásicamente en la literatura, como marcadores de la deformación extensional reciente, para identificar las estructuras y para calcular sus saltos (Simón, 1983; Gracia *et al.* 1988; Lozano, 1988; Gracia, 1990; Ezquerro *et al.* 2020). Este modelo de superficies de erosión defiende el origen extensional de las fosas estudiadas, en la línea de trabajos previos (Simón y Soriano, 1993; Rubio y Simón, 2007; Rubio *et al.*, 2007), pero existen otras interpretaciones, basadas en este u otros modelos, que les confieren un

origen compresivo (Cortés-Gracia y Casas-Sáinz, 2000; Casas-Sáinz y Cortés-Gracia, 2002) o kárstico (Gracia *et al*., 2003; Gutiérrez *et al*., 2008, 2009).

Existe un amplio repertorio de dataciones absolutas en las que nos fundamentamos en esta tesis para terminar de caracterizar correctamente la historia paleosismológica de las fallas estudiadas. Ezquerro (2017) y Ezquerro *et al*. (2020) datan con precisión las superficies de erosión por magnetoestratigrafía, al correlacionarse con megasecuencias que están bien acotadas en el sector norte de la cuenca de Teruel. Los depósitos plio-cuaternarios de las fosas de Teruel también están datados con magnetoestratigrafía, así como por yacimientos de macromamíferos, en el caso de los *glacis villafranquienses* (Adrover, 1975; Sinusía *et al*., 2004). Los diferentes niveles de terrazas fluviales mediante varios métodos: por un yacimiento de mamíferos (Moissenet, 1985), con U/Th (Arlegui *et al*., 2004; Gutiérrez *et al*., 2008, 2020b), por Espín Electrónico (*Electro Spin Resonance*, ESR; Santonja *et al*., 2014) y mayoritariamente con Luminiscencia Ópticamente Estimulada (*Optically Stimulated Luminiscence*, OSL; Gutiérrez *et al*. 2008, 2020b; Lafuente, 2011; Lafuente *et al*., 2008, 2011a, 2014; Santonja *et al*., 2014; Peña-Monné *et al*., 2022). En los trabajos previos de paleosismología de algunas de las fallas de la Cordillera Ibérica centro-oriental también se han datado clásicamente las unidades cuaternarias desplazadas por ellas con OSL (Gutiérrez *et al*., 2009, 2020b; Lafuente, 2011; Lafuente *et al*., 2011a, 2014; Simón *et al*., 2013, 2016, 2017, 2019), así como con ESR y con espectrometría de masas con acelerador para la datación del radiocarbono (*Accelerator Mass Spectrometry*, AMS; Gutiérrez *et al*., 2020a, b). Cabe destacar que muchas de estas dataciones regionales obtenidas con el método de OSL han sido puestas en cuestión por Gutiérrez *et al*. (2020b) y Moreno *et al*. (2021).

El desarrollo de las estructuras extensionales objeto de esta tesis responde al campo de esfuerzos activo en la región a lo largo del Mioceno superior-Cuaternario. Simón (1982, 1983, 1989) lo reconstruye para casi toda la región de la Cordillera Ibérica centro-oriental, para después ser precisado por Cortés y Simón (1997), Cortés-Gracia (1999), Cortés *et al*. (2000) y, especialmente, por Liesa (2000, 2011), Arlegui *et al*. (2004, 2005), Ezquerro y Simón (2017), Liesa *et al*. (2019). Herraiz *et al*. (2000) también lo corroboran a partir de tensores de esfuerzos obtenidos de mecanismos focales.

4. Situación geológica: la Cordillera Ibérica centro-oriental

4.1. Marco geográfico y geológico general

La Cordillera Ibérica es una cadena montañosa intraplaca de dirección NW-SE situada al NE de la Península Ibérica. Se extiende a lo largo de más de 400 km desde la Sierra de la Demanda, en Burgos y La Rioja, hasta el mar Mediterráneo, en Castellón (Fig. 1.1a,b). Está limitada por la cuenca del Ebro, en su margen noreste, y la Meseta, al suroeste, y constituye una cadena intraplaca tanto para los Pirineos como para la Cordillera Bética. La región geográfico-geológica a la que pertenece el sector centro-oriental de la Cordillera Ibérica es la Rama Aragonesa. En él aparecen varias depresiones rellenas por sedimentos neógeno-cuaternarios: la cuenca de Calatayud, el semigraben de Munébrega y la cuenca de Gallocanta, el semigraben de Daroca, la fosa del Jiloca y la cuenca de Teruel (Fig. 1.2), la cuenca de Sarrión-Mijares y el sistema de fosas del Maestrat (Fig. 1.1b).

Las depresiones tectónicas estudiadas en este trabajo están enmarcadas por diferentes macizos montañosos, y tienden a ser asimétricas: con márgenes occidentales suaves (u ocasionalmente fracturados) y márgenes orientales que corresponden con las fallas recientes y macroestructuras ya mencionadas. En el margen oriental de la cuenca de Calatayud juegan un papel fundamental las sierras de Vicort, Algairén, Peco, Cucalón y Pelarda (máxima altura: 1512 m). En el margen occidental de esta misma cuenca, así como en el semigraben de Munébrega, la cuenca de Gallocanta y el semigraben de Daroca, intervienen las sierras de Pardos y Santa Cruz (máxima altura: 1423 m). Por otro lado, la fosa del Jiloca se enmarca entre los macizos de Sierra Menera-Montes Universales-Albarracín (máxima altura: 1936 m), al W, y la Sierra Palomera (máxima altura: 1533 m) y los altos de Celadas (Cerro Gordo), al E. Estas sierras también limitan por el oeste la cuenca de Teruel, mientras que por el este se levantan las sierras del Pobo, Camarena y Javalambre (máxima altura: 2020 m). Por medio de la sierra de Gúdar (máxima altura: 2028 m), se enlaza con la cuenca de Sarrión-Mijares y el sistema de fosas del Maestrat, hacia el sureste.

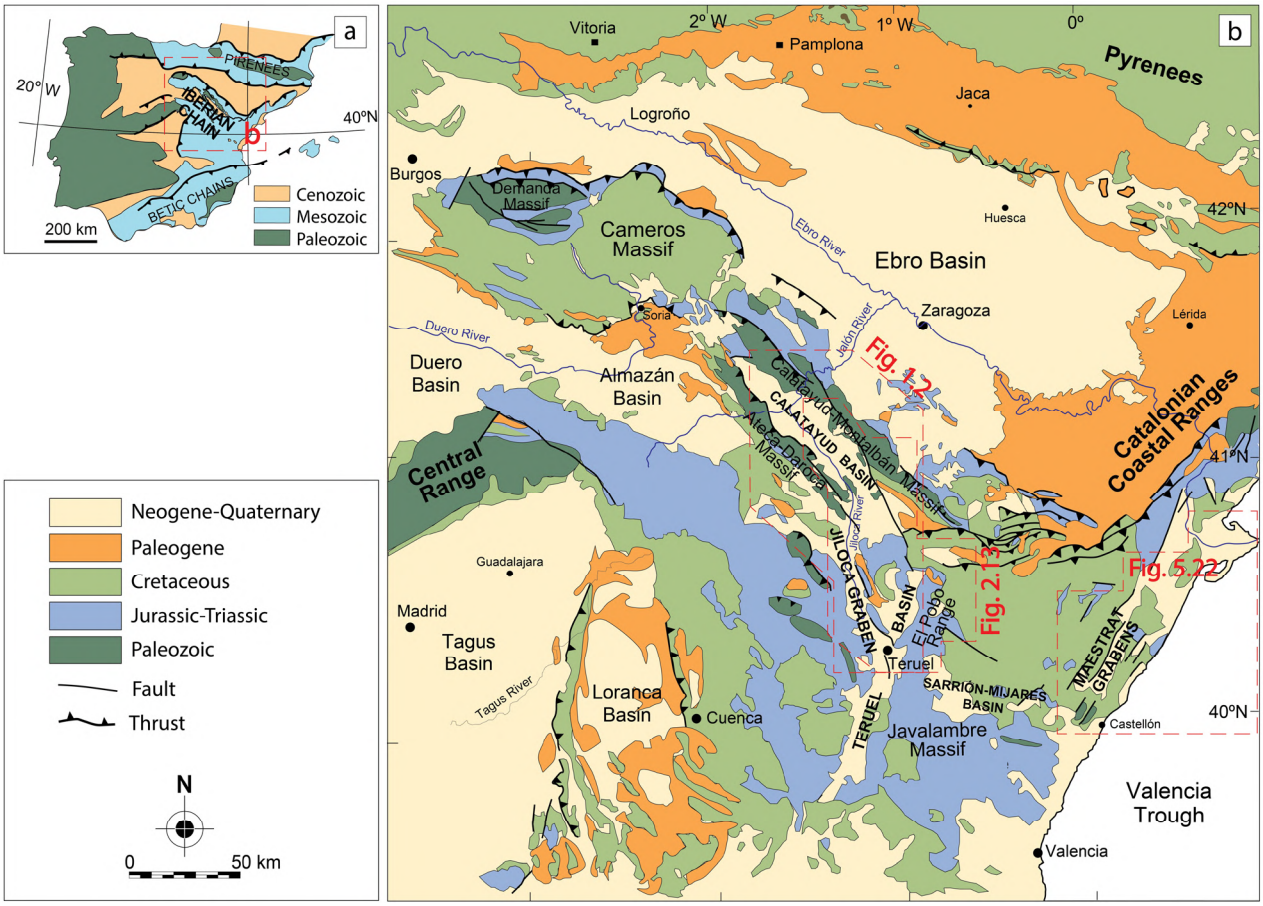

Fig. 1.1.- (a) Localización de la Cordillera Ibérica en la Península Ibérica. (b) Mapa geológico simplificado de la Cordillera Ibérica, en el que se señalan las principales cuencas extensionales neógeno-cuaternarias y la localización de las Figuras 1.2, 2.13 y 5.22.

Respecto a los cursos fluviales principales, en la actualidad el área de Calatayud-Daroca recibe aportes del río Jiloca, afluente del río Jalón (a su vez tributario del río Ebro) junto con los ríos Piedra y Perejiles, que drenan longitudinalmente las cuencas. Resulta interesante la incursión en la cuenca de Calatayud del Río Huerva, desde su nacimiento en la sierra de Cucalón y cortando la sierra de Algairén hasta llegar al río Ebro. El río Jiloca también es el principal curso fluvial longitudinal a la fosa del Jiloca, teniendo localizada su cabecera en el sector sur de esta depresión. No presenta continuidad, por tanto, hacia el sistema fluvial que drena directamente hacia el Mar Mediterráneo. El río colector longitudinal del sector norte de la cuenca de Teruel es el río Alfambra, que tras unirse al río Guadalaviar procedente de la sierra de Albarracín, forman el río Turia que drena el sector sur de la cuenca. Finalmente, es el río Mijares el que discurre desde la Sierra de Gúdar, pasando por la cuenca de Sarrión-Mijares, hasta su desembocadura en las cercanías de Castellón.

4.2. Marco estructural: hacia la extensión neógeno-cuaternaria

Se trata de una cadena que se originó durante la Orogenia Alpina debido a la inversión tectónica positiva de la cuenca mesozoica preexistente, la denominada Cuenca Ibérica (Álvaro *et al.*, 1979). Durante el Mesozoico, el NE de la Península Ibérica estaba sometido a una importante extensión ligada a la apertura del Atlántico norte y la expansión del Tetis hacia el oeste (Salas y Casas, 1993). Las subcuencas que se formaron estaban controladas por grandes fallas que conformarían la futura **herencia estructural** de la Cordillera Ibérica: fallas NW-SE, y en menor medida NE-SW, alguna de ellas ya formadas en etapas de deformación variscas y tardivariscas (Arthaud y Matte, 1975; Álvaro *et al.*, 1979; Vegas *et al.*, 1979; Capote *et al.*, 2002). A finales del Cretácico, la compresión generada por la convergencia oblicua entre las placas Africana, Ibérica y Euroasiática indujo al levantamiento de las dos principales cordilleras ligadas a los márgenes de placa (Pirineos y Béticas). A partir del Eoceno, esta deformación empezó a transmitirse hacia el interior de la placa Ibérica; comenzaba a formarse la Cordillera Ibérica, por reactivación e inversión de las fallas mesozoicas y paleozoicas previas (Capote *et al.*, 2002), y por el plegamiento

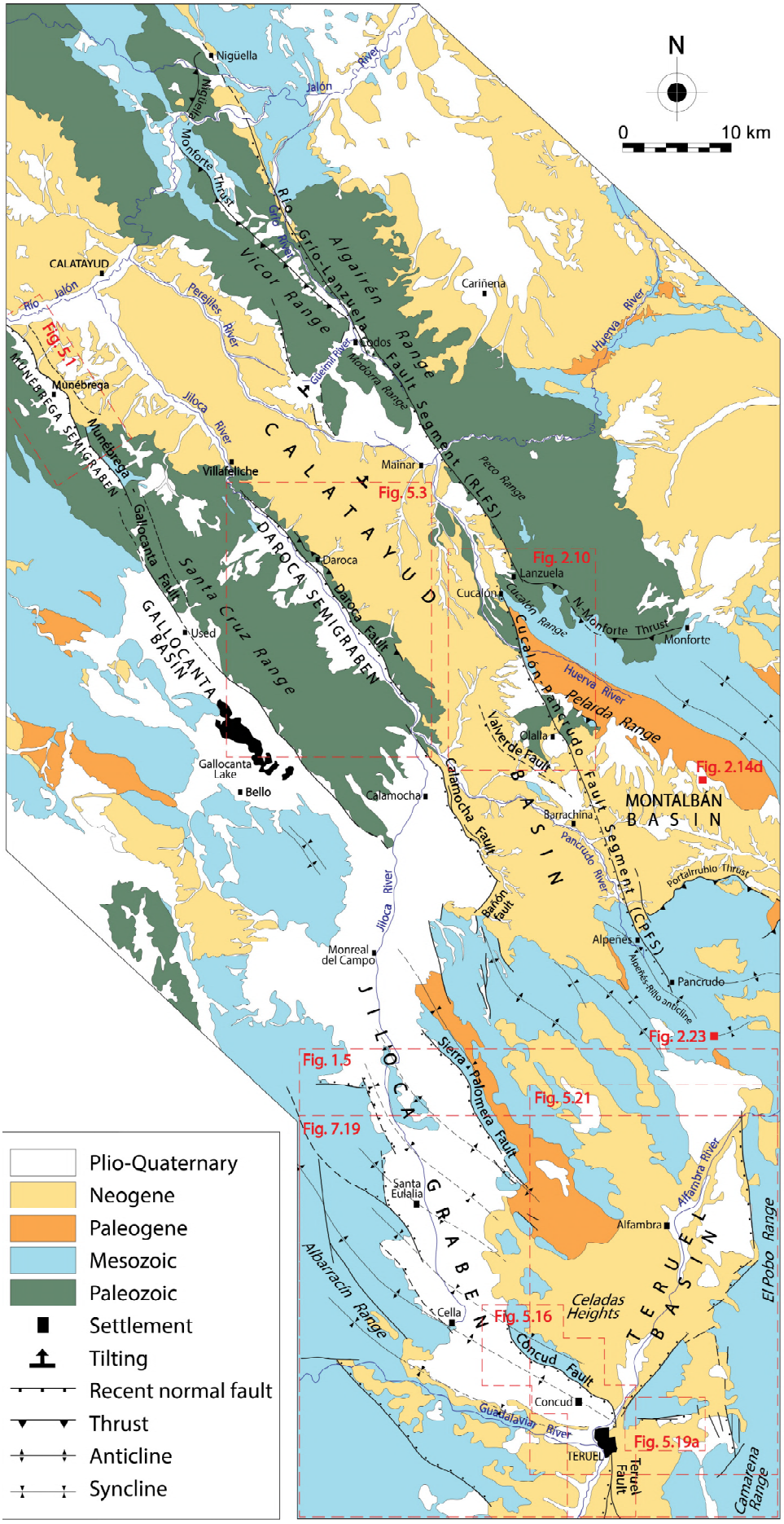

Fig. 1.2.- Mapa geológico simplificado de la cuenca de Calatayud, de la fosa del Jiloca y el sector norte de la cuenca de Teruel, en el que se indican las localizaciones de las Figuras 1.5, 2.10, 2.14d, 2.23, 5.1, 5.3, 5.16, 5.19a, 5.21 y 7.19.

en su zona central de potentes series paleozoicas ya deformadas (con hasta 11 km de espesor total; Cortés-Gracia y Casas-Sáinz, 1996). Este campo compresivo alpino incluye varios campos de esfuerzos independientes en la Cordillera Ibérica (Liesa, 2000; Liesa y Simón, 2009): *Bético temprano* (WNW-ESE, Eoceno), *Pirenaico-Ibérico* (NE-SW a ENE-WSW, Eoceno-Oligoceno Superior), *Bético intermedio* (NW-SE, Oligoceno Superior-Mioceno inferior), *Bético tardío* o *Guadarrama* (NNW-SSE, desde el Oligoceno Superior-Mioceno inferior), y *Pirenaico tardío* (NNE-SSW, desde el Oligoceno superior). Estas direcciones se sucederán o alternarán de forma irregular en toda la región a lo largo del tiempo, especialmente las dos últimas, hasta aproximadamente el Vallesiense (ca. 10-11 Ma), que es cuando se produce la transición del régimen de esfuerzos compresivo al extensional (Ezquerro y Simón, 2017). Durante los periodos compresivos, posiblemente en el tránsito Oligoceno-Mioceno, comenzaron a formarse varias grandes cuencas sedimentarias que están directamente relacionadas con la estructuración compresiva, entre las que están la cuenca del Ebro y la de Calatayud-Montalbán.

La **cuenca de Calatayud** (Fig. 1.2), de unos 65 km de longitud y dirección NW-SE, presenta dos márgenes de origen contractivo. En su margen SW interviene el cabalgamiento de Daroca, y en su margen NE el cabalgamiento de Nigüella-Monforte (inicialmente conocido como cabalgamiento de Datos; Calvín-Ballester y Casas, 2014; Casas *et al*., 2016), la zona de falla transpresiva de Río Grío-Pancrudo (Marcén y Román-Berdiel, 2015; Marcén, 2020; formada por dos segmentos: Río Grío-Lanzuela y Cucalón-Pancrudo) y el sistema de cabalgamientos de Pelarda. El cabalgamiento de Daroca se reconoce en sectores puntuales de su traza en los que no está *onlapado* por unidades posteriores a la compresión. Varios de sus segmentos están dispuestos *en échelon*, lo cual sugiere que esta estructura presentó una componente de desgarre dextral durante su última época compresiva (Julivert, 1954; Colomer y Santanach, 1988; Casas-Sáinz *et al*., 2018). Estuvo activo al menos hasta el Aragoniense (Mioceno medio; Julivert, 1954; Colomer, 1987; Guimerà, 2013; Simón *et al*., 2021). El cabalgamiento varisco de Nigüella-Monforte se reconoce únicamente en sus dos extremos. En su sector meridional, su traza no aparece en superficie o coincide con la zona de falla de Río Grío-Lanzuela, originada en época tardivarisca a partir de la reactivación de parte del trazado del cabalgamiento, posiblemente como estructura transpresiva-dextral (Marcén y Román-Berdiel, 2015; Casas *et al*., 2016; Marcén, 2020). El segmento de Cucalón-Pancrudo (Gracia *et al*., 1989; Gabaldón *et al*., 1991; Cortés-Gracia y Casas-Sáinz, 1996; IGME y ENRESA, 1998; Cortés-Gracia, 1999) pudo actuar de manera similar, aprovechando los cabalgamientos de Pelarda hasta su intersección con el cabalgamiento de Portalrubio (Guimerà *et al*., 1990; Simón y Liesa, 2011).

El tránsito al régimen de esfuerzos extensional en el sector centro-oriental de la Cordillera Ibérica fue un proceso progresivo, producido por un debilitamiento de la compresión intraplaca combinado con una intensificación de la extensión ligada al ***rifting* del Surco de Valencia** (Álvaro *et al*., 1979; Vegas *et al*. 1979; Simón 1982, 1986; Roca y Guimerà 1992; Maillard y Mauffret, 1999; Fig. 1.1b), desde el Mioceno inferior-medio hasta la actualidad. Existen diferentes interpretaciones de su origen, desde que se trate de la propagación hacia el sur del Rift Europeo (e.g., Ziegler, 1992) hasta que corresponda a la extensión retroarco asociada a la subducción en el mar de Alborán y el sector sur de las islas Baleares (e.g., Banda y Channel, 1979; Doglioni *et al*., 1997), y por lo tanto coetáneo a la compresión de la Cadena Bética (Banda y Santanach, 1992). La apertura del Surco de Valencia ocasionó la inversión negativa de gran parte de las estructuras heredadas, así como la neoformación de otras fallas normales (con geometría lístrica y un nivel de despegue común regional situado entre 11 y 15 km de profundidad según Roca y Guimerà, 1992, y entre 14 y 17 km según Ezquerro *et al*., 2020).

El proceso extensional tuvo tres etapas diferenciadas, comenzando por una **primera etapa** cuya dirección de extensión principal era de W-E a WNW-ESE (Mioceno inferior-medio), que es la responsable de la formación del sistema de fosas con dirección NNE-SSW en el Maestrat y el sector sur de la Fosa de Teruel, así como de las depresiones centrales de Sarrión-Mijares (Simón, 1982; Anadón y Moissenet, 1996). En una **segunda etapa** (Mioceno superior-Plioceno inferior), el campo extensional WNW-ESE de carácter triaxial (Simón, 1986, 1989) dio lugar al desarrollo del sector norte de la fosa de Teruel (Simón, 1983; Ezquerro *et al*., 2020).

El **sistema de fosas del Maestrat** (Fig. 1.1b) es la estructura localizada más al este de la Cordillera Ibérica, más interior por tanto respecto al Surco de Valencia (Simón 1982, Roca y Guimerà 1992). Al igual que la cuenca de

Teruel, la orientación NNE-SSW de estas estructuras corta la directriz ibérica, abarcando desde la ciudad de Castellón hasta aproximadamente el delta del río Ebro y enlazando prácticamente con las estructuras homólogas de las Catalánides (fallas del Baix Ebre, Camp, Vallès-Penedès, etc). Consiste en un gran sistema paralelo de *horst* y *graben* que se prolonga hasta 30-35 km hacia el interior de la costa mediterránea. Comenzó a formarse en la primera etapa de extensión, probablemente dando lugar a pequeñas subcuencas endorreicas que llegaron a rellenarse con entre 100 y 250 m de facies aluviales (Anadón y Moissenet, 1996). El movimiento posterior de estas fallas normales en una tercera etapa extensional durante el Plio-Cuaternario permitió el depósito de más sedimentos aluviales en los grábenes y la interacción entre las fallas y la red fluvial (Simón, 1982; Simón *et al*., 2013). Son abundantes las evidencias morfotectónicas de actividad de este sistema durante el Pleistoceno (Perea, 2006; Perea *et al*., 2012).

La **cuenca de Teruel** (Figs. 1.1b, 1.2) se extiende desde Fuentes Calientes (Teruel) hasta Mira (Cuenca), de manera que tiene una longitud de más de 100 km. El sector norte de la cuenca (desde la ciudad de Teruel hasta Fuentes Calientes) es un semigraben cuyo margen activo oriental está limitado por las fallas de El Pobo, Peralejos y Tortajada-Cabigordo. Se trata de una sucesión de segmentos alternantes NNE-SSW y NNW-SSE que basculan el relleno de la cuenca hacia su margen oriental (Moissenet, 1980, 1983; Simón *et al*., 2012; Ezquerro, 2017). Su sector central (Teruel-Villaespesa) pasa a ser un graben asimétrico con la falla N-S de Teruel como la estructura más influyente de todo el sector, y las fallas de la Hita, en su margen oriental. Su sector sur no es objeto de estudio en esta tesis. Probablemente, todas estas fallas también representan la reactivación y propagación, con componente normal, de estructuras preexistentes alpinas, a su vez heredadas de la etapa extensional mesozoica o de la deformación varisca o tardivarisca (Ezquerro, 2017). Es en su sector central la falla de Teruel, la macroestructura de Los Mansuetos-Valdecebro y la falla de Concud (que articula la cuenca de Teruel con la posterior fosa del Jiloca), cortan el relleno neógeno de la cuenca.

Entre el Maestrat y la cuenca de Teruel se sitúa la **cuenca de Sarrión-Mijares** (Fig. 1.1b), limitada al norte por la sierra de Gúdar y al sur por Javalambre. Se dispone en dirección WNW-ESE, y presenta unos bordes de cuenca muchos menos marcados que el resto, aunque no se descarta la existencia de fallas en ellos. La edad de su delgado relleno sedimentario indica que estas depresiones ya debían existir en el Mioceno superior, durante el segundo impulso distensivo, pero su estructura actual se debe básicamente a la tercera etapa de extensión (Simón, 1982).

En la **tercera etapa** extensiva (Plioceno superior-Cuaternario) el régimen de esfuerzos evolucionó a una **extensión radial o multidireccional** (σ_1 vertical, $\sigma_2 \approx \sigma_3$; Simón, 1986, 1989), con trayectorias primarias de σ_3 cercanas a ENE-WSW (Arlegui *et al*., 2005, 2006). Bajo él se reactivaron como fallas normales casi todos los bordes de fosa. En el margen SW de la cuenca de Calatayud se formaron el semigraben de Munébrega (Gutiérrez, 1998) y el semigraben de Daroca (Gracia, 1990, 1992; Gutiérrez *et al*., 2020a). Dadas las similitudes en cuanto a dirección y características de las estructuras, se considera que en esta tercera etapa también se conformó la zona de falla normal de Río Grío-Pancrudo en el margen NE de la cuenca. La reactivación extensional en el segmento de falla de Río Grío-Lanzuela se evidencia en su relación con los materiales aluviales cuaternarios que rellenan el valle del río Grío, así como en el condicionamiento que impone en la orientación de la red fluvial (Gutiérrez *et al*., 1996, 2013; Casas *et al*., 2016; Marcén, 2020). Asimismo, la deformación en este margen provocó un basculamiento suave de su relleno neógeno hacia la falla de Río Grío-Lanzuela (Moissenet, 1980; Gutiérrez *et al*., 2013). En el caso de la falla de Cucalón-Pancrudo, la reactivación se evidencia en los abanicos aluviales cuaternarios modelados en glacis que parten de su traza (Cortés-Gracia, 1999). El sector central de esta falla es el menos manifiesto y desplaza tanto materiales mesozoicos como neógenos; sin embargo, no presenta una clara relación con las fallas heredadas y podría ser de neoformación. Finalmente, en esta etapa también se formó la fosa del Jiloca y, como ya se ha mencionado, se rellenaron las fosas del Maestrat y tomó forma la cuenca de Sarrión-Mijares (Simón, 1982, 1989). La dirección de extensión máxima de la tercera etapa de extensión es similar a la ENE-WSW inferida a partir de los tensores de esfuerzos de mecanismos focales de sismos (Herraiz *et al*., 2000), asociados a fallas normales y alineaciones epicentrales NW-SE, que además indican que este campo extensional continua activo en la actualidad.

El **semigraben de Munébrega** (Fig. 1.2) limita parte del margen SW de la cuenca de Calatayud, y se dispone paralelo a la misma, con dirección NW-SE, a lo largo de casi 20 km. Su formación comenzó tras la culminación del relleno de la cuenca, después del Plioceno inferior (Gutiérrez, 1998). Su margen activo, el NE, está compuesto por la falla Munébrega E y, la falla principal, la Munébrega W (Gutiérrez, 1998; Gutiérrez *et al*., 2009, 2012). Esta última muestra continuidad hacia las lineaciones que conforman el margen NE de la **cuenca de Gallocanta** (Fig. 1.2). En un principio, tanto estas alineaciones como la cuenca en general, se consideraban de origen puramente neotectónico (Villena, 1969; del Olmo *et al*., 1983b; Hernández *et al*., 1983b). Estudios más recientes interpretan el conjunto como un semigraben tectónico, no activo, pero en el que predomina un sistema endorreico kárstico de tipo *polje* (Gracia *et al*., 2002; Gutiérrez *et al*., 2008; Gracia, 2014), del cual resulta la laguna de Gallocanta.

Al NE de estas depresiones, se encuentra el **semigraben de Daroca** (Fig. 1.2), que también limita la cuenca de Calatayud por el SW, con la misma dirección NW-SE y una longitud de más de 25 km. Al igual que la de Munébrega, también es más reciente que la cuenca de Calatayud y se empezó a formar en el Plioceno inferior (Adrover *et al*., 1982; Gracia, 1990, 1992; Gutiérrez *et al*., 2020a). Se trata de una depresión asimétrica controlada por la falla de Daroca en su margen NE. Ésta es el resultado de la inversión negativa del ya mencionado cabalgamiento de Daroca (Colomer, 1987; Gracia, 1990, 1992; Gutiérrez *et al*., 2008, 2020a) y, junto con la falla de Calamocha, conforman una macroestructura que es paralela a la estructura heredada y hunde el semigraben de Daroca y el sector norte de la fosa del Jiloca respecto a la cuenca de Calatayud.

La **fosa del Jiloca** (Figs. 1.1b, 1.2) constituye una depresión alargada de unos 70 km de longitud que corta la directriz ibérica con dirección NNW-SSE. Su estructura es claramente asimétrica: su límite occidental presenta un suave basculamiento hacia el este y se articula con algunos escalones de falla, mientras que su margen oriental es el resultado directo de la disposición escalonada diestra de las fallas normales de dirección ibérica de Calamocha, Sierra Palomera y Concud (Simón, 1983, 1989; Lafuente, 2011; Lafuente *et al*., 2011a). La fosa del Jiloca y la cuenca de Teruel se articularon por medio de las fallas de Concud y Teruel a partir del Plioceno superior, aunque en el Plioceno inferior ya existía un sistema lacustre central en la fosa del Jiloca que estaba conectado al de la cuenca de Teruel (Rubio y Simón, 2007; Lafuente, 2011; Lafuente *et al*., 2011b).

4.3. Marco morfotectónico

La evolución geomorfológica de la Cordillera Ibérica centro-oriental incluye varios episodios de aplanamiento del relieve durante el Neógeno. Aunque existe una superficie más antigua denominada tradicionalmente como Superficie de Erosión Intramiocena o SEI (Gutiérrez y Peña-Monné, 1976; S1 de Gutiérrez-Elorza y Gracia, 1997; datada recientemente en 11,2 Ma por Ezquerro, 2017), la superficie principal se conoce como **Superficie de Erosión Fundamental** o SEF (en los trabajos en inglés la denominamos *Fundamental Erosion Surface*, *FES*; Peña *et al*., 1984; Fig. 1.3). Ésta última consiste en una vasta planicie reconocible regionalmente a cotas altas y medias (Peña *et al*., 1984; S2+S3 de Gutiérrez-Elorza y Gracia, 1997), y es correlacionable con la parte más alta de los depósitos carbonatados ruscinienses (calizas del Páramo 2, que se explican en el siguiente apartado). Se formó bajo procesos de erosión, probablemente por disolución criptokárstica de las calizas (Gutiérrez-Elorza y Gracia, 1997), asociados a periodos de levantamiento (Casas-Sáinz y Cortés-Gracia, 2002; Gracia, 2020). Cada episodio tectónico interrumpía el desarrollo de la superficie de erosión, lo que derivaba en la formación de subniveles dentro de la misma. Se han diferenciado tres subniveles en el sistema de fosas de Teruel: SEF subnivel superior o SEF1 *(FES Upper Sublevel, FES1)*, SEF s.s. o SEF 2 *(FES s.s., FES2)* y SEF subnivel inferior o SEF3 *(FES Lower Sublevel, FES3;* Ezquerro, 2017; Simón-Porcar *et al*., 2019; Ezquerro *et al*., 2020). Las superficies SEF1 y SEF2 se correlacionan con el techo de la megasecuencia M7 definida por Ezquerro (2017), equivalente a la parte inferior de la unidad Páramo 2 (Rusciniense superior; zona MN15; mitad del cron C2Ar; 3,8 Ma; Ezquerro *et al*., 2020), mientras que la superficie SEF3 se correlaciona con el techo de M8 y es equivalente a la parte superior del Páramo 2 (Villafranquiense inferior, biozona MN16; hacia la base del cron C2An.3n; 3,5 Ma; Ezquerro *et al*., 2020). En ocasiones, estos aplanamientos se ven interrumpidos o están encajados en relieves que no fueron arrasados por

Fig. 1.3.- Ejemplo de disposición de la Superficie de Erosión Fundamental desarrollada sobre materiales jurásicos y paleógenos desde la Sierra Palomera enlazando, hacia el este, con el techo de las calizas ruscinienses del Páramo 2 de la Fosa de Teruel, en el entorno del pueblo de Celadas (tomada de Ezquerro, 2017).

la superficie de erosión en el momento de su formación. Éstos constituyen relieves residuales con frecuencia asociados a márgenes montañosos que ya lo eran en época neógena.

La tercera etapa extensiva (Plioceno superior-Cuaternario) produjo modificaciones locales en el nivel freático regional y, por lo tanto, en los procesos erosivos que desarrollaban la SEF, ocasionando su interrupción definitiva (Gracia, 2020). Como consecuencia, algunas depresiones de origen tectónico de la Cordillera Ibérica centro-oriental empezaron a experimentar **procesos de karstificación** interna. En el caso de la cuenca de Gallocanta, ésta pasó a evolucionar como un sistema endorreico de tipo *polje*, con un control estructural, pero mayormente influenciado por los cambios climáticos cuaternarios y las oscilaciones del nivel freático (Gracia *et al.*, 2002; Gracia, 2020). En la fosa del Jiloca también hay indicios de karstificación local, lo cual ha llevado a algunos autores a interpretar toda la fosa como otro *polje* (Gracia *et al.*, 2003). Sin embargo, existen pocas evidencias de dicha interpretación para una superficie tan extensa como la de la fosa del Jiloca, con su hundimiento asociado, mientras que sí las hay de su configuración tectónica (Rubio y Simón, 2007; Rubio *et al.*, 2007).

Durante este periodo, la Cordillera Ibérica también comenzó a estar sometida a un **levantamiento de tipo *doming*** (Simón, 1982, 1989), al menos desde hace 3 Ma (Scotti *et al.*, 2014, Giachetta *et al.*, 2015). Este mecanismo geodinámico fue postulado a partir de datos morfotectónicos, por el abombamiento de las superficies de erosión (Simón, 1982, 1989), y geofísicos, ya que se ha descrito una anomalía negativa de la densidad del manto superior y anomalías por baja velocidad de las ondas sísmicas en esta región, que podría haber producido un levantamiento de la topografía de amplitud hectométrica (Wortel y Spakman, 2000; Piromallo y Morelli, 2003; Boschi *et al.*, 2010; Faccenna *et al.*, 2010; Scotti *et al.*, 2014). También apuntan en esta dirección los modelos de Giachetta *et al.* (2015) de la evolución del paisaje y la red de drenaje. Este levantamiento es asimétrico a lo largo de gran parte de la Cordillera Ibérica, ya que tiene un máximo en su sector noreste (en el Maestrazgo, colaborando en el levantamiento de las sierras de Gúdar y Javalambre; Simón, 1982), y va disminuyendo hacia el sector suroeste (cuenca del alto Tajo), tal y como refleja la deformación registrada en las calizas del Páramo y en la SEF. Su efecto combinado con el movimiento de las fallas es responsable del hundimiento relativo de las depresiones en la región. Se trata de una deformación a gran escala
con tasas de levantamiento bajas. Como respuesta a esta deformación, la red fluvial todavía se está adaptando: con tasas de incisión también bajas pero que aumentan con el tiempo, patrones radiales y procesos de captura producidos progresivamente más hacia el interior de la cadena (Scotti *et al.*, 2014, Giachetta *et al.*, 2015; Peña-Monné *et al.*, 2022). Cabe destacar que los sistemas de drenaje pueden responder al levantamiento regional y la tectónica local, y pueden actuar conjuntamente o no con factores externos como son los cambios del nivel de base o el clima (e.g. Antoine *et al.*, 2000; Westaway *et al.*, 2002; Peña-Monné *et al.*, 2022).

Finalmente, la SEF está ocasionalmente cubierta por un sistema aluvial villafranquiense (transición Plioceno-Pleistoceno) modelado en glacis. En el conjunto de la región se conocen como ***glacis villafranquienses*** (Moissenet, 1982, 1985; Simón, 1983; Ezquerro *et al.*, 2012), y en su parte alta están datados en el Pleistoceno inferior por yacimientos de macromamíferos (zona MN17; 2,6-1,9 Ma; Adrover, 1975) y, con más precisión, por magnetoestratigrafía (1,95-2,1 Ma; Sinusía *et al.*, 2004). Este sistema de glacis también es reconocible en la cuenca de Calatayud, en sus depresiones limítrofes y en el sector norte de la fosa del Jiloca, donde presenta una pendiente media de entre el 1 y el 2% (Peiro y Simón, 2021). Asimismo, en toda la región aparecen otras morfologías cuaternarias, como son los abanicos aluviales pleistocenos que parten desde los escarpes de falla, o los depósitos de ladera holocenos.

4.4. Marco estratigráfico y sedimentológico: el Neógeno y Cuaternario

El estudio estratigráfico y sedimentológico de las sucesiones neógeno-cuaternarias de las depresiones analizadas en esta tesis se limita a las cuencas de Calatayud, Teruel y Jiloca (Fig. 1.4). En la **cuenca de Calatayud**, tanto bajo el régimen compresivo como extensional, la subsidencia tectónica permitió la sedimentación de la serie miocena más completa de toda la Cordillera Ibérica (Sanz-Rubio, 1999; Sanz-Rubio *et al.*, 2003). La marcada ciclicidad de su relleno sedimentario inducida por las oscilaciones de los parámetros orbitales terrestres, que ha

permitido la aplicación de estudios específicos (e.g. Abdul-Aziz *et al*., 2000), junto con el registro paleontológico (e.g. De Bruijn, 1967; Sesé, 2003), han permitido obtener un buen control cronológico de la cuenca. Tradicionalmente, en esta cuenca se han diferenciado varios sectores sobre la base de la cronoestratigrafía y sedimentología del relleno sedimentario (Anadón y Moissenet, 1996; Cortés-Gracia, 1999; Anadón *et al*., 2004).

En el sector septentrional, desde Calatayud hasta Villafeliche, los materiales neógenos se correlacionan con las unidades descritas por Pérez *et al*. (1985) para el margen suroeste de la depresión del Ebro (Gabaldón *et al*., 1991). Se trata de tres unidades genéticas mayores que integran, a su vez, varias unidades litoestratigráficas, y que están limitadas por rupturas sedimentarias a escala de cuenca (Sanz-Rubio, 1999; Anadón *et al*., 2004; Fig. 1.4):

- *Unidad Inferior* (Oligoceno superior?-Aragoniense inferior): más de 500 m, mayoritariamente de facies evaporíticas (yesos y halita, en parte descritos en sondeos; Marín, 1932) hacia el centro de la cuenca, que hacia los márgenes pasan a facies detríticas arcillosas.
- *Unidad Intermedia* (Aragoniense medio-Vallesiense): hasta 120 m, en gran parte de yeso, que cerca de los bordes de cuenca pasan a carbonatos dolomíticos.
- *Unidad superior* (Vallesiense superior-Rusciniense inferior): con una potencia variable entre 25 y 85 m, consta de depósitos terrígenos aluviales-fluviales y carbonatados fluvio-lacustres.

En el sector central de la cuenca de Calatayud, cerca de Daroca, el relleno sedimentario consta de hasta más de 200 m de materiales detríticos aluviales (conglomerados, lutitas rojas y areniscas) y carbonatados lacustres (margas y calizas) de edades que abarcan desde el Aragoniense hasta el Plioceno. Son equivalentes, en parte, a las unidades *Intermedia* y *Superior* descritas en el sector septentrional, faltando el registro de la unidad *Inferior* (Anadón *et al*., 2004; Fig. 1.4). Por último, en el sector meridional, entre Navarrete y Bañón, los depósitos neógenos muestran una disposición similar a la del sector septentrional: materiales detríticos en los márgenes de cuenca y evaporíticos hacia el centro, de edad Rambliense-Aragoniense. Los materiales más superiores de esta serie también son equivalentes a la unidad *Intermedia* (Anadón *et al*., 2004). En definitiva, la serie neógena de los sectores central y meridional de la cuenca de Calatayud se puede agrupar, según la nomenclatura propuesta inicialmente por Hernández *et al*. (1983a,b) y Colomer (1987), posteriormente adaptada por Martín-Bello *et al*. (2014), en las siguientes unidades (Fig. 1.4):

- Unidad Detrítica (*Clastic Unit; CU;* Ageniense superior-Aragoniense): conglomerados silíceos y lutitas. Se desglosa en tres subunidades (inferior o *CU1*, media o *CU2* y superior o *CU3*) a partir de sus relaciones verticales con los tramos carbonatados.
- Yesos de Navarrete (*Navarrete gypsum; NG;* Ageniense superior-Aragoniense inferior)
- Unidad de Bañón-Calizas de Nombrevilla (*Bañón Unit-Nombrevilla Limestone; NL;* Aragoniense): se diferencian dos subunidades carbonatadas (NL1 y NL2)
- Unidades Rojo 1, Páramo 1, Rojo 2, Páramo 2 y Rojo 3 (R1, P1, R2, P2 y R3; Vallesiense-Villafranquiense): alternancia de lutitas, limos y areniscas rojas, con calizas y margas. La unidad Páramo 1 no se cartografía ni se describe, y la unidad Rojo 1 no se describe con dicha nomenclatura, pero ambas figuran en los esquemas de correlación.
- *Glacis villafranquienses* (Villafranquiense tardío): conglomerados sin cementar con morfología de glacis.

Esta nomenclatura de unidades neógenas también se proponía simultáneamente para la **cuenca de Teruel** (Godoy *et al*., 1983 a, b). Existen otras divisiones estratigráficas propuestas para esta cuenca (Weerd, 1976; Alcalá *et al*., 2000; Alonso-Zarza y Calvo, 2000; Alonso-Zarza *et al*., 2012), y Ezquerro (2017) diferenció diez megasecuencias estratigráficas (M1 a M10) en su sector norte, basándose en cambios verticales granulométricos y sus características tectono-sedimentarias. Sin embargo, para facilitar la comparación entre cuencas, la nomenclatura más empleada va a ser la del Mapa Geológico Nacional 1:50.000 (MAGNA), pero actualizada y correlacionada con el modelo cronoestratigráfico de Ezquerro (2017). El relleno de los sectores centro y norte de la cuenca neógena de Teruel es de tipo mayoritariamente endorreico, incluyendo materiales detríticos, carbonatados y evaporíticos. Se depositaron en sistemas aluviales que partían de los dos márgenes de cuenca y vertían hacia sistemas lacustres hacia el centro de la misma (Moissenet, 1983; Alonso-Zarza y Calvo, 2000; Ezquerro,

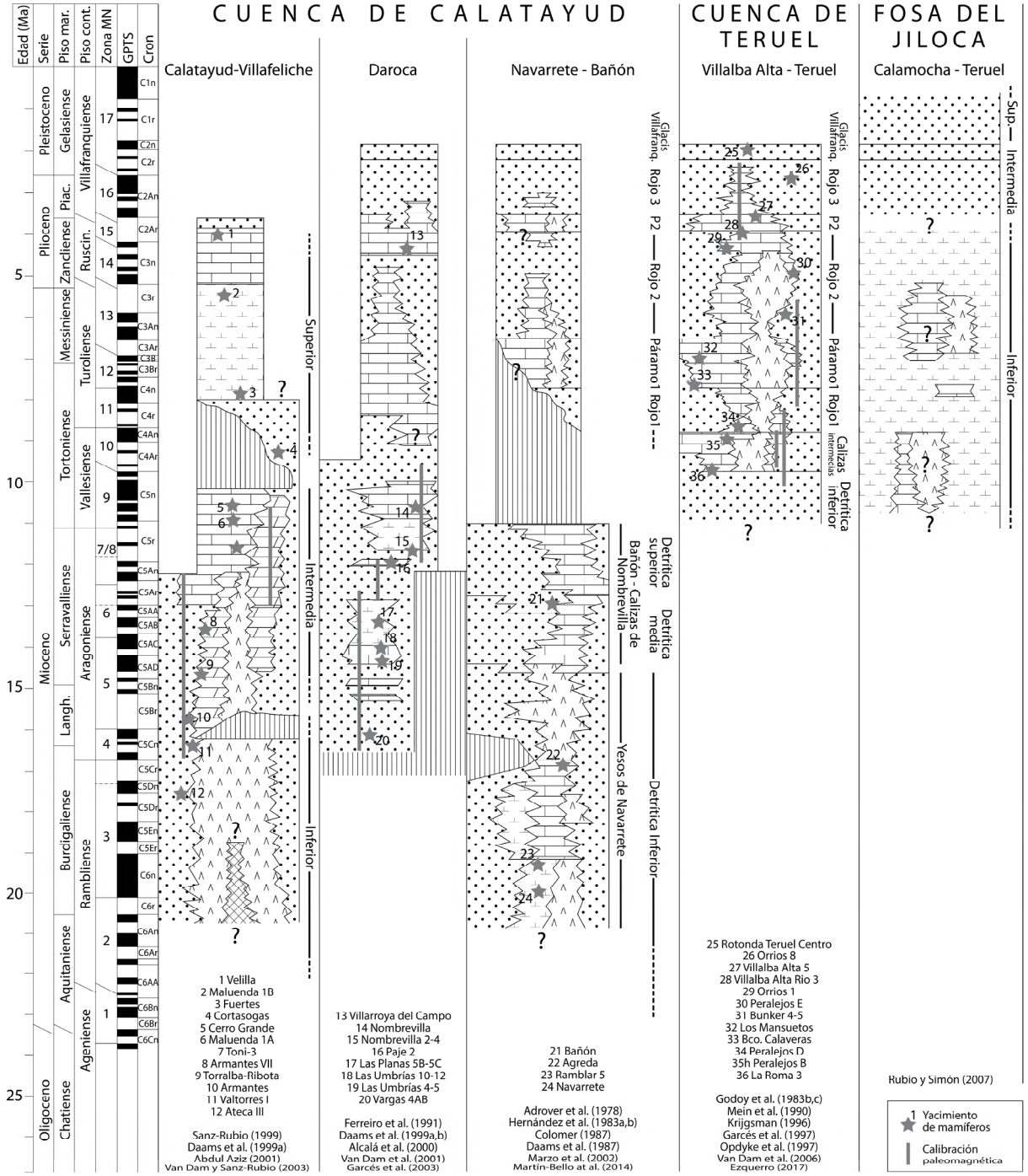

- Fig. 1.4.- Cuadro de correlación de las sucesiones neógeno-cuaternarias de los diversos sectores de las cuencas de Calatayud, Teruel y Jiloca. La escala de tiempo global o GPTS está basada en Cande y Kent (1995), con modificaciones basadas en Agustí *et al.* (2001) y Ogg (2012). Biozonación según Agustí *et al.* (2001), ligeramente modificada. Figura modificada de Anadón *et al.* (2004).

2017). El relleno abarca desde el Vallesiense inferior (~ 11,2 Ma) hasta el Villafranquiense superior (~ 1,8 Ma; Ezquerro, 2017; Ezquerro *et al.*, 2020). La división de Godoy *et al* (1983a, b) consiste en (Fig. 1.4):

- Unidad Detrítica inferior (Vallesiense-Rusciniense): conglomerados, areniscas, limos y arcillas asociados a ambientes aluviales en los márgenes de cuenca y dirigidos hacia el interior. Grada lateralmente al resto de unidades. Es una unidad diferente a la *CU1* de la cuenca de Calatayud.
- Calizas Intermedias (Vallesiense): calizas con intercalaciones de arcillas y margas lignitíferas sedimentadas en zonas lacustres.
- Toda la división de unidades informales detríticas-carbonatadas ("Rojos" y "Páramos"; Vallesiense-Villafranquiense). La unidad Páramo 1 se ha correlacionado con la parte superior de la megasecuencia M4 y la basal de la M5 (Turoliense; zonas MN12-MN13; cron C3Ar; alrededor de 7 Ma; Ezquerro, 2017); la unidad

Páramo 2, con el techo de la megasecuencia M7 y la M8 (Rusciniense superior-Villafranquiense inferior; MN15-MN16; C2Ar- C2An.3n; 3,8-3,5 Ma; Ezquerro *et al*., 2020).

- Otras unidades yesíferas que suelen constituir el cambio lateral de las unidades del Páramo.
- *Glacis villafranquienses* (Villafranquiense tardío): están datados por magnetoestratigrafía en 2,1-1,95 Ma (Sinusía *et al*., 2004).
- Otros depósitos cuaternarios de tipo aluvial que parten desde los escarpes de falla, coluviones y terrazas fluviales.

La estratigrafía neógena de estas cuencas es más conocida que la de la **fosa del Jiloca**, porque de ésta sólo aflora parte en su sector más meridional, y el encajamiento fluvial en el resto de la depresión es casi nulo (Lafuente *et al*., 2011a). En superficie sólo se muestra el dispositivo morfo-sedimentario correspondiente a los últimos depósitos aluviales pliocenos y cuaternarios. A partir de numerosos sondeos realizados en la zona, Rubio y Simón (2007) constatan la existencia de espesores de relleno sedimentario de la fosa del Jiloca notables, que de media alcanzan los 50 m y, en puntos concretos, llegan a superar los 100 m. Estos autores distinguen tres grandes unidades sobre el sustrato mesozoico (Fig. 1.4):

- Unidad inferior (Mioceno superior-Plioceno inferior): margas de origen palustre. Se correlaciona tentativamente con las formaciones carbonatadas mio-pliocenas de la fosa de Teruel (supuestamente, las unidades del Páramo y sus tránsitos a unidades yesíferas).
- Unidad intermedia (Plioceno inferior-Cuaternario): detrítica, compuesta de gravas y limos rojizos y anaranjados. Representa la mayor parte del relleno de la fosa, y culmina en superficie con el sistema de *glacis villafranquienses*.
- Unidad superior (Cuaternario): también de carácter detrítico y origen aluvial. Algunos de estos depósitos forman piedemontes que arrancan desde los escarpes de falla.

El **tránsito del endorreísmo al exorreísmo** en las cuencas neógenas de la Cordillera Ibérica centro-oriental es un proceso activo desde el Plioceno inferior hasta el día de hoy. Comenzó en el sector norte de la cuenca de Calatayud con la captura del primitivo río Jalón, y en el sector sur de la cuenca de Teruel con la captura del primitivo río Turia (Gutiérrez *et al*., 1996, 2008; Vacherat *et al*., 2018). El sector norte de la cuenca de Teruel fue progresando hacia el exorreísmo hasta el Villafranquiense medio (Ezquerro, 2017). La transición continuó con la captura por parte del río Jiloca, tributario del Jalón, del semigraben de Daroca a lo largo del Plioceno terminal-Pleistoceno inferior, y posteriormente del sector norte de la fosa del Jiloca hacia el Pleistoceno superior. Finalmente, también durante el Pleistoceno superior, se produjo la captura del sector sur de la cuenca de Calatayud por el río Huerva, así como del semigraben de Munébrega por un tributario menor del río Jalón (Gutiérrez *et al*., 1996, 2008; Vacherat *et al*., 2018).

Existe consenso en que la unidad Páramo 2 de edad Rusciniense (además de ser correlacionable con la SEF, como se explica en el apartado anterior) representa el final generalizado de la sedimentación endorreica y, sobre ella, se depositan las demás unidades durante el periodo exorreico y de actividad tectónica extensional plio-cuaternaria (e.g. Hernández *et al*., 1983a, b; Godoy *et al*., 1983a, b; Simón, 1983; Gabaldón *et al*., 1991). Sin embargo, la proliferación de los *glacis villafranquienses* hacia los centros de las depresiones no puede ser considerada un indicador clave del paso al exorreísmo, como es común en la literatura, ya que algunos de ellos pasan lateralmente a sedimentos palustres depositados en medios endorreicos (Ezquerro *et al*., 2012). Además, algunos de estos ambientes de tipo endorreico y palustre han permanecido hasta la actualidad, como es el caso de la cuenca de Gallocanta, o el sector central de la fosa del Jiloca (Gutiérrez *et al*., 1996, 2008; Rubio y Simón, 2007).

Al sur de la fosa del Jiloca, en su nexo con la cuenca de Teruel, se conformó una cubeta con mayor subsidencia que permaneció endorreica hasta el inicio del Pleistoceno (Ezquerro *et al*., 2012). Su origen está relacionado con el escalón que produce la falla de Concud y su zona de relevo con la falla de Teruel, junto con el *roll-over* del bloque superior de ambas. El movimiento de estas fallas bajo la etapa extensiva plio-cuaternaria hizo que en el sector de la cuenca de Teruel correspondiente al bloque levantado se interrumpiera la sedimentación

de tipo lacustre-palustre dentro de la unidad Rojo 3 (Moissenet, 1982; Lafuente *et al*., 2011b). Sin embargo, esta sedimentación prosiguió en la cubeta residual endorreica del bloque hundido como parte de la fosa del Jiloca.

Finalmente, y una vez se estableció la red fluvial exorreica en las depresiones del Jiloca y Teruel, los materiales cuaternarios de su intersección se depositaron formando cuatro niveles de terraza (Peña, 1981; Godoy *et al*., 1983a):

- Terraza superior (T3, a 80-90 m de altura sobre los cauces fluviales): niveles de gravas con cementación moderada de edad imprecisa.
- Terraza media (T2): nivel bastante continuo de arenas y gravas cementadas, con distribución altitudinal irregular (pero ca. 45-65 m), en parte debida a la actividad tectónica cuaternaria (Simón y Soriano, 1993). Está datada del Pleistoceno medio-superior por un yacimiento de mamíferos (Moissenet, 1985), por OSL y ESR entre ca. 264 y 350 ka (Santonja *et al*., 2014), y por OSL en 152 ± 17 y 173 ± 11 ka (Peña-Monné *et al*., 2022). Además, en el sector de Los Baños está acotada con U/Th entre 169 ± 10 y 116 ± 4 ka (Arlegui *et al*., 2004), así como entre 250+32/–25 y 213+33/–26 ka (Gutiérrez *et al*., 2008), y podría tener 327 ± 31 ka o ser más antigua de 285 ± 14 y de 228 ± 11 ka (Gutiérrez *et al*., 2020b). Existe un desdoble local de la T2 en otro nivel algo más bajo (Moissenet, 1993), que ha sido datado por OSL entre 46 ± 3 y 78 ± 5 ka (Simón et al., 2017) y por ESR en 307 ± 25 ka (Gutiérrez *et al*., 2020b).
- Terraza inferior (T1): arenas y gravas menos cementadas. Se encuentra desdoblada localmente en tres subniveles, los cuales cuentan con varias dataciones mediante OSL que indican una edad Pleistoceno superior. Los más importantes son los subniveles alto y medio. El alto (a 20-30 m de altura sobre los cauces fluviales) tiene una edad que podría ser de 22,0 ± 1,6 ka (Lafuente, 2011) o estar comprendida entre 136 ± 20, 111 ± 6 y 81 ± 5 (Peña-Monné *et al*., 2022). El subnivel medio (a 15-20 m de altura) tendría entre 15,0 ± 0,9 (Gutiérrez *et al*., 2008), 15,6 ± 1,3 ka, 14,9 ± 1,0 ka (Lafuente 2011; Lafuente *et al*., 2011a, 2014), 60 ± 2,5 ka (Gutiérrez *et al*., 2020b) y 22 ± 7 ka (Peña-Monné *et al*., 2022). El subnivel bajo sólo se identifica en un retazo en los alrededores de Masada Cociero (Simón *et al*., 2016).
- Terraza Subactual (T0): gravas, arenas y limos no cementados, datados como holocenos mediante OSL en 3,4 ± 0,7 ka (Lafuente, 2011), y entre 27 ± 2 y 10 ± 1 ka con OSL (Simón *et al*., 2017).

Este modelo cronológico cuaternario podría estar sujeto a revisión próximamente debido a determinadas incertidumbres respecto a la metodología seguida en el laboratorio que analizó muchas de estas dataciones, tal y como se plantea en Gutiérrez *et al*. (2020a) y Moreno *et al*. (2021). Se especifica y reflexiona más sobre esto en el ANEXO I de esta tesis.

4.5. Marco sismotectónico

La sismicidad histórica e instrumental de la región es baja a moderada. Los epicentros se concentran sobre todo en el margen oeste de la cuenca de Calatayud y en la zona de relevo entre las fallas de Sierra Palomera y Concud (IGN, 2022; Fig. 1.5). Los epicentros se pueden asociar razonablemente a algunas fallas recientes conocidas: Daroca, Sierra Palomera, Concud o Teruel.

Cabe destacar la actividad sísmica del margen oeste de la fosa del Jiloca y del sector sur de la cuenca de Teruel, en la zona de Ademuz (Giner-Robles *et al*., 2017, 2022). Son sectores con actividad notable originada por los sistemas de fallas del macizo de Albarracín y del borde de la fosa de Teruel. En el primer sector no existen depósitos cuaternarios importantes que registren esa actividad reciente y, en ambos sectores, se da el caso de que estos depósitos no han sido estudiados en profundidad con anterioridad a esta tesis, ni tampoco en la misma. Sí que se tiene constancia de desplazamientos en marcadores mio-pliocenos en los dos sectores, pero a pesar de ello no son objeto de estudio en esta tesis y simplemente se espera que se pueda profundizar en ellos en el futuro.

El catálogo del Instituto Geográfico Nacional (IGN, 2022) aporta todos los datos de intensidad máxima de terremotos históricos, de acuerdo con la Escala Macrosísimica Europea (*European Macroseismic Scale; EMS-98*), y los datos de magnitud de los terremotos ocurridos en época instrumental, asignada con diferentes criterios. Para unificar las magnitudes a magnitud momento (Mw), más comúnmente empleada, Cabañas *et al*. (2015) proponen

una buena correlación empírica entre los valores asignados con esos criterios y la Mw. Esta correlación se ha empleado en esta tesis para poder trabajar únicamente con valores de magnitud momento (Mw).

Con anterioridad a la época instrumental, IGN (2022) presenta registro de intensidades máximas de hasta VI-VII en la sierra de Albarracín (1848), y de IV-V en la fosa del Jiloca (1828; IGN, 2022). Según la relación propuesta por Cabañas *et al.* (2015), dichas intensidades podrían corresponder a magnitudes estimadas de 5-5.5, y 4-4.5, respectivamente. El registro instrumental regional hasta día de hoy incluye terremotos de magnitudes que suelen estar comprendidas entre 1.5 y 3.5, con magnitudes máximas de 4.1 en la sierra de Algairén, de 4.7 y 3.7 en los alrededores de las localidades de Daroca y Calamocha (Used, 1953), y de 3,8 en la Sierra Palomera.

No hay constancia de enjambres sísmicos importantes en el sector sur de la cuenca de Calatayud, ni en los sectores norte de las depresiones del Jiloca y Teruel. Se han obtenido seis mecanismos focales a profundidades que van desde los 2 hasta los 15 km en el sector de Calatayud, la sierra de Algairén, en Albarracín y Teruel (Herraiz *et al.*, 2000; IGN, 2022; Fig. 1.5). Están situados dentro de la corteza frágil, por encima del nivel de despegue regional situado entre 11 y 17 km de profundidad (Roca y Guimerà, 1992; Ezquerro *et al.*, 2020), y corresponden a fallas normales puras o con cierta componente direccional. Asimismo, son consistentes con las trayectorias primarias de σ_3 cercanas a ENE-WSW del campo de esfuerzos regional activo hoy en día (Herraiz *et al.*, 2000).

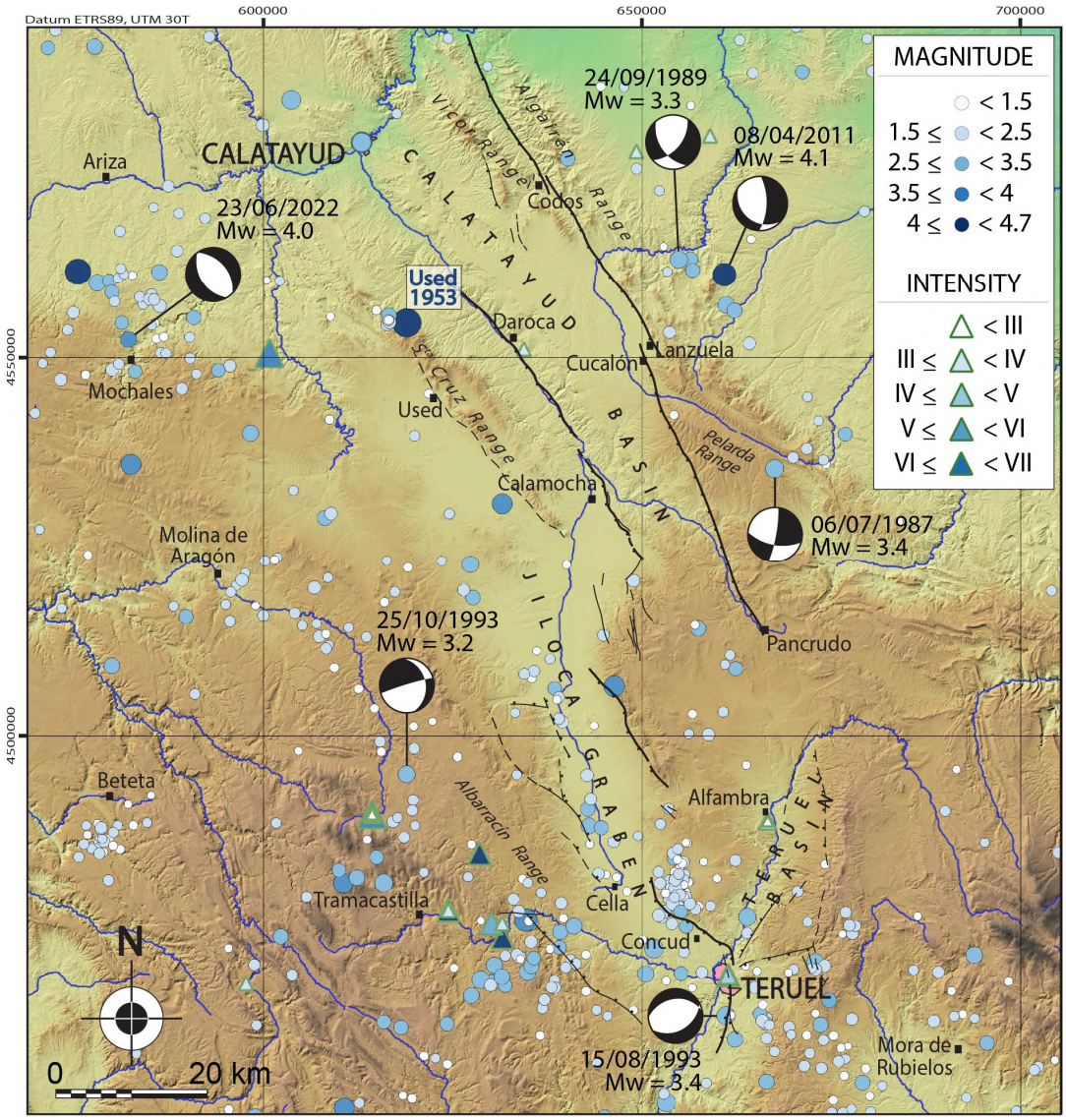

Fig. 1.5.- Mapa de epicentros de terremotos históricos e instrumentales en la cuenca de Calatayud, la fosa del Jiloca y el sector norte de la cuenca de Teruel (IGN, 2022).

5. Metodología

Para alcanzar los objetivos propuestos en este trabajo, se han seguido principalmente las metodologías del análisis estructural y morfotectónico en la mayoría de las fallas estudiadas, aplicándolas con un enfoque multidisciplinar que incluye el estudio paleosismológico en tres de ellas (fallas de Río Grío-Pancrudo, Calamocha y Sierra Palomera). Asimismo, una parte importante de este trabajo ha sido la revisión bibliográfica en torno a la estructura y evolución de otras fallas no estudiadas propiamente en él. Esta tesis también integra, de manera complementaria, información procedente de las zonas de relevo entre las fallas y de modelos analógicos. Todas las metodologías se detallan más en profundidad en sus respectivos capítulos, especialmente la de la modelización analógica (sección VII.1).

5.1. Revisión bibliográfica

La recopilación bibliográfica es el primer paso en cualquier trabajo científico para familiarizarse con los distintos estudios de ámbitos concretos realizados con anterioridad. Se ha recogido bibliografía relacionada con cinco aspectos fundamentales del sector centro-oriental de la Cordillera Ibérica: (1) la estratigrafía de sus cuencas (sobre todo de las de Teruel, Calatayud y Jiloca); (2) la geometría de sus estructuras compresivas cenozoicas, sobre todo fallas, posteriormente invertidas durante la extensión Plio-Cuaternaria; (3) la evolución tectónica de estas rupturas, y en general de su cinemática; (4) la dinámica cortical y el campo de extensión radial o multidireccional al que están sometidas; y (5) la sismicidad histórica e instrumental. Algunas de las fallas recientes estudiadas ya habían sido caracterizadas, en su totalidad o en parte, por autores previos, como es el caso sobre todo de las fallas de Teruel, Concud y Daroca. Existe, por tanto, gran variedad de bibliografía disponible del sector centro-oriental de la Cordillera Ibérica, por lo que esta tesis ha sido clave para clarificar, unificar y actualizar los conocimientos que se tienen de este sector, con la información procedente de esa revisión bibliográfica y la nueva información generada en esta tesis por medio de las demás metodologías.

Se ha recogido asimismo bibliografía de carácter teórico y metodológico, relacionada con la metodología del estudio paleosismológico, la geometría-cinemática-dinámica de procesos de fracturación similares en otros contextos mundiales de extensión radial o multidireccional, y las zonas de relevo entre fallas normales. También se ha profundizado en las diversas técnicas empleadas en el campo de la modelización analógica en contextos extensionales, dando importancia a aquellos dispositivos que hacen uso de una base dúctil.

5.2. Estudio estructural

Cualquier estudio estructural de una zona debe partir de una **cartografía geológica** de detalle que permita establecer las relaciones existentes entre los materiales y las estructuras de deformación. Dada la extensión del área de estudio, dicha cartografía se ha realizado, esencialmente, mediante estudio sobre ortoimágenes de satélite y modelos digitales de elevación (Digital Elevation Model, DEM; pixel = 2 m), así como en ocasiones sobre fotografías aéreas de escala 1:30 000. Siempre tomando como base la cartografía MAGNA de escala 1:50 000. Los DEM, cada vez más, son una herramienta muy empleada en cartografía de fallas (e.g., Cunningham *et al*., 2006; Chen *et al*., 2015), sobre todo en zonas densamente cubiertas, de fallas con tasas de desplazamiento bajas, y con escasas evidencias de fracturación secundaria (McCalpin, 2009).

Una vez obtenida una cartografía preliminar, se ha realizado de un **trabajo de campo** con el objetivo de comprobar determinados contactos estratigráficos, evidenciar la existencia de estructuras de deformación recientes y determinar su geometría (longitud, dirección, buzamiento, curvatura, ramificaciones, escalones…). Cuando la calidad de los afloramientos lo ha permitido, se ha llevado a cabo un estudio más en detalle, con especial atención a la toma de datos cinemáticos (estrías, desplazamiento de marcadores estratigráficos, disposición de cantos reorientados…) que han permitido inferir la dirección y sentido de movimiento de las fallas. Sin embargo, en casos de escasez de afloramientos que atraviesan o muestran directamente dichas estructuras, su estudio se ha limitado a la observación y caracterización de su expresión cartográfica sobre el terreno. Se han realizado análisis de paleoesfuerzos según el modelo de Anderson (1951) de fallas conjugadas para inferir sistemas de esfuerzos

hipotéticos. La escasez de planos con estrías ha hecho inviable la aplicación de otros métodos de inversión de esfuerzos más avanzados basados en la ecuación de Bott (1959) y que utilizan planos de falla reactivados de orientaciones aleatorias (e.g. Etchecopar *et al*., 1981; Simón, 1986).

La metodología del trabajo de campo se ha aplicado tanto a las rupturas de primer orden como a las de segundo orden (ramificaciones y otras fallas asociadas). Hay que tener en cuenta que las posibles fallas secundarias: (1) acomodan localmente la deformación de la falla principal, normalmente con menores desplazamientos cuanto más alejadas están de la misma (Bonilla, 1970), pero con análoga dirección de transporte; (2) pueden ayudar a caracterizar la dirección y sentido de movimiento de la falla principal, en el caso de conformar zonas de cizalla semifrágil (fracturas de Riedel); (3) pueden ofrecer información acerca de los eventos sísmicos provocados por el movimiento de la falla principal (Slemmons y dePolo, 1986). Esta metodología también ha permitido caracterizar algunas de las estructuras de las zonas de relevo entre las fallas principales.

Asimismo, para el estudio de la fracturación en las zonas de relevo entre fallas se incluye una parte experimental en el laboratorio, que comprende la elaboración de varios **modelos analógicos** (metodología detallada en sección VII.1). En ellos se simula y analiza en profundidad la evolución estructural de las zonas de relevo en contextos de fallas heredadas y campos de esfuerzos inestables, como es la extensión multidireccional, aplicando en ellos por primera vez una extensión biaxial.

Ocasionalmente se han aplicado también métodos de trabajo sedimentológicos, cuando la interpretación cinemática y evolutiva de algunas estructuras ha exigido tener en cuenta las relaciones tectosedimentarias en los bordes de cuenca o las direcciones de paleocorrientes. Por ejemplo, en la zona de falla de Río Grío-Pancrudo se han estudiado cantos imbricados en depósitos aluviales plio-cuaternarios y cuaternarios para obtener direcciones de **paleocorrientes**, debido a la ausencia de afloramientos 3D adecuados de otras estructuras sedimentarias, como cuerpos canaliformes o estratificación cruzada. Se trata de un aspecto clave para demostrar cambios en los patrones fluviales debidos a la posible actividad tectónica.

Las orientaciones de fallas, fracturas y estrías han sido representadas y analizadas mediante proyección estereográfica, utilizando el sistema de proyección equiareal desde el hemisferio inferior. Se ha empleado para ello el ***software* Stereonet 8** (Allmendinger *et al*., 2012; Cardozo y Allmendinger, 2013). El mismo paquete de *software* ha permitido elaborar los diagramas en rosa de las paleocorrientes y de las direcciones de fracturas medidas en campo y en modelos analógicos.

Por último, en esta tesis se incorpora información procedente de tres **sondeos mecánicos** realizados en la zona de relevo entre las fallas de Concud y Teruel, con el fin de obtener más información de la estratigrafía del subsuelo que permite profundizar en sus características estructurales. El sistema empleado ha sido el de sondeo a rotación con recuperación de testigo continuo, y los testigos recuperados fueron cortarlos longitudinalmente para proceder a su testificación. Se delimitaron tramos de características similares y se describió su litología, color y estructuras sedimentarias, orgánicas u otras. Por último, se levantaron e interpretaron los perfiles estratigráficos, correlacionando sus tramos, asignándoles una edad y el medio sedimentario en el que se depositaron.

5.3. Estudio morfotectónico

Algunas formas del relieve, como por ejemplo las superficies de erosión, se pueden usar como marcadores directos de la deformación en áreas activas. Se ha colaborado en la cartografía de las **superficies de erosión** en zonas cercanas a las fallas estudiadas y, en general, en las cuencas principales. Los mapas de restos conservados de estas superficies se han realizado a partir de fotografía aérea, mapas topográficos y modelos digitales de elevación (DEM), arrastrando desde otros sectores cercanos las superficies ya contrastadas en trabajos previos (Ezquerro, 2017; Simón-Porcar, *et al*., 2019; Simón *et al*., 2019; Ezquerro *et al*., 2020;). Después, la altitud de esos remanentes se ha interpolado para obtener mapas de contornos estructurales.

La reconstrucción y el análisis geométrico de las superficies de erosión sobre los mapas, traducidas en perfiles, ha permitido cuantificar los desplazamientos verticales de las fallas, así como detectar y evaluar otras características como los basculamientos. Dado que conocemos las edades de estos marcadores morfo-

sedimentarios, también hemos podido calcular tasas de deformación. Para más detalles sobre la metodología y problemática del uso de superficies de erosión como marcadores de la deformación, ir a la sección II.1.

Dada la extensión del área de estudio, dicha cartografía se ha realizado, esencialmente, mediante estudio sobre ortoimágenes de satélite, modelos digitales de elevación (Digital Elevation Model, DEM; pixel = 2 m), fotografías aéreas de escalas 1:18 000 y 1:30 000, y tomando como base la cartografía MAGNA de escala 1:50 000.

Las imágenes de satélite de alta resolución y los DEM también se pueden emplear para identificar superficies rotas y desplazadas en zonas poco accesibles. Las características que más se han identificado son **lineamientos** topográficos. Dado que éstos pueden desarrollarse a partir de una combinación de distintos factores geológicos, se han diferenciado cuidadosamente aquellos con evidencias claras de un origen tectónico, teniendo en cuenta su dirección y características asociadas (cambios en el drenaje, facetas triangulares, escarpes…).

5.4. Estudio paleosísmico

Para el estudio de las evidencias paleosísmicas se ha seguido la clasificación de McCalpin y Nelson (2009; tabla 1.1). Todas las evidencias que se han estudiado son de tipo primario, es decir, producidas por la deformación tectónica resultante del desplazamiento cosísmico a lo largo de un plano de falla. No se han encontrado las de tipo secundario, aquellas producidas por las ondas sísmicas, como son las sismitas. Las evidencias primarias descritas tienen expresión estratigráfica y geomorfológica, y se han hallado tanto lejos de las trazas de las fallas (de tipo *off-fault*), mediante trabajo de campo, como localizadas en las mismas trazas (de tipo *on-fault*), mediante la excavación de trincheras paleosismológicas y el estudio de taludes. En esta tesis se incluyen datos de la realización de dos trincheras en las fallas de Cucalón-Pancrudo y Sierra Palomera, y del estudio de varios taludes artificiales en la falla de Calamocha; el estudio paleosismológico de todos ellos supone una parte importante del trabajo. El estudio paleosísmico de la falla de Cucalón-Pancrudo y gran parte del de la falla de Calamocha son originales de esta tesis. La trinchera de la falla de Sierra Palomera se realizó con anterioridad a la misma, pero sus datos y resultados se han trabajado por completo y son inéditos.

Las **trincheras paleosismológicas** se han excavado lo más paralelas posible a la dirección de transporte de las fallas, normalmente transversalmente a sus trazas, en secciones que optimizan la obtención de datos precisos de desplazamiento o de recurrencia de paleoterremotos (Sieh, 1981). La localización y profundidad de cada una de ellas han estado dictaminadas por los objetivos de la investigación: para analizar los últimos paleoterremotos asociados a las fallas se han situado en depósitos cuaternarios recientes, tratando siempre de que las zanjas profundicen todo lo posible para obtener un registro más amplio. Se han tenido en cuenta también otras consideraciones, como los accesos en carretera para la maquinaria, los permisos de los propietarios de la tierra, etc. El estudio de los taludes antrópicos preexistentes se ha realizado siguiendo la misma metodología aplicada a las trincheras aunque, lógicamente, sin poder determinar su localización ni profundidad.

La **prospección geofísica** se utiliza muy comúnmente en paleosismología para localizar, cartografiar y caracterizar fallas y discontinuidades a poca profundidad (e.g. Green *et al.*, 2003; Stephenson y McBride, 2003; Vanneste *et al.* 2008; McCalpin, 2009). Aplicada antes de cada estudio paleosísmico, ha ayudado a determinar la sección óptima donde realizar la trinchera, así como a caracterizar la geometría de las fallas a más profundidad que la alcanzada por la excavación (McCalpin, 2009). Asimismo, ha permitido localizar posibles fallas ciegas en el subsuelo que no tienen expresión en superficie (Pueyo *et al.*, 2016), lo cual ha sido especialmente útil no sólo en los estudios paleosísmicos, sino en el estudio estructural de la fracturación de la zona de relevo entre las fallas de Concud y Teruel. Las técnicas empleadas en todos los casos han sido la magnetometría (Fig. 1.6a) y el georradar (GPR: Ground Penetrating Radar). La obtención de datos mediante estos dos métodos geofísicos, así como su procesado e interpretación, pueden resultar tareas muy complicadas, por lo que han sido realizadas con la colaboración de Óscar Pueyo, responsable del equipo de geofísica del grupo Geotransfer de la Universidad de Zaragoza. Los estudios previos llevados a cabo por el equipo en áreas cercanas a las fallas, que no muestran signos claros de actividad y que muchas veces no han roto en superficie, han facilitado la interpretación de los datos.

Nivel 1: Génesis	Primarias (fruto de deformación tectónica)			
Nivel 2: Localización	En la falla		Lejos de la falla	
Nivel 3: Momento	Cosísmicas	Post-sísmicas	Cosísmicas	Post-sísmicas
Expresión geomórfológica	o Escarpes de falla o Fisuras o Pliegues o Lomos de presión	o Contribuciones post-deslizamiento a las formas cosísmicas o Cuñas coluviales	o Superficies basculadas o Líneas de costa elevadas o inundadas	o Terrazas aluviales tectónicas o Contribuciones post-deslizamiento a las formas cosísmicas
Expresión estratigráfica	o Estratos fallados o Estratos plegados o Discordancias	o Cuñas coluviales derivadas de escarpes o Rellenos fisurales	o Depósitos de tsunami y discordancias erosivas causadas por tsunami	o Discordancias erosivas y depósitos inducidos por levantamiento, subsidencia y basculamiento
Abundancia de formas similares no sísmicas	Pocas	Pocas	Algunas	Comunes
Nivel 1: Génesis	Secundarias (fruto de la sacudida sísmica)			
Nivel 2: Localización	En la falla		Lejos de la falla	
Nivel 3: Momento	Cosísmicas	Post-sísmicas	Cosísmicas	Post-sísmicas
Expresión geomórfológica	o Volcanes de arena o Deslizamientos o Alteraciones en árboles	o Deslizamientos retrogresivos	o Volcanes de arena o Deslizamientos o Alteraciones en árboles y procesos de sackung o Subsidencia por compactación de sedimentos	o Deslizamientos retrogresivos
Expresión estratigráfica	o Diques de arena y sills o Deformaciones de sedimentos blandos	o Sedimentos depositados de deslizamientos retrogresivos	o Diques de arena o Cráteres rellenos o Estructuras de deformación en sedimentos blandos o Turbiditas	o Cambios en las tasas de sedimentación como respuesta a deslizamientos retrogresivos o características superficiales como fisuras, volcanes de arena u otras formas de perturbación del paisaje
Abundancia de formas similares no sísmicas	Algunas	Muy comunes	Algunas	Muy comunes

Tabla 1.1.- Clasificación jerárquica de evidencias paleosismológicas (tomada de McCalpin y Nelson, 2009).

La magnetometría es una técnica geofísica consistente en la medición de la intensidad del campo magnético terrestre y, según configuración empleada, también del gradiente magnético vertical. Ambos se ven modificados por la distribución de los materiales del subsuelo. Se ha empleado un magnetómetro de efecto Overhausser (GSM-19, con dos sensores con una separación de 0,5 m) con GPS integrado. Las variaciones de intensidad naturales del campo magnético terrestre y aquellas producidas a lo largo del día se han corregido con un magnetómetro de precesión protónica PMG-01 que ha servido de base en todo momento. Una vez obtenido el datum local de la zona, se ha realizado el cálculo de anomalías residuales para localizar los cambios relativos de la intensidad del campo magnético. Finalmente, los datos obtenidos se han integrado para poder obtener un mapa de variaciones de intensidad del campo.

Los datos obtenidos mediante georradar (GPR 2D) han complementado los obtenidos de la magnetometría. Se trata de un método que se basa en la emisión de ondas electromagnéticas hacia el subsuelo, a intervalos previamente definidos, para después recibir y registrar las reflexiones producidas por los contactos entre materiales diferentes. Para ello, se ha hecho uso de varios dispositivos con frecuencias centrales de 50, 100 y 250 MHz de RAMAC. La profundidad que se alcanza con esta técnica geofísica depende de la frecuencia utilizada y de las características de los materiales. En la zona de estudio de la trinchera de Lagueruela se han empleado los dos dispositivos, en todos los casos con doble recorrido, y con diferente configuración de profundidad de penetración (intervalos TWT), ya que los mayores contrastes entre los resultados a un lado y otro de la falla suelen encontrarse en condiciones profundas. Los perfiles de GPR se han procesado digitalmente para incrementos de señal con la profundidad, para filtrar las frecuencias fuera de rango y realizar el suavizado de los perfiles obtenidos.

Una vez excavada cada trinchera en la localización y con las características (orientación y profundidad) que se habían determinado mediante el trabajo de campo y la geofísica (Fig. 1.6b), se ha procedido al entibado de sus paredes para una mayor seguridad, y a la elección de la más propicia de ellas para su estudio (el otro permitirá solventar dudas puntuales). Esta pared se ha georreferenciado, limpiado (para exponer correctamente la estratigrafía y las estructuras) y subdividido (mediante un mallado ortogonal de 1 x 1 m, 1 x 0,5 m ó 0,5 x 0,5 m para disponer de referencias horizontales y verticales), todo según la **metodología paleosismológica** establecida por McCalpin (2009). Después se han diferenciado unidades litológicas y contactos según sus texturas, colores y granulometrías, entre otros (Fig. 1.6c). De igual forma se han distinguido las fallas, fracturas, fisuras y pliegues y se ha establecido su relación con las unidades sedimentarias. Cuando afecta a materiales no consolidados, la expresión de la fracturación es clara en los niveles inferiores, pero suele complicarse hacia la superficie (McCalpin, 2009). En tal caso, las rupturas se han identificado por cambios en la textura, precipitaciones de carbonato o alineaciones de cantos, entre otros. Hecho todo esto, se ha procedido al muestreo de puntos clave para las dataciones. Cuando todos los contactos, estructuras y muestras tomadas se han marcado en el talud de la trinchera, se ha procedido al dibujo detallado a mano de la sección (*log*), que comprenderá toda la información y facilitará su posterior digitalización sobre el fotomosaico del mismo. Este último se ha obtenido de la integración mediante software procesador de imágenes (Adobe Photoshop e Illustrator) de las múltiples fotografías del talud. Las fotografías se habían tomado lo más perpendiculares posible a los taludes, y aun así existen pequeños desajustes que se han podido corregir mediante software, gracias a que las fotografías siempre incluían parte del mallado de referencia. De esta manera, el resultado final es una imagen ortocorregida de cada celda de dicho mallado. Por otra parte, algunos de los taludes estudiados estaban originalmente inclinados, por lo que sus fotomosaicos han sido proyectados en un plano vertical. El *log* final del talud de la trinchera también se ha digitalizado mediante Adobe Illustrator. Terminado todo el trabajo, se ha procedido al rellenado de la trinchera y a la restauración del terreno.

Tanto en las trincheras como en los *logs* resultantes, se han cuantificado los **desplazamientos verticales** de las fallas e interpretado **paleoeventos** o paleoterremotos. El salto observado en los marcadores (o superficies de referencia), sobre todo estratigráficos, ha permitido evaluar el desplazamiento de las fallas, considerando la separación vertical de dichos marcadores. Este parámetro puede traducirse en un valor de desplazamiento neto si se conoce el buzamiento del plano de falla y la dirección de transporte dentro de él. El desplazamiento neto puede calcularse, bien para el total acumulado en una falla individual, o bien para el ocurrido durante un evento paleosísmico (salto neto cosísmico). Cada evento puede expresarse, además, en el registro estratigráfico mediante el horizonte de evento (*event horizon*; Pantosti *et al*., 1993), que corresponden a la superficie del terreno existente en el momento del paleoterremoto y su edad es la más próxima a la de éste. En las trincheras estudiadas, los horizontes de evento se han establecido sobre todo a partir de evidencias de terminaciones de fallas hacia arriba, interrumpidas en una discordancia bajo una unidad posterior no deformada que las fosiliza, o de rellenos fisurales en la parte más superficial de la falla. En estos casos, las muestras para datar los paleoeventos se han tomado lo

Fig. 1.6.- (a) Prospección con magnetómetro de efecto Overhausser. (b) Excavación de la trinchera. (c) Estudio de los taludes de la trinchera. (d) Toma de muestras para datación por OSL. Todas ellas con relación a la trinchera de Lagueruela.

más cerca posible a estos horizontes, mientras que en otros casos (como terminaciones de fallas hacia arriba, perdiéndose dentro de un estrato) sólo ha sido posible acotar la edad de los estratos más recientes a los que afecta la falla.

Conocer las edades de los depósitos cuaternarios implicados en cada estudio paleosísmico ha permitido calcular las edades de los eventos sísmicos y, por tanto, las tasas de desplazamiento vertical y de desplazamiento total para distintos intervalos de tiempo. Dada la escasez de sedimentos ricos en carbono, el método empleado en todas las dataciones de este trabajo es la **Luminiscencia Ópticamente Estimulada** (*Optically Stimulated Luminiscence*, OSL; Huntley *et al*., 1985), que se emplea sobre granos de cuarzo. Esta técnica está basada en la capacidad del cuarzo para acumular el efecto de la radiación ionizante. Como respuesta a la estimulación con luz,

el cuarzo responde con una señal luminiscente proporcional a la dosis recibida. La dosis acumulada y la correspondiente señal luminiscente se borra con la exposición a la luz solar, por lo que el momento cero que se data con esta técnica es la última vez que los granos de cuarzo estuvieron expuestos a la luz, es decir, el momento en el cual el cuarzo presente en el sedimento queda enterrado y oculto a la luz solar. Mediante la relación entre la dosis absorbida o equivalente (*equivalent dose*) y la tasa de dosis anual (*dose rate*) del material se puede obtener la edad precisa de enterramiento (Aitken, 1998). La tasa de dosis anual (*dose rate*) se obtiene a partir de la concentración de radionúclidos presentes en la matriz sedimentaria, bien utilizando espectrometría gamma o espectrometría de masas. Esta técnica permite datar sedimentos detríticos de hasta unos 400.000 años, dependiendo de la tasa de dosis y de las características luminiscentes del material a estudio.

Todas las muestras de OSL recogidas en esta tesis se han extraído usando tubos opacos para evitar su exposición a la luz solar (Fig. 1.6d), siguiendo escrupulosamente la metodología de Gray *et al*. (2015), y se han analizado en el Laboratorio de Luminiscencia del Centro Nacional de Investigación sobre la Evolución Humana (CENIEH, Burgos). La metodología seguida es la explicada en detalle en la sección III. Asimismo, el análisis OSL de varias muestras extraídas en campañas paleosismológicas llevadas a cabo con anterioridad a esta tesis, pero cuyas dataciones son interpretadas en la misma, habían sido procesadas por el Laboratorio de Datación y Radioquímica de la Universidad Autónoma (Madrid), y por el *Luminiscence Dating Laboratory* de la Universidad de Georgia (EEUU). Para la espectrometría gamma se han utilizado muestras de unos 200 g, consideradas como representativas de cada matriz sedimentaria, y se han medido por espectrometría gamma de alta resolución en el Servicio de Radioisótopos del Centro de Investigación, Tecnología e Innovación de la Universidad de Sevilla.

Una vez terminada la interpretación de las trincheras, se ha realizado su **análisis retrodeformacional**, mediante el cual se reconstruye gráficamente la secuencia de deformación invirtiendo el sentido de desplazamiento de las fallas y llevando las unidades estratigráficas a sus posiciones pre-deformación en cada evento (McCalpin, 2009). Este análisis se basa en asumir que originalmente las unidades desplazadas tenían continuidad física, y que las superficies de los niveles de grano fino eran horizontales.

5.5. Valoración del potencial sismogénico

Finalmente, la caracterización del **potencial sismogénico** de las fallas estudiadas (en las secciones II, III, IV y V) se ha realizado mediante diferentes parámetros sintetizados en una tabla recopilatoria (en la sección VI): saltos cosísmicos medios de los máximos terremotos esperables para cada falla (a lo largo de toda su traza), periodos de recurrencia y magnitudes momento máximas. Los saltos cosísmicos se pueden calcular durante el análisis paleosismológico directamente con los datos obtenidos de las trincheras, o bien estimarse haciendo uso de correlaciones empíricas de la literatura que sólo precisan de la geometría superficial de las fallas (obtenida tanto de datos de esta tesis como de trabajos previos). Respecto a los periodos de recurrencia, éstos también se pueden calcular de estas dos maneras: (1) datando paleoterremotos por separado y calculando la duración de los periodos intersísmicos entre ellos (método geológico), (2) obteniendo una recurrencia media para un periodo de movimiento que incorpore varios paleoterremotos y promedie el tiempo transcurrido entre ellos (método directo) (McCalpin, 2009). Por último, las relaciones empíricas también permiten estimar las magnitudes momento de los máximos terremotos generados por las fallas.

Las **regresiones empíricas** utilizadas en esta tesis, para relacionar la longitud de la ruptura superficial (*Surface Rupture Length*, *SRL*) con la magnitud momento (*Moment magnitude*, Mw) o el salto cosísmico medio (*Average Vertical Displacement*, *AVD*) del mayor terremoto generado por ella, son las establecidas por Wells y Coppersmith (1994), Stirling *et al*. (2002), Wesnousky (2008) y Leonard (2010) (Tabla 1.2; los resultados de aplicar dichas regresiones se han sintetizado en la tabla recopilatoria de la sección VI). Estos autores obtienen las relaciones empíricas a partir de las rectas o curvas de regresión que mejor se ajustan a la representación de los datos de longitud de la rupturas superficiales y magnitudes momento de terremotos históricos, ocurridos en diferentes contextos tectónicos y recogidos en diversas bases de datos. Las curvas de regresión de los valores de

Mw y *AVD* incluyen constantes empíricamente inferidas (*a*, *b*, *c* y *d* en Tabla 1.2). Cada autor calcula estas constantes, empleando en sus bases de datos muchas características de las fallas y de los terremotos que generan: contexto tectónico, edad, cantidad, distribución, longitud y tipo de estructuras, entre otros. Las desviaciones medias (σ) de los valores de Mw se incluyen en los resultados de esta tesis. Sin embargo, las desviaciones medias (σ) de los valores de *AVD* implican una horquilla de variación demasiado amplia, que para valores de *AVD* pequeños puede superar incluso a los mismos y, dado que son resultados que pueden considerarse como orientativos, en esta tesis optamos por indicarlos pero no incluirlos en los resultados.

El **método directo** de cálculo del periodo de recurrencia consiste en dividir el valor del salto cosísmico medio por la tasa de desplazamiento cosísmica media (Wallace, 1970). A esta última habría que restarle la tasa de desplazamiento por *creep*, pero para la mayoría de las fallas este valor se considera cero, a no ser que haya documentado *creep* en épocas históricas. En la tabla recopilatoria realizada (sección VI), este método se aplica tanto al salto cosísmico medio obtenido del análisis paleosismológico como al de las correlaciones empíricas anteriormente mencionadas, y siempre usando la tasa neta de desplazamiento desde el Pleistoceno superior. Dado que los saltos cosísmicos medios obtenidos con las correlaciones empíricas no incluyen las desviaciones medias, los periodos de recurrencia calculados con ellos también las arrastran y de nuevo han de considerarse como valores orientativos.

Wells y Coppersmith (1994)	
$M_W = a + b \cdot \log(SRL)$ ($\sigma \approx 0.3$) $\log(AVD) = c + d \cdot \log(SRL)$ ($\sigma \approx 0,4$)	$a = 4.86$ $b = 1.32$ $c = -1,99$ $d = 1,24$

Stirling *et al.* (2002)	
$M_W = a + b \cdot \log(SRL)$ ($\sigma \approx 0.2$) $\log(AVD) = c + d \cdot \log(SRL)$ ($\sigma \approx 0,3$)	$a = 5.89$ $b = 0.79$ $c = -0,09$ $d = 0,35$

Wesnousky (2008)	
$M_W = a + b \cdot \log(SRL)$ ($\sigma \approx 0.3$) $AVD = c \cdot SRL$ ($\sigma \approx 0,8$)	$a = 6.12$ $b = 0.47$ $c = 0,03$

Leonard (2010)	
$M_W = a + b \cdot \log(SRL)$ ($\sigma \approx 0.3$) $\log(AVD) = c + d \cdot \log(SRL)$ ($\sigma \approx 0,2$)	$a = 4.40$ $b = 1.52$ $c = -1,30$ $d = 0,83$

Tabla 1.2.- Correlaciones empíricas empleadas en esta tesis que relacionan los parámetros de las fallas, es decir, la longitud de la ruptura superficial o *SRL*, con los parámetros sísmicos, como son la magnitud momento o Mw y el salto cosísmico medio o *AVD*.
Las constantes *a*-*d* están empíricamente inferidas por cada autor. Se indican las desviaciones medias (σ) de los resultados sísmicos.

A día de hoy, la correlación de Stirling *et al.* (2002) se emplea más comúnmente que la de Wells y Coppersmith (1994) para la mayoría de los contextos tectónicos, ya que esta última subestima los resultados al ser las trazas cartográficas de las fallas en superficie más cortas que la longitud máxima de la superficie de rotura. Sin embargo, de entre las cuatro correlaciones empleadas en esta tesis, Stirling *et al.* (2013), en su trabajo para el *Global Earthquake Model* (*GEM*), recomiendan el uso de la de Wesnousky (2008) para obtener los parámetros sismogénicos de fallas normales de más de 15 km de longitud en contextos intraplaca del tipo *basin and range*, que es el caso de la mayoría de las fallas de la Cordillera ibérica centro-oriental. Muchas de las magnitudes obtenidas mediante este método son menores que las de Stirling *et al.* (2002), ya que tiene en cuenta el principio de que las fallas normales producen magnitudes menores que otros tipos de desplazamientos tectónicos (e.g., Schorlemmer *et al.*, 2005; Stirling *et al.*, 2013). Es por ello que, en esta tesis, para aquellas de más de 15 km, tendremos en cuenta los parámetros sismogénicos obtenidos mediante la regresión empírica de Wesnousky (2008) y se comparará con el rango de los parámetros de las demás regresiones. Para las de menor longitud, se dará únicamente el rango en el que oscilan los parámetros obtenidos mediante todas las relaciones empíricas empleadas.

La última fase del estudio sismogénico de fallas activas sería el **análisis de la peligrosidad sísmica** de la región. En esta tesis esto no se lleva a cabo, pero se hace una comparativa con la información actual de la que se dispone en la base de datos de fallas activas de Iberia (*Quaternary Active Faults Database of Iberia*, *QAFI*; García-Mayordomo *et al*., 2012; IGME, 2022) y en los mapas de peligrosidad sísmica de España (IGN-UPM, 2013; IGN, 2015). Toda la información geológica recogida en esta tesis sienta las bases para la futura aplicación de las herramientas de *Probabilistic Seismic Hazard Assessment* (*PSHA*), en la línea de la nueva norma sismorresistente NCSR-22 (en trámite de aprobación).

CAPÍTULO II.
FALLA DE RÍO GRÍO-PANCRUDO

Resumen:

La sección II aborda las características estructurales, morfotectónicas y paleosismológicas de la zona de falla de Río Grío-Pancrudo (Río Grío-Pancrudo Fault Zone, RPFZ), macroestructura de primer orden que limita la cuenca de Calatayud por el noreste. Las aborda, en un primer apartado, respecto a su segmento norte, aquel que va desde aproximadamente el pueblo de Nigüella hasta Lanzuela y hemos denominado segmento de falla de Río Grío-Lanzuela (Río Grío-Lanzuela Fault Segment, RLFS). En un segundo apartado, profundiza también en su segmento sur, que denominamos de Cucalón-Pancrudo (Cucalón-Pancrudo Fault Segment, CPFS).

El primer apartado se centra mayoritariamente en la configuración, ya publicada, del margen de la cuenca de Calatayud en relación con la RLFS, desde una metodología multidisciplinar en el sector de Codos, y mediante la metodología morfotectónica en todo el límite de cuenca. También presenta resultados preliminares del estudio de la CPFS. El sector de Codos constituye la fuente de información más importante de la RLFS: facetas triangulares, basculamientos del bloque hundido de la falla que han inducido la inversión del drenaje en época plio-cuaternaria, y afloramientos de la zona de falla en contacto con depósitos datados del Pleistoceno superior. El uso de las superficies de erosión regionales como marcadores de la deformación de la RLFS también ha permitido inferir desplazamientos considerables de la misma, en este caso posteriores al Plioceno.

En el segundo apartado se caracteriza la CPFS, empezando por introducir algunos de los aspectos de su pasado contractivo (necesarios para comprender su comportamiento y diferenciar las características asociadas a esta etapa de las de la extensión reciente), y continuando por su análisis morfotectónico, paleosismológico y de afloramientos. Se centra en los sectores de Lagueruela, Sierra Pelarda, Olalla y en zonas puntuales más al sur. Al igual que en el apartado anterior, las superficies de erosión regionales han registrado diferentes desplazamientos post-pliocenos a lo largo de la traza de la CPFS. Algunos afloramientos de la falla que llegan a poner en contacto depósitos cuaternarios con el basamento paleozoico evidencian su continuidad en el sector central y, en afloramientos diferentes, hacia el sur. La trinchera de Lagueruela expone rupturas que afectan a unidades holocenas, y su estudio ha permitido obtener sus características sismológicas y un primer registro paleosismológico de la CPFS para el periodo cuaternario. Este apartado al completo está escrito en inglés para, próximamente, ampliar la información contenida en él, preparar su publicación y enviarla.

Tanto en este apartado como en el anterior, se contextualiza la actividad de los segmentos de falla en el marco tectónico regional. Si se quiere consultar todos los valores inferidos relacionados con sus geometrías, tasas de desplazamiento y potencial sismogénico, se puede acudir a la tabla de la sección VI.

Geological Magazine

www.cambridge.org/geo

The Río Grío–Pancrudo Fault Zone (central Iberian Chain, Spain): recent extensional activity revealed by drainage reversal

Alba Peiro and José L. Simón

Dpto Ciencias de la Tierra, Grupo Geotransfer-IUCA, Universidad de Zaragoza, Pedro Cerbuna 12, 50009 Zaragoza, Spain

Original Article

Cite this article: Peiro A and Simón JL. The Río Grío–Pancrudo Fault Zone (central Iberian Chain, Spain): recent extensional activity revealed by drainage reversal. *Geological Magazine* https://doi.org/10.1017/S0016756821000790

Received: 7 January 2021
Revised: 7 July 2021
Accepted: 12 July 2021

Keywords:
Calatayud Basin; recent fault; active fault; tectonic geomorphology; planation surface; Plio-Quaternary; slip rate

Author for correspondence:
Alba Peiro, Email: apeiro@unizar.es

Abstract

The NNW–SSE-trending extensional Río Grío–Pancrudo Fault Zone is a large-scale structure that obliquely cuts the Neogene NW–SE Calatayud Basin. Its negative inversion during the Neogene–Quaternary extension gave rise to structural and geomorphological rearrangement of the basin margin. Geological mapping has allowed two right-relayed fault segments to be distinguished, whose recent extensional activity has been mainly characterized using a deformed planation surface (Fundamental Erosion Surface (FES) 3; 3.5 Ma) as a geomorphic marker. Normal slip along the Río Grío–Lanzuela Fault Segment has induced hanging-wall tilting, subsequent drainage reversal at the Güeimil valley after the Pliocene–Pleistocene transition, as well as morphological scarps and surficial ruptures in Pleistocene materials. In this sector, an offset of FES3 indicates a total throw of *c.* 240 m, resulting in a slip rate of 0.07 mm a^{-1}, while retrodeformation of hanging-wall tilting affecting a younger piedmont surface allows the calculation of a minimum throw in the range of 140–220 m after the Pliocene–Pleistocene transition, with a minimum slip rate of 0.07–0.11 mm a^{-1}. For the late Pleistocene period, vertical displacement of *c.* 20 m of a sedimentary level dated to 66.6 ± 6.5 ka yields a slip rate approaching 0.30–0.36 mm a^{-1}. At the Cucalón–Pancrudo Fault Segment, the offset of FES3 allows the calculation of a maximum vertical slip of 300 m for the last 3.5 Ma, and hence a net slip rate close to 0.09 mm a^{-1}. Totalling *c.* 88 km in length, the Río Grío–Pancrudo Fault Zone could be the largest recent macrostructure in the Iberian Chain, probably active, with the corresponding undeniable seismogenic potential.

1. Introduction

Recent tectonics can be revealed not only by direct observation of ruptures at the surface, but also by its imprint on landforms. Morphotectonics provides valuable information about the mechanisms responsible for deformation of the topography, and can decipher their relationship with crust uplift and subsidence due to folding or faulting (e.g. Ollier, 1981; Keller, 1986; Burbank & Anderson, 2012). In this way, geomorphological analysis contributes to the identification and mapping of active or recent faults, and therefore to the recognition of seismic sources and evaluate seismic hazard.

Some landforms, either planar (planation surfaces) or linear (shorelines, river terraces) can be used as direct markers of deformation. Their geometrical reconstruction, on maps or profiles, allows the quantification of fault displacement or overall relief uplift, while their dating permits the calculation of deformation rates (Bonow *et al.* 2006; Wagner *et al.* 2011; Ezquerro *et al.* 2020). In other cases, the tectonic signature on the landscape is subtler, and only qualitative diagnosis of recent tectonic movements can be achieved; drainage anomalies mostly fall within this category of evidence (Leeder & Jackson, 1993; Jackson *et al.* 1996; Goldsworthy & Jackson, 2000). Drainage reversal is a geomorphic sign that has been associated with extensional faulting and tilting in regions such as the East African Rift Valley (Ollier, 1981, pp. 175–6), the Tasman Sea rifting (Haworth & Ollier, 1992) or the Megara Basin in Greece (Leeder *et al.* 1991). In the latter, the present-day, S-flowing drainage pattern resulted from recent reversal; the previous N-flowing drainage system has been evinced by drainage and palaeocurrent analysis (Bentham *et al.* 1991).

The gentle relief of the central-eastern Iberian Chain (NE Spain), where relict landforms of diverse ages have been well preserved, provides an excellent laboratory for studying the interaction between tectonic and geomorphologic processes. Recent tectonic activity and seismicity of this intraplate region has been traditionally considered as low to moderate. It has been driven by extension linked to rifting of the Valencia Trough (Vegas *et al.* 1979; Roca & Guimerà, 1992), combined with crustal doming (Simón, 1982, 1989; Scotti *et al.* 2014). Since late Miocene time, the prevailing extension direction has changed from WNW–ESE to WSW–ENE (Simón, 1989), the latter being active up to the present day (Herraiz *et al.* 2000).

© The Author(s), 2021. Published by Cambridge University Press.

Downloaded from https://www.cambridge.org/core. Universidad de Zaragoza, on 04 Oct 2021 at 10:24:00, subject to the Cambridge Core terms of use, available at https://www.cambridge.org/core/terms. https://doi.org/10.1017/S0016756821000790

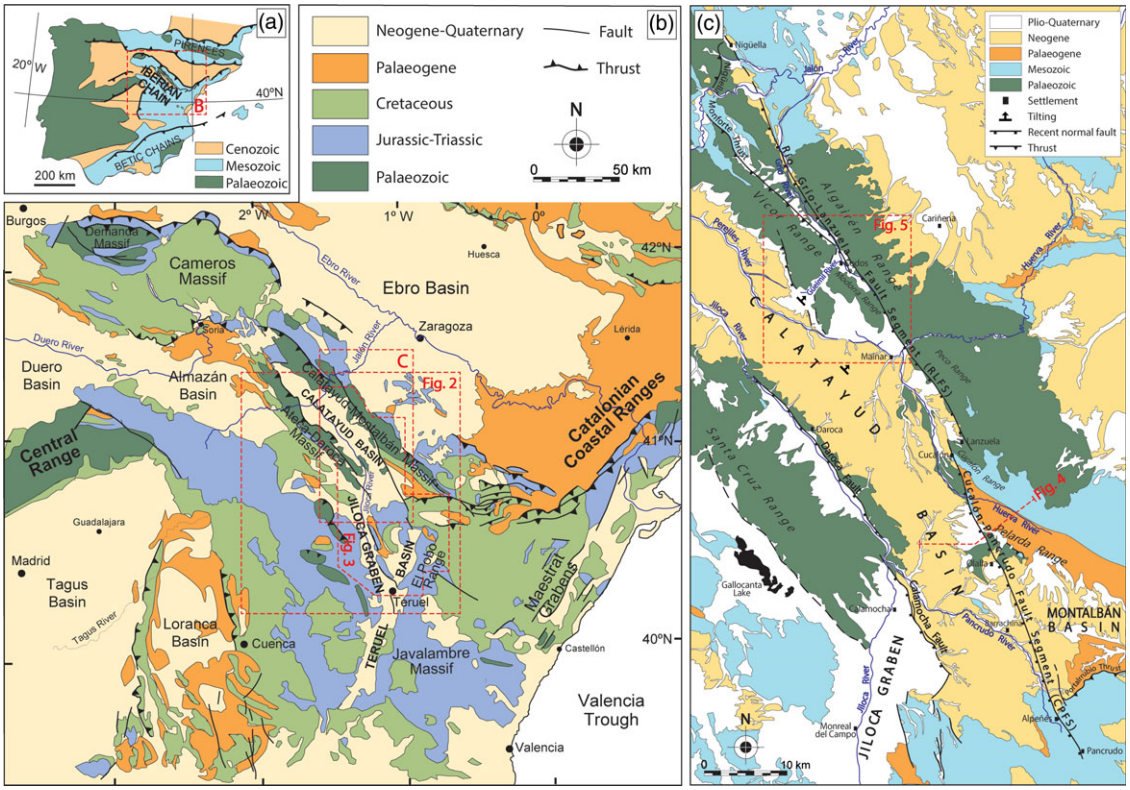

Fig. 1. (Colour online) (a) Location of the Iberian Chain within the Iberian Peninsula. (b) Geological sketch of the Iberian Chain, with location of the main Neogene–Quaternary extensional basins. (c) Geological map of the Río Grío–Pancrudo Fault Zone at the NE margin of the Neogene Calatayud Basin, with location of Figures 2–5.

Onshore extensional deformation has been accommodated by a number of large faults that bound grabens and half-grabens orthogonal to such extension directions: NNE–SSW (e.g. Teruel and Maestrat basins) and NNW–SSE (e.g. Jiloca Basin) (Fig. 1b). Recent (late Pliocene – Quaternary) activity of some of these faults (e.g. Concud, Sierra Palomera, Calamocha, Daroca, El Pobo, Peralejos, Teruel, La Hita and Valdecebro faults) has been characterized during the last decades from both structural and morphotectonic data. The contribution of late Neogene planation surfaces as widespread regional markers, allowing the calculation of fault throws and slip rates, has been decisive with this respect. These faults are modest in size, with lengths ranging from 5 to 19 km, maximum net displacements of 180–620 m and slip rates of 0.05–0.16 mm a^{-1} for the last 3.8 Ma (Rubio & Simón, 2007; Lafuente *et al.* 2014; Simón *et al.* 2017, 2019; Ezquerro *et al.* 2020). Since late Miocene – Quaternary times, a tendency for the progressive concentration of crustal deformation on a smaller number of faults has been inferred, while those that remain active increase their slip rate (Simón *et al.* 2012; Ezquerro *et al.* 2020).

In parallel to such tectonic evolution and overall uplift, the region has undergone transition from endorheic to exorheic conditions, that is, from internal drainage paths, guided by the Neogene intramontane basins, towards external drainage guided by the large, peripheral fluvial systems (mostly Ebro, Tagus, Júcar and Turia rivers). Such transition was modulated by local interaction of rivers with faults and tilted blocks. Examples of river capture and river beheading of tectonic origin have been mostly described at the easternmost Iberian Chain, where the onset of a new drainage network oriented towards the Mediterranean Sea interacted with the development of the conspicuous, NNE–SSW-trending Maestrat horst-and-graben system (Mateu, 1982; Pérez & Simón, 1993; Simón *et al.* 2013).

In this paper, we characterize a large recent extensional structure, very probably active, in a location further inland than those previously described in the Iberian Chain. It is here defined as the Río Grío–Pancrudo Fault Zone, comprising two segments separated by a narrow relay zone: Río Grío–Lanzuela (RLFS) and Cucalón–Pancrudo (CPFS). Its NNW–SSE-trending, 88-km-long trace cuts or bounds diverse geological domains (Calatayud–Montalbán Variscan folded block, Calatayud Cenozoic Basin, Alpine Utrillas Thrust), in which it has been locally identified using different names: Olalla Fault (Gabaldón *et al.* 1991), Alpeñés Fault (Tena & Casas, 1996), part of an interpreted Río Grío graben (Gutiérrez *et al.* 2013) or just the Río Grío Fault (Campos *et al.* 1996; Marcén, 2020). Its complex history since Variscan time, as well as the fragmented character of previous research, has prevented its identification as a single Neogene–Quaternary extensional structure (probably the largest within the Iberian Chain). Consequently, it has not received the attention that it merits as a potential first-order seismic source.

The purpose of this work is to shed some light on a series of ruptures, with diverse geological nature and history, that jointly define the Río Grío–Pancrudo Fault Zone. Because of the absence of widespread recent stratigraphic markers and the scarcity of outcrops where surface ruptures are exposed, the study of this large recent structure requires a geomorphological approach in addition to a purely structural approach. Our aims are to: (1) demonstrate Quaternary activity of the Río Grío–Pancrudo Fault Zone based on morphotectonic criteria, in particular using middle Pliocene – lower Pleistocene planation and pediment surfaces as deformation markers, and analyse two noteworthy cases of drainage reversal in

Downloaded from https://www.cambridge.org/core. Universidad de Zaragoza, on 04 Oct 2021 at 10:24:00, subject to the Cambridge Core terms of use, available at https://www.cambridge.org/core/terms. https://doi.org/10.1017/S0016756821000790

the framework of the regional transition from endorheism to exorheism; (2) achieve structural analysis of surficial ruptures along the RLFS (where the recent structure reactivates previous faults), discriminating between the kinematical imprint of contractive and extensional stages; and (3) infer fault throws and slip rates for distinct Plio-Quaternary time spans at the centre of the RLFS (Codos area) and in the CPFS (Cucalón–Olalla area).

2. Methods

The reconstruction of geomorphic markers and drainage anomalies are analysed using both geomorphological and sedimentological observations along the Río Grío–Pancrudo Fault Zone, while direct structural data at an outcrop scale allow us to characterize the geometry and kinematics of the RLFS. A detailed geological and geomorphological map has been constructed with the help of published maps at a 1:50 000 scale (Olivé *et al.* 1983), aerial photographs at a 1:30 000 scale, satellite orthoimages, digital elevation models (DEMs; pixel dimension 2 m) and the resulting hillshade images, and a field survey.

Palaeocurrent directions represent key data for demonstrating changes in fluvial patterns. The involved upper Pliocene and Pleistocene alluvial and fluvial sediments are mainly composed of gravel. In the absence of adequate three-dimensional (3D) exposures of sedimentary structures, such as channel bodies or cross-bedding, well defined sets of imbricated pebbles have allowed palaeocurrent directions to be interpreted at nine data sites. At each of these, 6–35 orientation data (average 16) of nearly plane pebble faces have been collected. The azimuth opposed to the average dip line of each imbricate pebble set has been taken as the local palaeocurrent direction.

Two good exposures of the damage zone at the trace of the RLFS have been surveyed. Data describing the orientation of rupture surfaces and associated kinematical indicators (slickenlines and small-scale drag folds) have been extracted from Palaeozoic materials of the footwall block. Two Pleistocene units affected by the fault zone at one of those localities have been dated by optically stimulated luminiscence (OSL) in the Luminiscence Dating Laboratory of Centro Nacional de Investigación de La Evolución Humana (CENIEH). Rose diagrams of palaeocurrents and stereoplots (equal-area, lower-hemisphere) of faults and slickenlines have been constructed using Stereonet 8 software (Allmendinger *et al.* 2012; Cardozo & Allmendinger, 2013).

In order to calculate vertical displacements of faults and infer net slip values, we have reconstructed the present-day geometry of Late Neogene planation surfaces and Plio-Pleistocene pediments offset by them. Maps of surface remnants were constructed using aerial photographs, topographic maps and DEMs, and the altitude of these remnants were interpolated for obtaining contour maps. The age of such morpho-sedimentary markers allows the calculation of fault slip rates. Further details on methodological problems concerning the use of planation surfaces as deformation markers are given in Section 4.a.

3. Geological setting

The Iberian Chain (Fig. 1a, b) is an intraplate, NW–SE-trending mountain chain located within the Iberian Plate, which developed during Cenozoic time under convergence with the European and African plates (Álvaro *et al.* 1979; Capote *et al.* 2002). It mainly resulted from inversion of several Mesozoic sedimentary basins, but also a thick succession of Palaeozoic units (up to 11 km; Cortés-Gracia & Casas-Sainz, 1996) was re-folded in its central zone. In this sector, two elongated Palaeozoic-cored structural highs, the Calatayud–Montalbán and the Ateca–Daroca massifs, are separated by the NW–SE-trending Neogene Calatayud Basin (Fig. 1b, c).

The sinking of the Calatayud Basin (Fig. 1c) initiated under late stages of the Alpine compression during the Palaeogene–Neogene transition. The tectonic nature of the NE basin boundary is not well known because it is entirely covered by recent (Pliocene and Quaternary) alluvial deposits, but its SW boundary is an unequivocal contractive structure. At least in its central sector (Daroca area), Cambrian rocks overthrust lower Miocene continental deposits of the basin infill, while younger, middle–upper Miocene units lap onto the thrust front (Julivert, 1954; Colomer, unpub. thesis, University of Barcelona, 1987; Colomer & Santanach, 1988; Casas *et al.* 2017).

At the beginning of late Miocene time, the central-eastern Iberian Chain underwent an extensional tectonic period associated with rifting of the Valencia Trough (Vegas *et al.* 1979; Simón 1982; Roca & Guimerà 1992; Maillard & Mauffret, 1999; Fig. 1b). Onshore deformation is expressed by a large network of Neogene–Quaternary basins (Teruel, Jiloca, Munébrega, Maestrat), whose bounding faults mostly represent the negative inversion of previous compressional faults (Álvaro *et al.* 1979; Fig. 1b). The Calatayud Basin underwent reactivation of faults at its NE boundary (supposedly dipping towards the SW), downthrowing the Neogene infill. At the SW margin, the deeper part of the reverse Daroca fault was inverted during late Pliocene–Pleistocene time, giving rise to the Calamocha–Daroca extensional fault zone (Fig. 1c). The latter sinks the northern sector of the Jiloca graben and the Daroca half-graben with respect to the Neogene infill of the Calatayud Basin. Its throw has been estimated in the range of 210–250 m for the Calamocha rupture, by considering the offset of the uppermost, middle Pliocene lacustrine unit of the basin (Julivert, 1954; Colomer & Santanach, 1988; Gracia, 1992; Gutiérrez *et al.* 2008; Martín-Bello *et al.* 2014). The structure of the Calatayud Basin is similar to the neighbouring Daroca and Gallocanta half-grabens (Fig. 1c), with their respective faults at their NE margins. It all gives rise to a stepped profile of adjacent basins, with their infill tilted in the hanging-wall blocks of extensional faults.

During Neogene–Quaternary times, the regional stress field has evolved from (1) uniaxial extension with WNW–ESE-trending σ_3 trajectories during a first extensional episode (late Miocene – early Pliocene), to (2) nearly biaxial or radial extension (σ_1 vertical, $\sigma_2 \approx \sigma_3$) with σ_3 trending nearly WSW–ENE during a second episode (late Pliocene – Quaternary) (Simón, 1989; Arlegui *et al.* 2005; Liesa *et al.* 2019).

Under both compressional and extensional regimes, tectonic subsidence of the Calatayud Basin allowed the most complete Neogene series in the Iberian Chain to accumulate (Anadón *et al.* 2004). The sedimentary record consists of clastic alluvial sediments sourced at the basin margins, which grade towards central sectors into lacustrine–palustrine environments characterized by both evaporite and carbonate sedimentation (Gabaldón *et al.* 1991; Sanz-Rubio, 1999; Sanz-Rubio *et al.* 2003). Endorheic sedimentation culminates with a thin sequence of lower Pliocene palustrine carbonates (Páramo 2 unit) (Gabaldón *et al.* 1991; Anadón *et al.* 2004).

The geomorphological evolution of the central-eastern Iberian Chain includes several episodes of relief planation. The main episode has been classically referred to the so-called Fundamental

Downloaded from https://www.cambridge.org/core. Universidad de Zaragoza, on 04 Oct 2021 at 10:24:00, subject to the Cambridge Core terms of use, available at https://www.cambridge.org/core/terms. https://doi.org/10.1017/S0016756821000790

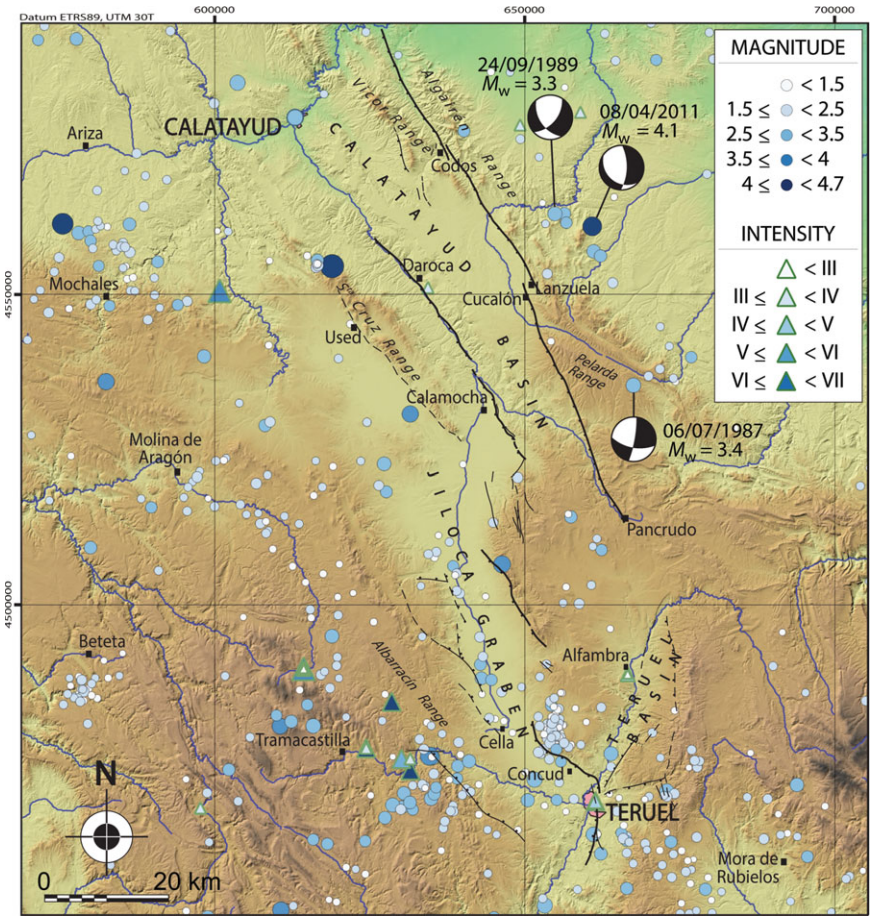

Fig. 2. (Colour online) Epicentre map of historic and instrumental earthquakes in the neighbourhood of the Calatayud Basin (https://www.ign.es/web/ign/portal/sis-catalogo-terremotos).

Erosion Surface (FES; Peña *et al.* 1984), and was traditionally correlated with the end of the endorheic filling of the Calatayud and Teruel basins (e.g. Simón, 1982). This surface has been recently divided into three sublevels, FES Upper Sublevel (FES1), FES *sensu stricto* (FES2) and FES Lower Sublevel (FES3), which in turn have allowed for finer physical correlation with sedimentary units, as well as more precise dating of planation episodes based on robust biostratigraphic and magnetostratigraphic data (Ezquerro, 2017; Simón-Porcar *et al.* 2019; Ezquerro *et al.* 2020). In this way, the age of FES3 is well constrained to the top of the M8 megasequence defined by Ezquerro (2017) (equivalent to the upper part of Páramo 2 unit; early Villafranchian in age; mammal biozone MN16; towards the base of chron C2An.3n; 3.5 Ma), while FES1 and FES2 merge into the top of M7 (lower part of Páramo 2 unit; late Ruscinian in age; MN15; middle part of C2Ar; 3.8 Ma) (Ezquerro *et al.* 2020). FES3 is overlaid by a Villafranchian (Pliocene–Pleistocene transition) alluvial system, comprising gravel and silt, that extends over most of the Neogene basins. The Villafranchian pediments of the Teruel area are dated to the earliest Pleistocene by macromammal fauna (Adrover, 1975; MN17 zone, 2.6–1.9 Ma) and, more accurately, by magnetostratigraphy (2.1–1.95 Ma; Sinusía *et al.* 2004).

The transition from endorheic to exorheic conditions in the study area is associated with the capture process of the Calatayud Basin. According to morphological and stratigraphical evidence, this is a diachronic process active since late Miocene time, which started with the capture of a primitive Jalón river NW of the Algairén and Vicor Ranges (Gutiérrez *et al.* 1996, 2008, 2020; Fig. 1c). The Villafranchian pediments that spread towards the basin do not necessarily represent this rearrangement (Gutiérrez *et al.* 1996, 2008), since alluvial systems laterally grading into endorheic palustrine areas have been documented from early Pleistocene times, for example, in the Teruel area (Ezquerro *et al.* 2012), and have even persisted to the present in the Gallocanta depression (Gutiérrez *et al.* 1996) and the southern Jiloca Basin (El Cañizar lake; Rubio, 2004; Rubio & Simón, 2007). The Jiloca river, the main tributary of the Jalón river, captured the Jiloca graben during early Pleistocene time (Gutiérrez *et al.* 1996, 2008, 2020; Vacherat *et al.* 2018), becoming the longitudinal drainage of the Calatayud Basin, together with the primitive Perejiles and Grío rivers (Fig. 1c). During late Pleistocene time, part of the Calatayud Basin was also captured by the Huerva river (Gutiérrez *et al.* 2008). This progressive transition to exorheic conditions is overall controlled by the base-level drop of the Ebro river, although locally influenced by tectonic activity.

Historical and instrumental seismicity of the region is low to moderate (Fig. 2). Epicentres are concentrated close to the western margin of the Jiloca graben, in the relay zone between Concud and Sierra Palomera faults, and in the western margin of the Calatayud Basin (https://www.ign.es/web/ign/portal/sis-catalogo-terremotos). No significant epicentre clustering occurs along the Río Grío–Pancrudo Fault Zone, the southern sector of the Calatayud Basin or the northern sector of the Jiloca graben (Fig. 1c). Before the instrumental period (maximum magnitude $M =$ 4.4), intensities

Downloaded from https://www.cambridge.org/core. Universidad de Zaragoza, on 04 Oct 2021 at 10:24:00, subject to the Cambridge Core terms of use, available at https://www.cambridge.org/core/terms. https://doi.org/10.1017/S0016756821000790

up to VI–VII were recorded in the Albarracín range (1848) and IV–V in the Jiloca graben (1828). Focal depths typically range from 5 to 15 km, that is, within the brittle crust above the basal detachment level identified by Roca & Guimerà (1992). Most of the available focal mechanisms correspond to normal faults, and are consistent with the WSW–ENE-σ_3-trending trajectories of the regional active stress field (Herraiz *et al.* 2000).

4. The Río Grío–Pancrudo Fault Zone: general structure and evidence of recent activity

4.a. Morphotectonic overview based on analysis of planation surfaces

Late Neogene planation surfaces have been recurrently used in the Iberian Chain for both identifying recent structures and assessing their vertical offsets and deformation rates (e.g. Peña *et al.* 1984; Gracia *et al.* 1988; Ezquerro *et al.* 2020). In our case, FES2 and FES3 surfaces and their coeval sedimentary levels provide potentially useful, mixed geomorphic–stratigraphic markers for this purpose, by allowing the construction of their corresponding structural contour maps.

Two main challenges have to be faced: constraining the age of each geomorphological marker, and ensuring its degree of flatness. The first issue has been adequately discussed and established in Section 3: FES2 and FES3 surfaces have been precisely dated to 3.8 and 3.5 Ma, respectively. The second issue should be justified, since continental planation surfaces can show gentle (short- to middle-wavelength) unevenness, or locally connect with residual, non-flattened reliefs through pediment slopes. Simón (1982, 1989) discussed this problem for the FES surface, recognizing that the amplitude of its unevenness meant that widely spaced contours (100 m) were required to represent its present-day geometry with adequate precision. At present, we realize that such an amplitude spans different sublevels that had not been recognized at that time; both the local difference in height between FES2 and FES3 and the local unevenness within each sublevel usually lies within the range 10–40 m. In consequence, we assume that: (1) vertical fault throws calculated from these sublevels implicitly include a maximum error bar of ± 40 m; and (2) a 50 m spaced contour map fits the precision of the actual roughness of FES2 and FES3 markers well, and can therefore be considered as reasonable for assessing recent movements (as previously proposed by Ezquerro *et al.* 2020). Such a level of uncertainty in the calculated fault throws results in errors for slip rates of *c.* 0.01 mm a^{-1}.

Such morphotectonic analysis should be primarily based on maps of planation surfaces covering large areas. In order to provide an overall morphotectonic view of the Río Grío–Pancrudo Fault Zone, we have synthesized several published maps in the Teruel region (Simón-Porcar *et al.* 2019; Ezquerro *et al.* 2020), as well as other maps constructed during our current research in the Jiloca and Calatayud basins. The result is shown in Figure 3, in which the (1) remains of several planation surfaces, (2) recent faults offsetting them and (3) contours of FES2 and FES3 depicting their present-day configuration jointly provide the best overall approach to describe the geometry of Plio-Quaternary deformation structures. FES2 contours have been drawn for the southern sector of the region, where the planation surface is better represented, while FES3 contours have been chosen for the northern sector. Despite such a difference, the systematic and continuous mapping over the entire region has ensured: (1) reliable identification of each erosion level, (2) age anchoring based on correlation with sedimentary units in the Teruel Basin (see Section 3) and (c) an overview of the large-scale morphostructure.

4.b. Río Grío area

The northernmost RLFS crops out nearly parallel to the Grío river (Figs 1c, 3). It represents the negative inversion of the Variscan Nigüella–Monforte Thrust, then reactivated as a transpressive structure during Palaeogene compression (Marcén & Román-Berdiel, 2015; Casas *et al.* 2016; Marcén, 2020), with occasionally coinciding rupture traces. Its recent extensional activity is revealed in different sectors of the Codos area, as extensively described in Section 5 and evidenced by: (1) tilting of the hanging wall deforming the FES3 and the Villafranchian pediment, (2) consequent post-Villafranchian drainage reversal and (3) local exposure of ruptures in Quaternary deposits.

4.c. Mainar–Lanzuela area

The prolongation of the RLFS to the SSE of the Grío river is clearly aligned with the NE margin of the Calatayud Basin, flanked by the Palaeozoic-cored Algairén and Peco Ranges (Figs 1c, 3). Both the Neogene series of the basin infill and FES3 are affected by a gentle, uniform tilting towards the structural highs. An extensional movement of the RLFS, similar to that registered at the Río Grío area, is inferred from this tilting. No outcrop of the fault trace has been found within this basin margin, partly because of the ensemble of Quaternary alluvial fans and pediments that overlies it. Nevertheless, the straight character of the contact between the lithological domains along the basin margin allows the fault trace to be identified. Near Lanzuela, an en échelon, right-relay arrangement occurs between the RLFS and the CPFS. The spacing between these is 2 km, with an overlap of less than 2 km. The offset of the FES3 in this area allows a maximum vertical displacement of about 200 m to be inferred (Fig. 3).

4.d. Cucalón–Olalla area

South of Cucalón, the CPFS shows noticeable features of contractive deformation in the form of tight, hectometre-scale folds affecting the Palaeogene series of the Montalbán Basin (Figs 1c, 3). This series is abruptly interrupted by the fault, and a wide Quaternary alluvial fan that spreads from the fault zone towards the centre of the Calatayud Basin is indicative of recent activity.

Nevertheless, it is not easy to calculate precisely the amplitude and age of its vertical displacement because of uncertainties in the composition and morphostructure of both the footwall and the hanging-wall block in this sector. A key piece of evidence is a striking conglomerate unit, comprising rounded cobbles and boulders of Palaeozoic quartzite and Lower Triassic sandstone, which crops out at the highest part of this block (Pelarda Range summits, up to 1510 m in height; Fig. 1c). Its anomalous elevation and origin have been the objective of many conjectures, and the low quality of outcrops makes its characterization difficult. Maps published by the Spanish geological survey (IGME; Martín *et al.* 1977; Gabaldón *et al.* 1989*a*, 1991) indicate that it represents a nearly horizontal Plio-Quaternary unit that unconformably overlies the Palaeogene series; a thickness of *c.* 150 m could be inferred from those maps. In contrast, Moissenet (1980), Adrover *et al.* (1982) and Pailhé (1984) consider that it comprises a part of that folded Palaeogene series, then partially levelled by a late Neogene planation surface and uplifted by the extensional displacement of the

Downloaded from https://www.cambridge.org/core. Universidad de Zaragoza, on 04 Oct 2021 at 10:24:00, subject to the Cambridge Core terms of use, available at https://www.cambridge.org/core/terms. https://doi.org/10.1017/S0016756821000790

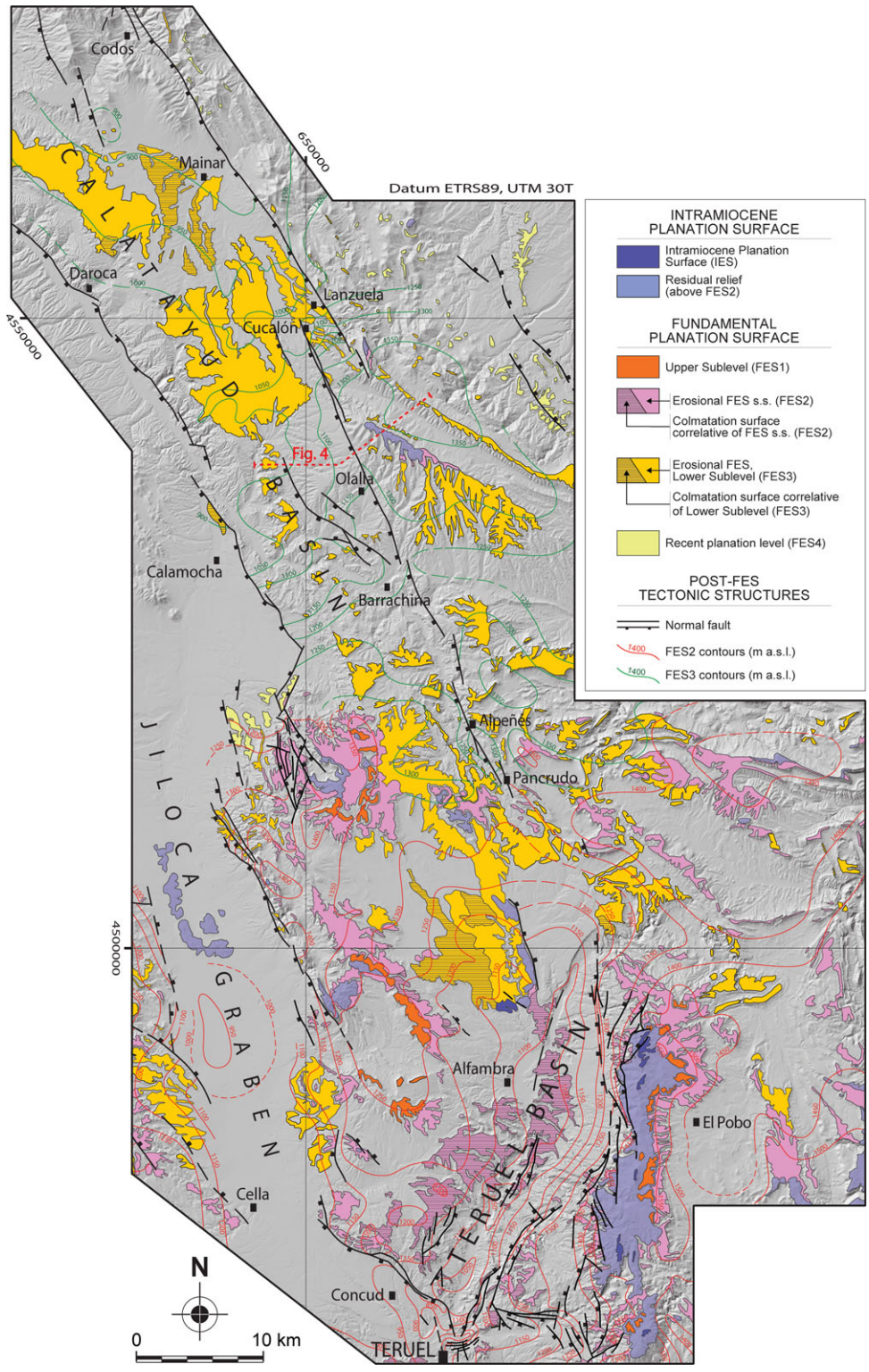

Fig. 3. (Colour online) Synthetic map of late Neogene planation surfaces in the surroundings of the Calatayud, Jiloca and Teruel basins, with location of Figure 4.

Cucalón–Olalla fault. The prominent Pelarda Range would represent a residual relief standing out above such a planation surface.

Recent and preliminary research conducted at the Pelarda Range revealed evidence in favour of the second interpretation (Fig. 4a, b). The quartzitic conglomerates probably correspond to the Oligocene Epoch (more specifically, to the upper part of unit T3 defined by Pérez *et al.* 1983), since bedding planes and several occasional interbedded mud and sand layers above 1450 m above sea level (asl) are tilted similarly to the underlying Palaeogene series and show continuity with the latter. More recent deposits are limited to a thin (1–5 m) surficial cover mostly consisting of the same quartzitic cobbles and boulders reworked from the underlying Palaeogene strata. Such sedimentary cover is linked

Downloaded from https://www.cambridge.org/core. Universidad de Zaragoza, on 04 Oct 2021 at 10:24:00, subject to the Cambridge Core terms of use, available at https://www.cambridge.org/core/terms. https://doi.org/10.1017/S0016756821000790

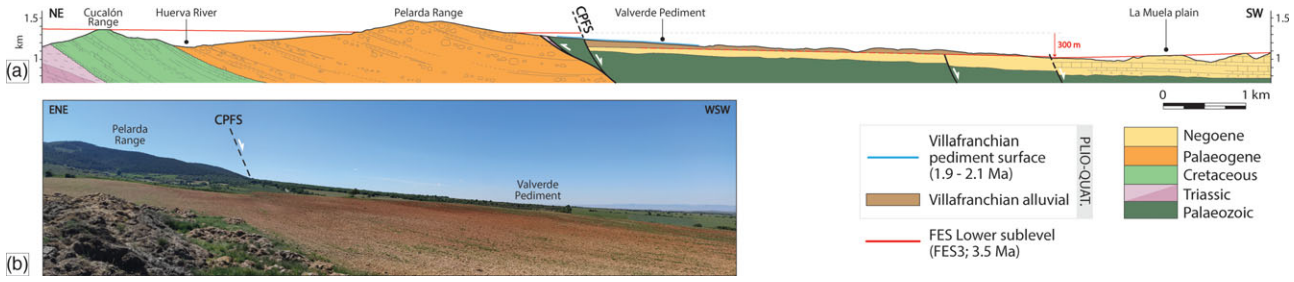

Fig. 4. (Colour online) (a) Cross-section through the Cucalón–Pancrudo Fault Segment (CPFS) at the Pelarda Range. Offset of the late Neogene planation surface (FES3) is indicated (see location in Figs 1c, 3). (b) Field view of the Pelarda Range mountain front.

to the FES3 planation surface, widely developed in the form of an extensive pediment (present-day mean slope *c.* 1.4°) lying between 1250 and 1390 m asl. Above this planation level, reduced remains of FES2 are preserved at 1400–1420 m, while the highest Pelarda summits, between 1420 and 1510 m, represent residual reliefs (Figs 3, 4a, b).

According to our present knowledge, the Neogene FES3 planation surface constitutes the only available deformation marker to obtain an overall estimate of post-3.5 Ma displacement on the fault zone. In the footwall block, at the western Pelarda Range transect (Figs 3, 4a), the remains of FES3 lie at 1320 m asl. In the hanging-wall block of the westernmost fault, FES3 is developed on Neogene materials of the Calatayud Basin, and to the NE of Daroca it correlates with the most recent lacustrine level capping the sedimentary sequence, analogue to that of the Teruel Basin (upper Páramo 2, Olivé *et al.* 1983; equivalent to M8 megasequence of Ezquerro, 2017; 3.5 Ma). Within this hanging-wall block, FES3 is downthrown to 1020–1030 m and is covered by red clastic deposits associated with a Villafranchian pediment. The overall fault zone has therefore undergone a total vertical offset of *c.* 300 m (the higher vertical offset recorded along the Río Grío–Pancrudo Fault Zone), partitioned among net slip on the faults depicted in Figure 4a and a gentle accommodation monocline. Assuming an approximate fault dip of 67° (which is similar to the average dip calculated for the RLFS, and lie within the 65–70° range of average dips for the main normal faults of the northern Teruel Basin; Ezquerro *et al.* 2020), its net slip for the last 3.5 Ma approaches 325 m, and its slip rate is *c.* 0.09 mm a^{-1}.

4.e. Barrachina area

The fault trace in this area is revealed by a succession of ruptures, not fully connected but markedly aligned. All of them cut and offset the Miocene and Pliocene carbonate units of the Calatayud Basin (Figs 1C, 3). Vertical offsets in the range of 50–120 m can be inferred for the FES3 surface.

4.f. Alpeñés–Pancrudo area

The CPFS shows visible contractive deformation (with a visible strike-slip component; Guimerà, 1988; Tena & Casas, 1996) in this area. It represents the limit where the Utrillas Thrust, in particular its western segment (Portalrrubio Thrust) is interrupted (Figs 1c, 3). Its recent extensional activation is not so evident. Once again, deformation registered by the FES3 has allowed a maximum vertical offset of about 100 m to be determined in this sector.

5. Detailed study at the Codos area

5.a. Morphostructure

The Codos area is located at the boundary between the central sector of the Calatayud Basin and the Calatayud–Montalbán massif (Figs 1c, 5). Crustal-scale thrusts and strike-slip faults inherited from Variscan and late Variscan tectonic periods, roughly parallel to the structural grain (NW–SE), are recognized within it (Cortés-Gracia & Casas-Sainz, 1996; de Vicente *et al.* 2009). The main Variscan structure is the Nigüella–Monforte Thrust (Figs 1c, 5; Casas *et al.* 2016), formerly referred as Datos Thrust (Calvín-Ballester & Casas, 2014). The RLFS probably originated as a strike-slip fault during late Variscan stages, and obliquely cuts the Nigüella–Monforte Thrust (Figs 1c, 5). Both structures partially share the rupture trace, but are distinguishable because the latter: (1) trends closer to NNW–SSE, (2) has a more pronounced dip and (3) shows noticeably thick fault rock bodies, especially at its northern sector (Casas *et al.* 2016). During the Palaeogene Period, the RLFS was reactivated as a dextral transpressive structure under the Alpine compression (variably oriented between N–S and NE–SW), giving rise to a complex internal structure made of anastomosing lenses of Ordovician and Triassic rocks exhibiting tight folds, pervasive foliation, fault breccia and fault gouge (Marcén & Román-Berdiel, 2015; Marcén, 2020).

The imprint of the Neogene negative inversion of the RLFS is much less noticeable than that of the contractive structure. The only macrostructural deformation feature extensively recognizable in geologic materials is gentle tilting of the Calatayud Basin Neogene infill towards the NE (Moissenet, 1980), particularly visible in the uppermost lacustrine carbonates (Páramo 1 and Páramo 2 units, early Pliocene in age; Olivé *et al.* 1983; Fig. 1c). Such tilting apparently represents roll-over accommodation of the hanging-wall block of the RLFS and Espigar fault, which jointly make the northeastern boundary of the Calatayud Basin in this sector (Figs 1c, 5).

As stated above, further evidence of recent fault activity can be expected from landforms. The bottom of the Calatayud Basin shows extensive remains of FES3 either topping the Páramo 2 carbonates or subtly cutting underlying Pliocene units (Figs 3, 5). Along the southern part of the study area, its altitude diminishes E-wards from about 950 up to 890 m asl, affected by the same tilting (*c.* 0.3°) already described for the Neogene units. The Villafranchian alluvial system is here associated with a wide embayment in the Espigar mountain front, NW of Langa del Castillo village (Campillo Plain, Fig. 5). Finally, both FES3 and the Villafranchian alluvium are incised by the drainage network tributary of the Perejiles river.

Downloaded from https://www.cambridge.org/core. Universidad de Zaragoza, on 04 Oct 2021 at 10:24:00, subject to the Cambridge Core terms of use, available at https://www.cambridge.org/core/terms. https://doi.org/10.1017/S0016756821000790

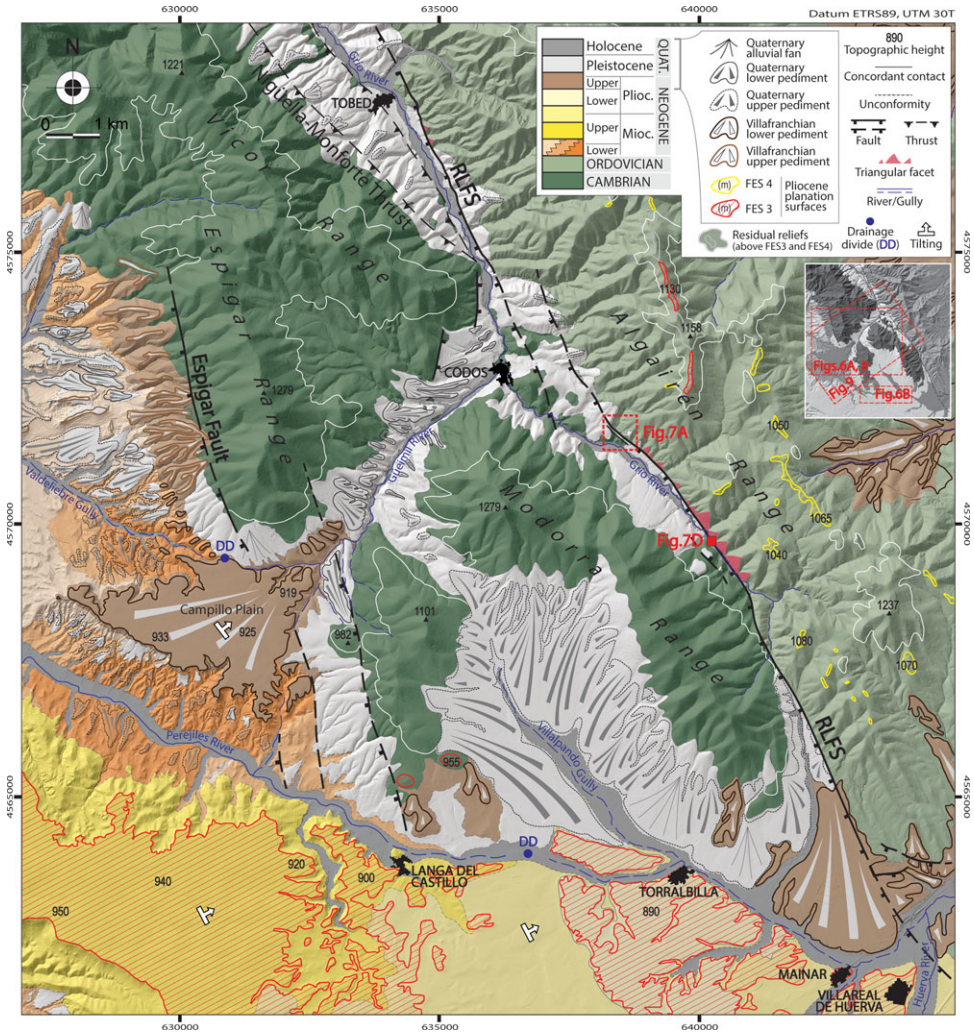

Fig. 5. (Colour online) Geological and morphostructural map of the Codos area affected by the Río Grío–Lanzuela Fault Segment (RLFS), in the NE margin of the Calatayud Basin (see location in Fig. 1c). Red squares and inset: location of Figures 6a, b, 7a, d, 8, 9.

FES3 has also been identified on the Palaeozoic massif (Algairén Range) at an altitude of 1130 m (Fig. 5). In this range, present-day heights of summits of the residual reliefs not levelled by this planation surface range from 1158 to 1237 m, and a new, more recent planation level (FES4) lies at 1040–1080 m asl (Fig. 5). Careful mapping and topographic correlation from the southern sector of the Calatayud Basin and neighbouring massifs have allowed the same FES3 planation surface to be determined in both the massif and the basin (Figs 3, 5). A post-FES3 vertical offset of about 240 m should therefore be interpreted for the RLFS in this area.

5.b. Evidence of drainage reversal

The northern sector of the Calatayud Basin and neighbouring ranges are drained by three main rivers (Jiloca, Perejiles and Grío) that flow towards the NNW, paralleling the Iberian structures. They join the transverse Jalón river, belonging to the Ebro drainage basin (Fig. 1b). To the south, the Huerva river also cross-cuts the eastern margin of the Calatayud Basin (Fig. 1c).

In the vicinity of Codos village, the Grío river is joined by a short, NE-flowing drainage, the Güeimil river, which exhibits a conspicuous drainage anomaly that reveals tilting of the overall Palaeozoic Vicor and Espigar ranges (Fig. 3). Today, the Güeimil river flows towards the NE, into the Grío river. Nevertheless, the relief setting strongly suggests that the present-day Güeimil valley represents the same drainage corridor that fed the Villafranchian alluvial system of the Campillo embayment, sourced from the northeastern basin margin (Fig. 5). This would require that (1) the drainage during late Pliocene time was directed towards the SW, and (2) the Villafranchian pediment had the same slope sense, despite the present-day opposite slope of 0.5° towards the NE that should be attributed to the same tilting process undergone by the FES3 surface at the Calatayud Basin.

Such hypothesized drainage reversal should be tested from sedimentological observation. While the Villafranchian alluvial system is set at the Campillo Plain, Pleistocene fluvial and alluvial gravel fills the entire Güeimil and Grío valleys. These Pleistocene deposits show increasing thickness downstream along the Güeimil valley from a minimum of 5 m at the headwaters up to 80 m near Codos. A maximum thickness of 90 m has been reported by Gutiérrez *et al.* (2013) in the Tobed sector (Fig. 5). Both sedimentary units have been surveyed with the purpose of interpreting their respective palaeocurrent patterns. In nine outcrops, consistent orientations of imbricate pebbles have allowed such interpretation. The results (Fig. 6a) show (1) palaeocurrents towards the SW, W and NW in Villafranchian gravel, compatible with an alluvial

Downloaded from https://www.cambridge.org/core. Universidad de Zaragoza, on 04 Oct 2021 at 10:24:00, subject to the Cambridge Core terms of use, available at https://www.cambridge.org/core/terms. https://doi.org/10.1017/S0016756821000790

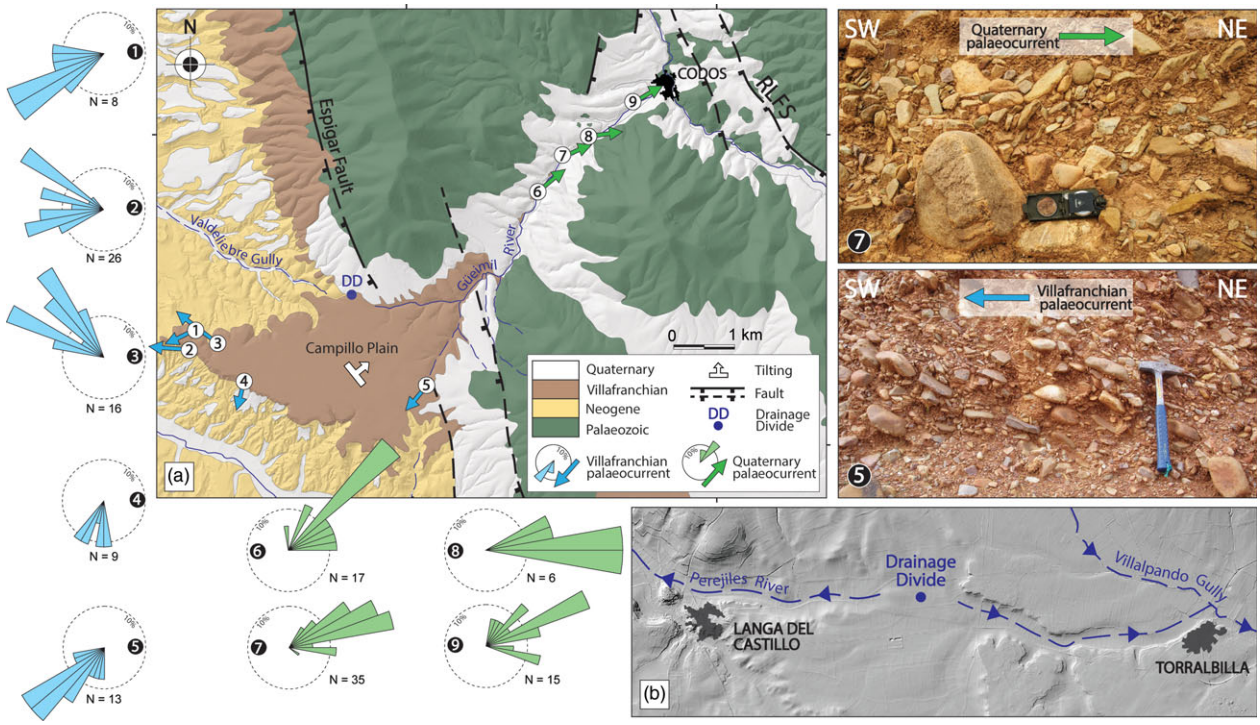

Fig. 6. (Colour online) (a) Drainage reversal at the Güeimil valley as indicated by opposite palaeocurrents recorded in Villafranchian and Quaternary deposits (see location in Fig. 5). Blue and green rose diagrams: palaeocurrent distributions inferred from imbricated pebbles measured at sites 1–5 (Villafranchian alluvial system; Pliocene–Pleistocene transition) and sites 5–9 (Quaternary fluvial deposits), respectively. Field views of sites 7 and 9 illustrate the opposite palaeocurrents. (b) Drainage divide of the Perejiles River between Langa del Castillo and Torralbilla (see location in Fig. 5).

fan drainage pattern, and (2) palaeocurrents towards the ENE in Pleistocene fluvial gravel, consistent with the Güeimil drainage. The hypothesis is therefore corroborated: the Güeimil valley, which in its normal way should drain towards the Perejiles river, was tilted back and then forced to drain into the Grío river, along the same riverbed but flowing in the opposite direction. The anomalous thickness of Pleistocene deposits in the Codos–Tobed sector can be interpreted as a consequence of the increase in accommodation space and subsequent river aggradation also produced by slip on the RLFS.

The regional drainage layout suggests that tilting of the hanging wall of the RLFS has induced other significant anomalies. Tributaries of the Jalón river, namely the Jiloca, the Perejiles and Grío rivers, flow towards the NW or NNW, parallel to recent extensional faults such as the RLFS (Fig. 1c). The high plain of the Calatayud Basin (specifically, the area south of Torralbilla and Mainar) should constitute the natural head of the Perejiles river. Nevertheless, this area drains into the Huerva river (see SE corner of Fig. 5). The continuous, E–W-trending flat-bottomed valley that extends between Torralbilla and Langa del Castillo surprisingly shows divergent drainage. Both the uppermost segment of the W-wards draining Perejiles river, and a short E-wards tributary of the Villalpando gully (flowing into the Huerva river), coexist within that valley. The subtle drainage divide is located on its flat bottom at the halfway point between Torralbilla and Langa del Castillo (Figs 5, 6b). This hydrographic anomaly can also be interpreted as a case of drainage reversal induced by tilting. This would be more recent in age than that interpreted for the Güeimil valley, since it occurred within a valley excavated during Pleistocene time. This evidence is consistent with the notion by Gutiérrez *et al.* (2008) of the capture of the Calatayud Basin by the Huerva river during late Pleistocene time.

5.c. Outcrop-scale structural observations

Beyond the geomorphological indicators of tectonic activity, the occurrence of Pleistocene slip on the RLFS should be confirmed by outcrop observations. One of the scarce exposures of the extensional rupture is located SE of Codos (Fig. 7a, b). In this sector, the main fault is accompanied by a smaller antithetic fault, both affecting Palaeozoic and Pleistocene units. Ancient Pleistocene deposits (Pleistocene 1 in Fig. 7a) consist of red conglomerate with sub-angular clasts and occasional silt layers. The Pleistocene 2 unit includes light-brown conglomerate, comprising Palaeozoic angular pebbles, with scarce silt layers. Two samples collected in Pleistocene 1 and 2 units have rendered OSL ages of 66.6 ± 6.5 ka and 40.2 ± 4.4 ka, respectively (see Table 1; location in Fig. 7). Pleistocene 1 is offset by both faults, while Pleistocene 2 deposits fill the intermediate graben (Fig. 7a–c) and could be considered as overall coeval with fault movement. The antithetic fault can be interpreted as a result of secondary accommodation of the hanging-wall block to slip on a curved upper segment of the main fault. The true throw measured at the base of the Pleistocene 1 unit (i.e. the significant vertical displacement, discounting the contribution of the antithetic fault; McCalpin, 1996) is therefore *c.* 20 m (Fig. 7c).

The RLFS is expressed in this outcrop as a 1–1.5-m-thick fault zone oriented 150, 67°W on average (Fig. 7b), in which Palaeozoic rocks are strongly deformed and partially brecciated. Their Variscan foliation is affected by small-scale drag folds (Fig. 7b'), whose axes are nearly orthogonal to striations observed on discrete rupture surfaces (Fig. 7b''). A nearly pure normal slip, with average transport direction towards 235°, is inferred from such kinematical indicators. Similarly oriented slickenlines have been measured in another outcrop located to the SE (Fig. 7d, d'; see location in

Downloaded from https://www.cambridge.org/core. Universidad de Zaragoza, on 04 Oct 2021 at 10:24:00, subject to the Cambridge Core terms of use, available at https://www.cambridge.org/core/terms. https://doi.org/10.1017/S0016756821000790

Table 1. Parameters and results of OSL dating of samples collected at the outcrop surveyed SE of Codos (Luminiscence Dating Laboratory of Centro Nacional de Investigación sobre la Evolución Humana, CENIEH, Burgos, Spain; Unit of Radioisotopes, Universidad de Sevilla, Spain)

Sample	Laboratory reference	Stratigraphic location	Depth (m)	H_2O (%)	Quartz grain (μm)	^{238}U (Bq kg^{-1})	^{232}Th (Bq kg^{-1})	^{40}K (Bq kg^{-1})	Dose rate (Gy ka^{-1})	Equivalent dose (Gy)	Age (ka)
CODOS_PLE-1	LM20132-08	Pleistocene 1	3	12	180–250	53 ± 27	63 ± 6	0.6 ± 0.1	4.1 ± 0.4	270.9 ± 8.9	66.6 ± 6.5
CODOS_PLE-2	LM20132-09	Pleistocene 2	20	10	180–250	40 ± 23	40 ± 23	0.2 ± 0.1	3.3 ± 0.3	132.8 ± 6.8	40.2 ± 4.4

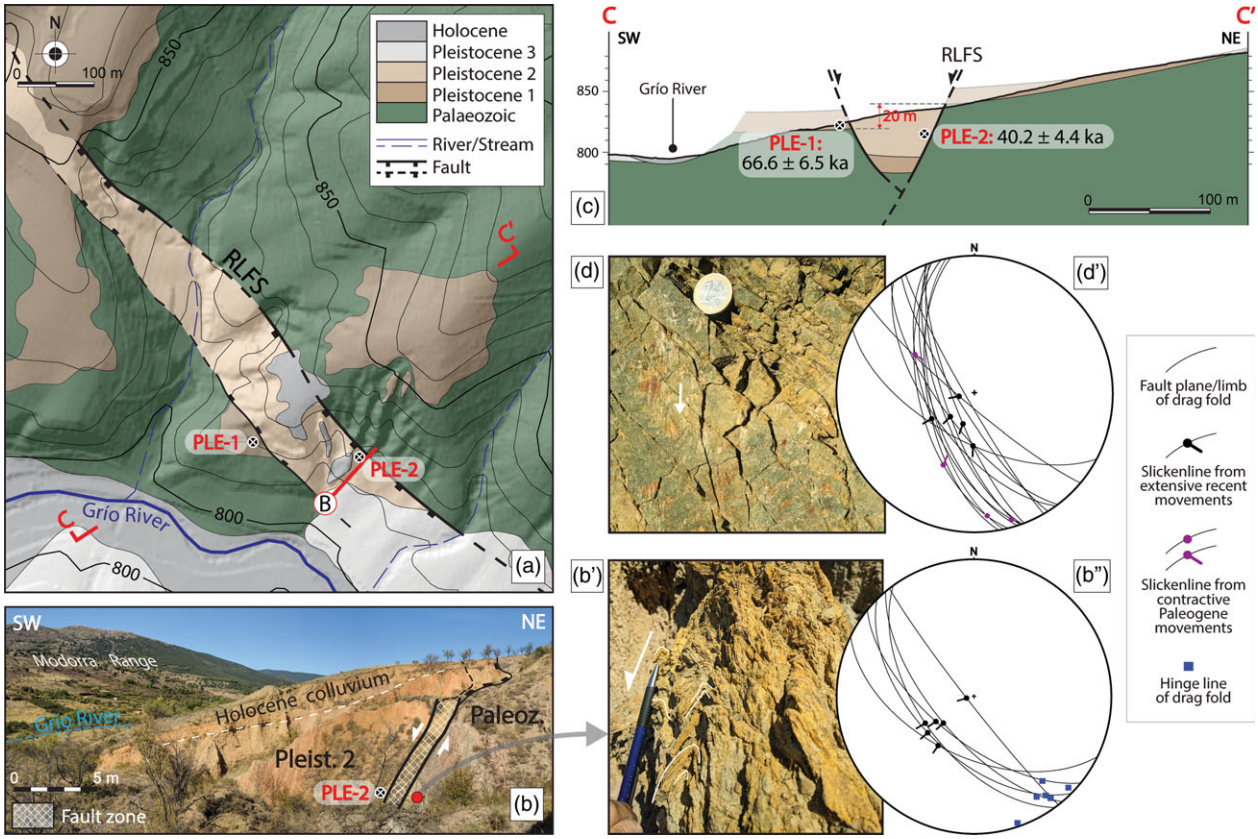

Fig. 7. (Colour online) (a) Geological map of the area SE of Codos showing evidence of Quaternary extensional activity on the Río Grío–Lanzuela Fault Segment (RLFS; see location in Fig. 5). (b) Exposure of the RLFS rupture affecting Quaternary and Palaeozoic units. (b', b'') Field view and orientation of the Variscan foliation affected by Quaternary small-scale drag folds. (c) Cross-section showing vertical displacement of the Pleistocene pediment discounting the contribution of the antithetic fault. (d, d') Secondary fault planes and slickenlines measured in an outcrop to the SE of map in (a) (see location in Fig. 5). Stereoplots: equal-area, lower hemisphere. The location and age of samples dated by OSL (PLE-1 and PLE-2) is indicated.

Fig. 5). In this second site, extensional slickenlines with accretion quartz fibres overprint previous reverse and strike-slip striations linked to contractive Alpine phases (Fig. 7d).

6. Interpretation and discussion

6.a. Assessing recent activity at the Río Grío–Pancrudo Fault zone

The fracture pattern described in previous sections defines a large recent extensional, NNW–SSE-trending structure, overall oblique to the Calatayud Basin: the Río Grío–Pancrudo Fault Zone, comprising two segments (Río Grío–Lanzuela, RLFS, and Cucalón–Pancrudo, CPFS; Fig. 1c). The maximum vertical offset calculated for the last 3.5 Ma has been identified within the CPFS (Cucalón–Olalla area; Fig. 4a), with a net slip of 325 m and slip rate of 0.09 mm a^{-1}.

Nevertheless, the most conspicuous geomorphological and structural evidence of recent, pure normal slip is found in the RLFS, which should be discussed in detail.

The FES3 planation surface has been used as a mixed, morpho-sedimentary marker for reconstructing the overall morphostructure of the area (Fig. 3). Its age is primarily constrained by robust biostratigraphic and magnetostratigraphic data in the coeval sedimentary units of the Teruel Basin, and secondarily correlated with similar units of the Calatayud Basin (Section 4.d). In this way, its map expression and its age are anchored in both basins at the northern and southern extremes of the study region. We are aware that the contour map of Figure 3 does not directly represent the geometry of tectonic deformation, since height variations of FES2 and FES3 are also partially controlled by their original, not completely flat topography. Nevertheless, the observed regional trends are palaeo-topographically and structurally consistent, and they allow the original slopes (e.g. at the FES3 pediment south

Downloaded from https://www.cambridge.org/core. Universidad de Zaragoza, on 04 Oct 2021 at 10:24:00, subject to the Cambridge Core terms of use, available at https://www.cambridge.org/core/terms. https://doi.org/10.1017/S0016756821000790

of Pelarda Range) and tectonic tilting (e.g. at the hanging-wall block of the Río Grío-Lanzuela Fault Segment) to be easily distinguished.

By using FES3 as a geomorphological, regionally dated marker (Ezquerro *et al.* 2020), a vertical displacement of *c.* 240 m can be inferred for the last 3.5 Ma in the Codos area (central sector of the RLFS; Fig. 5). Considering an average dip of 67°W and a pure normal slip, this involves a total net slip of *c.* 260 m, and a slip rate of 0.07 mm a^{-1}.

There is also evidence of persistent activity in RLFS during late Pliocene and Pleistocene time, although in this case slip values and slip rates are more uncertain. First, the post-FES4 slip rate cannot be estimated since the age of this marker remains unknown.

Second, a reasonable estimation of the Quaternary slip on RLFS can be made on the basis of roll-over deformation of the Villafranchian pediment, at the Campillo embayment. By extrapolating its tilted surface as far as the main fault trace, and comparing this present-day reconstructed profile with its hypothetical original profile, a minimum throw value has been calculated (Fig. 8a, b). The original slope of the Campillo pediment can be approached using other Villafranchian pediments of the surrounding region as a reference. We have selected 47 pediment remains mapped on the official 1:50 000 National Geological Map (Aragonés *et al.* 1981; del Olmo *et al.* 1983*a*, *b*; Hernández *et al.* 1983, 2005; Olivé *et al.* 1983, 2002; Gabaldón *et al.* 1989*b*) that have not undergone visible deformation. For each of them, the total length and the average slope have been measured and plotted on Figure 8c (see online Supplementary Table S1, available at http://journals.cambridge.org/geo). A significant correlation can be recognized between the variables, and a value in the range of 0.5–1° can be inferred as the typical slope of Villafranchian pediments longer than 4 km (which is the case for the Campillo pediment). Using this slope value, the hypothetical original profile of the Villafranchian pediment has been restored in Figure 8a, b, starting from the most distal visible point of the pediment surface (such a procedure implicitly assumes that this point coincides with the rotation axis of roll-over tilting). The difference in height between the original and the present-day profile close to RLFS provides an estimated post-Villafranchian minimum fault throw in the range of 140–220 m, and hence a minimum net slip of 155–235 m. Assuming that the tilted pediment is coeval to the Villafranchian pediments of the Teruel area (*c.* 2.0 Ma; average magnetostratigraphic age of La Puebla de Valverde, see Section 3), the minimum slip rate could be estimated in the range of 0.07–0.11 mm a^{-1}.

The maximum value above inferred for the fault throw (220 m) is close to that obtained from offset of FES3 (240 m), which supports the notion that almost the entire slip recorded at RLFS has occurred after the Villafranchian pediment was modelled. On the contrary, the Espigar fault moved during previous Neogene times and had become inactive by the Pliocene–Pleistocene transition. It generated the mountain front from which the Villafranchian alluvial system was sourced, but no surficial rupture subsequently propagated across the Campillo embayment. In summary, the extensional activity at the NE margin of the Calatayud Basin was transferred from the Espigar fault to the RLFS by early Pleistocene times, as the evolutionary model of Figure 9 illustrates. Both faults, together with local isostatic readjustment (shoulder uplift) at the footwall block of the Daroca fault, were responsible for the overall tilting of the Calatayud Basin. According to Jackson & Mckenzie (1983) and Jackson *et al.* (1988), the elevation of the footwall could represent about 10% of the subsidence of the hanging wall with respect to a regional reference level.

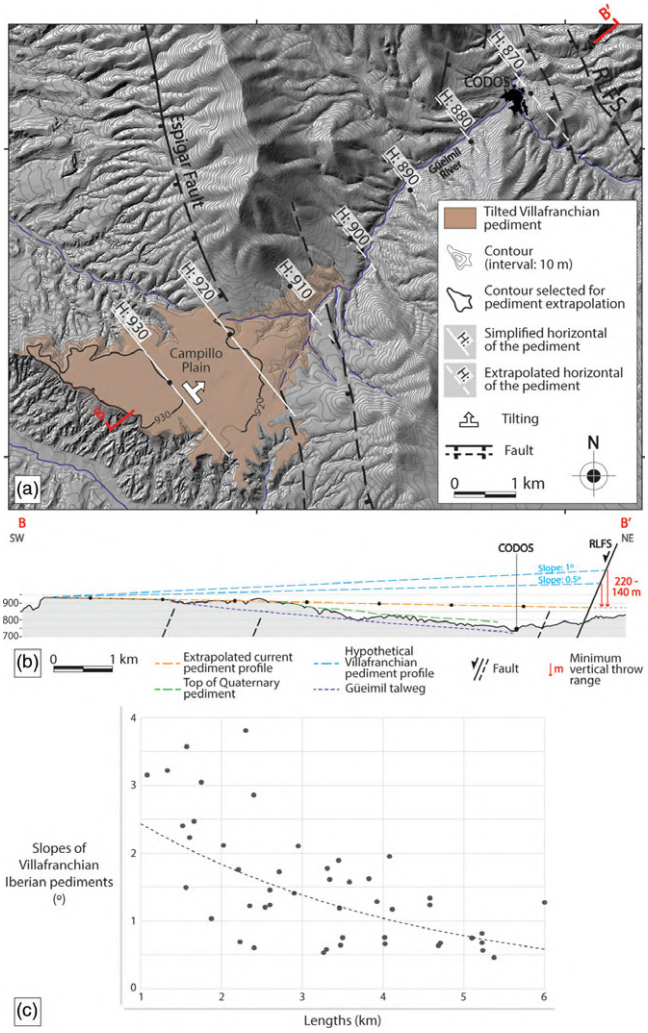

Fig. 8. (Colour online) (a) Extrapolation of the tilted Villafranchian pediment from the Campillo embayment as far as the main trace of the Río Grío–Lanzuela Fault Segment (RLFS; see location in Fig. 5). (b) Extrapolated profile and estimation of the RLFS minimum post-Villafranchian net slip. Topographic heights are expressed in metres above sea level. (c) Relationship between the total length (km) and the slope (°) of the Villafranchian Iberian pediments (see database in online Supplementary Table S1). The trend line (dotted) allows the slope of pediments longer than 4 km to be constrained within the range 0.5–1°.

Finally, concerning the intra-Pleistocene displacement recorded SE of Codos, a throw of 20 m (Fig. 7c) was measured at the base of the Pleistocene 1 unit. The OSL age provided by this unit (66.6 ± 6.5 ka) represents a close supradate of that sedimentary marker (the dated sample was extracted only 4 m above the base). Considering the dip of the fault plane (67°) and the nearly pure normal slip direction, a net slip of *c.* 21.7 m is calculated. A slip rate approaching 0.30–0.36 mm a^{-1} is therefore inferred for this time period.

6.b. Drainage reversals in the extensional tectonic setting

Sustained activity on the RLFS has produced noteworthy changes in local drainage paths, as well as other sedimentary effects.

(1) *Drainage reversal along the Güeimil valley (early? Pleistocene).* This flowed towards the SW during the Pliocene–Pleistocene transition (Villafranchian time), feeding a recognizable alluvial

Downloaded from https://www.cambridge.org/core. Universidad de Zaragoza, on 04 Oct 2021 at 10:24:00, subject to the Cambridge Core terms of use, available at https://www.cambridge.org/core/terms. https://doi.org/10.1017/S0016756821000790

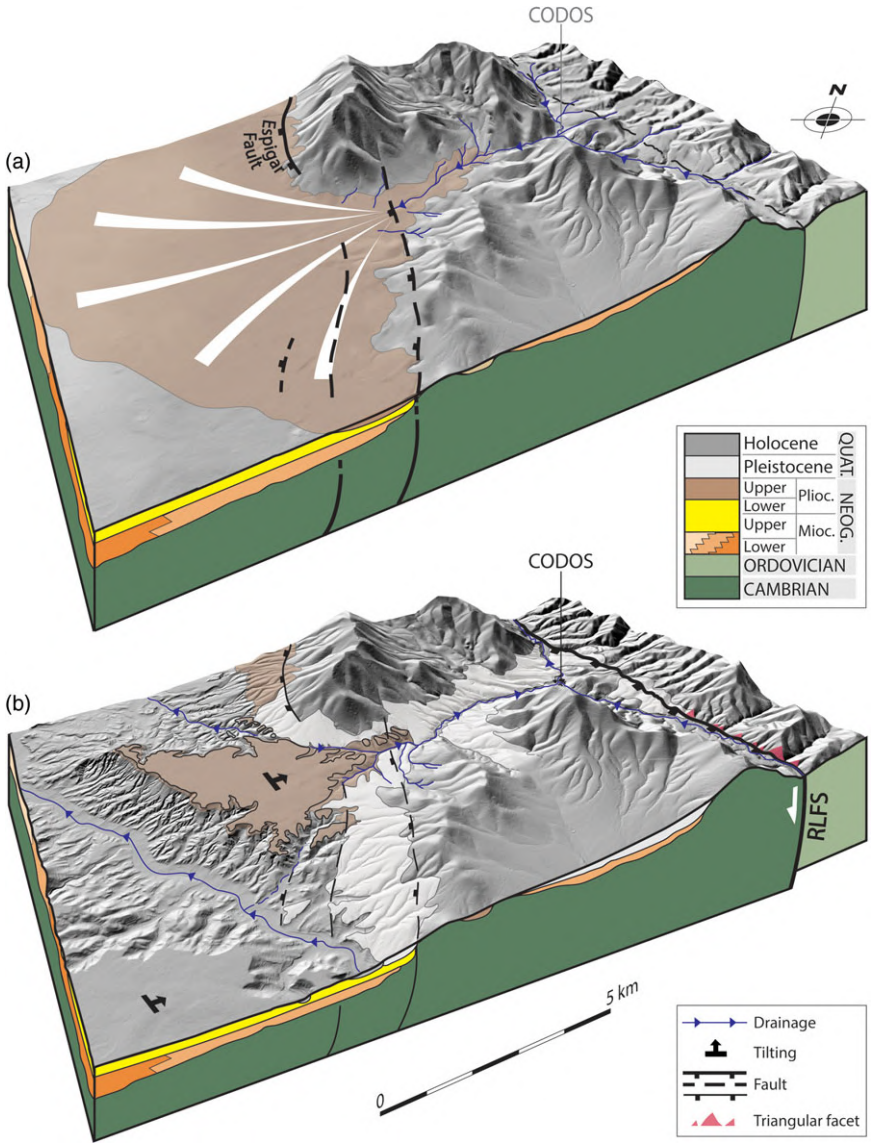

Fig. 9. (Colour online) (a, b) Proposed evolutionary model for the original Codos area, showing successive activation of the Espigar and Río Grío–Lanzuela (RLFS) faults and subsequent drainage reversal along the Güeimil valley. The latter occurred after the Pliocene–Pleistocene transition due to roll-over tilting of the hanging-wall block of the RLFS (see location in Fig. 5). The drainage pattern in the Codos area in (a) is hypothetic.

system in the Calatayud Basin (Fig. 5). Apart from tilting the Neogene units and the FES3 planation surface, roll-over accommodation of the hanging wall of the RLFS switched the slope of the riverbed and forced the Güeimil river to drain towards the NE into the Grío river. Migration of the alluvial apex towards the source area during late Neogene time, as well as aggradation of the Güeimil and Grío valleys during Pleistocene time, could also result from progressive tilting and consequent increase in accommodation space towards the NE. The block diagrams in Figure 9 illustrate the proposed evolutionary model. In order to estimate the hypothetic extent of the Güeimil palaeo-catchment area illustrated in Figure 9, the relationship between the size of the alluvial fan and its catchment area can be taken into account. According to Dade & Verdeyen (2007), a 15–20 km^2 alluvial fan (similar to the hypothetic original Campillo) would be associated with a catchment area of *c.* 35 km^2. If the palaeo-divide was further from Codos (see Figs 5, 9), the catchment area would attain about 50 km^2, while with a hypothetic palaeo-divide west of Codos (i.e. originally disconnected Grío and Güeimil basins) would be 20–25 km^2 in size. This means that the location of this palaeo-divide had probably gone beyond Codos village, although it is not certain that the catchment area was exactly that represented in Figure 9.

(2) *Drainage reversal along the high Perejiles valley (late Pleistocene).* The natural head of the Perejiles river was captured by the Huerva river, so that a segment of its original, W-wards-draining flat-bottomed valley (between Torralbilla and Langa del Castillo) became a tributary of the Huerva river (Figs 5, 6b).

Examples of drainage reversal were described by Ollier (1981, p. 175–6) west of Lake Victoria (Uganda), induced by tectonic tilting linked to the formation of the Western Rift Valley. Along the SE-flowing Clarence river (eastern Australia), Haworth & Ollier (1992) described evidence of aligned streams that represent the remains of an earlier NW-flowing system, reversed after the tectonic opening of the Tasman Sea. River reversals are also caused by isostatic arching triggered by active tectonics (e.g. opening of the Dead Sea Transform and Rift Valley; Matmon *et al.* 1999). All these examples represent regional-scale drainage anomalies caused by tilting and subsequent migration of drainage divides on footwall blocks of normal faults.

Downloaded from https://www.cambridge.org/core. Universidad de Zaragoza, on 04 Oct 2021 at 10:24:00, subject to the Cambridge Core terms of use, available at https://www.cambridge.org/core/terms. https://doi.org/10.1017/S0016756821000790

A drainage reversal very similar to that studied in this paper is found in the Megara Basin (central Greece), whose infill currently shows tilting towards the south and is enclosed between ENE–WSW- and WNW–ESE-striking normal faults. The present-day drainage pattern flows S-wards, but sedimentological and drainage analyses reveal that it is the result of a drainage reversal that occurred during late Pleistocene time due to tectonic uplift and tilting (Leeder *et al.* 1991). During the Plio-Pleistocene transition, alluvial clastics from the basin infill were deposited by a NW-flowing system, also corroborated by local palaeocurrents (Bentham *et al.* 1991).

As highlighted in Section 3, the drainage rearrangement of this area of the eastern Iberian Chain took place during a progressive transition from endorheic to exorheic conditions. The overall process is controlled in the distance by base-level changes, in this case of the Ebro river, although it is locally modelled in certain sectors by the activity of nearby faults. The individual influence of each of these factors can be difficult to determine. In our study case, the regional base-level drop would have resulted in divide retreat of the Huerva head, while local NE-tilting of the Calatayud Basin would have contributed to the final drainage reversal.

6.c. Slip rates and seismogenic potential of the Río Grío–Pancrudo Fault Zone within the Iberian Chain context

Slip rates inferred at the Río Grío–Pancrudo Fault Zone for the overall late Pliocene – Quaternary period are close to those reported for the main extensional faults in the eastern Iberian Chain. Since late Pliocene time, faults in both the neighbouring Jiloca graben (Calamocha, Sierra Palomera and Concud faults) and the Teruel Basin show slip rates within the range of 0.05–0.16 mm a^{-1} (Simón *et al.* 2012, 2013; Ezquerro *et al.* 2020). These authors noticed that fault slip rates in both basins tend to increase with time (e.g. the slip rate calculated from detailed palaeo-seismological analysis in the Concud fault for late Pleistocene time is 0.29 mm a^{-1}; Simón *et al.* 2016). The same tendency has been inferred for the Río Grío–Lanzuela Fault Segment studied here: while the average net slip since 3.5 Ma was 0.07 mm a^{-1}, it has increased to a minimum of 0.07–0.11 mm a^{-1} since 2.0 Ma and has been approaching 0.30–0.36 mm a^{-1} for the last 66.6 ± 6.5 ka. On the contrary, slip rates on faults closer to the Valencia Trough, such as those of the Maestrat grabens (easternmost Iberian Chain; Simón *et al.* 2012, 2013) and the Catalonian grabens (Masana, 1995; Masana *et al.* 2001; Perea *et al.* 2006), have tended to decrease.

Such a pattern of evolution during Pleistocene time has been associated (Simón *et al.* 2012, 2013; Ezquerro *et al.* 2020) with a number of tectonic processes: (1) progressive W-wards propagation of rifting, from inner parts of the Valencia Trough towards more external domains, as suggested by Capote *et al.* (2002) from the evolutionary trend along Neogene times; (2) favourable orientation of the main Variscan and late Variscan faults that control the macrostructure of the Iberian Chain (NW–SE to NNW–SSE) within the most recent stress field (with dominant extension σ_3 axis trending WSW–ENE; Arlegui *et al.* 2005); (3) fault linkage processes, well documented from tectono-sedimentary analysis in the case of the northern Teruel Basin (Ezquerro, 2017; Ezquerro *et al.* 2019), and also supported by analysis of T-D curves (Ezquerro *et al.* 2020); and (4) (chiefly as a consequence of (2) and (3)), progressive localization of displacement into a few faults, a tendency that has been observed for example in the central Apennines, Italy, since 0.9 Ma (Roberts *et al.* 2002).

There is evidence of Quaternary activity at the Río Grío–Pancrudo Fault Zone, with decametre-scale displacement at a significant slip rate (close to 0.30–0.36 mm a^{-1}) during late Pleistocene time, allowing us to consider it as an active structure. Its seismogenic potential should therefore be taken into account in the evaluation of seismic hazard of the Iberian Chain. The probability of a single deep fault entirely moving is significant, since the relay zone between the fault segments may not have enough width to act as a barrier to the co-seismic propagation of the surficial rupture. According to Biasi & Wesnousky (2016), ruptures in dip-slip faults manage to cross 54% of relay zones 1 km wide or less, and this percentage increases in the case of normal faults. If we consider the Río Grío–Pancrudo Fault Zone as a single structure, it would generate earthquakes of magnitude 7.3–7.4 (considering a total length of 88 km, and following the correlation of Wells & Coppersmith, 1994). Future detailed palaeo-seismological studies should be focused on assessing the probability of such a scenario.

7. Conclusions

The Río Grío–Pancrudo Fault Zone represents a late Variscan strike-slip structure, reactivated under the Alpine compression during Palaeogene time, and finally inverted during the Neogene–Quaternary extension. It comprises two NNW–SSE-trending fault segments that total about 88 km in length, separated by a right-relay zone 2 km in width and overlapping less than 2 km: Río Grío-Lanzuela (RLFS) and Cucalón-Pancrudo (CPFS). The Río Grío–Pancrudo Fault Zone partially coincides with the northeastern boundary of the Neogene Calatayud Basin, leading to the sinking and overall tilting of its infill (probably with a small contribution of isostatic readjustment at the Daroca fault). Nevertheless, the general trend of the Río Grío–Pancrudo Fault Zone is oblique to the basin boundary: the northern sector of RLFS enters the Palaeozoic Calatayud–Montalbán massif, and the central sector of the CPFS obliquely crosses the basin. Propagation of such a large NNW–SSE-trending extensional structure was possible because of its favourable orientation with respect to the prevailing WSW–ENE σ_3 trajectories of the coeval stress field.

The recent extensional activity of the Río Grío–Lanzuela Fault Segment has been demonstrated and evaluated through its imprint on landforms and drainage. In the Codos area, morphotectonic and palaeocurrent analysis indicate that the Güeimil valley has experienced a drainage reversal from flowing into the Calatayud Basin through a wide alluvial fan during Villafranchian time (Pliocene–Pleistocene transition), to flowing into the Grío river following the Río Grío–Lanzuela fault trace after Pleistocene time. The total throw at this sector of the Río Grío–Lanzuela Fault Segment has been calculated at *c.* 240 m (pure normal net slip of *c.* 260 m) from offset of an upper Neogene planation surface (FES3; 3.5 Ma), resulting in a long-term slip rate of 0.07 mm a^{-1}. Within the Quaternary, the minimum fault throw is estimated in the range of 140–220 m (pure normal net slip in the range of 155–235) for the last 2.0 Ma (slip rate, 0.07–0.11 mm a^{-1}).

Data are more scarce at the Cucalón–Pancrudo Fault Segment, but preliminary results indicate that FES3 has undergone vertical offset of *c.* 300 m (pure normal net slip, *c.* 325 m), which implies a slip rate of *c.* 0.09 mm a^{-1}.

Slip rates obtained in both fault segments are comparable to those averaged on other faults in the central Iberian Chain for late

Downloaded from https://www.cambridge.org/core. Universidad de Zaragoza, on 04 Oct 2021 at 10:24:00, subject to the Cambridge Core terms of use, available at https://www.cambridge.org/core/terms. https://doi.org/10.1017/S0016756821000790

Pliocene – Pleistocene time. Decametre-scale displacement during late Pleistocene time, at slip rates close to 0.30–0.36 mm a^{-1}, suggests that the fault has undergone an increase in slip rate during Pliocene–Quaternary times, a tendency also previously reported for other faults in the neighbouring Jiloca and Teruel basins.

The seismogenic potential of the Río Grío–Pancrudo Fault Zone, which might be one of the largest active macrostructures in the Iberian Chain, should be considered in the evaluation of seismic hazard of the region. The probability that the coseismic rupture within this fault zone could manage to cross the relay zone between both fault segments, generating earthquakes of magnitude 7.3–7.4, should not be neglected.

Supplementary material. To view supplementary material for this article, please visit https://doi.org/10.1017/S0016756821000790

Acknowledgements. This research was financed by Programa Operativo del Fondo Europeo de Desarrollo Regional Aragón 2014-2020 (project LMP127_18) and Ministerio de Ciencia e Innovación of the Spanish Government (project PID2019-108705-GB-I00). This work is a contribution by the Geotransfer-IUCA research group (E32_17R) funded by Aragon Government and FEDER-Aragón 2014–2020 ('*Construyendo Europa desde Aragón*'). A Peiro benefitted from an FPU contract (FPU17/02470) of the Spanish Government. We thank Alicia Medialdea, as well as the Luminiscence Dating Laboratory of CENIEH (Centro Nacional de Investigación sobre la Evolución Humana, Burgos, Spain) and the Unit of Radioisotopes at the Universidad de Sevilla, for the OSL dating. CL Liesa, LE Arlegui and A Luzón contributed to field survey and interpretation on which the cross-section of Figure 4a is based. MA Soriano helped us with mapping Quaternary pediments in Figure 5. L Ezquerro, L Alcalá and MD Pesquero advised us on issues related to palaeontological dating of planation surfaces and Villafranchian pediments. Finally, we sincerely thank the two anonymous reviewers for their comments and suggestions, which have greatly improved the paper.

Declaration of interest. The authors declare that they have no known competing financial interests or personal relationships that influenced the work reported in this paper.

References

Adrover R (1975) Principales yacimientos paleomastológicos de la provincia de Teruel y su posición estratigráfica relativa. In *Actas I Coloquio Internacional sobre Bioestratigrafía Continental del Neógeno Superior-Cuaternario Inferior* (eds MT Alberdi and E Aguirre), pp. 31–48. Madrid-Montpellier: Trabajos sobre Neógeno-Cuaternario.

Adrover R, Feist M, Hugueney M, Mein P and Moissenet E (1982) L'âge et la mise en relief de la formation detritique culminante de la Sierra Pelarda (Prov. Teruel, Espagne). *Comptes rendus de l'Académie des sciences, Paris* **295**, 231–6.

Allmendinger RW, Cardozo NC and Fisher D (2012) *Structural Geology Algorithms: Vectors & Tensors*. Cambridge: Cambridge University Press, 289 p.

Álvaro M, Capote R and Vegas R (1979) Un modelo de evolución geotectónica para la Cadena Celtibérica. *Acta Geologica Hispánica* **14**, 172–7.

Anadón P, Alcalá L, Alonso-Zarza AM, Calvo JP, Ortí F, Rosell L and Sanz-Rubio E (2004) Cuencas de la Cordillera Ibérica. In *Geología de España* (ed JA Vera), pp. 562–69. Madrid: Sociedad Geológica de España-Instituto Geológico y Minero de España.

Aragonés E, Hernández A, Aguilar MJ, Ramírez J, García-Alcalde GL and Arbizu M (1981) Mapa Geológico de España 1: 50.000, hoja no. 409 (Calatayud). Madrid: Instituto Geológico y Minero de España.

Arlegui LE, Simón JL, Lisle RJ and Orife T (2005) Late Pliocene–Pleistocene stress field in the Teruel and Jiloca grabens (eastern Spain): contribution of a new method of stress inversion. *Journal of Structural Geology* **27**, 693–705.

Bentham P, Collier RE, Gawthorpe RL, Leeder R and Stark C (1991) Tectono-sedimentary development of an extensional basin: the Neogene Megara Basin, Greece. *Journal of the Geological Society* **148**, 923–34.

Biasi GP and Wesnousky SG (2016) Steps and gaps in ground ruptures: empirical bounds on rupture propagation. *Bulletin of the Seismological Society of America* **106**, 1110–24.

Bonow JM, Lidmar-Bergström K and Japsen P (2006) Palaeosurfaces in central West Greenland as reference for identification of tectonic movements and estimation of erosion. *Global and Planetary Change* **50**, 161–83.

Burbank DW and Anderson RS (2012) *Tectonic Geomorphology*. Oxford: Wiley-Blackwell, 454 p.

Calvín-Ballester P and Casas A (2014) Folded Variscan thrusts in the Herrera unit of the Iberian Range (NE Spain). In Deformation Structures and Processes within the Continental Crust (eds S Llana-Fúnez, A Marcos and F Bastida), pp. 39–52. Geological Society of London, Special Publication no. 394.

Campos S, Aurell M and Casas A (1996) Origen de las brechas de la base del Jurásico en Morata de Jalón. *Geogaceta* **20**, 887–9.

Capote R, Muñoz JA, Simón JL, Liesa CL and Arlegui LE (2002) Alpine tectonics I: The Alpine system north of the Betic Cordillera. In *Geology of Spain* (eds W Gibbons and T Moreno), pp. 367–400. Geological Society of London.

Cardozo N and Allmendinger RW (2013) Spherical projections with OSXStereonet. *Computers & Geosciences* **51**, 193–205.

Casas A, Aurell M, Revuelto C, Calvín P, Simón JL, Pueyo Ó, Pocoví A and Marcén M (2017) El embalse de Mularroya (Zaragoza): problemas geológicos de una obra en estado avanzado de construcción. *Revista de la Sociedad Geológica de España* **30**, 51–64.

Casas A, Marcén M, Calvín P, Gil A, Román-Berdiel T and Pocoví A (2016) Deformación varisca, tardivarisca y alpina en la Rama Aragonesa de la Cordillera Ibérica: propuesta para diferenciación y denominación de estructuras. *Geo-Temas* **16**, 495–8.

Colomer M and Santanach P (1988) Estructura y evolución del borde sur-occidental de la Fosa de Calatayud-Daroca. *Geogaceta* **4**, 29–31.

Cortés-Gracia AL and Casas-Sáinz A (1996) Deformación alpina de zócalo y cobertera en el borde norte de la Cordillera Ibérica (Cubeta de Azuara-Sierra de Herrera). *Revista de la Sociedad Geológica de España* **9**, 51–66.

Dade WB and Verdeyen ME (2007) Tectonic and climatic controls of alluvial-fan size and source-catchment relief. *Journal of the Geological Society*, **164**, 353–8.

de Vicente G, Vegas R, Muñoz-Martín A, Wees JDVan, Casas-Sáinz A, Sopeña A, Sánchez-Moya Y, Arche A, López-Gómez J, Olaiz A and Fernández-Lozano J (2009) Oblique strain partitioning and transpression on an inverted rift: The Castilian Branch of the Iberian Chain. *Tectonophysics* **470**, 224–42.

del Olmo P, Hernández A, Aragonés E, Gutiérrez M, Puigdefábregas C, Giner J, Aguilar MJ, Leal MC, Gutiérrez JC, Gil M, Adrover R, Portero JM and Gabaldón V (1983a) Mapa Geológico de España 1: 50.000, hoja no. 437 (Ateca). Madrid: Instituto Geológico y Minero de España.

del Olmo P, Portero JM, Villena J, Pardo G, Gutiérrez M, Puigdefábregas C, Giner J, Aguilar MJ, Leal MC, Goy A, Comas MJ and Gabaldón V (1983b) Mapa Geológico de España 1: 50.000, hoja no. 490 (Odón). Madrid: Instituto Geológico y Minero de España.

Ezquerro L (2017) El sector norte de la cuenca neógena de Teruel: tectónica, clima y sedimentación. Ph.D. thesis, Universidad de Zaragoza. Published thesis.

Ezquerro L, Lafuente P, Pesquero MD, Alcalá L, Arlegui LE, Liesa CL, Luque L, Rodríguez-Pascua MA and Simón JL (2012) Una cubeta endorreica residual Plio-Pleistocena en la zona de relevo entre las fallas de Concud y Teruel: implicaciones paleogeográficas. *Revista de la Sociedad Geológica de España* **25**, 157–75.

Ezquerro L, Luzón A, Liesa CL and Simón JL (2019) Alluvial sedimentation and tectono-stratigraphic evolution in a narrow extensional zigzag basin margin (northern Teruel Basin, Spain). *Journal of Palaeogeography* **8**, 1–25.

Ezquerro L, Simón JL, Luzón A and Liesa CL (2020) Segmentation and increasing activity in the Neogene-Quaternary Teruel Basin rift (Spain) revealed by morphotectonic approach. *Journal of Structural Geology* **135**, published online 26 March 2020. doi: 10.1016/j.jsg.2020.104043

Gabaldón V, Lendínez A, Ferreiro E, Ruiz V, López de Alda F, Valverde M, Lago San José M, Meléndez A, Pardo G, Ardevol L, Villena J, González A, Hernández A, Álvaro M, Leal MC, Aguilar Tomás M, Gómez JJ and

Downloaded from https://www.cambridge.org/core. Universidad de Zaragoza, on 04 Oct 2021 at 10:24:00, subject to the Cambridge Core terms of use, available at https://www.cambridge.org/core/terms. https://doi.org/10.1017/S0016756821000790

Carls P (1991) Mapa Geológico de España 1: 200.000, hoja no. 40 (Daroca). Madrid: Instituto Geológico y Minero de España.

Gabaldón V, Lendínez A, Ruiz V, Carls P, Alvaro M, Guitérrez M, Hernández A, Gómez JJ, Meléndez A, Perez A, Pardo G, Villena J, Aguilar M, Leal MC, Comas MJ, Goy A, Lago M and Conte JC (1989a) Mapa Geológico de España 1: 50.000, hoja no. 466 (Moyuela). Madrid: Instituto Geológico y Minero de España.

Gabaldón V, Lendínez A, Ruiz V, Carls P, Alvaro M, Guitérrez M, Soriano MA, Hernández A, Gómez JJ, Meléndez A, Aurell M, Pérez A, Pardo G, Villena J, Aguilar M, Leal MC, Comas MJ, Goy A, Lago M and Conte JC (1989b) Mapa Geológico de España 1: 50.000, hoja no. 439 (Azuara). Madrid: Instituto Geológico y Minero de España.

Goldsworthy M and Jackson J (2000) Active normal fault evolution in Greece revealed by geomorphology and drainage patterns. *Journal of the Geological Society* **157**, 967–81.

Gracia FJ, Gutiérrez M and Leránoz B (1988) Las superficies de erosión neógenas en el sector central de la Cordillera Ibérica. *Revista de la Sociedad Geológica de España* **1**, 135–42.

Gracia J (1992) Tectónica pliocena de la Fosa de Daroca (prov. de Zaragoza). *Geogaceta* **11**, 127–9.

Guimerà J (1988) Estudi estructural de l'enllaç entre la Serralada Iberica y la Serralada Costanera Catalana. Ph.D. thesis, Universitat de Barcelona. Published thesis.

Gutiérrez F, Gracia FJ and Gutiérrez M (1996) Consideraciones sobre el final del relleno endorreico de las fosas de Calatayud y Teruel y su paso al exorreismo: implicaciones morfoestratigráficas y estructurales. In *IV Reunión de Geomorfología* (eds A Grandal and J Pagés), pp. 23–43. O Castro, A Coruña: Sociedad Española de Geomorfología.

Gutiérrez F, Gutiérrez M, Gracia FJ, McCalpin JP, Lucha P and Guerrero J (2008) Plio-Quaternary extensional seismotectonics and drainage network development in the central sector of the Iberian Chain (NE Spain). *Geomorphology* **102**, 21–42.

Gutiérrez F, Lucha P and Jordá L (2013) The Río Grío depression (Iberian Chain, NE Spain). Neotectonic graben vs. Fluvial valley. *Cuaternario y Geomorfología* **27**, 5–32.

Gutiérrez F, Moreno D, López GI, Jiménez F, del Val M, Alonso MJ, Martínez-Pillado V, Guzmán O, Martínez D and Carbonel D (2020) Revisiting the slip rate of Quaternary faults in the Iberian Chain, NE Spain. Geomorphic and seismic-hazard implications. *Geomorphology*, **363**, 107233.

Haworth RJ and Ollier CD (1992) Continental rifting and drainage reversal: the Clarence River of eastern Australia. *Earth Surface Processes and Landforms* **17**, 387–97.

Hernández A, Olivé A, Moissenet E, Pardo G, Villena J, Portero JM, Gutiérrez M, Puigdefábregas C, Giner J, Aguilar MJ, Leal MC, Gutiérrez JC, Gil MD, Adrover R and Gabaldón V (1983) Mapa Geológico de España 1: 50.000, hoja no. 491 (Calamocha). Madrid: Instituto Geológico y Minero de España.

Hernández A, Ramírez JI, Navarro JJ, Cortes AL, Rodríguez R, Babiano F, Gómez D, Ramírez J, Cuenca G, Pozo M and Casas J (2005) Mapa Geológico de España 1: 50.000, hoja no. 411 (Longares). Madrid: Instituto Geológico y Minero de España.

Herraiz M, De Vicente G, Lindo-Ñaupari R, Giner J, Simón JL, González-Casado JM, Vadillo O, Rodríguez-Pascua MA, Cicuéndez JL, Casas A, Cabañas L, Rincón P, Cortés AL, Ramírez M and Lucini M (2000) The recent (upper Miocene to Quaternary) and present tectonic stress distributions in the Iberian Peninsula. *Tectonics* **19**, 762–86.

Jackson J, Norris R and Youngson J (1996) The structural evolution of active fault and fold systems in central Otago, New Zealand: evidence revealed by drainage patterns. *Journal of Structural Geology* **18**, 217–34.

Jackson JA and McKenzie D (1983) The geometrical evolution of normal fault systems. *Journal of Structural Geology* **5**, 471–82.

Jackson JA, White NJ, Garfunkel Z and Anderson H (1988) Relations between normal fault geometry, tilting and vertical motions in extensional terrains: an example from the southern Gulf of Suez. *Journal of Structural Geology* **10**, 155–70.

Julivert M (1954) *Observaciones sobre la tectónica de la Depresión de Calatayud*. Sabadell: Museo de Sabadell, 17 p.

Keller EA (1986) Investigation of active tectonics: use of surficial earth processes. In *Active Tectonics: Impact on Society* (ed RR Wallace), pp. 136–147. Washington DC: National Academic Press.

Lafuente P, Arlegui LE, Liesa CL, Pueyo O and Simón JL (2014) Spatial and temporal variation of paleoseismic activity at an intraplate, historically quiescent structure: the Concud fault (Iberian Chain, Spain). *Tectonophysics* **632**, 167–87.

Leeder MR and Jackson JA (1993) The interaction between normal faulting and drainage in active extensional basins, with examples from the western United States and central Greece. *Basin Research* **5**, 79–102.

Leeder MR, Seger MJ and Stark CP (1991) Sedimentation and tectonic geomorphology adjacent to major active and inactive normal faults, southern Greece. *Journal of the Geological Society* **148**, 331–43.

Liesa CL, Simón JL, Ezquerro L, Arlegui LE and Luzón A (2019) Stress evolution and structural inheritance controlling an intracontinental extensional basin: the central-northern sector of the Neogene Teruel *Basin. Journal of Structural Geology* **118**, 362–76.

Maillard A and Mauffret A (1999) Crustal structure and riftogenesis of the Valencia Trough (north-western Mediterranean Sea). *Basin Research*, **11**, 357–79.

Marcén M (2020) Fábricas Magnéticas aplicadas al estudio de Zonas de Falla: Ejemplos de la Península Ibérica. Ph.D. thesis, Universidad de Zaragoza. Published thesis.

Marcén M and Román-Berdiel MT (2015) Geometría y cinemática de la zona de falla de Río Grío: evidencias de transpresión alpina en la Cadena Ibérica. *Geogaceta* **58**, 180–3.

Martín M, Canerot J, Linares-Rivas A, Grambast L, Quintero I, Mansilla H, De las Heras A, Fernández MC, Leyva F and Martínez JU (1977) Mapa Geológico de España 1: 50.000, hoja no. 492 (Segura de los Baños). Madrid: Instituto Geológico y Minero de España.

Martín-Bello L, Arlegui LE, Ezquerro L, Liesa CL and Simón JL (2014) La falla de Calamocha (fosa del Jiloca, Cordillera Ibérica): estructura y actividad pleistocena. In *Una aproximación multidisciplinary al studio de las fallas activas, los terremotos y el riesgo sísmico* (eds A Álvarez-Gómez and F Martín-González), pp. 55–58. Lorca, Murcia, 22–24 October 2014. 2ª Reunión Ibérica sobre Fallas Activas y Paleosismología.

Masana E (1995) L'activitat neotectònica a les cadenes Costaneres Catalanes. Ph.D. thesis, Universitat de Barcelona. Published thesis.

Masana E, Villamarín JA and Santanach P (2001) Paleoseismic results from multiple trenching analysis along a silent fault: the El Camp fault (Tarragona, northeastern Iberian Peninsula). *Acta Geologica Hispánica* **36**, 329–54.

Mateu J (1982) El Norte del País Valenciano. Geomorfología litoral y prelitoral. Ph.D. thesis, Universitat de Valencia. Published thesis.

Matmon A, Enzel Y, Zilberman E and Heimann A (1999) Late Pliocene and Pleistocene reversal of drainage systems in northern Israel: tectonic implications. *Geomorphology* **28**, 43–59.

McCalpin JP (1996) *Paleoseismology*. San Diego: Academic Press, 588 p.

Moissenet É (1980) Relief et déformations récentes: trois transversales dans les fossés internes des chaînes ibériques orientales. *Revue géographique des Pyrénées et du Sud-Ouest, Sud-Ouest Européen* **51**, 315–44.

Olivé A, del Olmo P, Portero JM, Carls P, Sdzuy K, Collande CV, Kolb S, Teyssen T, Gutiérrez M, Puigdefábregas C, Giner J, Aguilar MJ, Leal MC, Goy A, Comas MJ, Adrover R and Gabaldón V (1983) Mapa Geológico de España 1: 50.000, hoja no. 438 (Paniza). Madrid: Instituto Geológico y Minero de España.

Olivé A, Hernández A, Moissenet E, Pardo G, Villena J, Gutiérrez M, Puigdefábregas C, Giner J, Aguilar MJ, Leal MC, Goy A, Comas MJ, Adrover R, Portero JM and Gabaldón V (2002) Mapa Geológico de España 1: 50.000, hoja no. 516 (Monreal del Campo). Madrid: Instituto Geológico y Minero de España.

Ollier C (1981) Tectonics and Landforms. London: Longman, 324 pp.

Pailhé P (1984) La Chaîne Ibérique Orientale. Étude géomorphologique. Ph.D. thesis, Université de Bordeaux. Published thesis.

Peña JL, Gutiérrez M, Ibáñez MJ, Lozano MV, Rodríguez J, Sánchez-Fabre M, Simón JL, Soriano MA and Yetano LM (1984) *Geomorfología de la provincia de Teruel*. Teruel: Instituto de Estudios Turolenses, 149 p.

Downloaded from https://www.cambridge.org/core. Universidad de Zaragoza, on 04 Oct 2021 at 10:24:00, subject to the Cambridge Core terms of use, available at https://www.cambridge.org/core/terms. https://doi.org/10.1017/S0016756821000790

Perea H, Masana E and Santanach P (2006) A pragmatic approach to seismic parameters in a region with low seismicity: the case of Eastern Iberia. *Natural Hazards* **39**, 451–77.

Pérez A, Pardo G, Villena J and González A (1983) Estratigrafía y sedimentología del Paléogeno de la cubeta de Montalbán, prov. de Teruel, España. *Boletín de la Real Sociedad Española de Historia Natural, Sección Geológica* **81**, 197–223.

Pérez A and Simón JL (1993) Cambios en el trazado de la red fluvial producidos por la tectónica cuaternaria en el sistema de fosas del Maestrat. *El Cuaternario de España y Portugal, ITGE-AEQUA, Madrid* **2**, 707–15.

Roberts GP, Michetti AM, Cowie P, Morewood NC and Papanikolaou I (2002) Fault slip-rate variations during crustal-scale strain localisation, central Italy. *Geophysical Research Letters* **29**, 9-1.

Roca E and Guimerá J (1992) The Neogene structure of the eastern Iberian margin: structural constraints on the crustal evolution of the Valencia trough (western Mediterranean). *Tectonophysics* **203**, 203–18.

Rubio JC (2004) *Estudio hidrogeológico e histórico arqueológico de los humedales del alto Jiloca.* Zaragoza: Consejo de Protección de la Naturaleza de Aragón, 216 p.

Rubio JC and Simón JL (2007) Tectonic subsidence vs. erosional lowering in a controversial intramontane depression: the Jiloca basin (Iberian Chain, Spain), *Geological Magazine* **144**, 1–15.

Sanz-Rubio E (1999) Análisis de los sistemas deposicionales carbonáticos y evaporíticos del Neógeno de la Cuenca de Calatayud (provincia de Zaragoza). Ph.D. thesis, Universidad Complutense de Madrid. Published thesis.

Sanz-Rubio E, Sánchez-Moral S, Cañaveras JC, Abdul-Aziz H, Calvo JP, Cuezva S, Mazo AV, Rouchy JM, Sesé C and Van Darn J (2003) Síntesis de la cronoestratigrafía y evolución sedimentaria de los sistemas lacustres evaporíticos y carbonatados neógenos de la cuenca de Calatayud-Montalbán. *Estudios Geológicos* **59**, 83–105.

Scotti VN, Molin P, Faccenna C, Soligo M and Casas-Sainz A (2014) The influence of surface and tectonic processes on landscape evolution of the Iberian Chain (Spain): quantitative geomorphological analysis and geochronology. *Geomorphology* **206**, 37–57.

Simón JL (1982) Compresión y distensión alpinas en la Cadena Ibérica Oriental. Ph.D. thesis, Universidad de Zaragoza. Published thesis.

Simón JL (1989) Late Cenozoic stress field and fracturing in the Iberian Chain and Ebro Basin (Spain). *Journal of Structural Geology* **11**, 285–94.

Simón JL, Arlegui LE, Ezquerro L, Lafuente P, Liesa CL and Luzón A (2016) Enhanced palaeoseismic succession at the Concud Fault (Iberian Chain, Spain): new insights for seismic hazard assessment. *Natural Hazards* **80**, 1967–93.

Simón JL, Arlegui LE, Ezquerro L, Lafuente P, Liesa CL and Luzón A (2017) Assessing interaction of active extensional faults from structural and paleoseismological analysis: The Teruel and Concud faults (eastern Spain). *Journal of Structural Geology* **103**, 100–19.

Simón JL, Arlegui L, Lafuente P and Liesa CL (2012) Active extensional faults in the central-eastern Iberian Chain, Spain. *Journal of Iberian Geology* **38**, 127–44.

Simón JL, Ezquerro L, Arlegui LE, Liesa CL, Luzón A, Medialdea A, García A and Zarazaga D (2019) Role of transverse structures in paleoseismicity and drainage rearrangement in rift systems: the case of the Valdecebro fault zone (Teruel graben, eastern Spain). *International Journal of Earth Sciences* **108**, 1429–49.

Simón JL, Pérez-Cueva AJ and Calvo-Cases A (2013) Tectonic beheading of fluvial valleys in the Maestrat grabens (eastern Spain): insights into slip rates of Pleistocene extensional faults. *Tectonophysics* **593**, 73–84.

Simón-Porcar G, Simón JL and Liesa CL (2019) La cuenca neógena extensional de El Pobo (Teruel, Cordillera Ibérica): sedimentología, estructura y relación con la evolución del relieve. *Revista de la Sociedad Geológica de España* **32**, 17–42.

Sinusía C, Pueyo EL, Azanza B and Pocoví A (2004) Datación magnetoestratigráfica del yacimiento paleontológico de La Puebla de Valverde (Teruel). *Geo-Temas* **6**, 339–42.

Tena S and Casas A (1996) Estructura y cinemática de la falla de Alpeñés (Cordillera Ibérica). *Geogaceta* **20**, 789–91.

Vacherat A, Bonnet S and Mouthereau F (2018) Drainage reorganization and divide migration induced by the excavation of the Ebro basin (NE Spain). *Earth Surface Dynamics* **6**, 369–387.

Vegas R, Fontboté JM and Banda E (1979) Widespread Neogene rifting superimposed on alpine regions of the Iberian Peninsula. Proceedings of the Symposium on Evolution and Tectonics of the Western Mediterranean and Surrounding Areas, EGS, Vienna. Madrid: Instituto Geográfico Nacional, Special Publication no. 201, 109–128.

Wagner T, Fritz H, Stüwe K, Nestroy O, Rodnight H, Hellstrom J and Benischke R (2011) Correlations of cave levels, stream terraces and planation surfaces along the River Mur: Timing of landscape evolution along the eastern margin of the Alps. *Geomorphology* **134**, 62–78.

Wells DL and Coppersmith KJ (1994) New empirical relationships among magnitude, rupture length, rupture width, rupture area and surface displacement. *Bulletin of the Seismological Society of America* **84**, 974–1002.

Downloaded from https://www.cambridge.org/core. Universidad de Zaragoza, on 04 Oct 2021 at 10:24:00, subject to the Cambridge Core terms of use, available at https://www.cambridge.org/core/terms. https://doi.org/10.1017/S0016756821000790

2. The Cucalón-Pancrudo Fault Segment (CPFS)

2.1. General structure

The CPFS spreads from Cucalón to Pancrudo villages for nearly 40 km long, striking N155ºE and steeply dipping towards WSW (Fig. 1.2). Near its tip points, it intersects previous contractive structures. In the Cucalón-Olalla sector, there is clear evidence of recent activity, while between Olalla and Pancrudo this is not so evident. The main indicative of its Plio-Quaternary extensional activation is the rupture and displacement of the regional planation surface FES along the whole fault trace.

At its northern sector, between Cucalón and Lagueruela villages, the CPFS brings into contact Cambrian and Pliocene rocks, at the western block, with the Mesozoic and Paleogene series, at the eastern block (Fig. 2.10). The CPFS is here expressed as an anastomosing fault zone with a strong structural heritage, as it sometimes shares the trace with the Pelarda thrust.

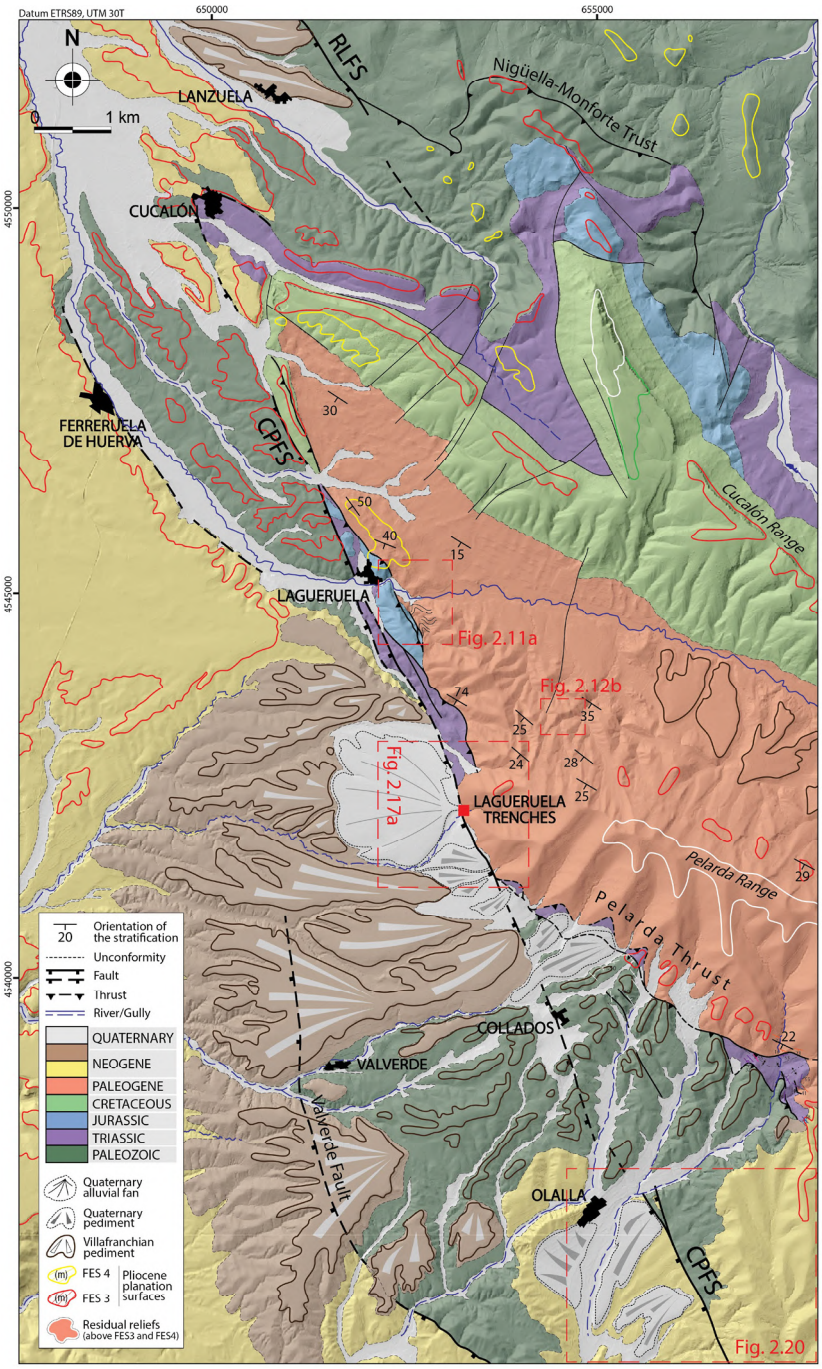

Fig. 2.10.- Geological-geomorphological map of the Lanzuela-Olalla area (on DEM image from Instituto Geográfico Nacional) showing the main structures associated to the Cucalón-Pancrudo Fault Segment (CPFS). Locations of Figs. 2.11a, 2.12b, 2.17a and 2.20 are indicated.

The north-central sector of the CPFS, more or less between Lagueruela and Olalla villages, shows the most noticeable features of recent reactivation. Several Villafranchian and Quaternary alluvial systems are interrupted by the fault zone, spreading from the latter, and it clearly offsets the Miocene series in different sites (Fig. 2.10). Along this section, other intrabasin normal faults run parallel to the CPFS, such as the Valverde fault, which generates metric offsets in the Villafranchian alluvial systems.

The trace of the south-central sector, between Olalla and Alpeñés villages (Fig. 1.2), can be inferred from certain almost straight lineaments cutting the Neogene Calatayud basin. They represent a succession of ruptures, not fully connected but markedly aligned, which are noticeable in both aerial photographs and DEM. It also offsets the FES, which allows to infer a recent normal extensional slip for this sector (not extensible to Quaternary times due to the absence of evidence). However, a number of outcrops of rupture surfaces that have been surveyed only show evidence of the previous contractive movements of the fault. This lineament is less manifest around the Barrachina area. As an indicative of the possible activation of this segment, several Villafranchian-Quaternary pediments and fans spread from it towards the centre of the Calatayud basin.

The southern sector, between Alpeñés and Pancrudo villages, mainly shows evidence of control by the structural heritage, related with the Alpeñés-Rillo anticline. In addition, it intersects another contractive structure, the Portalrubio thrust (Fig. 1.2).

2.2. Contractive framework

In order to fully understand the recent behaviour of the Río Grío-Pancrudo Fault Zone (RGPFZ), its past contractive history should be considered. This macrostructure crosses the Aragonian branch of the Iberian Chain and limits the northeastern margin of the Calatayud basin. This sector of the Aragonian branch is characterised by the presence of two anticlines, that spread for more than 100 km long, and exhibit Paleozoic and Precambrian outcrops at their cores, and a folded Mesozoic series at their limbs (Cortés-Gracia and Casas-Sainz, 1996). They are limited by thrusts and high-dipping faults at their margins, two of them being the RLFS and CPFS. The former has been deeply analysed in previous studies, but the latter has only been briefly mentioned in the literature, so a humble survey has been carried out in the present work.

As stated in section II.1, the NNW-SSE striking RLFS runs partially parallel to the Nigüella-Monforte thrust (Casas *et al*., 2016) till almost its tip at Lanzuela village, where both structures branch out and the thrust continues striking NW-SE (Fig. 2.10). It constitutes a fault zone enclosing anastomosing lenses of Triassic and Paleozoic fragments, with associated folds, foliation and fault breccia. These structures show strong reverse and dextral components, although there are also indicators of sinistral components. The whole structure is interpreted as the result of the reactivation, during the Cenozoic compression, of weakness areas probably formed during the Late-Variscan stage (Marcén & Román-Berdiel, 2015; Casas *et al*., 2016; Marcén, 2020).

The origin of the CPFS (Gracia *et al*., 1988; Gabaldón *et al*., 1991; Cortés-Gracia, 1999) might be the same as for the RLFS. At the northern sector of this main fault, this fault zone runs parallel to a thrust system in the surroundings of Lagueruela village, and shares part of its trace with the Pelarda NW-SE-striking thrust (Fig. 2.10). This thrust system, made of several almost parallel or anastomosing branches, lifted its southern block with Paleozoic and Mesozoic rocks onto the Paleogene series that constitute the Pelarda range, and enclosed part of the Mesozoic series between its branches. The Paleogene complex also shows noticeable features of contractive deformation, as it comprises the core of a gentle monocline or syncline fold in the closest areas to the main contractive ruptures (Moissenet, 1980; Adrover *et al*., 1982; Pailhé ,1984; Cortés-Gracia and Casas-Sainz, 1996; Peiro and Simón, 2021).

In the surroundings of Lagueruela village, anastomosing lenses at map and outcrop scale within the Jurassic units occur (Fig. 2.10). Along these rupture traces, several outcrops allow to obtain kinematic information of the fault. In a first site, Paleogene conglomerates appear affected by foliation planes oriented close to 020,70W, that are contiguous to a rupture plane oriented 140,60W, conforming a shear zone (Fig. 2.11a, d). A transport direction towards N312ºE can be inferred from its stereoplot (Fig. 2.11d). In a second site, there is a sigmoidal structure affecting the same conglomerates associated to a local fault bend or fault relay between fault segments

oriented close to 170,80W (Fig. 2.11a, b, c). This relay zone shows local foliation oriented 060,90. Such structural relationships constitute kinematical indicators that allow to interpret the shear zone as sinistral reverse. A transport direction towards N357ºE can be inferred from its stereoplot (Fig. 2.11c). Data collected in the surroundings of the village have corroborated the prevalent fracture direction with slickenlines indicating very scattered transport directions, with both reverse and sinistral components (Fig. 2.11e). Moreover, a group of tight, hectometre-scale folds affect the Paleogene series in this area (Fig. 2.11a). They consist in several plunging inclined synclines and anticlines that are consecutive, with hinge lines and axial planes that are almost parallel between them (oriented ca. 35,185 and 145,50W, respectively; Fig. 2.11f, g, h), and also parallel to the whole shear zone.

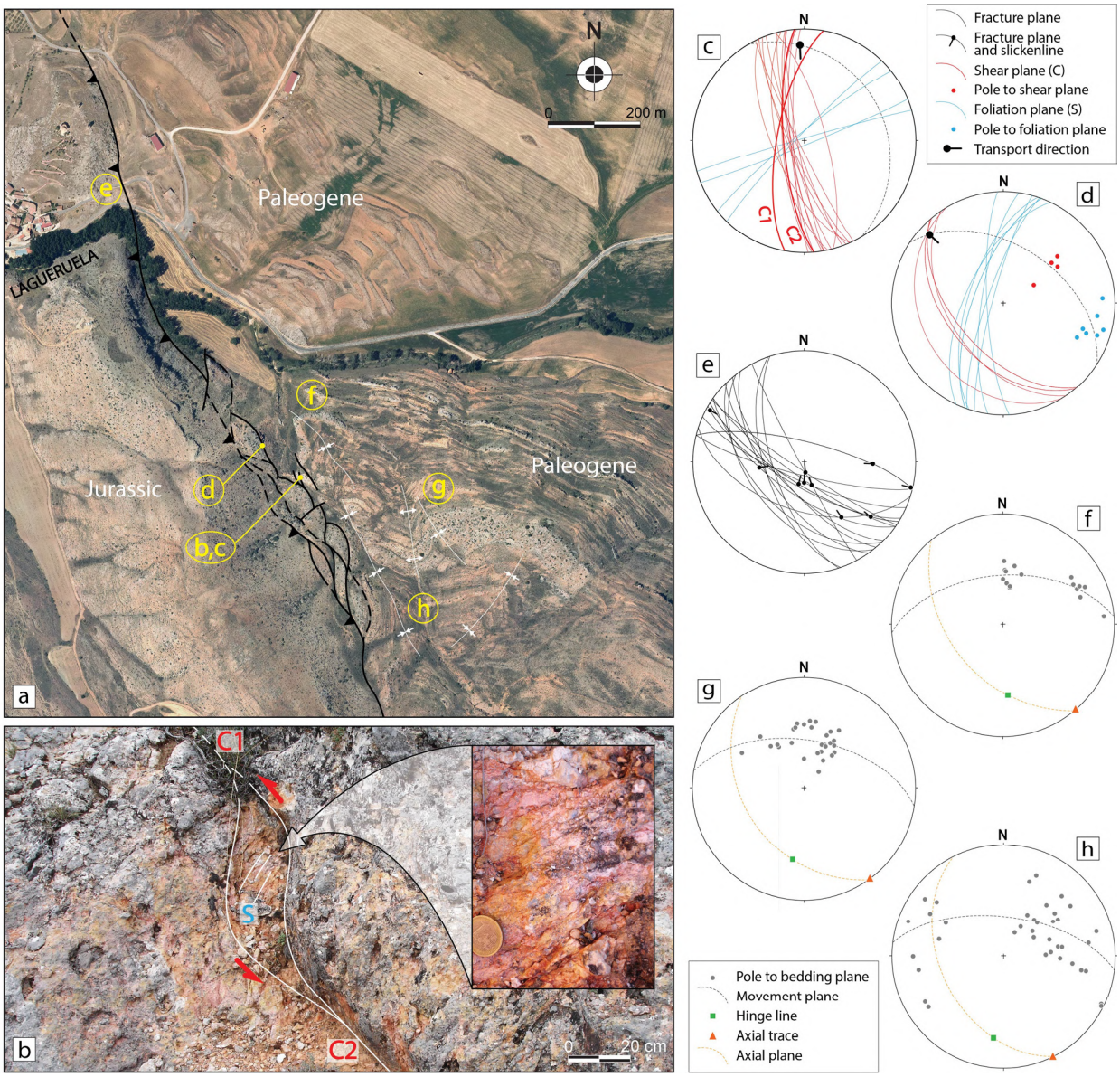

Fig. 2.11.- (a) Orthoimage of the Laguerela area, showing an anastomosing compressive fault zone of the CPFS, location of outcrops b-h is indicated, see location in Figure 2.10. (b, c) Photograph and stereoplot (equal area, lower emisphere) of a compressive relay zone between two C-planes, in which a secondary foliation (S) has been developed. (d) Stereoplot of S and C planes at the shear zone. (e) Stereoplot of minor faults with slickenlines. (f, g, h) Stereoplots of three tight folds within the Paleogene series.

These Paleogene outcrops are not the only ones with contractive features. The same series constitutes the Pelarda range, which makes part of a possible syncline structure (Fig. 2.5a; Moissenet, 1980; Adrover *et al.*, 1982; Pailhé, 1984) or a monocline series, according to our measures of layers dipping homogeneously to the SW (from 35º-25ºS at its northern sector, till 22ºS at its southern one, with no evidence of an opposite dip that could be associated with the other limb of the syncline) (Fig. 2.12). The parallelism between this series and the Pelarda thrust suggests a possible genetic relationship. Its contractive activity could have originated the tilting of the Paleogene

series, later uplifted and abruptly interrupted by normal slip on the CPFS. The NW-SE striking Pelarda thrust limits this complex at its SW sector. The eastern sector of the Pelarda thrust (to the northeast of Olalla village) is key for characterising this structure. Here both the northern and southern branches are recognisable due to the contact between the Paleogene and Triassic series, or between the latter and the Paleozoic, but only the southern branch plane could be measured, at around 124,38S. To the west, the southern branch has been verified in other outcrops, in contrast to the lack of exposures of the northern branch. However, the latter has then been extrapolated to the west, following the contrast between the Paleogene and Triassic series, that generates heterogeneities in aerial photographs and DEM. These Triassic series also appears intensely folded within the eastern sector of the Pelarda thrust (with two sets of plunging inclined folds: one also striking NW-SE and another NE-SW; Fig. 2.10).

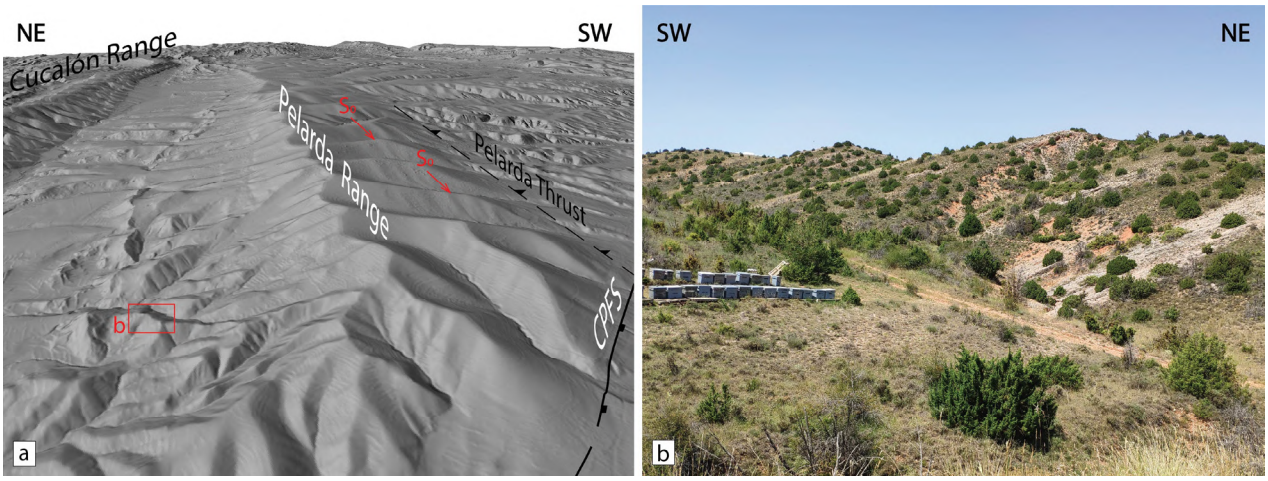

Fig. 2.12.- (a, b) 3D view of the DEM and photograph showing the oblique dipping of the Paleogene series within the Pelarda range. Location of "b" is shown both in "a" and in Figure 2.10.

The southern sector of the CPFS limits the western margin of the Paleogene Montalbán basin. Here, associated to this rupture, the Alpeñés-Rillo anticline (Tena and Casas, 1996) is the main contractive structure (Fig. 1.2). It strikes almost parallel with the CPFS, showing a Triassic core and limbs that consist in Jurassic and Cretaceous rocks. Slickenlines measured in this sector indicate a dextral directional movement with a reverse component (Guimerà, 1988). It also occurs that the Portalrubio thrust sheet is interrupted near this southern sector of the CPFS (Fig. 1.2; Guimerà *et al*., 1990; Simón and Liesa, 2011). It is an arc-shaped front, oriented transversely to the CPFS, NE–SW to NW–SE. This structure overlaps the Tertiary rocks of the Montalbán basin and, to its easternmost sector, it is cut and overthrust by the adjacent Utrillas thrust. It was active under the diverse regional compression directions from almost the middle Oligocene till the early Miocene (Simón and Liesa, 2011).

The compressive features associated with the whole RGPFZ can be summarized in three: (i) the main ruptures (RLFS and CPFS), considered as both reverse and dextral or sinistral structures, with associated almost parallel folds (e.g. the Alpeñés-Rillo anticline); (ii) the main thrusts (Nigüella-Monforte and Pelarda), that seem to belong to a common NW-SE trending compressive complex; and (iii) punctual outcrops, where again both dextral and sinistral indicators are inferred from their structural analysis. As the contractive history of the rupture system is not the main objective of this thesis, an approach to an evolutionary compressive model could be made in this section. The NW-SE trending thrust system could have been generated under the regional Iberian stress field (NE-SW; active during the Eocene-Late Oligocene time lapse; Liesa and Simón, 2009) or under the Pyrenean one (NNE-SSW; active since Late Oligocene). In this context, the NNW-SSE trending RGPFZ could have also emerged due to reactivation of previous weakness areas in the basement, moving under a mainly dextral component. Due to the lack of evidence, at this point it is not possible to stablish a structural chronology of these structures. What is sure is that, occasionally, a different stress field like the Early Betic one (ESE-WNW; Eocene; Liesa and Simón, 2009) acted on the RGPFZ and could explain the sinistral indicators inferred along its trace.

2.3. Evidence of Plio-Pleistocene and Holocene extensional activity

2.3.1. Revealed by morphotectonic analysis

As followed for the RLFS, planar landforms like planation surfaces can be used as direct markers of recent deformation for the CPFS. It is already a recurrent methodology used in the whole Iberian Chain for both identifying recent structures and assessing their vertical offsets and deformation rates (e.g. Peña *et al*. 1984; Gracia *et al*. 1988; Ezquerro *et al*. 2020). Reconstruction of the FES and its sublevels, and of pediments and alluvial deposits, has allowed to generate a regional contour map (Fig. 2.13), which is the basis for this task. In the case of the CPFS, the Neogene FES3 planation surface constitutes the vastest deformation marker and allows to estimate its post-3.5 Ma displacement. FES3 is developed in the form of an extensive pediment on Paleozoic, Mesozoic, Paleogene and Neogene materials, around residual reliefs, at both sides of the CPFS. In the case of the Pelarda range, a thin surficial sedimentary layer (1-5 m) is associated to this planation surface, and unconformably lies over the tilted Paleogene layers (Fig. 2.14c, d). These deposits have been surveyed in two explorative trenches and consist in non-cohesive brown gravel with sparse, muddy to sandy matrix and subrounded quartzitic clasts (centimetric to decimetric in size), result of reworking of the Paleogene conglomerates (Fig. 2.14d). It is believed that the presence of this thin sedimentary cover is the explanation for other geological interpretations of the Pelarda range as the one from Martín *et al*. (1977) and Gabaldón *et al*. (1989a, 1991). The basis of these interpretations was that this sedimentary unit seemed as a thick Neogene to Quaternary deposit that horizontally crowned the whole range and unconformably lied over Paleogene deposits (Fig.2.14b).

Within the footwall block of the CPFS, the FES3 flattens the Upper Cretaceous limestones in the monocline of the Cucalón range, reaching an altitude of 1380 m. Towards the central sector of the footwall block, there is an altitude loss of the FES3 from around the Pelarda range, where FES3 is developed at ca. 1300-1350 m (below both an older FES2 surface and a residual relief), to the Barrachina sector, where it is estimated to drop till an altitude of less than 1250 m. Near Alpeñés village, FES3 also gains altitude, standing at around 1300-1350 m (Fig. 2.13).

Within the hanging-wall block, there is an almost homogeneous altitude gain from the northern to the southern sector (Fig. 2.13). Around Cucalón village and to the Calatayud basin centre, the FES3 is an almost planar pediment developed over the informal units Páramo 1 and Rojo 2 at an average altitude of 1000 m. Towards the southern tip point of the CPFS, the FES3 remains indicate a gradient to higher altitudes till the Alpeñés-Pancrudo area. Here the deposits mainly associated with the Aragonian Clastic Unit, as part of the southern termination of the Calatayud basin, are modelled by the FES3 reaching an altitude slightly higher than 1300 m. This altitude diminishes up to ca. 1200 m in a local depression, where it approaches the fault plane. Along the Cucalón-Olalla sector of the hanging-wall block, the FES3 surface includes a bending component and shows a stepped-shape, because several remains are truncated by intrabasin secondary faults like the Valverde fault. Locally, the hanging-wall block hosts red clastic deposits of Villafranchian age, several tens of metres thick, whose tops are modelled into pediments (Fig. 2.13).

Within the relay zone between the RLFS and the CPFS, the FES3 is preserved through dispersed irregular remains, that are degraded by erosive incision and level both the Paleozoic materials and the Aragonian Clastic Unit (Fig. 2.13). There is an altitude loss of FES3 from de southeastern sector of the relay zone, at almost 1300 m, till the Calatayud basin centre, where it lies at ca. 1000 m. It follows the common arrangement of a relay ramp between the main faults, due to bending and soft-linkage interaction between them. It was not possible the identification of favourable outcrops for measuring minor faults and fractures affecting the relay zone.

As stated in the study by Peiro and Simón (2021), this deformation registered by the FES3 allows determining maximum vertical offsets along the CPFS. Such fault throw, and its variation along the fault, have been analysed on a series of transects across the fault trace on the contour map of Figure 2.13. The result is shown in the throw vs. distance (T-D) graph of Figure 2.15 and the topographic profiles of Figure 2.16.

In Figure 2.15 four distinct T-D curves depict values of: (1) RLFS fault throw s.s., (2) CPFS fault throw s.s., (3) tectonic throw of the CPFS together with the bending component and the Valverde fault, (4) total throw of all the

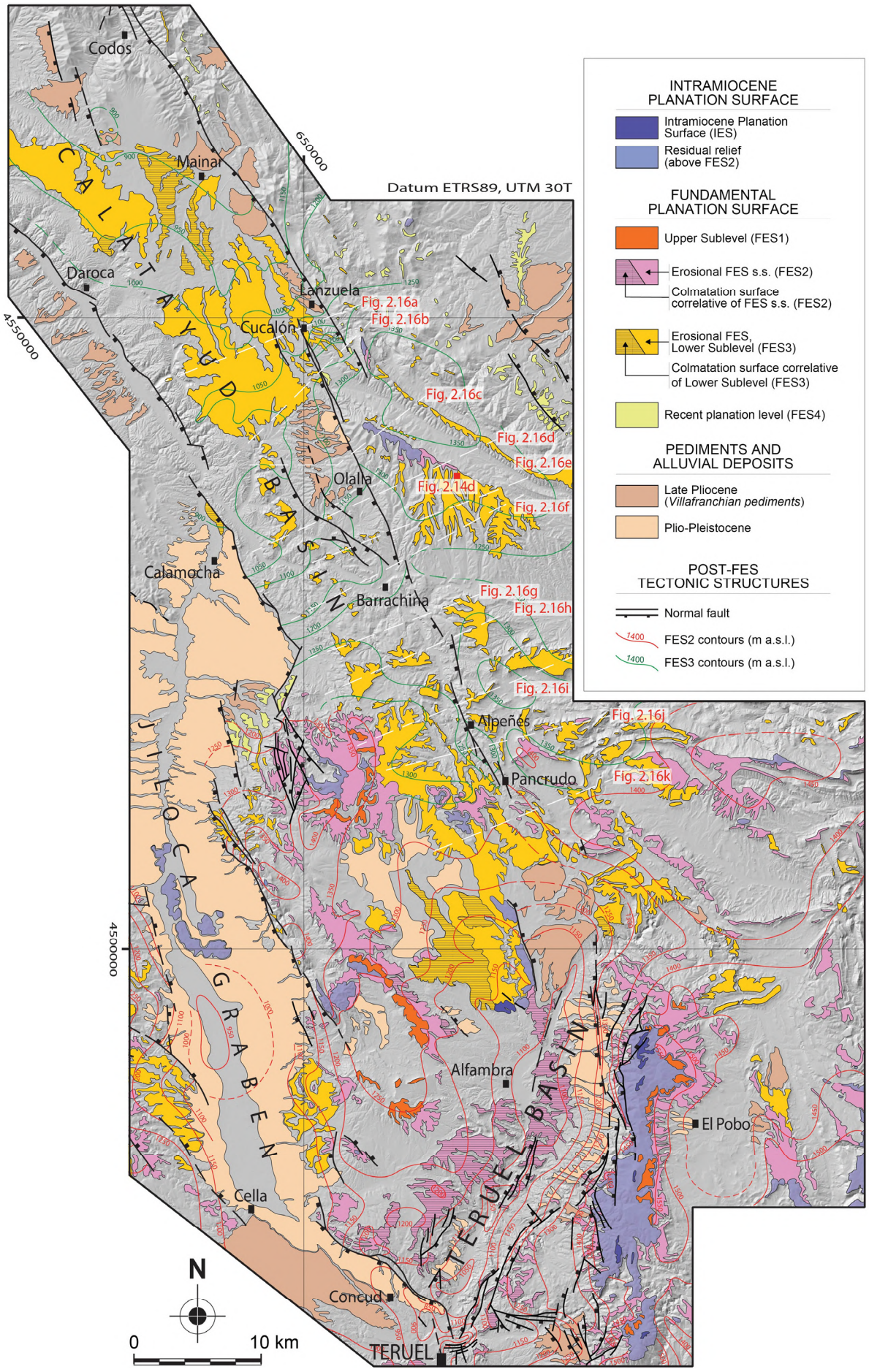

Fig. 2.13.- Synthetic map of late Neogene planation surfaces, pediments and alluvial deposits in the surroundings of the Calatayud, Jiloca and Teruel basins, with location of Figures 2. 14d and 2.16a-k (modified from Peiro and Simón, 2021).

structures combined. The T-D curve of the RLFS is incomplete due to the lack of FES3 remains within the northern sector of the fault. However, the first maximum values of the RLFS curve, of 240 m (depicted around kilometre 27 in Fig. 2.15; Peiro and Simón, 2021) suggest a possible bell-shape. Its tendency points to the existence of a maximum throw that could be equal or higher than 240 m within the northern sector of the RLFS. The T-D curve of the CPFS shows two maxima of ca. 190 and 100 m (around kilometres 55 and 86 in Fig. 2.15), corresponding to two sectors of the main fault, from Cucalón to Barrachina, and from the latter to Pancrudo, respectively. The first sector shows a very symmetrical bell-shape while the second one is more irregular. Between these two maxima, there is a throw drop around Barrachina village to 30 m (kilometre 73 in Fig. 2.15; Fig. 2.16g). According to the evolutive models of fault coalescence through relay zones (e.g., Peacock and Sanderson, 1994; Gawthorpe and Leeder, 2000), this throw drop could correspond to the junction point between two fault segments, separated at the beginning, now linked through the old relay zone. Moreover, the steeper displacement showed in the RLFS and CPFS curves within their relay zone fits the evolutive model from literature of two faults interacting and transferring displacement. If the bending component and the intrabasin Valverde fault are taken into account, the maximum fault throw increases from 190 m to almost 300 m (the higher one recorded along the Río Grío-Pancrudo Fault Zone; Peiro and Simón, 2021).

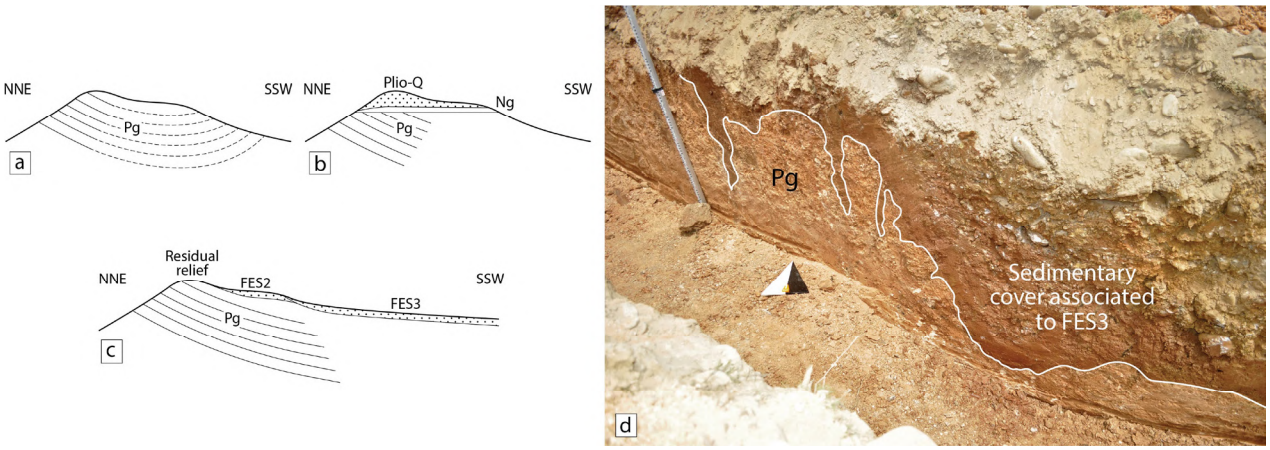

2.14.- (a) Interpretation of the Pelarda complex by Moissenet (1980), Adrover *et al.* (1982) and Pailhé (1984). (b) Interpretation of the Pelarda complex by Martín *et al.* (1977) and Gabaldón *et al.* (1989a, 1991). (c) Interpretation of the Pelarda complex by Peiro and Simón (2021) and this thesis. (d) Erosive contact between the Paleogene series and the clastic cover associated to the FES3 surface. See location in Figure 1.2.

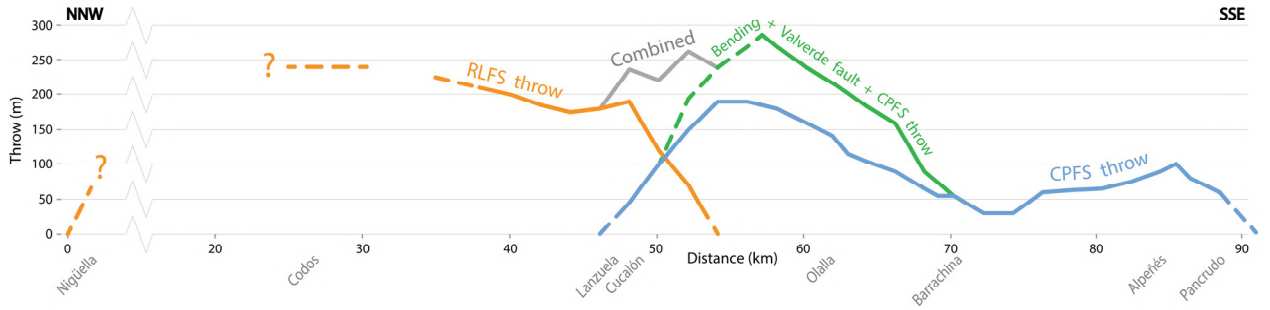

2.15. Throw vs. distance (T-D) graph along the whole Río Grío-Pancrudo fault zone (RLFS, depicted in orange, and CPFS, depicted in blue), together with the bending component and the Valverde fault (depicted in green). Curves represent the throw s.s. recorded by the FES3 marker.

Transversal topographic profiles of Fig. 2.16, crossing the relay zone and the CPFS, corroborate these calculations. Along the relay zone and in the surroundings of Cucalón village, vertical offsets of the main fault are in the range of ca. 30-150 m when comparing the altitude of FES3 remains at one side and the other of the CPFS (Fig. 2.16a, b). Displacement is more visible in the profile of Fig. 2.16a, as two remains of FES3 are confronted closely to the CPFS. In the case of Fig. 2.16b (and in other profiles from this point forward mentioned), when the FES3 surface cut by the topographic profile is far from the main fault, its arrangement is interpolated from nearby reliable remains and the defined contour lines.

Within the sector of the CPFS adjacent to the Pelarda range, the movement of its hanging-wall block has thrown down the FES3 to ca. 1020-1040 m, which its covered by the red clastic deposits of the Villafranchian pediment (Fig. 2.16c). In the footwall block, the remains of FES3 lie at around 1320 m, surrounding the residual relief of the Pelarda summit. Therefore, the overall fault zone has undergone a total vertical offset of about 280-300 m, partitioned among net slip on the Valverde fault and a gentle accommodation monocline.

Between villages of Olalla and Barrachina, remains of FES3 are quite far from CPFS at both the hanging-wall and footwall blocks, but within the latter its height is well constrained along the Pelarda range. This implies a reliable use of the contour lines for inferring vertical offsets (Fig. 2.16d, e). In this sector, the main fault generates vertical displacements of 90-110 m. However, they are higher when the bending component and the intrabasin Valverde fault is included, resulting in throws of ca. 160-190 m.

To the south, there is a clear lack of FES3 remains within the hanging-wall block of the CPFS, but within the footwall block it is still well constrained along the Pelarda range and the plain of Mas de Teller (Fig. 2.16f, g, h). Our interpretation is based on the extrapolation of the inferred contour lines from the surrounding sectors, and according to this the vertical offset of the main fault system in this sector is low, between 30 and 65 m. However, a more conservative interpretation could be approached, which would consider that in this sector there is no surficial expression of the CPFS and that the FES3 simply shows a gentle tilting from its western remains to the eastern ones.

Displacement on the CPFS increases when approaching the fault tip, between Alpeñés and Pancrudo villages. Here the contour map points to a local roll-over structure affecting the hanging-wall block, identified in the profile of Fig. 2.16j and interpolated to that of Fig. 2.16i. Vertical offsets in the range of 70 to 100 m can be inferred for the FES3 surface in this sector. Finally, no significant vertical deformation is inferred from mapping of the FES3 surface south of Pancrudo village, reinforcing the hypothesis of the CPFS termination in this sector (Fig. 2.16k).

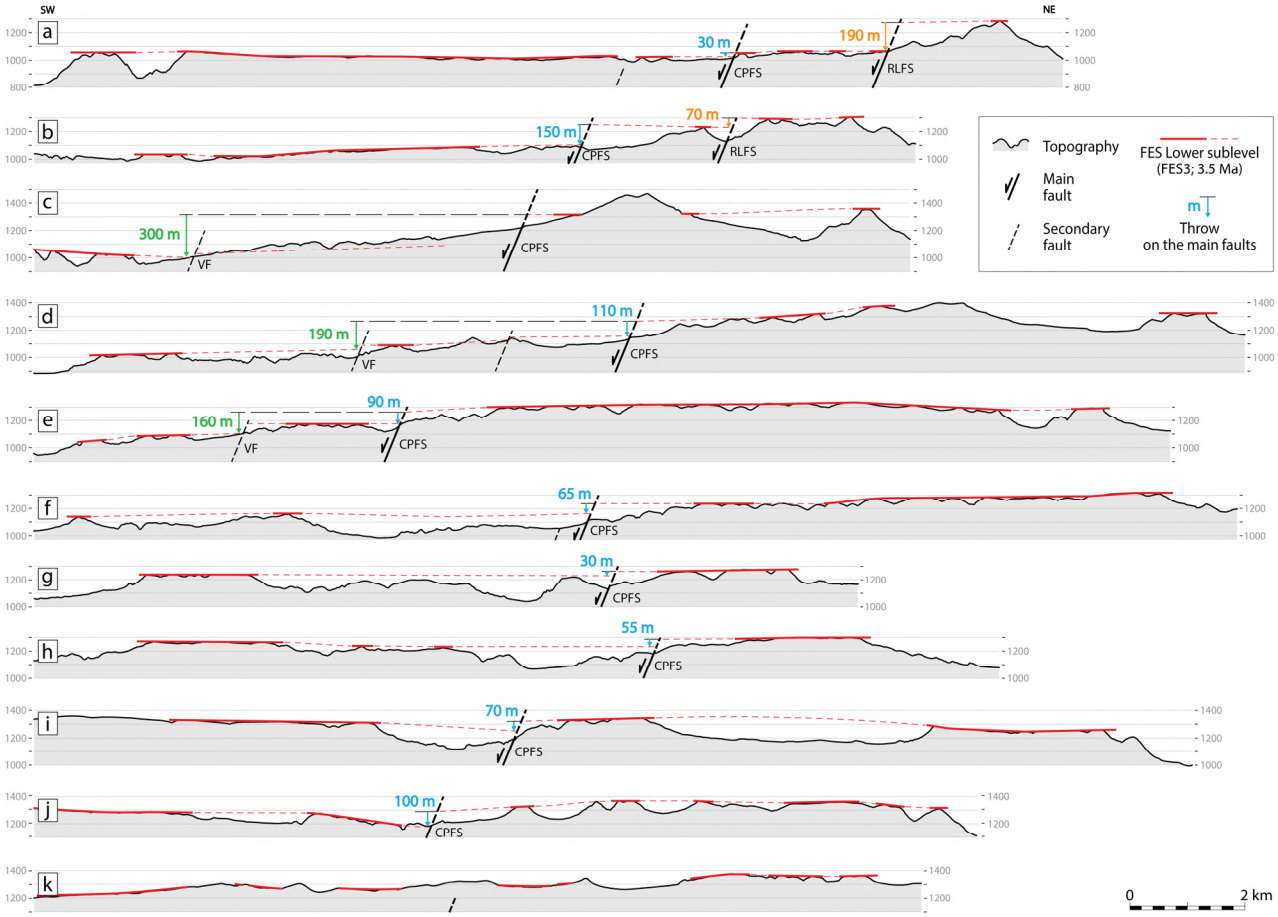

2.16. (a-k) Topographic profiles across the Cucalón-Pancrudo Fault Segment (CPFS; depicted in blue), together with the Valverde Fault (VF; depicted in green) and its relay zone with the Río Grío-Lanzuela Fault Segment (RLFS; depicted in orange). Estimations of post-FES3 vertical slips are shown. See location in Figure 2.13.

Considering the age of the FES3 morphosedimentary marker (3.5 Ma), and assuming a pure normal movement and an average dip of 67º (which is the average calculated for the RLFS, and lies within the 65-70° range of average dips for the main normal faults of the northern Teruel Basin; Ezquerro *et al.* 2020), the throw value of the RLFS, 240 m, involves a total net slip of ca. 260 m, and a slip rate of 0.07 mm/a (Peiro and Simón, 2021). In the case of the CPFS, the higher vertical displacement of 190 m results into a net slip of ca. 205 m, and a slip rate of 0.06 mm/a. If the CPFS is considered together with the bending component and the Valverde fault, the maximum throw is 280-300 m and implies a net slip of ca. 305-325 m and a slip rate of 0.09 mm/a (Peiro and Simón, 2021).

2.3.2. The Lagueruela trench site

The Lagueruela trench site is in the northern sector of the CPFS, around 3 km to the south of Lagueruela town (Figs. 2.10, 2.17). The paleoseismological analysis at the Lagueruela site is focused on the intersection between the fault trace and the apex of a Pleistocene alluvial fan, which to the west overlays and rearranges the underneath Villafranchian alluvial pediment. Two trenches where dug, one on the alluvial fan surface, and the other one close to the incised Valdelafuente gully, the latter draining from the Pelarda range to the Calatayud basin perpendicularly to the CPFS, and exhibiting its own Holocene fluvial sediments. Two flat landforms can be recognised within the trench site: the Pleistocene fan surface, that dips 7-8º towards W and is located ca. 8-10 m above the present thalweg, and a local fluvial terrace, that dips ca. 10º towards SW and raises 2 m from the thalweg of the gully. The fan is characterised by an alluvial deposit mostly made of rounded cobbles and boulders that are more abundant when closer to the apex. These clasts correspond to the characteristic Paleozoic and Triassic ones reworked from the Paleogene of the Pelarda range.

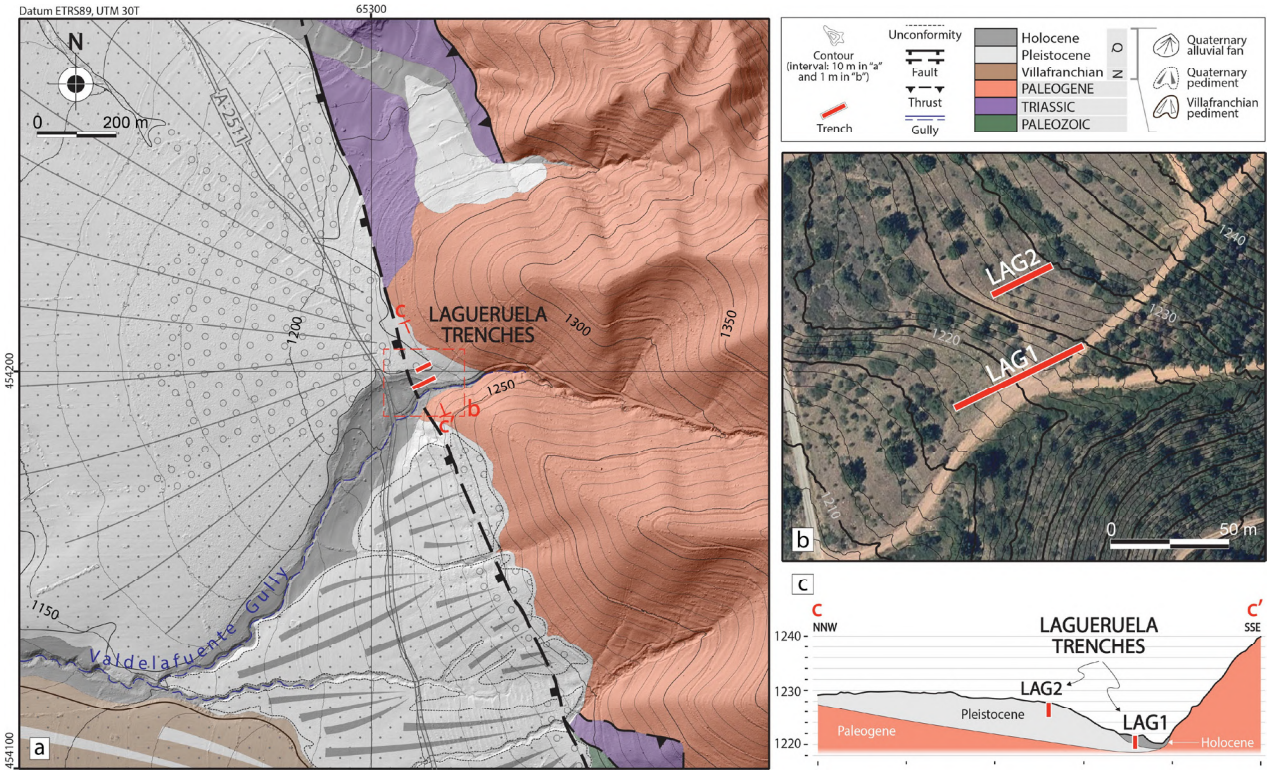

2.17.- (a, b) Geological–geomorphological map (see location in Figure 2.10) and aerial view of the Lagueruela area, where trenches LAG1 and LAG2 were dug; elaborated from field survey, analysis of aerial images, DEM and orthoimages.
(c) Geological cross section parallel with the CPFS, where the arrangement of the Pleistocene and Holocene deposits can be observed.

The sites for trenching were selected after their favourable geophysical survey (not described in this study): (i) LAG1 trench, 60 m long, on the Holocene fluvial terrace in an eroded bend of the Valdelafuente gully; (ii) LAG2 trench, 25 m long, on the top of the Pleistocene alluvial fan. Both trenches cross the main fault trace at right angles,

with a trend close to N065ºE. LAG1 was excavated with a maximum depth of approx. 2 m, and LAG2 with 2.5 m. The western part of the LAG1 trench (from meter 11 to 16) constitutes the main source of paleoseismological information. Within it, ruptures associated with the CPFS cut both the Holocene sediments of the gully at the top of LAG1 trench, and the Pleistocene deposits at the bottom. The latter are almost contemporary with the sedimentary Pleistocene series where the LAG2 trench was dug. Both trenches have been surveyed and dated by Optically Stimulated Luminescence (OSL).

Materials

Materials cropping out in the LAG1 trench entirely correspond to Quaternary alluvial and fluvial sediments (Fig. 2.18a, c). Several units are distinguished:

Unit 1 (up to 30 cm in thickness): grey and ochre mudstone with crude parallel lamination.

Unit 2 (up to 1.20-thick): whitish gravel with muddy matrix and angular to subrounded clasts up to 46 cm in diameter. Towards the top of the unit, which is marmorized and locally encrusted, fine sediments are more abundant.

Unit 3 (35 cm-thick): ochre and brown mudstone, darker and sandier at top, where rare disperse clasts can be observed.

Unit 4 (25 cm-thick): brown grain-supported gravels with angular to subrounded clasts (up to 17 cm in diameter). They form a plane-convex up level that fades laterally.

Unit 5 (45 cm-thick): grey and dark brown mudstone with organic matter remains, bioturbation evidence and millimetric, rarely centimetric, disperse angular-subangular clasts.

Unit 6 (35 cm-thick): grey mudstone with floating clasts. A gravel level with angular to subrounded cm-sized clasts can be recognized in the base.

Unit 7 (30 cm-thick): brown mudstone, orangish in the middle part. Two gravel levels, with clasts up to 17 in diameter, are intercalated near the base and the top of the unit.

Unit 8 (33 cm-thick): brown mudstone with disperse subangular-subrounded clasts up to 12 cm in diameter.

Unit 9 (35 cm-thick): soil.

These units have been identified at the southern wall of LAG1 trench and correlated with the northern wall, considering their lithological characteristics and two vertical profiles of magnetic susceptibility measurements at both trench walls (Fig. 2.18a, c). They allowed to identify that the highest values of magnetic susceptibility correspond to units 7 and 8.

LAG2 was dug in an almost homogeneous alluvial fan deposit in which no significant stratigraphic marker was identified. It consists in brown gravels with subrounded to subangular clasts, with occasional levels of reddish mudstones with disperse clasts.

OSL dating

Eight samples were collected to constrain the chronology of the sedimentary units: seven samples from the LAG1 trench (from LAG1-1 to LAG1-F in Table 2.1), and one from the LAG2 trench (LAG2-1 in Table 2.1). They were generally collected using opaque tubes to avoid exposure to daylight. In one case, due to backhoe damage to the trench walls and water filtration, one sample (LAG1-F) was collected from the inside of a removed block under the darkness conditions of the laboratory. These eight OSL samples were processed by the Luminiscence Dating Laboratory of CENIEH (Burgos, Spain).

The OSL response from the eight samples measured is fast-component dominated, and their reliability to estimate the accumulated dose has been confirmed through dose recovery tests performed in the laboratory. The derived natural dose populations are normally distributed with overdispersion values below 30% after removing outliers. Estimated burial doses, total dose rates and derived numerical ages are summarized in Table 2.1.

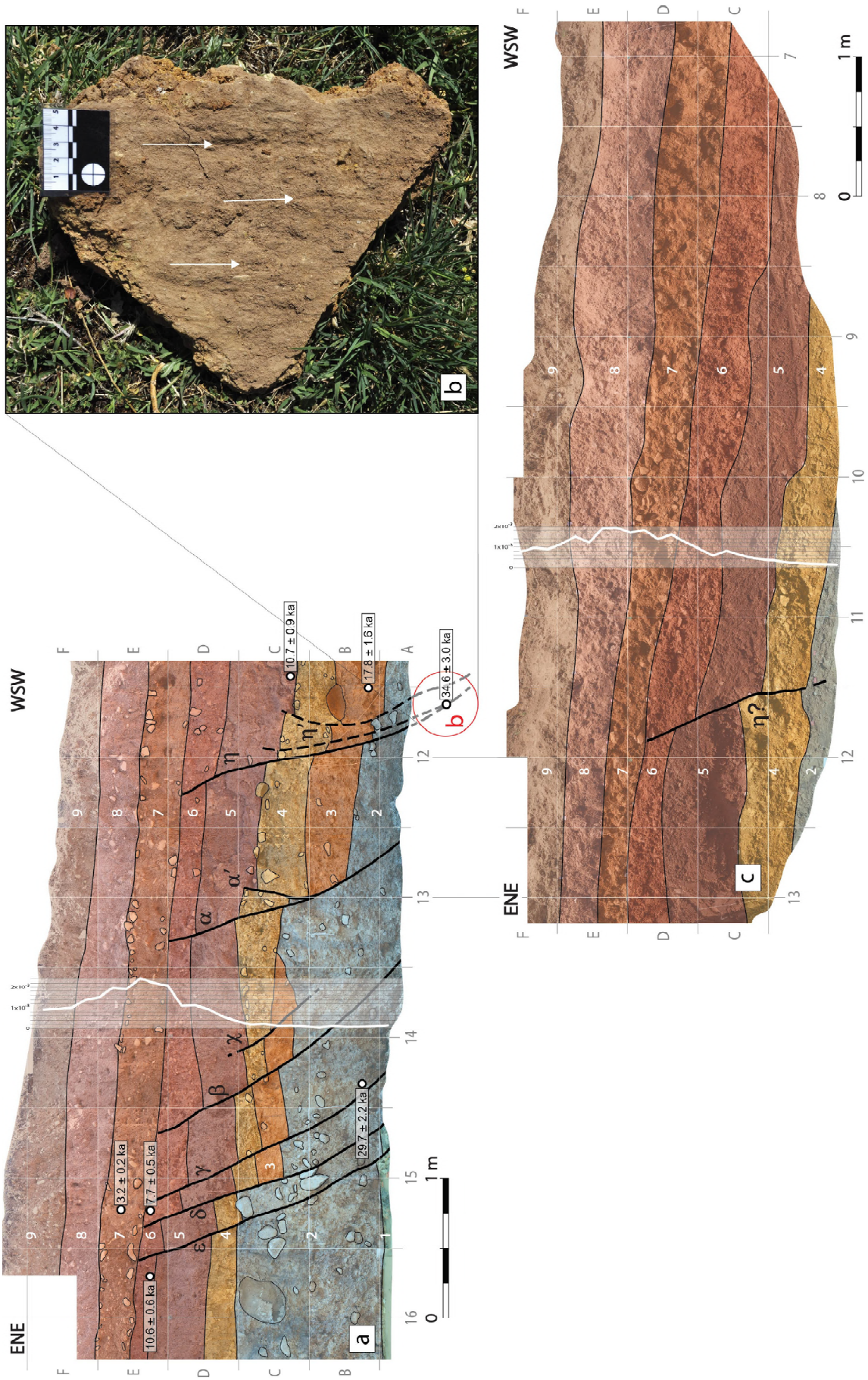

2.18.- (a) Detailed log from meter 11 to 16 of the southern wall of LAG1 trench (b) Slickenlines associated to fault η-η' in an intact non-orientated fallen block. (c) Detailed log from meter 7 to 13 of the northern wall of LAG1 trench. See location in Figures 2. 10 and 2. 17. 1 to 9: Quaternary units described in the text. Greek characters: faults referred in the text. The location and age of samples dated by OSL is indicated. The profiles of magnetic susceptibility (white line) are shown vertically and their values are expressed in SI.

Sample	Laboratory reference	Depth (m)	Dose rate (Gy/ka)	Equivalent dose (Gy)	Age (ka)
LAG1-1	LM20132-01	1.1	3.1 ± 0.2	24.1 ± 0.9	7.7 ± 0.5
LAG1-2	LM20132-02	1.2	3.1 ± 0.2	32.4 ± 0.9	10.6 ± 0.6
LAG1-3	LM20132-03	0.9	3.0 ± 0.2	9.8 ± 0.3	3.2 ± 0.2
LAG1-5	LM20132-04	1.6	3.1 ± 0.3	33.6 ± 0.7	10.7 ± 0.9
LAG1-6	LM20132-05	2.1	3.6 ± 0.3	64.2 ± 2.1	17.8 ± 1.6
LAG1-7	LM20132-06	2.4	3.0 ± 0.2	90.7 ± 3.1	29.7 ± 2.2
LAG1-F	LM20132-10	2.6	3.1 ± 0.3	106.8 ± 2.3	34.6 ± 3.0
LAG2-1	LM20132-07	1	3.1 ± 0.3	99.5 ± 2.1	31.7 ± 2.8

Table 2.1.- Summary of the parameters and derived ages of samples dated with OSL from the Lagueruela trenches (Luminescence Dating Laboratory of CENIEH, Burgos, Spain). All ages are reported at 1-sigma (k=1).

Structural description

Several extensional, domino-style faults are exposed within the LAG1 trench (Fig. 2.18a). Only one of them can be recognised at both trench walls (Fig. 2. 18c). No orientation of the rupture planes could be measured due to degradation of the trench walls. However, the possible identification of the westernmost fault (η) at the northern and southern walls allows inferring a general N142ºE strike of the fault system along the trench. No in situ measurement of kinematic indicators could be collected, neither. Nevertheless, occurrence of shear along rupture planes (more precisely, on fault η-η) is evidenced by slickenlines observed in the same removed block in which OSL sample LAG1-F was extracted (Fig. 2. 18b).

Every fault exposed within the LAG1 trench is synthetic with the CPFS. Two groups of ruptures can be recognised (Fig. 2. 18a, c): 1) faults χ, α' and η', that produced centimetric slip in the base of unit 5, vanishing inside this unit; and 2) faults ε, δ, λ, β, α and η, that underwent decimetric vertical displacement after sedimentation of unit 6, and are covered by unit 7. Faults α' and η' are splay faults of α and η, respectively; therefore, they are sometimes referred as α-α' and η-η'. Faults δ and α-α' are in contact with remains of unit 3, and produce a higher vertical separation to the base of this unit than to the base of unit 4. We interpret that both faults underwent displacement before sedimentation of unit 4, and were then reactivated after deposition of unit 6.

Successive slip on this fault system has therefore produced displacement of units 1-6, resulting in sinking and thickening of the series to the SW block. Both the fault geometries and the stratigraphical thickening are consistent with the geophysical inferences from reflectors of the GPR profiles (interruptions and tilting changes).

The aggregate, visible throw of the synthetic fault system is ≈ 1 m, as seen when comparing the height of the top of unit 2 at both ends of the southern log (Fig. 2. 18a). There is a lack of information about slip vectors on the surveyed faults, but a rough translation of this throw value into net slip can be done. Assuming a nearly pure normal movement and a fault dip of 65º (the average apparent dip of the trench fault system), the net slip could be estimated at about 1,1 m.

No deformation has been registered within the LAG2 trench, probably due to the lack of clear stratigraphic markers. Slight heterogeneities in the gravel complex have allowed to infer a possible channelled structure, only associated with the alluvial fan dynamics.

Paleoseismic events and retrodeformational analysis

Two clear deformation events (X and Z), and an additional uncertain one (Y), have been interpreted at the LAG1 trench after delving into the sedimentary units and their relationship with faults. Retrodeformational analysis of the southern-wall trench log (Fig. 2. 18a) has been achieved as an auxiliary tool. It allows contrasting the succession of deformation events, and testing its kinematic consistence. A number of identifiable faults were either formed, propagated or reactivated during each deformation event. For each event, fault throws have been computed, and the horizontal extensions visually expressed in the successive cross sections of Figure 2.19 have been measured.

The interpreted events at the LAG1 trench are as follows (Fig. 2.19):

Event X: Inferred from the presence of discontinuous remains of unit 3 in contact with faults δ and α-α′, explained by slip on those faults after deposition of unit 3 and prior to unit 4. This event is predated by unit 3 (17.8 ± 1.6 ka), and postdated by unit 4 and the base of unit 5 (10.7 ± 0.9 ka). The more probable event age would be closer to the age of unit 3, and adopted as ca. 15 ka. The total, synthetic throw of this event is ≈ 0.6 m, net slip estimated at ≈ 0.7 m, and horizontal extension ≈ 0.1 m.

Event Y (?): Tentatively interpreted from rupture and displacement of the base of unit 5 due to sin/post-sedimentary slip by faults χ, α-α′ and η-η′. It could be more or less coeval with the base of unit 5 (10.7 ± 0.9 ka), assuming a more probable event age near 10 ka. A second scenario where this deformation takes place simultaneously with Event Z can not be ruled out. The total, synthetic net slip of this event would be ≈ 0.2 m, and its horizontal extension less than 0.1 m.

Event Z: Identified from rupture and displacement of the base of unit 6 due to domino-style slip on faults ε, δ, λ, β, α and η, prior to deposition of unit 7. This event is predated by top of unit 6 (7.7 ± 0.5 ka), and postdated by unit 7 (3.2 ± 0.2 ka). The more probable event age is ca. 5 ka. The total, synthetic throw of this event is ≈ 0.25 m, net slip estimated at ≈ 0.3 m, however it should be higher due to the domino-style slip. Its horizontal extension is close to 0.2 m.

Paleoseismological interpretation

The CPFS has undergone slip during late Pleistocene and Holocene times, as evinced in the LAG1 trench. Detailed study of this trench has provided a succession of 2-3 deformational events for the time window from 17.8 ± 1.6 ka till 3.2 ± 0.2 ka. On the contrary, LAG2 trench has only allowed to date the top of the Pleistocene alluvial fan in 31.7 ± 2.8 ka.

Considering both scenarios (either 2 or 3 events), and taking into account the error bars, the paleoseismological succession of LAG1 trench results in an average recurrence period in the range of 4.2 to 8.2 ka. Net coseismic displacements range from 0.2 to 0.7 m, with an average value of 0.5 m. The total net slip estimated at about 1,1 m provides a slip rate of 0.07-0.08 mm/a for the time window from 17.8 ± 1.6 ka till 3.2 ± 0.2 ka.

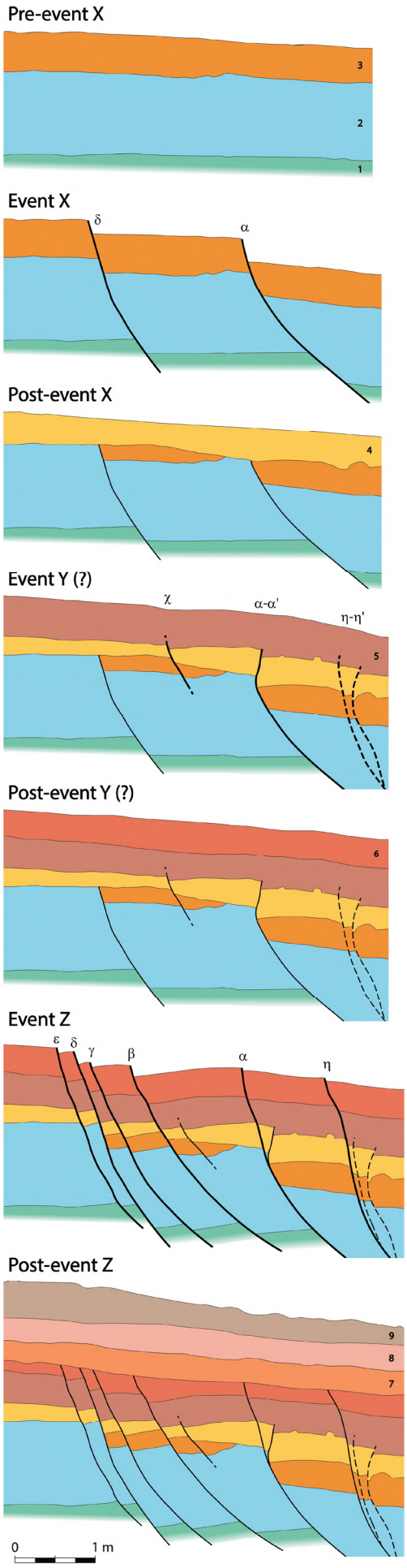

2.19.- Evolutionary model of sedimentation and deformation recorded at the southern-wall of LAG1 trench from retrodeformational analysis. Each sketch represents a stage subsequent to the paleoseismic event labelled above. Unexposed sectors below the trench have been locally reconstructed in the sketches in order to complete the evolutionary model. Bold traces indicate which faults are active during each event.

Displacement associated with these deformation events is accumulated on the main fault, so the inferred paleoseismic notions can be considered as accurate for late Pleistocene-Holocene times. However, more trenches would be needed for building a robust paleoseismic record of the CPFS, but for the moment no other favourable locations for this purpose have been identified along the fault trace. In any case, the calculated parameters definitely allow classifying this sector of the CPFS as an active fault, according to most scientific classifications and legal regulations (e.g., NRC, 1997; Machette, 2000; Strom, 2017).

2.3.3. Southern fault outcrops

Olalla site

To the east of Olalla village, and following the A-2513 road, there is a piece of evidence of the presence of the CPFS to the south, as it is clearly exposed at El Caño slope (Figs. 2.20 and 2.21). The latter is a slope of ca. 150 m in length and 20-40 m high, nearly perpendicular to the CPFS, which has been excavated by erosive incision of La Riera gully. In this site, the CPFS brings into contact the Paleozoic materials, within the footwall block, and the Neogene units, within the hanging-wall block. Quaternary sediments crop out far from the main rupture, at the southwestern sector of the slope. However, to the southeast of the Olalla site, these recent sediments show continuity with a Quaternary alluvial pediment that spreads from the fault scarp to the depression of La Riera gully.

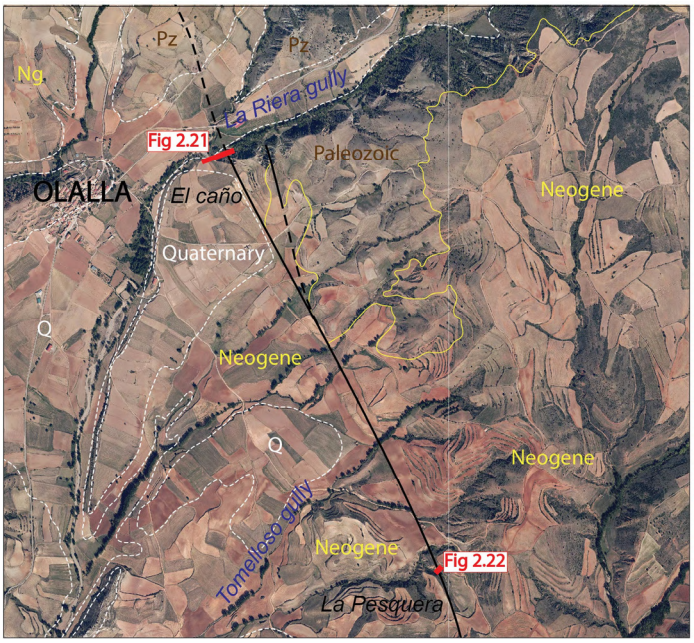

2.20.- Orthoimage showing the CPFS between the Olalla and Nueros sector (see location in Figure 2. 10), affecting the Paleozoic, Neogene and Quaternary units. Location of Figures 2.21 and 2.22 are indicated.

Figure 2.21.- Synthetic cross section of El Caño slope, where the CPFS brings into contact the Paleozoic materials and the Neogene units. Quaternary sediments crop out at the western part of this section. See location in Figure 2.20.

Within the Olalla slope, the CPFS emerges as a ca. 10-m-thick fault zone that strikes N147ºE with an almost vertical dip. This fault zone consists in Paleozoic rocks strongly deformed and partially brecciated. No geometric feature nor kinematical indicator could be described or measured within the fault zone itself, due to the inaccessible characteristics of the outcrop. Several minor faults offset the Neogene layers at both the footwall and hanging-wall blocks. The two westernmost ruptures at the hanging-wall block have an orientation of 175,60E and 167,85W, respectively. Within this block, the Neogene layers show an average dip of 45º to the SW, representing a probable bending monocline.

La Pesquera site

A second exposure of the CPFS is located halfway between Olalla and Nueros villages, in a secondary gully of the Tomelloso gully (Fig. 22a, b). The fault zone is oriented ca. 125,60S, shows a thickness of approximately 1.3 m and affects two different Miocene units: an orange mudstone or claystone unit with disperse clasts (M1) within its footwall block, and a brownish gravel of angular centimetric clasts (of Paleozoic origin) in a muddy matrix with decimetric layers of interbedded limestone (M2) within the hanging-wall block. Bedding of M2 is noticeably tilted, being oriented 112,40S. A set of minor faults (oriented 118,55S in average; Fig. 22b) offsets the layers of M2 with centimetric offsets and showing clear slickenlines in their planes with very low pitches, associated to a strike-slip past stage of the fault zone (Fig. 22c, d). No clear kinematical indicator of the sense of movement has been identified.

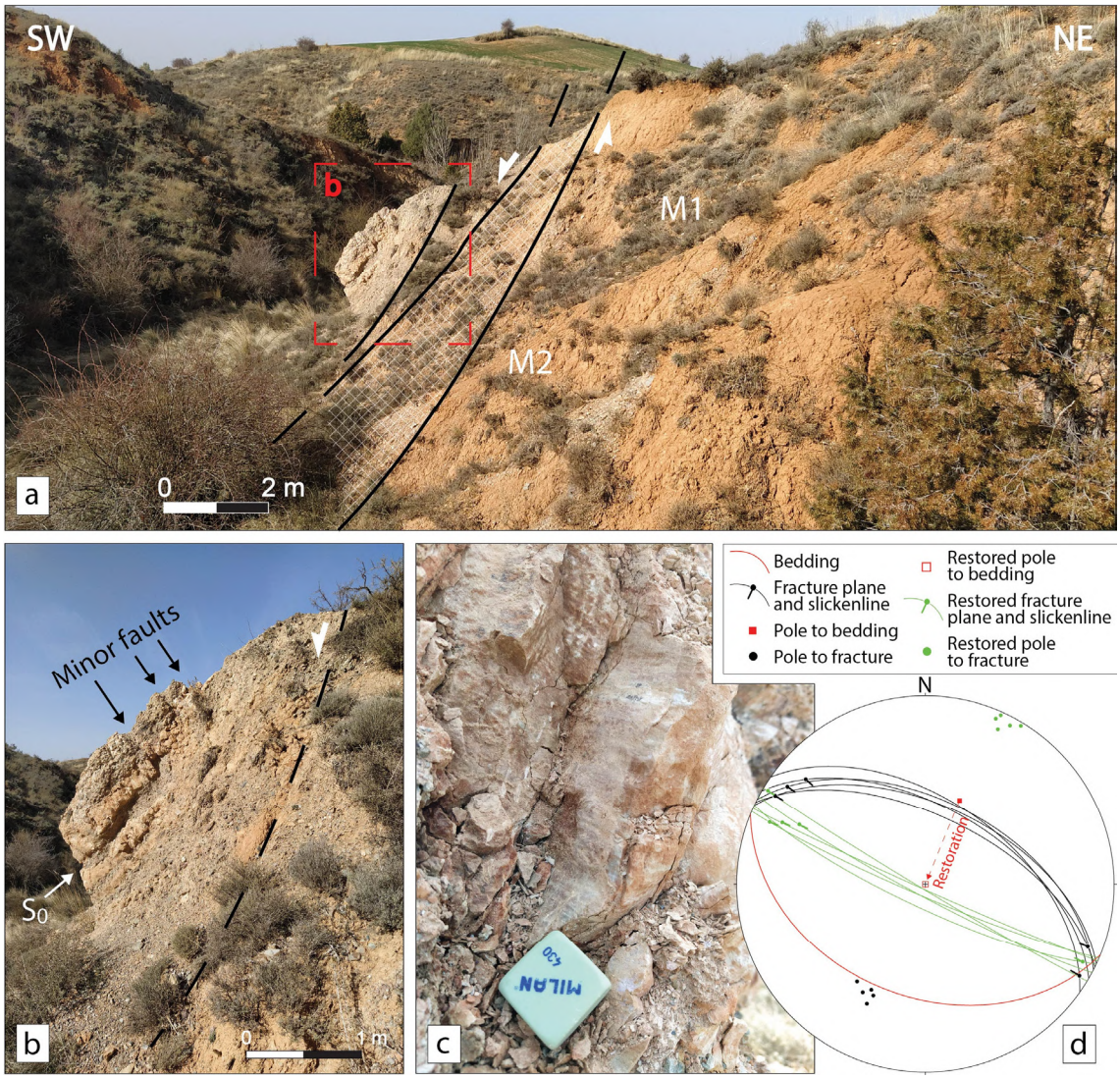

2.22.- (a) Exposure of the CPFS rupture affecting two Miocene units (M1 and M2) in La Pesquera site. (b) Unit M2 fractured by minor faults and affected by a drag fold associated to the hanging-wall block of the fault. (c) Stereoplot (equal area, lower emisphere) of slickenlines on a minor fault plane located in the opposite side of photo "b". See location of this outcrop in Figure 2.20.

Tilting on the hanging-wall bedding is interpreted as part of a drag fold associated with recent normal slip of the main fault zone. If we restore the bedding to its original disposition, including the set of minor strike-slip faults, the planes of these ones seem to be originally vertical (ca. 110,90; Fig. 22d), while the slickenlines remain nearly horizontal. In summary, this set of minor faults can be interpreted as nearly strike-slip faults previous to the drag fold and the normal fault zone. The centimetric displacements of M2 would be result of an initial reverse component of this strike-slip movement or, less probable due to the absence of a different set of slickenlines superimposed to the strike-slip ones, result of the later normal slip. In general, this set of ruptures could have been generated under one of the regional stress fields of the last compressive pulses undergone by the Iberian Chain during Early Miocene times. The subsequent extensional stress fields reactivated this fault segment as a normal fault with the drag fold associated to it.

Fuentes Calientes site

The CPFS s.s. spread till Pancrudo village, but a rupture system aligned with this macrostructure can be recognised close to Fuentes Calientes village at published geological maps (Martín *et al.*, 1979; Gabaldón *et al.*, 1991), aerial photographs and outcrop scale. Upper Cretaceous limestone beds show a stepped arrangement produced by several faults with two main directions: N150ºE and N010ºE. There is also a natural spring at the foot of this outcrop that could be associated with a westernmost, non-visible fault. This kind of regional outcrops could evince the possible recent propagation of ruptures southwards from Pancrudo. However, fracturing in this area does not affect recent deposits, so this hypothesis can not be tested.

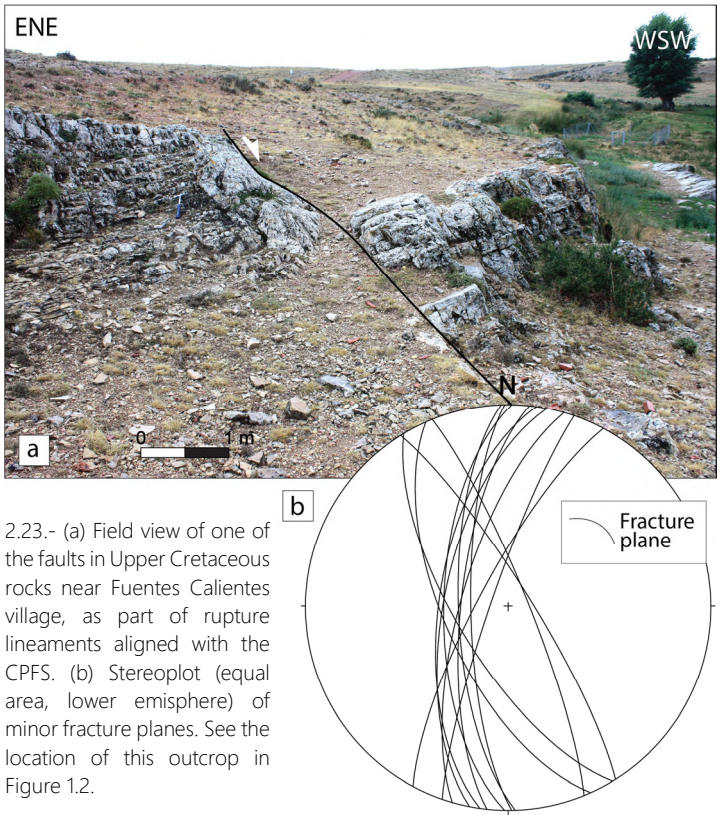

2.23.- (a) Field view of one of the faults in Upper Cretaceous rocks near Fuentes Calientes village, as part of rupture lineaments aligned with the CPFS. (b) Stereoplot (equal area, lower emisphere) of minor fracture planes. See the location of this outcrop in Figure 1.2.

2.4. Assessing the recent activity of the CPFS within the regional framework

The long-term slip rate inferred at the Cucalón-Pancrudo fault segment since the late Pliocene (0.06 mm/a), or the one obtained for this main fault together with the bending component and the Valverde fault (0.09 mm/a), do not differ from the one reported for its adjacent Río Grío-Lanzuela fault segment for that time period (0.07 mm/a; Peiro and Simón, 2021), neither from those of the main extensional faults in the eastern Iberian Chain. The latter range between 0.05 and 0.16 mm/a for faults at both the neighbouring Jiloca graben and the Teruel basin (Simón *et al.*, 2012, 2013; Ezquerro *et al.*, 2020). The short-term slip rate during Late Pleistocene-Holocene times (0.07-0.08 mm/a) remains almost equal to the long-term slip rate. Therefore, it disagrees with the regional tendency to increase within these two basins from Late Pliocene to Quaternary times (Simón *et al.*, 2016), and also with the tendency to diminish within the Maestrat grabens and the Catalonian grabens (Masana, 1995; Masana *et al.*, 2001; Perea *et al.*, 2006).

The fact that the activity of the CPFS is not reflecting the regional increasing tendency could be associated with: (i) Low representativeness of data collected for calculating the slip rate during the Late Pleistocene, from only one paleoseismological trench. (ii) Strain partitioning between different unknown fault branches or other deformation structures, the recorded slip rate being a part of a total. This could explain why the bending component of the monocline, together with the Valverde fault, generate such a maximum displacement of the whole system, and allow to accommodate a high amount of deformation on the CPFS. (iii) Fault linkage processes, supported by

the analysis of T-D curves (Fig. 2.15). The CPFS is interacting and transferring displacement to the RLFS through their relay zone, and the northern sector of the CPFS, where the short-term slip rate has been calculated, corresponds to an old fault segment recently linked to a southern one. After linkage, the southern segment could be the one accommodating more deformation (in fact it has already been described as as a new formed fault, in opposition to the essentially inherited northern segment), but no slip data are available for supporting this assumption. (iv) Limit of the progressive westwards propagation of rifting and the doming, from inner parts of the Valencia Trough towards more external domains (Fig. 1.1b).

In order to infer the seismogenic potential of the CPFS, the regression model by Wesnousky (2008) can be applied, as it is the one recommended for approaching seismogenic parameters in slow intraplate normal faults according to the analysis carried out by Stirling *et al.* (2013) for the Global Earthquake Model (GEM). Considering the length of the CPFS trace (40 km) and the absence of structural segmentation, such regression provides a potential moment magnitude Mw = 6.9 ± 0.3 for earthquakes generated by this structure. This Mw value fits the range obtained from other common regression proposals (Mw = 6.8-7.2; Wells and Coppersmith, 1994; Stirling *et al*., 2002; Leonard, 2010), but should be regarded as more precise. Moreover, Wesnousky's (2008) model gives a potential average coseismic slip of ca. 1.2 m, while the other regressions (Wells and Coppersmith, 1994; Stirling *et al*., 2002; Leonard, 2010) point to values in the range of 1-3 m.

Reliability of the paleoseismic parameters obtained at the Lagueruela trench for Holocene times can now be tested: slip rate of 0.07-0.08 mm/a, average recurrence period of 4.2 to 8.2 ka and coseismic displacements that range from 0.2 to 0.7 m, with an average value of 0.5 m. Assuming a stick-slip fault regime at a rate of 0.07 mm/a, a recurrence period of 4.2 ka involves a coseismic slip of 0.3 m, and considering a rate of 0.08 mm/a and a recurrence period of 8.2 ka the coseismic slip would be 0.7 m. These values lie within the range estimated from field data (0.2-0.7 m), but are low with respect to the ones obtained from regression models (1.0-3.0 m, being closer to 1.2 m). The latter are considered for a rupture of the whole fault length, so the most realistic scenario is that the CPFS has registered, within the Lagueruela area, only the activity of a certain segment. From the range of coseismic displacement obtained at the trench (0.2-0.7 m), a surface rupture length between 5.3 and 30.2 km is expected (based on Wells and Coppersmith, 1994; Leonard, 2010) and, more accurately, in the range of 6.7-23.3 km (using Wesnousky, 2008). The northern bell-shaped T-D curve of the CPFS (Fig. 2.15) is ca. 25 km long, therefore it perfectly fits the scenario of this sector rupturing and registering its activity within the Lagueruela area. Wesnousky's (2008) regression provides a potential moment magnitude Mw = 6.8 ± 0.3 for earthquakes generated by this sector of the CPFS, which also fits the range obtained from the other regressions (Mw = 6.2-7.2; Wells and Coppersmith, 1994; Stirling *et al*., 2002; Leonard, 2010).

The Cucalón-Pancrudo fault segment shows evidence of Quaternary activity and, at least its northern sector from Cucalón to Barrachina villages, has moved during Late Pleistocene-Holocene times. This allows us to consider it as an active structure able to produce maximum earthquakes of Mw 6.9 ± 0.3, whose northern sector has a recurrence period under 10 ka. Future studies at the fault trace will allow to complete the paleoseismic record of the CPFS, but for the moment it already represents a seismic source that should be considered in seismic hazard assessment of the region.

Finally, a scenario of rupture propagation along the whole Río Grío-Pancrudo fault zone, that means of both the RLFS and the CPFS, should not be completely ruled out. This scenario has not been included in Table 6.1 because it is not considered as the more realistic, due to the scale of this macrostructure and to the already mentioned evidence of fault rupture through limited segments. However, they are separated by a right relay-zone 2.5 km wide (Figs. 1.2, 2.10) and, according to Biasi and Wesnousky (2016), it might not represent a barrier to propagation. These authors determined that 54% of relay zones ≥ 1 km wide, in dip-slip faults longer than 10 km, are overcome during fault propagation, and that such relay zones are less effective at stopping normal than reverse ruptures. In the hypothetical case of the occurrence of a maximum earthquake generated by the entire Río Grío-Pancrudo fault zone, of 95 km long, it could reach a magnitude of 7.0 ± 0.3 (according to the regression model by Wesnousky, 2008).

CAPÍTULO III.

FALLA DE CALAMOCHA

Resumen:

La sección III es la corresponde a la publicación, ya aceptada, de la falla de Calamocha, la cual forma el límite entre las cuencas de Calatayud y del Jiloca. Mayoritariamente muestra los resultados de su estudio en cartografía y de afloramientos, que han permitido el análisis paleosismológico de diferentes ramas de la falla principal. Su actividad post-pliocena también ha quedado registrada en las superficies de erosión regionales. Los afloramientos estudiados muestran claros desplazamientos de depósitos datados en el Pleistoceno superior, pero muchas de esas rupturas no son las principales y no representan la deformación total de las mismas. A partir de todo ello, se estiman algunas de las posibles características sismológicas de la falla de Calamocha y se enmarcan en el contexto tectónico regional. Todos los valores inferidos para la falla de Calamocha se pueden consultar sintetizados en la tabla de la sección VI.

PUBLICACIÓN:

Actividad reciente y paleosismicidad de una falla extensional intraplaca: la falla de Calamocha (Fosa del Jiloca, Cordillera Ibérica centro-oriental) / *Recent activity and paleoseismicity of an intraplate extensional fault: the Calamocha fault (Jiloca graben, central Iberian Chain).*

Peiro, A., Simón, J.L., Martín-Bello, L., Arlegui, L.E., Ezquerro, L., Luzón, A., Medialdea, A., Corral, B., Liesa, C.L. (2022). *International Journal of Earth Sciences*, online. doi: 10.1007/s00531-022-02265-3

★ Equivalencia de Figuras: en la publicación hay Fig. 1-Fig. 13, y corresponden a las Fig. 3.1-Fig. 3.13 de esta tesis.

International Journal of Earth Sciences
https://doi.org/10.1007/s00531-022-02265-3

ORIGINAL PAPER

Recent activity and paleoseismicity of an intraplate extensional fault: the Calamocha fault (Jiloca graben, central Iberian Chain)

Alba Peiro[1] · José L. Simón[1] · Leticia Martín-Bello[1] · Luis E. Arlegui[1] · Lope Ezquerro[1] · Aránzazu Luzón[1] · Alicia Medialdea[2] · Belén Corral[1] · Carlos L. Liesa[1]

Received: 23 May 2022 / Accepted: 24 October 2022
© The Author(s) 2022

Abstract

The Calamocha fault is an 18-km-long, NNW–SSE striking pure normal fault that moves down the northern sector of the Jiloca graben with respect to the Neogene infill of the Calatayud basin (central Iberian Chain). Its structure and kinematics are characterized by means of detailed geological mapping, morphotectonic analysis and data recording at the outcrop scale. The Calamocha fault represents the inversion of a previous contractional fault zone under the recent tensional stress field (WSW–ENE trending σ_3 trajectories). The extensional activity started during the Late Pliocene (ca. 3.8 Ma), accumulating a maximum net slip of 190–230 m (long-term slip rate of 0.05–0.06 mm/a). The palaeoseismological study of three artificial exposures near Calamocha town evidenced recurrent slip during the Late Pleistocene, which proves its active character. Analysis of faulted clastic alluvial units, dated by means of optically stimulated luminescence (OSL), reveals at least eight slip events since 145.9 ± 9.1 ka, the last one being younger than 13.8 ± 0.9 ka. Only a few events represent visible accumulated displacement on the main synthetic rupture surfaces; this allows a rough estimate of the short-term slip rate (during the Late Pleistocene) of about 0.1 mm/a, faster than the long-term rate. The Calamocha fault could potentially produce a characteristic earthquake (in the sense of Schwartz and Coppersmith, J Geophys Res 89:5681–5698, 1984) with moment magnitude $M_w \approx 6.7 \pm 0.3$ ($M_w \approx 6.9 \pm 0.3$ in a scenario of activation of the whole Calamocha–Daroca fault zone), average coseismic displacement of 0.5–1.3 m and average recurrence period under 15 ka.

Keywords Normal fault · Slip rate · Trench study · OSL dating · Morphotectonics · Late Pleistocene

✉ José L. Simón
jsimon@unizar.es

Alba Peiro
apeiro@unizar.es

Leticia Martín-Bello
leticia.martin.bello@gmail.com

Luis E. Arlegui
arlegui@unizar.es

Lope Ezquerro
lopezquerro@gmail.com

Aránzazu Luzón
aluzon@unizar.es

Alicia Medialdea
alicia.medialdea@cenieh.es

Belén Corral
riveraesvida@gmail.com

Carlos L. Liesa
carluis@unizar.es

[1] Dpto. de Ciencias de la Tierra, Grupo Geotransfer-Instituto Universitario de Investigación en Ciencias Ambientales de Aragón (IUCA), Universidad de Zaragoza, Pedro Cerbuna 12, 50009 Saragossa, Spain

[2] Centro Nacional de Investigación sobre la Evolución Humana (CENIEH), Paseo Sierra de Atapuerca 3, 09002 Burgos, Spain

Published online: 25 November 2022

Introduction

Intraplate regions usually exhibit low to moderate seismicity, and their active faults have large return periods (in the order of 10^3 years; Liu and Zoback 1997), which means that they tend to be underestimated in seismic hazard analyses. Therefore, it is critical to study the geological record for identifying and dating large ancient earthquakes by means of palaeoseismological methods (Allen 1986; McCalpin 2009; Yeats et al. 1997). Such is the case of the Iberian Chain, in the eastern Iberian Peninsula (Fig. 1a, b), a region that exhibits low to moderate historical and instrumental seismicity, but contains numerous slow active normal faults. Among the latter, those located at the junction of the Teruel and Jiloca grabens (Sierra Palomera, Concud, Teruel and Valdecebro faults) have been the focus of a number of detailed palaeoseismological studies during the last decade, which have demonstrated their Pleistocene activity and seismogenic potential (Lafuente et al. 2011, 2014; Simón et al. 2012, 2016, 2017; 2019; Ezquerro et al. 2015, 2016; Peiro et al. 2020, 2022).

The Calamocha fault is a NNW–SSE striking normal fault that brings into contact the Neogene units of the Calatayud basin with the Pleistocene sediments that infill the northern sector of the Jiloca graben (Fig. 1c). Together with the Daroca fault, they define a conspicuous extensional fault zone along the central Iberian Chain. Contractional structures have also been reported along this fault zone, mostly in the surrounding area of Daroca town (Daroca thrust: Colomer and Santanach 1988; Casas et al. 2018; Simón et al. 2021) and the area NW of Calamocha (Corral 2014; Liesa et al. 2021). This suggests a compressional origin for the overall structure, probably due to Alpine reactivation of a Variscan fault that formed the SW boundary of the Calatayud basin. During Plio-Quaternary times, its inversion gave rise to the Calamocha–Daroca normal fault zone.

The Calamocha fault shows signs of Quaternary activity, already noticed by Simón (1983), and documented in detail by Simón et al. (2012) and Martín-Bello et al. (2014). It has been incorporated into the national database of active faults created by IGME (Instituto Geológico y Minero de España), but no exhaustive palaeoseismic research aiming

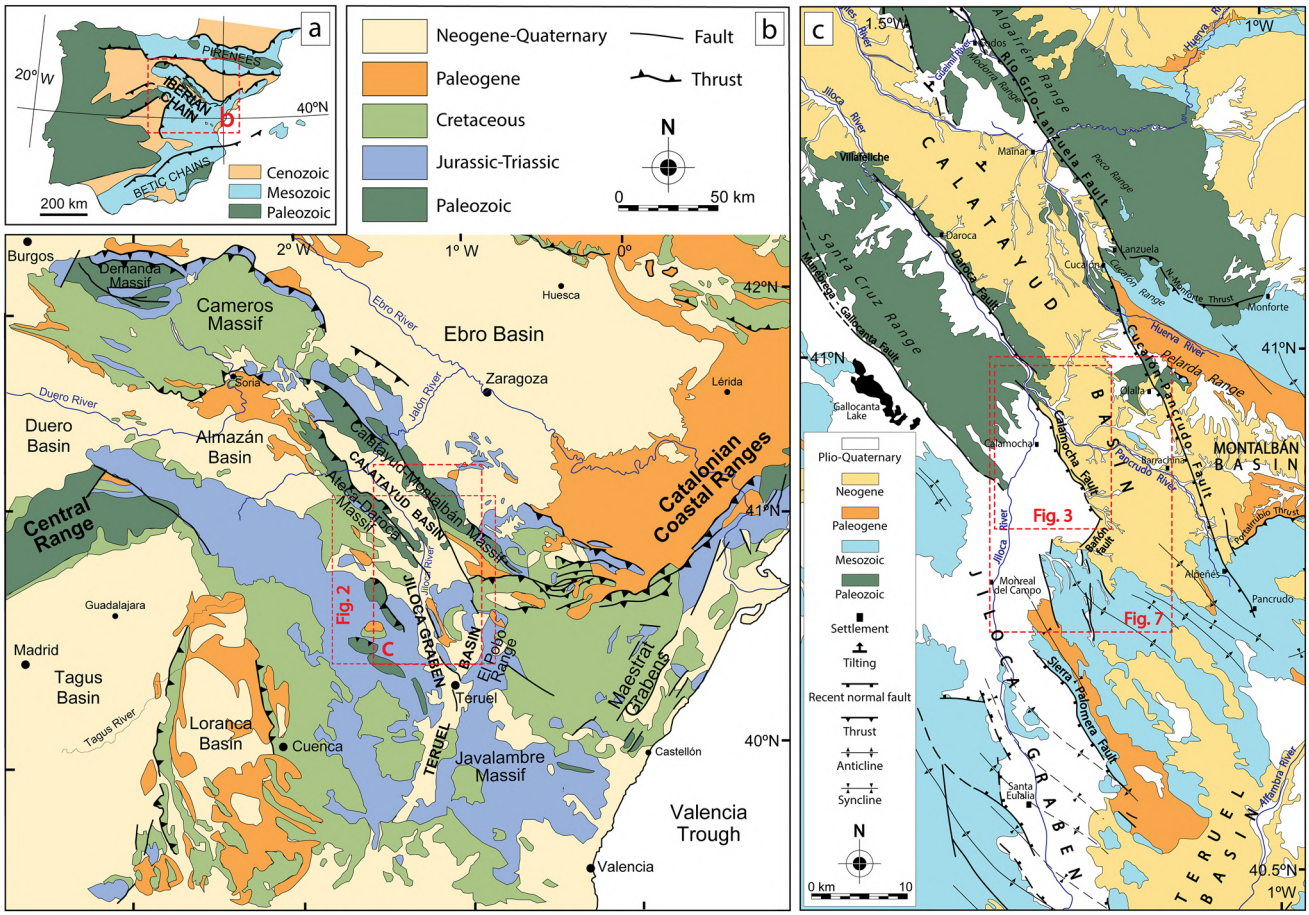

Fig. 1 **a** Location of the Iberian Chain within the Iberian Peninsula. **b** Geological sketch of the Iberian Chain, with location of the main Neogene–Quaternary extensional basins. **c** Simplified geological map of the Calatayud and Jiloca basins, with location of Figs. 2, 4 and 8

to reconstruct its recent faulting history has been conducted yet.

The objective of this paper is to document the structure and recent activity of the Calamocha fault. In particular, its geometry, kinematics and evolution are characterized, including an estimate of long-term and short-term slip rates. Moreover, some rupture events dated to the Pleistocene have been identified from palaeoseismological analysis of a number of artificial exposures in the vicinity of Calamocha. In this way, we aim to contribute to an overall understanding of extensional tectonic processes in the central–eastern Iberian Chain during Neogene and Quaternary times.

Geological setting

Overall view

The Iberian Chain is a NW–SE trending, intraplate mountain chain located within the Iberian Peninsula (Fig. 1a, b), which developed during Cenozoic time owing to its convergence with both the European and African plates (Álvaro et al. 1979; Capote et al. 2002). The chain mainly resulted from the inversion of several Mesozoic basins (Liesa et al. 2018) during compressional episodes of the Alpine Orogeny (Palaeogene to early Neogene; Liesa and Simón 2009). Within the central sector of the chain, an up to 11,000 m thick Palaeozoic sequence was re-folded during the Cenozoic compression, the macrostructures exhibiting a prevalent NW–SE trend (Cortés-Gracia and Casas-Sainz 1996; Calvín-Ballester and Casas 2014). In this sector, two large, Palaeozoic structural highs, the Calatayud–Montalbán and the Ateca–Daroca massifs, each one with wavelength of about 25 km and estimated amplitude of 2 km (Casas et al. 2016), are separated by the Cenozoic Calatayud basin (Fig. 1c).

Since the beginning of the Late Miocene, the central–eastern Iberian Chain underwent an extensional tectonic period linked to rifting of the Valencia Trough (Vegas et al. 1979; Simón 1982; Roca and Guimerà 1992; Maillard and Mauffret 1999). Onshore extensional deformation has been accommodated by normal faults that bound large Neogene–Quaternary basins (Maestrat, Teruel, Jiloca, Gallocanta, Munébrega), and mostly represent the inversion of previous compressional faults (Álvaro et al. 1979).

Two extensional stages, Late Miocene to Early Pliocene and Late Pliocene–Quaternary, have traditionally been distinguished (Moissenet, 1980; Simón, 1982, 1983, 1989; Anadón and Moissenet, 1996; Ezquerro et al., 2020). They are characterized by two distinct tensional stress fields (σ_1 vertical): (i) uniaxial tension with WNW–ESE trending σ_3 trajectories, prevailing during the first episode; (ii) nearly radial tension ($\sigma_2 \approx \sigma_3$) with σ_3 trajectories trending WSW–ENE, prevailing during the second episode (Simón 1982, 1989; Arlegui et al. 2005; Liesa et al. 2019). The latter has essentially remained until the present day (Herraiz et al. 2000). The overall NNW–SSE trend of the Jiloca graben, developed during the second extensional episode, constitutes the most conspicuous macrostructural expression of the regional stress trajectories (Simón 1989). Besides, the oblique, NW–SE striking individual faults resulting from inversion of Palaeogene thrusts represent the structural inheritance.

The Mio-Pliocene Calatayud basin

The NW–SE trending, 65-km-long Calatayud basin, developed in a compressional setting bounded by the Palaeozoic Ateca–Daroca and the Calatayud–Montalbán massifs (Fig. 1c). In particular, the SW margin corresponds to the Daroca thrust, where Cambrian rocks overthrust the Lower Miocene continental deposits of the basin infill, while younger, Middle–Upper Miocene units overlap the thrust front from the SW margin of the basin (Julivert 1954; Colomer and Santanach 1988; Casas et al. 2018; Liesa et al. 2021; Simón et al. 2021).

Subsidence within the Calatayud basin developed in a complex compressional–extensional setting during the entire Neogene, allowing the accumulation of the most complete Neogene series in the Iberian Chain (Anadón et al. 2004). The sedimentary record consists of clastic alluvial sediments sourced at the basin margins, which grades towards central sectors into lacustrine–palustrine evaporites and carbonates (Gabaldón et al. 1991; Sanz-Rubio 1999; Sanz-Rubio et al. 2003).

Several non-formal lithostratigraphic units were distinguished within the Neogene series of the south-eastern sector of the Calatayud basin by Hernández et al. (1983), then adapted by Martín-Bello et al. (2014):

- The Daroca clastic unit (CU; late Agenian–middle Aragonian), made of siliceous gravel and silt, is divided into three subunits (CU1, CU2 and CU3) based on its vertical relationships with the carbonate units.
- Navarrete gypsum (NG; early Aragonian).
- The carbonate succession of the Bañón unit-Nombrevilla limestone (NL; Aragonian) is separated into two subunits (NL1 and NL2) by the clastic unit CU2.
- Rojo 1 (R1; Vallesiensian-Turolian) is made of red siltstone with interbedded gravel and sandstone
- Páramo 1 (P1; Turolian) is made of limestone and marl.
- Rojo 2 (R2) and Páramo 2 (P2) (Ruscinian) consist of red siltstone and marly limestone, respectively, the latter culminating the endorheic sedimentary succession of the Calatayud basin. Within the Calamocha fault

domain, both units only crop out in the hanging-wall block.
– Rojo 3 (R3; Ruscinian–Villafranchian) is made up of red mudstone with interbedded sandstone and siliceous gravel.

Plio-Quaternary normal faults linked to the Calatayud basin

Under the Plio-Quaternary extensional regime, some of the thrusts that bound the Calatayud basin were inverted. The NE margin of the Calatayud basin is now partially controlled by the Río Grío–Pancrudo normal fault zone (Gutiérrez et al. 2013; Peiro and Simón 2021a, b), while its SW margin is represented by the Munébrega–Gallocanta (Gutiérrez et al. 2009) and the Daroca–Calamocha normal fault zones (Gracia 1992; Gutiérrez et al. 2008, 2020a; Fig. 1c). The present-day structure represents a stepped array of half-grabens, with their respective faults at their north-eastern margins.

Normal slip along the NNW–SSE trending extensional Río Grío–Pancrudo Fault Zone has produced a vertical displacement of 300 m in a late Neogene planation surface (FES3; "Morphotectonic evolution: late neogene planation surfaces", hanging-wall tilting, and subsequent drainage reversal after the Pliocene–Pleistocene transition (Peiro and Simón 2021a, b). Surficial faulting of Late Pleistocene materials has provided a slip rate approaching 0.30–0.36 mm/a (Peiro and Simón 2021b).

The Munébrega–Gallocanta fault zone bounds the Munébrega Plio-Quaternary, NW–SE trending half-graben, as well as the endorheic Gallocanta lacustrine basin (Gracia et al. 2002; Gutiérrez et al. 2008). Offset of a Late Pleistocene pediment has provided a vertical slip rate in the range of 0.02–0.10 mm/a (Gutiérrez et al. 2009, 2020b).

The recent Daroca–Calamocha fault zone bounds the northern sector of the Jiloca graben and the Daroca half-graben with respect to the Neogene infill of the Calatayud basin (Julivert 1954; Gracia 1992; Gutiérrez et al. 2008; Fig. 1c). Most of the Calatayud basin lies at its footwall block, but small portions of its Neogene infill were sunk and covered by Plio-Pleistocene deposits in the Jiloca basin. The fault zone is made up of two NNW–SSE to NW–SE trending segments (Daroca and Calamocha faults, 27 and 18 km long, respectively), connected by a right-stepping relay zone 1.8 km wide. The normal Daroca fault forms the north-eastern margin of the Daroca half-graben and tilts its Upper Pliocene–Pleistocene infill. A vertical slip rate of 0.02–0.06 mm/a has been estimated from the offset of a Pleistocene erosional–aggradation pediment, with the youngest event being dated to 2354–1544 cal yr BP (Gutiérrez et al. 2020a).

The Jiloca graben

The Calamocha fault, together with the Sierra Palomera and Concud faults, form the eastern boundary of the asymmetric Jiloca graben (Fig. 1c). They show an en-échelon, right-stepping arrangement that results in an NNW–SSE trend for the overall basin. A number of Palaeogene folds are obliquely cut by the graben; nevertheless, they are nearly parallel to the Sierra Palomera and Concud faults, which also represent the inversion of Palaeogene contractional faults (Lafuente et al. 2011; Simón et al. 2021).

The Sierra Palomera fault is a 15.5-km-long, NNW–SSE striking normal fault with a nearly pure normal sense of slip. Its activity since Late Pliocene times is mainly revealed by the tilting and offset of regional planation surfaces, which allows the estimation of a throw in the range of 350–400 m (Rubio and Simón 2007; García-Lacosta et al. 2014; Peiro et al. 2022). A subsidiary antithetic fault, induced by rollover bending associated with the Sierra Palomera fault, shows evidence of recurrent activity during Late Pleistocene times (Peiro et al. 2022).

The relay zone between the Calamocha and the Sierra Palomera faults is controlled by the NE–SW striking Bañón fault (Fig. 1c), an incipient connecting fault that is unlikely to evolve into a complete hard linkage. Instead, recent deformation within the relay zone is mainly accommodated by distributed along-strike minor faults, controlled by both the regional stress field and the structural inheritance (Peiro et al. 2020). As of today, the Calamocha and Sierra Palomera faults behave as independent structures from the geometrical and kinematical point of view (Peiro et al. 2020).

The Jiloca basin infill is made of an Upper Pliocene–Pleistocene alluvial succession, in which two units are distinguished: (i) a Villafranchian pediment (V) represents an alluvial system covering wide sectors of the hanging wall, made up of several metres to several tens of metres of red gravel and silt; (ii) Quaternary sediments mostly correspond to alluvial systems made up of unconsolidated polygenetic gravel associated with the fault scarp, although palustrine lutites and carbonates are also recognized in local endorheic areas (Cañizar lake; Rubio 2004; Rubio et al. 2007).

Morphotectonic evolution: late Neogene planation surfaces

Mountains surrounding the Jiloca basin show extensive erosion surfaces developed through successive planation episodes, which model Palaeozoic, Mesozoic and Palaeogene rocks and level compressional structures. The main planation surface, classically referred to as *Fundamental Erosion Surface* (FES; Peña et al. 1984), has recently been divided into three sublevels, FES upper sublevel (FES1), FES *s.s.* (FES2) and FES lower sublevel (FES3)

(Simón-Porcar et al. 2019; Ezquerro et al. 2020). FES2 and FES3 are probably equivalent to the S1 and S2 surfaces, respectively, defined by Gutiérrez and Gracia (1997).

Physical correlation of such sublevels with distinct sedimentary horizons of the Teruel basin made it possible for them to be dated precisely, based on robust biostratigraphic and magnetostratigraphic data (Ezquerro 2017; Ezquerro et al. 2020). The age of FES3 (3.5 Ma) is well constrained to the top of the M8 megasequence defined by Ezquerro (2017), equivalent to the upper part of Páramo *2* unit (Early Villafranchian; mammal biozone MN16; near the base of chron C2An.3n), while FES 1 and FES2 merge into the top of M7 (3.8 Ma; lower part of Páramo 2 unit; Late Ruscinian; MN15; middle part of C2Ar) (Ezquerro et al. 2020).

FES3 is either locally incised by a lower erosional surface (FES4), or overlaid by the Rojo 3 unit (R3) and the *Villafranchian pediments* that extend over most of the Jiloca basin and its margins. The associated Villafranchian alluvial system is dated to the earliest Pleistocene by macromammal fauna (Adrover 1986; MN17 zone, 2.6–1.9 Ma) and, more accurately, by magnetostratigraphy (1.95–2.1 Ma; Sinusía et al. 2004). Development of this pediment system represented the transition to external drainage in the whole region, except for certain sectors in which endorheic conditions remained until the Early Pleistocene (Teruel area; Ezquerro et al. 2012) or even until historical and present times (Gallocanta lake; Cañizar lake, Rubio and Simón 2007).

Seismicity

Historic and instrumental seismicity of the region is low to moderate. The epicentres are clustered: (i) close to the margins of the southern Jiloca graben; (ii) in the Albarracín massif, with a maximum intensity of VI–VII at Orihuela del Tremedal (1848) (IGN 2022), and (iii) along the Molina de Aragón plateau (Fig. 2). Nevertheless, the most recent and strong earthquakes have been recorded north of those domains, west of Daroca: Cimballa (1912; intensity VI–VII) and Used (1953; intensity VII; magnitude 4.7) (IGN 2022). Earthquakes located at the Calatayud basin and its active bounding fault zones are very scarce. Focal depths typically range from 5 to 15 km, which corresponds to the brittle layer above the basal detachment level identified by Roca and Guimerà (1992). Most of the available focal mechanisms correspond to normal faults and are consistent with the regional active stress field (Herraiz et al. 2000).

Methods

Structural and morphotectonic study

The structure of the Calamocha fault zone has been characterized by means of a detailed geological map, elaborated with the help of published maps at a 1:50.000 scale (Hernández et al. 1983), aerial photographs at a 1:30.000 scale, satellite orthoimages, digital elevation models (DEM, pixel = 2 m) and the resulting hillshade images, and field survey. Three geological cross sections through the northern, central and southern sector of the Calamocha fault were constructed based on mapping and outcrop information, partially inspired by those of Martín-Bello et al. (2014), Corral (2014), and Liesa et al. (2021).

Recent structures have also been analysed on a morphotectonic map, elaborated from photogeological and DEM studies, which includes remnants of the Late Neogene planation surfaces (sublevels FES1 to FES4 of the *Fundamental Erosion Surface*). Among them, the most extensively represented (FES2 and FES3) have been used as geomorphological markers of recent deformation. Their topographical reconstruction (height contours) and dating ("Morphotectonic evolution: late neogene planation surfaces") have provided tools for calculating the maximum displacement and the long-term slip rate for the Calamocha fault.

Palaeoseismological study

Direct palaeoseismological and structural data at outcrop scale contribute to characterize the geometry and kinematics of the Calamocha fault. Three fresh artificial slopes adjacent to civil constructions have been investigated following the procedure proposed by McCalpin (2009): Zaragoza–Sagunto Railway (ZSR), Polígono Agroalimentario (PA), and A-23 highway (A23H). Slopes displaying the best palaeoseismic information were cleaned, equipped with a square grid (0.5–3 m on each side, depending on the overall dimensions of each section and the level of detail required), and logged with sketches and detailed photographs. Sedimentary units and structures were marked after being classified based on characteristics such as colour, grain size, composition and texture.

Analysis of the relationships between sedimentary units and faults have allowed the reconstruction of deformation episodes, and hence to chronologically constrain palaeoseismic events. Depending on whether the slip vector is known or not, either the net slip or the throw (vertical separation of a marker) is estimated on each individual fault. Throw values are reliable for horizontal markers, while calculations of net slip are only approximate in most cases owing to the lack of information on fault kinematics. Another source of error in reconstructing the geometry of structures is the fact that the surveyed artificial exposures are not vertical but dipping slopes. Detailed logs of such slopes are projected into vertical planes, but they are not equivalent to true vertical sections.

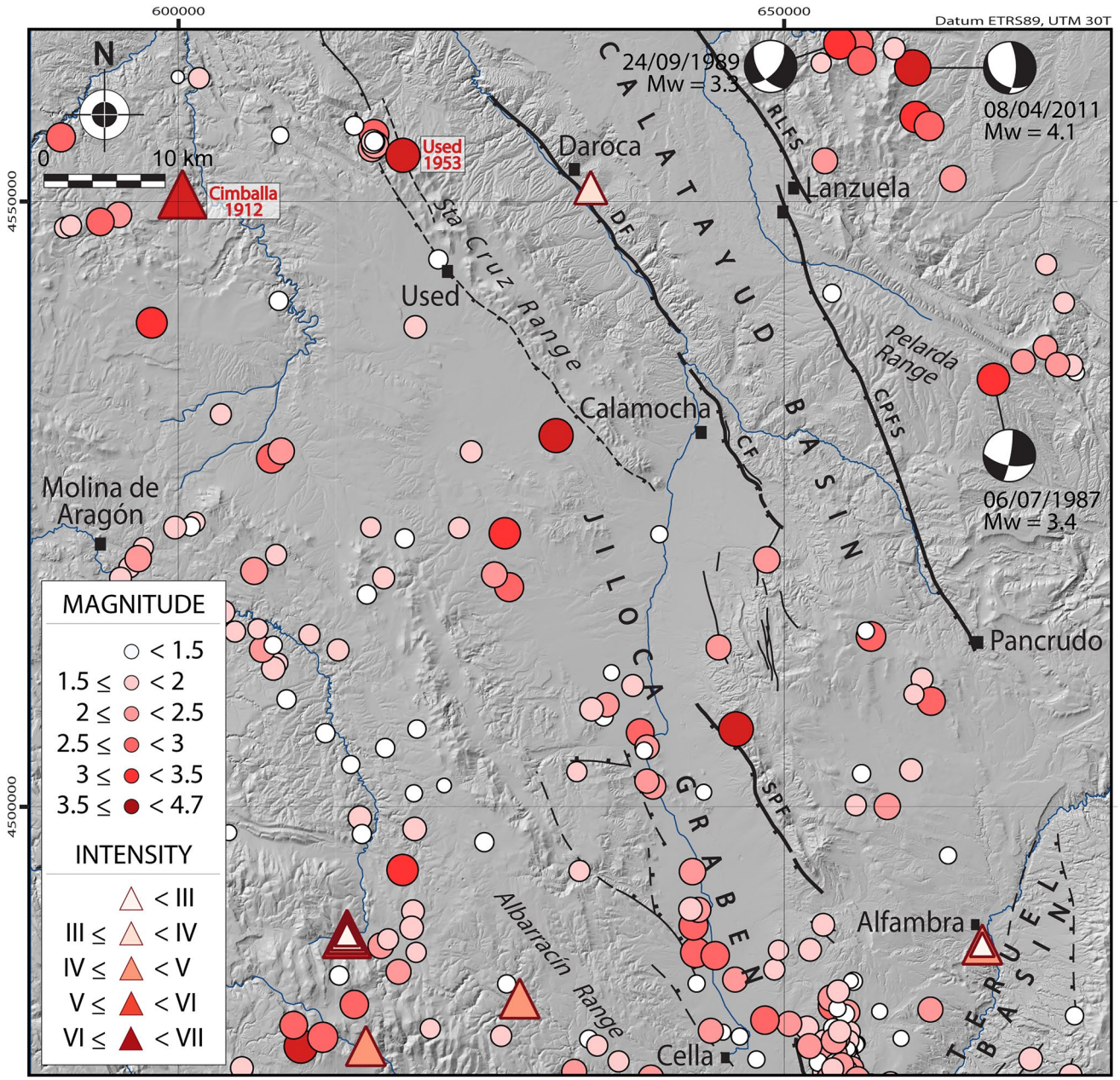

Fig. 2 Epicentre map of historic and instrumental earthquakes in the central Iberian Chain (data source: IGN 2022). *RLFS* Río Grío–Lanzuela fault, *CPFS* Cucalón–Pancrudo fault, *DF* Daroca fault, *CF* Calamocha fault

OSL dating

Because of the lack of organic matter samples, the sedimentary units were dated using the optically stimulated luminescence (OSL) method. A total of 16 samples of fine clastic sediments were collected using opaque tubes to avoid exposure to daylight.

Ten samples were collected during a field campaign in 2019 at the main surveyed trench (ZSR), then processed by the Luminescence Dating Laboratory of CENIEH (Burgos, Spain). They were treated under controlled light conditions following standard procedures (Wintle 1997) to extract the quartz grains of sizes 180–250 µm. The procedure involved: (i) treatment with HCl and H_2O_2 to remove carbonates and organic matter, respectively; (ii) density separation isolating the fraction between 2.62 and 2.7 g/cm^3; and (iii) treatment with HF 40% for 50 min to dissolve any possible remaining feldspar and to etch the outer layer of the quartz grains.

Luminescence measurements were carried out in an automated Risø OSL/TL reader (TL-DA 20). Dose distributions derived from the measurement of 48–60 multigrain aliquots per sample were reduced by excluding the identified outliers; outliers have been defined as those values out of 1.5 times outside of the interquartile range. Central age model (CAM, Galbraith et al. 1999) on the reduced distributions was used to estimate the burial dose of each sample.

Environmental dose rates were calculated from the contribution of beta, gamma and cosmic radiation. Beta and gamma were based on the radionuclide concentration measured at the Centro de Investigación, Tecnología e Innovación (CITIUS) of the University of Sevilla by using a hyperpure germanium spectrometer HPGe with a germanium semiconductor detector type REGe (brand CAMBERRA, model GR6022) (Table 1). Gamma measurements were also carried out at sample locations using a NaI scintillation probe. Gamma contribution derived from in situ measurements was compared to that derived from high-resolution gamma spectrometry finding no significant differences. High-resolution gamma spectrometry was preferred over in situ measurements as it allows storing the samples in tight containers and left to reach secular equilibrium before measurement. A linear accumulation of sediments has been assumed in order to calculate the contribution of cosmic radiation according to varying burial depth (Prescott and Hutton 1994). Attenuation caused by moisture and grain size (Bell 1979; Guerin et al. 2012) was taken into account. An uncertainty of 5% has been added to water contents to account for variability during the burial period. Total dose rates were calculated using the dose rate and age calculator (DRAC, Durcan et al. 2015) and are summarized in Table 1.

Additionally, six samples had been previously collected (field campaigns in 2010, 2012 and 2014) at PA and A23H outcrops, then processed by Laboratorio de Datación y Radioquímica de la Universidad Autónoma de Madrid. These samples were measured over the polymineral fine grain (2–10 μm) fraction. Anomalous fading tests indicated that fading of the OSL signal was not significant for these samples. Annual dose rates were derived from the contribution of K-40, measured with a Geiger–Müller system, and the contribution of uranium and thorium measured with a ZnS solid scintillator. Uncertainties associated with the calculated annual dose rates for these samples were not reported, but considered for age estimation.

Structure and morphotectonics of the Calamocha fault

Structural description

The northern sector of the Calamocha normal fault zone brings into contact Palaeozoic and middle Miocene rocks, at the footwall block, with Late Neogene units (R2, P2 and R3), at the hanging-wall block (Figs. 3 and 4a). A reverse fault, inherited from the Early Miocene contractional structuration of the Calatayud basin, is kept between the normal faults. The fault trace trends N140º E and veers to N120º E close to its northern tip, where the fault surface is clearly exposed (Fig. 5a, c). At the Venta de los Céntimos

Table 1 Summary of the parameters and derived ages of samples dated with OSL from the ZSR trench (at the Luminescence Dating Laboratory of CENIEH, Burgos, Spain), and from the PA and A23H slopes (at the Laboratorio de Datación y Radioquímica de la Universidad Autónoma, Madrid, Spain)

Sample	Trench location	Depth (m)	Dose rate (Gy/ka)	Equivalent dose (Gy)	Age (ka)
CALT-3B	ZSR	2.5	1.93 ± 0.07	236.7 ± 9.9	122.6 ± 7.0
CALT-3Bb	ZSR	1.7	3.35 ± 0.14	295.3 ± 10.1	88.2 ± 4.9
CALT-4D	ZSR	0.5	2.88 ± 0.10	294.5 ± 13.4	102.2 ± 5.9
CALT-5B	ZSR	2.0	2.10 ± 0.10	144.5 ± 8.7	68.9 ± 5.2
CALT-7D	ZSR	0.5	2.32 ± 0.08	171.6 ± 10.0	73.8 ± 5.0
CALT-7A	ZSR	3.0	2.26 ± 0.07	329.1 ± 17.4	145.9 ± 9.1
CALT-8B	ZSR	2.3	1.57 ± 0.06	210.2 ± 13.8	134.0 ± 10.3
CALT-8Bb	ZSR	2.1	1.62 ± 0.07	205.5 ± 8.8	126.7 ± 7.6
CALT-5Ua	ZSR	1.7	1.84 ± 0.08	265.0 ± 11.1	144.1 ± 8.5
CALT-8C	ZSR	1.3	2.14 ± 0.08	233.0 ± 16.6	108.9 ± 8.8
MAD-5764SDA	PA	0.8	3.6	253.80	69.9 ± 5.5
MAD-6334BIN	PA	10.0	1.8	168.86	95.4 ± 6.3
MAD-6332BIN	A23H	0.5	4.8	66.26	13.8 ± 0.9
MAD-6165rBIN	A23H	1.7	3.4	119.00	35.3 ± 0.9
MAD-6177rBIN	A23H	3.0	2.1	114.26	53.1 ± 3.7
MAD-6180rBIN	A23H	2.0	3.6	150.85	41.9 ± 2.9

Uncertainties associated with the estimated dose rates and equivalent doses from PA and A23H slopes were not reported. All ages are reported at 1-sigma ($k = 1$)

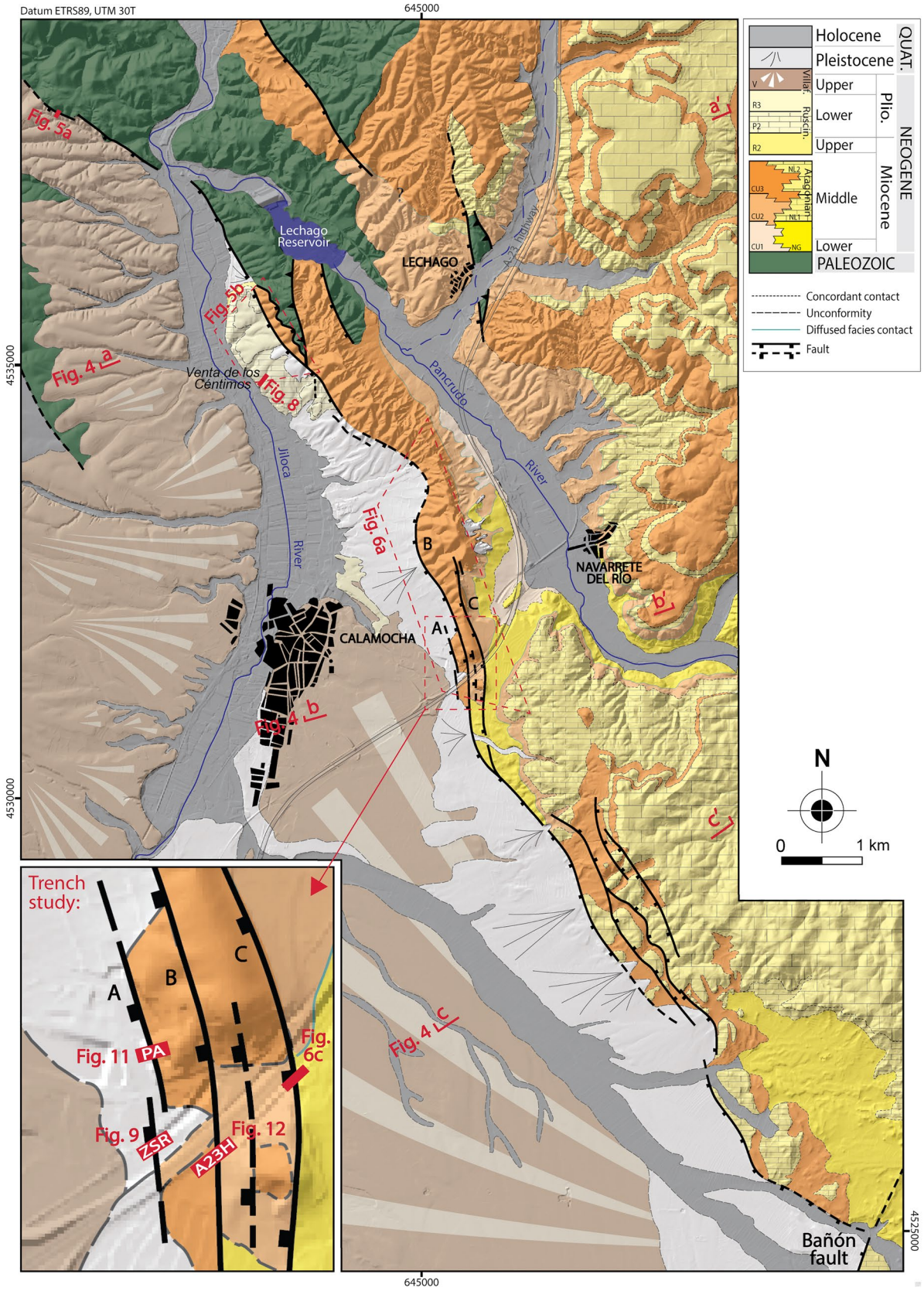
Datum ETRS89, UTM 30T
645000
4535000
4530000
4525000
Holocene
Pleistocene
Upper
Lower
Upper
Middle
Lower
PALEOZOIC
QUAT.
NEOGENE
Plio.
Miocene
Villaf.
Ruscin.
Aragonian
Concordant contact
Unconformity
Diffused facies contact
Fault
Lechago Reservoir
LECHAGO
A-23 highway
Fig. 5a
Fig. 5b
Fig. 4 a
Venta de los Céntimos
Fig. 8
Jiloca River
Pancrudo River
Fig. 6a
B
C
A
CALAMOCHA
Fig. 4 b
NAVARRETE DEL RÍO
a
a'
b
b'
c
c'
N
0
1 km
Trench study:
A
B
C
Fig. 11
PA
Fig. 6c
Fig. 9
ZSR
Fig. 12
A23H
Fig. 4 c
Bañón fault

◂**Fig. 3** Geological map of the Calamocha area (on DEM image from IGN) showing the main structures associated with the Calamocha fault (modified from Martín-Bello et al. 2014). Location of Figs. 6a, b, 7a, c, 9, 10, 12 and 13, and cross sections of Fig. 5a, b, c, are indicated. The inset shows the location of trenches: Zaragoza–Sagunto Railway (*ZSR*), Polígono Agroalimentario (*PA*), and A-23 highway (A23H)

area (Fig. 3), the main fault does not crop out, but the abrupt contact between slightly tilted P2 limestones and Palaeozoic materials can be recognized (Fig. 5b). Numerous minor fractures, mostly striking NNW–SSE, have been observed close to the fault within unit R3 (Fig. 5d). To the south, the fault trace becomes more sinuous, and brings into contact Miocene clastic materials (CU3) with Pleistocene alluvial fans that spread from the fault scarp.

In the central sector, the Calamocha fault splits into several, nearly parallel synthetic branches (faults A, B, C in Figs. 3, 4b and 6a). Two of them (faults B and C) crop out in the A-23 highway slopes and bring into contact different Miocene clastic units (NL2, CU2 and CU3; Fig. 6b, c). In particular, fault branch B, locally oriented N178º E, 75º W, can be clearly observed on a slope adjacent to the highway; at its hanging-wall block, the CU3 unit, made of quartzitic pebbles with interbedded red siltstones, strongly dips to the west suggesting the occurrence of a sharp normal drag fold. Unit CU3 finally lies in contact with the Pleistocene alluvial deposits through the westernmost fault (A), with average orientation N160º E, 70º W. The ca. 1-km-long trace of this fault branch can be recognized both in the field and orthoimages, and was excellently exposed for several years in an artificial slope at the Polígono Agroalimentario (agri-food industrial estate) of Calamocha.

At its southern sector, the Calamocha fault brings into contact Miocene units with Pleistocene alluvial fans that partially cover the Villafranchian pediment (Fig. 4c). The footwall block is affected by a monocline whose shortest limb dips up to 17º SW and is offset by two antithetic faults that duplicate the CU3-NL2 sequence in surface. At the SSE tip of the Calamocha fault, it abuts the transverse Bañón fault (Fig. 3).

Fault kinematics

Kinematic data of the Calamocha fault are only available from its central sector. As reported below ("The Calamocha fault and associated deformation within the regional framework and "Seismogenic characterization"), slickenlines observed on fault branches A and B show prevailing transport directions (azimuth of the slip vector on the hanging-wall block) towards W and SW, representing slip vectors with rake mostly constrained between 85º N and 75º S on the local fault surfaces, i.e., nearly pure normal slip.

Calculating the fault throw is not an easy task, owing to the lack of unambiguous stratigraphic markers recognizable at both fault walls. Rubio and Simón (2007) estimated a minimum vertical throw of 160–180 m in the northern segment based on a hypothetical contemporaneity of units R2 and/or P2 of the hanging-wall block with a clastic unit that crops out to the east of Lechago village (unit 38 of Hernández et al. 1983; lower Pliocene).

At present, a better approach is feasible thanks to geomorphological markers, i.e., the planation surfaces described in "Morphotectonic evolution: late neogene planation surfaces". The morphotectonic map of Fig. 7 shows the remains of such surfaces in the area surrounding the Calamocha fault, together with the contours of FES2 and FES3, and recent faults that offset them. FES3 is the most useful marker since it is present in both fault blocks. East of Calamocha, it constitutes a widespread erosion level modelling the Miocene materials of the footwall block, at heights that decrease northwards from ca. 1150 to 1040 m a.s.l. North of Calamocha, it is exposed within the hanging-wall block at the Venta de los Céntimos area, represented by its correlative sedimentary level, i.e., the stratigraphic limit between units P2 and R3, at about 880–900 m a.s.l. Such a morpho-sedimentary setting is analogous to that widely described in the Teruel basin (e.g., Ezquerro et al. 2020). Further north-east, at the hanging-wall block of the Cucalón–Pancrudo fault, erosional FES3 is also overlaid by the R3 unit, the latter being 60–80 m thick and modelled by a Villafranchian pediment. In this case, FES3 is expressed as the stratigraphic boundary between middle Miocene carbonates and R3 alluvial clastics, its height being constrained from map information.

The throw recorded by FES3 in the northern sector of the Calamocha fault is calculated to 150–180 m, similar to that estimated by Rubio and Simón (2007) based on less precise morpho-sedimentary correlation. According to the contours of Fig. 7, the throw accommodated at the central sector approaches 130–150 m, while it decreases to about 100 m in the southern one.

Assuming the basic geometric and kinematical parameters formerly referred (fault dip: 70–75º W; slip vector rake: 85º N to 75º S), as well as the aforementioned maximum throw (150–180 m), the maximum post-FES3 net slip in the northern and central sectors of the Calamocha fault can be estimated in the range of 155–195 m. Considering the age of the FES3 planation surface (3.5 Ma; "Morphotectonic evolution: late neogene planation surfaces"), this results in a slip rate of 0.045–0.055 mm/a.

Although FES3 constitutes the most valuable marker for calculating the long-term slip and slip rate, this does not mean that the entire history of the fault started after that planation event. The possibility of earlier movements has been directly explored at the only area where materials slightly older than FES3 crop out close to the fault (P2 unit in Venta

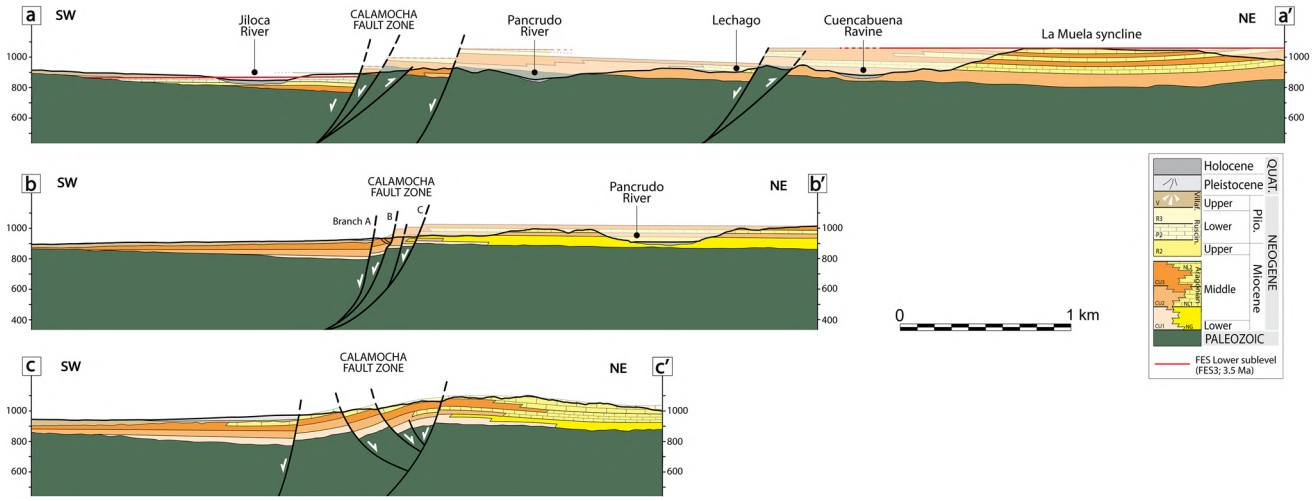

Fig. 4 Cross sections of the Calamocha fault at its northern **a**, central (**b**; modified from Martín-Bello et al. 2014) and southern sectors **c**. See location in Fig. 4

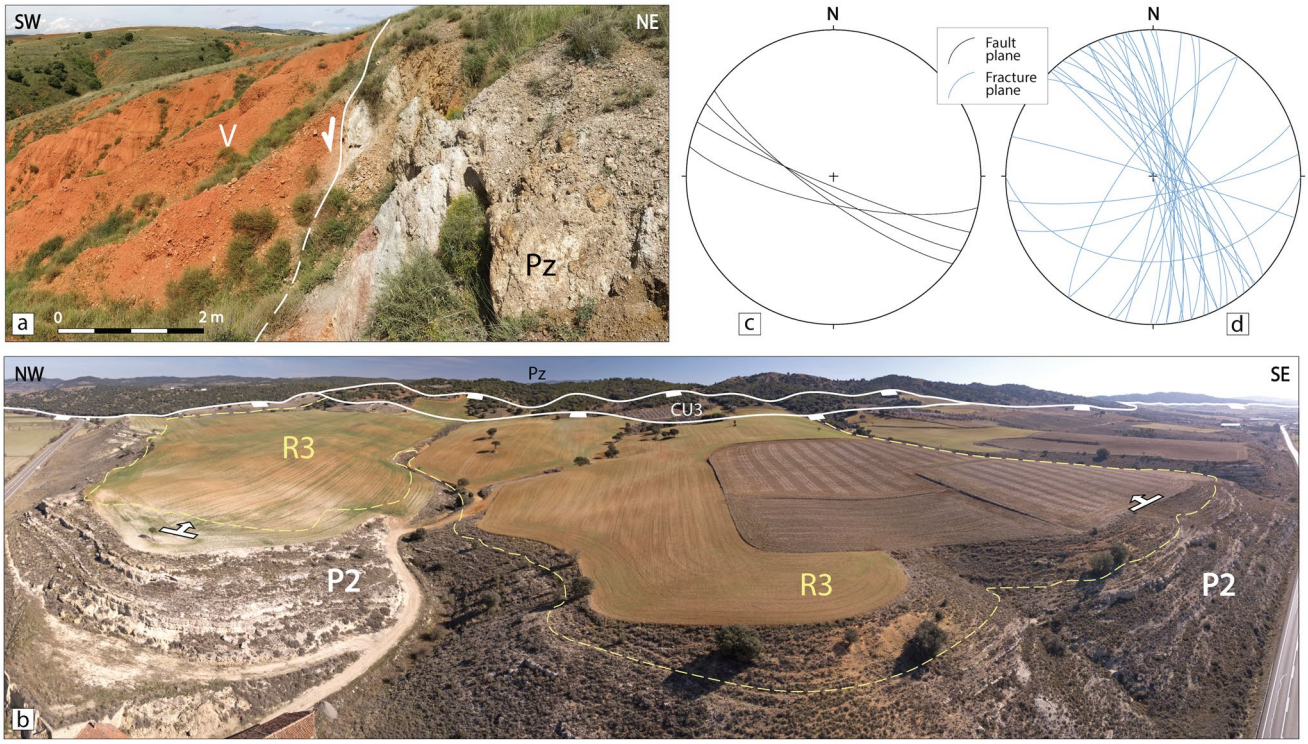

Fig. 5 **a** Exposure of the Calamocha fault close to its northern tip, separating Villafranchian red clastics (V) from Palaeozoic (Pz). **b** Oblique aerial view of Venta de los Céntimos area (VC in Fig. 4), showing the fault scarp separating the slightly tilted (about 5º towards E) limestones of P2 unit and red clastics of R3 unit from CU3 and Palaeozoic. **c** Stereoplot (equal area, lower hemisphere) depicting orientations of fault surfaces measured in outcrop a. **d** Stereoplot (equal area, lower hemisphere) depicting orientations of fractures measured in R3 unit. See location in Fig. 4

de los Céntimos area). Limestone and marl beds of P2 in the hanging-wall block show metre- to decametre-scale normal faults with associated changes in the thickness of certain stratigraphic levels (Fig. 8a), therefore being interpreted as coeval with sedimentation. These synsedimentary faults have NNW–SSE strike and east dip, i.e., they are synthetic to the Calamocha fault and nearly parallel to fractures measured in the R3 unit (Fig. 5d). A few metres apart, the same

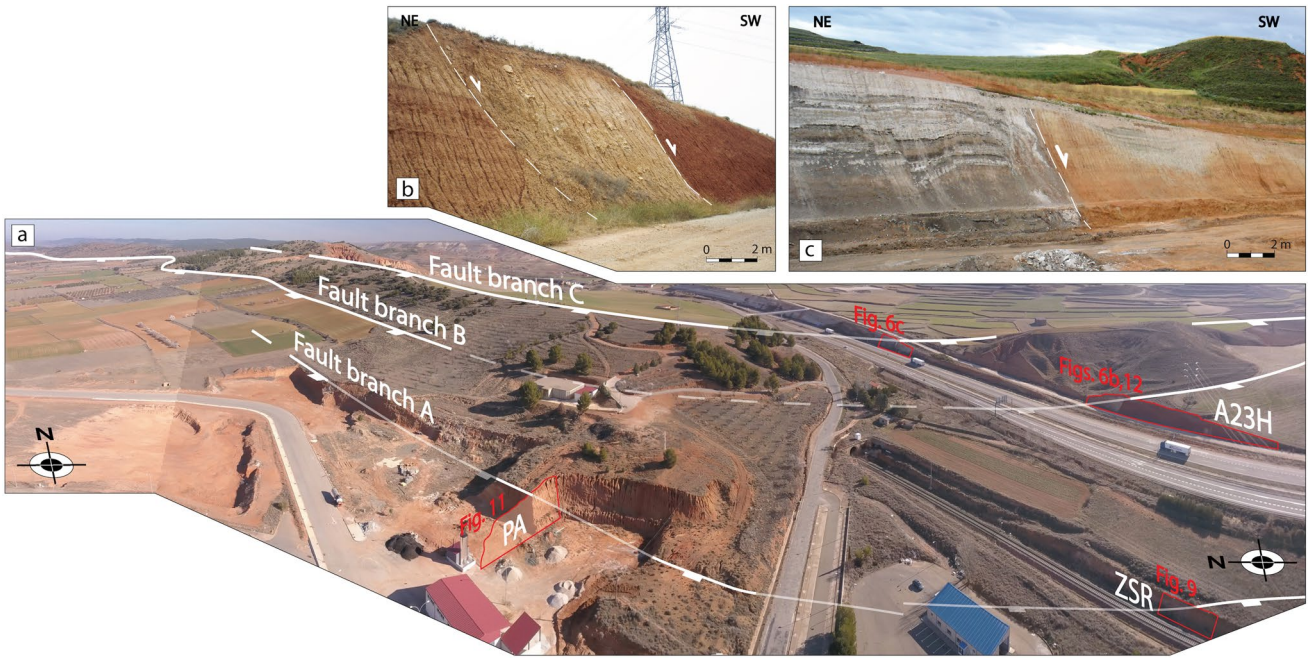

Fig. 6 **a** Oblique aerial view of the area east of Calamocha town, where the traces of fault branches A, B and C representing the central sector of the Calamocha fault zone are drawn. **b** Branch B exposed at a service road adjacent to A-23 highway. **c** Branch C exposed at the A-23 slope. Location of the slopes ZSR, PA and A23H, and their respective Figs. 10, 12 and 13, are indicated

deformed beds also show gentle, upright folds with local thickening and thinning, interpreted as soft-sediment deformation structures.

Such tectono-sedimentary setting suggests that: (i) the negative inversion of the Calamocha fault would have initiated prior to development of FES3 surface, at least coeval with the deposition of the P2 unit (so probably coeval with onset of the Concud fault, close to the age of FES2, ca. 3.8 Ma; Ezquerro et al. 2020); (ii) the total accumulated displacement on the fault could be slightly higher than that formerly established, increased by a value equivalent to a fraction of the thickness of unit P2 (up to a 30 m). In such a scenario, the maximum throw at the Calamocha fault is in the range of 180–210 m, and the maximum net slip in the range of 190–230 m. The estimate of average long-term slip rate (3.8 Ma) does not change significantly: 0.05–0.06 mm/a.

Trench study

The target of our palaeoseismological study has been the western branches of the Calamocha fault (A and B), east of Calamocha town. Three artificial slopes, trending nearly orthogonal to the fault traces and dipping about 45–50° have been the object of detailed study (see location in Figs. 3 and 6a): Zaragoza–Sagunto railway (ZSR), Polígono Agroalimentario (PA), and A-23 highway (A23H). The ZSR site constitutes the main source of palaeoseismological information, while PA and A23H have provided complementary data about structures whose ages are less constrained.

Zaragoza–Sagunto Railway (ZSR)

A segment of artificial slope of the Zaragoza–Sagunto railway was surveyed, representing an N055° E trending, 45-m-long trench that exposes branch A (ZSR; Fig. 9; see location in Figs. 3 and 6A).

Materials

Materials cropping out in the trench are alluvial Pleistocene sediments unconformably lying on Neogene greyish mudstone with interbedded grey limestone and ochre sand, all of them in decimetre-scale tabular strata dipping to the SW. Seven Pleistocene units have been distinguished on the basis of their lithology (Fig. 9a, b):

– Unit 1 (50 cm thick, in average) is made of orange mudstone with white carbonate nodules up to 25 cm in diameter, the latter disappearing towards the uppermost sandy part of the unit. This unit is only present within the western block.

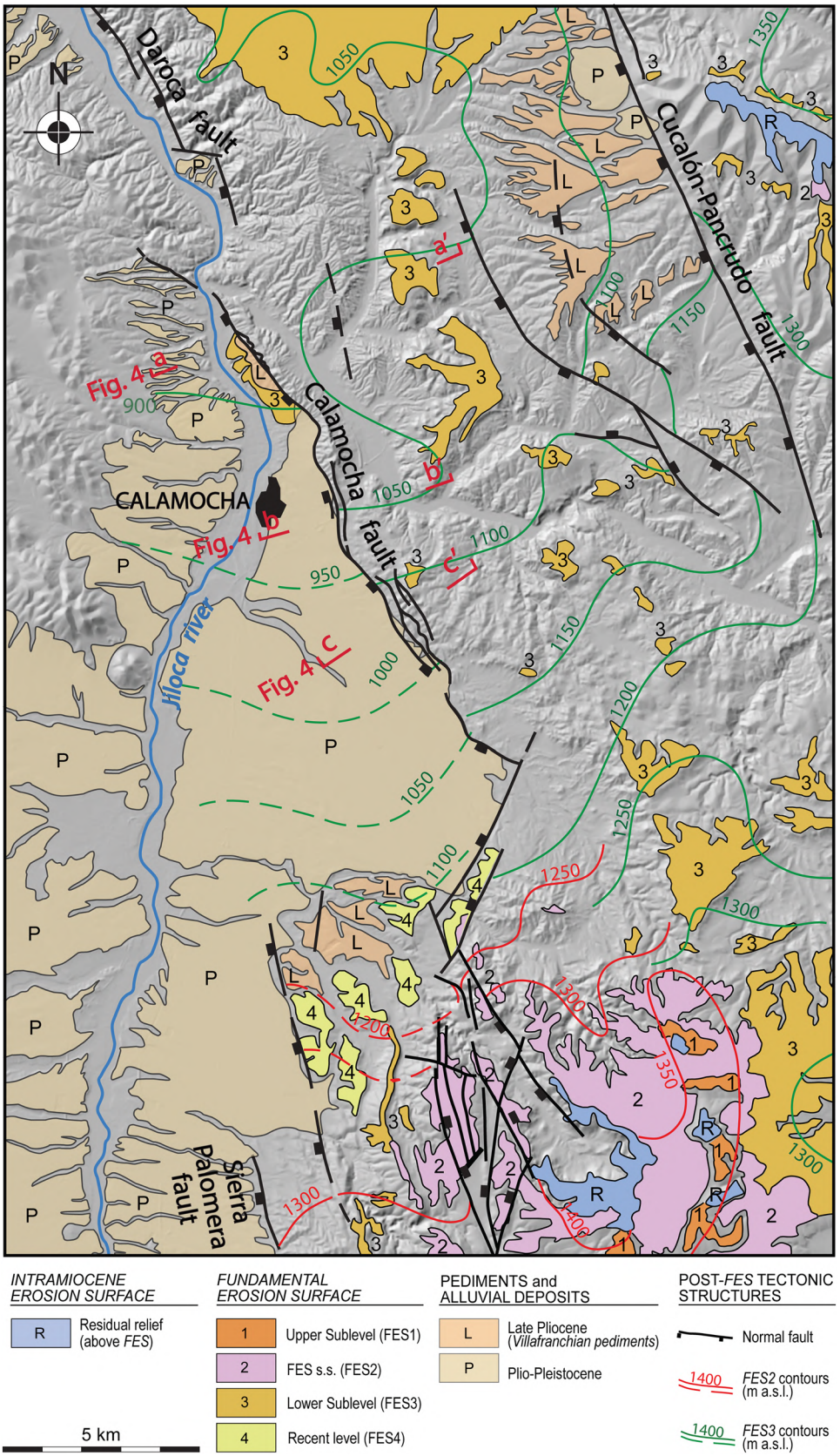

Fig. 7 Morphotectonic map of the study area, showing remains of late Neogene planation surfaces, their height contours and recent faults. See location in Fig. 1b

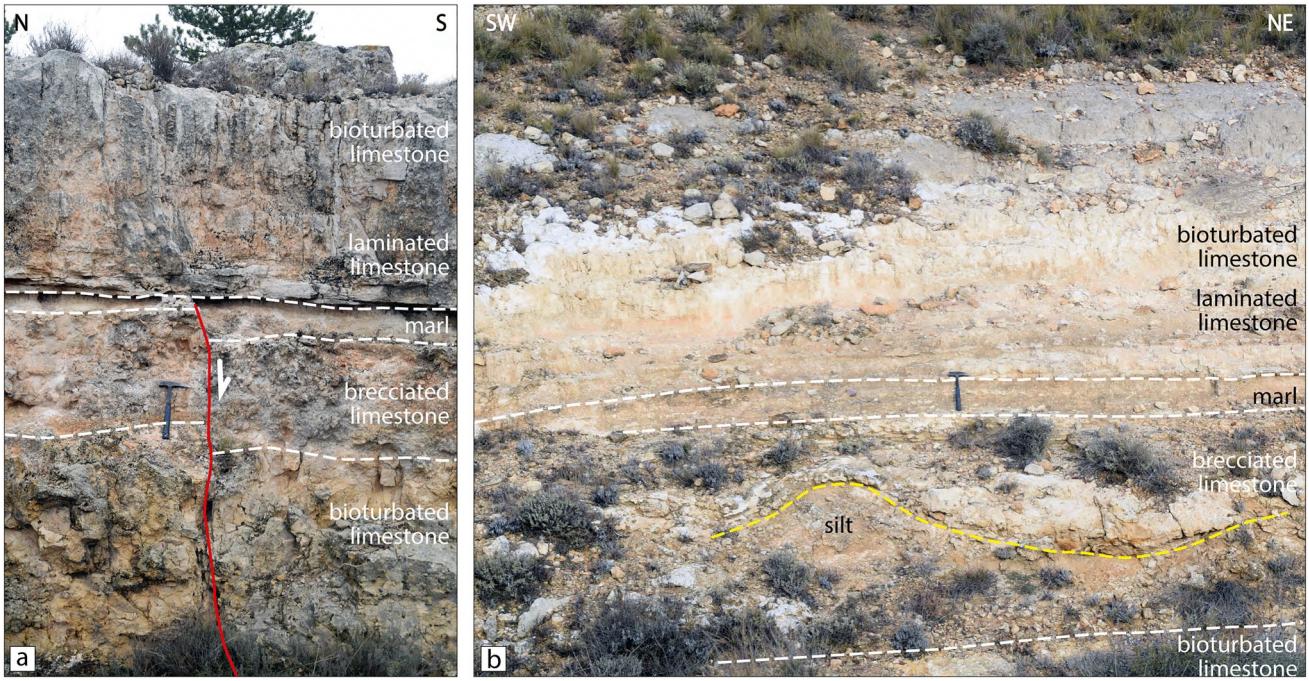

Fig. 8 Synsedimentary structures in P2 unit at the Venta de los Céntimos area. **a** Normal fault exhibiting differential displacement in successive beds. **b** Soft-sediment deformation structures (SSDS, gentle folds). See location in Fig. 4

- Unit 2 (35–75 cm) corresponds to a fining-upwards irregular bed with erosional base, made of whitish, grain-supported pebble gravel with brownish sandy matrix. Clasts of quartzite and limestone are mainly subangular to subrounded in shape. Some rip-up mud clasts were also identified.
- Unit 3 (25 cm) consists of whitish, grain-supported gravel with angular to subangular, mm- to dm-scale clasts, making up a tabular, calcrete-topped, fining-upwards cycle. This unit is only present within the western block.
- Unit 4 (40 cm) is made up of reddish, grain-supported gravel with angular to subangular mm- to dm-scale clasts arranged in a fining-upwards cycle. This unit is only present within the western block.
- Unit 5 (140 cm) consists of brown, pedogenized mudstone with carbonate nodules up to 25 cm in size, dispersed angular–subangular clasts, and rare interbedded grey sand levels. Carbonate nodules are less common towards the base and the top of the unit. This unit is only present within the eastern block.
- Unit 6 (110 cm) is formed by light orange, disorganized gravel with subangular clasts (up 25 cm in size) and white carbonate nodules.
- Unit 7 (until 140 cm) is made up of grain-supported gravel, orange in colour, with channel geometry. This unit is only present within the western block.
- Unit 8 is a nearly vertical structureless body of orange silt with scarce floating, angular to subangular limestone clasts.
- Unit 9 (20 cm) corresponds to a surficial regolith made up of reddish sandy mudstone with disperse granules.

OSL dating

The OSL response from the ten samples measured is fast-component dominated, and their reliability to estimate the accumulated dose has been confirmed through dose recovery tests performed in the laboratory. The derived natural dose populations are normally distributed with overdispersion values below 30% after removing outliers. Estimated burial equivalent doses, total dose rates and derived numerical ages are summarized in Table 1. Sample CALT-3Bb showed an anomalously large dose rate compared to the rest of the samples from this trench. This led to too young an age, disagreeing with the sedimentary succession. This age has therefore been discarded from the study and from any further discussion. Ages finally adopted are labelled in Fig. 9b.

Structural description

An extensional fault zone, with faults that are both synthetic and antithetic to the Calamocha fault system, is exposed

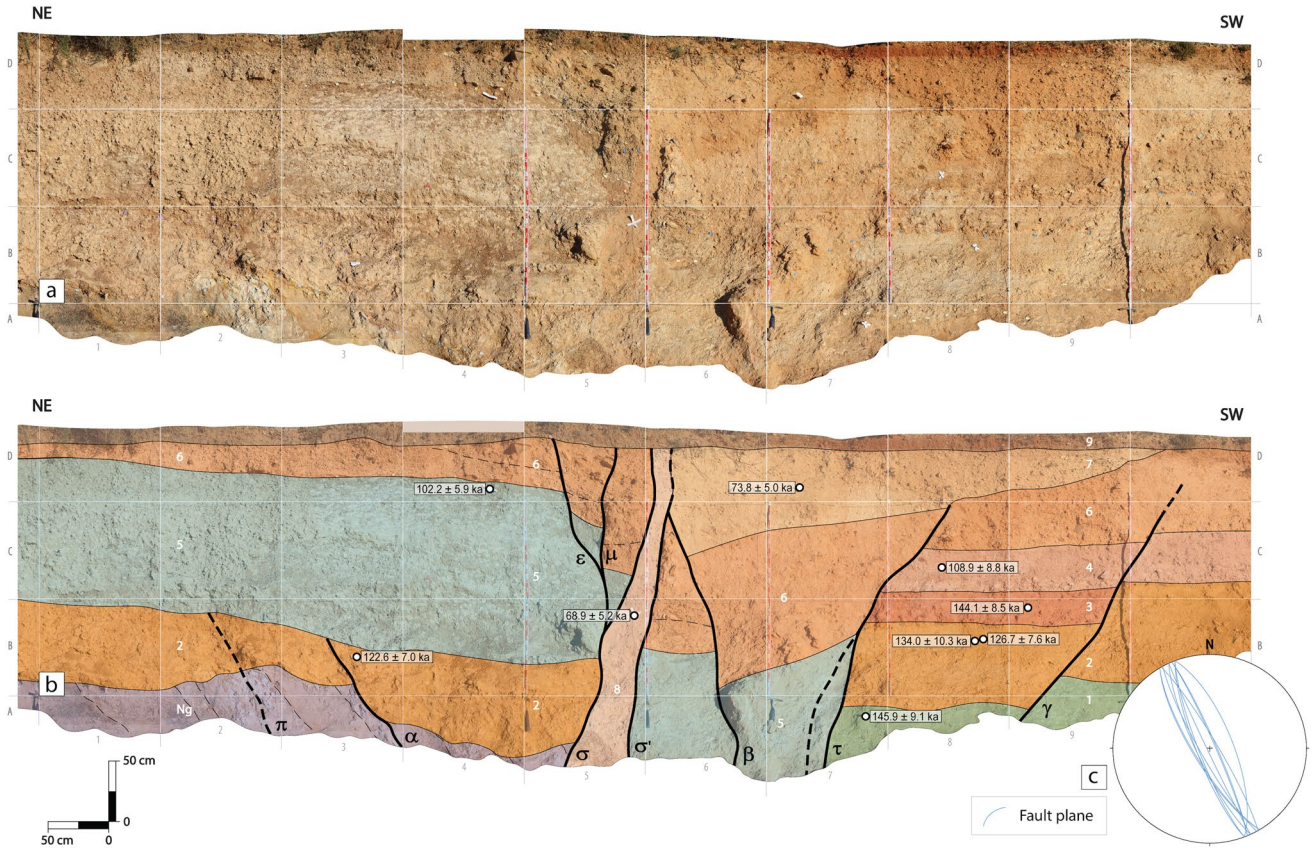

Fig. 9 **a** Photomosaic of the ZSR trench that crosses branch A; see location in Figs. 4 and 7a. **b** Detailed log. 1–9: Quaternary units described in the text. Greek characters: faults referred in the text. The location and age of samples dated by OSL is indicated. **c** Stereoplot (equal area, lower hemisphere) showing orientations of fault planes measured within the trench

within the ZSR log (Fig. 9b). It cuts the trench wall obliquely and can be identified with the southern prolongation of synthetic branch A (Fig. 3), although antithetic faults are also exposed. The stereoplot of Fig. 9c shows the homogeneous NNW–SSE strike and ca. 80º dip of every fault plane measured along the trench. No kinematic indicator has been observed on them.

Faults at both the eastern and central sectors are synthetic with the Calamocha fault (Fig. 9b). The eastern sector of the trench is cut by fault α (accompanied by fracture π), which underwent vertical displacement (throw) ≈ 0.3 m after sedimentation of unit 2 and is covered by unit 5. Faults ε, μ, σ, σ' and β make up the central fault zone, with an associated open fissure bounded by surfaces σ and σ' and filled with unit 8. Surfaces σ and σ' are irregular and show high apparent projected dips that mainly respond to the oblique orientation of the structure with respect to the trench direction, and the subsequent projection of the slope onto the vertical plane. Faults ε and μ are associated with σ as two splay faults, jointly producing a throw of more than 0.7 m in the contact between units 5 and 6. The rock body enclosed by surfaces σ and σ' (unit 8) is interpreted as a fissure infill based on its nearly vertical, transverse attitude and its massive, disorganized internal constitution. According to this interpretation, such surfaces would have represented both walls of a single fracture, then they were disengaged and partially crumbled before infilling took place. Fault propagated through units 5, 6 and 7 producing a localized rollover structure.

Faults exposed at the western sector, γ and τ, are antithetic to the Calamocha fault (Fig. 9b). Fault γ offsets ≈ 0.4 m the base of unit 2, while producing a smaller separation (ca. 0.1 m) in the base of unit 4. We have interpreted that it underwent displacement ≈ 0.3 m before sedimentation of unit 2, and was then reactivated after the deposition of unit 6. Fault τ played an important role producing the highest antithetic displacement and allowing syntectonic deposit of unit 5 (as it is only visible in its hanging-wall block). It also offsets unit 6, so it has undergone reactivation after the deposition of this unit and has been covered by unit 7, in the same way as fault γ.

After deposition of unit 2, the aggregate, visible throw of the synthetic faults (≈ 2 m) is virtually counterbalanced by the antithetic throw, as can be seen by comparing the height of the base of unit 2 at both ends of the log (Fig. 9b). In

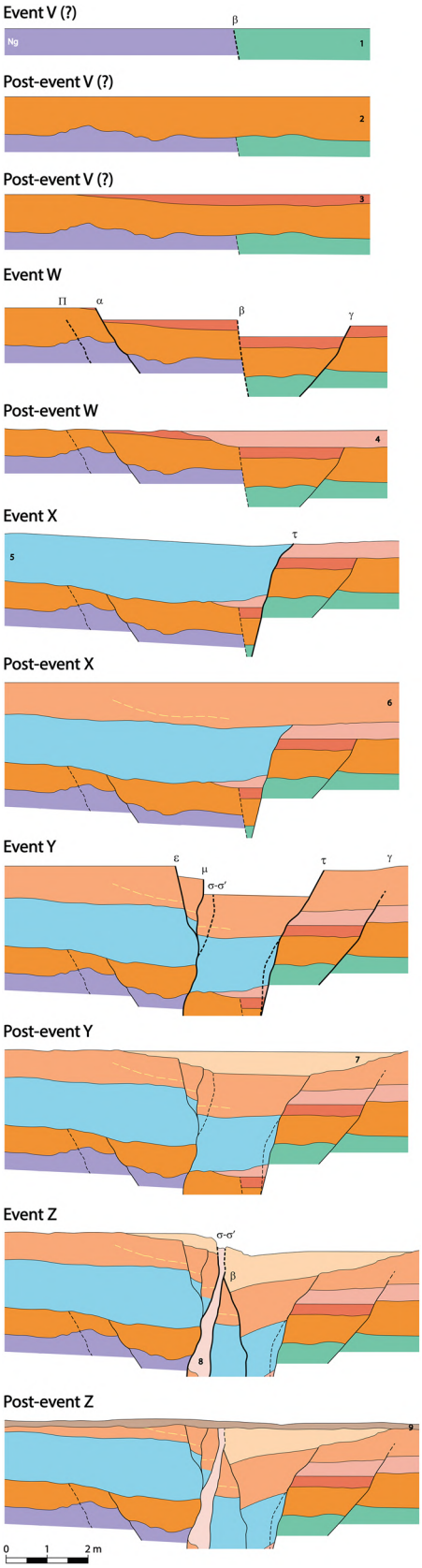

Fig. 10 Evolutionary model of sedimentation and deformation recorded at the ZSR trench from retrodeformational analysis. Each sketch represents a stage subsequent to the palaeoseismic event (and, in some cases, to deposition of sedimentary units) labelled above. Unexposed sectors below the trench have been locally reconstructed in the sketches to complete the evolutionary model. Bold traces represent faults active during each event

addition, a supposed synthetic offset of unit 1 (with throw equal of greater than its own thickness), previous to deposition of unit 2, could justify the absence of the former in the western block and the deeper position of the Neogene/Pleistocene boundary in the eastern one.

As explained above, throw values cannot be translated into net slip due to the lack of information about slip vectors on the surveyed faults. In addition, doubts about the kinematical meaning of antithetic faults and weak chronological constrains also prevent a reliable approach to slip rates.

Interpretation of palaeoseismic events and retrodeformational analysis

Detailed study of sedimentary units, deformation and relationship with faults allows interpreting four clear deformation events (W to Z), and an additional uncertain one (V), at the ZSR. As an auxiliary tool, retrodeformational analysis of the trench log (Fig. 10) was achieved to contrast the succession of deformation events and to test its kinematic consistence. Several identifiable faults were either formed, propagated or reactivated during each deformation event. For each event, fault throws were computed, while progressive horizontal extension is visually expressed in the successive cross sections of Fig. 10.

The interpreted events at the ZSR are as follows (see Figs. 10b and 11):

- Event V (?) is tentatively inferred from the absence of unit 1 above the Neogene in the eastern block, which can be reliably explained by slip on fault β after deposition of unit 1 and prior to unit 2. A second scenario, i.e., an erosional unconformity between both units, cannot be ruled out. Event V would be pre-dated by the top of unit 1 (145.9 ± 9.1 ka) and post-dated by unit 2 (with a range age of 144.3–135.6 ka, result of the overlap of 122.6 ± 7.0, 126.7 ± 7.6, 134.0 ± 10.3 and 144.1 ± 8.5 ka). The more probable event age would be adopted as ca. 140 ka. The throw associated with this hypothetic event should be equal to or greater than the exposed thickness of unit 1 (≈ 0.5 m).
- Event W is initially identified from rupture and displacement of units 2 and 3 by the antithetic fault γ, prior to deposition of unit 4. This explains why the offset in unit 2 is greater than that in unit 4, and why unit 3 is only present in its hanging-wall block. Hypotheti-

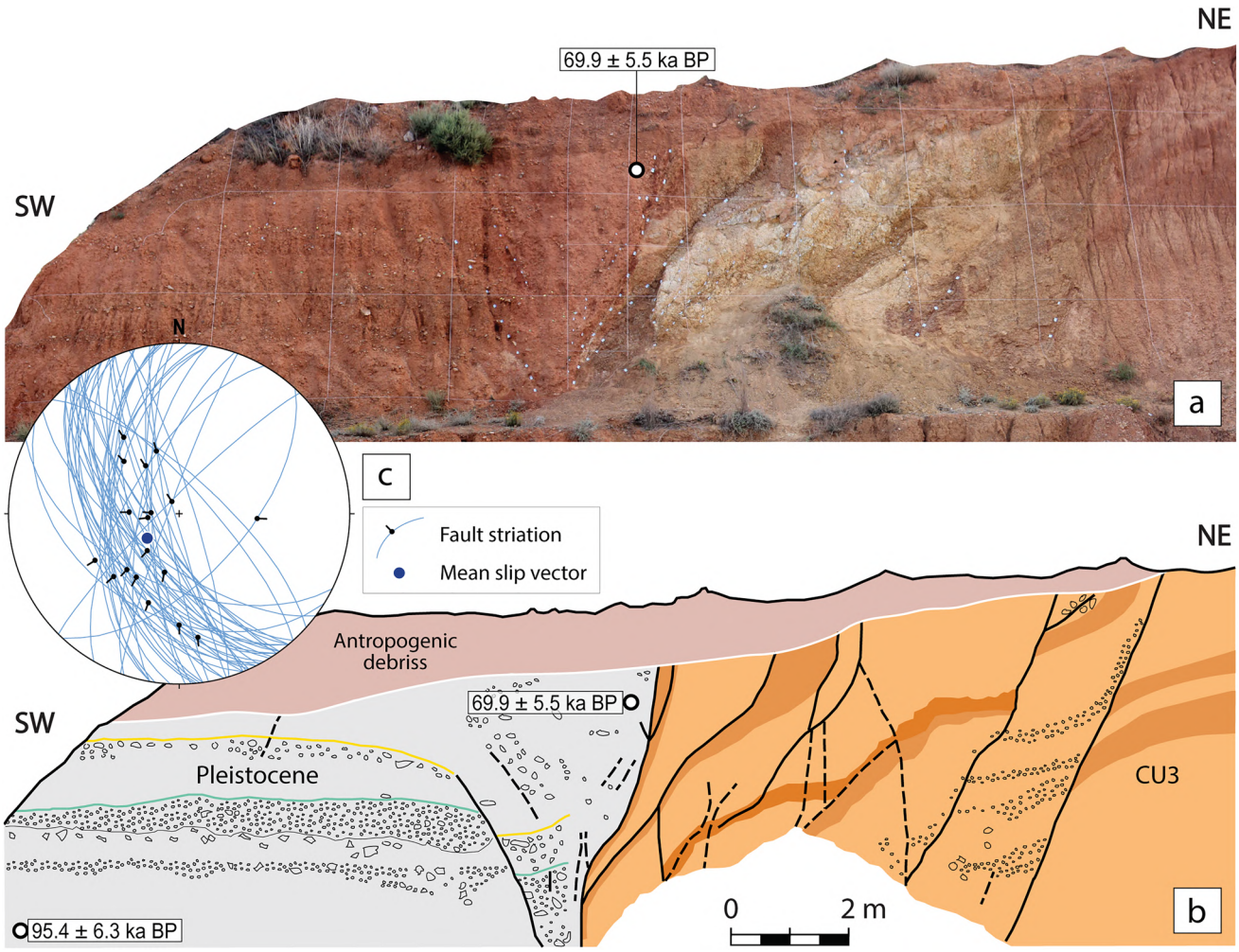

Fig. 11 **a** Photomosaic of the PA slope that crosses branch A; see location in Figs. 4 and 7a. **b** Synthetic log showing the Miocene Clastic Unit 3 (CU3) and Pleistocene deposits (modified from Martín-Bello et al. 2014). The location and age of samples dated by OSL is indicated. **c** Stereoplot (equal area, lower hemisphere) showing orientations of fault planes and slickenlines measured within the outcrop

cal simultaneous slip on fault β could justify the loss of unit 3 in the eastern block. Faults α and π, overlaid by unit 5, have been also attributed to this event on the basis of the principle of parsimony (in order to minimize the number of events necessary for explaining the observed structures). This event is pre-dated by unit 2 (in the range of 144.3−135.6 ka) and post-dated by unit 4 (108.9 ± 8.8 ka). The more probable event age would be closer to the first range, and adopted as ca. 125 ka. Synthetic and antithetic slip has been counterbalanced in this event, resulting in a total synthetic throw of ≈ 0.45 m and a horizontal extension of ≈ 0.45 m.

– Event X is interpreted from the existence of unit 5 only within the eastern block due to syn/post-sedimentary displacement by fault τ. It should be pre-dated by unit 4 (108.9 ± 8.8 ka) and post-dated by the top of unit 5 (102.2 ± 5.9 ka). The more probable event age would be adopted as ca. 105 ka. The total, antithetic throw of this event is ≈ 1.1 m and its horizontal extension ≈ 0.3 m.
– Event Y is identified from rupture and displacement of unit 6 by faults ε, μ, σ-σ', τ and γ. It is pre-dated by unit 5 (102.2 ± 5.9 ka) and post-dated by unit 7 (73.8 ± 5.0 ka). The more probable event age would be closer to the second age and adopted as ca. 80 ka. The total throw of this event is virtually null due to counterbalancing of synthetic and antithetic slip, and its horizontal extension ≈ 0.2 m.
– Event Z is interpreted from the displacement and rollover tilting of unit 7 by fault β and from the disengagement of surfaces σ and σ' that results in fissure opening and infill with unit 8. It is pre-dated by unit 7 (73.8 ± 5.0 ka) and post-dated by unit 8 (68.9 ± 5.2 ka). The more probable event age adopted is ca. 70 ka. The total synthetic throw

of this event is ≈ 0.5 m and its horizontal extension ≈ 0.25 m.

Polígono agroalimentario (PA)

PA site was an N075º E trending, 20-m-long artificial slope at the margin of the Calamocha agri-food industrial estate, which also intersected fault branch A. It was removed during recent widening of the industrial area, but it had already been analysed and fully documented before.

The trace of fault branch A, bringing into contact Pleistocene sediments within the hanging-wall and unit CU3 within the footwall, was recognized in this outcrop (Fig. 11a, b). Quaternary sediments are significantly homogeneous, so that no well-defined unit could be distinguished at that formerly existing slope. Pleistocene alluvial sediments consist of gravel with quartzitic clasts and red lutite matrix. Some clasts are aligned defining subtle levels that can be locally recognized. Lithology of unit CU3 mainly consists of marl and limestone, bedding being strongly disrupted due to both brittle and ductile deformation.

The chronology of the involved Pleistocene sediments has been constrained from two OSL ages. These were provided by two samples collected, respectively, at the base of the visible Pleistocene succession (95.4 ± 6.3 ka) and within the youngest sediments cut by the fault (69.9 ± 5.5 ka) (see Table 1). The overlying materials are present-day debris of anthropogenic origin.

The main fault surface has an average orientation N160º E, 70º W. Subsidiary rupture surfaces exposed at the slope mainly affected the footwall block and were synthetic with the main fault A, striking NNW–SSE and dipping between 45º and 80º W (Fig. 11c). There were some antithetic faults propagated through the hanging-wall block, one of them with a throw of ca. 1.1 m. The slickenlines measured within the fault zone indicate a prevailing normal slip, with most slip vectors towards W and SW (mean transport direction towards N234º E; Fig. 11c).

The described features suggest that fault A was active as a nearly pure normal fault during the Late Pleistocene, probably during deposition of the alluvial sediments occupying the hanging-wall block (95.4 ± 6.3 to 69.9 ± 5.5 ka, approximately), and definitely after them. The minimum fault throw accumulated during that time span can be approached from: (i) the sedimentary thickness between both dated samples (ca. 4.5 m), assuming that slip rate and sedimentation rate are similar to each other; (ii) the difference between the visible throw at the main fault minus the throw accommodated by the antithetic fault: (4.8 − 1.1) m = 3.7 m. Considering the average fault dip (70º) and assuming the slip direction previously inferred (N234º E), the resulting net slip would be in the range of 3.9–4.8 m, and the slip rate could be roughly estimated to 0.1–0.3 mm/a.

A-23 highway slope (A23H)

A23H site is a N055º E trending, 110-m-long slope segment of the service road adjacent to the A-23 highway. It exposes fault branch B, which brings into contact two middle Miocene units: siltstone and claystone of CU2, within the footwall block, and gravel of subrounded clasts CU3, within the hanging-wall block (Figs. 6b, 12a). Bedding of the unit CU2 is difficult to identify owing to intense bending and brecciation, while conspicuous alignments of quartzitic pebbles and carbonated crusts define bedding within CU3. The main fault plane (δ in Fig. 12b) is locally oriented N178º E, 75º W, with slickenlines indicating a slip vector towards N270º E (Fig. 12d).

The footwall block is affected by minor synthetic faults and fractures, which strike close to N–S and dip between 50º and 80º W (Fig. 12d). Within the hanging-wall block a high number of antithetic faults can be recognized, also striking around N–S and dipping 30–50º E. They produce apparent displacements of 0.5–3 m in the pebble alignments that define the bedding, the latter dipping 25º–45º W (see close view in Fig. 12c).

Such fault association suggests a rollover structure induced by listric geometry of the main fault. Passive accommodation of the hanging-wall deformation would have occurred through a mechanism of antithetic simple shear achieved by slip over discrete planes. However, bedding does not dip towards the main fault, but synthetic with it (up to a maximum of 45° SW in an inflection zone at 60 m to the fault). The bedding attitude suggests the occurrence of additional normal drag folding. The reduced dip of the antithetic faults and, on the contrary, the wide angle between these faults and bedding indicates that these faults were formed prior to the drag fold, and then reduced their dips while bedding was tilted. We interpret that such deformation sequence could be achieved by slip of the hanging-wall block on an undulated rupture surface made of a shallow listric segment, then on an increasingly dipping deep segment.

Some of the antithetic faults (mainly those propagating further down into the hanging-wall block) are overlaid by two colluvial bodies (Q1 and Q2 in Fig. 12a) with erosive base. Both are made of gravel (angular limestone pebbles) with interbedded medium-fine sand, and are dated to 41.9 ± 2.9 and 53.1 ± 3.7 ka, respectively (see Table 1).

Two other colluvial bodies (Q3 and Q4) are affected by faults (Fig. 12a, b):

– Colluvium Q3 is made of grain-supported gravel (angular limestone pebbles up to 20 cm in diameter). The sedimentary body is channel-shaped, shows subhorizontal layering marked by interbedded fine sand levels, and is dated to 35.3 ± 2.3 ka. It also overlies two of the antithetic faults, but another one (ρ) in the hanging-wall

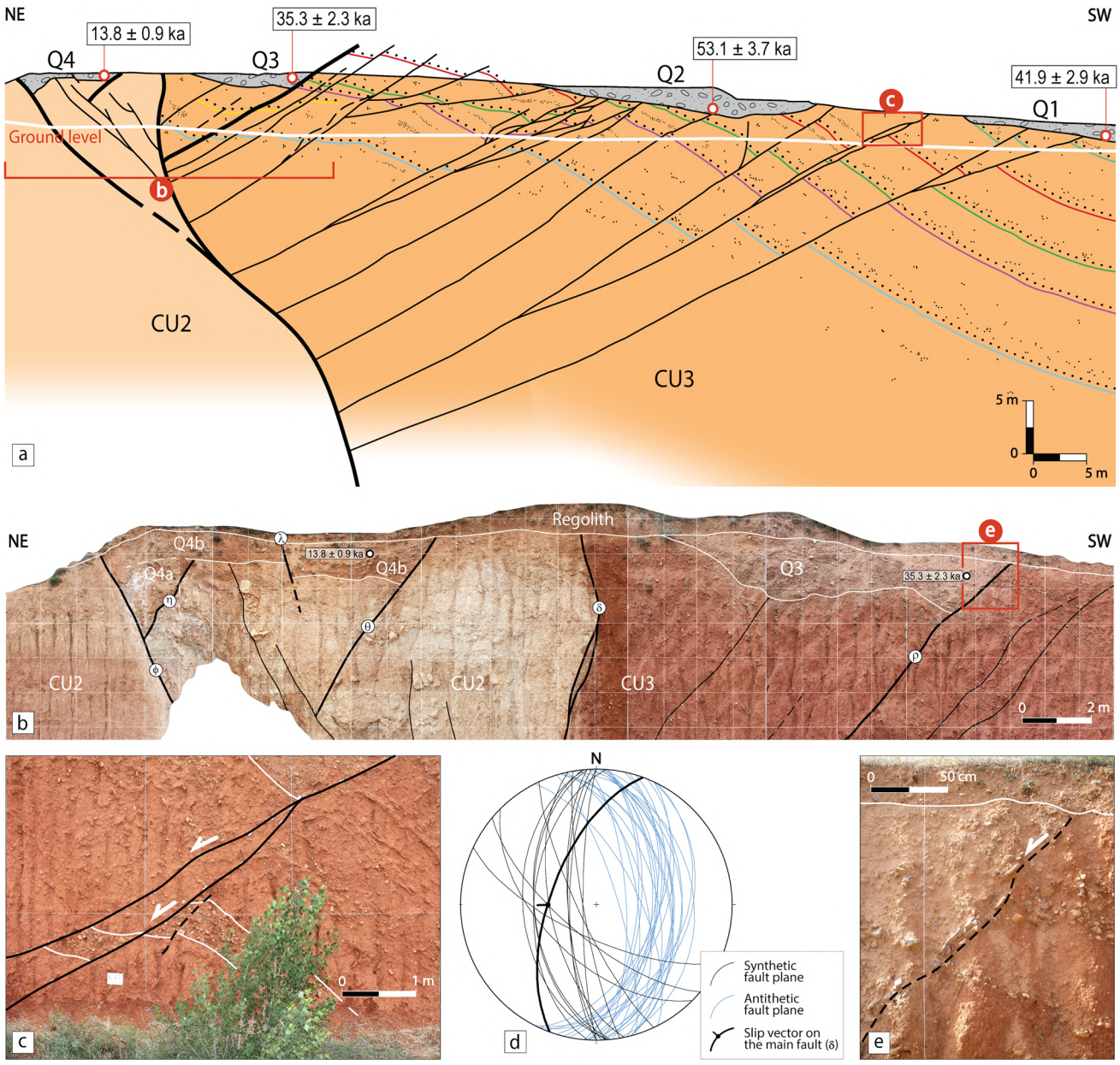

Fig. 12 **a** Synthetic cross section (aboveground) of the A23H slope that crosses branch B, and its interpretation (belowground). Bedding of the Miocene clastic unit CU3 in the hanging-wall block can be recognized by conspicuous quartzitic gravel horizons, unconformably underlying Quaternary colluviums Q1–Q4. The position and age of samples dated by OSL is indicated. See location in Figs. 4 and 7a. Modified from Martín-Bello et al. (2014). **b** Interpreted photomosaic of deformed colluvium bodies Q3 and Q4. Sections a and b are drawn from photomosaics of the artificial slope projected onto the vertical plane. **c** Details of bedding of unit CU3 cut by antithetic faults. **d** Stereoplot (equal area, lower hemisphere) showing orientations of synthetic and antithetic faults, as well as striation on the main fault plane (δ). **e** Details of aligned pebbles of Q3 along the fault (ρ)

block, striking N005° E and dipping 64° E, cuts the deposit and produces reorientation of pebbles (Fig. 12e), with a minimum throw of 1.5 m. Assuming a slip vector towards N090° E (within the same movement plane of fault δ; i.e., nearly pure normal movement), this involves a net slip of ~ 1.7 m (Fig. 12b).

– Colluvium Q4 is a massive and nearly tabular body of fine sand with two interbedded levels of matrix-supported gravel (angular-subangular limestone pebbles up to 15 cm in diameter). It has delivered an OSL age 13.8 ± 0.9 ka. The sedimentary body overlies the main fault zone, and is delimited by two main mechanical

boundaries which correspond to a synthetic fault (ϕ), oriented 175, 52 W, and an antithetic one (θ), oriented 174, 60 E. They produce throws of 2,4 m and 1,3 m, respectively, which would correspond to net slips ~ 3.0 m and ~ 1.4 m. Another two faults (η and λ) also cut the base of Q4, showing net slip of ~ 1.6 m and ~ 0.4, respectively (Fig. 12b). Very probably, the displacement recorded at fault ϕ does not represent a single event. Fault η cuts subunit Q4a and is overlaid by the base of Q4b, which in turn is offset by faults ϕ, λ and θ. At least two faulting episodes are therefore required for explaining the deformation of Q4.

According to the proposed kinematic model, recent reactivation of antithetic faults should have been induced by slip events on fault branch B. Overall, activation of subsidiary rupture surfaces would have developed progressively closer to the main fault. It all corroborates that the Calamocha fault has undergone recurrent slip events during the Late Pleistocene: some of them prior to 53.1 ± 3.7, 41.9 ± 2.9 and 35.3 ± 2.3 ka, others after 35.3 ± 2.3 ka and 13.8 ± 0.9, respectively.

Discussion

Assessing long-term and short-term activity of the Calamocha fault and its palaeoseismic significance

The geometry, kinematics and evolution of the Calamocha fault have been characterized from structural and morphotectonic approaches. The fault sinks the northern sector of the Jiloca graben with respect to the Neogene infill of the Calatayud basin, both basins therefore being articulated as two adjacent tilted steps (Fig. 1c). The fault trace trends NNW–SSE (N150º E in average) and is 18 km long, splitting into three or four nearly parallel branches in certain sectors (Figs. 3, 6a). Where the fault surfaces are exposed, they usually dip 70–75º E. Kinematical indicators observed in some of them in the central sector show nearly pure normal slip, with prevailing transport directions towards W and SW (mean slip vector towards N234º E reported at branch A; Fig. 11c).

The occurrence of older contractional structures near its northern sector (Liesa et al. 2021) suggests that the normal Calamocha fault resulted from inversion of a previous, Palaeogene to Early Miocene compressional structure, in the same way as it has been interpreted for the neighbouring Daroca Fault (Colomer and Santanach 1988; Casas et al. 2018). The onset of extensional activity has been documented in the Late Pliocene, 3.8 Ma ago.

The maximum normal throw at the northern and central sectors of the fault is in the range of 180–210 m, and the maximum net slip in the range of 190–230 m. The average long-term (3.8 Ma) slip rate has therefore been calculated to 0.05–0.06 mm/a.

Branches A and B at the central sector of the Calamocha fault have undergone recurrent slip during the Late Pleistocene, as evidenced by detailed study at three artificial exposures in the neighbourhoods of Calamocha town: Zaragoza–Sagunto railway (ZSR), Polígono Agroalimentario (PA), and the A-23 highway (A23H; Fig. 6a). A chronological synthesis of faulting episodes during the Pleistocene is depicted in Fig. 13. Site ZSR has provided a succession of four to five deformational events for branch A within the time lapse between 145.9 ± 9.1 and 68.9 ± 5.2 ka. Considering both scenarios (4 or 5 slip events), and seeing the age

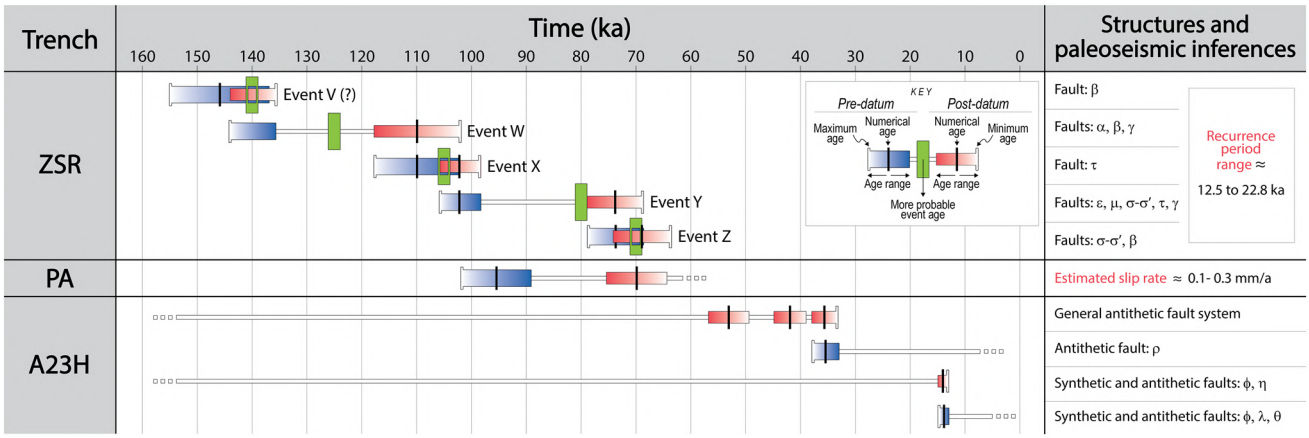

Fig. 13 Chronological summary of faulting events interpreted from trench study at branches A and B of the Calamocha fault

error bars, this results in an average recurrence period in the range of 12.5–22.8 ka. Site PA shows evidence of slip on branch A during/after the time lapse between 95.4 ± 6.3 and 69.9 ± 5.5 ka. Site A23H reveals that branch B has undergone slip events prior to 53.1 ± 3.7, 41.9 ± 2.9 and 35.3 ± 2.3 ka, as well as others after 35.3 ± 2.3 and 13.8 ± 0.9 ka. Overall, (i) the ZSR trench records older deformation episodes; (ii) event Z in ZSR could be correlated with an indistinguishable fraction of the total fault slip recorded in PA (on the same fault branch A); (iii) the A23H slope has recorded imprecise faulting episodes, including the younger ones.

It is unfortunate that these data are not able to build a robust palaeoseismic succession for the Calamocha fault. Some of the deformation events interpreted in site ZSR do not represent visible accumulated displacement on the main fault; the slip balance on the ensemble of synthetic and antithetic faults is very small indeed (not much greater than 0.3 m). Only events W and Z could correspond to true slip episodes on fault branch A. Faulting episodes inferred at sites PA (branch A) and A23H (branch B) are not constrained enough in age for being correlated to build a complete evolutionary model. Nevertheless, from the available data, general notions can be retained about (i) the recurrent nature of deformation events since ca. 146 ka ago, (ii) their average recurrence period (12.5–22.8 ka for branch A), (iii) the slip rate (roughly estimated to 0.1–0.3 mm/a where visible slip has effectively accumulated; PA trench), and (iv) the proximity in time of the latest slip episodes (younger than 13.8 ka; Fig. 13).

These parameters definitely allow classifying the Calamocha fault as an active fault, according to most scientific classifications and legal regulations (e.g., NRC 1997; Machette 2000; Strom 2017). Moreover, the slip rate approached for a limited time window in the Late Pleistocene suggests that it has been higher than the long-term rate (0.1–0.3 mm/a vs. 0.05–0.06 mm/a).

The Calamocha fault and associated deformation within the regional framework

The maximum net slip (190–230 m) and average slip rate (0.05–0.06 mm/a) reported for the last 3.8 Ma at the Calamocha fault are of the same order, but generally lower, than those of neighbouring faults in the region (Table 2).

The above-mentioned apparent increase of short-term (Late Pleistocene) with respect to the long-term (since Late Pliocene) slip rate that we have inferred for the Calamocha fault represents a common tendency in the central Iberian Chain (Table 2). Only for the E–W trending Valdecebro fault zone (transverse structure within the Teruel basin), the slip rate for the last 142 ka (0.05–0.07 mm/a) is similar to the long-term one (Simón et al. 2019). Nevertheless, it should be noted that such slip rate is partial, since it corresponds to a single fault branch among several branches active during the Late Pleistocene.

The same tendency towards an increasing slip rate had already manifested during Neogene times at the eastern margin of the Teruel basin, the main extensional macrostructure within the region. All things considered, the total slip rate (fault throw and associated bending) accommodated on distinct transects across the entire basin margin shows a similar value (0.07–0.09 mm/a). However, comparing both extensional episodes defined in the region, a clear increase has been evidenced: from 0.05 to 0.07 mm/a during Late Miocene to Early Pliocene times, to 0.12–0.16 mm/a during Late Pliocene–Quaternary times (Ezquerro et al. 2020).

Three contributing factors have been invoked by Ezquerro et al. (2020) for explaining such an increase in slip rate: (i) onshore, westwards propagation of extensional deformation from the inner parts of the Valencia Trough; (ii) onset of crustal doming at the central–eastern Iberian Chain, which induced the recent multidirectional tension; (iii) progressive fault linkage since the beginning of the Late Miocene.

Table 2 Summary of net slip values and slip rates calculated for the Calamocha fault and other recent extensional faults within the central–eastern Iberian Chain

Fault	Net slip (m)	Long-term slip rate (mm/a) (3.8–3.5 Ma)	Short-term slip rate (mm/a)	References
Calamocha	190–230	0.05–0.06	0.1–0.3 (since 95.4–69.9 ka)	This work
Sierra Palomera	330–480	0.09–0.15		Peiro et al. (2022)
Concud	255–290	0.07–0.08	0.29 (since 74 ka)	Lafuente et al. (2011, 2014), Simón et al. (2016), Ezquerro et al. (2020)
Teruel	270	0.07	0.18–0.20 (since 46 ka)	Simón et al. (2017)
Valdecebro	190	0.05	0.05–0.07 (since 142 ka)	Simón et al. (2019)
Eastern margin of the Teruel basin	490–690	0.13–0.17		Ezquerro et al. (2020)
Río Grío–Pancrudo	260–325	0.07–0.09	0.3–0.36 (since 67 ka)	Peiro and Simón (2022)

The geometry and kinematics of the Calamocha fault are consistent with the recent tensional stress field, characterized by σ_3 trajectories trending WSW–ENE (Simón 1982, 1989; Arlegui et al. 2005; Liesa et al. 2019). Most rupture surfaces observed in the surveyed outcrops are either closely parallel (sites ZSR and PA) or antithetic (site A23H) to the map-scale faults, but, in any case, they are parallel to the NNW–SSE trending S_{Hmax} (σ_2) stress trajectories. Therefore, all of them are favourably oriented to move as nearly pure normal faults, as the observed slickenlines indicate.

Nevertheless, the nature of the relationship between each fault branch and its subsidiary rupture surfaces, and hence the tectonic and palaeoseismic meaning of the latter, are different for each exposure studied. Faults are entirely synthetic with the main branch A in site PA, and mostly antithetic to branch B (associated with rollover kinematics of the hanging-wall block) in site A23H; however, in both cases, minor rupture surfaces are kinematically related to slip on the main faults. If the position and characteristics of Quaternary sediments linked to them would have made it possible to establish an almost complete succession of deformation events, their palaeoseismic significance would have been complete. This was not the case owing to: (i) the impossibility of identifying sedimentary units with distinct tectono-sedimentary relationships within Pleistocene sediments in site PA, and (ii) the laterally discontinuous occurrence of the colluvial deposits in site A23H. In the case of site ZSR, the quality of the available information has made it possible to reconstruct a succession of faulting episodes, but these cannot be directly linked to progressive slip of fault branch A. Consequently, we do not have direct information about the seismogenic behaviour of branch A, beyond overall perception on repeated deformation during the Late Pleistocene, with an average recurrence period in the order of 10^1 ka.

Relationships of the faulting succession interpreted at site ZSR with the Calamocha fault itself should not be sought at the kinematical level but at the dynamical level: both have a common origin within the regional stress framework. Maps of surface fractures resulting from large earthquakes (e.g., Philip and Meghraoui 1983; Lavecchia et al. 2012; Choi et al. 2019) reveal the structural complexity resulting from hierarchical development of (i) a large fault that propagates from the subsoil to the surface, (ii) subsidiary fractures and folds induced by the kinematics of the main fault, and (iii) accompanying faults directly controlled by the same regional stress field. The succession of faulting events at ZSR represents progressive deformation within the hanging-wall block of the Calamocha fault in response to the remote tensional stress field. The faulting succession indicates alternating slip on synthetic and antithetic faults, which has accommodated overall absolute horizontal stretching at this section of ca. 100 cm (local β factor = 1.1). The case is similar to the one recently studied at a trench excavated in the hanging-wall block of the neighbouring Sierra Palomera fault (Peiro et al. 2022). It is not feasible that propagation or reactivation of those small ruptures occurred fully independently; more likely, it accompanied a major slip event in one of the main branches. Hence, although such minor faults do not directly represent a progressive slip of that fault, they have some palaeoseismological significance from a temporal point of view.

Seismogenic characterization

According to the analysis carried out by Stirling et al. (2013) for the Global Earthquake Model (GEM), application of the regression model by Wesnousky (2008) is recommended for approaching seismogenic parameters in slow intraplate normal faults. Considering the length of the Calamocha fault trace (18 km) and the absence of structural segmentation, such regression provides a potential moment magnitude $M_w = 6.7 \pm 0.3$ for earthquakes generated by this structure. This M_w value fits the range obtained from other common regression proposals (central values of M_w ranging from 6.3 to 6.9; Wells and Coppersmith 1994; Stirling et al. 2002; Leonard 2010), but should be regarded as more precise. Concerning the coseismic slip, despite the wide deviation bar that all regression models show, it should be noted that Wesnousky's (2008) model gives a potential average coseismic slip of ca. 0.5 m, while the other regressions (Wells and Coppersmith 1994; Stirling et al., 2002; Leonard 2010) point to values in the range of 0.4–2.2 m.

Testing the reliability of such values of coseismic slip is a difficult task since the results from our trench study are not robust enough, but they seem reasonably consistent. Some pieces of field information could provide an approach to the coseismic slip on individual branches of the Calamocha fault ("Seismogenic characterization"): (i) synthetic throws measured for two deformational events in trench ZSR (events W and Z; 0.45 and 0.5 m, respectively; Figs. 9b, 10); (ii) synthetic throw estimated for the hypothetical event V (> 0.5 m; Figs. 9b, 10); (iii) synthetic throw inferred from the rupture of colluvium Q4 along fault ϕ in A23H (2.4 m; Fig. 12b). As explained above, Q4 had to undergo at least two deformation episodes, so the hypothesis that the 2.4 m throw in fault ϕ was distributed among at least two events seems reasonable. From such premises, the average of estimated coseismic throws for events V, W, Z, and fault ϕ would be in the range of 0.45–1.2 m, which approximately corresponds to net slip of 0.5–1.3 m (considering the orientation of fault planes and transport direction). Such quantities are within the range derived from the regressions mentioned above; we can therefore assume that they represent realistic values for the seismogenic behaviour of the Calamocha fault.

Once compiled and critically assumed the above information, it is also possible to calculate the potential moment

magnitude M_w by using the equation proposed by Hanks and Kanamori (1979), based on the notion of seismic moment M_0. For achieving such calculation, we have considered: (i) the average coseismic slip of 0.5–1.3 m; (ii) the rupture area expressed as the product of the trace length (18 km) and the fault width along dip (13–19 km, up to the regional detachment level, whose depth has been located by Roca and Guimerà 1992, and Ezquerro et al. 2020, at 11–17 km); (iii) the average shear modulus μ commonly used for typical upper crustal rocks, $3–3.5 \cdot 10^{10}$ Pa. The resulting M_w value lies in the range of 6.3–6.7. This M_w range lies within the aforementioned range estimated from regression models ($M_w = 6.3–6.9$), so it can be assumed as the most accurate for the Calamocha fault.

Reliability of the other palaeoseismic parameters approached from trench study for Late Pleistocene times can be now assessed: slip rate of 0.1–0.3 mm/a (PA site), and average recurrence period of 12.5–22.8 ka (ZSR site). For both parameters, values in the lowest range are needed to be consistent with the formerly approached coseismic slip. Assuming a stick–slip fault regime at a rate of 0.1 mm/a, a recurrence period of 12.5 ka involves a coseismic slip of 1.25 m, which lies within the range estimated from field data (0.5–1.3 m), and also within that obtained from the regression models. Conversely, increasing the slip rate over 0.12 mm/a or the recurrence period over 15 ka would result in less realistic coseismic slip values. In summary, the following palaeoseismic parameters are adopted as the most probable and realistic for the Calamocha fault: $M_w = 6.3–6.9$; coseismic slip = 0.5–1.3 m; recurrence period ≤ 15 ka; slip rate ≈ 0.1 mm/a.

An active fault able to produce earthquakes of M_w 6.3–6.9 with recurrence period under 15 ka certainly represents a seismic source that should be considered in seismic hazard assessment of the region. Unfortunately, the incompleteness of the palaeoseismic data and, in particular, the lack of knowledge about the elapsed time, precludes the possibility of achieving a probabilistic assessment at this moment.

Finally, a scenario of rupture propagation along both the Calamocha and Daroca faults should not be ruled out. They are separated by a right relay zone 1.8 km wide (Figs. 1c, 3), which might not represent a barrier to propagation given their parallelism and favourable orientation with respect to the regional stress field. According to Biasi and Wesnousky (2016), 54% of relay zones ≥ 1 km wide, in dip-slip faults longer than 10 km, are overcome during fault propagation; moreover, such relay zones are less effective at stopping normal than reverse ruptures. If we consider the Calamocha-Daroca fault zone as a single structure 42 km long (27 km + 18 km − 3 km overlap), its complete rupture could generate earthquakes of magnitude 6.9 ± 0.3, according to the regression model by Wesnousky (2008).

Conclusions

The Calamocha fault is a NNW–SSE striking, 70–75º E dipping, 18-km-long, nearly pure normal fault with an average transport direction (azimuth of the slip vector on the hanging-wall block) towards WSW. It was the result of the inversion of a previous compressional structure, in full coherence with the recent, WSW–ENE trending σ_3 trajectories of the tensional stress field active since the Late Pliocene.

The maximum throw, recorded by a Late Pliocene planation surface (FES2, 3.8 Ma), is in the range of 180–210 m. This involves a maximum net slip of 190–230 m and slip rate of 0.05–0.06 mm/a since that age.

The Calamocha fault has undergone recurrent slip during the Late Pleistocene. On branch A, two artificial exposures have evidenced: (i) a probable slip event (V in ZSR site), with coseismic throw exceeding 0.5 m, dated to ca. 140 ka; (ii) two well-constrained slip events (W and Z), with coseismic throws of 0.45 and 0.5 m, dated to ca. 125 ka and ca. 70 ka, respectively; (iii) two other intercalated deformation events, dated to ca. 105 and 80 ka (*X* and *Y*), not explicitly linked to slip on the main fault; (iv) undifferentiated slip episodes that totalize net slip of 3.9–4.8 m (PA site) during/after the time lapse between 95.4 ± 6.3 and 69.9 ± 5.5 ka, one of them hypothetically correlated with event Z. Branch B has undergone (A23H site): (i) at least two slip episodes on the main rupture surface, totalizing a minimum throw of 2.2 m, older and younger, respectively, than 13.8 ± 0.9 ka; (ii) undetermined events indirectly revealed by activation of antithetic faults prior to 53.1 ± 3.7, 41.9 ± 2.9 and 35.3 ± 2.3 ka, and after 35.3 ± 2.3 ka and 13.8 ± 0.9 ka. The lack of Quaternary deposits affected by fault branch C prevents from knowing its recent activity.

The short-term slip rate has been roughly calculated to 0.1–0.3 mm/a for a narrow time window within the Late Pleistocene, although it should be estimated in the lowest range (ca. 0.1 mm/a) in order to fit realistic palaeoseismic parameters. In any case, it would be higher than the long-term rate, thus following the same tendency previously observed in most faults at the central Iberian Chain.

The seismogenic ability of the Calamocha fault is characterized by the following parameters: (i) potential moment magnitude Mw ≈ 6.3–6.7 (Mw ≈ 6.6–7.2 in a scenario of activation of the whole Calamocha-Daroca fault zone); (ii) average coseismic slip estimated in the range of 0.5–1.3 m; (iii) average recurrence period under 15 ka.

Acknowledgements The research has been financed by projects LMP127_18 (Gobierno de Aragón-Programa Operativo del Fondo Europeo de Desarrollo Regional Aragón 2014–2020), and PID2019-108705-GB-I00 of the Agencia Estatal de Investigación (AEI/10.13039/501100011033) of the Spanish Government. This work is a contribution of the Geotransfer Research Group (E32_20R) funded by Gobierno de Aragón. A. Peiro benefits from a FPU contract

(FPU17/02470) of the Spanish Government. We thank P. Beneítez for the OSL dating at the Laboratorio de Datación y Radioquímica of the Universidad Autónoma de Madrid, as well as J. Brizuela for the drone photographs, and A. Whitehead for the English revision of the manuscript.

Funding Open Access funding provided thanks to the CRUE-CSIC agreement with Springer Nature.

Open Access This article is licensed under a Creative Commons Attribution 4.0 International License, which permits use, sharing, adaptation, distribution and reproduction in any medium or format, as long as you give appropriate credit to the original author(s) and the source, provide a link to the Creative Commons licence, and indicate if changes were made. The images or other third party material in this article are included in the article's Creative Commons licence, unless indicated otherwise in a credit line to the material. If material is not included in the article's Creative Commons licence and your intended use is not permitted by statutory regulation or exceeds the permitted use, you will need to obtain permission directly from the copyright holder. To view a copy of this licence, visit http://creativecommons.org/licenses/by/4.0/.

References

Adrover R (1986) Nuevas faunas de roedores en el Mio-Plioceno continental de la región de Teruel (España). Interés bioestratigráfico y paleoecológico. Instituto de Estudios Turolenses, Teruel

Allen CR (1986) Seismological and paleoseismological techniques of research in active tectonics. In: Wallace RE (ed) Active tectonics studies in geophysics. National Academy Press, Washington, pp 148–154

Álvaro M, Capote R, Vegas R (1979) Un modelo de evolución geotectónica para la Cadena Celtibérica. Acta Geol Hisp 14:172–177

Anadón P, Moissenet E (1996) Neogene basins in the Eastern Iberian Range. In: Friend PF, Dabrio CF (eds) Tertiary basins of Spain. The stratigraphic Record of Crustal kinematics. World and Regional Geology series 6. Cambridge University Press, Cambridge, pp 68–76

Anadón P, Alcalá L, Alonso-Zarza AM, Calvo JP, Ortí F, Rosell L, Sanz-Rubio E (2004) Cuencas de la Cordillera Ibérica. In: Vera JA (ed) Geología de España. Sociedad Geológica de España-Instituto Geológico y Minero, Madrid, pp 562–569

Arlegui LE, Simón JL, Lisle RJ, Orife T (2005) Late Pliocene-Pleistocene stress field in the Teruel and Jiloca grabens (eastern Spain): contribution of a new method of stress inversion. J Struct Geol 27:693–705

Bell WT (1979) Attenuation factors for the absorbed radiation dose in quartz inclusions for thermoluminescence dating. Ancient TL 8:1–12

Biasi GP, Wesnousky SG (2016) Steps and gaps in ground ruptures: empirical bounds on rupture propagation. Bull Seismol Soc Am 106(3):1110–1124

Calvín-Ballester P, Casas A (2014) folded variscan thrusts in the herrera unit of the iberian range (NE Spain). Geol Soc London Spec Publ 394:39–52

Capote R, Muñoz JA, Simón JL, Liesa CL, Arlegui LE (2002) Alpine tectonics I: the alpine system north of the Betic Cordillera. In: Gibbons W, Moreno T (eds) Geology of Spain. The Geological Society, London, pp 367–400

Casas A, Marcén M, Calvín P, Gil A, Román-Berdiel T, Pocoví A (2016) Deformación varisca, tardivarisca y alpina en la Rama Aragonesa de la Cordillera Ibérica: propuesta para diferenciación y denominación de estructuras. Geo-Temas 16(2):495–498

Casas AM, Gil A, Simón JL, Izquierdo E, Aldega L, Román T, Osácar C, Pueyo O, Ansón M, García C, Corrado S, Invernizzi C, Caricchi C (2018) Strain indicators and magnetic fabric in intraplate fault zones: case study of daroca thrust, Iberian Chain, Spain. Tectonophysics 730:29–47

Choi JH, Ko K, Gihm YS, Cho CS, Lee H, Song SG, Bang ES, Lee HJ, Bae HK, Kim SW, Choi SJ, Lee SS, Lee SR (2019) Surface deformations and rupture processes associated with the 2017 M w 5.4 Pohang, Korea, earthquake. Bull Seismol Soc Am 109(2):756–769

Colomer M, Santanach P (1988) Estructura y evolución del borde suroccidental de la Fosa de Calatayud-Daroca. Geogaceta 4:29–31

Corral MB (2014) Estructura y relaciones tectónica-sedimentación en el contacto del Paleozoico de Villafeliche-Calamocha y la cuenca neógena de Calatayud. Universidad de Zaragoza, Trabajo Fin de Grado

Cortés-Gracia A, Casas-Sainz AM (1996) Deformación alpina de zócalo y cobertera en el borde norte de la Cordillera Ibérica (Cubeta de Azuara-Sierra de Herrera). Rev Soc Geol España 9(1–2):51–66

Durcan JA, King GE, Duller GAT (2015) DRAC: Dose rate and age calculator for trapped charge dating. Quat Geochron 28:54–61

Ezquerro L (2017) El sector norte de la cuenca neógena de Teruel: tectónica, clima y sedimentación. PhD Thesis, Universidad de Zaragoza http://zaguan.unizar.es/record/77098#

Ezquerro L, Lafuente P, Pesquero MD, Alcalá L, Arlegui LE, Liesa CL, Luque L, Rodríguez-Pascua MA, Simón JL (2012) Una cubeta endorreica residual del Pleistoceno inferior en la zona de relevo entre las fallas neógenas de Concud y Teruel, Cordillera Ibérica: implicaciones paleogeográficas. Rev Soc Geol España 25:157–175

Ezquerro L, Moretti M, Liesa CL, Luzón A, Simón JL (2015) Seismites from a well core of palustrine deposits as a tool for reconstructing the palaeoseismic record of a fault. Tectonophysics 655:191–205

Ezquerro L, Moretti M, Liesa CL, Luzón A, Pueyo E, Simón JL (2016) Controls on space-time distribution of soft-sediment deformation structures: applying palaeomagnetic dating to approach the apparent recurrence period of paleoseisms at the Concud fault (eastern Spain). Sed Geol 344:91–111

Ezquerro L, Simón JL, Luzón A, Liesa CL (2020) Segmentation and increasing activity in the Neogene–Quaternary Teruel Basin rift (Spain) revealed by morphotectonic approach. J Struct Geol 135:104043. https://doi.org/10.1016/j.jsg-2020.104403

Gabaldón V, Lendínez A, Ferreiro E, Ruiz V, López de Alda F, Valverde M, Lago San José M, Meléndez A, Pardo G, Ardevol L, Villena J, González A, Hernández A, Álvaro M, Leal M C, Aguilar Tomás M, Gómez JJ, Carls P. (1991) Mapa Geológico de España 1: 200.000, hoja nº 40 (Daroca). IGME, Madrid

Galbraith RF, Roberts RG, Laslett GM, Yoshida H, Olley JM (1999) Optical dating of single and multiple grains of quartz from Jinmium rock shelter, Northern Australia: part 1, experimental design and statistical models. Archaeometry 41:339–364

García-Lacosta AI, Pueyo Ó, Arlegui LE, Liesa CL, Ezquerro L, Simón JL. (2014) La zona de falla reciente de Sierra Palomera (fosa del Jiloca, Cordillera Ibérica): contribución de la geofísica a la caracterización estructural. 2ª Reunión Ibérica sobre Fallas Activas y Paleosismología-Iberfault (Lorca, Murcia), IGME, pp 51–54

Gracia FJ (1992) Tectónica pliocena de la Fosa de Daroca (prov. de Zaragoza). Geogaceta 11:127–129

Gracia FJ, Gutiérrez F, Gutiérrez M (2002) Origin and evolution of the Gallocanta polje (Iberian Range, NE Spain). Z Geomorphol 46:245–262

Guerin G, Mercier N, Nathan R, Adamiec G, Lefrais Y (2012) On the use of the infinite matrix assumption and associated concepts: a critical review. Radiat Meas 47:778–785

Gutiérrez M, Gracia FJ (1997) Environmental interpretation and evolution of the Tertiary erosion surfaces in the Iberian Range (Spain). Geol Soc, London, Special Publ 120(1):147–158
Gutiérrez F, Gutiérrez M, Gracia FJ, McCalpin JP, Lucha P, Guerrero J (2008) Plio-Quaternary extensional seismotectonics and drainage network development in the central sector of the Iberian Chain (NE Spain). Geomorphology 102(1):21–42
Gutiérrez F, Masana E, González A, Guerrero J, Lucha P, McCalpin JP (2009) Late quaternary paleoseismic evidence on the Munébrega Half-graben fault (Iberian Range, Spain). Int J Earth Sci 98:1691–1703. https://doi.org/10.1007/s00531-008-0319-y
Gutiérrez F, Lucha P, Jordá L (2013) The Río Grío depression (Iberian Chain, NE Spain). Neotectonic graben vs. Fluvial Valley. Cuaternario y Geomorfología 27:5–32
Gutiérrez F, Carbonel D, Sevil J, Moreno D, Linares R, Comas X, Zarroca M, Roqué C, McCalpin JP (2020a) Neotectonics and late holocene paleoseismic evidence in the Plio-Quaternary Daroca half-graben, Iberian Chain, NE Spain Implications for fault source characterization. J Struct Geol 131:103933
Gutiérrez F, Moreno D, López GI, Jiménez F, del Val M, Alonso MJ, Martínez-Pillado V, Guzmán O, Martínez D, Carbonel D (2020b) Revisiting the slip rate of Quaternary faults in the Iberian Chain, NE Spain. Geomorphic Seismic-Hazard Implic Geomorphol 363:107233
Hanks TC, Kanamori H (1979) A moment magnitude scale. J Geophys Res 84:2348–2350
Hernández A, Olivé A, Moissenet E, Pardo G, Villena J, Portero JM, Gutiérrez M, Puigdefábregas C, Giner J, Aguilar MJ, Leal MC, Gutiérrez JC, Gil MD, Adrover R, Gabaldón V. (1983) Mapa Geológico de España 1: 50.000, Hoja nº 491 (Calamocha). IGME, Madrid
Herraiz M, De Vicente G, Lindo-Ñaupari R, Giner J, Simón JL, González-Casado JM, Vadillo O, Rodríguez-Pascua MA, Cicuéndez JL, Casas A, Cabañas L, Rincón P, Cortés AL, Ramírez M, Lucini M (2000) The recent (upper Miocene to Quaternary) and present tectonic stress distributions in the Iberian Peninsula. Tectonics 19:762–786
IGN (2022) Servicio de Información Sísmica del Instituto Geográfico Nacional. https://www.ign.es/web/ign/portal/sis-catalogo-terremotos
Julivert M. (1954) Observaciones sobre la tectónica de la Depresión de Calatayud. Arrahona, Museo de Sabadell, pp 3–18
Lafuente P, Arlegui LE, Liesa CL, Simón JL (2011) Paleoseismological analysis of an intraplate extensional structure: the Concud fault (Iberian Chain, Eastern Spain). Int J Earth Sci 100:1713–1732
Lafuente P, Arlegui LE, Liesa CL, Pueyo O, Simón JL (2014) Spatial and temporal variation of paleoseismic activity at an intraplate, historically quiescent structure: the Concud fault (Iberian Chain, Spain). Tectonophysics 632:167–187
Lavecchia G, de Nardis R, Cirillo D, Brozzetti F, Boncio P (2012) The May-June 2012 Ferrara Arc earthquakes (northern Italy): structural control of the spatial evolution of the seismic sequence and of the surface pattern of coseismic fractures. Ann Geophys. https://doi.org/10.4401/ag-6173
Leonard M (2010) Earthquake fault scaling: self-consistent relating of rupture length, width, average displacement, and moment release. Bull Seismol Soc Am 100(5A):1971–1988
Liesa CL, Simón JL (2009) Evolution of intraplate stress fields under multiple compressions: The case of the Iberian Chain (NE Spain). Tectonophysics 474:144–159
Liesa CL, Simón JL, Casas AM (2018) La tectónica de inversión en una región intraplaca: La Cordillera Ibérica. Rev Soc Geol España 31:23–50
Liesa CL, Simón JL, Ezquerro L, Arlegui LE, Luzón A (2019) Stress evolution and structural inheritance controlling an intracontinental extensional basin: the central-northern sector of the Neogene Teruel Basin. J Struct Geol 118:362–376
Liesa CL, Corral MB, Arlegui LA, Peiro A, Simón JL. (2021) Inversión tectónica negativa y estructuración de la zona de relevo entre las fallas normales plio-cuaternarias de Calamocha y Daroca. X Congreso de Geología de España, Sociedad Geológica de España, Vitoria, Spain
Liu L, Zoback MD (1997) Lithospheric strength and intraplate seismicity in the New Madrid seismic zone. Tectonics 16(4):585–595
Maillard A, Mauffret A (1999) Crustal structure and riftogenesis of the Valencia Trough (north-western Mediterranean Sea). Basin Res 11(4):357
McCalpin J (2009) Paleoseismology, 2nd edn. Academic Press
Machette MN (2000) Active, capable, and potentially active faults—a paleoseismic perspective. J Geodyn 29:387–392
Martín-Bello L, Arlegui LE, Ezquerro L, Liesa CL, Simón JL. (2014) La falla de Calamocha (fosa del Jiloca, Cordillera Ibérica): estructura y actividad pleistocena. 2ª Reunión Ibérica sobre Fallas Activas y Paleosismología-Iberfault (Lorca, Murcia), IGME, pp 55–85
Moissenet E (1980) Relief et déformations récentes: trois transversales dans les fossés internes des chaînes Ibériques orientales. Revue De Géographie Des Pyrenées Et Sud-Ouest 51:315–344
NRC (1997) Regulatory Guide 1.165, Identification and Characterization of Seismic Sources and Determination of Safe Shutdown Earthquake Ground Motions US. Nuclear Regulatory Commission, Office of Nuclear Regulatory Research, Washington
Peiro A, Simón JL (2021a) Caracterización preliminar de la zona de falla de Río Grío-Pancrudo: estructura extensional de primer orden en la evolución reciente de la Cordillera Ibérica. Geo-Temas 18:846–849
Peiro A, Simón JL (2021b) The Río Grío-Pancrudo Fault Zone (central Iberian Chain, Spain): recent extensional activity revealed by drainage reversal. Geol Mag 159:21–36. https://doi.org/10.1017/S0016756821000790
Peiro A, Simón JL, Román-Berdiel T (2020) Fault relay zones evolving through distributed longitudinal fractures: the case of the Teruel graben system (Iberian Chain, Spain). J Struct Geol 131:103942. https://doi.org/10.1016/j.jsg.2019.103942
Peiro A, Simón JL, Arlegui LE, Ezquerro L, García-Lacosta AI, Lamelas MT, Liesa CL, Luzón A, Martín-Bello L, Pueyo-Anchuela Ó, Russo N (2022) Hanging-wall deformation at the active Sierra Palomera extensional fault (Jiloca basin, Spain) from structural, morphotectonic, geophysical and trench study. Tectonophysics 828:229274
Peña JL, Gutiérrez M, Ibáñez M, Lozano MV, Rodríguez J, Sánchez M, Simón JL, Soriano MA, Yetano LM. (1984) Geomorfología de la provincia de Teruel. Instituto de Estudios Turolenses, Teruel
Philip H, Meghraoui M (1983) Structural analysis and interpretation of the surface deformations of the El Asnam earthquake of October 10, 1980. Tectonics 2(1):17–49
Prescott JR, Hutton JT (1994) Cosmic ray contributions to dose rates for luminescence and ESR: large depths and long-term time variations. Radiat Meas 23:497–500
Roca E, Guimerà J (1992) The Neogene structure of the eastern Iberian margin: structural constraints on the crustal evolution of the Valencia trough (western Mediterranean). Tectonophysics 203:203–218
Rubio JC. (2004) Los humedales del Alto Jiloca: estudio hidrogeológico e histórico-arqueológico. Consejo de Protección de la Naturaleza de Aragón, Zaragoza
Rubio JC, Simón JL (2007) Tectonic subsidence vs. erosional lowering in a controversial intramontane depression: the Jiloca basin (Iberian Chain, Spain). Geol Mag 144:1–15

Rubio JC, Simón JL, Soriano A (2007) Interacting tectonics, hydrogeology and karst processes in an intramontane basin: the Jiloca graben (NE Spain). Hydrogeol J 15:1565–1576

Sanz-Rubio E (1999) Análisis de los sistemas deposicionales carbonáticos y evaporíticos del Neógeno de la Cuenca de Calatayud (provincia de Zaragoza). PhD Thesis, Universidad Complutense de Madrid

Sanz-Rubio E, Sánchez-Moral S, Cañaveras JC, Abdul-Aziz H, Calvo JP, Cuezva S, Mazo AV, Rouchy JM, Sesé C, Van Darn J (2003) Síntesis de la cronoestratigrafía y evolución sedimentaria de los sistemas lacustres evaporíticos y carbonatados neógenos de la cuenca de Calatayud–Montalbán. Estud Geol 59:83–105

Schwartz DP, Coppersmith KJ (1984) Fault behavior and characteristic earthquakes: examples from Wasatch and San Andreas fault zones. J Geophys Res 89:5681–5698

Simón JL (1982) Compresión y distensión alpinas en la Cadena Ibérica Oriental. PhD Thesis, Universidad de Zaragoza (publ. Instituto de Estudios Turolenses, Teruel, 1984)

Simón JL (1983) Tectónica y neotectónica del sistema de fosas de Teruel. Teruel 69:21–97

Simón JL (1989) Late Cenozoic stress field and fracturing in the Iberian Chain and Ebro Basin (Spain). J Struct Geol 11:285–294

Simón JL, Arlegui L, Lafuente P, Liesa CL (2012) Active extensional faults in the central–eastern Iberian Chain, Spain. J Iber Geol 38:127–144

Simón JL, Arlegui LE, Ezquerro L, Lafuente P, Liesa CL, Luzón A (2016) Enhaced paleoseismic succession at the Concud Fault (Iberian Chain, Spain): new insights for seismic hazard assessment. Na Hazards 80(3):1967–1993

Simón JL, Arlegui LE, Ezquerro L, Lafuente P, Liesa CL, Luzón A (2017) Assessing interaction of active extensional faults from structural and paleoseismological analysis: the Teruel and Concud faults (eastern Spain). J Struct Geol 103:100–119

Simón JL, Ezquerro L, Arlegui LE, Liesa CL, Luzón A, Medialdea A, García A, Zarazaga D (2019) Role of transverse structures in paleoseismicity and drainage rearrangement in rift systems: the case of the Valdecebro fault zone (Teruel graben, eastern Spain). Int J Earth Sci 108:1429–1449. https://doi.org/10.1007/s00531-019-01707-9

Simón JL, Casas-Sainz AM, Gil-Imaz A (2021) Controversial epiglyptic thrust sheets: the case of the daroca thrust (Iberian Chain, Spain). J Struct Geol 145:104298

Simón-Porcar G, Liesa CL, Simón JL (2019) La cuenca neógena extensional de El Pobo (Teruel, Cordillera Ibérica): sedimentología, estructura y relación con la evolución del relieve. Revista De La Sociedad Geológica De España 32:17–42

Sinusía C, Pueyo EL, Azanza B, Pocoví A (2004) Datación magnetoestratigráfica del yacimiento paleontológico de la Puebla de Valverde (Teruel). Geo-Temas 6(4):339–342

Stirling M, Rhoades D, Berryman K (2002) Comparison of earthquake scaling relations derived from data of the instrumental and preinstrumental era. Bull Seismol Soc Am 92(2):812–830

Stirling M, Goded T, Berryman K, Litchfield N (2013) Selection of earthquake scaling relationships for seismic-hazard analysis. Bull Seismol Soc Am 103(6):2993–3011

Strom A. (2017) Active faults at structure's foundations: Definition and its influence on hazard assessment. Proceedings 16th World Conference on Earthquake Engineering, Santiago de Chile

Vegas R, Fontboté JM, Banda E (1979) Widespread Neogene rifting superimposed on alpine regions of the Iberian Peninsula. Proceedings Symposium Evolution and Tectonics of the Western Mediterranean and Surrounding Areas, EGS, Viena, Instituto Geográfico Nacional, Madrid, Special Publ 201:109–128

Wells DL, Coppersmith KJ (1994) New empirical relationships among magnitude, rupture length, rupture width, rupture area, and surface displacement. Bull Seismol Soc Am 84:974–1002

Wesnousky SG (2008) Displacement and geometrical characteristics of earthquake surface ruptures: Issues and implications for seismic-hazard analysis and the process of earthquake rupture. Bull Seismol Soc Am 98(4):1609–1632

Wintle AG (1997) Luminescence dating: laboratory procedures and protocols. Radiat Meas 27:769–817

Yeats RS, Sieh K, Allen CR (1997) The geology of earthquakes. Oxford University Press, New York


IV

CAPÍTULO IV.

FALLA DE SIERRA PALOMERA

Resumen:

En la sección IV se estudia la falla de Sierra Palomera, que conforma el margen este de la fosa del Jiloca en su sector central, en la publicación en la que la abordamos desde el punto de vista geofísico, morfotectónico, estructural y paleosismológico. De nuevo, las superficies de erosión regionales evidencian un salto vertical importante de la misma, que permite inferir su tasa de desplazamiento para el Plio-Cuaternario. Mediante análisis estructural y geofísica se terminan de caracterizar algunas de sus ramas en el bloque hundido. La trinchera de La Sima corta una de estas fallas antitéticas a la principal, la cual muestra evidencias de actividad durante el Pleistoceno medio-superior. Se infiere un modelo de evolución de la deformación en el bloque superior de la misma pero, dada la escasez de dataciones apropiadas, no se puede establecer una secuencia paleosismológica representativa. Sin embargo, sí que permite arrojar luz sobre la cronología de los patrones de fracturación y su control cinemático y dinámico. Todos los valores inferidos para la falla de Sierra Palomera también se pueden consultar sintetizados en la tabla de la sección VI.

PUBLICACIÓN:

Deformación en el bloque hundido de la falla activa extensional de Sierra Palomera (Fosa del Jiloca, España) desde su estudio estructural, morfotectónico, geofísico y de trinchera / *Hanging-wall deformation at the active Sierra Palomera extensional fault (Jiloca basin, Spain) from structural, morphotectonic, geophysical and trench study.*

Peiro, A., Simón, J.L., Arlegui, L.E., Ezquerro, L., García-Lacosta, A.I., Lamelas, T., Liesa, C.L., Luzón, A., Martín-Bello, L., Pueyo-Anchuela, O., Russo, N. (2022). *Tectonophysics* 828, 229274. doi: 10.1016/j.tecto.2022.229274

★ Equivalencia de Figuras: en la publicación hay Fig. 1-Fig. 15, y corresponden a las Fig. 4.1-Fig. 4.15 de esta tesis.

Tectonophysics 828 (2022) 229274

Contents lists available at ScienceDirect

Tectonophysics

journal homepage: www.elsevier.com/locate/tecto

Hanging-wall deformation at the active Sierra Palomera extensional fault (Jiloca basin, Spain) from structural, morphotectonic, geophysical and trench study

A. Peiro [a,*], J.L. Simón [a], L.E. Arlegui [a], L. Ezquerro [b], A.I. García-Lacosta [a], M.T. Lamelas [c], C. L. Liesa [a], A. Luzón [a], L. Martín-Bello [a], Ó. Pueyo-Anchuela [a], N. Russo [a]

[a] Departamento de Ciencias de la Tierra and GEOTRANSFER Research Group-IUCA, Universidad de Zaragoza, Pedro Cerbuna, 12, 50009 Zaragoza, Spain
[b] GEOBIOTEC, Department of Earth Sciences, NOVA School of Science and Technology, Campus de Caparica, P-2829 516 Caparica, Portugal
[c] Centro Universitario de la Defensa, Academia General Militar, and GEOFOREST Research Group-IUCA, Ctra. de Huesca s/n, 50090 Zaragoza, Spain

ARTICLE INFO

Keywords:
Active fault
Antithetic fault
Rollover
Magnetometry
Pleistocene
Iberian Chain

ABSTRACT

The NNW-SSE trending Sierra Palomera fault is characterized as an active, nearly pure extensional fault with mean transport direction towards N230°E, consistent with the ENE-WSW extension trajectories of the recent to present-day regional stress field. Its macrostructure is described from surface geology and magnetometric and electromagnetic surveys, which have allowed identifying two subsidiary, nearly parallel normal faults (antithetic and synthetic, respectively). The structural contour map of an extensive planation surface, dated to 3.8 Ma, provides a maximum fault throw *s.s.* of 330 m for the main fault (480 m including bending), and a net slip rate of 0.09–0.10 mm/a (0.13–0.15 mm/a including bending). Trench study focussed on the subsidiary antithetic fault shows evidence of its activity during Middle-Late Pleistocene times, offsetting ca. 2.5 m the slope of a well-preserved alluvial fan. Detailed analysis and retrodeformation of the antithetic fault and other minor ruptures in the trench has allowed defining seven deformation events. The lack of a consistent age model for the involved sedimentary sequence makes them almost meaningless in terms of paleoseismic history. However, geometry and sequential development of meso-scale faults (intermediate between seismic-scale and analogue models) allows unravelling the extensional deformation history within the hanging-wall block of the Sierra Palomera fault. Progressive rupture patterns reveal shifting from dominantly synthetic to dominantly antithetic faulting, suggesting both kinematical control linked to rollover growth, and dynamical control by the regional stress field.

1. Introduction

Our understanding of geometry and kinematics of extensional fault systems has been significantly improved thanks to analytical and scaled analogue models, particularly concerning deformation of the hanging-wall block of listric faults. Such models provide interesting inferences about controls that the shape of the main fault surface exerts on the development of hanging-wall folds and fractures. Fault surfaces with irregular geometry induce antithetic simple shear along a deformation band that nucleates at shallowing fault bends, while synthetic shear is induced at steepening fault bends (McClay and Scott, 1991; Xiao and Suppe, 1992; Withjack et al., 1995; Delogkos et al., 2020). Depending on the mechanical behaviour of materials, such overall simple shear mechanism results in either fault-related folding (rollover and drag folds, respectively) or faulting (antithetic and synthetic, respectively). Analogue models provide insights into both differential behaviours, e.g., by comparing experimental materials as clay and sand (e.g., Withjack et al., 1995). Nevertheless, as discussed by Xiao and Suppe (1992), models give limited information about the actual small-scale mechanisms that accommodate deformation. Therefore, contribution of data directly supplied by field examples is necessary for full understanding of kinematics of extensional systems.

The Sierra Palomera fault, at the central sector of the Jiloca basin, is one of the most conspicuous recent, hypothetically active extensional faults in the central Iberian Chain (Spain; Fig. 1), but less known than other neighbouring structures. The Calamocha and Concud faults, which

* Corresponding author.
E-mail addresses: apeiro@unizar.es (A. Peiro), jsimon@unizar.es (J.L. Simón), arlegui@unizar.es (L.E. Arlegui), tlamelas@unizar.es (M.T. Lamelas), carluis@unizar.es (C.L. Liesa), aluzon@unizar.es (A. Luzón), opueyo@unizar.es (Ó. Pueyo-Anchuela).

https://doi.org/10.1016/j.tecto.2022.229274
Received 24 September 2021; Received in revised form 12 February 2022; Accepted 17 February 2022
Available online 22 February 2022
0040-1951/© 2022 Elsevier B.V. All rights reserved.

bound the northern and southern sectors of the Jiloca basin (Fig. 1c), offset early Pliocene lacustrine deposits of the Calatayud and Teruel basins, respectively. This allows calculating their total throws at about 210 m for the Calamocha fault (Martín-Bello et al., 2014), and 260 m for the Concud fault (Ezquerro et al., 2020). On the contrary, no recent stratigraphic marker is available for the Sierra Palomera fault. The tectonic nature of the basin boundary itself, and particularly the relative role of erosive lowering and fault displacement in the creation of the mountain scarp, has been the object of controversy indeed. After Cortés and Casas (2000), its topography is essentially a result of erosive incision in response to orogenic uplift during the Paleogene. Gracia et al. (2003) reinterpret the Jiloca depression as a polje developed during the Late Pliocene-Quaternary. Rubio and Simón (2007) and Rubio et al. (2007) provide new sedimentary, geomorphological and hydrogeological evidence on the tectonic origin of the Jiloca depression, concluding that the Sierra Palomera fault has a maximum throw approaching 350–400 m.

Concerning the signs of Quaternary activity, these are again conspicuous in the northern and southern sectors of the Jiloca graben but not in the central one. The Concud fault has been object of intense paleoseismological research, which has allowed reconstructing a succession of eleven events since ca. 74 ka BP, with average recurrence period of 7.1–8.0 ka, total accumulated net slip of about 20 m, and average slip rate of 0.29 mm/a (Lafuente, 2011; Lafuente et al., 2011a, 2011b, 2014; Simón et al., 2016). Quaternary activity of the Calamocha fault is revealed by the mechanical contact between Neogene units of the Calatayud basin and Late Pleistocene alluvial deposits that infill the northernmost Jiloca basin (Martín-Bello et al., 2014). Other neighbouring faults (Munébrega, Teruel, Valdecebro) have also been object of trench studies in the last two decades (Gutiérrez et al., 2009; Simón et al., 2017, 2019). On the contrary, no exposure of the Sierra Palomera fault cutting Quaternary deposits has been reported, and no paleoseismological analysis has been carried out. This is mainly due to the fact that the Quaternary fluvial incision is virtually absent, and there is a lack of appropriate sites for digging trenches across the main fault.

In such a situation, the study of the Sierra Palomera fault should be focussed on obtaining indirect evidence of its recent activity from hanging-wall deformation. This can be achieved by (i) exploring the subsoil of the associated pediment by means of geophysical techniques, (ii) analysing the effects of fault activity on the relief through morphotectonic analysis, and (iii) recognizing deformation of Quaternary materials in trenches. Methodology of trench analysis, extensively used and standardized for paleoseismological studies (e.g., McCalpin, 1996), offers new insights for detailed analysis of progressive extensional deformation. Concerning scale, trenches have the advantage of delivering valuable information on faults at an intermediate scale between seismic profiles and laboratory analogue models. Concerning timing, each identified event can be considered as an incremental or 'infinitesimal' deformation episode, and hence the reconstructed paleoseismic succession provides a detailed and realistic view of extension kinematics (although ineludibly constrained to a given space and time window).

The present work has been carried out in that perspective. Our specific objectives are: (1) improving our overall knowledge on the

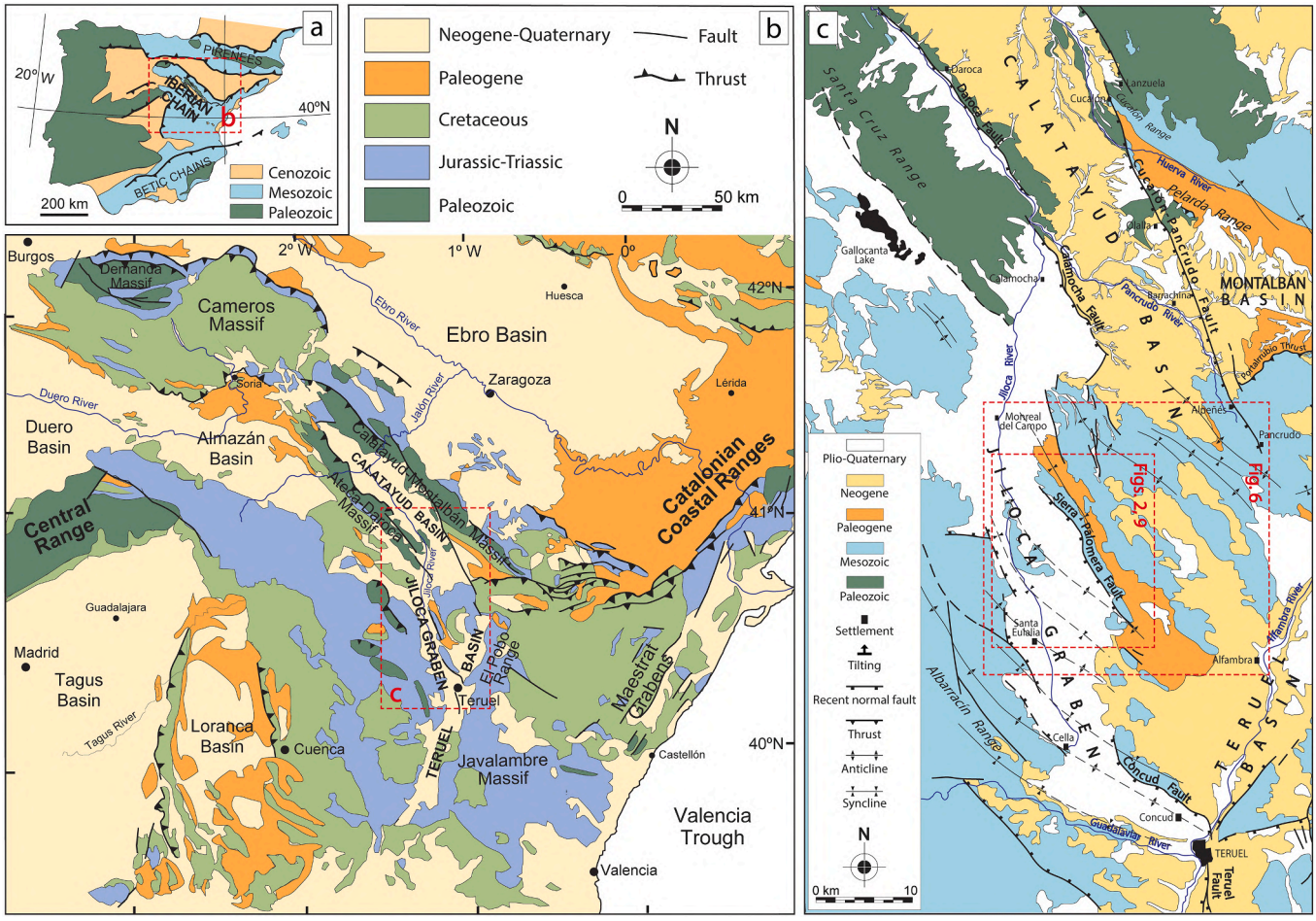

Fig. 1. (a) Location of the Iberian Chain within the Iberian Peninsula. (b) Geological sketch of the Iberian Chain, with location of the main Neogene-Quaternary extensional basins. (c) Simplified geological map of the Jiloca graben, with location of Figs. 2, 6 and 9.

structure and evolution of the Sierra Palomera fault and the Jiloca basin; (2) reporting evidence on the activity of the Sierra Palomera fault during the Quaternary, and (3) characterizing the patterns of progressive extensional deformation within its hanging-wall block.

2. Geological setting

The Iberian Chain is a NW-SE trending, 450 km long intraplate mountain range located in the eastern Iberian Peninsula (Fig. 1a). This chain developed in Paleogene to Early Miocene times due to positive inversion of the extensional Mesozoic Iberian basin, under the convergence between the Africa and Eurasia plates (Álvaro et al., 1979; Guimerà and Alvaro, 1990; Capote et al., 2002; Liesa et al., 2018). After a transition period during the Early Miocene, in which the longitudinal Calatayud basin developed under a transpressional regime (Colomer and Santanach, 1988; Simón et al., 2021), a new extensional stage associated to rifting of the Valencia Trough took place.

Extensional deformation propagated onshore towards the central part of the Iberian Chain (Álvaro et al., 1979; Vegas et al., 1979) in two stages, inducing both reactivation of the main inherited Mesozoic faults and formation of new normal faults, and generating a number of diversely oriented intracontinental grabens and half-grabens (Simón, 1982, 1989; Gutiérrez et al., 2008, 2012; Ezquerro, 2017; Liesa et al., 2019). During the first stage (Late Miocene to Early Pliocene in age), the 90-km-long, NNE-SSW to N-S trending Teruel half-graben basin developed, filled with terrestrial sediments up to 500 m thick (Simón, 1982, 1983; Moissenet, 1983; Anadón and Moissenet, 1996; Ezquerro, 2017; Ezquerro et al., 2019, 2020). The second extensional stage that started by the mid-Pliocene has produced a more widespread deformation in the central Iberian Chain. A large number of inherited structures were reactivated, producing new NNW-SSE trending grabens and half-grabens that are inset or cross-cut the pre-existent Teruel and Calatayud basins (Simón, 1983, 1989; Gutiérrez et al., 2008, 2020; Liesa et al., 2019). They include, among others (Fig. 1c), the 80-km-long Jiloca graben, which results from en-échelon, right releasing arrangement of the NW-SE striking Concud, Sierra Palomera and Calamocha faults (Simón, 1983; Rubio and Simón, 2007; Simón et al., 2012, 2017; Peiro et al., 2019, 2020). In the first extensional phase, the direction of maximum extension (σ_3) was *E*-W to ESE-WNW (under a triaxial extensional regime), while 'multidirectional' extension with ENE-WSW σ_3 trajectories characterizes the second phase (Simón, 1982, 1983, 1989; Cortés, 1999; Capote et al., 2002; Arlegui et al., 2005, 2006; Liesa, 2011; Ezquerro, 2017; Liesa et al., 2019).

Geometric construction of normal fault profiles of the Teruel half-graben system allows locating the sole detachment at a depth of 14–17 km b.s.l., and estimating an average E-W stretching factor $\beta = 1.1$ since its onset (11.2 Ma ago) (Ezquerro et al., 2020). Major faults accumulated slip of a few hundred metres to ca. 1 km (computing both fault throw *s.s.* and associated bending). The resulting slip rate, around 0.09 mm/a in average, is very similar for distinct transects across the structure, but shows a clear increase between both extensional phases: from 0.05–0.07 mm/a to 0.12–0.16 mm/a (Ezquerro et al., 2020). Such slip rate increase has been attributed to: (i) onshore, westwards propagation of extensional deformation from the inner parts of the Valencia Trough, enhanced by crustal doming that would have affected the eastern Iberian Chain; (ii) onset of the multidirectional extension stress field driven by crustal doming mechanism; (iii) progressive fault linkage since the beginning of the Late Miocene (Ezquerro et al., 2020).

Mountains surrounding the Teruel and Jiloca basins show extensive erosion surfaces modelling Mesozoic-Palaeogene rocks and bevelling compressional structures. Two large planation surfaces, whose remnants appear at different heights either on the upthrown blocks or in the basin floors, have been traditionally defined (Gutiérrez and Peña, 1976; Peña et al., 1984; Sánchez-Fabre et al., 2019): (i) *Intra-Miocene Erosion Surface* (*IES*, middle Miocene), generally recognized in the upper part of the main reliefs, and (ii) *Fundamental Erosion Surface* (*FES*, middle Pliocene), easily recognizable as a vast planation level at lower heights. They approximately correspond to the *Iberian Chain Surface* and the *Lower Pliocene Surface* by Pailhé (1984), and the S1 and S2 by Gutiérrez and Gracia (1997), respectively. Recent detailed studies (Simón-Porcar et al., 2019; Ezquerro et al., 2020) have demonstrated that the *FES* splits into three different surfaces: an Upper Sublevel, the *FES s.s.* (the most widely developed), and a Lower Sublevel. In this work, these surfaces will be called as *FES1*, *FES2* and *FES3*, respectively. Planation surfaces have been physically correlated with different coeval sedimentary horizons (lacustrine-palustrine carbonates) within the sedimentary infill of the Teruel basin (Ezquerro, 2017), whose ages are well-constrained on the basis of mammal sites and magnetostratigraphy. In this way, the *Intra-Miocene Erosion Surface* has been dated close to the Aragonian-Vallesian limit (~11.2 Ma; Alcalá et al., 2000; Ezquerro, 2017), *FES1* and *FES2* to the Late Ruscinian (both merging around ~3.8 Ma), and *FES3* to the Early Villafranchian (~3,5 Ma) (Ezquerro et al., 2020).

Qualitative and quantitative geomorphological features of the mountain fronts and the associated piedmonts of the eastern margin of the Jiloca graben are those typical of active normal faults. At the Concud fault, Lafuente et al. (2011b) described conspicuous triangular facets and short, non-incised alluvial fans, and provided a significantly low value of the mountain-front sinuosity index defined by Bull and McFadden (1977) ($S_{mf} = 1.24$). At the Sierra Palomera fault, García-Lacosta (2013) described trapezoidal facets and V-shaped gullies, and provided a similar value for the sinuosity index ($S_{mf} = 1.27$). The fault scarps are connected with the depression bottom by gentle pediments mostly draining towards the Jiloca river, although endorheic conditions have locally remained until historical times, with development of a palustrine area at the basin centre (ancient Cañizar lake; Rubio and Simón, 2007).

Historic and instrumental seismicity of the central-eastern Iberian Chain is low to moderate. In the Teruel region, the epicentres are concentrated at the Jiloca graben margins, the central-southern sector of the Teruel basin, and the Albarracín and Javalambre massifs. Apart from the Albarracín massif, epicentres can be reasonably associated to Neogene-Quaternary known faults. Measured magnitudes (Mb) usually range from 1.5 to 3.5, with maximum Mb = 4.4 in the Teruel Graben and Mb = 3.8 in the Albarracín massif (IGN, 2021).

3. Methodology

3.1. Structural and morphotectonic study

The structural study is based on recognizing and mapping the main structures on aerial photographs at 1: 18,000 and 1: 33,000 scale, and satellite imagery, complemented with field surveys involving outcrop-scale observations. Data of orientation of rupture surfaces and slickenlines have been collected in a number of sites within the Sierra Palomera fault damage zone, as well as within the trench described below. Stereoplots (equal-area, lower hemisphere) of those data sets have been elaborated using Stereonet 8 software (Allmendinger et al., 2012; Cardozo and Allmendinger, 2013).

To characterize the geometry of recent vertical deformation, the three erosional planation surfaces (*FES1, FES2* and *FES3*) described above were used as markers. This required mapping of erosion surfaces and morphotectonic analysis based on aerial photographs (scales 1: 18,000 and 1: 33,000) and orthorectified photographs (1: 5000), as well as on digital elevation models (DEM, pixel = 5 m) and the resulting

hillshade images. A structural contour map of *FES2* was elaborated by interpolating the altitude of their remnants, which permits measuring throw across the main fault and hence calculating slip rate. Changes of throw along the fault zone were calculated from 1-km-spaced transects orthogonal to the fault trace and analysed on a throw vs. distance (T-D) graph.

Once constrained the age of a planation surface (see Section 2), the main challenge to be addressed is ensuring its degree of flatness, being aware of the degree of error involved in height management. Continental planation surfaces can show gentle (short- to middle-wavelength) unevenness, or locally connect with residual, non-flattened reliefs through pediment slopes. Amplitude of the unevenness advises to use an adequate contour interval for *FES2* in order to represent its present-day geometry with the suitable precision. Both the local difference in height between *FES2* and *FES3* and the local unevenness within each one usually lies within the range of 10–40 m. Therefore, we assume that: (i) fault throws calculated from them implicitly include a maximum error bar of ±40 m, and (ii) a 50-m-spaced contour map can be considered as reasonable for assessing recent movements (as previously proposed by Ezquerro et al., 2020). Such level of uncertainty in the calculated fault throws results in errors for slip rates around 0.01 mm/a.

3.2. Subsoil exploration

Subsurface information was acquired by means of geophysical exploration. Two different techniques were utilised, which had rendered interesting results in other neighbouring sectors (e.g., Pueyo et al., 2016): magnetometry and electromagnetic (EM) multifrequency survey. A twofold approach was taken: first, a regional analysis by means of ten transects approximately orthogonal to the Sierra Palomera mountain front; second, a detailed analysis of a sector where the highest geophysical anomalies were identified and also where geomorphological evidences hinted at the presence of a previously unknown antithetic fault. For the magnetometry survey, a GSM-19 equipment with built-in GPS was used to measure both Earth magnetic field intensity and vertical magnetic gradient (sensors separation of 0.5 m). Diurnal correction was performed from a second, stationary, magnetometer (PMG-01) that permitted to exclude natural earth magnetic field changes during the survey and to compare the results performed during different days. Then, the regional general trend was identified and subtracted to earth magnetic data to highlight anomalies in the form of residual values. The EM multifrequency survey was performed by a GEM-02 device for a range of frequencies between 65 and 0.5 kHz.

Subsoil information has been complemented with borehole data extensively compiled by Rubio (2004), whose synthetic results were presented by Rubio and Simón (2007). Together with surface geology, it was used for constructing geological cross sections that have allowed characterizing the general geometry of macrostructure. Moreover, they were used for extending the contour map of FES2 to the centre of the Jiloca basin.

3.3. Trench analysis

A trench study focussed on the northwards prolongation of the La Peñuela fault, antithetic to the main Sierra Palomera fault, has been carried out following the classical methodology (see, e.g., McCalpin, 1996): excavating and shoring; cleansing and gridding the most suitable wall; identifying and marking sedimentary boundaries and deformation structures; drawing a detailed log and taking photographs of each grid cell; analysing the relationship between units and faults to identify individual events; and sampling materials for dating. Sedimentary units were defined on the basis of lithology, bed geometry, texture, colour and sedimentary structures.

Individual deformation events identified within the trench have been carefully verified by retrodeformational analysis, following the common practice in paleoseismological reconstruction (McCalpin, 1996). Several post-event sedimentary stages have also been included for a better understanding and representation of the evolutionary model. A number of identifiable faults were either formed, propagated or reactivated during successive deformation events. For each fault involved in each event, dip separation has been measured and equated to net slip (with precision of 5 cm). In addition, the resulting horizontal extension has been calculated taking into account the average dip of each fault. Further details are given in Section 7.4.

Dating of trench samples was achieved by the Luminiscence Dating Laboratory of University of Georgia, USA, using the Optically Stimulated Luminiscence (OSL) technique. Unfortunately, five of them were saturated samples that only provided minimum ages, which drastically decreased the consistency of the age model. Additional, preliminary OSL dating of shallow alluvial fan sediments had been achieved by Laboratorio de Datación y Radioquímica de la Universidad Autónoma de Madrid.

4. Structure and morphotectonics of the Sierra Palomera area

The NNW-SSE trending Sierra Palomera extensional fault makes the eastern boundary of the Jiloca graben at its central sector (Figs. 1b, 2). In the footwall block, Jurassic marine carbonates are unconformably covered by Paleogene continental clastics (Figs. 2, 3). In the hanging-wall block, i.e., the central sector of the Jiloca basin, the sedimentary infill is made of: (i) Late Pliocene (Villafranchian) to Pleistocene alluvial and episodic palustrine deposits, all of them exposed at the surface; (ii) an underlying carbonate unit, only observed in boreholes, that could represent an early lacustrine stage of Late Miocene-Early Pliocene age (Rubio and Simón, 2007). Borehole information indicates that the maximum thickness of the total infill approaches 100 m (Rubio and Simón, 2007).

The Jiloca basin runs slightly oblique to previous Paleogene, NW-SE trending folds (Fig. 1b; Rubio and Simón, 2007; Rubio et al., 2007). In particular, the Sierra Palomera fault follows the eastern limb, nearly vertical, of an eastwards verging anticline (Fig. 3). Its core is represented by Lower-Middle Triassic rocks that crop out in the neighbourhoods of Singra village, and its periclinal closure is partially preserved close to the southern tip of Sierra Palomera fault (Fig. 2). Such structural setting suggests that the main extensional fault resulted from negative inversion, during Late Pliocene-Pleistocene times, of a previous reverse fault linked to that anticline and developed during the Paleogene compression (Rubio and Simón, 2007).

The Sierra Palomera fault trace is ca. 26 km long and trends N152°E in average. The main fault surface only crops out in a few small exposures (1 to 4 m^2 in area). A number of rupture surfaces observed within the damage zone show orientations consistent with the map trend: strike between NW-SE and N-S, and dip between 54° and 87° W (mean orientation: N155°E, 70° W; Fig. 4). Slickenlines show pitch ranging from 75°N to 70°S, therefore indicating almost pure normal movement, with mean transport direction towards N230°E.

Two wide right relay zones separate the Sierra Palomera fault from the Calamocha and Concud faults. The dominant trend of recent, extensional faults and fractures distributed within both relay zones is similar to that of the main fault or slightly deviates to approach the N-S direction. These relay zones dominated by along-strike fractures were described in detail by Peiro et al. (2019, 2020).

The Sierra Palomera fault is expressed in the landscape by a conspicuous, 20-km-long fault mountain front (Fig. 5a,b), which attains heights of 200 to 300 m above its toe, 450 to 550 with respect to the bottom of the Jiloca depression. The mountain front shows a significantly low value of the sinuosity index (S_{mf} = 1.27; García-Lacosta, 2013). A number of gullies (most of them exhibiting V-shaped transverse profiles) run across the fault scarp and delimit some well-preserved trapezoidal facets (Fig. 5c). Gullies feed short, high-slope alluvial fans (Fig. 5d) that are barely incised, only partially connected to the axial fluvial system, and exhibit signs of present-day functionality (e.g., gravel

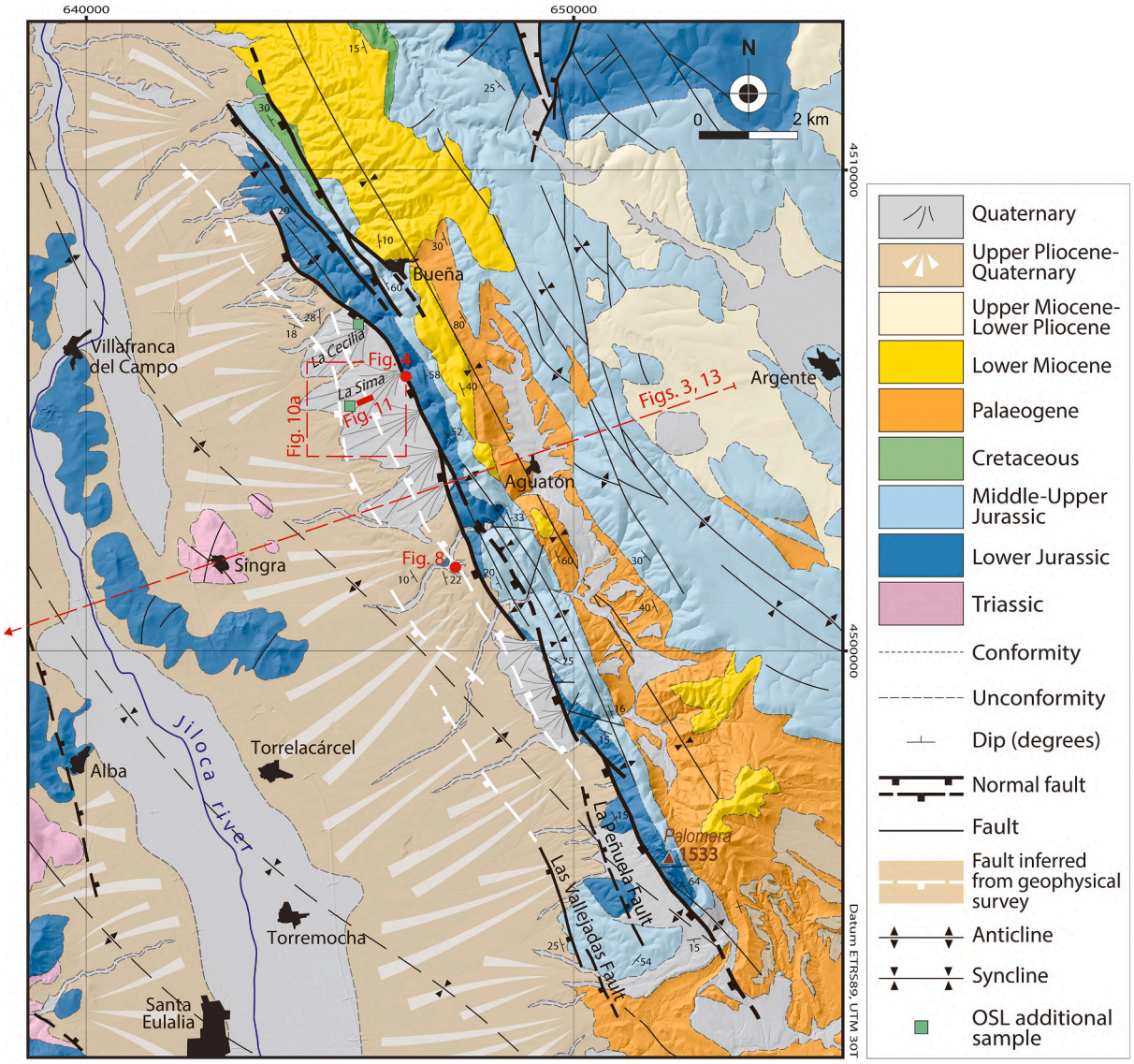

Fig. 2. Geological map of the Sierra Palomera area (on DEM image from Instituto Geográfico Nacional) showing the main structures associated to the Sierra Palomera fault. Location of Figs. 3, 4, 8, 10a, 11 is indicated, as well as that of OSL samples in La Cecilia and La Sima alluvial fans (see Table 1).

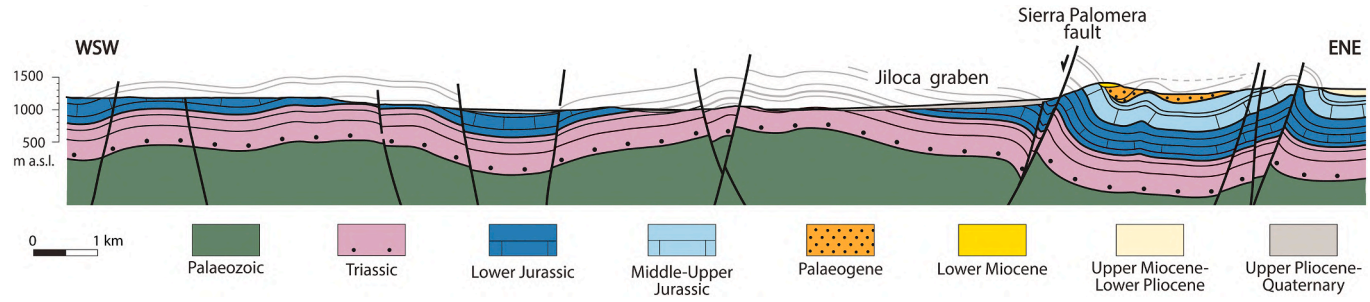

Fig. 3. Cross section of the Jiloca Graben at its central sector, initially reconstructed from surface geology and shallow borehole data (modified from Rubio and Simón, 2007). See location in Fig. 2.

aggradation affecting bush vegetation).

The difference in height of the geomorphological markers *FES2* and *FES3* between the footwall and the hanging-wall blocks reasonably allows approaching the Sierra Palomera fault throw. The envelope of relief at the footwall block is largely represented by the *FES2* planation surface cutting pre-Neogene units, which attains a maximum height of 1430 m close to the edge (Fig. 6). The summit of Sierra Palomera (1533 m a.s.l.) and its surrounding area constitutes a residual relief that stands out from *FES2*, while remains of an upper erosion sublevel (*FES1*) extend at the eastern foothills. A lower sublevel (*FES3*, usually lying 10–40 m below *FES2*) is also present: (i) eastwards of Sierra Palomera, over large areas of the northern Teruel basin; (ii) northwards and southwards, at the relay zones with the Calamocha and Concud faults, respectively; and (iii) along a narrow band westwards of the Sierra Palomera divide.

The height of *FES2* and *FES3* within the Jiloca depression can only be inferred indirectly. Both have been mapped at the eastern margin of the Jiloca depression, W of Santa Eulalia town, where they descend to ca. 1100 and 1050 m, respectively (Fig. 6). Then they are supposed to be covered by the Plio-Pleistocene infill, while gentle residual reliefs at the Singra-Villafranca del Campo area (made of Triassic and Jurassic rocks belonging to the core of the Sierra Palomera anticline) stand out above the depression bottom. The subsoil data provided by Rubio and Simón (2007); Fig. 6) for the central Jiloca basin constrain the heights of those planation surfaces. The boundary between Plio-Pleistocene alluvial deposits and the underlying carbonate unit, lying at about 950 m a.s.l. in the Santa Eulalia area, could be correlated with either *FES2* or *FES3*.

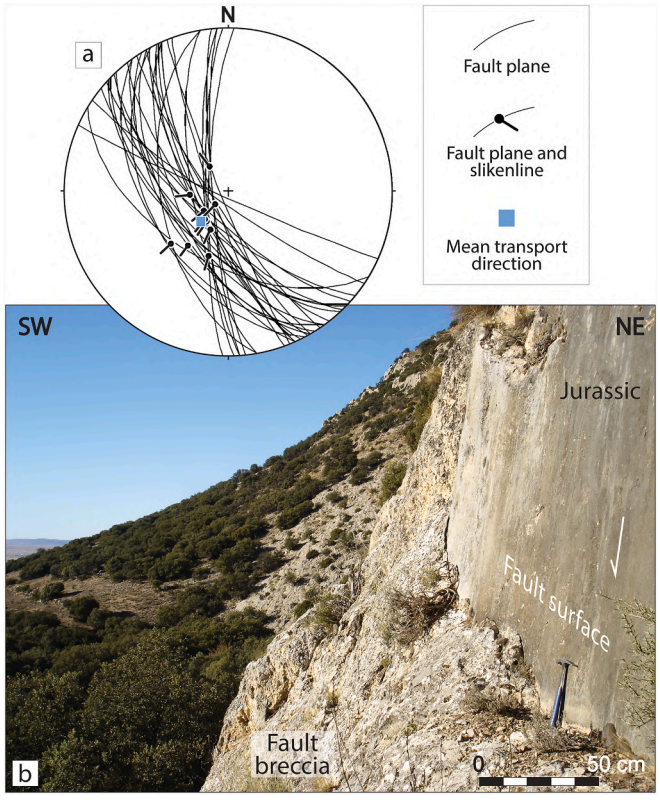

Fig. 4. (a) Field view of one of the rupture surfaces within the damage zone of the Sierra Palomera fault; it cuts Lower Jurassic limestones and shows associated fault breccia. (b) Stereoplot (equal area, lower hemisphere) showing orientations of fault planes and slickenlines collected in that zone.

Within the Sierra Palomera block, *FES2* and its correlative Late Ruscinian carbonates are in continuity with each other and show a quite homogeneous slope of about 1.5–2% along a distance of 20 km, in which the altitude of this morphosedimentary marker diminishes from 1400-1430 m (central sector of Sierra Palomera) to 1090–1120 m (Alfambra area) (Fig. 6). This morphotectonic setting defines a conspicuously tilted block whose edge has undergone a tectonic uplift of about 300 m relative to the bottom of the Teruel depression, as can be visualized from structural contours in Fig. 6.

The latter value closely approaches the topographic amplitude of the Sierra Palomera scarp itself, and is comparable to the fault throw inferred from offset of the *FES2* marker. Such fault throw, and its variation along the Sierra Palomera fault, have been analysed on a series of 1-km-spaced transects across the fault trace on the contour map of Fig. 6, assuming that *FES2* within the Jiloca basin coincides with the base of the Plio-Pleistocene infill. The result is shown in the throw vs. distance (T-D) graph of Fig. 7, where two distinct curves depict values of (i) fault throw *s.s.*, and (ii) total tectonic throw of *FES2* between the Sierra Palomera summits and the Jiloca depression bottom (including the bending component). The T-D curves show an overall bell-shape, although slightly bimodal in detail. The maximum values, 330 m and 480 m, respectively, are found at the central sector. Considering the age of the *FES2* morphosedimentary marker (3.8 Ma), and assuming an average dip of 70° for the fault plane and a pure normal movement, a maximum net slip rate of 0.09 mm/a can be inferred (0.13 mm/a for the total rate between Sierra Palomera and the Jiloca bottom).

Despite the initial appearance of the Sierra Palomera fault is that of a single major rupture that accommodates the entire throw, there is evidence of a parallel, synthetic fault (Las Vallejadas fault) located west of the main escarpment at its southern sector (Fig. 2). Both delimit an intermediate step within the mountain front, in which *FES2* lies at an altitude of 1140–1220 m, furthermore offset (ca. 10 m) by a minor antithetic rupture (La Peñuela fault). Recent activation of both subsidiary faults is revealed by local deformation of Villafranchian alluvial deposits: (i) back tilting (up to 25°E), due to rollover kinematics, observed at the foot of the morphological escarpment of Las Vallejadas fault (Fig. 2); (ii) accommodation monocline (dip up to 22°E) in the case of La Peñuela fault (Fig. 8; see location in Fig. 2).

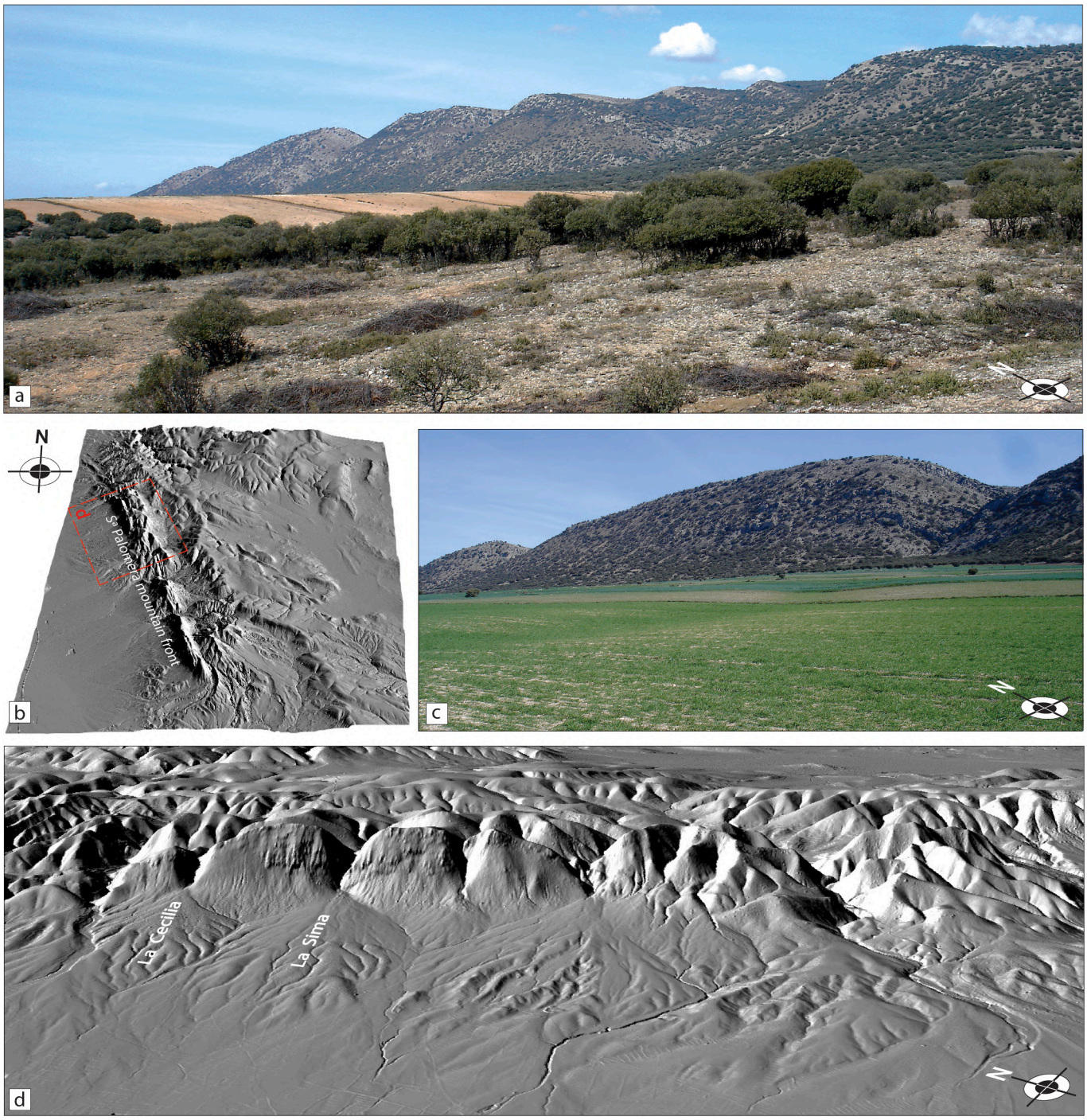

Fig. 5. The Sierra Palomera mountain front. (a) Field panoramic view. (b) Hillshade oblique image rendered from Digital Elevation Model (5 m grid) of Instituto Geográfico Nacional (IGN). (c) Detail of a trapezoidal facet within the fault scarp. (d) Hillshade oblique image (5-m-grid DEM, IGN) showing a close view to the alluvial fans sourced at the mountain front; La Cecilia and La Sima alluvial fans are identified.

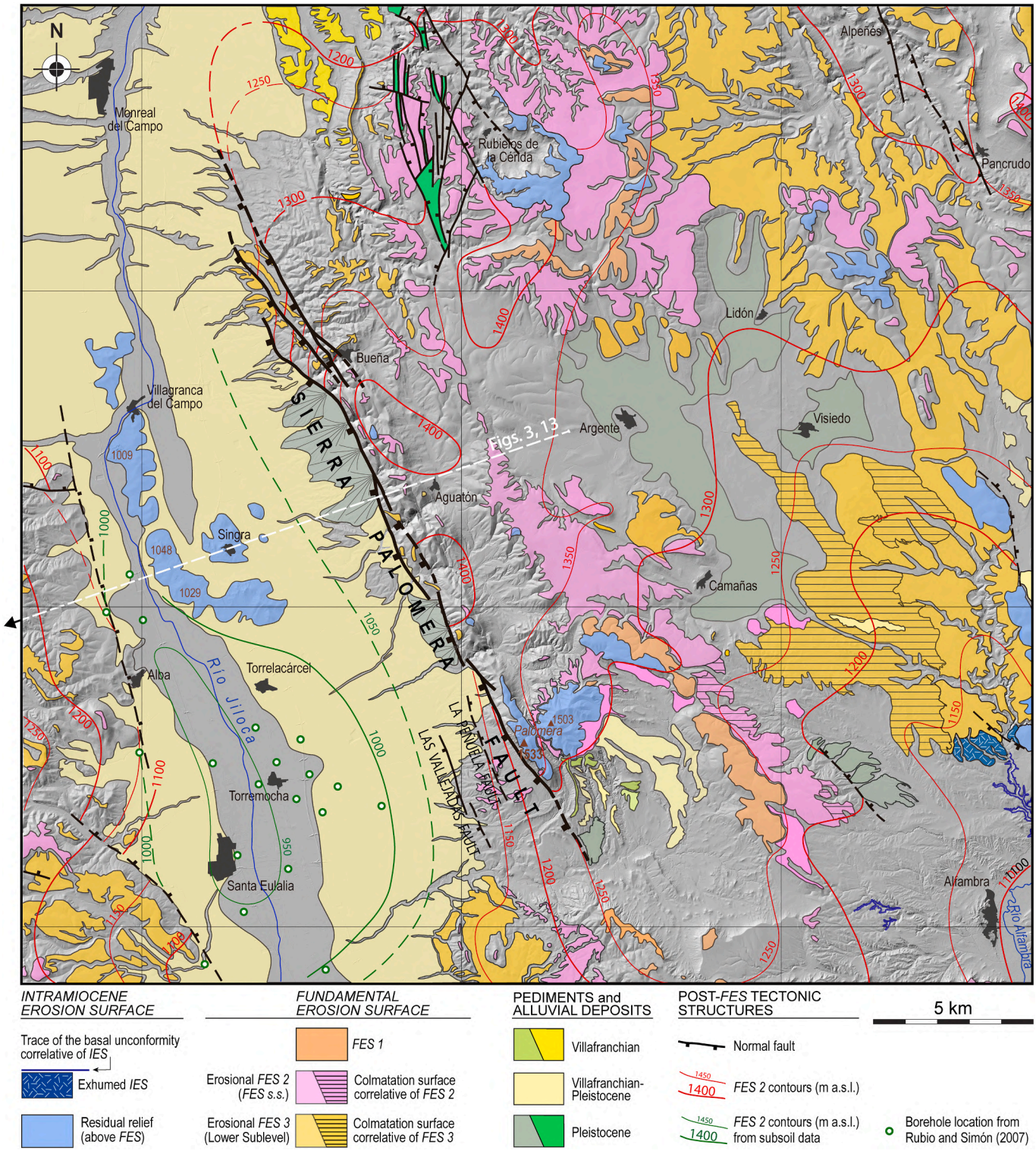

Fig. 6. Morphotectonic map of the Sierra Palomera area.

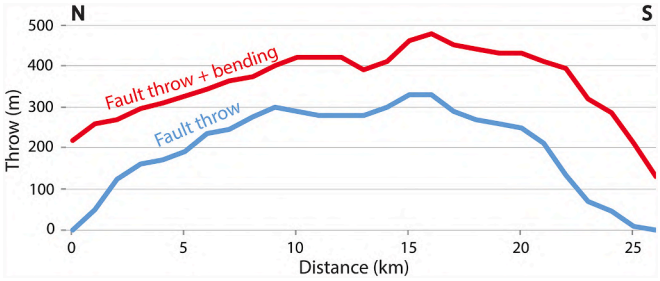

Fig. 7. Throw vs. distance (T-D) graph along the Sierra Palomera fault. Lower curve: fault throw *s.s.* recorded by the *FES2* marker. Upper curve: total tectonic throw of *FES2* including the bending component.

Fig. 8. Villafranchian alluvial deposits (V) tilted by an accommodation monocline above La Peñuela fault. Jurassic limestones (J) of the footwall block crops out at the bottom of the gully. See location in Fig. 2.

5. Geophysical exploration of the overall Sierra Palomera piedmont

Data of magnetic intensity field and vertical magnetic gradient were extensively collected along ten transects, roughly orthogonal to the Sierra Palomera fault trace along its hanging-wall block and ranging from 2.0 to 5.2 km in length (Fig. 9a). Spacing between successive measurement points was about 0.8 m. The two northernmost transects (profiles 01 and 02) and the southernmost one (profile 10) show a narrow distribution of residuals due to their lesser contrast with respect to the general, regional trend (Fig. 9b). The central transects (03 to 09) have spikes and lows that depart considerably from the general trend, and therefore, when data of the ten transects are considered as a whole, they define the range of the distribution (more specifically, profile 03 has the lowest and the highest values of residual magnetic intensity). Nonetheless, transects 01, 02 and 10 show a similar (albeit reduced in magnitude) outline to the rest.

The variation pattern of residuals in magnetometric profiles (also corroborated by EM profiles) allows portraying three domains (A, B and C) that are broadly parallel the Sierra Palomera fault (Fig. 9b). In the northern section of the studied area, the boundary between domains A and B is largely evident, due to the sudden change and amplitude of the anomaly. Moreover, these profiles show a more direct correlation between them than the southern ones, where the contact progresses through a magnetic dipole (Fig. 9a, b). These three domains are characterized by:

a) Closer to the Sierra Palomera fault, domain A is an area where residual values of magnetic intensity are close to zero and barely change, except for a subtle decrease to the west.
b) Westwards, a sharp change of attitude marks the onset of domain B, a zone of anomalies expressed as variations of residuals up to 20–30 nT over decametric distances. Such anomalies reflect the presence of small magnetic dipoles and a slightly higher mean value of Earth magnetic field. Values for apparent conductivity are still homogeneous.
c) Finally, domain C is separated from domain B by a sharp decrease in magnetic intensity (it goes down about 100 nT) with lower relative values of Earth magnetic field and presence of a lower density of magnetic dipoles (including those of higher wavelength). Apparent conductivity and magnetic susceptibility are higher.

The reported geophysical results (Earth magnetic field, together with apparent conductivity and susceptibility) suggest the presence of a body of relatively higher magnetic susceptibility underlying domain A, which gets shallower under domain B, and gets again deeper under domain C. Boundaries between those domains are sharp and clear. This setting can be interpreted as an uplifted block (made of Paleozoic and Triassic materials belonging to the core of the Sierra Palomera anticline) bounded by faults nearly parallel to the Sierra Palomera fault trace.

6. La Sima alluvial fan: linear topographic anomaly and its geomagnetic expression

In the absence of any visible surficial rupture across Quaternary sediments of the Sierra Palomera piedmont, evidence of recent tectonic activity should be obtained from trenching. Owing to non-favourable topographic, lithologic and access conditions at the Sierra Palomera fault trace itself, our search was focused on the surface of two alluvial fans sourced at the mountain front, at La Cecilia and La Sima areas (see location in Figs. 2 and 5d). Both exhibit well-preserved alluvial fan morphology at its proximal sectors, with evidence of present-day aggradation at the apex. Shallow sand and silty sedimentary horizons in those alluvial fans have provided ages of 28.9 ± 2.0 ka BP (La Cecilia) and 19.2 ± 1.1 ka BP (La Sima) (see Table 1; location in Fig. 2).

In the middle sector of La Sima alluvial fan, a sharp NNW-SSE trending lineament is clearly visible on aerial photographs and DEM images, beyond which the fan surface is more deeply incised by the local drainage network (Fig. 10a). That lineament involves a morphological anomaly, a break in the fan slope, which becomes null or even negative up to take locally the appearance of a gentle, degraded uphill-facing scarplet (Fig. 10c). These features suggest the occurrence of an antithetic fault that would have sunk the proximal sector of the fan with respect to the middle one by about 2.5 m. This lineament coincides with the boundary between domains A and B defined from geophysical results (Fig. 9b), and is virtually prolonged towards SSE up to connect with the antithetic La Peñuela fault (Fig. 2).

In order to test the hypothesis of an antithetic fault cutting the La Sima alluvial fan, the subsoil in the neighbourhoods of the morphological lineament was intensively explored by means of a magnetic and electromagnetic survey. The coincidence of the lineament with the A/B boundary is clearly expressed in the detailed map of residual magnetic anomalies shown in Fig. 10b. The area east of the sharp linear NNW-SSE trending limit, clearly visible on this map, shows low residual values with wide (hectometre-scale) wavelength variations. To the west of this limit, an increase of more than 30 nT is observed, as well as a decrease of more than 50 mS/m in the total conductivity; moreover, the texture of

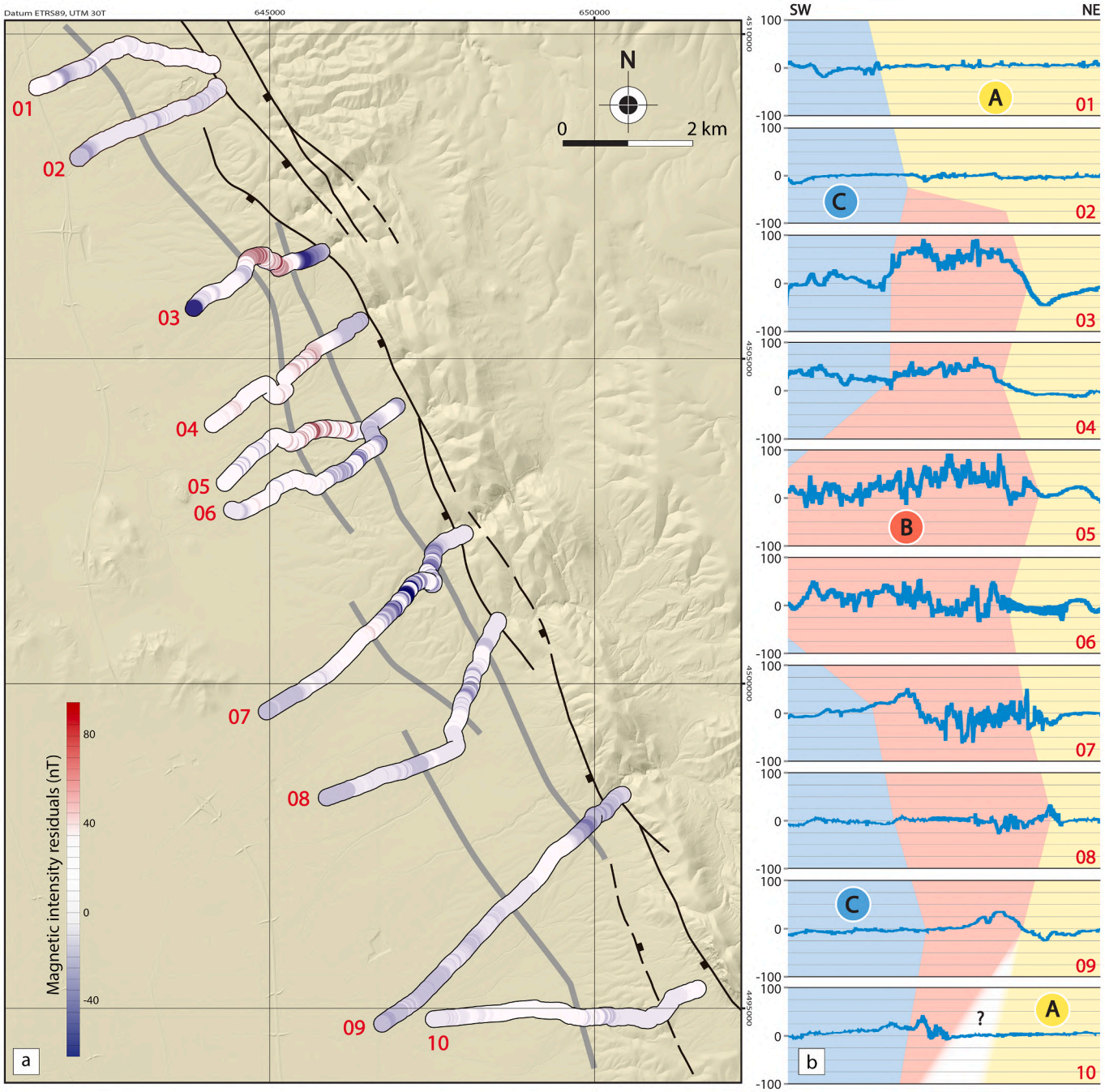

Fig. 9. Results of the magnetometric survey covering the Sierra Palomera piedmont. (a) Location of profiles 01 to 10 (which is the same as for the electromagnetic survey), with the residual values of field intensity (nT) plotted as a colour palette. Black thin lines depict the Sierra Palomera fault trace. Grey thick lines depict the spatial correlation of trending changes on the successive transects, and therefore of the described domains (A, B and C). (b) Residual earth magnetic field profiles plotted with a normalized horizontal length, in which domains A, B and C roughly parallel to the Sierra Palomera fault are defined (data are in nT; see text for details).

the residual map changes noticeably, showing sharper magnetic dipoles of decametric wavelength.

The amplitude and morphology of the linear anomaly is not consistent with the susceptibility values of surficial sediments, and suggest the contrast, at shallow levels, between a high-susceptibility rock body to the west (domain B, as defined in Section 5) and the domain A to the east. In addition, Fig. 10b shows other NW-SE trending linear anomalies in domain B, which involve a lower contrast of magnetic field values. Both the main anomaly and the secondary ones show high gradient and sharpness of the observed dipoles, suggesting near-surface, high dipping discontinuities or rock boundaries compatible with recent faults.

7. Trench study at La Sima alluvial fan

Once verified that geophysical and topographic analysis of La Sima lineament reinforced our preliminary hypothesis about the northwards prolongation of the antithetic La Peñuela fault, we selected an easily accessible site for trench study. A 40 m long, 1.4 m wide trench was dug along a N067°E direction, roughly orthogonal to the linear anomaly that separates domains A and B. A segment of 19 m on its southern wall, with depth ranging from 3.0 to 3.5 m, was logged and analysed in detail (Fig. 11a,b).

Table 1
Parameters and results of OSL dating of samples collected at the La Sima trench (S1 to S7; Luminiscence Dating Laboratory of University of Georgia, USA), and La Cecilia and La Sima alluvial fans (Laboratorio de Datación y Radioquímica de la Universidad Autónoma de Madrid, Spain).

Sample	Laboratory reference	Stratigraphic location	Depth (m)	H_2O (%)	Quartz Grain (μm)	^{238}U (ppm)	^{232}Th (ppm)	K (%)	Dose rate (Gy/ka)	Equivalent dose (Gy)	Age (ka)
S1	UGA15OSL-1013	Unit 9 (top)	1.0	5 ± 2.5	80–125	1.42 ± 0.33	5.86 ± 1.14	0.6 ± 0.1	1.50 ± 0.15	146.0 ± 3.9	97.4 ± 10.2
S2	UGA15OSL-1014	Unit 9b	2.1	5 ± 2.5	80–250	0.73 ± 0.12	2.24 ± 0.46	0.2 ± 0.1	0.68 ± 0.10	>256	>378
S3	UGA15OSL-1015	Unit 8	1.6	5 ± 2.5	125–250	0.95 ± 0.15	2.45 ± 0.54	0.3 ± 0.1	0.84 ± 0.11	>300	>355
S4	UGA15OSL-1017	Unit 6 (base)	2.8	5 ± 2.5	150–250	1.35 ± 0.25	5.42 ± 0.88	0.5 ± 0.1	1.27 ± 0.13	>300	>236
S5	UGA15OSL-1018	Unit 11	0.4	5 ± 2.5	125–250	1.29 ± 0.20	4.15 ± 0.71	0.5 ± 0.1	1.26 ± 0.12	62.0 ± 3.4	49.2 ± 5.4
S6	UGA15OSL-1019	Unit 7 (top)	0.7	5 ± 2.5	125–250	0.96 ± 0.20	4.73 ± 0.71	0.5 ± 0.1	1.21 ± 0.12	>300	>248
S7	UGA15OSL-1020	Unit 6 (top)	1.2	5 ± 2.5	80–125	1.41 ± 0.21	4.54 ± 0.75	0.8 ± 0.1	1.56 ± 0.13	>300	>193
La Cecilia	MAD-6326BIN	Alluvial fan	3.0	2.31	2–10	2.97	1.54	0.01 ± 0.1	1.63	47.1 ± 2.5	28.9 ± 2.0
La Sima	MAD-6327BIN	Alluvial fan	0.4	6.25	2–10	3.73	1.90	0.18 ± 0.1	2.31	44.3 ± 1.4	19.2 ± 1.1

7.1. Sedimentary units

The materials exposed at La Sima trench essentially correspond to relatively well-bedded Pleistocene alluvial sediments (Fig. 11a). Sedimentary features indicate alternating energetic flows, sometimes flash floods, recorded by gravel channel and bar deposits, and waning discharges that settled fines over the gravel deposits. All the succession includes clear signs of calcrete development and periods of time with negligible sedimentation. Bioturbation signs and carbonate precipitation are related to pedogenesis, suggesting wetting and drying episodes of the sedimentary surface. The sedimentary succession has been subdivided into twelve lithological units (Fig. 11b):

Unit 1 (up to 50 cm in thickness): Massive reddish mudstone with isolated, mm- to cm-sized angular limestone clasts (more abundant at the base), with bioturbation traces and smooth carbonate nodules.

Unit 2 (25 to 55 cm): Orange massive sandy mudstone with floating angular-subangular grey limestone granules and pebbles, and some irregular cm-thick gravel bed. Grey mudstones laminae towards the top.

Unit 3 (55 to 75 cm): Tabular laminated, indurated and brecciated, carbonate crust with some cm-thick interbedded silts with carbonate clasts. Carbonate fragments are smaller in the upper part; laminated fragments are less abundant towards W.

Unit 4 (20 to 35 cm): Reddish massive silty sand and mudstone in a tabular level with vertical root traces filled by fine sands. Some carbonate nodules, plant remains and scattered grey, angular limestone and caliche clasts up to 10 cm in size can be recognized.

Unit 5 (15 to >50 cm): Clast-supported gravel with silty to sandy matrix in a tabular, locally channelized sedimentary body with crude horizontal stratification. Gravel is made of angular-subrounded limestone clasts (up to 8 cm) and smaller caliche clasts.

Unit 6 (25–55 cm): Orange to brownish massive silt and mudstone with greyish limestone angular clasts and floating whitish caliche rounded nodules (up to 2 cm). Clast content increases locally. Root traces, plant remains and organic matter patches can be recognized in the western sector.

Unit 7 (30 to >150 cm): Heterogeneous unit mainly made of grain-supported gravel, locally cemented, with angular-subrounded limestone clasts (up to 15 cm in size) and caliche nodules. It includes red mudstone discontinuous intercalations, up to 20 cm in thickness, with floating cm-sized angular clasts. The overall geometry of the unit is tabular in the footwall block and channelized in the hanging-wall block. A level of calcrete gravel, >50 cm in thickness, appears at the top of this unit within the footwall block.

Unit 8 (10–60 cm): Reddish silt with floating limestone angular granules and pebbles (up to 8 cm) with evidence of bioturbation.

Unit 9 (45–120 cm): Grey gravel in a channeled body with limestone angular clasts (up to 12–14 cm in size) and rounded caliche clasts. Crude finning upwards cycles can be recognized. Pedogenic features increase towards the top, where brecciated limestones locally appear.

Unit 10 (55 to 70 cm): Reddish massive silts with floating subangular limestone clasts (up to 7 cm), whitish carbonate nodules and an interbedded discontinuous clast-supported gravel level with subangular clasts up to 10 cm in size.

Unit 11: Wedge-shaped body of orange and whitish massive, highly cemented silt, with carbonate floating subangular limestone clasts (up to 10 cm) and caliche clasts arranged with the A-axis subvertical.

Unit 12 (20 to 50 cm): Surface regolith made of silt with angular to subangular clasts, reworked by agricultural labours.

7.2. OSL dating

Seven samples (S1 to S7) of alluvial sediments within the trench (see Fig. 11b for location) have been dated, although unfortunately the results show a high level of uncertainty (see Table 1). Other three collected samples did not contain enough sand grains for providing a representative dose distribution and therefore OSL dates were not reliable in this

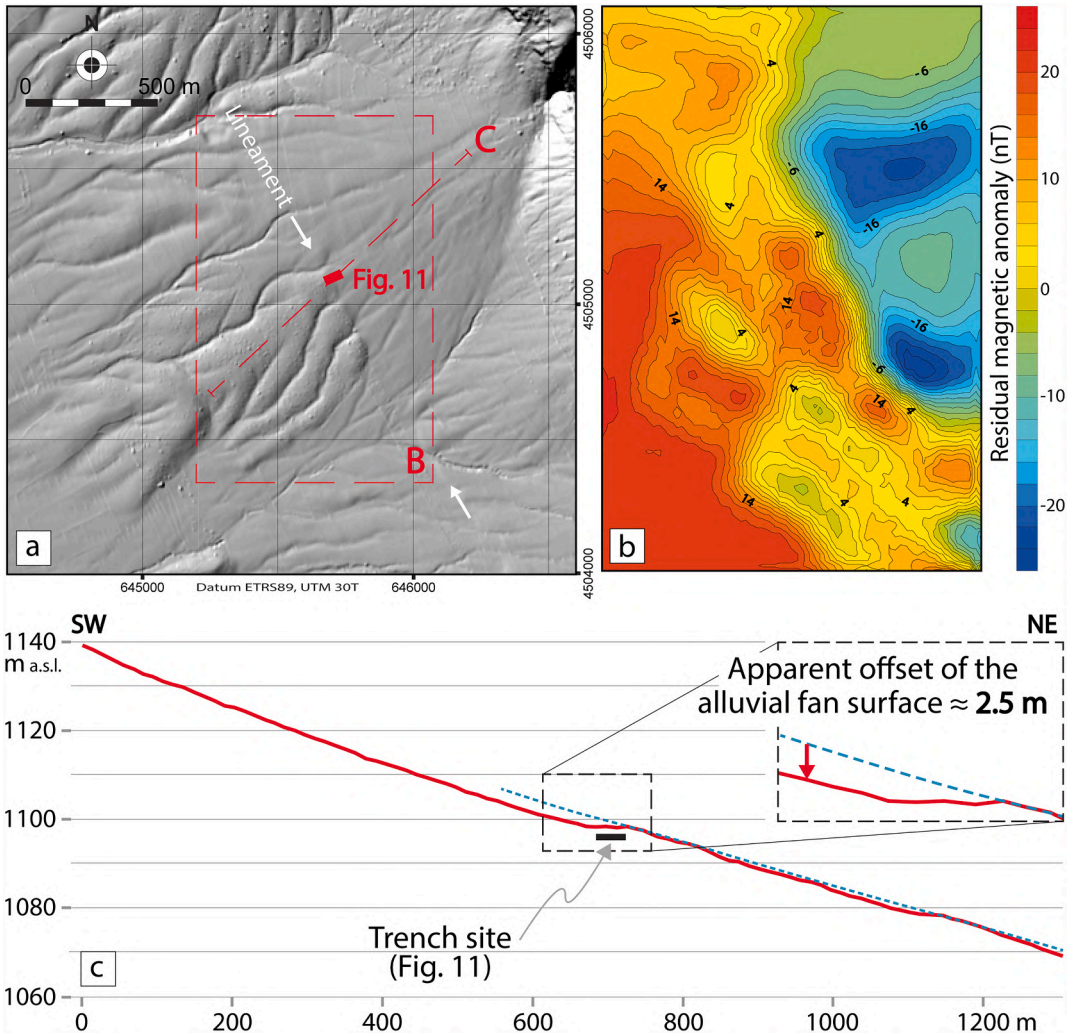

Fig. 10. (a) Hillshade relief map of the barranco de la Sima alluvial fan rendered from digital elevation model (DEM, 5 m grid) of the Instituto Geográfico Nacional. See location in Fig. 2. (b) Residual magnetic field anomalies at the central sector of the alluvial fan, at the contact between domains A and B. (c) Detailed topographic profile showing a slope anomaly in the longitudinal profile of the alluvial fan surface, from which an apparent antithetic throw of ca. 2.5 m can be inferred.

case. These samples are not located in Fig. 11b.

Samples S2, S3, S4, S6 and S7 have presented signal saturation, i.e., their natural luminescence signal lies beyond the saturation of the OSL response with dose, making it impossible to provide adequate results. According to laboratory results, their ages should be older than 193 to 378 ka, although such figures should not be taken sensu stricto. Only one of the alluvial sedimentary units is directly dated: S1 provides an age 97.4 ± 10.2 ka for the top of unit 9. Unit 11 (sample S5), which will be next interpreted as a fissure infill, is dated to 49.2 ± 5.4 ka. As a result, the chronology of unit 10, overlapping unit 9 and being cut by the fissure, can be broadly constrained between both numerical ages.

Without the support of further anchors, building an age model for the overall alluvial succession exposed in the trench is not feasible. In any case, the ensemble of OSL dating results and geomorphological observations in the study area suggest that: (i) most of that alluvial succession belongs to the Middle Pleistocene; (ii) a rapid decrease of sedimentation rate occurs by the Middle-Late Pleistocene transition; and (iii) sedimentation persisting in proximal and middle sectors of the alluvial fans during Late Pleistocene to present-day times only represents a small contribution to the surficial aggradation and landscape modelling.

7.3. Deformation structures

The trench log shows a main extensional fault zone at the central sector, dipping eastward and hence antithetic with respect to the Sierra Palomera fault (Fig. 11b), and full consistent with the uphill-facing scarplet described in Section 6. These features allow identifying such antithetic fault zone with the map-scale La Peñuela fault (Fig. 2). The footwall block of that fault zone shows a gentle monocline, while other normal (both synthetic and antithetic) faults, cutting most of the sedimentary succession, are distributed along the entire section. The orientations of all these structures are overall consistent, as depicted in stereoplots of Fig. 11c,d,e,f.

The central fault zone is made of three significant structural elements:

1) Main fault, expressed by θ_1 and θ_2 individual rupture surfaces.
2) Splay faults κ1, κ2, κ3 and κ4, associated to the tip of the main rupture and propagated through unit 7. Both the main, westwards dipping rupture surfaces and the nearly vertical splay faults consistently strike NNW-SSE (Fig. 11c). Such structural arrangement suggests that, at certain stage of its development, the main rupture θ_1-θ_2 was covered by the upper part of unit 7, and then reactivated in the form of splay faults related to refraction at the extensional tip (horsetail structure, in the sense of Granier, 1985). That is the key, purely instrumental criterium for separating lower and upper unit 7 in Fig. 12; therefore, such separation is not based on a visible lithological boundary (we have defined a single unit 7 indeed).

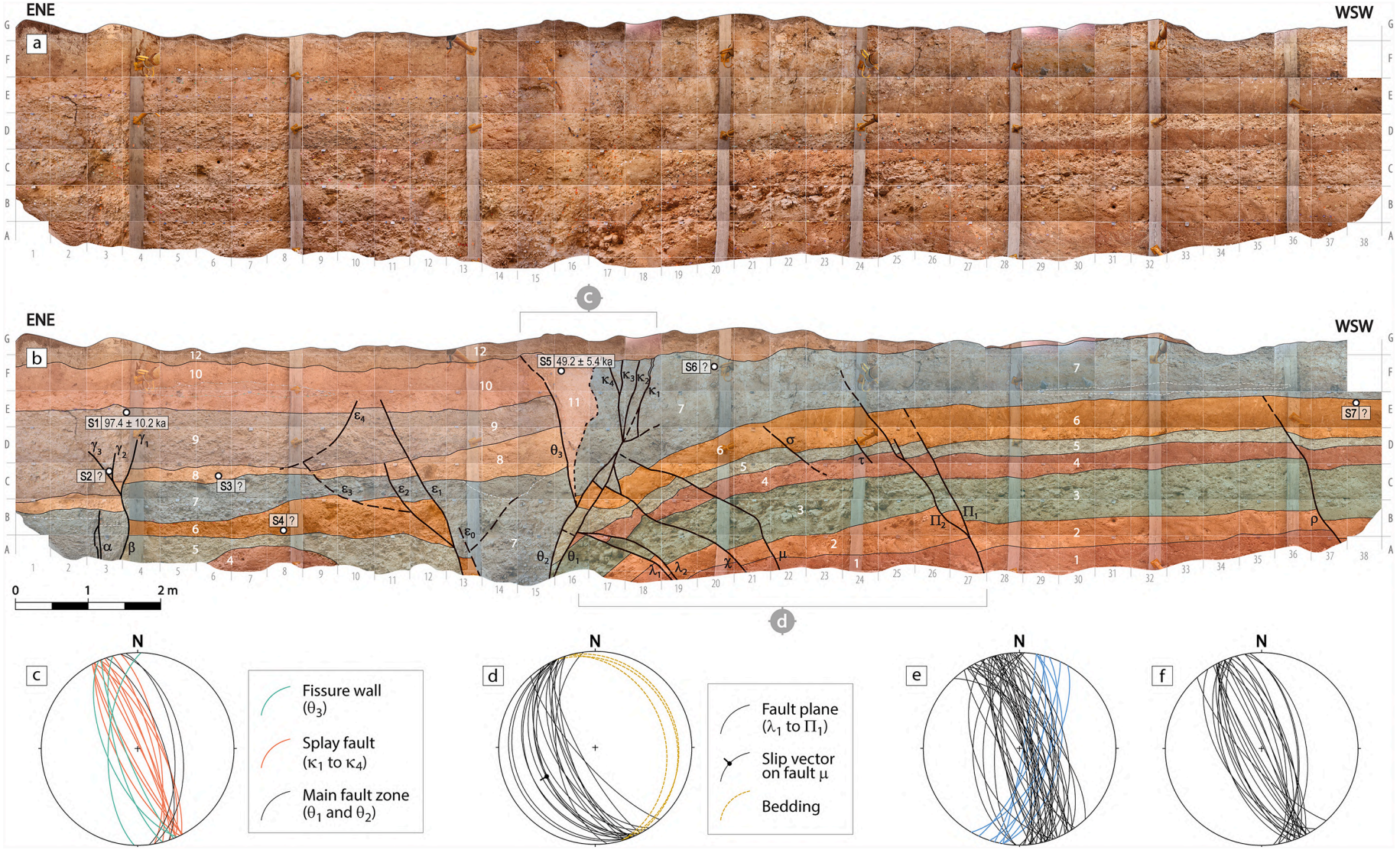

Fig. 11. (a) Uninterpreted photomosaic of La Sima trench, see location in Fig. 2. (b) Detailed log. 1 to 12: Quaternary units described in the text. Greek characters: faults referred in the text. The location and age of samples dated by OSL is indicated. Stereoplots (equal area, lower hemisphere) show orientations of faults and fractures measured within the trench: (c) Central fault zone. (d) Footwall block, including monocline. (e) Synthetic stereoplot of fault planes, including a main set parallel to the prevailing structural trend (NNW-SSE, black great circles) and a subsidiary set oriented NNE-SSW (blue great circles); fault planes rotated at the monocline have been restored to their original orientation. (f) Synthetic stereoplot of fractures without displacement. (For interpretation of the references to colour in this figure legend, the reader is referred to the web version of this article.)

3) Open fissure bounded by fault θ_3 and another irregular surface, and filled with unit 11. The interpretation is based on its wedge shape, the massive internal structure of the infill, and the occurrence of clasts with nearly vertical A-axes. According to this interpretation, both bounding surfaces would have represented both walls of a single, also NNW-SSE striking fault, then disengaged from each other when the fissure opened up and partially crumbled before infilling took place.

The footwall block is deformed by the monocline and cut by a number of NNW-SSE striking normal faults (Fig. 11d), all of them synthetic with the Sierra Palomera fault and exhibiting dip separations in the range of 10 to 20 cm (Fig. 11b). Faults ρ, π_1 and π_2 cut the horizontal limb of the monocline, and have apparently kept their original, high dip. The rest of faults (τ, σ, μ, χ, λ_1 and λ_2) appear at the hinge and the abrupt limb of the monocline. They show a progressive decrease in dip towards the east as the bedding dip increases, and some individual faults (μ, λ_1, λ_2) exhibit conspicuously arched traces, so that the angle between faults and bedding remains broadly constant (mostly within the range of 55–65°). Such geometrical setting strongly suggests that they were folded by the monocline. Concerning the relationships between faults and sedimentary units, ρ and π_1 uniformly offset (15–20 cm) the base of units 2 to 6, while they suddenly vanish and does not affect the base of unit 7. Also fault σ shows similar relationships, although in this case it does not propagated through the lower units, probably detached within low-viscosity materials of unit 4. As a consequence, ρ, π_1 and σ produce a noticeable thickening of unit 6 in their respective hanging-wall blocks. Faults π_2, τ, μ, χ, λ_1 and λ_2) also offset rather uniformly the sedimentary boundaries, and at least two of them (π_2 and μ) propagated across unit 7.

The hanging-wall block shows two ensembles of intersecting faults that cut units that are younger than the ones from the footwall block (Fig. 11b). Individual faults show distinct slip for different sedimentary markers, which indicates diachronic development. The ε_0-ε_1 couple offsets more than 1.2 m the base of unit 7, while it produces a rather uniform dip separation of 8–10 cm in the bases of units 8, 9 and 10. We should therefore interpret that ε_0-ε_1 underwent most of its present-date displacement (>1.3 m) before sedimentation of unit 8, and was then reactivated after the lower part (at least) of unit 10 was deposited. Splaying from ε_1, fault ε_2 cuts units 7 and 8, and is covered by unit 9, while ε_3 cuts the base of unit 9, thus making the three faults a footwall rupture sequence. The antithetic ε_4 propagated thorough unit 9 and the lowermost unit 10. At the easternmost trench sector we find a similar pattern in the NNW-SSE striking faults α and β. Fault β offsets more than 0.7 m the base of unit 7, while (together with its splay faults γ_1, γ_2 and γ_3) produces a smaller separation (0.4 m) in the bases of units 8 and 9. We interpret that β underwent displacement ≈ 0.3 m before sedimentation of unit 8, and was then reactivated after deposition of unit 9. Fault α propagated through unit 7, previous to sedimentation of unit 8, and did not undergo further reactivation.

The orientations of the described structures have a strict consistence. All faults systematically strike NNW-SSE (Fig. 11f), and so does the limb of the monocline (Fig. 11d). There is no doubt that the latter is (i) genetically linked to faults, and (ii) responsible for the decrease in dip of faults σ, μ, χ, λ_1 and λ_2. Bedding and fault surfaces are rotated around a common, well-defined horizontal axis ca. N160°E (Fig. 11d). Strikes of minor fractures measured along the trench are also clustered around NNW-SSE, although a small number among them are oriented NNE-SSW (in blue in Fig. 11e). A brief discussion about the dynamic framework (stress fields) in which such fault and fracture pattern developed will be made in Section 8.5.

7.4. Retrodeformational analysis and evolutionary model: deformation events

Based on the former structural description, in particular on the relationships between structures and the sedimentary units, a careful retrodeformational analysis has been achieved, with a double purpose: (i) building an evolutionary model, i.e. a systematic succession of deformation events, and (ii) testing its kinematic consistence (Fig. 12).

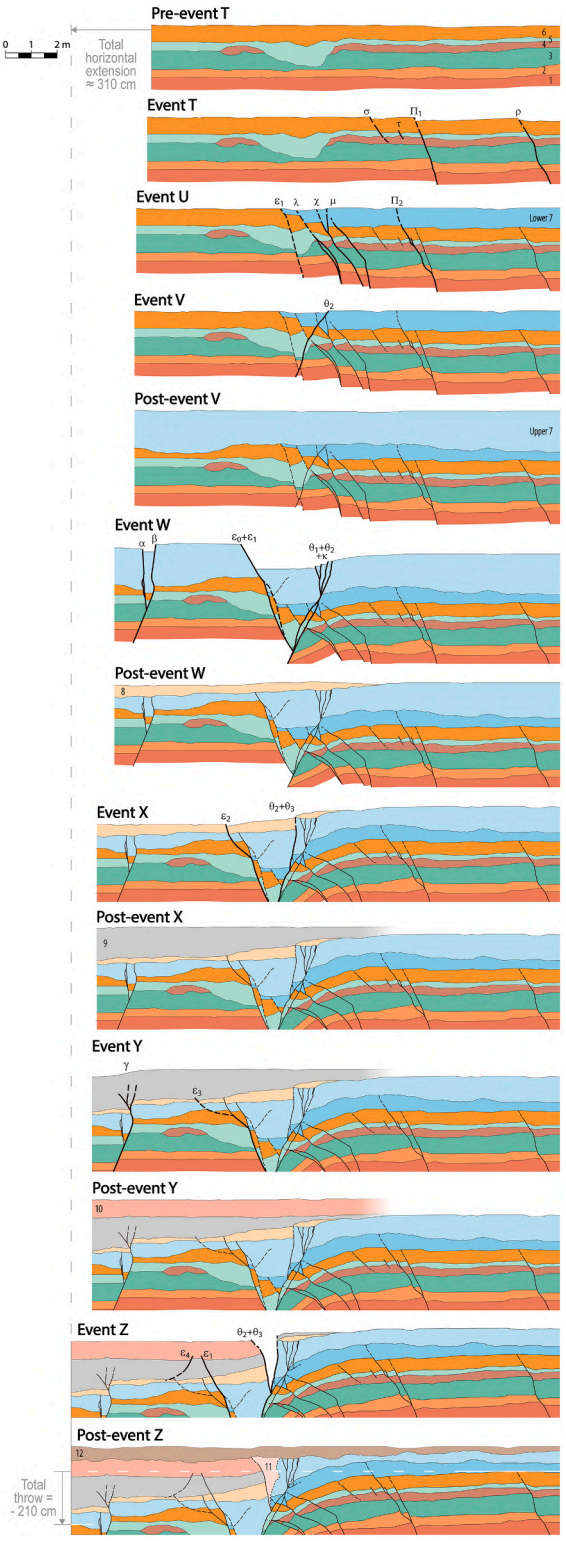

Fig. 12. Evolutionary model of sedimentation and deformation recorded at the La Sima trench from retrodeformational analysis. Each sketch represents a stage subsequent to the paleoseismic event (and, in some cases, to deposition of sedimentary units) labelled above. Unexposed sectors below the trench have been locally reconstructed in the sketches in order to complete the evolutionary model. Bold traces indicate which faults are active during each event. Total horizontal extension and throw calculated in Table 2 are shown.

A number of identifiable faults were either formed, propagated or reactivated during each deformation event (Fig. 12 and Table 2). Dip separation directly measured on the trench log is taken as practically representing the net slip on each fault, since: (i) bedding is roughly horizontal, (ii) the trench, oriented N067°E, is nearly orthogonal to the prevailing strike of faults, and (iii) the only kinematical indicator observed during trench survey (slickenlines with pitch 82°S on fault μ; Fig. 11d), as well as those collected at the Sierra Palomera fault zone itself (see Fig. 4b), suggest nearly pure normal slip for the overall extensional fault system.

Net slip for every individual fault (with positive sign for synthetic faults and negative sign for antithetic ones), together with the resulting horizontal extension (considering the average fault dip), are depicted in Table 2. Such measurements exclude offset accommodated by the bending monocline. The latter has been only considered for computing the total accumulated deformation, since it is not possible to accurately calculate which fraction of bending occurred during each event. The total slip per event, taken as the algebraic sum of slip values on individual faults, is also shown. The total horizontal extension per event considers the aggregate of extension values on individual faults, but also includes an estimate of the contribution of bending, in order to jointly accommodate the horizontal extension visually expressed in the successive cross sections of Fig. 12.

Below we summarize the main features of each of the seven deformation events (T to Z) defined at the La Sima trench (Fig. 12; see measurements in Table 2):

Event T: Slip on faults ρ, π_1, τ and σ after deposition of unit 6 and previous to unit 7. Accumulated net slip: +45 cm.

Event U: Slip on faults π_2, μ, χ, λ_1, λ_2 and ε_1, subsequent or coeval with deposition of the lower part of unit 7. Accumulated net slip: +105 cm.

Event V: Slip on fault θ_2, subsequent to deposition of lower unit 7, then covered by upper unit 7. Development of the monocline begins; according to our progressive deformation model depicted in Fig. 12, in which the main rupture had always propagated through units 1 to 6, this monocline should be interpreted as a drag fold. Net slip: −10 cm.

Event W: Reactivation of the main, central fault through the rupture surfaces θ_1-θ_2, which propagates across upper unit 7 splitting into κ1, κ2, κ3 and κ4. Progress of the monocline produces rotation of faults τ, σ, μ, χ, λ_1 and λ_2. Slip on faults ε_0-ε_1, α and β, all of them subsequent to top of unit 7 and previous to unit 8. Accumulated net slip: +125–65 = +60 cm.

Event X: Propagation of the main fault zones, θ and ε, through new rupture surfaces: θ_2-θ_3 and ε_2, respectively. Both are younger than unit 8 and older than unit 9. Accumulated net slip: +5–50 = −45 cm.

Event Y: Activation of fault ε_3, and propagation of β splitting into γ_1, γ_2 and γ_3. Both processes are subsequent to deposition of unit 9 and probably previous to unit 10, therefore close to (or slightly younger than) the numerical age provided by sample S1 (97.4 ± 10.2 ka). Accumulated net slip: −35 cm.

Event Z: Formation of fault ε_4 and propagation of ε_1 cutting the lower part of unit 10. Slip on θ_2 that induces extensional movement on the θ_3 surface, giving rise to an open fissure that tears apart units 7 to 10 and is subsequently filled with unit 11. This event should be dated just prior to the numerical age provided by sample S5 (49.2 ± 5.4 ka). Accumulated net slip: +10–120 = −110 cm.

8. The Sierra Palomera fault: synthesis and discussion

8.1. Geometry and kinematics of macrostructures

Structural information from field survey has allowed characterizing geometry and kinematics of the Sierra Palomera fault itself (Figs. 4, 6, 13). The attitude of the main fault surface is N155°E, 70° W in average, while most ruptures visible along and close to it are systematically parallel. The fault shows pure normal movement, with mean transport direction towards N230°E. In addition, the use of two geomorphological markers (mid-Pliocene *FES2* and *FES3* planation surfaces; Fig. 13b) has permitted measuring the fault throw *s.s.* (330 m) and the total tectonic throw (480 m, including bending) at the Sierra Palomera fault, resulting in slip rates of 0.09 and 0.13 mm/a, respectively.

Table 2
Synthesis of deformation events inferred at La Sima trench: faults activated during each event; net slip values calculated from the trench log and the retrodeformational analysis (positive: synthetic with the Sierra Palomera fault; negative: antithetic; Figs. 11, 12), and associated values of horizontal extension. Further explanation in text.

Event	Active faults	Net slip[1] (cm)	Average dip (°)	Horizontal extension[1] (cm)	Net slip[1] per event (cm)	Horizontal extension[2] per event (cm)
T	σ	+ 10	53	6	+ 45	15
	τ	+ 5	60	2		
	π1	+ 15	70	5		
	ρ	+ 15	64	7		
U	ε1	+ 15	74	4	+ 105	45
	λ1 + λ2	+ 40	60	20		
	χ	+ 20	59	10		
	μ	+ 15	60	7		
	π2	+ 15	60	7		
V	θ2	− 10	63	5	− 10	5
W	α	+ 10	86	1	+ 60	80
	ε0 + ε1	+ 115	64	50		
	β	− 30	74	8		
	θ1 + θ2 + κ1 to κ4	− 35	63	16		
X	ε2	+ 5	62	2	− 45	65
	θ2 + θ3	− 50	74	14		
Y	ε3	0	55	0	− 35	20
	γ1 + γ2 + γ3	− 35	80	6		
Z	ε1	+ 10	64	4	− 110	80
	ε4	− 10	42	7		
	θ2 + θ3 (+ open fissure)	− 110	74	30		
Total synthetic faults		+ 290		125 (7.8%)[3]		
Total antithetic faults		− 280		86 (5.4%)[3]		

Accumulated deformation:	Throw[2] (cm)	Horizontal extension[2] (cm)
Bending monocline	≈ − 220	≈ 100 (6.2%)[3]
Total structures	− 210	≈ 310 (19.4%)[3]

[1] Excluding deformation associated to the monocline.
[2] Including deformation associated to both faults and monocline.
[3] Percentage with respect to the restored log length ≈ 1600 cm.

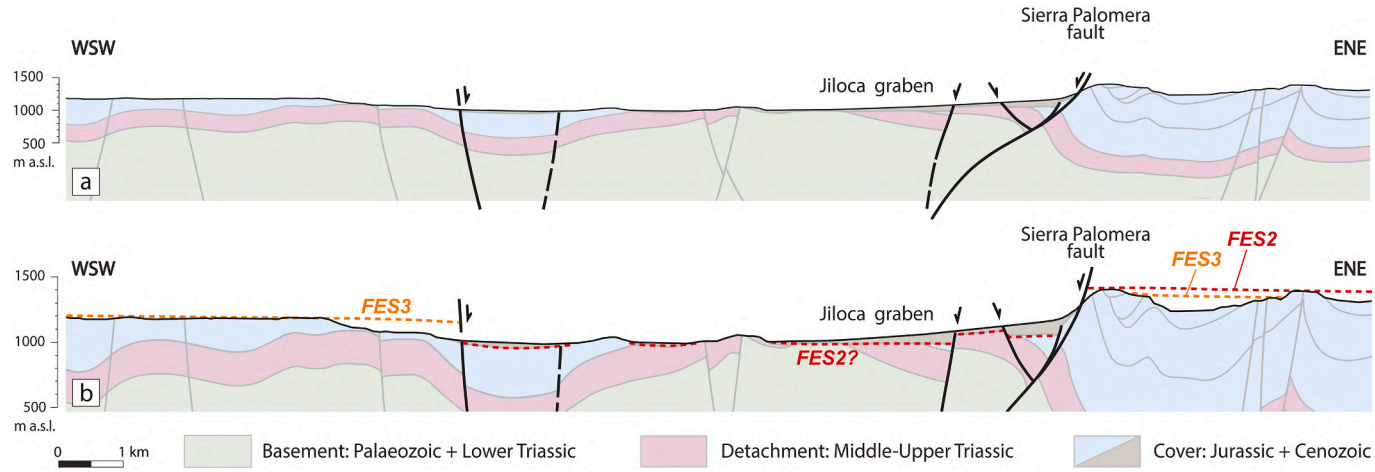

Fig. 13. (a) Refined cross section of the Jiloca graben at its central sector, in which the new inferred, subsidiary faults have been incorporated. (b) Upper fringe of the same cross section (vertical scale x2) showing offset of planation surfaces *FES2* and *FES3*.

Geophysical results reported in Section 5, defining three adjacent, NNW-SSE trending elongated domains (A, B, C) suggest the existence of an uplifted block bounded by faults nearly parallel to the Sierra Palomera fault trace. At the southern sector of the study area, local coincidence of the A/B and B/C domain boundaries with La Peñuela and Las Vallejadas faults, respectively, strongly supports such interpretation. The antithetic rupture exposed in La Sima trench, revealed in the landscape by a gentle uphill-facing scarplet across the La Sima alluvial fan (Section 6), unequivocally represents that map-scale antithetic La Peñuela fault and corroborates the extensional character of such structure.

In this way, the results of subsoil exploration by geophysical methods and trench survey, together with structural and morphotectonic data, allow refining the structural model of the central Jiloca graben, beyond the apparently flat appearance of the Sierra Palomera pediment. The synthetic Las Vallejadas fault and the antithetic La Peñuela fault have been incorporated to the geological map of Fig. 2, as well as to a new version of the cross section (Fig. 13a). Furthermore, the latter depicts a reinterpretation of the geometry of the master fault. It is known that the shape of the main fault surface strongly controls the style of accommodation folding and subsidiary faulting in the hanging-wall block of extensional faults. Rollover folds and antithetic faults develop above concave-upward fault bends, whereas drag folds and synthetic faults form above convex-upward fault bends, their propagation being facilitated by high curvature of such fault bends (McClay and Scott, 1991; Xiao and Suppe, 1992; Withjack et al., 1995; Delogkos et al., 2020). In our case, the occurrence of the antithetic and the synthetic inferred subsidiary faults strongly suggests the presence, at a depth of less than 1 km, of a relative flat in the main fault surface (i.e., a double, convex-concave bend), probably located at the Middle-Upper Triassic lutite and evaporite units (Middle Muschelkalk and Keuper facies).

Concerning the along-strike propagation of the Sierra Palomera fault, the slightly bimodal throw vs. distance (T-D) curve depicted in Fig. 7 suggests that it could result from coalescence of two distinct fault segments (although the amplitude of the relative minimum between both maxima, close to the error bar adopted for throw estimations, casts doubt on the significance of this detail). In any case, the overall bell-shape of the T-D curve indicates full linkage along the fault zone. Moreover, the persistence of a bending component beyond both tips of the fault trace reveals that the total length of the Sierra Palomera fault is larger than that exposed at the surface, thus being propagated towards NNW and SSE as a blind fault.

According to Peiro et al. (2020), the overall fault system at the eastern boundary of the Jiloca basin is at a transient stage towards coalescence, and will probably evolve to an along-strike propagation of the master faults through distributed longitudinal fractures. The relay zones between Sierra Palomera, Calamocha and Concud faults, dominated by longitudinal fractures, represent a type of fault relay controlled by both inherited structures and the remote stress field (Peiro et al., 2019, 2020). It strongly contrasts with the classical models reported in the literature (e.g., Peacock and Sanderson, 1994; Young et al., 2001; Fossen and Rotevatn, 2016), in which transverse connecting faults controlled by the own relay kinematics prevail.

Such fault system makes a geometrically and kinematically consistent, genetically related major extensional fault system. The N230°E mean transport direction at the Sierra Palomera fault is similar to those of Concud (N220°E; Lafuente et al., 2014) and Calamocha (W to SW; Martín-Bello et al., 2014). Moreover, all them probably resulted from negative inversion, during the Late Pliocene-Quaternary times, of previous contractive structures developed under the Paleogene-Early Miocene compression (Rubio and Simón, 2007; Lafuente et al., 2011a; Liesa et al., 2021).

8.2. *Morphotectonic approach to assessing recent fault activity within the context of eastern Spain*

In the absence of stratigraphic markers recognized in both fault blocks, the fault throw *s.s.* and the total tectonic throw at the Sierra Palomera graben margin (up to 330 m and 480 m, respectively) have been reasonably estimated from offset of Late Neogene planation surfaces. Nevertheless, uncertainties linked to such geomorphological markers should be highlighted.

Our main geomorphological marker, *FES2*, is poorly represented within the Jiloca bottom, i.e., the hanging-all block of the Sierra Palomera fault, which makes difficult to calculate the actual throw. We interpret that the boundary between Plio-Pleistocene alluvial deposits and the underlying carbonate unit probably represents the position of *FES2* (Fig. 13b), although it also could be correlated with *FES3*. According to the results provided by Ezquerro et al. (2020), such uncertainty introduces a potential error of either 10–40 m in the height of the marker (equivalent to the thickness of Villafranchian palustrine carbonates ≈ M8 megasequence of Ezquerro, 2017), or 0.3 Ma in its age. If the top of the buried carbonate unit would be Early Villafranchian in age (3.5 Ma, therefore correlative of *FES3*): (i) the fault throw *s.s.* and the total tectonic throw calculated in Section 4 (330 m and 480 m, respectively) should be applied to a 3.5 Ma time span, therefore resulting in slightly higher slip rates (0.10 vs. 0.09 mm/a, 0.15 vs. 0.13 mm/a, respectively); (ii) *FES2* would lie 10–40 m lower within the downthrown block, and hence the fault throw *s.s.* and the maximum total tectonic throw could increase up to 370 m and 520 m, respectively, giving rise to

slip rates of 0.10 and 0.15 mm/a for the last 3.8 Ma. In any case, such height uncertainty is of the same order as the unevenness of the planation surfaces themselves, and results in a very small error in slip rate (0.01 mm/a).

The consistency of this interpretation is further reinforced if the whole morphotectonic setting is considered. We have explained how the morphosedimentary *FES2* marker defines a tilted Sierra Palomera-Alfambra block whose edge is tectonically uplifted ca. 300 m relative to the bottom of the Teruel basin. A similar morphostructural outline can be drawn for the Sierra de Albarracín-Jiloca block, in which the *FES2* altitude progressively decreases eastwards, from 1400-1500 m to <1100 m. Therefore, the inference that the fault separating such tilted blocks has a throw in the range of 300–400 m seems well-founded. On the other hand, the notion of recent throw on the Sierra Palomera fault being larger than those on Calamocha and Concud faults (210 and 260 m, respectively; Martín-Bello et al., 2014; Ezquerro et al., 2020) fits a common structural feature of segmented extensional fault zones, in which maximum throws are found in central segments (self-similar pattern as that of individual faults; Cowie and Roberts, 2001). Gracia et al. (2003) aimed to minimize the role of tectonic slip on the Sierra Palomera fault in benefit of erosional lowering in the development of the central Jiloca depression, but that controversy is currently out of place.

We should compare the displacement and slip rates on the Sierra Palomera fault with those in the neighbouring Teruel graben. During the last 3.8 Ma (Late Pliocene-Quaternary extensional phase), fault zones making the eastern margin of the Teruel basin underwent total throw (including bending component) in the range of 440 to 620 m, and hence long-term vertical slip rates of 0.12 to 0.16 mm/a (Ezquerro et al., 2020). Assuming an average dip of 70° for the fault plane and a pure normal movement, the resulting total net slip rates for this period are 0.13 to 0.17 mm/a, similar to that calculated for the Sierra Palomera fault (0.09–0.15 mm/a) and higher than those for the Concud (0.07–0.08 mm/a; Lafuente et al., 2011a), Calamocha (0.06–0.09 mm/a; Martín-Bello et al., 2014), and Teruel (0.075 mm/a; Simón et al., 2017) faults.

It is also pertinent to consider geomorphic indices as auxiliary tools for assessing fault activity (e.g., Bull and McFadden, 1977; McCalpin, 1996; Silva et al., 2003; Burbank and Anderson, 2012), and compare the values obtained for the Sierra Palomera mountain front with those of other faults in the same geodynamic framework. At Sierra Palomera, García-Lacosta (2013) calculated the mountain-front sinuosity (S_{mf} = 1.27), and valley width/height ratio (V_f = 0.22). These values, together with qualitative attributes as trapezoidal facets, V-shaped gullies, and small alluvial fans not connected to the regional fluvial system, indicate 'rapid' fault slip according to the classification by McCalpin (1996), and 'active' (according to Silva et al., 2003) (Fig. 14). The range of slip rates that those authors estimate for such categories in their respective classifications (0.08 to 0.5 mm/a) encloses the value calculated for the Sierra Palomera fault from offset of the *FES2* marker (0.09–0.13 mm/a).

The sinuosity index S_{mf} at the Sierra Palomera mountain front is very similar to those published for the Concud fault (S_{mf} = 1.24; Lafuente et al., 2011b), Maestrat grabens in eastern Iberian Chain (S_{mf} = 1.04–1.60; mean = 1.27; Perea, 2006), or Carboneras, Lorca-Alhama and Baza faults in the Betic Chains (S_{mf} usually ranging from 1.05 to 1.4; Silva et al., 2003; García-Tortosa et al., 2008). The V_f index computed for the Sierra Palomera fault does not differ from that of the Concud fault (V_f = 0.30; Lafuente et al., 2011b), while higher and more variable values have been reported in the Maestrat grabens (Silva et al., 2003; Perea, 2006; García-Tortosa et al., 2008).

Plotting S_{mf} vs. V_f values on the diagram proposed by Silva et al. (2003) allows assessing the relative position of the Sierra Palomera fault among extensional fault-generated mountain fronts of eastern Spain (Fig. 14). The relatively low values of both S_{mf} and V_f indices found at the Sierra Palomera mountain front (1.27 and 0.22, respectively) represent a morphotectonic signal similar to that of the Concud fault, and also consistent with the tendency of extensional faults studied by Silva et al. (2003) in the Valencia area and Betic Chains.

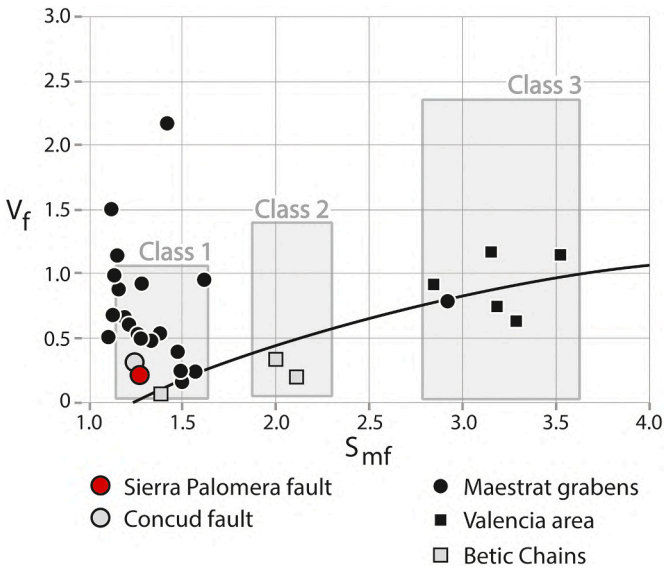

Fig. 14. Plot of S_{mf} (mountain-front sinuosity index) vs. V_f (valley width/height ratio, measured 250 m upstream from the fault trace), showing the relative position of the Sierra Palomera Fault among extensional fault-generated mountain fronts of eastern Spain. For comparison, the S_{mf} -V_f plots for the neighbouring Concud fault (Lafuente et al., 2011b), faults bounding the Maestrat grabens (eastern Iberian Chain; Perea, 2006), and Valencia region and Betic chains (Silva et al., 2003) are also included. Class 1, 2, 3: activity classes (active, moderate and inactive, respectively); the curve represents the tendency for normal faults in SE Spain according to Silva et al. (2003).

8.3. *Pleistocene fault activity and its paleoseismological relevance*

Morphotectonic data indicate that the Sierra Palomera fault has a significant degree of activity, but no outcrop observation on the main trace has unequivocally evidenced Quaternary displacement on it. Therefore, it is very relevant the finding, in La Sima trench, of Pleistocene faults that accommodate extensional deformation associated to the hanging-wall rollover, since they indirectly confirm, for the first time, Pleistocene activity of the Sierra Palomera fault.

As explained in section 6.4, seven deformation events (T to Z) have been recognized after detailed trench analysis, which could be conventionally considered as paleoseismic events according to usual criteria in Paleoseismology. Individual faults activated in each event have been recognized, and slip on them has been quantified (individual net slip in the range of 5 to 115 cm; Table 2). Finally, the overall faulting history has been carefully reconstructed by means of retrodeformational analysis (Fig. 12). Nevertheless, we should critically admit that the meaning of these results in relation to paleoseismicity of the Sierra Palomera fault is very imprecise, since:

(i) Instead of crossing the main fault, the trench only represents a short transect within the hanging-wall block, at a distance of 1.0 km from the fault trace.
(ii) During each event, faults widely distributed along the surveyed transect underwent both synthetic slip with Sierra Palomera fault (downthrown block to the west; positive values in Table 2) and antithetic slip (negative). The algebraic sum of those values does not necessarily have any meaning in relation to the real slip on the main fault.
(iii) The poor quality of OSL results precludes us from having an age model of the exposed sedimentary succession; therefore, the age constraints of the individual events are very limited. Only the last

two events, Y and Z, could be dated to ca. 97 ± 10 ka and 49 ± 5 ka, respectively.

Concerning the net slip accumulated by faults (see Table 2), three among the first four events (T, U and W) involve significant synthetic slip (+45, +105 and + 60 cm, respectively), while the last three ones (X, Y, Z) involve significant antithetic slip (−45, −35 and − 110 cm, respectively). The global aggregate fault slip for the ensemble of deformation events is virtually null (+10 cm). Nevertheless, a total accumulated antithetic throw of 210 cm can be directly measured on the log from offset of the top of unit 6, the youngest sedimentary marker previous to the recorded faulting episodes (compare the first and the last picture in Fig. 12). Consequently, that resulting throw should be entirely attributed to the bending monocline (i.e., accommodated in the form of continuous deformation, not computed within fault slip measurements depicted in Table 2). That value reasonably approaches the apparent vertical offset of the natural slope of La Sima alluvial fan (ca. 2.5 m; Fig. 10c). In summary, the morphological expression (up-facing scarplet) of the fault zone exposed in the trench fits well the antithetic sign of the accumulated slip during the youngest faulting episodes.

These youngest, antithetic faulting events (X, Y and Z) have associated net slip values (−35 to −110 cm) that should be accommodated on faults several km long (in the range of 10 to 40 km, according to the empirical relationships proposed by Wells and Coppersmith, 1994). This inference plays in favour of: (i) the interpretation of the antithetic fault exposed at La Sima trench as a large structure, comparable in length to the Sierra Palomera fault itself, as the macrostructural and geophysical data suggested (see Sections 5, 6 and 8.1); (ii) the notion that faulting events recorded at the trench, in particular those dated to ca. 97 ± 10 ka and 49 ± 5 ka, should respond to coseismic events on the main fault.

Could the timing of those younger events be taken as a reference for approaching seismic recurrence periods and slip rates of the Sierra Palomera fault during Pleistocene times? The tempting hypothesis that the two aforementioned ages correspond to the last two major paleoearthquakes would suggest a single interseismic period of around 48 ka. According to Villamor and Berryman (1999), this would be reliable for faults showing average slip rate around 0.1 mm/a, as the Sierra Palomera fault does. Nevertheless, the space and time window examined in our trench is too narrow for providing a representative paleoseismological record. Subsidiary faults similar to those exposed at La Sima could have form at other sites within the hanging-wall block in response to other events on the main fault. Furthermore, each event on this main fault did not necessarily reactivate the antithetic fault exposed at La Sima trench. Accordingly, the actual slip rate on the Sierra Palomera fault during Late Pleistocene times could be significantly higher than the long-term one (0.09–0.15 mm/a since mid-Pliocene times; see Sections 8.1 and 8.2), following the same tendency found in other active structures of the region, such as the Concud fault (Lafuente et al., 2014; Simón et al., 2016), Teruel fault (Simón et al., 2017), Teruel basin (Ezquerro et al., 2020; see Section 2) and Calatayud basin (Peiro and Simón, 2021).

8.4. *Internal deformation of the hanging-wall fault block: a close look from trench analysis*

Although the succession of deformation events identified at La Sima trench have a very limited paleoseismic meaning, it allows understanding progressive stretching within the hanging-wall block of the Sierra Palomera fault. In particular, sequential activation of synthetic and antithetic individual faults has been carefully reconstructed by means of retrodeformational analysis (Fig. 12) and can be precisely compared with faulting patterns linked to rollover deformation at both smaller and larger scales (analogue models and field or seismic-profile examples, respectively).

Usually, the hanging-wall rollover geometry is not entirely achieved through ductile deformation. Examples from analogue models (e.g., Withjack and Schlische, 2006), outcrops and high-resolution seismic profiles (e.g., Song and Cawood, 2001; Delogkos et al., 2020) indicate that a portion of deformation is accommodated by smaller-scale faults. Antithetic faults directly materialize the antithetic simple shear that nucleates at the transition from the main ramp to the basal detachment (Withjack et al., 1995), frequently abutting the connection line between the steep and flat segments of the main fault surface (Bruce, 1973; Song and Cawood, 2001; Withjack and Schlische, 2006). In addition, together with subsidiary synthetic faults, they can accommodate layer-parallel extension along the rollover, giving rise to crestal collapse grabens in both analogue models (e.g., McClay, 1990; McClay and Scott, 1991; Buchanan and McClay, 1991; Soto et al., 2007) and field examples (e.g., Imber et al., 2003; Back and Morley, 2016; Fazli Khani et al., 2017). The locus of active hanging-wall antithetic faulting, as well as that of crestal graben formation, have the appearance of having migrated landwards during development of extensional systems: each individual antithetic fault moves passively beyond the fault bend and becomes inactive, while a new fault propagating from the same bend replaces it. Thus, secondary faults tend to be progressively older basinwards (Christiansen, 1983; McClay, 1990; Withjack et al., 1995; Withjack and Schlische, 2006). In any case, periods of activity of the hanging-wall growth faults can overlap (Imber et al., 2003). The great majority of analogue models of rollovers show a faulting sequence that begins with an antithetic fault, then alternating synthetic and antithetic ones eventually joining and reciprocally offsetting at depth (McClay, 1990; McClay et al., 1991; T. Román-Berdiel, personal communication). The same pattern has been reported in actual examples (e.g., Fazli Khani and Back, 2015, Fig. 10). Nevertheless, sandbox experiments have also been described in which alternating activation of synthetic and antithetic faults is initiated with a synthetic one (e.g., Buchanan and McClay, 1991).

The fault sequence interpreted at La Sima trench share some of the former evolutionary patterns typical of rollover deformation, such as the relevance and persistence of a subsidiary antithetic fault, the activation of younger antithetic ruptures closer to the main fault, and overall alternating onset of synthetic and antithetic ruptures. However, we have also found a non-typical feature: the oldest recorded meso-scale faults are synthetic with the Sierra Palomera fault, despite having formed in the same area where the persistent antithetic fault will later appear. The first deformational events (T to W) mainly involve accumulation of significant synthetic net slip (+200 cm), while the last three ones (X, Y, Z) involve substantial antithetic net slip (−190 cm). Briefly, progressive deformation in the hanging-wall block is shifted from dominantly synthetic faulting to dominantly antithetic faulting. Such particular deformation pattern suggests the existence of other controls on the hanging-wall deformation in addition to the rollover kinematics itself, as discussed in the next section.

Finally, the accumulated net slip has an associated component of horizontal extension that enables a further quantitative kinematical approach (see Table 2). The total extension recorded at La Sima trench is ≈310 cm, which represents about 19% of the restored length of the logged transect (local β factor = 1.19). Horizontal extension accommodated by faults totalizes ca. 210 cm (125 cm by synthetic ones and 86 cm by antithetic ones). Development of the bending monocline involves additional extension of about 100 cm.

Overall considered, our results represent a high-resolution, subseismic-scale picture of hanging-wall deformation that complements natural case studies based on seismic profiles and 'fills the gap' with the scale of laboratory analogue models. It documents both (i) earlier stages of a process of hanging-wall deformation (those mostly governed by synthetic faulting) that usually are not recognized from seismic reflection data, and (ii) later stages governed by antithetic faulting that better correlate with seismic-reflection-based models.

8.5. Kinematic and dynamic controls on deformation of the hanging-wall block: relevance of the tectonic stress framework

It is not easy to discriminate whether faults propagated through the hanging-wall block are kinematically or dynamically controlled, i.e., they essentially accommodate extensional deformation associated to the rollover monocline, or they are directly linked to regional stress. Geometry and kinematics of faults surveyed at both map and trench scales overall fits the expected deformation within the hanging-wall block of the Sierra Palomera fault. But they are also consistent with the regional extensional stress field, whose σ_3 trajectories trend EN*E*-WSW (Simón, 1982, 1989; Arlegui et al., 2005, 2006; Liesa et al., 2019), orthogonal to the overall trend of the Jiloca graben, and only slightly oblique to the Sierra Palomera fault trace itself. Stress inversion from the most representative, non-rotated conjugate faults measured within the trench, according to Anderson (1951), provides local stress axes matching those regional trajectories (Fig. 15).

The extension direction expectable for the kinematical scenario could be constrained between N065°E (orthogonal to the average strike of the Sierra Palomera fault; an inherited feature indeed) and N050°E (transport direction). The extension trend expectable for the dynamical scenario would approach N075°E (seeing at the average trend of the Jiloca graben), or would range from N055°E to N080°E (seeing at paleostress results reported by Arlegui et al., 2005, and Liesa et al., 2019). The similarity between both inferences prevents us from discriminating among those hypothetical controls based solely on the orientation of structures (stereoplots of Fig. 11 show how the strongly clustered directions of normal faults in La Sima trench fit equally well the two scenarios). Nevertheless, some details of the faulting succession suggest that both controls probably coexist. The kinematical control has been attested and discussed in Sections 8.1 and 8.5. The dynamical one could explain the occurrence of early synthetic meso-scale faults (an unusual feature in kinematically-driven models) at La Sima site.

Additionally, there also seems to be a certain degree of control by a recent ESE-WNW extension direction. Both E-W to ESE-WNW, and ENE-WSW extension directions (characterizing the Late Miocene-Early Pliocene and the Plio-Quaternary rift episodes, respectively) are recorded during the entire extensional period indeed (Liesa et al., 2019). This suggests stress partitioning (in the sense of Simón et al., 2008) of the composite extensional field that results from combination of intraplate NNW-SSE compression (Africa-Iberia convergence) and WNW-ESE extension (rifting of the Valencia trough) (Simón, 1989; Herraiz et al., 2000; Capote et al., 2002). Among fractures observed at La Sima trench that do not show any sign of displacement, a minority NNE-SSW trending set can be distinguished (Fig. 11f), which records the WNW-ESE extensional component of the regional, locally and episodically partitioned stress field.

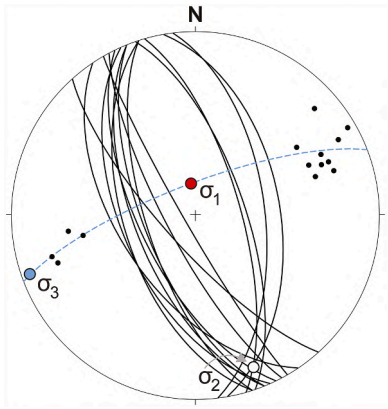

Fig. 15. Interpretation of paleostress axes from orientation of non-rotated, conjugate fault planes measured within La Sima trench. Stress inversion based on model by Anderson (1951).

9. Conclusions

The NNW-SSE trending, 26 km long Sierra Palomera extensional fault has been active during Late Pliocene-Quaternary times. It has undergone nearly pure normal movement with mean transport direction towards N230°E, consistent with the ENE-WSW extension trajectories of the recent to present-day regional stress field.

The hanging-wall block of the Sierra Palomera fault is cut by two subsidiary parallel ruptures: (i) the synthetic Las Vallejadas fault, located at about 1.5 km basinwards, and (ii) the antithetic La Peñuela fault, at a distance of 0.7–1.0 km, which apparently offsets ca. 2.5 m the surface of the La Sima alluvial fan giving rise to a gentle uphill-facing scarplet.

In the absence of recent stratigraphic markers, the *FES2* planation surface (3.8 Ma) has allowed calculating a maximum value of 330 ± 40 m for the fault throw *s.s.*, and ca. 480 ± 40 m for the total tectonic throw at the half-graben margin (including the bending component), resulting in a net slip rate of 0.09 – 0.10 mm/a (0.13–0.15 mm/a including bending).

Results from La Sima trench have demonstrated the existence of the antithetic La Peñuela fault, accompanied by a number of minor synthetic and antithetic ones, and its activity during Middle-Late Pleistocene times. Their detailed kinematical analysis has allowed building an evolutionary model made of seven deformation events. Net slip on individual faults ranges from 5 to 115 cm. The cumulative antithetic throw at the exposed fault zone, including fault slip *s.s.* and bending, is estimated at 210 cm, which reasonably approaches the apparent offset of the natural slope of La Sima alluvial fan.

The significance of the paleoseismic results is certainly limited. The surveyed trench within the hanging-wall block does not cross the main fault itself. In addition, it was not feasible to achieve a consistent age model for the entire sedimentary sequence; only the last two deformation events have been dated to ca. 97 ± 10 ka and 49 ± 5 ka, respectively. Nevertheless, Pleistocene activity of the Sierra Palomera fault has been proved for the first time, although indirectly from hanging-wall deformation.

The succession of faulting events at La Sima trench study allows unravelling the progressive extensional deformation within the hanging-wall block of the Sierra Palomera fault. The total horizontal extension recorded at La Sima trench is ≈310 cm (local β factor = 1.19). The faulting succession indicates that synthetic slip prevailing in early deformation events was shifted to antithetic slip during the younger ones. Geometry and sequential development of meso-scale faults suggest the concurrence of: (1) a kinematic control, i.e., antithetic simple shear linked to rollover kinematics (mostly resulting in the main antithetic fault zone), eventually accompanied by layer-parallel extension orthogonal to the rollover axis, and (2) a dynamic control, i.e., response to the remote extensional stress field, characterized by ENE-WSW (occasionally ESE-WSW) extension trajectories.

CRediT authorship contribution statement

A. Peiro: Methodology, Formal analysis, Investigation, Writing – original draft, Visualization. **J.L. Simón:** Conceptualization, Validation, Investigation, Writing – original draft, Supervision. **L.E. Arlegui:** Investigation, Visualization. **L. Ezquerro:** Validation, Investigation. **A.I. García-Lacosta:** Formal analysis, Investigation, Visualization. **M.T. Lamelas:** Formal analysis, Investigation, Visualization. **C.L. Liesa:** Validation, Investigation, Writing – review & editing. **A. Luzón:** Validation, Investigation, Writing – original draft. **L. Martín-Bello:** Investigation. **Ó. Pueyo-Anchuela:** Investigation, Methodology, Formal analysis, Writing – original draft. **N. Russo:** Investigation, Visualization.

Declaration of Competing Interest

The authors declare that they have no known competing financial

interests or personal relationships that could have appeared to influence the work reported in this paper.

Acknowledgments

The research has been financed by projects LMP127_18 (Gobierno de Aragón-Programa Operativo del Fondo Europeo de Desarrollo Regional Aragón 2014-2020), and PID2019-108705-GB-I00 of the Agencia Estatal de Investigación (AEI/10.13039/501100011033) of the Spanish Government. This work is a contribution of the Geotransfer Research Group (E32_20R) funded by the Regional Aragón Government. A. Peiro benefits from an FPU contract (FPU17/02470) of the Spanish Government. We thank G. Brook (Luminiscence Dating Laboratory of University of Georgia, USA), and P. Beneítez (Laboratorio de Datación y Radioquímica of the Universidad Autónoma de Madrid, Spain) for OSL dating. A. Medialdea advised us on issues related to OSL dating, and T. Román-Berdiel helped us comparing the results with analogue models. Finally, we sincerely thank the thorough reviews and valuable comments of Hamed Fazli Khani and an anonymous reviewer, which have greatly improved the paper.

References

Alcalá, L., Alonso-Zarza, A.M., Álvarez, M.A., Azanza, B., Calvo, J.P., Cañaveras, J.C., van Dam, J.A., Garcés, M., Krijgsman, W., van der Meulen, A.J., Morales, J., Peláez, P., Pérez-González, A., Sánchez, S., Sancho, R., Sanz, E., 2000. El registro sedimentario y faunístico de las cuencas de Calatayud-Daroca y Teruel. Evolución paleoambiental y paleoclimática durante el Neógeno. Rev. Soc. Geol. Esp. 13, 323–343.

Allmendinger, R.W., Cardozo, N., Fisher, D., 2012. Structural Geology Algorithms: Vectors and Tensors in Structural Geology. Cambridge University Press.

Álvaro, M., Capote, R., Vegas, R., 1979. Un modelo de evolución geotectónica para la Cadena Celtibérica. Acta Geol. Hisp. 14, 172–177.

Anadón, P., Moissenet, E., 1996. Neogene basins in the Eastern Iberian Range. In: Friend, P.F., Dabrio, C.F. (Eds.), Tertiary Basins of Spain. The Stratigraphic Record of Crustal Kinematics. World and Regional Geology Series 6. Cambridge University press, Cambridge, pp. 68–76.

Anderson, E.M., 1951. The Dynamics of Faulting and Dyke Formation with Application to Britain. Oliver & Boyd, Edinburgh.

Arlegui, L.E., Simón, J.L., Lisle, R.J., Orife, T., 2005. Late Pliocene-Pleistocene stress field in the Teruel and Jiloca grabens (eastern Spain): contribution of a new method of stress inversion. J. Struct. Geol. 27, 693–705. https://doi.org/10.1016/j.jsg.2004.10.013.

Arlegui, L.E., Simón, J.L., Lisle, R.J., Orife, T., 2006. Analysis of non-striated faults in a recent extensional setting: the Plio-Pleistocene Concud fault (Jiloca graben, eastern Spain). J. Struct. Geol. 28, 1019–1027. https://doi.org/10.1016/j.jsg.2006.03.009.

Back, S., Morley, C.K., 2016. Growth faults above shale–Seismic-scale outcrop analogues from the Makran foreland, SW Pakistan. Mar. Pet. Geol. 70, 144–162. https://doi.org/10.1016/j.marpetgeo.2015.11.008.

Bruce, C.H., 1973. Pressured shale and related sediment deformation: mechanism for development of regional contemporaneous faults. AAPG Bull. 57, 878–886. https://doi.org/10.1306/819A4352-16C5-11D7-8645000102C1865D.

Buchanan, P.G., McClay, K.R., 1991. Sandbox experiments of inverted listric and planar fault systems. Tectonophysics 188, 97–115. https://doi.org/10.1016/0040-1951(91)90317-L.

Bull, W.B., McFadden, L.D., 1977. Tectonic Geomorphology north and south of the Garlock fault California. In: Doehring, D.O. (Ed.), Geomorphology in Arid Regions. Allen & Unwin, London, pp. 115–138.

Burbank, D.W., Anderson, R.S., 2012. Tectonic Geomorphology. Wiley-Blackwell, Oxford.

Capote, R., Muñoz, J.A., Simón, J.L., Liesa, C.L., Arlegui, L.E., 2002. Alpine tectonics I: The Alpine system north of the Betic Cordillera. In: Gibbons, W., Moreno, T. (Eds.), Geology of Spain. The Geological Society, London, pp. 367–400.

Cardozo, N., Allmendinger, R.W., 2013. Spherical projections with OSXStereonet. Comput. Geosci. 51, 193–205. https://doi.org/10.1016/j.cageo.2012.07.021.

Christiansen, A.F., 1983. An example of a major syndepositional listric fault. In: Bally, A.W. (Ed.), Seismic Expression of Structural Styles. AAPG Studies in Geology, 15, pp. 36–40 (2.3.1).

Colomer, M., Santanach, P., 1988. Estructura y evolución del borde sur-occidental de la Fosa de Calatayud-Daroca. Geogaceta 4, 29–31.

Cortés, A.L., 1999. Evolución tectónica reciente de la Cordillera Ibérica, Cuenca del Ebro y Pirineo centro-occidental. Unpublished PhD thesis. Univ. Zaragoza.

Cortés, A.L., Casas, A.M., 2000. ¿Tiene el sistema de fosas de Teruel origen extensional? Rev. Soc. Geol. Esp. 13 (3-4), 445–470.

Cowie, P., Roberts, G.P., 2001. Constraining slip rates and spacings for active normal faults. J. Struct. Geol. 23, 1901–1915. https://doi.org/10.1016/S0191-8141(01)00036-0.

Delogkos, E., Saqab, M.M., Walsh, J.J., Roche, V., Childs, C., 2020. Throw variations and strain partitioning associated with fault-bend folding along normal faults. Solid Earth 11, 935–945. https://doi.org/10.5194/se-11-935-2020.

Ezquerro, L., 2017. El sector norte de la cuenca neógena de Teruel: tectónica, clima y sedimentación. PhD thesis. Univ. Zaragoza. http://zaguan.unizar.es/record/77098#.

Ezquerro, L., Simón, J.L., Luzón, A., Liesa, C.L., 2019. Alluvial sedimentation and tectono-stratigraphic evolution in a narrow extensional zigzag basin margin (northern Teruel Basin, Spain). J. Palaeogeogr. 8, 1–25. https://doi.org/10.1186/s42501-019-0044-4.

Ezquerro, L., Simón, J.L., Luzón, A., Liesa, C.L., 2020. Segmentation and increasing activity in the Neogene-Quaternary Teruel Basin rift (Spain) revealed by morphotectonic approach. J. Struct. Geol. 135, 104043. https://doi.org/10.1016/j.jsg.2020.104403.

Fazli Khani, H., Back, S., 2015. The influence of pre-existing structure on the growth of syn-sedimentary normal faults in a deltaic setting, Niger Delta. J. Struct. Geol. 73, 18–32. https://doi.org/10.1016/j.jsg.2015.01.011.

Fazli Khani, H., Back, S., Kukla, P.A., Fossen, H., 2017. Interaction between gravity-driven listric normal fault linkage and their hanging-wall rollover development: a case study from the western Niger Delta, Nigeria. Geol. Soc. Lond., Spec. Publ. 439 (1), 169–186. https://doi.org/10.1144/SP439.20.

Fossen, H., Rotevatn, A., 2016. Fault linkage and relay structures in extensional settings-A review. Earth Sci. Rev. 154, 14–28. https://doi.org/10.1016/j.earscirev.2015.11.014.

García-Lacosta, A.I., 2013. La falla de Sierra Palomera: evolución estructural y actividad reciente. Unpublished MSc thesis. Univ. Zaragoza.

García-Tortosa, F.J., Sanz de Galdeano, C., Sánchez-Gómez, M., Alfaro, P., 2008. Geomorphologic evidence of the active Baza Fault (Betic Cordillera, South Spain). Geomorphology 97, 374–391. https://doi.org/10.1016/j.geomorph.2007.08.007.

Gracia, F.J., Gutiérrez, F., Gutiérrez, M., 2003. The Jiloca karst polje-tectonic graben (Iberian Range, NE Spain). Geomorphology 52, 215–231. https://doi.org/10.1016/S0169-555X(02)00257-X.

Granier, T., 1985. Origin, damping, and pattern of development of faults in granite. Tectonics 4, 721–737. https://doi.org/10.1029/TC004i007p00721.

Guimerà, J., Alvaro, M., 1990. Structure et evolution de la compression alpine dans la Chaine Cotiere Catalane (Espagne). Bulletin Société Géologique France 8, 339–348. https://doi.org/10.2113/gssgfbull.VI.2.339.

Gutiérrez, M., Gracia, F.J., 1997. Environmental interpretation and evolution of the Tertiary erosion surfaces in the Iberian Range (Spain). In: Widdowson, M. (Ed.), Palaeosurfaces: Recognition, Reconstruction and Palaeoenvironmental Interpretation, 120. Geological Society. London, Special Publications, pp. 147–158.

Gutiérrez, M., Peña, J.L., 1976. Glacis y terrazas en el curso medio del río Alfambra (provincia de Teruel). Bol. Geol. Min. 87, 561–570.

Gutiérrez, F., Gutiérrez, M., Gracia, F.J., McCalpin, J.P., Lucha, P., Guerrero, J., 2008. Plio-Quaternary extensional seismotectonics and drainage network development in the central sector of the Iberian Range (NE Spain). Geomorphology 102, 21–42. https://doi.org/10.1016/j.geomorph.2007.07.020.

Gutiérrez, F., Masana, E., González, Á., Lucha, P., Guerrero, J., McCalpin, J.P., 2009. Late Quaternary paleoseismic evidence on the Munébrega half-graben fault (Iberian Range, Spain). Int. J. Earth Sci. 98, 1691–1703. https://doi.org/10.1007/s00531-008-0319-y.

Gutiérrez, F., Gracia, F.J., Gutiérrez, M., Lucha, P., Guerrero, J., Carbonel, D., Galve, J.P., 2012. A review on Quaternary tectonic and nontectonic faults in the central sector of the Iberian Chain, NE Spain. J. Iber. Geol. 38, 145–160. https://doi.org/10.5209/revJIGE.2012.v38.n1.39210.

Gutiérrez, F., Carbonel, D., Sevil, J., Moreno, D., Linares, R., Comas, X., Zarroca, M., Roqué, C., McCalpin, J.P., 2020. Neotectonics and late Holocene paleoseismic evidence in the Plio-Quaternary Daroca Half-graben, Iberian Chain, NE Spain. Implications for fault source characterization. J. Struct. Geol. 131, 103933. https://doi.org/10.1016/j.jsg.2019.103933.

Herraiz, M., De Vicente, G., Lindo, R., Giner, J., Simón, J.L., González, J.M., Vadillo, O., Rodríguez, M.A., Cicuéndez, J.I., Casas, A., Rincón, P., Cortés, A.L., Lucini, M., 2000. The recent (Upper Miocene to Quaternary) and present tectonics stress distributions in the Iberian Peninsula. Tectonics 19, 762–786. https://doi.org/10.1029/2000TC900006.

IGN, 2021. Catálogo de terremotos. https://www.ign.es/web/ign/portal/sis-catalogo-terremotos (accessed August 2021).

Imber, J., Childs, C., Nell, P.A.R., Walsh, J.J., Hodgetts, D., Flint, S., 2003. Hanging wall fault kinematics and footwall collapse in listric growth fault systems. J. Struct. Geol. 25 (2), 197–208. https://doi.org/10.1016/S0191-8141(02)00034-2.

Lafuente, P., 2011. Tectónica activa y paleosismicidad de la falla de Concud (Cordillera Ibérica central). Unpublished PhD thesis. Univ. Zaragoza.

Lafuente, P., Arlegui, L.E., Liesa, C.L., Simón, J.L., 2011a. Paleoseismological analysis of an intraplate extensional structure: the Concud fault (Iberian Chain, Eastern Spain). Int. J. Earth Sci. 100, 1713–1732. https://doi.org/10.1007/s00531-010-0542-1.

Lafuente, P., Lamelas, T., Simón, J.L., Soriano, M.A., 2011b. Comparing geomorphic and geologic indices of activity in an intraplate extensional structure: the Concud fault (central Iberian Chain, Spain). Geodin. Acta 24, 107–122. https://doi.org/10.1007/S00531-010-0542-1.

Lafuente, P., Arlegui, L.E., Liesa, C.L., Pueyo, O., Simón, J.L., 2014. Spatial and temporal variation of paleoseismic activity at an intraplate, historically quiescent structure: the Concud fault (Iberian Chain, Spain). Tectonophysics 632, 167–187. https://doi.org/10.1016/j.tecto.2014.06.012.

Liesa, C.L., 2011. Evolución de campos de esfuerzos en la Sierra del Pobo (Cordillera Ibérica, España). Rev. Soc. Geol. Esp. 24, 49–68.

Liesa, C.L., Simón, J.L., Casas, A.M., 2018. La tectónica de inversión en una región intraplaca: La Cordillera Ibérica. Rev. Soc. Geol. Esp. 31, 23–50.
Liesa, C.L., Simon, J.L., Ezquerro, L., Arlegui, L.E., Luzón, A., 2019. Stress evolution and structural inheritance controlling an intracontinental extensional basin: The central-northern sector of the Neogene Teruel Basin. J. Struct. Geol. 118, 362–376. https://doi.org/10.1016/j.jsg.2018.11.011.
Liesa, C.L., Corral, M.B., Arlegui, L.A., Peiro, A., Simón, J.L., 2021. Inversión tectónica negativa y estructuración de la zona de relevo entre las fallas normales plio-cuaternarias de Calamocha y Daroca. X Congreso de Geología de España, Sociedad Geológica de España, Vitoria, Spain.
Martín-Bello, L., Arlegui, L.E., Ezquerro, L., Liesa, C.L., Simón, J.L., 2014. La falla de Calamocha (fosa del Jiloca, Cordillera Ibérica): Estructura y actividad pleistocena. In: Álvarez-Gomez, J.A., Martín González, F. (Eds.), Una aproximación multidisciplinar al estudio de las fallas activas, los terremotos y el riesgo sísmico. Segunda reunión ibérica sobre fallas activas y paleosismología, Lorca, (Murcia, España), pp. 55–85.
McCalpin, J.P., 1996. Paleoseismology. Academic Press, San Diego.
McClay, K.R., 1990. Extensional fault systems in sedimentary basins: a review of analogue model studies. Mar. Pet. Geol. 7, 206–233. https://doi.org/10.1016/0264-8172(90)90001-W.
McClay, K.R., Scott, A.D., 1991. Experimental models of hangingwall deformation in ramp-flat listric extensional fault systems. Tectonophysics 188, 85–96. https://doi.org/10.1016/0040-1951(91)90316-K.
McClay, K.R., Waltham, D.A., Scott, A.D., Abousetta, A., 1991. Physical and seismic modelling of listric normal fault geometries. Geol. Soc. Lond., Spec. Publ. 56, 231–239. https://doi.org/10.1144/GSL.SP.1991.056.01.16.
Moissenet, E., 1983. Aspectos de la Neotectónica en la fosa de Teruel. In: Comba, J.A. (Ed.), Geología de España. Libro Jubilar J.M. Ríos. 2. IGME, Madrid, pp. 427–446.
Pailhé, P., 1984. La Chaîne Ibérique Orientale. Étude géomorphologique. PhD thesis. Univ. Bordeaux.
Peacock, D.C.P., Sanderson, D.J., 1994. Geometry and development of relay ramps in normal fault systems. Bull. Am. Ass. Petrol. Geol. 78, 147–165. https://doi.org/10.1306/BDFF9046-1718-11D7-8645000102C1865D.
Peiro, A., Simón, J.L., 2021. The Río Grío-Pancrudo Fault Zone (central Iberian Chain, Spain): recent extensional activity revealed by drainage reversal. Geol. Mag. 159 (1), 21–36. https://doi.org/10.1017/S0016756821000790.
Peiro, A., Simón, J.L., Román-Berdiel, T., 2019. Zonas de relevo de falla en el margen oriental de la fosa del Jiloca (Cordillera Ibérica): geometría, cinemática y modelización analógica. Bol. Geol. Min. 130 (3), 393–416. https://doi.org/10.21701/bolgeomin.130.3.002.
Peiro, A., Simón, J.L., Román-Berdiel, T., 2020. Fault relay zones evolving through distributed longitudinal fractures: the case of the Teruel graben system (Iberian Chain, Spain). J. Struct. Geol. 131, 103942. https://doi.org/10.1016/j.jsg.2019.103942.
Peña, J.L., Gutiérrez, M., Ibáñez, M., Lozano, M.V., Rodríguez, J., Sánchez, M., Simón, J.L., Soriano, M.A., Yetano, L.M., 1984. Geomorfología de la provincia de Teruel. Instituto de Estudios Turolenses, Teruel.
Perea, H., 2006. Falles actives i perillositat sísmica al marge nord-occidental del solc de Valencia. Unpublished PhD thesis. Univ. Barcelona.
Pueyo, Ó., Lafuente, P., Arlegui, L.E., Liesa, C.L., Simón, J.L., 2016. Geophysical characterization of buried active faults: the Concud Fault (Iberian Chain, NE Spain). Int. J. Earth Sci. 105, 2221–2239. https://doi.org/10.1007/s00531-015-1283-y.
Rubio, J.C., 2004. Los humedales del Alto Jiloca: estudio hidrogeológico e histórico-arqueológico. Unpublished PhD thesis. Univ. Zaragoza.
Rubio, J.C., Simón, J.L., 2007. Tectonic subsidence vs. erosional lowering in a controversial intramontane depression: the Jiloca basin (Iberian Chain, Spain). Geol. Mag. 144, 1–15. https://doi.org/10.1017/S0016756806002949.
Rubio, J.C., Simón, J.L., Soriano, A., 2007. Interacting tectonics, hydrogeology and karst processes in an intramontane basin: the Jiloca graben (NE Spain). Hydrol. J. 15, 1565–1576. https://doi.org/10.1007/s10040-007-0190-0.
Sánchez-Fabre, M., Peña-Monné, J.L., Sampietro-Vattuone, M.M., 2019. Geomorphology of the northern sector of the Alfambra-Teruel depression (Iberian ranges, NE Spain). J. Map 15, 112–121. https://doi.org/10.1080/17445647.2018.1551157.
Silva, P.G., Goy, J.L., Zazo, C., Bardají, T., 2003. Fault-generated mountain fronts in southeast Spain: geomorphologic assessment of tectonic and seismic activity. Geomorphology 50, 203–225. https://doi.org/10.1016/S0169-555X(02)00215-5.
Simón, J.L., 1982. Compresión y distensión alpinas en la Cadena Ibérica oriental. PhD thesis. Universidad de Zaragoza. Instituto de Estudios Turolenses, Teruel.
Simón, J.L., 1983. Tectónica y neotectónica del sistema de fosas de Teruel. Teruel 69, 21–97.
Simón, J.L., 1989. Late Cenozoic stress field and fracturing in the Iberian Chain and Ebro Basin (Spain). J. Struct. Geol. 11, 285–294. https://doi.org/10.1016/0191-8141(89)90068-0.
Simón, J.L., Arlegui, L.E., Lafuente, P., Liesa, C.L., 2012. Active extensional faults in the central-eastern Iberian Chain, Spain. J. Iber. Geol. 38, 127–144. https://doi.org/10.5209/rev_JIGE.2012.v38.n1.39209.
Simón, J.L., Arlegui, L.E., Ezquerro, L., Lafuente, P., Liesa, C.L., Luzón, A., 2016. Enhanced palaeoseismic succession at the Concud Fault (Iberian Chain, Spain): new insights for seismic hazard assessment. Nat. Hazards 80, 1967–1993. https://doi.org/10.1007/s11069-015-2054-6.
Simón, J.L., Arlegui, L.E., Ezquerro, L., Lafuente, P., Liesa, C.L., Luzón, A., 2017. Assessing interaction of active extensional faults from structural and paleoseismological analysis: The Teruel and Concud faults (eastern Spain). J. Struct. Geol. 103, 100–119. https://doi.org/10.1016/j.jsg.2017.08.003.
Simón, J.L., Ezquerro, L., Arlegui, L.E., Liesa, C.L., Luzón, A., Medialdea, A., García, A., Zarazaga, D., 2019. Role of transverse structures in paleoseismicity and drainage rearrangement in rift systems: the case of the Valdecebro fault zone (Teruel graben, eastern Spain). Int. J. Earth Sci. 108, 1429–1449. https://doi.org/10.1007/s00531-019-01707-9.
Simón, J.L., Arlegui, L.E., Liesa, C.L., 2008. Stress partitioning: a practical concept for analysing boundary conditions of brittle deformation. Geodin. Acta. 53, 1057–1065.
Simón, J.L., Casas-Sainz, A.M., Gil-Imaz, A., 2021. Controversial epiglyptic thrust sheets: the case of the Daroca Thrust (Iberian Chain, Spain). J. Struct. Geol. 145, 104298. https://doi.org/10.1016/j.jsg.2021.104298.
Simón-Porcar, G., Simón, J.L., Liesa, C.L., 2019. La cuenca neógena extensional de El Pobo (Teruel, Cordillera Ibérica): sedimentología, estructura y relación con la evolución del relieve. Rev. Soc. Geol. Esp. 32, 17–42.
Song, T., Cawood, P.A., 2001. Effects of subsidiary faults on the geometric construction of listric normal fault systems. AAPG Bull. 85 (2), 221–232. https://doi.org/10.1306/8626C7A3-173B-11D7-8645000102C1865D.
Soto, R., Casas-Sainz, A.M., Del Río, P., 2007. Geometry of half-grabens containing a mid-level viscous décollement. Basin Res. 19 (3), 437–450. https://doi.org/10.1111/j.1365-2117.2007.00328.x.
Vegas, R., Fontboté, J.M., Banda, E., 1979. Widespread neogene rifting superimposed on alpine regions of the Iberian Peninsula. In: Proceedings Symposium Evolution and Tectonics of the Western Mediterranean and Surrounding Areas, EGS, Viena. Instituto Geográfico Nacional, Madrid, Special Publication, 201, pp. 109–128.
Villamor, P., Berryman, K.R., 1999. La tasa de desplazamiento de una falla como aproximación de primer orden en las estimaciones de peligrosidad sísmica. I Congreso Nacional de Ingeniería Sísmica, Asociación Española de Ingeniería Sísmica, pp. 153–163.
Wells, D.L., Coppersmith, K.J., 1994. New empirical relationships among magnitude, rupture length, rupture width, rupture area, and surface displacement. Bull. Seismol. Soc. Am. 84, 974–1002.
Withjack, M.O., Schlische, R.W., 2006. Geometric and experimental models of extensional fault-bend folds. Geol. Soc. Lond., Spec. Publ. 253 (1), 285–305.
Withjack, M.O., Islam, Q.T., La Pointe, P.R., 1995. Normal faults and their hanging-wall deformation: an experimental study. AAPG Bull. 79, 1–18. https://doi.org/10.1144/GSL.SP.2006.253.01.15.
Xiao, H., Suppe, J., 1992. Origin of Rollover. Am. Assoc. Pet. Geol. Bull. 76, 509–529.
Young, M.J., Gawthorpe, R.L., Hardy, S., 2001. Growth and linkage of a segmented normal fault zone; the Late Jurassic Murchison-Statfjord North Fault, northern North Sea. J. Struct. Geol. 23, 1933–1952. https://doi.org/10.1016/S0191-8141(01)00038-4.


V

CAPÍTULO V.

REVISIÓN DE OTRAS FALLAS ACTIVAS Y RECIENTES

Resumen:

La sección V pretende completar la información nueva aportada en esta tesis con la del resto de fallas de la Cordillera Ibérica centro-oriental descritas por otros autores. Casi todas han sido analizadas en la literatura desde el punto de vista estructural, morfotectónico y paleosismológico. Se comienza sintetizando las características de las fallas asociadas al margen suroeste de la cuenca de Calatayud: fallas de Munébrega y Daroca. Respecto a esta última, también se profundiza en la publicación sobre la memoria social y geológica de su posible último terremoto, el de Used de 1953. Después se continúa con las fallas que limitan la fosa del Jiloca por el sur y su intersección con el sector norte de la cuenca de Teruel: fallas de Concud (con el registro paleosismológico más completo de todas), Teruel y Valdecebro. También en la cuenca de Teruel, se recopila la información estructural y morfotectónica de las zonas de falla de El Pobo, Peralejos-Tortajada-Cabigordo y La Hita. Para acabar con el sistema de fosas del Maestrat, únicamente estudiadas desde el punto de vista morfotectónico dada la escasez de afloramientos.

La cronología del modelo evolutivo de muchos de estos sectores podría estar sujeta a revisión próximamente debido a determinadas incertidumbres respecto a la metodología seguida en el laboratorio que analizó muchas de las dataciones que se muestran en la literatura. En el Anexo I de esta tesis se habla más extensamente de estas incertidumbres.

De todas las fallas de esta sección, los autores infieren tasas de desplazamiento y parámetros sismogénicos cuando es posible. De manera complementaria en esta tesis, se hacen ciertas aportaciones a la interpretación de los datos procedentes de la literatura, y se aplican regresiones empíricas para estimar sus potenciales parámetros sismogénicos. Al igual que en las fallas estudiadas en secciones anteriores, los valores descritos por los autores para todo el conjunto de fallas también se han añadido a la síntesis de la sección VI.

1. Falla de Munébrega

La falla de Munébrega es una falla normal que forma el borde noreste del semigraben de Munébrega, desde el NW del pueblo de Valtorres hasta Castejón de Alarba (del Olmo *et al*., 1983a; Echeverría, 1988; Gutiérrez 1996; Gutiérrez *et al.* 2008, 2009, 2012) (Figs. 1.2, 5.1). Su actividad extensional reciente comenzó en la tercera etapa extensional, en el Plio-Cuaternario (Gutiérrez, 1998), y permitió el desarrollo de orlas de glacis y abanicos cuaternarios en el semigraben que parten hacia y desde el plano de falla (Gutiérrez *et al*., 2009). Su dirección media es N150ºE, con buzamiento hacia el SW, y pone en contacto los materiales miocenos que rellenan la cuenca de Calatayud, en el bloque levantado, con los depósitos aluviales cuaternarios, en su bloque hundido. Tiene una longitud aflorante de cerca de 20 km, repartida en dos segmentos de aproximadamente 14 y 6 km, respectivamente, que están separados por una zona de relevo sinestral. Estas fallas dan lugar a parte de una estructura en *horst* junto con otra falla situada al E de características similares, que discurre paralelamente a ellas y hunde parte del margen suroeste de la cuenca de Calatayud (Gutiérrez *et al*., 2008, 2012). Se trata de un lineamiento topográfico de 10 km de longitud, que sigue una dirección N155ºE, y cambia progresivamente hacia una dirección próxima a ESE-WNW en su terminación sur (Gutiérrez *et al*., 2008, 2012).

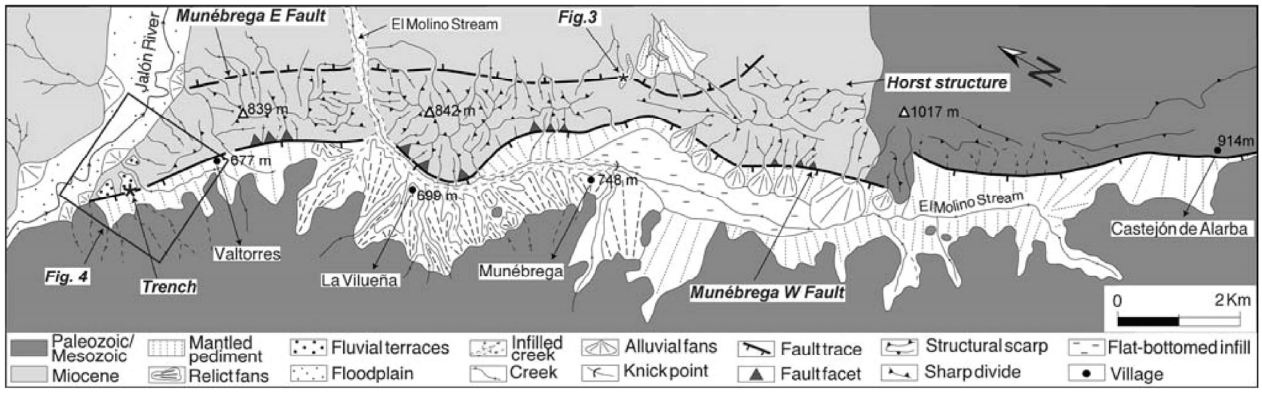

Fig. 5.1.- Mapa geológico de las dos ramas de la falla de Munébrega, se indica la localización de la trinchera (tomada de Gutiérrez *et al*., 2009). Ver su localización en Figura 1.2.

A lo largo de este margen activo, se reconocen facetas triangulares de falla, cambios en el trazado de algunos barrancos y lineamientos que continuarían hacia la cuenca de Gallocanta. El margen NE de esta cuenca limita de manera muy neta el Paleozoico de la Sierra de Santa Cruz con los materiales plio-cuaternarios que rellenan la cuenca (Figs. 1.2, 5.1). Este margen le confiere las características de un semigraben de origen tectónico, que mantiene la dirección NW-SE de la falla de Munébrega y que, a través de una zona de relevo, supone una prolongación de la estructura de cerca de 20 km, totalizando aproximadamente 40 km. A pesar de ello, se ha interpretado como un segmento sin actividad reciente (Gracia *et al*., 2002; Gutiérrez *et al*., 2008; Gracia, 2014), por lo que las inferencias paleosismológicas no pueden aplicarse a todo el conjunto tectónico de Munébrega-Gallocanta.

El estudio paleosísmico llevado a cabo por Gutiérrez *et al.* (2009) de una trinchera excavada en la terminación NW de la falla principal de Munébrega, donde desplaza un glacis asociado a terrazas del río Jalón, muestra varias ramas de falla cortando materiales cuaternarios (Fig. 5.2). Los autores dividen estos depósitos en tres unidades estratigráficas: A y B, que son las afectadas por la deformación, y C, que está sin deformar. Las fallas que afloran se han interpretado como *splay faults* que se unen en profundidad para dar lugar a la falla principal. Se trata de una zona de falla normal, con fallas verticales en el centro y fallas de bajo ángulo en las zonas más alejadas (F1-F9 en Fig. 5.2), así como con pliegues monoclinales asociadas a algunas de ellas. Entre las fallas F1 y F2, Gutiérrez *et al.* (2009) interpretan un relleno fisural (F en Fig. 5.2) entre dos planos de geometría similar. Las fallas F7 y F8 son de bajo ángulo y muestran movimiento inverso como consecuencia de la geometría curvada de su plano de falla en profundidad. El salto vertical total acumulado, calculado como el sumatorio de los saltos de cada falla de la trinchera, es de aproximadamente 7,4 m (Fig. 5.2). Teniendo en cuenta las dataciones OSL obtenidas

en el estudio, tomadas directamente en la trinchera, este salto supone una tasa de desplazamiento vertical de 0,09-0,11 mm/a para los últimos 71,8 ± 5,5 ka. Teniendo en cuenta las nuevas dataciones ESR de Gutiérrez *et al.* (2020b), tomadas en el mismo glacis pero en un afloramiento distinto, se estimaría una edad de 241 ± 50 ka y una tasa de desplazamiento vertical de 0,02-0,04 mm/a.

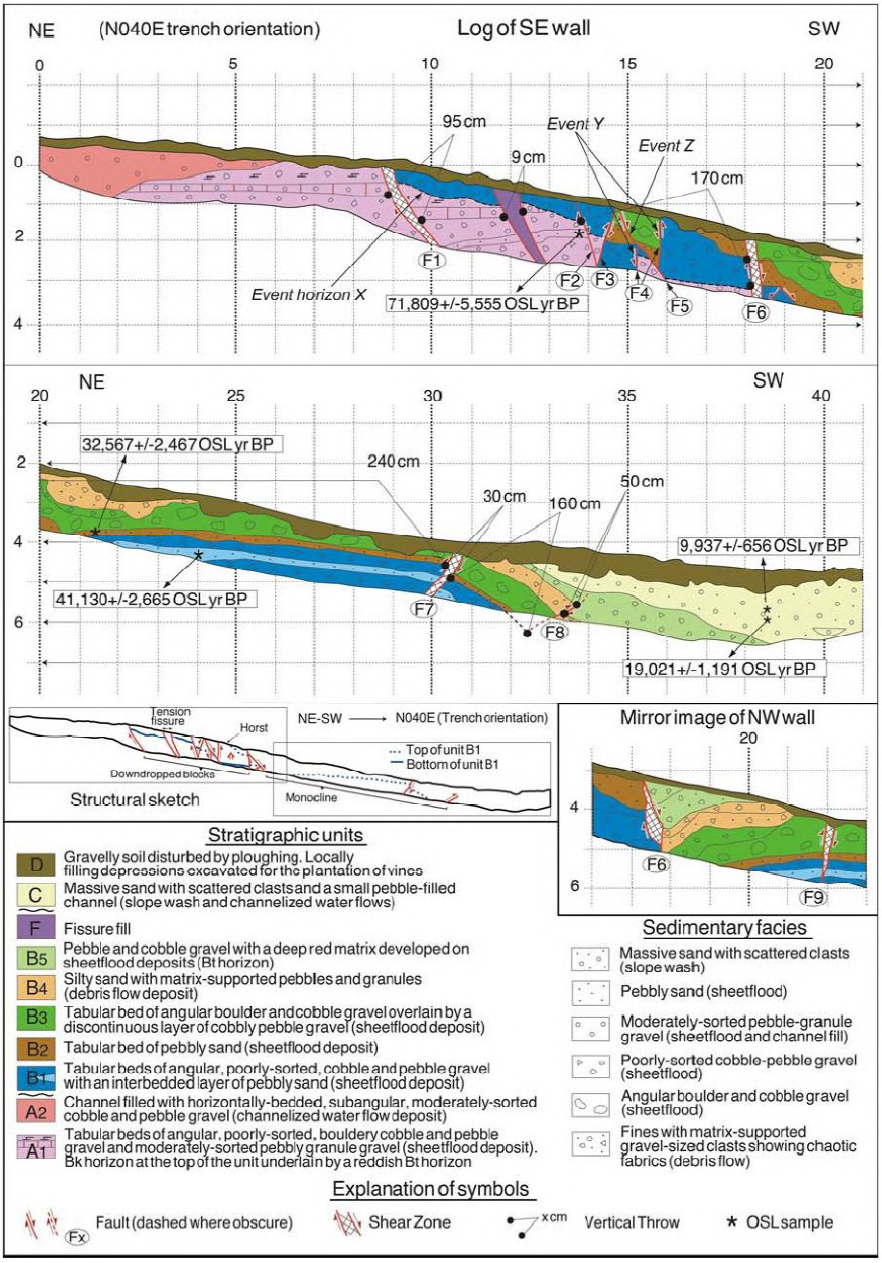

Fig. 5.2.- Log del talud SE de la trinchera de la falla de Munébrega (parte superior) y de parte de su talud NW (parte inferior) (tomada de Gutiérrez *et al.*, 2009). Ver localización en Figura 5.1.

Gutiérrez *et al.* (2009) interpretan una sucesión de al menos tres eventos posiblemente comprendidos entre 71,8 ± 5,5 ka y 19,0 ± 1,2 ka, o, tras la revisión de dataciones anteriormente aludida, posteriores a 241 ± 50 ka (Gutiérrez *et al.*, 2020b). Son los siguientes: evento X (ocurrido después del depósito de la serie A, datada hacia la mitad de su potencia en 71,8 ± 5,5 ka, o 241 ± 50 ka, y antes que la serie B, cuya edad más cercana a la base es 41,1 ± 2,7 ka); eventos Y y Z (entre el depósito de la serie B, cuya datación más cercana es de 32,6 ± 2,5 ka, y el depósito de la serie C, con una edad de 19,0 ± 1,2 ka; Gutiérrez *et al.*, 2009). El salto acumulado en la trinchera es de 7,4 m, y da lugar a un desplazamiento vertical medio por evento de 2,5 m.

En cuanto al cálculo del periodo de recurrencia media de la falla de Munébrega, Gutiérrez *et al.* (2009) parten de los datos paleosismológicos, que abarcan una ventana temporal para los tres eventos (X,Y,Z) desde 72 ka hasta la actualidad, estimando su periodo de recurrencia media en 24 ka. Los autores consideran este periodo

como un valor máximo, ya que: (i) la edad del primer terremoto es menor de 72 ka, y (ii) podrían haberse producido más terremotos que los interpretados en el registro. En el caso de que los tres eventos estuvieran comprendidos entre 241 ka y la actualidad, su periodo de recurrencia media sería de unos 80 ka (Gutiérrez *et al.*, 2020b).

Por nuestra parte en esta tesis, podemos aplicar correlaciones empíricas para comparar y verificar los datos obtenidos mediante dicho estudio paleosismológico. El valor de desplazamiento vertical medio de 2,5 m es coherente con el desplazamiento medio cosísmico de 2,3 m calculado a partir de la regresión empírica de Stirling *et al.* (2002) para terremotos pre-instrumentales, asumiendo que un posible terremoto rompería toda la traza de la falla (ca. 20 km; Gutiérrez *et al.*, 2009). Según la regresión de Wesnousky (2008) obtenemos un salto cosísmico medio menor, de 0,6 m. Tampoco difieren los periodos de recurrencia medios obtenidos de los datos paleosismológicos y los de la regresión de Stirling *et al.* (2002), que apuntan hacia un periodo de 21-26 ka o de 58-116 ka mediante el cálculo directo. Con los saltos cosísmicos resultantes de otras regresiones (Wells y Coppersmith, 1994; Wesnousky, 2008; Leonard, 2010) el periodo de recurrencia sería más corto, de entre 4 y 7 ka, o entre 11-30 ka. Por último, con la correlación de Wesnousky (2008) el mayor terremoto esperable para la falla de Munébrega alcanzaría una magnitud de Mw = 6.7 ± 0.3. Mediante el resto de regresiones empíricas, la magnitud momento estaría en el rango 6.4-6.9 (aplicando Wells y Coppersmith, 1994; Stirling, 2002; Leonard, 2010).

2. Falla de Daroca

El semigraben de Daroca está limitado en su margen NE por la falla normal de Daroca, estructura que discurre en dirección NW-SE, paralelamente y al SW del cabalgamiento con su mismo nombre (Figs. 1.2, 5.3). El espacio de acomodación generado por la falla de Daroca, desde el inicio de su actividad en el Plioceno inferior, comenzó a rellenarse con depósitos plio-cuaternarios en forma de glacis y abanicos que parten mayoritariamente del SW hacia el plano de falla (Gutiérrez *et al.*, 2020b). La falla de Daroca pone en contacto los materiales del Cámbrico de la lámina de cabalgamiento, en el bloque levantado, con el relleno plio-cuaternario del semigraben, en el bloque hundido. Su dirección media es N145ºE, abarcando desde el pueblo de Murero hasta Luco de Jiloca, y su buzamiento está en torno a 40-50º hacia el SW (Gutiérrez *et al.*, 2020a). Su traza es casi rectilínea y está dividida en varios segmentos que totalizan 27 km de longitud (Gutiérrez *et al.*, 2020a). Éstos limitan varias zonas de relevo de pequeña extensión (<1 km de espaciado) que presentan evidencias de interacción por *soft-linkage* y algunas evidencias de propagación oblicua de la fracturación (Gutiérrez *et al.*, 2020a). En varios puntos a lo largo de la traza, la falla muestra facetas triangulares (de hasta 90 m de altitud) en el Paleozoico del bloque levantado que, en gran medida, se atribuyen a erosión diferencial de los materiales más blandos del bloque hundido (Gutiérrez *et al.*, 2020a).

El plano de la falla de Daroca aflora en diferentes puntos a lo largo de su traza. Gutiérrez *et al.* (2020a) describen, al SE de la ciudad de Daroca, sedimentos plio-cuaternarios del bloque hundido que están basculados hacia el plano de falla en torno a 17-20º, mediante una estructura en *roll-over*, y que en diferentes localidades están afectados por fracturación. Asimismo, muestran cómo en una gravera local la falla pone en contacto, con orientación 140, 50 SW, las rocas paleozoicas con varias unidades plio-cuaternarias, y cómo ésta queda aparentemente fosilizada por una unidad coluvial holocena. La unidad superior pleistocena está modelada en glacis y está datada mediante OSL entre 118,7 ± 16,2 y 112,9 ± 9,1 ka (Gutiérrez *et al.*, 2008). Con las nuevas dataciones ESR aportadas por Gutiérrez *et al.* (2020a,b) y Moreno *et al.* (2021) el glacis pleistoceno tendría una edad de 329 ± 43 ka.

Los ápices de las facetas triangulares de la falla de Daroca desarrolladas en el bloque levantado son consideradas por los autores como remanentes del glacis pleistoceno, y utilizadas por tanto como un marcador de desplazamiento. Mediante tres perfiles topográficos hechos a lo largo de las divisorias del drenaje de las facetas, perpendicularmente a la falla, Gutiérrez *et al.* (2020a) calculan un desplazamiento vertical de dicho marcador de entre 8,5 y 16,8 m. Si consideramos que el glacis pleistoceno tiene una edad aproximada con OSL de 112,9 ± 9,1 ka (Gutiérrez *et al.*, 2008), la tasa de desplazamiento para esa ventana temporal estaría entre 0,07 y 0,16 mm/a. Si, tenemos en cuenta su datación más antigua, la tasa sería de 0,02-0,06 mm/a (Gutiérrez *et al.*, 2020a,b).

La trinchera paleosismológica excavada al SE de Daroca (cerca del afloramiento de la gravera) por Gutiérrez *et al.* (2020a) corta la falla afectando al Paleozoico (Unidad 1 en dicho artículo), los sedimentos aluviales del glacis pleistoceno (Unidad 2; que se correlacionan con los de la gravera), otros aluviales (Unidad 3) y unos primeros depósitos de ladera holocenos (Unidad 4; Fig. 5.4). Estos últimos además generan una cuña coluvial y un relleno fisural (Unidades 5 y 6). Finalmente, unos segundos depósitos de ladera holocenos acaban fosilizando la falla (Unidad 7 en adelante). Ésta aflora en forma de zona de falla de 1,2 m de espesor que abarca parte del Paleozoico (con fracturación paralela a la falla y estructuras S-C), unas lineaciones arcillosas intermedias y parte de los depósitos aluviales plio-cuaternarios (deformados por alguna falla sintética y antitética a la principal, y por la fisura; Gutiérrez *et al.*, 2020a). Esta zona de falla es reconocible en ambos taludes, por lo que los autores infieren que su orientación es 130, 43 S. El depósito de ladera holoceno afectado por la falla, la Unidad 4, está datado por radiocarbono AMS en 2354–2180 cal ka BP. Aquellos que fosilizan la falla (Unidad 7 en adelante) tienen una edad máxima comprendida entre 1708-1564 y 1697-1544 cal ka BP (Gutiérrez *et al.*, 2020a).

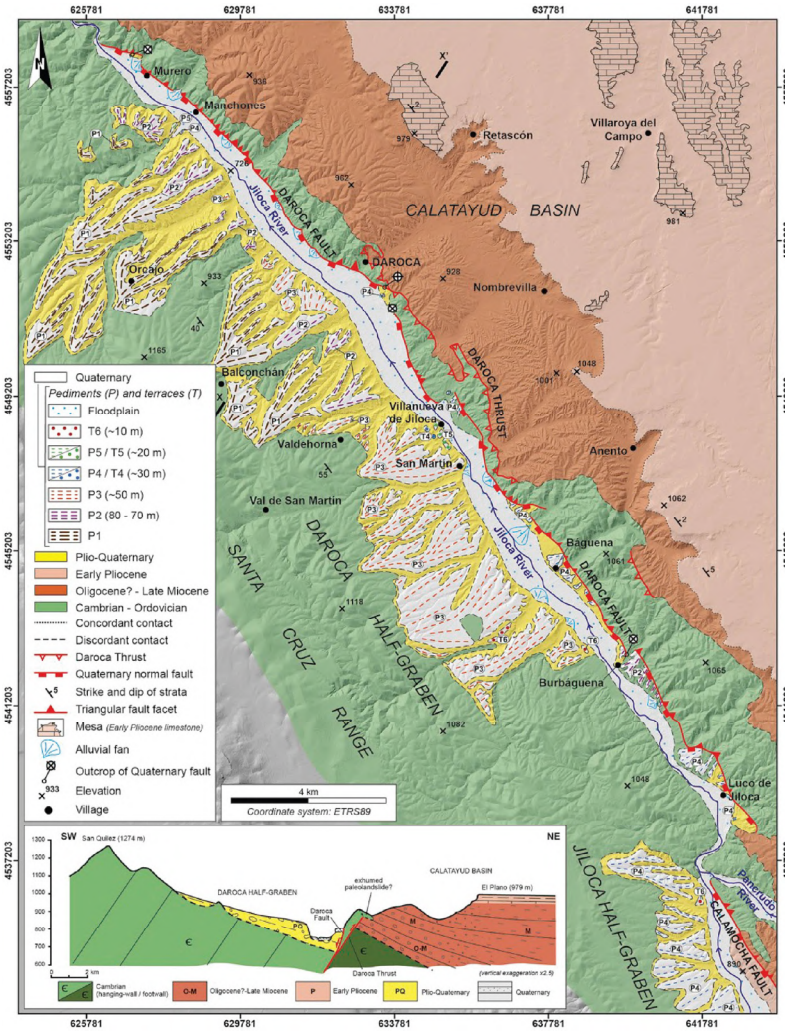

Fig. 5.3.- Mapa geológico de la falla de Daroca y corte geológico perpendicular a la misma a la altura del pueblo de Daroca (marcado como X-X'). La trinchera estudiada se localiza ca. 1,4 km al SE del pueblo de Daroca (tomada de Gutiérrez *et al.*, 2020a). Localización en Figura 1.2.

Los autores interpretan un número indeterminado de eventos en la trinchera, posteriores al depósito de la Unidad 2 (post 112,9 ± 9,1 ka o 329 ± 43 ka), y anteriores a la Unidad 4 (pre 2354–2180 cal ka BP) (Fig. 5.4). Sí describen el evento más reciente (*Most Recent Event; MRE*) de la falla de Daroca, el ocurrido después del depósito de la Unidad 4 y antes de la Unidad 7, es decir, en el periodo temporal de 2354-1564 cal ka BP (Gutiérrez *et al.*, 2020a). Éste estaría representado por una rotura en el plano de falla principal, por la fisura y la cuña coluvial. Indican que, en general, se trata de un registro paleosísmico incompleto que no permite obtener saltos cosísmicos ni una tasa de desplazamiento fiable, para un periodo de actividad más corto que el calculado a partir de las facetas triangulares y el desplazamiento del glacis pleistoceno (Gutiérrez *et al.*, 2008, 2020a).

Sin embargo, en esta tesis proponemos una ampliación de la interpretación del log original (Fig. 5.4). Nos basamos en que las cuñas coluviales han de estar limitadas por el plano de falla que las ha generado (McCalpin, 2009), por lo que la falla que limita el relleno fisural de la Unidad 5 debería extenderse hasta la cuña coluvial de la Unidad 6. Asimismo, no es posible abrir, rellenar y fosilizar una fisura con una cuña coluvial en un mismo evento, como ocurriría en el MRE interpretado por Gutiérrez *et al.* (2020a). Si este fuera el caso, el depósito coluvial no tendría la geometría actual, sino que la mayor parte del mismo habría rellenado la fisura (McCalpin, 2009) y, según la descripción litológica de las Unidades 5 y 6, éstas son diferentes. Por ello, nuestra propuesta sería diferenciar dos eventos diferentes en lo que los autores interpretan como el MRE, sin posibilidad de determinar la acotación temporal de cada uno de ellos.

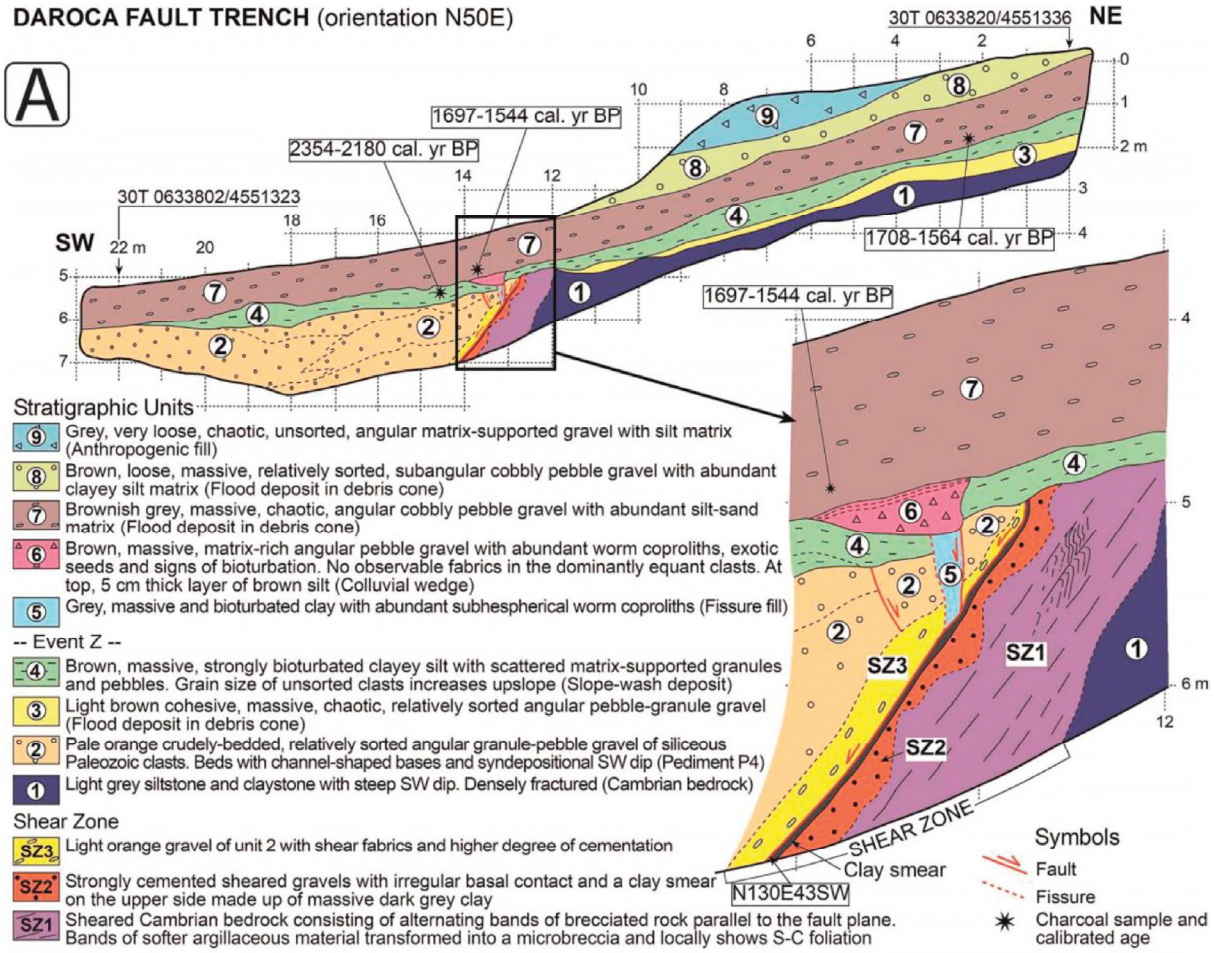

Fig. 5.4.- Log del talud N de la trinchera excavada en la falla de Daroca (tomada de Gutiérrez *et al.*, 2020a). Ver localización en Figura 5.3.

De manera complementaria, vamos a realizar inferencias sismogénicas con las correlaciones empíricas. Si rompiera la traza superficial de 27 km de longitud de la falla de Daroca en su conjunto, el terremoto esperable podría producir un salto cosísmico medio de 0,8 m (aplicando Wesnousky, 2008). Con este último y la tasa de desplazamiento de los datos de Gutiérrez *et al.* (2008), se obtiene un posible periodo de recurrencia de 5-12 ka, bastante similar al resultante de las regresiones de Wells y Coppersmith (1994) y Leonard (2010), pero inferior al de Stirling *et al.* (2002). Con la tasa de Gutiérrez *et al.* (2020b), el periodo sería de 14-41 ka (con Wesnousky, 2008). La correlación de Wesnousky (2008) también indica una magnitud de Mw = 6.8 ± 0.3 para dicho terremoto. Mediante el resto de regresiones empíricas, la magnitud momento oscila entre 6.6 y 7.0 (aplicando Wells y Coppersmith, 1994; Stirling, 2002; Leonard, 2010). Los datos ponderados de localización y profundidad del foco sísmico del terremoto de Used de 1953 permiten asociarlo, con una alta probabilidad, a la falla de Daroca. Su Mw = 4.7 (IGN, 2022) nos indicaría que no rompió toda su traza sino sólo una parte menor.

Geoheritage (2022) 14:123
https://doi.org/10.1007/s12371-022-00758-w

ORIGINAL ARTICLE

Memory of the Earth and Human Memory of Natural Disasters: the 1953 Earthquake in Western Aragón (Spain)

José L. Simón[1] · Guillermo Simón-Porcar[2] · Alba Peiro[1]

Received: 24 April 2022 / Accepted: 31 October 2022
© The Author(s) 2022

Abstract
Occurred in 1953 in Used (Zaragoza province), an earthquake of magnitude 4.7 and intensity VII was the last destructive earthquake in the Aragón region, Spain. The remaining social memory of that event (a type of intangible geological heritage) and its influence on the perception of seismic hazard in the area are explored by means of interviews and a population survey. The results indicate that the memory is lively amongst the population within the epicentral area, both in the generation that experienced it and, to a lesser extent, in the following generations. However, this does not translate into a significant perception of seismic hazard, the latter being more influenced by cultural factors: in the epicentral area it is greater amongst people who did not live through the earthquake, but who have heard familiar stories or have had external information highlighteing its importance. The study of social perception is part of a citizen science project, in which the social memory enters into dialogue with the *Memory of the Earth*, i.e. the record left by that and other previous earthquakes in geology and landscape. The research on the effects of the shake on people, buildings, and environment has benefited from numerous testimonies from the elderly. Reciprocally, such knowledge is scientifically processed and returned to the citizens in the form of scientific outreach products (book, documentary film, talks), with the aim of promoting scientific culture about natural disasters.

Keywords Seismic hazard · Active fault · Population survey · Citizen science · Used · Iberian Chain

Introduction: Scope and Objectives

Geological heritage represents the *Memory of the Earth*, i.e. the record of the Earth's history inscribed in rocks and landscapes (*Declaration of the Rights of the Memory of the Earth*; Martini 1992). Most of that *Memory of the Earth* concerns its remote past, e.g. ancient orogenies or catastrophic faunal extinctions. Their study has relevance for reconstructing the history of our Planet, a cultural resource as important for our present and our future as the history of Humanity itself is. On the other hand, knowledge of Earth history and dynamics is necessary for adequately and efficiently using mineral and energy resources that we humans consider vital for our socioeconomic development.

But the *Memory of the Earth* also deals with events of a more recent past, and the most relevant amongst them undoubtedly are those that refer to natural disasters that recurrently shake cities and countries. Where these phenomena have occurred in the last centuries or decades, they offer the possibility to connect and establish a dialogue with the human memory, either with that individual, personal memory, or with the social memory (the one collected in books, historical documents, or press). The possibility of such a dialogue being established depends on two main factors: (i) the natural recurrence of processes and the elapsed time since the last event and (ii) the extent of individual and social memory, something that is often conditioned by the cultural development of each community. Processes with short recurrence, e.g. river floods, may (or should) be present either in individual memory or in intergenerational memory preserved by oral transmission. On the contrary, processes with secular recurrence require, for the consolidation of their memory, the documentary record.

✉ José L. Simón
jsimon@unizar.es

Guillermo Simón-Porcar
g.simon_12@hotmail.com

[1] Departamento de Ciencias de la Tierra, Fac. Ciencias - Geotransfer Research Group-IUCA, Universidad de Zaragoza, Pedro Cerbuna, 12, 50009 Saragossa, Spain

[2] C/Antares, 21. 50012 Saragossa, Spain

Published online: 15 November 2022

Collective memory about catastrophic phenomena, and in general about negative events, tends to be lost too quickly. Concerning, e.g. catastrophic flood events, their memory depends on the presence of eye-witnesses, so that after the latter die out, the historical memory tends to disappear (Fanta et al., 2019). This probably represents a psychological defence mechanism, whereby societies tend to cope with traumatic events by repressing the memory, forgetting the negative; the socio-cultural construction of risk, determined by collective memory, is therefore biased (Páez et al., 2001; Noria, 2015). After the news of a river flood, it is commonplace to hear on radio or television a local official who has been surprised by the phenomenon, claiming that "not even the oldest people in the area could remember such a thing". Societies thus often adopt an "ostrich strategy", closing their eyes to the obstinate reality of natural processes. Our modern, technological *society of knowledge* also makes this mistake, frequently faking the collective memory and demonstrating a worrying lack of scientific culture indeed (Simón, 2015).

In this context, it is understandable that people have difficulties in taking seriously into account the *Memory of the Earth*. Even if our reverence for science nominally gives value to the scientific knowledge that is being achieved about geological processes, our subjective judgements and pre-scientific notions are often more decisive. This collective attitude does not befit a cultured and wise society.

Natural hazard assessment requires widening the time window of our memory. In the case of earthquakes, for example, such an assessment cannot be based only on the inventory of historical and instrumental earthquakes, but must extend to paleoearthquakes. In intraplate regions where significant earthquakes have large recurrence intervals (in the order of 10^3 years; Liu and Zoback 1997), the latest event could be older than the existing historical documents. In such regions, studying the geological record for identifying active faults and the resulting ancient quakes is therefore a critical task (Allen 1986; Yeats et al. 1997). Paleoseismic events can be identified and dated from both *primary* and *secondary* geological evidences (McCalpin and Nelson, 1996). *Primary* or *on-fault* evidences are usually found at trenches excavated across fault traces, in which relationships between rupture surfaces and sedimentary units are carefully analysed for building a model of the local paleoseismic succession (e.g. Allen, 1986; Pantosti et al., 1993; McCalpin, 2009). *Secondary* paleoseismic evidences are mostly provided by soft-sediment deformation structures (SSDSs) induced by the shake at a distance of the source fault, during or after sedimentation and before complete lithification. Since the pioneer works by Seilacher (1969) and Sims (1973), many others describing regional examples or discussing the methodology for their analysis have been published (e.g. Scott and Price, 1988; Alfaro et al., 1999; Alsop and Marco, 2013; Moretti and Van Loon, 2014; Moretti et al., 2016; Basilone 2017).

The dialogue between Earth's and human memory also demonstrates the complementarity between tangible and intangible geological heritage. As is the case with the cultural heritage in general, geological heritage mostly includes material objects (rocks, fossils, landscapes; Dos Reis and Henriques, 2009), but also intangible entities: customs and folk wisdom, oral traditions, language, myths, and religious ceremonies linked to the geological record (Martini, 2009). Ancient mining techniques (Muntoni et al., 2020), traditional folk wisdom linked to salt pond operations (Mansur and Souza 2011), or orally transmitted accounts of geological processes belong to this category. In particular, chronicles and personal reports of the effects of an earthquake are valuable pieces of immaterial geological heritage. First of all, they represent an essential part of scientific earthquake research, in particular for the location of the macroseismic epicentre and the assignment of intensity. At the same time, they constitute an expression of human perception of natural phenomena, and therefore of high ethno-geological value.

The earthquake occurred on 28 September 1953 in Used (Zaragoza province; see location in Fig. 1), with magnitude 4.7 and intensity VII, was the last destructive earthquake in the Aragón region, Spain. It caused considerable material damage in Used and, to a lesser extent, in other surrounding villages, and a major landslide that cut the main road in the county. The event was widely reported in regional and national press (Fig. 2), and resulted in the death of a girl (Simón et al., 2021). It occurred in a region of low to moderate historical seismic activity, but where geological studies have shown the presence of active, potentially seismogenic faults (Gutiérrez et al., 2009, 2012, 2020; Simón et al., 2012; Peiro and Simón, 2021a, b), i.e. in a region where the geological record provides a wider temporal perspective that provides an adequate explanation to this extraordinary event.

Most people who lived through the earthquake are no longer around to recount it, and those who remain mostly were children or teenagers whose memories are fragmentary or biased. At present, it would be unrealistic to search for new data of that earthquake based on oral testimonies (e.g. for refining the macroseismic zonification). However, there have been strong reasons for our research group to undertake an interdisciplinary project focusing on that earthquake. From a scientific point of view, personal and documentary sources of information can contribute to increase our knowledge of the geomorphological-environmental effects of the earthquake, an aspect not studied to date that can now be addressed in the perspective of citizen science. From a social point of

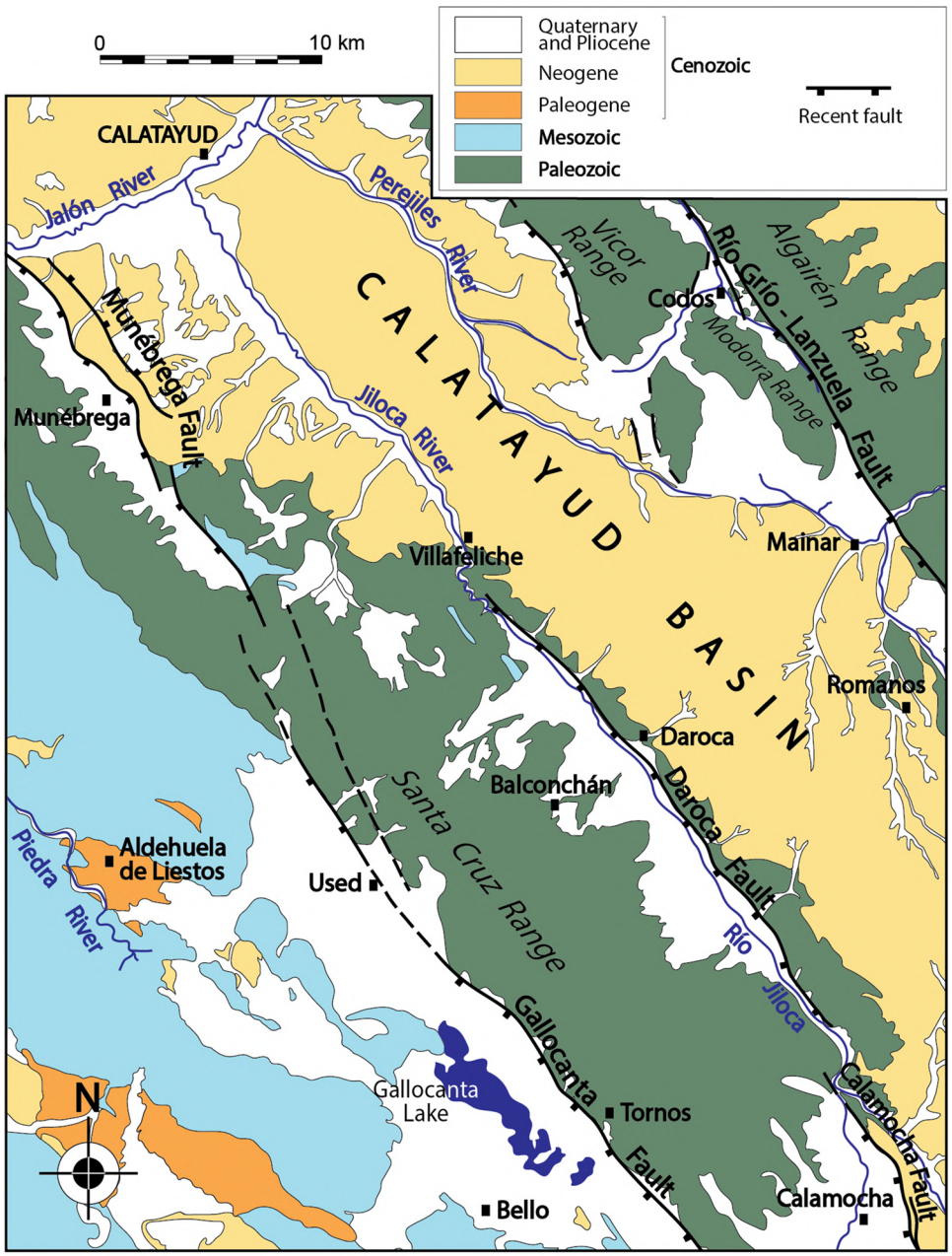

Fig. 1 Geological setting. **a** Location of the study area within the Iberian Chain (inset: location within NE Spain). **b** Geological map of the Used area

view, there is a need to transfer knowledge to the local population, and to deepen the collective perception of seismic hazard.

The objectives of this work are the following:

(1) Establishing a dialogue between the *Memory of the Earth* (record of geological processes interpreted on scientific bases) and the human (individual and social) memory of the Used earthquake of 1953.
(2) Assessing the remaining social memory of the earthquake, comparing the epicentral area with the rest of the Aragón region, as well as between successive generations.
(3) Using human memory for increasing the scientific knowledge of the geomorphological-environmental effects of the earthquakes.
(4) Assessing the influence of human memory on the social perception of seismic hazard.
(5) Developping the social dimension of seismology, implementing an exercise of citizen science, and giving back scientifically processed knowledge to the population in the form of outreach products.

EL NOTICIERO

Año LIII—Núm. 16.601 Zaragoza, martes 29 de septiembre de 1953 Setenta céntimos

Movimiento sísmico en Zaragoza

El fenómeno produjo gran alarma y fueron numerosas las personas que abandonaron sus hogares. — En Huesca y Calatayud fué percibido el sismo intensamente

EL OBSERVATORIO DEL EBRO LO CALIFICA DE TIPO PROXIMO Y DE INTENSIDAD BASTANTE CONSIDERABLE, Y ES UNO DE LOS MAS FUERTES OBSERVADOS EN AQUEL CENTRO

Aproximadamente a las once menos cuarto de anoche se observó en Zaragoza un movimiento sísmico de alguna intensidad.

Sobre todo fué percibido en los pisos altos y en la parte alta de la ciudad.

El temblor de tierra hizo estremecerse durante algunos segundos los muebles, oscilar las lámparas y las vajillas y cristales de los aparadores.

Fueron numerosas las personas que llamaron a nuestro periódico dando cuenta de las sacudidas que, a lo que parece, fueron dos, una más brusca que otra.

En el barrio de la Magdalena, calle de Moncasi, Coso y otros puntos de la población, grupos de vecinos salieron a la calle al instante de apreciarse el movimiento sísmico, llenos de alarma.

Los bomberos recibieron numerosas llamadas de los más variados puntos de la población, hasta el punto de que hicieron un recorrido por las calles, pudiendo apreciar que ningún daño se había producido.

Acerca de la duración del movimiento se oyeron diversas opiniones: mientras unos afirmaban haber sido de cuatro a cinco segundos, algunas personas la hacían llegar hasta más de treinta.

En relación con su intensidad también oímos referencias tan dispares como las de numerosas gentes que no observaron el fenómeno y la de un matrimonio de la calle Madre Vedruna que afirmó que el temblor de tierra les había tirado desde la cama al suelo.

(Pasa a la página cuarta)

Fig. 2 News on the earthquake in *El Noticiero* regional newspaper

Methodology: Documentary Sources

The essential part of this work, dealing with human memory of the 1953 earthquake and perception of seismic hazard, has essentially involved social research. We have first compiled the relevant information that exists in documentary sources: scientific literature, administrative documents, and printed press.

Concerning scientific literature, there is an only monograph published a few years after the earthquake (Rey Pastor and Bonelli, 1957), apart from occasional mentions in articles on regional active faults and seismotectonics (Gracia and Gutiérrez, 1996; Gutiérrez et al., 2009, 2020; Samardjieva et al., 1999) and the logical inclusion in official seismic catalogues (Mezcua and Martínez-Solares 1983; IGN, 2021).

Scientific (unpublished) and administrative documents have been obtained from the following institutions: Observatori Fabra, belonging to the Reial Academia de Ciències i Arts de Barcelona; Institut Cartogràfic y Geològic de Catalunya (ICGC); Instituto Geográfico Nacional (IGN); Instituto Geológico y Minero de España (IGME); civil registry and archive of the Used municipality; Archivo de la Diputación Provincial de Zaragoza (provincial council); Archivo Arciprestal de Daroca (ecclesiastical archive of Daroca archpriesthood); and Demarcación de Carreteras del Estado en Aragón, Ministerio de Transportes (state roads, ministry of transport, Spanish government).

Printed news was recovered from local, regional, and national papers, mainly *Heraldo de Aragón* and *El Noticiero* (Zaragoza; Fig. 2), *ABC* (Madrid), and *El Correo Catalán* and *La Vanguardia* (Barcelona). These journals were accessed at the Archivo-Hemeroteca Municipal de Zaragoza (archive of the Zaragoza municipality), archive of the Observatori Fabra-Reial Academia de Ciències i Arts de Barcelona, and a dossier previously compiled by IGN.

Second, an interview campaign was conducted with older people who lived through the 1953 earthquake in Used and other villages in the epicentral zone. Significant direct testimony was obtained from a total of 19 informants, which are cited in the "Acknowledgements" section. The information obtained concerns the effects of the shake on people, buildings, and environment.

Third, we carried out a population survey focused on assessing the degree of knowledge and social memory of the 1953 earthquake amongst the population of the epicentral area and the rest of Aragón (as a result of either personal experience or oral transmission), as well as the social perception of seismic hazard. Table 1 shows the template used for such survey. The latter was carried out on-site amongst the inhabitants of affected villages, in addition to being distributed in web format through social networks and other electronic media. A total of 198 responses were collected.

Table 1 Template used for the population survey on the memory and perception of seismic hazard

GENDER: Man Woman			**AGE:**	
LOCALITY OF RESIDENCE:				
Level of education: Primary Secondary University Other				
1) Do you know if an earthquake occurred in your locality some decades ago? YES NO **Can you remember in which year?**				
2) Why do you know it?	You lived through the seism	Your family told you about it	You know it from other sources	You do not know it
3) Can you remember any other earthquake in your zone in the past? YES NO **If YES, where did it occurred?**				
4) Do you consider that your locality is under significant seismic hazard? YES NO				
5) Which of the following natural disasters do you consider most likely to occur in your locality?				
a) Flooding		b) Karst subsidence		
c) Landslide		d) Earthquake		

In parallel with the social research, geological work has been carried out to understand the seismotectonic framework of the Used earthquake (possible seismic source, geodynamic context…) and its geoenvironmental effects. Different methodological approaches, mostly structural and geomorphological, have been used for exploring the record of seismogenic fault activity in rocks and landscape. The structural study is based on recognizing and mapping the main structures in aerial photographs and satellite orthoimages, complemented with field surveys involving outcrop-scale observations. The geomorphological study is focused on mapping and reconstructing planation surfaces for being used as markers of vertical deformation, as well as landforms linked to fault mountain fronts (linear escarpments, triangular facets, alluvial fans). Intensive field surveys have been carried out searching for evidence of slope unstability resulting from seismic shaking (landslides, falling blocks…), on the basis of indications provided by aged informants.

Geological, Geographical, and Social Setting

The geological region in which the 1953 earthquake took place (Fig. 1a) is the so-called Aragonese Branch of the Iberian Chain. The latter extends for more than 400 km in a NW–SE direction, from Sierra de la Demanda, in the Burgos province, to the Mediterranean Sea, in Castellón and Valencia. It is an intraplate chain located within Iberia, which resulted from inversion of several Mesozoic basins (Liesa et al., 2018) during Paleogene to early Neogene compressional episodes (Liesa and Simón, 2009), under the convergence with the European and African plates (Álvaro et al., 1979; Capote et al., 2002).

The area surrounding Used includes a series of mountain ranges (Santa Cruz, Algairén) and depressions (Calatayud, Gallocanta), which largely follow the general NW–SE direction of the chain (Fig. 1b). The Calatayud basin was onset under the compressional regime during late Palaeogene time, and is infilled by alluvial and lacustrine sediments mainly of the Lower Miocene. It is bounded at its SW margin by the Palaeozoic Ateca-Daroca massif, both being separated by the Daroca thrust (Julivert, 1954; Colomer and Santanach, 1988; Casas-Sainz et al. 2018). The latter was subsequently inverted into the Daroca extensional fault, which sinks the Daroca half-graben with respect to the Neogene infill of the Calatayud basin (Julivert, 1954; Gracia, 1992; Gutiérrez et al., 2008). Within and SW of the Paleozoic massif, a second large extensional structure, the Munébrega-Gallocanta fault zone bounds the Munébrega and Gallocanta Plio-Quaternary half-grabens.

The Grío, Perejiles, Jiloca, and Piedra rivers, tributaries of the Jalón river and, finally, of the Ebro Basin, drain most of the area. Nevertheless, the centre of the Gallocanta depression remains endorheic, hosting the Gallocanta lake (considered as the largest natural lake in Spain, 14.4 km^2) and La Zaida lake. The latter is submitted to artificial management for agricultural use in alternate years, through a sluice gate built in the sixteenth century.

With an average altitude exceeding 1000 m a.s.l., the area has an extreme continental climate, with average minimum temperatures in winter of 0–1 °C (absolute minimum of − 30 °C in the Calamocha Observatory), and average maximum temperatures in summer around 30 °C. Although rainfall is relatively low (400–500 mm/year), the high altitude allows the soil to keep moist enough for fairly regular cereal harvests.

The municipality of Used, as well as the rest of villages in the southern sector of the epicentral area of the 1953 earthquake, belongs to the Campo de Daroca county. The northern sector belongs to Comunidad de Calatayud, whilst other more marginally affected areas belong to the neighbouring counties of Jiloca (Teruel province) and Molina de Aragón (Guadalajara, Castilla-La Mancha region). With the exception of the city of Calatayud, all of them are located in rural Spain and have suffered a severe depopulation process since the mid-twentieth century. Overall population density is 6.7 inhabitants per km^2.

Economy of the zone is mainly based on rain-fed agriculture, with a lesser contribution of farming, small industries (mainly in the agri-food sector), construction, and services (mostly commerce and tourism). Industry and services are mainly concentrated in the county seats: Calatayud, Daroca, and Calamocha.

Memory of the Earth: Tectonic Framework of Seismicity at the Central Iberian Chain

Since the beginning of the Late Miocene, the central-eastern Iberian Chain underwent an extensional tectonic regime linked to rifting of the Valencia Trough (Vegas et al. 1979; Simón, 1982; Roca and Guimerà 1992). Onshore extensional deformation was accommodated by a large network of Neogene-Quaternary grabens (Maestrat, Teruel, Jiloca, Gallocanta, Munébrega), whose bounding faults mostly represent the negative inversion of previous contractive faults (Álvaro et al., 1979). The last stage of tectonic activity started by the mid-Pliocene (approximately 3.8 Ma ago), under a crustal stress regime characterized as a multidirectional or radial extension (σ_1 vertical, $\sigma_2 \approx \sigma_3$) with prevailing ENE-WSW σ_3 trajectories (Simón, 1982, 1989; Arlegui et al., 2005; Liesa et al., 2019). This stress field has remained up to the present day (Herraiz et al., 2000).

Along the central Aragonese Branch, the main extensional faults activated since mid-Pliocene time trend NW–SE to NNW-SSE (Fig. 1b). They are grouped into three major alignments: Río Grío-Pancrudo (Gutiérrez et al., 2013; Peiro and Simón, 2021a, 2021b), Munébrega-Gallocanta (Gutiérrez et al., 2009), and Daroca-Calamocha (Gracia, 1992; Gutiérrez et al., 2008, 2020). All these faults dip towards SW, making the NE margins of half-graben basins, and show traces that exceed 15 km in length (88 km in the case of the Río Grío-Pancrudo; Peiro and Simón, 2021a). The Río Grío-Pancrudo fault zone has undergone vertical displacement of ~ 300 m during the last 3.5 Ma, with net slip rate close to 0.09 mm/a. Vertical displacement of ~ 20 m of a sedimentary level dated to 66.6 ± 6.5 ka gives a more recent slip rate approaching 0.30–0.36 mm/a (Peiro and Simón, 2021b). The Munébrega fault also shows evidence of Late Pleistocene activity: vertical displacement of about 7 m in an alluvial unit initially dated to 72 ± 6 ka (Gutiérrez et al., 2009) would result in a vertical slip rate of approximately 0.1 mm/a. Such dating has been recently revised and brought forward to 241 ± 50 ka, which diminishes the slip rate to 0.02–0.04 mm/a (Gutiérrez et al., 2020). At the Daroca fault, offset of an erosional-aggradation pediment dated to 329 ± 43 ka provides a vertical slip rate of 0.02–0.06 mm/a (Gutiérrez et al., 2020). For the Calamocha fault, a throw of about 210 m for the Late Pliocene–Quaternary stage (long-term slip rate of 0.06 mm/a), as well as evidence of recurrent movement during the Pleistocene, have been reported (Martín-Bello et al., 2014).

The activity of these faults is probably responsible for the earthquakes that occasionally affect the region. Most of them have their epicentre in the transition from the Iberian Chain to the Ebro Basin (Algairén, Herrera, and Oriche mountain ranges) and to the Castilian Plateau (Gallocanta-Molina de Aragón highlands). The most important recent earthquakes, apart from the 1953 one, were those of Cimballa (1912, intensity VI–VII), Calatayud (1944, intensity VI, magnitude 3.8), and Herrera de los Navarros (2011, intensity IV–V, magnitude 4.1).

It can be assumed that the 1953 earthquake was caused by one of these large faults. However, it is not easy to know which exactly was, due to high uncertainties in both location of the epicentre (see Fig. 3) and focal depth: either 7.3 km (Rey Pastor and Bonelli, 1957), 15 km (Samardjieva et al., 1999), or 31 km (J. V. Cantavella and J. Fernández, personal communication on an unpublished calculation based on *Hypocenter* software). Most of the focal depths attributed to earthquakes in the region are between 5 and 15 km, i.e. within the brittle upper crust. Geophysical exploration of the eastern Iberian crust indicates that the detachment level for the main extensional faults is located at a depth of 13–15 km (Roca and Guimerà, 1992). Below this level, deformation becomes more ductile and the frequency of earthquakes sharply decreases. Consequently, only the focal depths calculated by Rey Pastor and Bonelli (1957) and Samardjieva et al. (1999) are compatible with the geodynamic framework. Combining those parametres with the average dip of the fault plane (65 to 75° in shallow levels, decreasing in depth), the epicentre should be geometrically located between 2 and 15 km SW of the fault trace responsible for the earthquake. Consequently, the fault most likely to have caused the 1953 earthquake was the Daroca fault. The elongation of isosists along that fault (Fig. 3) is consistent with this interpretation.

In summary, despite this sector of the Iberian plate is characterized by low to moderate seismicity, it hosts a number of active faults, for which the geological record shows evidence of recurrent displacement during the Quaternary, and should be therefore considered as potentially seismogenic. Such knowledge of active faults based upon the *Memory of the Earth* is increasingly guiding seismic hazard

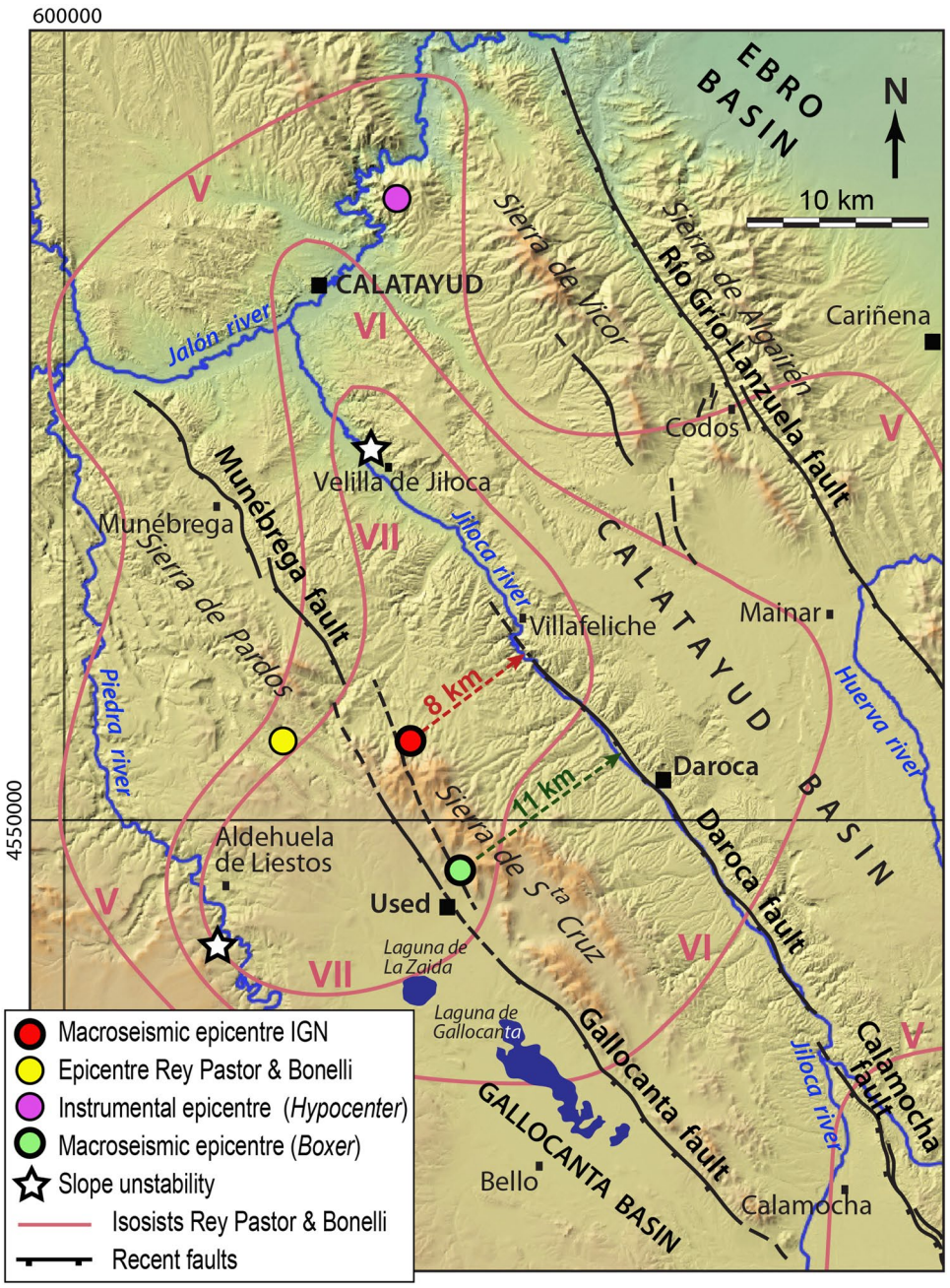

Fig. 3 Synthetic seismotectonic map. The compatibility between distinct locations proposed for the epicentre and potential source faults is analysed. From the available data, the most probable seismogenic source was the Daroca fault

assessment in scientifically advanced countries. In Spain, it has given rise to new hazard maps elaborated by IGN (Martínez Solares et al., 2013). These should soon replace the obsolete map currently considered in seismic codes (Ministerio de Fomento, 2002), in which a null seismic hazard level is assigned to the entire Iberian Chain.

A recent case in the region illustrates how using the geological record of prehistoric earthquakes can provide the basis for more rational seismic hazard assessment. In 2012 the Aragón regional government presented the project for a new hospital in Teruel city, which, according to current regulations, did not initially include any anti-seismic design. The site chosen for it is about 400 m from the Concud fault, which makes the boundary of the Jiloca graben in its southern sector. This is the best-known active fault in the region: it has been object of intense paleoseismological research that have allowed reconstructing a wide succession of 11 events since approximately 74 ka BP, with average recurrence period of 7.1–8.0 ka, total net accumulated slip of about 20 m, and average slip rate of 0.29 mm/a (Lafuente, 2011; Lafuente et al., 2011, 2014; Simón et al., 2016). The maximum expectable earthquake within a 500-year period is estimated to be $M = 5.3 \pm 0.3$, whilst the peak ground acceleration could

attain $a_p = 0.105$ g (Simón et al., 2014). In the light of reports written by our research team, IGN and IGME, the Aragón government decided to modify the building project and provide it with anti-seismic design according to the newly proposed seismic parameters.

Human Memory of the Used Earthquake of 1953

Individual and social memory on the 1953 earthquake is enough to reconstruct its effects in Used and the other villages of the epicentral area. Testimonies collected amongst informants who experienced the quake (Fig. 4) illustrate how they felt and reacted. Scientific and administrative documents and press recorded seismological data and numerous consequences derived from the shake.

In Used, there was a general panic; people went out into the streets without knowing what had happened. The doctor and the vet tried to calm them down; despite most people did not know what an earthquake was indeed, they were comforted to see that initially there was no great misfortune. Another thing was to see, the following day, the destruction caused to buildings: almost all of them were damaged and some even collapsed. A wall of the church was cracked and part of the bell tower crowning the frontal façade fell (Fig. 5). A 19-year-old girl, Victorina Liarte, was terrified and went into shock; as a result, she fell seriously ill and died a week later.

The earthquake was strongly felt in other numerous villages of the Daroca and Calatayud counties, although damage to buildings was minor. Special mention should be made of what happened in Daroca. According to the complete and personal account by the correspondent of *El Noticiero* journal "…the ground rippled repeatedly, making the effect of a giant cat crawling under a carpet (…). The walls also shook as if they had been made of paper (…). People walking in the street were shaken (…). In many places, terrified of new movements, they lay down in their clothes". Without going into how accurate this description is, the earthquake caused significant damage in Daroca, and even today noticeable cracks can be observed in façades that were not repaired (Fig. 6).

In addition to *El Noticiero*, other regional and national newspapers reported on the earthquake and its effects, mostly *Heraldo de Aragón* and *Amanecer* (Zaragoza), *El*

Fig. 4 Some people who lived through the earthquake have provided valuable information. **a** Marcelina Ferrer. **b** Santiago Muñoz. **c** Silvina López. **d** Silvestre Gálvez. Photographs: Jorge Brizuela

Fig. 5 Frontal façade of the Used parish church in 1947, showing the bell tower that collapsed during the earthquake of 1953 (source: Archivo Mas)

Correo Catalán and *La Vanguardia* (Barcelona), and *ABC* (Madrid). The press quickly published some of the first data from the seismographs. *El Noticiero* contacted the Ebro Observatory (Tortosa, Tarragona province) only 15 min after the earthquake. The journalist not only received first-hand scientific information, but also contributed to assess the intensity of the earthquake and the possible location of the epicentre. Such interesting conversation constituted a splendid example of collaborative science. The Ebro Observatory had initially attributed to the earthquake an intensity of IV on the Mercalli scale, but the journalist pointed out that in mountains SW of Zaragoza the movement had been more intense. In view of that exchange of information, it was suspected that the epicentre could be located in the Daroca area.

In the days that followed, not only did the press report on the phenomenon, but local institutions and individuals carried out an interesting exercise of citizen science, providing valuable testimonies. Much data collected at the time for evaluation of the seismic intensity is preserved in the correspondence that town councils, parish priests, and individuals maintained with the Fabra Observatory in Barcelona. The informants responded to the call made by Eduard Fontseré, director of the meteorology and seismology section of that observatory, as well as to press announcements published by the Reial Acadèmia de Ciències i Arts de Barcelona, the institution to which it belongs. It is amazing that, in their survey sheets, some informants themselves assigned a Mercalli intensity to the observed effects. According to the overall results, the epicentral intensity was initially estimated to VIII (Fontseré, 1955). Later, and independently, Rey Pastor and Bonelli (1957) used the testimony files collected by the Toledo Observatory (which, unfortunately, we have not been able to locate) and carried out their own field surveys. From these, they (i) located the epicentre more precisely to the north of Used (longitude 1°40′W, latitude 41°08′N), (ii) calculated the focal depth at 7.3 km, and (iii) estimated a maximum intensity of VII (Fig. 3).

Fig. 6 Symmetrical cracks in the façade of a building in Calle Mayor of Daroca town

So far, we have referred to the social memory documentally recorded. But what is the individual memory kept by those who lived through the earthquake? We must bear in mind that the current testimonies by older people may be different from those given by their parents in 1953. Time filters often distort stories. The contrast between both pointviews is exemplified in Calatayud town. *Heraldo de Aragón* emphasized in its 2 October edition the great alarm amongst the population, stating that "only sick people did not leave their homes, (…) and 99% of the neighbourhood took to the streets". However, a present-day, 94-year-old informant lucidly recalled the earthquake in Calatayud but claimed not to have felt any fear.

We wanted to objectify the memory that currently persists in the municipalities more affected by the earthquake, and also to compare it with that in other areas of Aragon. With this purpose, a survey was carried out in person amongst the inhabitants of the epicentral area, in addition to being distributed in web format through social networks and other electronic media. A total of 198 responses were collected, of which 90 belonged to people in the Used-Daroca-Maluenda area (included in isosists VI and VII; Fig. 3), 54 correspond to the rest of the Zaragoza province, and 54 to the Teruel province. Concerning the responses obtained in the epicentral area, 42 were from people over 72 years old (of whom 27 lived through the earthquake and, because of their age, could remember it), 42 were between 40 and 71 years, and 6 were from people under 40.

The results of this survey (Table 2 and Fig. 7a) show that a great majority (81%) of people living in the more affected area who were over 4 years old at the time of the earthquake remember it, generally because they experienced it firsthand. More than half can date it with reasonable accuracy (±2 years). This proportion drops to 71% amongst those aged 40–71, who know about it only from oral transmission within the family (about half of the total in this age group), or from other sources. Within this age segment, only 43% know the approximate date. Amongst those under 40 years of age, for whom the sample is very small, only half knew about the earthquake, generally from sources outside the family.

If we aggregate these results and compare them with those of other areas of Zaragoza and Teruel provinces, we see significant differences. In the Daroca-Used-Maluenda area, 74% of people of all ages are aware of the existence of the 1953 earthquake, whilst only 4% in the rest of the Zaragoza province. In Teruel, 32% of individuals surveyed were aware of the occurrence of an earthquake in their locality; in 13% of the cases, given the approximate date on which they placed it, it was also very probably the 1953 earthquake.

In short, the memory of the earthquake is quite vivid in the municipalities of the epicentral area, both in the generation that lived through it and, to a lesser extent, in younger generations. In areas of the Iberian Chain and the Ebro Basin where it was felt with less intensity, knowledge of the earthquake is logically more limited, but it is noteworthy that it is quite greater in the Teruel province than in Zaragoza province.

Geomorphological and Geoenvironmental Effects of the Earthquake: Dialogue Between Earth's and Human Memory

The most worrying and reported effects of earthquakes are those on people, household goods, and buildings. These are a priority when classifying the degrees of intensity, both in the Mercalli scale and in the current European Macroseismic

Table 2 Results of the population survey on the memory and perception of seismic hazard

	EPICENTRAL ZONE					REST OF ZARAGOZA PROVINCE	TERUEL PROVINCE
	Age	>71	40-71	<40	TOTAL	TOTAL	TOTAL
	N	42	42	6	90	54	54
1) Do you know if an earthquake occurred in your locality some decades ago?	YES (%)	81	71	50	74	4	32
	NO (%)	19	29	50	26	96	68
Can you remember in which year?	RIGHT (%)	57	43	50	51		
	WRONG / DK / NA (%)	43	57	50	49		
2) Why do you know it?	Lived through (%)	64	0	0	30		
	Family (%)	7	47.5	16	26.5		
	Other sources (%)	10	23.5	34	17.5		
	DK / NA (%)	19	29	50	26		
4) Do you consider that your locality is under significant seismic hazard?	YES (%)	2.5	9	0	5.5	2	33
	NO (%)	95	86	50	90	87	54
	DK / NA (%)	2.5	5	50	4.5	11	13
5) Which of the following natural disasters do you consider most likely to occur in your locality?	Flooding (%)	69	67	67	68	70	48
	Karst subsidence (%)	2.5	10	33	8	54	17
	Landslide (%)	40	31	50	37	20	39
	Earthquake (%)	0	7	17	4	2	28

Scale (EMS-98). Scientists consider the latter as a good instrument for damage analysis of current or very recent earthquakes, but it has serious limitations for analysing old earthquakes. Not only does it exclude data on environmental effects, but also on historical-artistic and archaeological heritage. This limitation has been countered by the introduction of an Environmental Effects Macroseismic Intensity Scale (ESI-07), promoted by the International Union for Quaternary Research (INQUA) and published by the Geological Institute of Italy (Michetti et al., 2007).

In the case of the 1953 earthquake, the only observed geomorphological-environmental effects were related to instability of hillsides and slopes. Two relevant cases have been recognized from direct personal testimonies, documents, and press reports, as well as from geomorphological field observations, i.e. thanks to confluence of Earth's and human memory.

The most conspicuous geomorphological effect was the landslide that cut the N-234 road between Velilla de Jiloca and Maluenda, south of Calatayud. Almost all the regional and national newspapers highlighted this event. *ABC* and *Heraldo de Aragón* described it as a "landslide from a nearby mountain, with more than 800 tonnes of earth and stones falling. Some blocks were more than 2 *Tm*, and several of them ended up in the river Jiloca, while others cut off the road to Valencia". The works for removing the collapsed material and opening the road again took 4 days. Older people in both municipalities remember perfectly well what happened. In Velilla de Jiloca, they advised us that, on top of the mountain where the landslide occurred, a large open crack (*La Raja*) does exist "since ever", where they used to play as children.

The collapsed slope belongs to an abrupt escarpment that extends along, and close to, the right bank of the Jiloca river. It is made of horizontal Miocene gypsum and marl beds, deeply cut by a network of fractures with dominant NW–SE and NE-SW directions, in its northern part, and NNW-SSE and ENE-WSW, in its southern part. The escarpment is markedly unstable, as evidenced by its current appearance, with multiple partially disconnected gypsum blocks, some of them modelled in the form of monoliths. Satellite images (Fig. 8a) show how some blocks bounded by two fracture sets are separated from the escarpment without losing their parallelepipedal shape. At the roadside, other blocks that were overturned in the past show steeply dipping bedding (Fig. 8b).

A second geomorphological effect, verified with considerable reliability, is fall of one or two large rock blocks in Barranco del Montecillo, a narrow, winding canyon embedded in Upper Cretaceous limestones south of Aldehuela de Liestos. An elderly informant, Santiago Muñoz, told us that, as a boy, he worked as a shepherd and regularly led his sheep

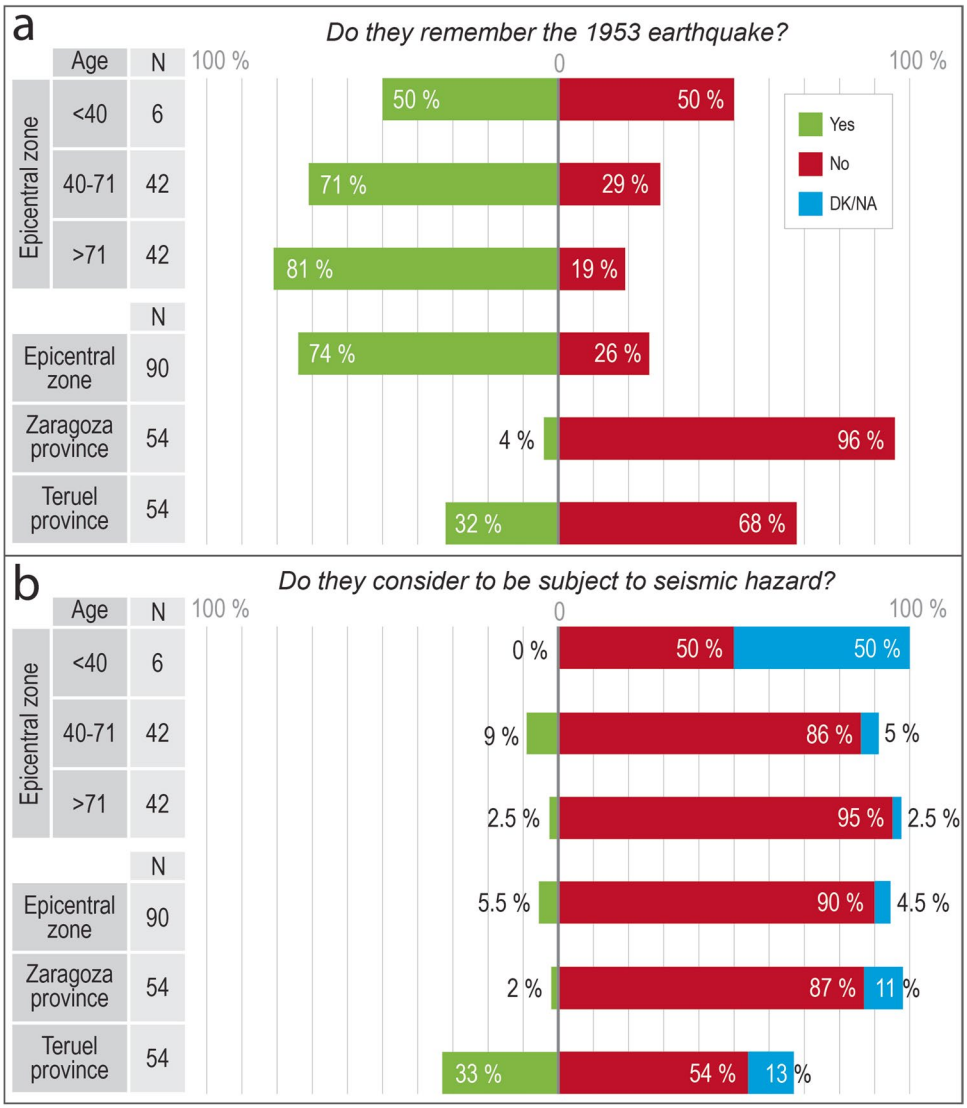

Fig. 7 **a** Results of the survey carried out in the Zaragoza and Teruel provinces exploring social memory on the 1953 earthquake. **b** Idem exploring perception of seismic hazard. Number of individuals interviewed: 198; date: December 2020 to February 2021

along this canyon. Next to one of the meanders, halfway up the slope, there was "a menacing boulder". Years later, at an imprecise date after 1953, he returned to the site and saw that the large rock had indeed fallen to the valley bottom, probably during the earthquake.

We assessed the likelihood of this hypothesis by carefully surveying the area described by the informant. According to his testimony, the boulder (i) was very large, (ii) came from the left slope of the canyon, and (iii) in its fall, it slightly overtopped the bottom and crossed to the right bank. Three candidate blocks were found at the bottom of Barranco del Montecillo. One of them was excluded since it is on the left side of the talweg, and with a fair degree of certainty is already observable on aerial photographs taken in 1947, before the earthquake. The other two blocks are compatible with the description, as they lie on the right bank, and they do not appear on 1947 aerial photographs whilst are observable on those taken in 1957. Particularly, one of these two boulders, about 3 m high, shows internal bedding in a nearly vertical position (Fig. 9). This suggests that it was overturned whilst falling and, with the inertia, it could have surpassed the talweg and risen approximately 1 m on the opposite bank.

Social Perception of Seismic Hazard

How do memory and knowledge on the 1953 earthquake translate into the perception of seismic hazard in the region? The second part of the population survey carried out inside and outside the epicentral area sought to assess the degree of perception amongst the population living in or linked to the Used-Daroca-Maluenda area, making a comparative assessment between successive generations of people and with other areas of Aragon (Table 2 and Fig. 7b). In the area most affected by the 1953 earthquake, the vast majority of people

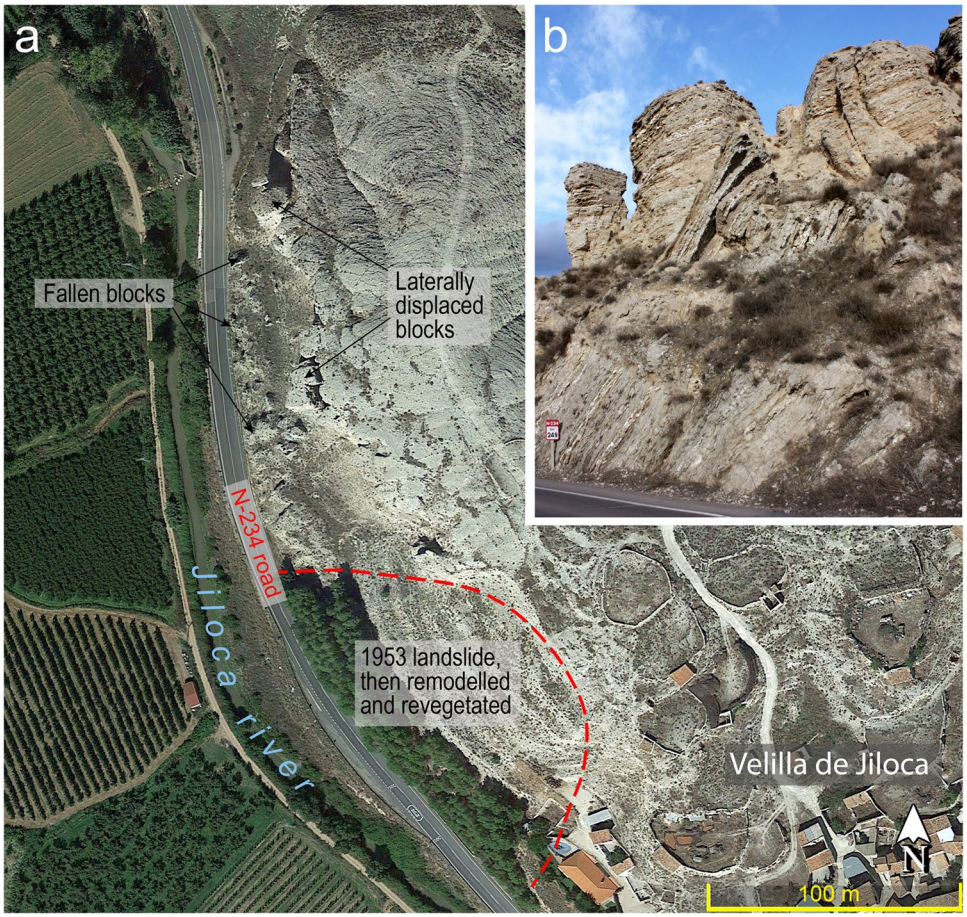

Fig. 8 **a** Vertical *Google Earth* image of the unstable slope in which a landslide triggered by the earthquake cut the N-234 road. **b** Current appearance of the N-234 road slope. Blocks of Miocene gypsum bounded by tectonic fractures are displaced laterally and, in some cases, collapsed and overturned

Fig. 9 Limestone block at the bottom of Barranco del Montecillo, very probably fallen during the 1953 earthquake

do not consider themselves to be subject to significant seismic hazard. Overall, only 5.5% of people do. By age group, this perception is higher amongst people aged between 40 and 71 (9%) than amongst those over 72 (2.5%). Earthquakes worry people much less than other natural disasters that could affect their territory. Ahead of them, and in this order, the danger of floods, landslides, or karstic subsidence are considered much higher. The same order is maintained irrespective of the age range analysed.

If we compare these results with those of the other areas covered by the survey, we notice certain differences. Both in the rest of the Zaragoza and Teruel provinces, those who believe they inhabit an area with a certain seismic hazard are again in the minority, but whilst in Zaragoza they are only 2%, and in Teruel they reach 33%. Compared with the other types of geological disasters, the order of concern in the province of Teruel is similar as in the epicentral area, whilst in Zaragoza the perception of danger of karstic subsidence (a frequent process in the central Ebro basin) prevails over that of slope movement (Table 2).

The main conclusion to be drawn is that the existing social memory of the 1953 earthquake does not translate into a significant perception of seismic hazard. This perception is miniscule and very similar in the area most affected by the earthquake, where it is very largely remembered, and in the rest of the province of Zaragoza, where the memory is almost non-existent. The perception of seismic hazard seems to be more influenced

by cultural factors: in the epicentral zone it is higher amongst people who did not live through the earthquake, but who have heard stories within the family and have had external information that has probably highlighted its importance.

This hypothesis is corroborated by the results obtained in Teruel: in spite of having felt the earthquake of 1953 more remotely, there seems to be a slightly greater awareness of it than in Zaragoza, and even though there is no other quake comparable in intensity and proximity in time in the register of the whole province of Teruel, there is a greater perception of the seismic risk. The explanation is probably to be found in the fact that, especially in Teruel city, the seismic phenomenon has been the subject of press reports and social debate due to the above-mentioned issue of the project of new public hospital.

The Outreach Project

One of the main objectives of the present project was promoting scientific culture about natural disasters amongst population, based on their own memory and experience. In this way, knowledge generated has been processed and returned to locals in the form of scientific outreach products. Three tools have been used: a written publication, a documentary film, and public talks. These help them both to consolidate the social memory of the 1953 earthquake and, at the same time, to rationally understand geological processes involved in natural disasters.

The main results of the research work, both those related to geology (evaluation of the fault responsible for the earthquake, geomorphological-environmental effects) and those concerning human memory and social perception, are collected in an outreach style booklet (Simón et al., 2021; Fig. 10a). The latter also summarizes the main seismological data compiled from both scientific literature and unpublished documents. The edition has been promoted by the Zaragoza University in collaboration with local study centres of Daroca (Zaragoza) and Jiloca (Teruel). The printed copies have been distributed free of charge, most of them to the population of Campo de Daroca, Comunidad de Calatayud, and Jiloca counties.

A documentary film, 15 min in duration, shows the essential contents of the project in a synthetic and lively format (Fig. 10b). The narration is supported by drone scenes, documentary images, interviews, and short expert dissertations. The script and documents have been prepared by two of the authors of the present paper (J. L. S., A. P.), whilst filming and editing of the documentary was carried out by Jorge Brizuela.

A number of public talks have been carried out in municipalities of the Campo de Daroca, Comunidad de Calatayud, and Jiloca counties (Used, Daroca, Calamocha, Maluenda…), in which the book has been presented, printed copies have been given to the public attending the event, the documentary

Fig. 10 **a** Cover of the outreach short book: *The 1953 Used earthquake: science and memory*. **b** Photogram of the documentary film, filmed and edited by J. Brizuela: A. Peiro interviewing an aged informant

film has been exhibited, and the chronicle of the project has been released.

Concluding Remarks

Our study on the 1953 earthquake has tried to deepen the knowledge and rescue the memory of what was the last destructive earthquake to occur in Aragon. As Earth

scientists, we have first attempted to characterize the tectonic framework in which the quake took place, mostly based on the geological and geomorphological record, i.e. on Earth's memory printed on rocks and reliefs. But we have also been interested in the social memory of that event, complementing scientific knowledge with popular knowledge of it.

The 1953 earthquake caused considerable material damage in Used (Zaragoza province) and, to a lesser extent, in other surrounding municipalities. The event was widely reported in regional and national press. It also produced the death of a girl, a fact that had never been explicitly reported before.

The earthquake was studied at the time by seismologists from the Fabra Observatory in Barcelona and the Instituto Geografico Nacional (IGN) in Madrid, and was assigned a magnitude of 4.7 and an epicentral intensity of VII. Uncertainties in focal location make it difficult to determine which fault in the area was responsible for the earthquake; the Daroca fault is the most compatible one with the available seismologic and tectonic information. The only documented geomorphological-environmental effects are a major landslide that cut the N-234 road and the fall of large boulders in a canyon tributary to the Río Piedra.

Based on direct testimonies from people who lived through it, as well as on a population survey carried out inside and outside the epicentral area, we conclude that the memory of the 1953 earthquake is very much alive in the more affected municipalities, both in the elderly and somewhat less so in younger generations. Nevertheless, that social memory does not translate into a significant perception of seismic hazard, the latter being more influenced by cultural factors than by direct personal experience of the earthquake.

Our study has a citizen science dimension: much information has been provided by the population itself and, after being processed and interpreted, has a return to the inhabitants of the territory in the form of cultural products. It somehow represents a dialogue between the *Memory of the Earth* and the social memory, trying to contribute to the remembrance of the 1953 earthquake not being lost. As stated by Fanta et al. (2019) referring to catastrophic floods, people remember and understand natural processes, but only for a limited period of time. Knowledge that is not repeated often enough fades away from the memory. Therefore, communitary protection from natural disasters cannot uniquely rely on folk memory, but on scientific knowledge. It is necessary to teach people about the occurrence of catastrophic events in the past, which requires exploring their record in rocks and landscapes, i.e. in the geological heritage.

Acknowledgements We acknowledge the following informants who gave us their personal testimonies and useful data on the effects of the earthquake: Josefa García, Fortunato Tajada, Marcelina Ferrer, Carmen Muñoz, Antonio Ballestín, Paula Liarte, Ramón Aliaga, and Alberto Sánchez (Used); Santiago Muñoz (Aldehuela de Liestos); Silvestre Gálvez and Silvina López (Torralba de los Frailes); Juan Catalán (Velilla de Jiloca); José A. Lavilla (Villanueva de Jiloca); Ángel Aranda (Orcajo); Mª Pilar Lorente (Daroca); Mercedes Oliete and Eugenia Acero (Calatayud); and Luis Martín Ballesteros and Jesús Gil (Maluenda). The following institutions provided us with scientific, administrative, and press documents: Observatori Fabra-Reial Academia de Ciències i Arts de Barcelona, Institut Cartogràfic y Geològic de Catalunya (ICGC), Instituto Geográfico Nacional (IGN), Instituto Geológico y Minero de España (IGME), municipalities of Used and Zaragoza, Diputación Provincial de Zaragoza, Arciprestazgo de Daroca, and Demarcación de Carreteras del Estado en Aragón-Ministerio de Transportes (Spanish government). Useful seismological and geological observations and comments are due to Josep Batlló (ICGC), Juan V. Cantavella and Javier Fernández (IGN), Miguel Á. Rodríguez Pascua and Jesús Causapé (IGME), Antonio Aretxabala, and Álvaro González. Luis Arlegui prepared DEM images for Fig. 3. Jorge Brizuela took photographs of Fig. 4, and filmed and edited the outreach documentary. Centro de Estudios del Jiloca (CEJ) y Centro de Estudios Darocenses (Daroca, Zargoza) collaborated in editing the outreach book.

Author Contribution Study conception and design was due to José L. Simón. All authors contributed to data collection and analysis, material preparation, and figures. The first draft of the manuscript was written by José L. Simón. All authors commented on previous versions of the manuscript, read, and approved the final manuscript.

Funding Open Access funding provided thanks to the CRUE-CSIC agreement with Springer Nature. This study has been funded by (i) Aragón regional government and FEDER, Aragón Operational Programme 2014–2020, research project LMP127_18; (ii) Aragón regional government, research group Geotransfer, E32_20R; (iii) Agencia Estatal de Investigación, Ministerio de Ciencia e Innovación, Spanish government, project PID2019-108705-GB-I00; and (iv) Instituto Universitario de Ciencias Ambientales (IUCA), University of Zaragoza.

Data Availability Not applicable: all relevant data are included in the manuscript.

Code Availability Not applicable.

Declarations

Conflict of Interest The authors declare no competing interests.

Open Access This article is licensed under a Creative Commons Attribution 4.0 International License, which permits use, sharing, adaptation, distribution and reproduction in any medium or format, as long as you give appropriate credit to the original author(s) and the source, provide a link to the Creative Commons licence, and indicate if changes were made. The images or other third party material in this article are included in the article's Creative Commons licence, unless indicated otherwise in a credit line to the material. If material is not included in the article's Creative Commons licence and your intended use is not permitted by statutory regulation or exceeds the permitted use, you will need to obtain permission directly from the copyright holder. To view a copy of this licence, visit http://creativecommons.org/licenses/by/4.0/.

References

Alfaro P, Estévez A, Moretti M, Soria JM (1999) Structures sédimentaires de déformation interprétées comme séismites dans le Quaternaire du Bassin du Bas Segura (Cordillère Bétique orientale). Compt Rend de l'Acad de Sci de Paris 328:17–22

Allen CR (1986) Seismological and paleoseismological techniques of research in active tectonics. In: Wallace RE (ed) Active Tectonics. National Academy Press, Washington, Studies in Geophysics, pp 148–154

Alsop GI, Marco S (2013) Seismogenic slump folds formed by gravity-driven tectonics down a negligible subaqueous slope. Tectonophysics 605:48–69

Álvaro M, Capote R, Vegas R (1979) Un modelo de evolución geotectónica para la Cadena Celtibérica. Acta Geologica Hispanica 14:172–177

Arlegui LE, Simón JL, Lisle RJ, Orife T (2005) Late Pliocene-Pleistocene stress field in the Teruel and Jiloca grabens (eastern Spain): contribution of a new method of stress inversion. J Struct Geol 27:693–705

Basilone L (2017) Seismogenic rotational slumps and translational glides in pelagic deep-water carbonates. Upper Tithonian-Berriasian of Southern Tethyan margin (W Sicily, Italy). Sed Geol 356:1–14

Capote R, Muñoz JA, Simón JL, Liesa CL, Arlegui LE (2002) Alpine tectonics I: The Alpine system north of the Betic cordillera. In: Gibbons W, Moreno T (eds) The Geology of Spain. The Geological Society, London, pp 367–400

Casas-Sainz AM, Gil-Imaz A, Simón JL, Izquierdo-Llavall E, Aldega L, Román-Berdiel T, Osácar MC, Pueyo-Anchuela Ó, Ansón M, García-Lasanta C, Corrado S, Invernicci C, Caricchi C (2018) Strain indicators and magnetic fabric in intraplate fault zones: case study of Daroca thrust, Iberian Chain, Spain. Tectonophysics 730:29–47

Colomer M, Santanach P (1988) Estructura y evolución del borde sur-occidental de la Fosa de Calatayud-Daroca. Geogaceta 4:29–31

Dos Reis RP, Henriques MH (2009) Approaching an integrated qualification and evaluation system for geological heritage. Geoheritage 1:1–10

Fanta V, Šálek M, Sklenicka P (2019) How long do floods throughout the millennium remain in the collective memory? Nat Commun 10:1–9

Fontseré E (1955) Los temblores de tierra catalanes de los años 1952 y 1953. Boletín Del Observatorio Fabra (reial Academia De Ciències i Arts De Barcelona) 42:79–84

Gracia FJ (1992) Tectónica pliocena de la Fosa de Daroca (prov. de Zaragoza). Geogaceta 11:127–129

Gracia FJ, Gutiérrez F (1996) Neotectónica y sismicidad del valle del Jiloca y sus alrededores. Xiloca 17:165–206

Gutiérrez F, Gutiérrez M, Gracia FJ, McCalpin JP, Lucha P, Guerrero J (2008) Plio-Quaternary extensional seismotectonics and drainage network development in the central sector of the Iberian Chain (NE Spain). Geomorphol 102:21–42

Gutiérrez F, Masana E, González A, Guerrero J, Lucha P, McCalpin JP (2009) Late Quaternary paleoseismic evidence on the Munébrega Half-graben fault (Iberian Range, Spain). Int J Earth Sci 98:1691–1703

Gutiérrez F, Gracia FJ, Gutiérrez M, Lucha P, Guerrero J, Carbonel D, Galve JP (2012) A review on Quaternary tectonic and nontectonic faults in the central sector of the Iberian Chain, NE Spain. J Iber Geol 38:145–160

Gutiérrez F, Lucha P, Jordá L (2013) The Río Grío depression (Iberian Chain, NE Spain). Neotectonic graben vs. Fluvial Valley Cuaternario y Geomorfología 27:5–32

Gutiérrez F, Carbonel D, Sevil J, Moreno D, Linares R, Comas X, Zarroca M, Roqué C, McCalpin JP (2020) Neotectonics and late holocene paleoseismic evidence in the Plio-Quaternary Daroca half-graben, Iberian Chain, NE Spain Implications for fault source characterization. J Struct Geol 131:103933

Herraiz M, De Vicente G, Lindo-Ñaupari R, Giner J, Simón JL, González-Casado JM, Vadillo O, Rodríguez-Pascua MA, Cicuéndez JL, Casas A, Cabañas L, Rincón P, Cortés AL, Ramírez M, Lucini M (2000) The recent (upper Miocene to Quaternary) and present tectonic stress distributions in the Iberian Peninsula. Tectonics 19:762–786

IGN (2021) Servicio de Información Sísmica del Instituto Geográfico Nacional. https://www.ign.es/web/ign/portal/sis-catalogo-terremotos. Accessed 30 Jan 2022

Julivert M (1954) Observaciones sobre la tectónica de la Depresión de Calatayud. Arrahona, Museo de Sabadell 3–18

Lafuente P, Arlegui LE, Liesa CL, Simón JL (2011) Paleoseismological analysis of an intraplate extensional structure: the Concud fault (Iberian Chain, Spain). Int J Earth Sci 100:1713–1732

Lafuente P, Arlegui LE, Liesa CL, Pueyo Ó, Simón JL (2014) Spatial and temporal variation of palaeoseismic activity at an intraplate, historically quiescent structure: the Concud fault (Iberian Chain, Spain). Tectonophysics 632:167–187

Lafuente P (2011) Tectónica activa y paleosismicidad de la falla de Concud (Cordillera Ibérica central). PhD Thesis, Universidad de Zaragoza

Liesa CL, Simón JL (2009) Evolution of intraplate stress fields under multiple remote compressions: the case of the Iberian Chain (NE Spain). Tectonophysics 474:144–159

Liesa CL, Casas AM, Simón JL (2018) La tectónica de inversión en una región intraplaca: la Cordillera Ibérica. Revista De La Sociedad Geológica De España 31:23–50

Liesa CL, Simón JL, Ezquerro L, Arlegui LE, Luzón A (2019) Stress evolution and structural inheritance controlling an intracontinental extensional basin: the central-northern sector of the Neogene Teruel Basin. J Struct Geol 118:362–376

Liu L, Zoback MD (1997) Lithospheric strength and intraplate seismicity in the New Madrid seismic zone. Tectonics 16:585–595

Mansur KL, de Souza CI (2011) Characterization and valuation of the geological heritage identified in the Peró dune field, state of Rio de Janeiro, Brazil. Geoheritage 3:97–115

Martín-Bello L, Arlegui LE, Ezquerro L, Liesa CL, Simón JL (2014) La falla de Calamocha (fosa del Jiloca, Cordillera Ibérica): estructura y actividad pleistocena. 2ª Reunión Ibérica sobre Fallas Activas y Paleosismología-Iberfault (Lorca, Murcia), IGME: 55–85

Martínez Solares JM, Cabañas L, Benito MB, Ribas A, Gaspar JM, Ruiz S, Rodríguez O (2013) Actualización de mapas de peligrosidad sísmica de España 2012. Centro Nacional de Información Geográfica (CNIG-IGN), Madrid

Martini G (1992) The Digne Symposium on the conservation of our geological heritage. Earth Sci Conserv 30:3–4

Martini G (2009) Geoparks… a vision for the future. Revista Do Instituto De Geociências-USP 5:85–90

McCalpin J (2009) Paleoseismology, 2nd edn. Academic Press

McCalpin JP, Nelson AR (1996) Introduction to paleoseismology. Int Geophys 62:1–32

Mezcua J, Martínez-Solares JM (1983) Sismicidad del Área Ibero-Mogrebí. IGN, Madrid

Michetti AM, Esposito E, Guerrieri L and collaborators (2007) Intensity Scale ESI 2007. In: Guerrieri L, Vittori E (Eds.) Memorie Descrittive Carta Geologica d'Italia, 74. Servizio Geologico d'Italia–Dipartimento Difesa del Suolo, APAT, Roma

Ministerio de Fomento (2002) Real Decreto 997/2002, de 27 de septiembre, por el que se aprueba la norma de construcción sismorresistente: parte general y edificación (NCSR-02). BOE 244:35898–35967

Moretti M, Van Loon AJ (2014) Restrictions to the application of 'diagnostic' criteria for recognizing ancient seismites. J Palaeogeogr 3:162–173

Moretti M, Alfaro P, Owen G (2016) The environmental significance of soft-sediment deformation structures: key signatures for sedimentary and tectonic processes. Sed Geol 344:1–4

Muntoni F, Balvis T, Rizzo R, Loru P (2020) Territorial planning of geological mining historical and environmental park of Sardinia. Geoheritage 12:1–11

Noria A (2015) "El tiempo todo lo olvida". El desastre de El Limón del 6 de septiembre de 1987 en Venezuela: apuntes para su estudio. HIB: revista de historia iberoamericana 8: 55–78

Páez D, Fernandez I, Beristain M (2001) Catástrofes, traumas y conductas colectivas: procesos y efectos culturales. Departamento de Psicología Social y Metodología, Universidad del País Vasco. http://www.uned.es/dpto-psicologíasocial. Accessed 25 Oct 2021

Pantosti D, Schwartz DP, Valensise G (1993) Paleoseismology along the 1980 surface rupture of the Irpinia fault: implications for earthquake recurrence in the southern Apennines, Italy. J Geophys Res: Solid Earth 98(B4):6561–6577

Peiro A, Simón JL (2021a) Caracterización preliminar de la zona de falla de Río Grío-Pancrudo: estructura extensional de primer orden en la evolución reciente de la Cordillera Ibérica. Geo-Temas 18:846–849

Peiro A, Simón JL (2021b) The Río Grío-Pancrudo Fault Zone (central Iberian Chain, Spain): recent extensional activity revealed by drainage reversal. Geol Mag 159:21–36

Rey Pastor A, Bonelli J (1957) El sismo de Daroca-Used de 28 de septiembre de 1953 y su relación con la línea sismotectónica del Jiloca. Instituto Geográfico y Catastral, Madrid

Roca E, Guimerà J (1992) The Neogene structure of the eastern Iberian margin: structural constraints on the crustal evolution of the Valencia trough (western Mediterranean). Tectonophysics 203:203–218

Samardjieva E, Payo G, Badal J (1999) Magnitude formulae and intensity–magnitude relations for early instrumental earthquakes in the Iberian region. Nat Hazards 19:189–204

Scott B, Price S (1988) Earthquake-induced structures in young sediments. Tectonophysics 147:165–170

Seilacher A (1969) Fault-graded beds interpreted as seismites. Sedimentol 13:155–159

Simón JL (1982) Compresión y distensión alpinas en la Cadena Ibérica oriental. PhD Thesis, Universidad de Zaragoza

Simón JL (1989) Late Cenozoic stress field and fracturing in the Iberian Chain and Ebro Basin (Spain). J Struct Geol 11:285–294

Simón JL (2015) La Geología: ¿ciencia útil para una sociedad del desconocimientio? El Ecologista 85:56–58

Simón JL, Arlegui LE, Lafuente P, Liesa CL (2012) Active extensional faults in the central-eastern Iberian Chain, Spain. J Iber Geol 38:127–144

Simón JL, Arlegui LE, Ezquerro L, Lafuente P, Liesa CL (2014) Aproximación a la peligrosidad sísmica en la ciudad de Teruel asociada a la falla de Concud (NE España). Geogaceta 56:7–10

Simón JL, Arlegui LE, Ezquerro L, Lafuente P, Liesa CL, Luzón A (2016) Enhanced paleoseismic succession at the Concud Fault (Iberian Chain, Spain): new insights for seismic hazard assessment. Nat Hazards 80:1967–1993

Simón JL, Simón-Porcar G, Peiro A (2021) El terremoto de Used de 1953: ciencia y memoria. Universidad de Zaragoza-Centro de Estudios del Jiloca-Centro de Estudios Darocenses, Zaragoza

Sims JD (1973) Earthquake-induced structures in sediments of Van Norman Lake, San Fernando, California. Sci 182:161–163

Vegas R, Fontboté JM, Banda E (1979) Widespread Neogene rifting superimposed on alpine regions of the Iberian Peninsula. Proceedings Symposium Evolution and Tectonics of the Western Mediterranean and Surrounding Areas, EGS, Viena. Instituto Geográfico Nacional, Madrid, Special Publ 201:109–128

Yeats RS, Sieh K, Allen CR (1997) The geology of earthquakes. Oxford University Press, New York

3. Falla de Concud

La falla de Concud es una falla normal plio-cuaternaria que limita el margen noreste de la terminación sur de la fosa del Jiloca, y desplaza el relleno del sector meridional de la cuenca de Teruel respecto a esta última (Figs. 1.2, 5.16). Tiene una longitud aflorante de 14,2 km, desde el este del pueblo de Cella hasta los alrededores de la ciudad de Teruel, y su dirección media es NW-SE, que cambia a cercana a N-S en sus extremos. En su sector central, el plano de falla, con buzamientos medios entre 65 y 70º SW, se divide en dos segmentos casi paralelos y pone en contacto los depósitos aluviales pleistocenos en el bloque hundido y las unidades triásicas y jurásicas en el bloque levantado (Lafuente, 2011; Lafuente *et al.*, 2011a, 2014). Las estrías medidas en afloramientos de los planos de falla indican un movimiento normal casi puro en el segmento principal de dirección NW-SE, mientras que en su segmento sur NNW-SSW las estrías muestran una pequeña componente de desgarre sinestral. De ello se infiere que el bloque superior se mueve con una dirección de transporte media hacia N 220º E. La herencia estructural regional ejerce un claro control en ella, ya que su traza discurre paralela a la de un sinclinal vergente al norte relacionado con la estructuración compresiva previa, entre otras características. Ello sugiere que su configuración extensional actual es el resultado de la inversión negativa de la estructura compresiva previa durante la última fase extensional regional (Plioceno superior-Cuaternario).

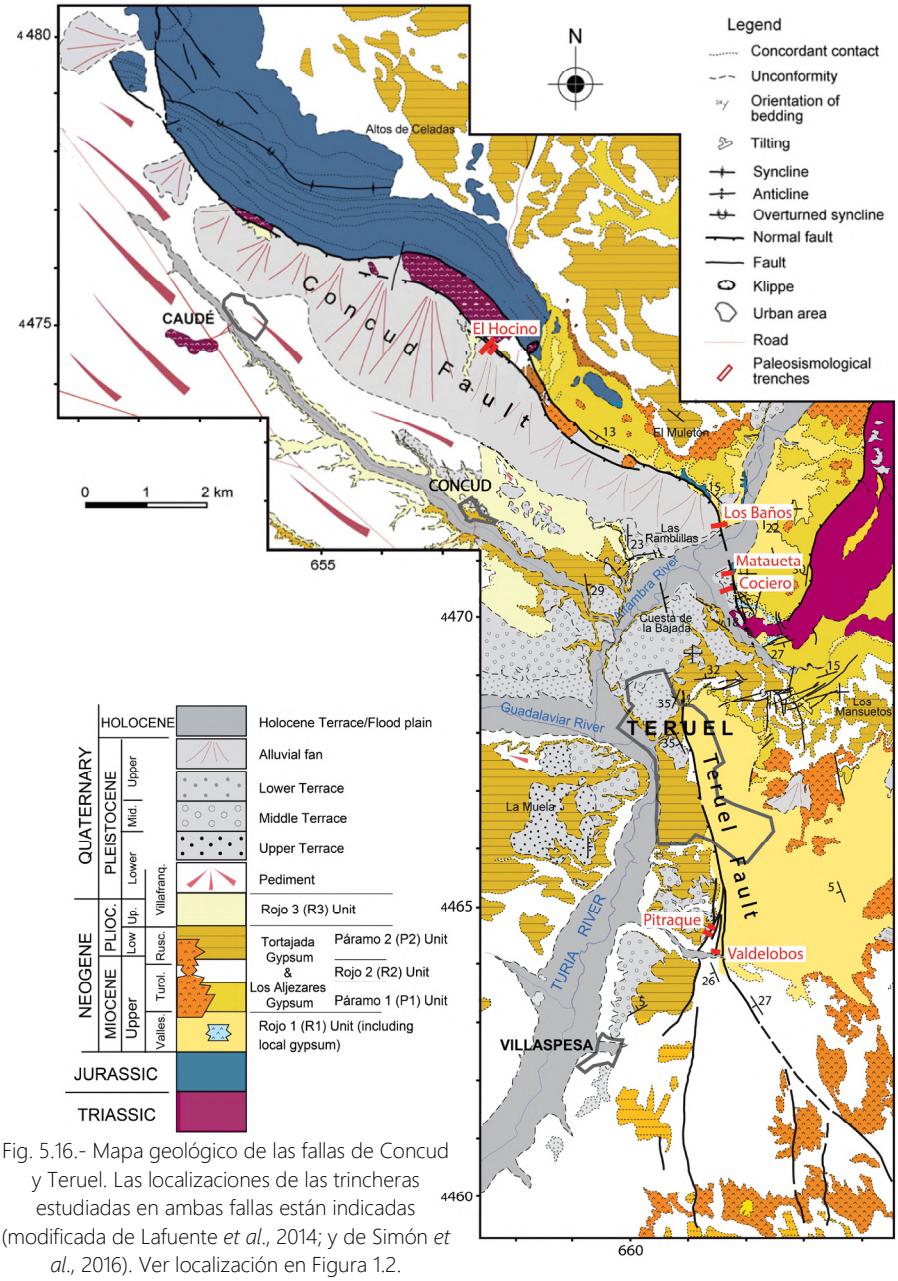

Fig. 5.16.- Mapa geológico de las fallas de Concud y Teruel. Las localizaciones de las trincheras estudiadas en ambas fallas están indicadas (modificada de Lafuente *et al.*, 2014; y de Simón *et al.*, 2016). Ver localización en Figura 1.2.

La falla de Concud ha estado activa desde el Plioceno superior, y el techo de la serie pretectónica se identifica con la superficie SEF, tanto en el bloque hundido de la falla como en el levantado, con una diferencia de altura de 260 m (Lafuente, 2011; Lafuente *et al*., 2011a; Ezquerro *et al*., 2020). Teniendo en cuenta un buzamiento medio del plano de 70º SW y un movimiento normal casi puro, se trata de un desplazamiento neto de 277 m, que podría aumentar hasta casi los 300 m si se tiene en cuenta el basculamiento en *roll-over* que caracteriza su bloque hundido en profundidad. La SEF aquí está datada en ca. 3,8 Ma (Rusciniense superior; Ezquerro *et al*., 2020), por lo que se calcula una tasa de desplazamiento de la falla de 0,07–0,08 mm/a para esa ventana temporal (Simón *et al*. 2005; Lafuente 2011; Lafuente *et al*. 2011a).

El registro paleosismológico de la falla de Concud se ha estudiado a partir del análisis de cinco trincheras excavadas en su segmento centro-sur (Fig. 5.16): Los Baños (Lafuente, 2011; Lafuente *et al*., 2011a), El Hocino (1 y 2), Masada Cociero (Lafuente, 2011; Lafuente *et al*., 2014) y La Mataueta (Simón *et al*., 2016). Se trata del registro más completo de todas las fallas de la Cordillera Ibérica centro-oriental, y consta de once eventos, de los cuales cinco están correlacionados en varias de las trincheras (Fig. 5.17).

La falla de Concud se expone bien preservada en el afloramiento de Los Baños (Fig. 5.16, poniendo en contacto la Formación Alfambra (Mioceno superior) en su bloque levantado, con una serie de depósitos pleistocenos en su bloque hundido. El bloque levantado está afectado por un suave pliegue de arrastre de escala hectométrica y numerosas fallas menores sintéticas y antitéticas a la principal, que está orientada 170, 75 W, con estrías de cabeceo 75º S. Estas fallas menores, sobre todo las sintéticas, también cortan parte del bloque inferior (Arlegui *et al*., 2006; Lafuente *et al*., 2011a). Cabe destacar la existencia de tres fisuras rellenas con diferentes unidades pleistocenas, que están asociadas a la ruptura principal en la parte más alta de la trinchera. Lafuente *et al*. (2011a) interpretan que se formaron por el *bending* desencadenado por el movimiento de una falla ciega en su bloque hundido. Estos autores infieren, a partir de los datos estructurales, estratigráficos, y las edades OSL, una sucesión de hasta seis eventos sísmicos en esta trinchera: evento U (de edad anterior a 71,7 ± 5,2 ka), evento V (inmediatamente posterior a 71,7 ± 5,2 ka y anterior a 64,2 ± 4,4 ka), evento W (datado probablemente en 64,2 ± 4,4 ka y, en cualquier caso, anterior a 63,7 ± 4,0 ka), evento X (entre 64,2 ± 4,4 ka y 63,7 ± 4,0 ka), evento Y (cercano a 38,6 ± 2,3 ka) y evento Z (cercano a 32,1 ± 2,4 ka; Fig. 5.17).

Las trincheras del Hocino están excavadas en la rama sur, de las dos en que se desdobla la falla de Concud en su sector central (Fig. 5.16). En este sector la falla corta las unidades neógenas que rellenan la fosa del Jiloca en su bloque levantado y las pone en contacto con sedimentos aluviales pleistocenos en su bloque hundido (Lafuente *et al*., 2014). En ambas trincheras la fracturación se concentra en una zona de falla central de dirección media 163, 60 W, con estrías mayoritariamente dispuestas 75º S, pero también 53º N. La zona de falla se compone de varias fallas menores sintéticas con la principal y, en el caso de la trinchera Hocino 1, de una estructura S-C acorde con el movimiento normal de la estructura, de la cual se infiere una dirección de transporte N 295º E. El movimiento a lo largo de esta falla ha inducido el basculamiento de la parte basal de la secuencia pleistocena de su bloque hundido en un *roll-over*, mientras el depósito del resto de la secuencia forma una cuña sintectónica. El salto medible en este basculamiento es de 5,5 m, que se traduce en un salto neto de 6,5 m. La unidad aluvial en la que se identifica este desplazamiento está datada con OSL en 74,2 ± 8,2 ka, lo cual deriva en una tasa de desplazamiento para esa ventana temporal de 0,08-0,10 mm/a. Lafuente *et al*. (2014) interpretan una sucesión de cinco eventos en total, cuatro de ellos en Hocino 1 y uno más en Hocino 2 (las edades OSL que se indican son las que mejor acotan los eventos en una trinchera u otra): Evento V (después de 77,3 ± 4,3 ka, y antes de 71,3 ± 4,7 ka, en el Hocino 1), Evento W (posterior a 71,3 ± 4,7 ka y anterior a 74,2 ± 8,2 ka, del Hocino 1), Evento X (entre 46,9 ± 4,2 ka y 51,2 ± 4,1 ka, del Hocino 1), Evento Y (entre 43,8 ± 3,0 ka y 40,4 ± 3,4 ka, del Hocino 2), Evento Z (después de 19,5 ± 2,1 ka y antes de 22,3 ± 2,0 ka, del Hocino 2; Fig. 5.17).

En el caso de los afloramientos de Masada Cociero, éstos muestran una falla menor sintética con la falla de Concud (con dirección NNW-SSE en este sector) que desplaza los depósitos villafranquienses y la Terraza baja (T1) del río Alfambra, de edad Pleistoceno superior (Fig. 5.16; Lafuente *et al*., 2014). Se trata de una zona de falla compleja que, en las unidades inferiores villafranquienses, desarrolla varias *splay faults* de las cuales sólo un par

sintéticas afectan a dicha terraza. El salto neto en estos afloramientos es de 1,7-2,2 m (calculado a partir de la reconstrucción de este plano de falla y la dirección de transporte media N 220º E de toda la falla de Concud). Los autores del estudio infieren un único evento bien acotado con dataciones OSL alrededor de los 15 ka, entre 15,6 ± 1,3 ka y 15,0 ± 1,0 ka (Fig. 5.17).

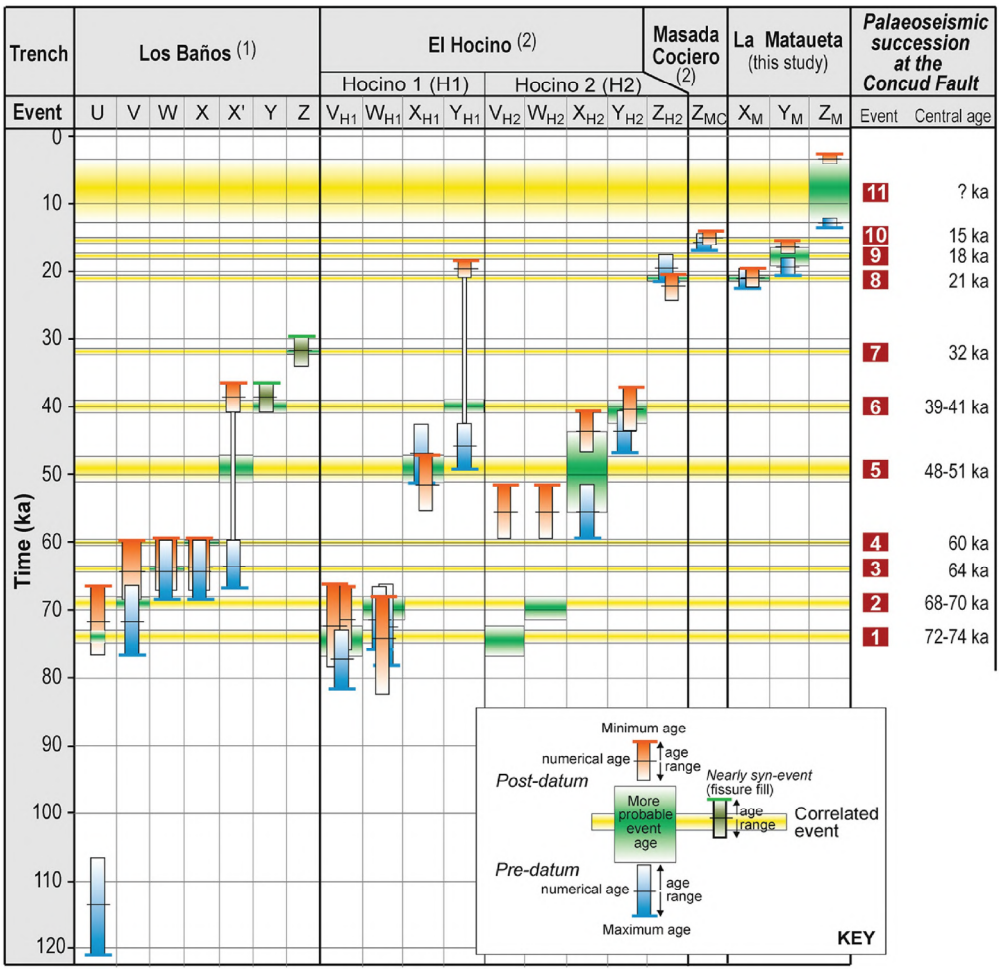

Fig. 5.17.- Registro paleosismológico integrado de la falla de Concud, a partir de los eventos inferidos en todas las trincheras analizadas. Se indican con detalle los rangos temporales en los que se basan las correlaciones (tomada de Simón *et al.*, 2016).

Por último, la trinchera de La Mataueta está excavada al norte de Masada Cociero, en un glacis de corto recorrido y edad Pleistoceno superior, que cubre localmente retazos de la Terraza baja (T1) del río Alfambra (Fig. 5.16). Éste parte desde el escarpe de la traza principal de la falla Concud, y está deformado por una falla sintética paralela a la rama principal, que es el objeto del estudio paleosismológico de Simón *et al.* (2016). La falla expuesta en la trinchera de La Mataueta está orientada 165, 67 W y desplaza todas las unidades aluviales pleistocenas. No se han encontrado estrías en sus planos de rotura pero, teniendo en cuenta la dirección de transporte media de falla de Concud, se infiere un vector desplazamiento con cabeceo de 77º S. En su bloque hundido, la serie está basculada en *roll-over* hacia la falla principal y cortada por una falla antitética de dirección 160, 65 E. El análisis en detalle del log de la trinchera, y de las edades OSL de sus unidades, ha permitido la interpretación de los tres eventos más recientes de la falla de Concud (Simón *et al.*, 2016): Evento X (ocurrido entre 21,3 ± 1,5 ka y 21,0 ± 1,4 ka, siendo 21 ka su edad más probable), posible etapa de *creep* (entre 21,0 ± 1,3 ka y 19,2 ± 1,2 ka), Evento Y (después de 19,2 ± 1,2 ka y antes de 16,4 ± 1,0 ka), Evento Z (más reciente de 12,8 ± 0,7 ka; Fig. 5.17).

Todos los eventos han ocurrido en los últimos 74 ka y han generado un salto total acumulado en la falla de Concud de 20,5 m, con saltos cosísmicos medios de 1,9 m (Lafuente, 2011; Simón *et al.*, 2016). Esto se traduce en una tasa de desplazamiento media de 0,29 mm/a que ha variado en el tiempo, siendo de 0,53 y 0,42 mm/a en los periodos de 74-60 ka y 21-8 ka, respectivamente, y de 0,13 mm/a en el periodo comprendido entre 60 y 21 ka. El periodo de recurrencia medio obtenido de los datos paleosismológicos se encuentra entre 7,1 ± 3,5 y 8,0 ± 3,3

ka, dependiendo del margen de error en la acotación temporal del último evento (11) y la posibilidad de no haber dado con el evento más reciente (MRE) de la falla de Concud. La secuencia paleosísmica está bien reconstruida porque este periodo de recurrencia no difiere demasiado del calculado mediante el método directo, de aprox. 6,5 ka.

Para caracterizar el potencial sísmico de la falla de Concud se han calculado diferentes magnitudes momento (Mw): en el rango 6.4-6.8 (Lafuente, 2011; aplicando Wells y Coppersmith, 1994; Stirling *et al*., 2002; Pavlides y Caputo, 2004) y en el rango 6.5-6.6 (Ezquerro *et al*., 2015; Simón *et al*., 2016; aplicando Hanks y Kanamori, 1979).

En esta tesis, inferimos una Mw = 6.2-6.8 para el máximo terremoto esperable de la falla de Concud (usando las regresiones de Wells y Coppersmith, 1994; Stirling *et al*., 2002; Wesnousky, 2008; Leonard, 2010). El salto cosísmico medio, obtenido mediante el estudio paleosismológico, de 1,9 m, es similar al calculado mediante la regresión de Stirling *et al*. (2002), de 2,1 m. Con el resto de correlaciones este valor es menor, en torno a 0,3-0,5 m (aplicando Wells y Coppersmith, 1994; Wesnousky, 2008; Leonard, 2010). Los saltos cosísmicos inferidos mediante estas regresiones permiten calcular periodos de recurrencia bajos, de 1-2 ka, mientras que el de Stirling *et al*. (2002) los cifra en aproximadamente 7 ka.

4. Falla de Teruel

La falla de Teruel es una falla normal intracuencal del sector central de la fosa de Teruel que presenta una dirección N-S (Fig. 5.16). En su sector norte, en los alrededores de la ciudad de Teruel, la falla consiste en una única rama de dirección N 170º E, mientras que en su sector sur, a la altura del pueblo de Villaspesa, se divide en dos ramas orientadas N-S y NNW-SSE, respectivamente. El buzamiento medio de su plano de falla es de 68º hacia el E, y las estrías medidas en él indican una dirección de transporte hacia N 275º E, lo que significa un movimiento normal casi puro (Simón *et al*., 2017). La longitud aflorante de su traza principal es de ca. 9 km; sin embargo, existen fallas menores y fracturas que afectan a terrazas fluviales cuaternarias y están alineadas con la traza de la falla de Teruel (Peiro *et al*., 2017). Son indicios de su posible prolongación hacia el norte, mediante la cual pasaría a superar los 11 km de longitud (Simón *et al*., 2017). De esta forma, la falla de Teruel se aproxima a la de Concud, y cabe pesar que ambas podrían llegar a formar una estructura sismogénica conjunta de 23 km de longitud (Gutiérrez *et al*., 2012). Sin embargo, los datos estructurales indican que son estructuras geométrica y cinemáticamente independientes (Lafuente *et al*., 2011b; Peiro *et al*., 2017), lo que sugiere que también lo son desde el punto de vista sísmico. La estructura transversal de Los Mansuetos-Valdecebro (Fig 5.16), que consiste en un sinforme fracturado y transversal a ambas fallas, también interfiere en la estructura y contribuye a la transferencia del desplazamiento entre las fallas principales (Lafuente *et al*., 2011b; Peiro *et al*., 2017).

La falla desplaza la mayor parte de las unidades informales detríticas-carbonatadas que forman el relleno neógeno de la cuenca de Teruel, así como un remanente de la Terraza fluvial media (T2) de los ríos Alfambra y Turia, del Pleistoceno medio. El bloque hundido de la falla de Teruel, el situado al W, está basculado aproximadamente 2º hacia el E mediante un *roll-over* que afecta hasta la unidad Páramo 2. En este mismo bloque, hacia las proximidades de la falla, la serie neógena define un monoclinal de adaptación con buzamientos próximos a los 17º W. Como consecuencia del desplazamiento neto sobre la falla y el acomodado por el *bending* del monoclinal, la base del Páramo 2 pasa de estar a 880 m s.n.m. de altura al oeste de la ciudad de Teruel a alcanzar los 1130 m s.n.m. al este de la misma. Esto se traduce en un salto vertical de 250 m (Simón *et al*., 2017; Ezquerro 2017; Ezquerro *et al*., 2020). Teniendo en cuenta este salto, el buzamiento del plano y el movimiento normal casi puro, los autores infieren un net slip de ca. 270 m para la base del Páramo 2. Dada la correlación hecha entre la parte media de dicha unidad con la SEF y el techo de la megasecuencia M7 definida por Ezquerro (2017), datada en 3,8 Ma (Ezquerro *et al*., 2020), se obtiene una tasa de desplazamiento de ca. 0,07 mm/a para esa ventana temporal.

El estudio paleosísmico llevado a cabo por Simón *et al*. (2017) en la falla de Teruel tiene lugar en su sector central, donde se ramifica en varios segmentos de falla que desplazan la Terraza media (Fig. 5.16). Las tres

trincheras fueron excavadas en dos de sus ramas principales más occidentales, en dos localidades: Pitraque (Pitraque 1 y 2) y Valdelobos.

En la trinchera de Pitraque 1 los autores muestran la fracturación tanto de las unidades neógenas Rojo 2 y Páramo 2 como de las unidades suprayacentes pleistocenas. La falla situada más al este de la serie neógena presenta una dirección NE-SW y produce un salto de 10 cm en la base de la unidad pleistocena, mientras que el resto están orientadas NNW-SSE y quedan fosilizadas por dichos depósitos. La deformación del Pleistoceno se expresa en forma de numerosas fracturas, algunas fallas con desplazamientos centimétricos y dos grandes grietas de extensión, una de ellas con relleno carbonatado de hasta 2 m de altura y 20 cm de separación. Los autores interpretan que esta fracturación más reciente está inducida por el *bending* de un monoclinal de acomodación al movimiento de una falla ciega en profundidad. Considerando las relaciones estructurales entre las fallas, las unidades sedimentarias y sus edades OSL, Simón *et al.* (2017) identifican tres eventos paleosísmicos: evento X (anterior a 70,7 ± 5,3 ka), evento Y (entre 70,7 ± 5,3 ka y 71,8 ± 5,1 ka) y evento Z (entre 48,5 ± 3,8 ka y el regolito de edad aproximada holocena). Asimismo, considerando la amplitud del monoclinal, estiman un salto cosísmico mínimo de 1 m para la falla ciega hipotética (net slip de más de 1,1 m si el plano buzara ca. 70º).

La trinchera Pitraque 2 corta las mismas unidades estratigráficas que Pitraque 1, pero en esta ocasión claramente desplazadas por dos fallas normales (Fig. 5.18a). La situada más al oeste tiene una dirección N 035º E y queda fosilizada por las unidades pleistocenas, mientras que la falla normal del sector este, que está orientada N 019º E, rompe y desplaza hasta tres unidades recientes con un salto de 50 cm (Fig. 5.18b). Las estrías medidas en esta última indican un movimiento normal puro para la falla de Teruel (Fig. 5.18c, e; Simón *et al.*, 2017). Al monoclinal de acomodación interpretado en Pitraque 1 también se le asocia una grieta de extensión que discurre paralelamente a esta falla normal. Los autores también infieren tres eventos: evento X (antes de 70,7 ± 5,3 ka), evento Y (después de 46,5 ± 3,1 ka), evento Z (entre 46,5 ± 3,1 ka y el regolito holoceno).

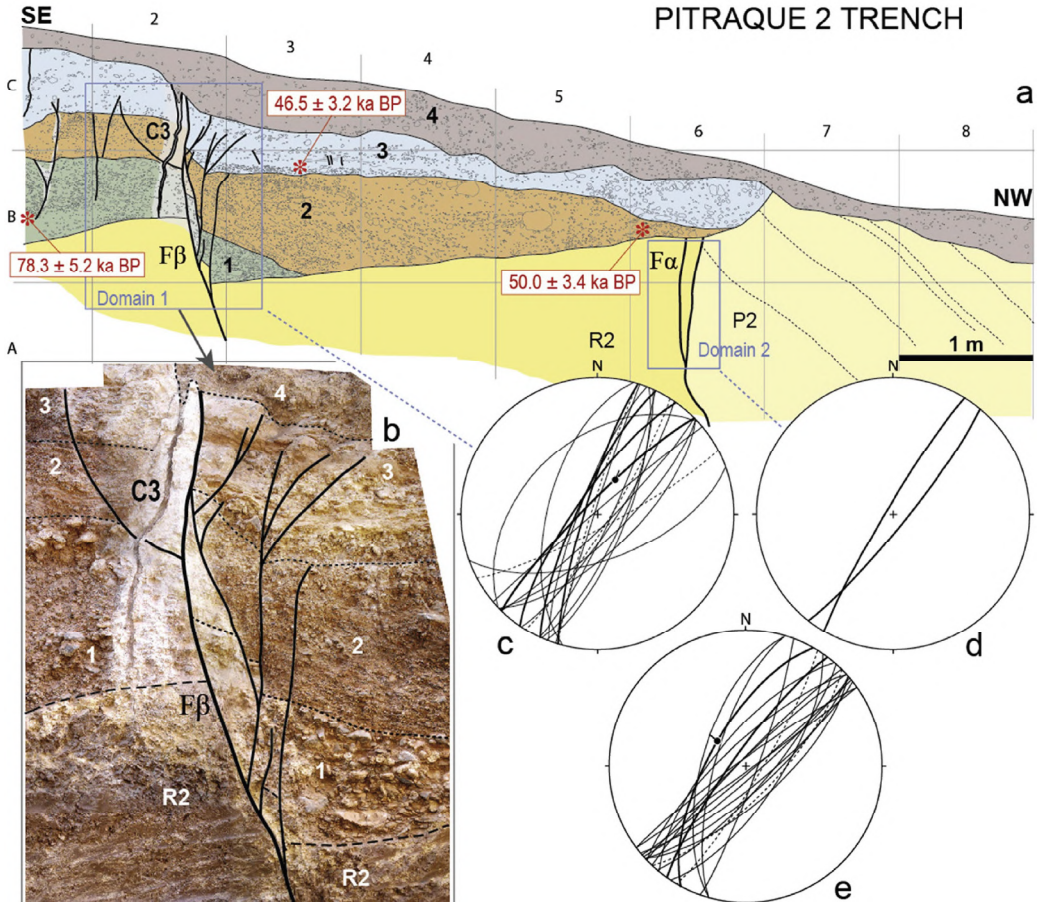

Fig. 5.18.- (a) Log del talud S de la trinchera Pitraque 2 excavada en la falla de Teruel. R2: unidad Rojo 2; P2: unidad Páramo 2; 1-4: unidades Pleistocenas. Se indica la localización (con asteriscos) y la edad de las muestras datadas con OSL. (b) Fotografía de detalle del dominio 1 indicado en "a". (c, d) Estereogramas de fracturas de los dominios 1 y 2. (e) Ídem en el talud contrario (tomada de Simón *et al.*, 2017). Ver localización en la Figura 5.16.

La trinchera de Valdelobos corta la unidad neógena Rojo 2 desplazada por otra rama de la falla de Teruel distinta a la estudiada en Pitraque. Se trata de una falla normal de dirección N 155º E que también afecta a los depósitos basales de la terraza más reciente de la rambla de Valdelobos. Es por ello que Simón *et al.* (2017) interpretan únicamente un evento Z, datado entre 26,7 ± 1,9 ka y 9,9 ± 0,7 ka.

Los autores del estudio realizan una correlación entre los eventos interpretados en las tres trincheras para acotar el registro paleosísmico de la falla de Teruel en varios eventos: evento 0 (engloba los eventos X de las dos trincheras de Pitraque, y se produjo antes del depósito de las unidades datadas por OSL en 70,7 ± 5,3 ka y 78,3 ± 5,2 ka), evento 1 (corresponde al evento Y de Pitraque 1, está acotado entre 70,7 ± 5,3 ka y 66,7 ka, que sería la edad mínima de la datación 71,8 ± 5,1 ka), evento 2 (es el evento Y de Pitraque 2, que se produjo antes de 46,5 ± 3,1 ka), evento 3 (agrupa los dos eventos Z de Pitraque 1 y 2, de después de 46,5 ± 3,1 ka) y evento 4 (identificado con el único evento de la trinchera de Valdelobos y, por lo tanto, asociado a una rama diferente de la falla de Teruel, está acotado entre 26,7 ± 1,9 ka y 9,9 ± 0,7 ka).

A partir de estos cuatro eventos recientes acotados entre aproximadamente 76,0-66,7 ka y 28,6-9,2 ka, Simón *et al.* (2017) calculan un periodo de recurrencia medio en el rango 9,5-16,7 ka para las ramas investigadas de la falla de Teruel. Los eventos 1-3 llevan asociado un salto neto acumulado de 1,7 m y un salto medio cosísmico de ca. 0,6 m para su rama de la falla. El evento 4 no supone una variación sustancial en estos valores, y con todos ellos se obtiene una tasa de desplazamiento de 0,03-0,05 mm/a para una ventana temporal de ca. 70-20 ka en el conjunto de la falla.

Las unidades pleistocenas estudiadas en las trincheras de Pitraque corresponden con la Terraza fluvial media (T2) de los ríos Alfambra y Turia, del Pleistoceno medio. Sus retazos están desplazados hasta 8,2 m en la vertical a un lado y a otro de las ramas oeste de la falla de Teruel (desplazamiento neto de 8,8 m teniendo en cuenta un buzamiento medio del plano de falla de ca. 70º, y su dirección de transporte hacia N 275º E) (Simón *et al.*, 2017). Tomando para su techo la edad mínima obtenida en las trincheras (46,5 ± 3,1 ka), los autores calculan una tasa de desplazamiento de 0,18-0,20 mm/a para ese rango temporal más concreto, acumulando en este caso el movimiento en casi todas las ramas de la falla. La tasa total para toda la falla de Teruel probablemente sea superior, pero la ausencia de afloramientos cuaternarios en las otras ramas imposibilita la contrastación de esta hipótesis en el artículo. Con la tasa calculada para el Pleistoceno superior (0,18-0,20 mm/a) y el salto medio cosísmico (0,6 m), se obtiene (mediante el método directo) un periodo de recurrencia de 3 ka.

El terremoto esperable para la falla de Teruel, calculado en esta tesis tanto en el caso de que rompiera la traza inicialmente considerada para la falla, a lo largo de sus 9 km de longitud, como si lo hiciera por los 11 km de longitud que se estiman con su posible prolongación hacia el norte, llegaría a producir un salto cosísmico medio en ambos casos en el rango de 0,2-1,9 m, y se le asociaría una magnitud Mw = 5.9-6.7 (aplicando Wells y Coppersmith, 1994; Stirling, 2002; Wesnousky, 2008; Leonard, 2010). El valor de salto medio cosísmico obtenido de los datos paleosismológicos (0,6 m), se encuentra en el rango obtenido mediante las correlaciones empíricas. Asimismo, con estos datos se ha calculado el periodo de recurrencia, con dos agrupaciones en torno a 1-2 ka y a 9-10 ka. En el hipotético caso de que la falla de Teruel sí que formara una estructura sismogénica conjuntamente a la de Concud, de 23 km de longitud, su Mw sería de 6.8 ± 0.3 (aplicando Wesnousky, 2008), pudiendo oscilar entre 6.5 y 7.0 (aplicando Wells y Coppersmith, 1994; Stirling, 2002; Leonard, 2010), y su salto cosísmico medio sería de hasta 2,4 m (Stirling, 2002).

5. Falla de Valdecebro

La zona de falla de Valdecebro es una estructura transversa a la cuenca de Teruel que, junto con las fallas de Concud y Teruel, compartimenta intracuencalmente la fosa con directrices diferentes (Figs 1.2, 5.19a). Está orientada con una dirección WNW-ESE, con buzamientos en el rango de 46º-86º (con una media de 69º) tanto hacia el norte como hacia el sur, y se extiende a lo largo de unos 5,2 km, hundiendo su bloque sur mediante un basculamiento en *roll-over* para dar lugar a la depresión de Valdecebro. Se compone de una serie de fallas normales, que generalmente ponen en contacto las calizas jurásicas, en su bloque levantado, con los

conglomerados del Mioceno superior, en su bloque hundido. Las estrías medidas en un plano de falla representativo indican un cabeceo de 85º W, lo cual implica un movimiento normal casi puro de la estructura y una dirección de transporte media hacia N 202° E (Fig. 5.19c; Simón *et al.*, 2019). Según la composición estratigráfica de sus dos bloques, puede inferirse que la falla de Valdecebro comenzó su actividad en el Rusciniense superior, se mantuvo activa durante el Villafranquiense y a lo largo del Cuaternario (Ezquerro, 2017), dadas las evidencias de fracturación encontradas en superficies de glacis pleistocenos. Esta actividad queda, por tanto, reflejada en la superficie SEF, que aparece desplazada por las fallas con un salto vertical de hasta 190 m. Este valor se traduce en un salto neto de 205 m y, teniendo en cuenta su edad de 3,8 Ma, se calcula una tasa de desplazamiento medio de ca. 0.05 mm/a para esa ventana temporal (Simón *et al.*, 2019; Ezquerro *et al.*, 2020).

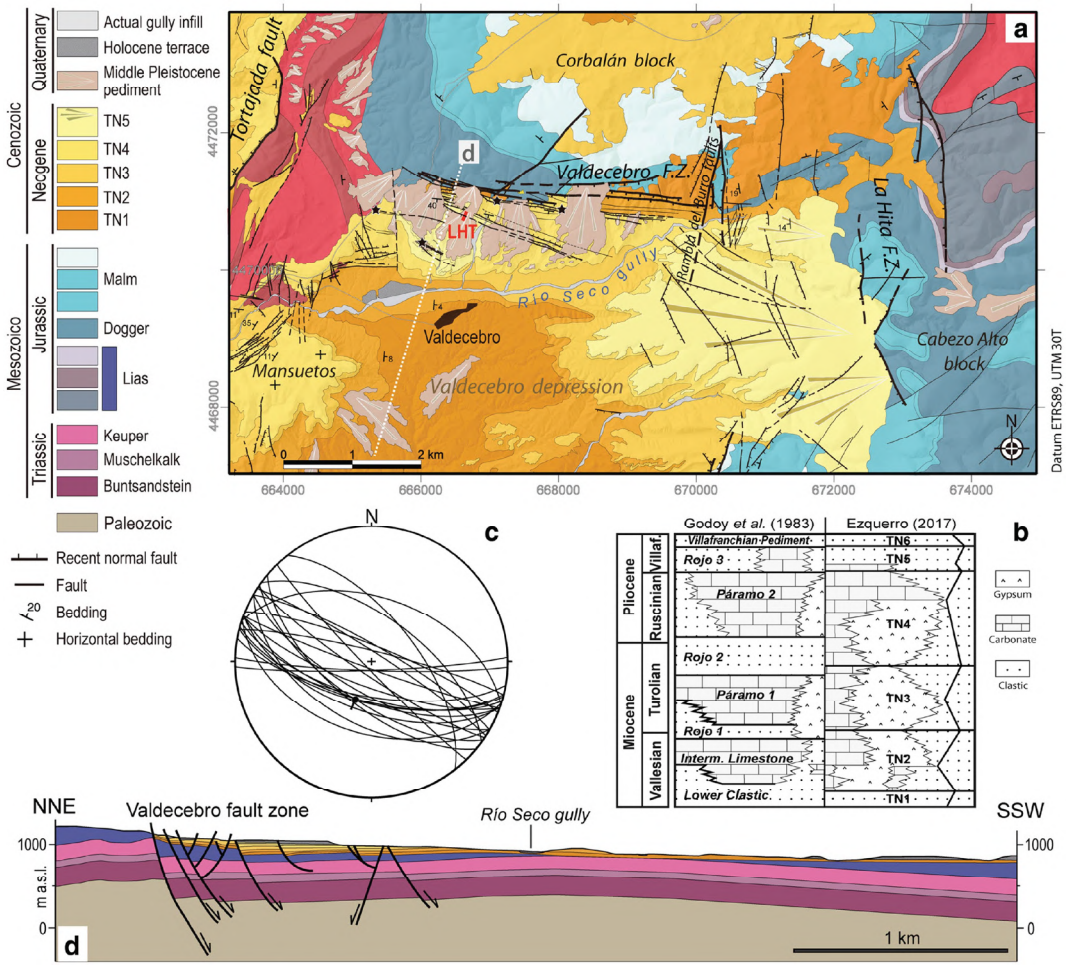

Fig. 5.19.- (a) Mapa geológico de la falla de Valdecebro, que incluye las unidades genéticas (TN1-TN6) definidas por Ezquerro (2017) y la localización de la trinchera de Los Huesares (LHT). (b) Correlación de las unidades genéticas con las unidades informales de Godoy *et al.* (1983). (c) Orientaciones de planos y estría medidos sobre superficies de la falla. (d) Corte geológico de la zona de falla de Valdecebro, su localización se indica en el mapa (tomada de Simón *et al.*, 2019).

La actividad cuaternaria de la falla de Valdecebro ha sido registrada por Simón *et al.* (2019) en la trinchera de Los Huesares (Fig. 5.20), excavada en uno de los glacis pleistocenos que mostraba un escalón en superficie debido al desplazamiento de la rama de falla situada más al sur. Esta rama pone en contacto la unidad informal miocena Rojo 3 con los sedimentos aluviales pleistocenos. Estos últimos son los aflorantes en la trinchera, cortados por dos fallas normales principales, así como por varias fallas sintéticas y antitéticas intermedias. Las siete unidades aluviales definidas por los autores van registrando los desplazamientos verticales de algunas fallas y a su vez fosilizando otras. El salto neto acumulado de todas ellas alcanza los 7 m.

Simón *et al.* (2019) interpretan, a partir de las relaciones estratigráficas y estructurales, y de las edades OSL y el modelo de edad, un mínimo de 6-7 eventos asociados a la falla de Valdecebro (Fig. 5.20a): Evento T (comprendido entre los 149,1 ± 8,1 ka y los 142 ka), Evento U (entre los 130 y los 125 ka), Eventos V, W y X (después de 125 ka), Evento Y (entre 95 y 50,1 ± 2,0 ka) y Evento Z (con posterioridad a 50,1 ± 2,0 ka). A lo largo de todos

ellos, las dos zonas de falla principales se van desarrollando casi a la vez y de manera similar, produciendo saltos cosísmicos variados en el rango 58-117 cm, y periodos de recurrencia medios de entre 8,4 y 28,4 ka. Independientemente de cuál sea el escenario, Simón *et al.* (2019) calculan una tasa de desplazamiento medio para la falla de Valdecebro de entre 0,05 y 0,07 mm/a para los últimos 142 ka, aunque este registro paleosismológico corresponde a una única rama de las varias que componen la falla de Valdecebro y que presentan evidencias de actividad durante el Pleistoceno superior. Con los datos de salto cosísmico y las tasas, se obtienen por el método directo unos periodos de recurrencia de alrededor de 1-4 ka y 21-29 ka, similares a los obtenidos mediante datos paleosismológicos.

Por nuestra parte en esta tesis, realizamos inferencias sismogénicas de la falla de Valdecebro utilizando las regresiones empíricas. Con sus 5,2 km de ruptura superficial, podría llegar a generar terremotos en el rango de Mw = 5.5-6.5, y desplazamientos cosísmicos medios de entre 0,1 y 1,4 m (aplicando Wells y Coppersmith, 1994; Stirling, 2002; Wesnousky, 2008; Leonard, 2010). Los saltos cosísmicos medios obtenidos en la trinchera, de entre 0,6 y 1,2 m, encajan bien en este marco. Los periodos de recurrencia obtenidos mediante correlaciones empíricas rondan los 1-4 ka (aplicando Wells y Coppersmith, 1994; Leonard, 2010), y los 21-29 ka (Stirling, 2002).

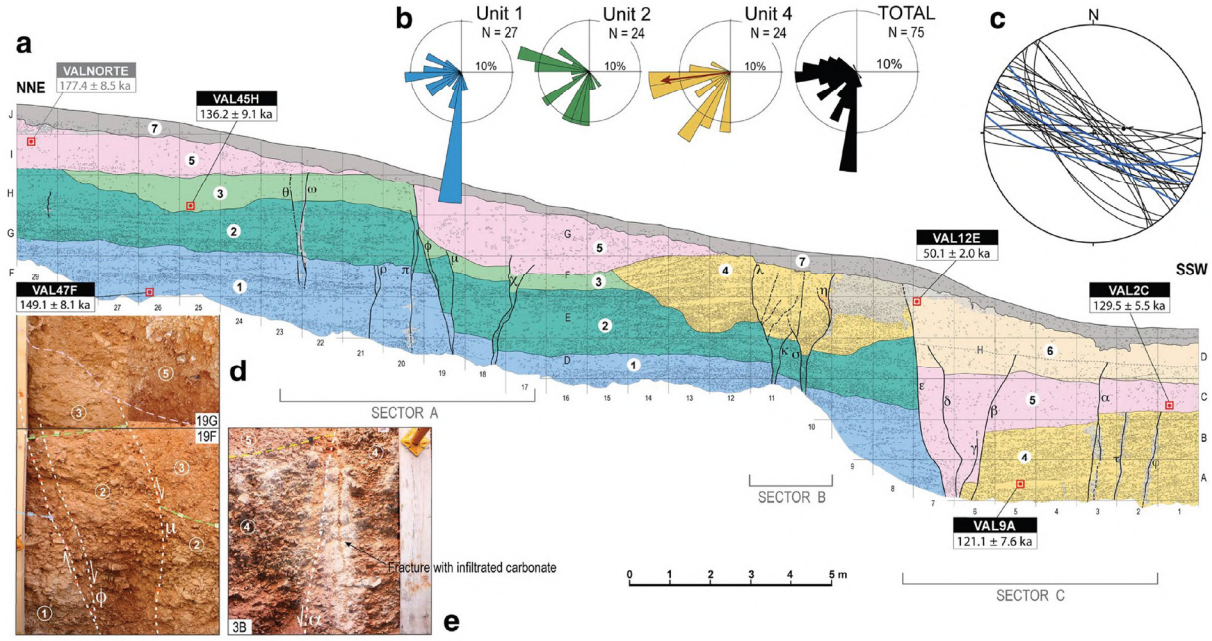

Fig. 5.20.- (a) Log de la trinchera de Los Huesares. Ver localización en Figura 5.19a. (b) Diagramas en rosa de paleocorrientes inferidas de cantos imbricados en las unidades sedimentarias cuaternarias. (c) Orientaciones de planos de fallas y fracturas medidos en la trinchera. (d) Fotografías de detalle de las celdas 3B, 19F y 19G de la trinchera (tomada de Simón *et al.*, 2019).

6. Zonas de falla de El Pobo, Peralejos-Tortajada-Cabigordo y La Hita

El margen activo del semigraben de la parte norte de la cuenca de Teruel corresponde con una zona de falla que presenta una longitud aproximada de 35 km y está compuesta por distintos planos de falla (Figs. 1.2, 5.21). La zona de falla de la Sierra de El Pobo es la situada más al norte y alcanza los 16 km de longitud en dirección N-S, desde el NE del pueblo de Villalba Alta hasta el SE de Escorihuela. En su sector norte se desarrollan numerosas fallas, tanto sintéticas como antitéticas, que marcan un contacto neto entre los materiales neógenos que rellenan la cuenca y los mesozoicos del borde. Presentan longitudes menores a 1 km y buzamientos elevados, con pocas estrías pero que indican un movimiento claramente normal de todo el conjunto (Ezquerro, 2017; Ezquerro *et al.*, 2020). Algunas de las fallas antitéticas de su bloque hundido cortan los depósitos pliocenos con desplazamientos de algunos metros. Todas ellas se han interpretado como la expresión superficial, a modo de *splay faults*, de una falla ciega que bien podría alinearse con el plano de falla principal único del sector sur de la falla de El Pobo. Su sector sur abarca los últimos 9 km de la estructura, donde se observa un contacto muy neto entre los glacis pleistocenos depositados en su bloque hundido y las unidades mesozoicas de la Sierra de El Pobo, en su bloque levantado (Simón *et al.*, 2012; Ezquerro, 2017; Ezquerro *et al.*, 2020). Este último presenta algunos planos de falla

menores, escalonados y de orientación paralela al plano principal, en los que se han medido dos familias de estrías: una con cabeceos bajos y movimiento dextral-normal, y otra con cabeceos que indican un movimiento normal puro, que indican una dirección de transporte N 260º E (Ezquerro, 2017; Ezquerro *et al*., 2020). El relleno neógeno de su bloque hundido está basculado en una estructura en *roll-over* contra la falla principal, en cuyas inmediaciones también hay un monoclinal de arrastre. Toda la estructura de falla de la Sierra de El Pobo produce un desplazamiento vertical de la SEF (3,8 Ma) de entre 180 y 520 m, a partir del cual se obtiene una tasa de desplazamiento medio para ese espacio temporal en el rango 0,05-0,14 mm/a (Ezquerro *et al*., 2020).

Hasta casi la ciudad de Teruel, el margen activo de la cuenca se expresa por medio de las zonas de falla de Peralejos, Tortajada y Cabigordo (Fig. 5.21). Suponen la continuidad hacia el sur de la falla de El Pobo, aunque con una directriz más NNE-SSW en las fallas de Peralejos-Tortajada, y volviendo a la N-S en Cabigordo. En el caso de las primeras, éstas ponen en contacto las unidades del Mioceno superior que rellenan la cuenca con los materiales triásicos y jurásicos (Ezquerro, 2017; Ezquerro *et al*., 2020). En algún caso, los depósitos neógenos llegan a disponerse en *onlap* sobre los materiales del bloque levantado. Son escasos y de muy corto recorrido los glacis pleistocenos que se desarrollan únicamente en las cercanías de la zona de falla de Tortajada. Ambas zonas de falla están compuestas por varios segmentos con disposición *en échelon* y zonas de relevo diestro menores. Las estrías medidas en sus planos de falla indican un movimiento normal casi puro, con dirección de transporte N 295º E en Peralejos y N 315º E en Tortajada (Ezquerro, 2017), y en menor medida dextral-normal. Respecto a la zona de falla de Cabigordo, ésta se localiza en el bloque levantado de las anteriores, y genera un monoclinal de adaptación en la serie mesozoica que permite el depósito de la misma serie neógena y de un glacis pleistoceno sin contacto tectónico claro entre ambos dominios (Ezquerro, 2017; Ezquerro *et al*., 2020). Se trata de un conjunto de fallas N-S con buzamientos al W que son la expresión superficial de la falla en profundidad. La cartografía de la SEF en estos sectores ha permitido calcular un salto vertical en este sector de 440-520 m y una tasa de desplazamiento medio de 0,12-0,14 mm/a para los últimos 3,8 Ma.

Por último, la zona de falla de La Hita es una estructura que está situada al sur de Cabigordo y al este de la falla de Valdecebro (Fig. 5.21), conformando el margen oriental del sector central de la cuenca de Teruel. Su geometría no está bien definida, pero consiste en un conjunto de fallas de orientación variable (NNW-SSE, NNE-SSW, y de media N-S) que afectan tanto a las rocas jurásicas del bloque levantado, como al relleno neógeno y los depósitos villafranquienses de su bloque hundido. Estos últimos también las fosilizan en algunos puntos. El conjunto de fallas desplaza la SEF aproximadamente 250-620 m, resultando una tasa de desplazamiento de 0,07-0,16 mm/a (Ezquerro, 2017; Ezquerro *et al*., 2020).

El estudio de los diagramas distancia-salto vertical de la SEF llevado a cabo por Ezquerro (2017) arroja evidencias de que todas estas estructuras, a excepción del conjunto de las fallas de La Hita y Teruel, se han comportado como una estructura única de casi 30 km de longitud, cinemáticamente coherente y que correspondería a una sola falla de escala cortical. La coalescencia en profundidad con la falla de La Hita no habría culminado. Existen evidencias de estructuras de licuefacción sísmicamente inducidas (sismitas) en los depósitos villafranquienses de los glacis que parten desde la falla de El Pobo. Se estima que podría tratarse de una sucesión de seis eventos, posiblemente comprendidos entre 2,9 y 2,6 Ma (Ezquerro, 2017). Sin embargo, las malas condiciones del afloramiento, la distribución irregular de las capas y la falta de un control preciso de su edad, no permiten inferir nada con seguridad acerca de estos periodos de actividad más recientes para las fallas próximas. No existen evidencias directas de actividad reciente en toda la estructura, debido a la falta de depósitos cuaternarios afectados por la misma.

Dada la coherencia cinemática de toda la zona de falla de El Pobo y Peralejos-Tortajada-Cabigordo, si se comportara como una única estructura sismogénica, su máximo terremoto esperable calculado en esta tesis alcanzaría una Mw = 6.8 ± 0.3 (aplicando la regresión de Wesnousky, 2008). Sin embargo, consideramos que dadas las pocas evidencias paleosismológicas de actividad, parece bastante improbable que, en el caso de que se moviera esta estructura, rompiera a lo largo de toda esta extensión. En cambio, lo haría a lo largo de los diferentes segmentos mediante terremotos de menor magnitud, con menores saltos cosísmicos y periodos de recurrencia.

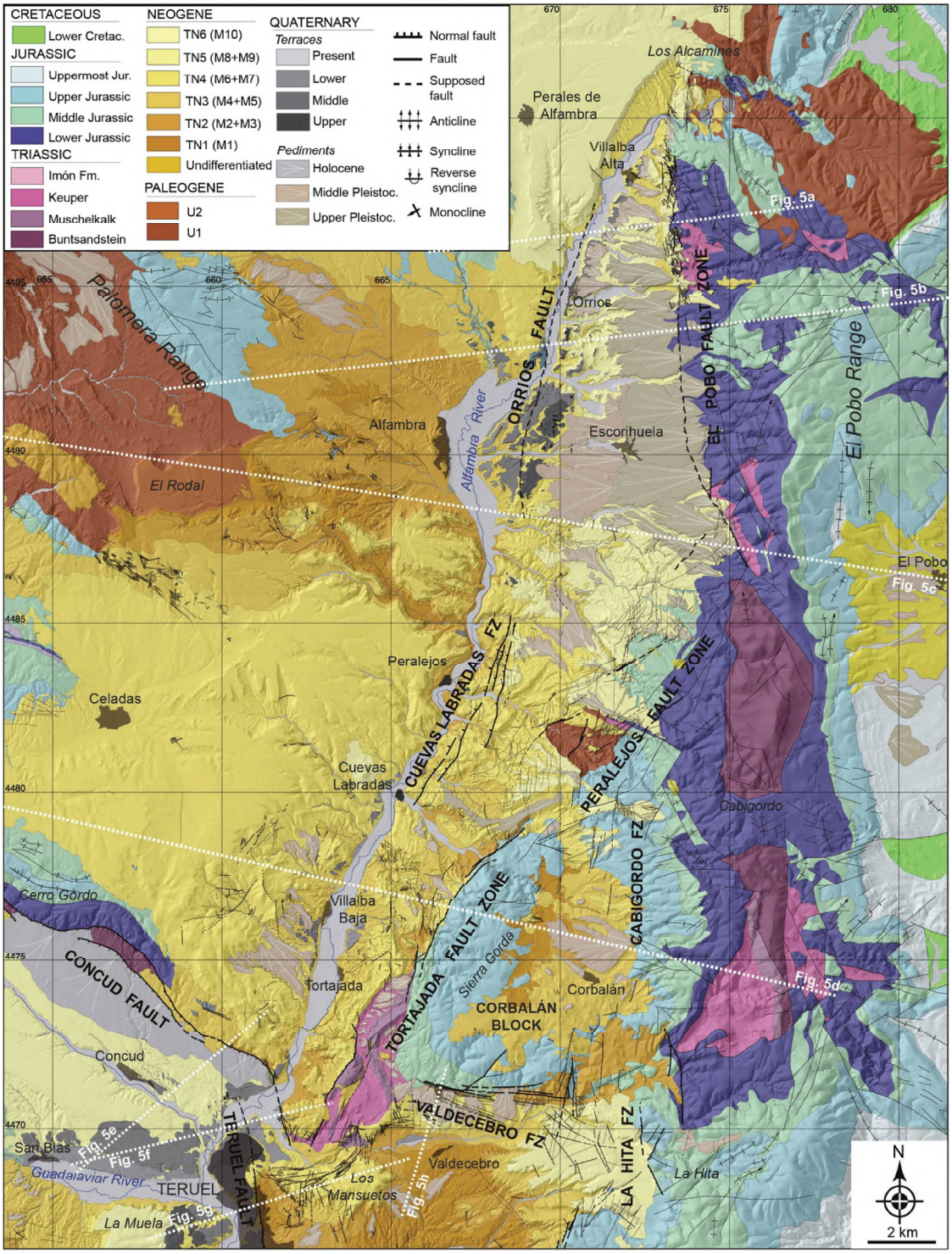

Fig. 5.21.- Mapa geológico de los sectores norte y central de cuenca de Teruel, y su borde activo con la zona de falla de El Pobo, Peralejos-Tortajada-Cabigordo y zona de falla de La Hita (tomada de Ezquerro *et al.*, 2020). Ver su localización en Figura 1.2.

7. Sistema de fosas del Maestrat

Este último sector se compone de un sistema de fallas normales, de dirección cercana a NNE-SSW y extensión decamétrica o hectométrica generalizadas, que desplaza de manera sintética y antitética las unidades mesozoicas y los rellenos neógenos y cuaternarios de las distintas cuencas (Fig. 5.22a,b). Este sistema de *horst* y *graben* no sólo se extiende costa adentro en el Maestrat, sino que también en la plataforma marina se han localizado fallas con la misma dirección y comportamiento (Fig. 5.22a; Roca, 1992; Perea, 2006; Perea *et al.*, 2012). Todo ello responde a la propagación y acomodación tierra adentro de la deformación asociada a la apertura del Surco de Valencia en esta región.

Las fallas mejor documentadas son las siguientes: fallas de Irta, Torreblanca, Xivert o Alcalà de Xivert, Talaies, Vall d'Àngel, Salzedella, Torre Endomènech, La Valltorta, Rambla de la Viuda o Ivarsos, Albocàsser, Catí, Atzeneta y Montsià (Perea, 2006; Perea *et al.*, 2012; Simón *et al.*, 2012; Simón *et al.*, 2013). A pesar de que son pocas las medidas de planos de falla consideradas como representativas, su dirección está en torno a N 030º E, el buzamiento observado está alrededor de 65º tanto hacia el NW como hacia el SE, y las estrías tienen cabeceos de entre 70 y 75º, indicando un movimiento normal casi puro (Fig. 5.22c; Simón, 1982). Estas estrías definen, a su vez, una dirección de transporte cercana a E-W. La falla marina más estudiada es la de Amposta (con sus tres ramas: oeste, central y este; Roca, 1992; Roca y Guimerà, 1992; Perea, 2006; Perea *et al.*, 2012), por su relación con la fracturación reactivada por la inyección de gas en el almacén "Castor" (Cesca *et al.*, 2014). Sus tres ramas buzan ca. 60º, hacia el SE en el caso de las ramas oeste y central, y hacia el NW en el caso de la oriental (Roca, 1992; Cesca *et al.*, 2014).

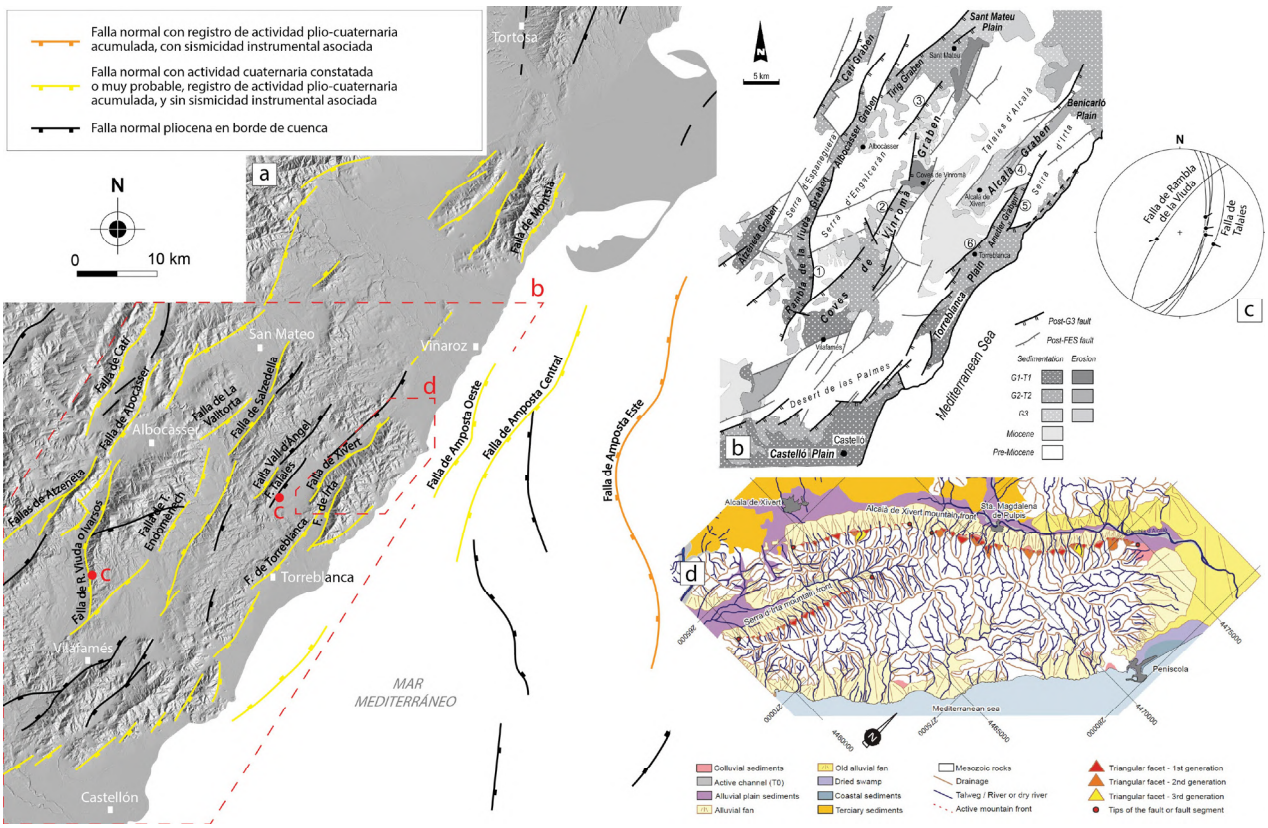

Fig. 5.22.- (a) Cartografía del sistema de fosas del Maestrat, sobre Modelo Digital de Elevación (*DEM*), basado en Simón (1982) y Perea *et al.* (2012). Ver localización en Figura 1.1b. (b) Mapa geológico (tomado de Simón *et al.*, 2012; modificado de Simón, 1982). (c) Orientaciones de planos y estrías medidos sobre superficies principales de dos de las fallas. (d) Mapa geomorfológico de la Sierra de Irta, con las fallas de Irta y Xivert, y sus facetas triangulares (tomada de Perea *et al.*, 2012).

Son claras las evidencias de actividad plio-cuaternaria de las fallas del Maestrat; sin embargo, no se dispone de marcadores estratigráficos fiables que permitan obtener información paleosismológica completa acerca de las mismas. Se han llevado a cabo aproximaciones a sus tasas de desplazamiento vertical desde cuatro metodologías morfotectónicas (Tabla 6.1):

(1) El salto vertical de muchas de las fallas de este sector se ha calculado a partir del desplazamiento de la superficie de erosión SEF. Ésta no está correlacionada con las presentes en el sistema de fosas de Teruel, por lo que no se puede especificar su subnivel ni su edad exacta. Sin embargo, se considera que, al igual que en aquéllas, su edad se acerca a los 3,8 Ma (Simón-Porcar *et al.*, 2019; Ezquerro *et al.*, 2020; ver sección II.4.3). Destaca la falla de la Rambla de la Viuda (o Ivarsos en los trabajos de Perea; Fig. 5.22a,b), ya que desplaza notablemente esta superficie hasta 620-640 m, dando lugar a una tasa de 0,16-0,17 mm/a (Simón *et al.*, 2012). Las fallas de Irta y Torre Endomènech producen unos saltos máximos en el rango 300-350 m de este marcador, obteniendo una tasa de desplazamiento vertical de 0,08-0,09 mm/a (Fig. 5.22a,b). Las fallas de Torreblanca y Xivert, en cambio, del orden de 200-220 m, y tasas de 0,05-0,06 mm/a (Simón *et al.*, 2012, 2013).

(2) Asimismo, para un espacio temporal parecido, las tasas de desplazamiento de las fallas también se han obtenido teniendo en cuenta la máxima altura de las facetas triangulares más recientes presentes a lo largo de sus trazas (todas presentan 2-3 generaciones), y considerándola asimilable a su salto acumulado desde el Plioceno (Perea, 2006; Perea *et al.*, 2012). No se tiene un control directo de su edad, pero los autores correlacionan tentativamente estas facetas triangulares con las del frente de Tet-Cerdanya (de edad pliocena), y estiman su edad (hasta el Cuaternario) en torno a 2-5 Ma. Se trata, por tanto, de una estimación, no basada en una correlación fina entre aplanamientos del relieve y niveles sedimentarios. La generación última y de mayor altura de facetas triangulares asociadas a las fallas del Maestrat (Irta, Xivert, Vall d'Àngel, Salzedella, Rambla de la Viuda o Ivarsos, Albocàsser, Catí, Atzeneta y Montsià) ronda siempre la centena de metros, lo que se traduce en unas tasas de desplazamiento verticales de alrededor de 0,02-0,09 mm/a, y en ocasiones mayores. En el caso de las fallas marinas (Amposta; Fig 5. 22a), su desplazamiento se ha calculado a partir del salto que producen en la base de una unidad plio-cuaternaria observada en los perfiles de sísmica de reflexión. De los desplazamientos de entre 50 y 200 m que producen, se obtienen unas tasas mínimas para el periodo plio-cuaternario de 0,01-0,03 mm/a y 0,04-0,10 mm/a (Roca, 1992; Perea, 2006; Perea *et al.*, 2012).

(3) En algunos casos, el salto vertical también se ha calculado a partir del desplazamiento de unos depósitos aluviales más recientes que podrían corresponder a otra superficie diferente, la de los *glacis villafranquienses* datados en ca. 2,0 Ma (ver sección II.4.3). Es el caso de las fallas de Irta y Torreblanca, que desplazan este marcador 100-140 m, y de las fallas Torre Endomènech y La Valltorta, que la desplazan 40-70 m. La tasa de las dos primeras en ese periodo oscila entre 0,05-0,07 mm/a, y la de las dos segundas fallas habría sido de 0,02-0,03 mm/a (Simón *et al.*, 2012).

(4) Finalmente, en el caso de la falla de Torreblanca (Fig 5.22a), se ha podido acotar su actividad en el Cuaternario a partir del análisis de dos valles decapitados por el movimiento de la misma. Los valles de Portell y La Coma discurren perpendicularmente a la falla, y sus cabeceras durante el Plioceno superior se encontraban en la sierra de Irta. En la actualidad la extensión de estos valles es menor, y sus cabeceras originales ahora drenan hacia el sur, al nuevo graben del Ametler creado en el interior de la Sierra de Irta (Simón *et al.*, 2013). El salto vertical de la falla de Torreblanca posterior a la interrupción del drenaje original de estos valles es de cerca de 70 m, y la base de los depósitos aluviales que rellenan la fosa del Ametler están datados mediante OSL en 253,3 ± 18,0 ka. Esto lleva a los autores a calcular una tasa de desplazamiento vertical máxima para la falla de Torreblanca de 0,26-0,30 mm/a.

Los trabajos realizados en esta región se basan principalmente en el análisis morfoestructural de las cuencas, dado que existen muy pocos afloramientos de los planos de falla que las limitan. Se desconocen muchas de sus características estructurales y sismológicas, y aquellas que sí se conocen podrían considerarse como poco fiables. En consecuencia, la caracterización del potencial sísmico de la región realizada en esta tesis mediante correlaciones empíricas debe agrupar algunas de las fallas y ser únicamente orientativa. Las fallas de longitud de traza menor de 15 km (Irta, Xivert, Talaies, Vall d'Àngel, Torre Endomènech, La Valltorta, y Montsià) llegarían a producir terremotos de Mw entre 5.8 y 6.6, y saltos cosísmicos medios de entre 0,1 y 1,7 aproximadamente (aplicando las regresiones de Wells y Coppersmith, 1994; Stirling *et al.*, 2002; Wesnousky, 2008; Leonard, 2010). De la misma manera, las de mayor longitud (Torreblanca, Salzedella, Rambla de la Viuda o Ivarsos, Albocàsser, Catí y Atzeneta) alcanzarían magnitudes de entre 6.2 y 6.9, y saltos de entre 0,5 y 2,3 m aprox. Estos valores también corresponderían en líneas generales a la falla marina de la Amposta, a excepción de su rama este, de más longitud, que alcanzaría Mw = 7.2 y saltos métricos.


VI

CAPÍTULO VI.

SÍNTESIS DE LA ACTIVIDAD DE LAS FALLAS RECIENTES EN LA CORDILLERA IBÉRICA CENTRO-ORIENTAL

	Falla o zona de falla		Longitud de la rotura superficial o *SRL* (km)	Salto neto máximo desde hace 3,8-3,5 Ma (m)	Dirección de transporte promedio	Tasa neta desde hace 3,8-3,5 Ma (mm/a)	Tasa neta durante el Cuaternario (mm/a)	Evento más reciente o *MRE* (ka)	Salto cosísmico medio o *AVD* (m) (de datos paleosismológicos)	Periodo de recurrencia (ka) (de datos paleosismológicos)	Periodo de recurrencia (ka) (del método directo) [+]	Referencia	Parámetros obtenidos de regresiones empíricas											
													Wells y Coppersmith (1994)			Stirling et al. (2002)			Wesnousky (2008)			Leonard (2010)		
													Salto cosísmico medio o *AVD* (m)	Periodo de recurrencia (ka) (del método directo) [++]	Magnitud momento o Mw	Salto cosísmico medio o *AVD* (m)	Periodo de recurrencia (ka) (del método directo) [++]	Magnitud momento o Mw	Salto cosísmico medio o *AVD* (m)	Periodo de recurrencia (ka) (del método directo) [++]	Magnitud momento o Mw	Salto cosísmico medio o *AVD* (m)	Periodo de recurrencia (ka) (del método directo) [++]	Magnitud momento o Mw
													σ ≈ 0,4		σ ≈ 0,3	σ ≈ 0,3		σ ≈ 0.2	σ ≈ 0,8		σ ≈ 0.3	σ ≈ 0,2		σ ≈ 0.3
Cuenca de Calatayud	*RPFZ*	Río Grío-Lanzuela o *RLFS*	55	260	N235ºE	0,07	0,30-0,36 (desde 67 ka)					Peiro y Simón (2021), esta tesis	1,5	4-5	7.2	3,3	9-11	7.3	1,7	5-6	6.9	1,4	4-5	7.0
		Cucalón-Pancrudo o *CPFS*	40	205		0,06	0,07-0,08 (desde 18 ka)	5,0	0,5	4,2-8,2	6-7	Esta tesis	1	12-14	7.0	3	37-43	7.2	1,2	15-17	6.9	1,1	14-16	6.8
		CPFS+Valverde		305-325		0,09																		
	Munébrega		20				0,09-0,11 (desde 72 ka)	Post 32,6 Pre 19,0	2,5	18-24	23-28	Gutiérrez (1998) Gutiérrez *et al.* (2009)	0,4	4-5	6.6	2,3	21-26	6.9	0,6	5-7	6.7	0,6	6-7	6.4
							0,02-0,04 (desde 241 ka)			60-80	62-125	Gutiérrez *et al.* (2020a)		11-21			58-116			15-30			15-30	
	Daroca		27				0,07-0,16 (desde 113 ka)					Gracia (1990, 1992) Gutiérrez *et al.* (2008)	0,6	4-9	6.7	2,6	16-37	7.0	0,8	5-12	6.8	0,8	5-11	6.6
							0,02-0,06 (desde 330 ka)	Post 2,3 Pre 1,6 BP				Gutiérrez *et al.* (2020a,b)		10-30			43-129			14-41			13-39	
Fosa del Jiloca	Calamocha		18	190-230	N234ºE	0,05-0,06	0,10-0,30 (de 95 a 70 ka)	Post 13,8	0,5	8-10	5	Peiro *et al.* (2022), esta tesis	0,4	1,3-4	6.5	2,2	7,3-22	6.9	0,5	1,7-5	6.7	0,6	2-6	6.3
	Sierra Palomera		26	330-480	N230ºE	0,09-0,15						Peiro *et al.* (2022), esta tesis	0,6		6.7	2,5		7.0	0,8		6.8	0,8		6.6
		La Peñuela	14		N240ºE			49,2					0,3		6.4	2		6.8	0,4		6.7	0,5		6.1
	Concud		14,2	255-290	N220ºE	0,07-0,08	0,29 (desde 74 ka)	13,0-3,0	1,9	7-8	6,5	Lafuente (2011), Lafuente *et al.* (2011, 2014), Simón *et al.* (2016)	0,3	1	6.4	2,1	7	6.8	0,4	1	6.7	0,5	2	6.2
Cuenca del Teruel	Teruel		9-11	270	N275ºE	0,07	0,18-0,20 (desde 46 ka)	28,6-9,2	0,6	9-17	3	Simón *et al.* (2017)	0,2	1	6.1-6.2	1,8-1,9	9-10	6.6-6.7	0,3	1-2	6.6	0,3-0,4	2	5.9-6.0
	Valdecebro		5	190	N202ºE	0,05	0,05-0,07 (desde 142 ka; en una rama)	Post 50,1	0,6-1,2	8-28	8,5-24	Simón *et al.* (2019)	0,1	1-2	5.8	1,4	21-29	6.5	0,2	2-3	6.5	0,2	3-4	5.5
	El Pobo		9	380-520	N260ºE	0,10-0,14						Ezquerro *et al.* (2020)	0,2		6.1	1,8		6.6	0,3		6.6	0,3		5.9
	Peralejos		8,5	520	N295ºE	0,14							0,1		6.1	1,7		6.6	0,3		6.6	0,3		5.8
	Tortajada		11,6	260	N315ºE	0,07							0,2		6.3	1,9		6.7	0,3		6.6	0,4		6.0
	Cabigordo		4	180		0,05							0,1		5.7	1,3		6.4	0,1		6.4	0,2		5.0
	La Hita		3	250-620		0,07-0,16							0,04		5.5	1,2		6.3	0,1		6.3	0,1		5.1
Maestrat	Irta		6	300-350		0,08-0,09	0,05-0,07 (desde 2 Ma)					Simón *et al.* (2012, 2013), esta tesis	0,1	1-2	5.9	1,5	21-30	6.5	0,2	3-4	6.5	0,2	3-4	5.6
				110*		0,02-0,06*						Perea *et al.* (2012)												
	Torreblanca		15-25	200-220		0,05-0,06	0,05-0,07 (desde 2 Ma)					Simón *et al.* (2012, 2013), esta tesis	0,3-0,6	4-12	6.4-6.7	2,1-2,5	30-50	6.8-7.0	0,5-0,8	7-16	6.7-6.8	0,5-0,7	7-14	6.2-6.5
							0,26-0,30 (desde 253 ka)							1-2			7-10			2-3			2-3	
	Xivert		14,5	200		0,05						Simón *et al.* (2012), esta tesis	0,3		6.4	2,1		6.8	0,4		6.7	0,5		6.2
				105-135*		0,02-0,07*						Perea *et al.* (2012)												
	Talaies		8		N088ºE							Simón (1982), esta tesis	0,1		6.1	1,7		6.6	0,2		6.5	0,3		5.8
	Vall d'Àngel		8,5	100*		0,02-0,05*						Perea *et al.* (2012)	0,1		6.1	1,7		6.6	0,3		6.6	0,3		5.8
	Salzedella		23,5	70-85*		0,01-0,04*							0,5		6.7	2,5		7.0	0,7		6.8	0,7		6.5
	Torre Endomènech		8	300		0,08	0,02 (desde 2 Ma)					Simón (1982), Simón *et al.* (2012), esta tesis	0,1	5	6.1	1,7	85	6.6	0,2	10	6.5	0,3	15	5.8
	La Valltorta		8	120		0,03	0,02-0,03 (desde 2 Ma)						0,1	3-5	6.1	1,7	57-85	6.6	0,2	7-10	6.5	0,3	10-15	5.8
	Rambla de la Viuda o Ivarsos		15-20	620-640	N252ºE	0,16-0,17						Simón *et al.* (2012), esta tesis	0,3-0,4		6.4-6.6	2,1-2,3		6.8-6.9	0,5-0,6		6.7	0,5-0,6		6.2-6.4
				85-270*		0,02-0,14*																		
	Albocàsser		20,4	130-240*		0,03-0,14*						Perea *et al.* (2012)	0,4		6.6	2,3		6.9	0,6		6.7	0,6		6.4
	Catí		19	150-225*		0,03-0,11*							0,4		6.5	2,3		6.9	0,6		6.7	0,6		6.3
	Atzeneta		18	165-175*		0,03-0,09*							0,4		6.5	2,2		6.9	0,5		6.7	0,6		6.3
	Montsià		11	155*		0,03-0,09*							0,2		6.2	1,9		6.7	0,3		6.6	0,4		6.0
	Amposta	oeste	18	53*		0,01-0,03*							0,4		6.5	2,2		6.9	0,5		6.7	0,6		6.3
		central	35	57*		0,01-0,03*							0,8		6.9	2,8		7.1	1,1		6.8	1		6.7
		este	51	193*		0,04-0,10*							1,3		7.1	3,2		7.2	1,5		6.9	1,3		7.0

(*) Saltos y tasas calculados a partir del desplazamiento de alturas de facetas triangulares, a las que se les atribuye tentativamente un rango de edad de 5-2 Ma.

(†) Calculado a partir de dividir el *AVD* paleosismológico por la tasa neta durante el Cuaternario

(‡) Calculado a partir de dividir el *AVD* de las correlaciones empíricas por la tasa neta durante el Cuaternario


VII

CAPÍTULO VII.

MECANISMOS DE INTERACCIÓN Y PROPAGACIÓN EN LAS ZONAS DE RELEVO DE FALLAS

Resumen:

La sección VII busca complementar la caracterización de las fallas principales hecha en las secciones anteriores extendiéndola a sus zonas de relevo. Se plantea un nuevo modelo de zona de relevo en contexto extensional, que contrasta con los modelos clásicos de la literatura, y que está dominado por fracturas que rompen longitudinalmente sus rampas de relevo. Este modelo se basa en tres fuentes de información entre las que está, en primer lugar, el estudio estructural de tres casos ya publicados sobre las zonas de relevo regionales entre las fallas de Calamocha, Sierra Palomera, Concud y Teruel. Dicha publicación se completa en esta tesis con reseñas más breves sobre las zonas de relevo entre los segmentos de falla de Río Grío-Lanzuela y Cucalón-Pancrudo, Munébrega y Gallocanta, Daroca y Calamocha. En segundo lugar, el modelo se basa en el estudio de modelos analógicos bajo una extensión biaxial lo más parecida posible al campo regional actual. Y en tercer lugar, en el análisis de los datos de sismicidad instrumental recogidos en el catálogo y las aportaciones del nuevo sismógrafo de Celadas. Con todo ello, se contribuye a conocer los mecanismos de interacción de fallas extensionales en relevo y se profundiza en las condiciones genéticas bajo las cuales se desarrollan los patrones de fracturación.

Journal of Structural Geology 131 (2020) 103942

Contents lists available at ScienceDirect

Journal of Structural Geology

journal homepage: http://www.elsevier.com/locate/jsg

Fault relay zones evolving through distributed longitudinal fractures: The case of the Teruel graben system (Iberian Chain, Spain)

Alba Peiro *, José Luis Simón, Teresa Román-Berdiel

Dpto. de Ciencias de la Tierra, Grupo Geotransfer - Instituto Universitario de Investigación en Ciencias Ambientales de Aragón (IUCA), Universidad de Zaragoza, Pedro Cerbuna 12, 50009, Zaragoza, Spain

ARTICLE INFO

Keywords:
Fault interaction
Jiloca graben
Along-strike propagation
Biaxial extension
Analogue modelling

ABSTRACT

A new type of fault relay zone in extensional contexts, dominated by distributed along-strike or longitudinal fractures, is defined. It contrasts with the classical models reported in the literature, in which transverse connecting faults controlled by the own relay kinematics prevail. The new model is based on structural features of the Teruel graben system, as well as on analogue modelling. Relay zones between the NW-SE to NNW-SSE striking faults that delimit the eastern boundary of the Jiloca Graben (Calamocha, Sierra Palomera and Concud faults), together with the Teruel Fault, have been studied. All of these relay faults show recent (Neogene-Quaternary) ruptures at different scales, mostly parallel to the macrostructural trend and to the maximum horizontal stress (S_{Hmax}) trajectories (i.e., orthogonal to the ENE-WSW regional extension direction that characterises the nearly biaxial or radial stress regime active during Upper Pliocene-Quaternary times). Transverse ruptures are almost absent, with the exception of the northern relay zone (Calamocha-Sierra Palomera), where an incipient NE-SW striking connecting fault does exist. Analogue models have been run under a biaxial extension regime similar to the regional one. They allowed analysing the main factors controlling fracture propagation, depending on the ratio of extension velocities and the orientation of the master faults relative to extension directions. Laboratory fracture patterns, as in the natural studied examples, are mostly controlled by the inherited anisotropies and, in a greater extent, by the imposed extension trajectories, which results in a clear prevalence of longitudinal fractures. Such external controls, usually disregarded in numerical and analogue modelling, tend to induce fault coalescence through along-strike (parallel or at very-low-angle) propagation resulting in a final braided fault pattern.

1. Introduction

Fault relay zones within extensional settings have been widely studied (e.g., Peacock and Sanderson, 1994; Childs et al., 1995; Willemse, 1997; Crider and Pollard, 1998; Peacock, 2002; Fossen and Rotevatn, 2016). Many publications reveal increasing interest on relationships between fault relay zones and oil or gas reservoirs (Fossen et al., 2005; Rotevatn et al., 2007), as well as on their behaviour during seismic events (Machette et al., 1991; Manighetti et al., 2009; Finzi and Langer, 2012). Models of fault linkage controlled by fault interaction and propagation, based on numerical and analogue modelling as well as on natural examples, have been extensively developed. The basic evolutionary model from two non-interacting overstepping segments to a single fault includes development of a relay ramp (*soft linkage*) followed by a breached ramp stage (*hard linkage*) (e.g. Walsh and Watterson, 1991; Peacock and Sanderson, 1994; Young et al., 2001; Fossen and Rotevatn, 2016). Concerning hard linkage, this could have been achieved through full connecting faults, or lie in a transient, incomplete stage (*incipient hard linkage*). Those evolutionary stages can be related to characteristic displacement-length profiles that express the degree and type of fault interaction prior to linkage (Peacock and Sanderson, 1991; Cartwrigth et al., 1995; Gawthorpe and Leeder, 2000; Mansfield and Cartwright, 2001).

Most published pictures and sketches that represent the conceptual model of a breached relay zone show secondary faults at high angles (>45-50°) to the master faults (Fig. 1A,B,C,D; Ramsay and Huber, 1987, p. 533; Peacock and Sanderson, 1994, figs. 1, 3d and 12; Ferrill and Morris, 2001, fig. 8d; Peacock, 2002, fig. 3c; Fossen and Rotevatn, 2016). Such conceptual model obeys the notion that breaching occurs at a given level of bending curvature at the relay ramp, owing to

* Corresponding author.
E-mail addresses: apeiro@unizar.es (A. Peiro), jsimon@unizar.es (J.L. Simón), mtdjrb@unizar.es (T. Román-Berdiel).

https://doi.org/10.1016/j.jsg.2019.103942
Received 6 June 2019; Received in revised form 26 November 2019; Accepted 26 November 2019
Available online 28 November 2019
0191-8141/© 2019 Elsevier Ltd. All rights reserved.

lengthening of material parallel to the master faults (Fossen and Rotevatn, 2016). Nevertheless, comparatively few works describe actual visible examples of such transverse connecting faults (e.g. Peacock and Sanderson, 1994, figs. 2, 14 and 15; Young et al., 2001). We set aside the case of nearly vertical, dominantly strike-slip faults that transfer displacement between two adjacent fault zones with differential extension rate (transfer faults s.s.; Gibbs, 1984, 1990), which in our opinion should not be assimilated to *hard linkage* as some authors implicitly do (e.g. Gawthorpe and Hurst, 1993; Acocella et al., 2005).

Indeed, as illustrated in literature, relay zones in both nature and laboratory experiments show a wide variety of faulting geometries that do not fit that conceptual model. In contrast with the scarce above-mentioned cases of high-angle connecting faults (Peacock and Sanderson, 1994; Young et al., 2001), low-angle oblique faults (usually in the range of 20-40° to the major faults) are very frequent in relay zones, either as single ruptures propagated from one of the fault tips (Fig. 1E,G; e.g., Peacock and Sanderson, 1994, fig. 7a,b; Childs et al., 1995, fig. 12; Walsh et al., 1999, fig. 3d; Peacock, 2002, fig. 1b; Le Calvez and Vendeville, 2002, fig. 15; Moustafa and Khalil, 2016, fig. 12), or as distributed ruptures (fig. 1F,H; e.g., Peacock and Sanderson, 1994, fig. 2; Gupta and Scholz, 2000, fig. 2). Fracture patterns nearly parallel, <20° to the major faults, are also frequent (Fig. 1I and J): (i) along-strike faults or fault zones propagated from a major fault tip, which can abut the second major fault without any significant deviation since its incidence angle lies within the strike variability (Peacock and Sanderson, 1994, Fig. 16a; Childs et al., 1995; Crider and Pollard, 1998; Walsh et al., 1999, figs. 3d and 5a; Nicol et al., 2005, fig. 3; Fossen and Rotevatn, 2016, fig. 6); (ii) longitudinal distributed fracture patterns that randomly extend within and near the relay zone, frequently including both synthetic and antithetic faults (Huggins et al., 1995; Peacock and Sanderson, 1994, figs. 4a and 9a; Trudgill and Cartwright, 1994, figs. 3b, 5 and 6; Morley and Wonganan, 2000; Mansfield and Cartwright, 2001, fig. 7; Moustafa and Khalil, 2016, fig. 9; Fossen and Rotevatn, 2016, fig. 3a). Finally, multiple fracture sets derived from inherited structures can also develop (e.g. Trudgill and Cartwright, 1994, fig. 3b; Fossen and Rotevatn, 2016), eventually giving rise to zigzag basin margins after full linkage (e.g., Younes and McClay, 2002; Gawthorpe et al., 2003; Moustafa and Khalil, 2016).

Fig. 1 compiles such diverse typology of fracture patterns associated to fault relay zones, considering: (i) the angle of the newly propagating ruptures with respect to the master faults (high-angle or transverse, low-angle oblique, and very-low-angle or along-strike propagating ruptures are distinguished); (ii) cases of complete breaching (*hard linkage*) vs. incomplete breaching (*incipient hard linkage*); (iii) cases where deformation is accommodated on a single fault and others where it is distributed among several ruptures. We should pay special attention to along-strike propagated ruptures in relay zones (Fig. 1I and J), as most actual fault zones show an anastomosing geometry made of distinct traces oriented at very-low-angles to each other. They likely developed from initially relay-arranged individual segments, which should coalesce into a merged fault zone without mediation of any high-angle, transverse connecting fault.

Most conceptual, analogue and numerical models initially consider (i) a non-deformed rock body in which new fault systems develop, and (ii) just kinematic boundary conditions (velocities and displacements), so that reciprocal interaction between master faults and secondary fractures is only subject to such kinematic constraints (e.g. Childs et al., 1993; Gupta and Scholz, 2000; Ferrill and Morris, 2001). However, extensional faulting (i) frequently develops in areas with inherited faults and fractures, and (ii) is controlled by the coeval regional and local stress fields. The influence of structural inheritance and dynamical boundary conditions on fracture propagation within fault relay zones has not received enough attention in the literature.

The purpose of the present work is to provide insight into the genetic conditions in which other structural patterns, different from transverse connecting faults typically identified with *hard linkage*, can develop. Our analysis is based upon both field examples and analogue models, controlled, in both cases, by an extensional stress regime. First, we describe and analyse fracture patterns within relay zones between major faults of the Teruel graben system (Jiloca and Teruel basins), active during Upper Pliocene-Quaternary times under a nearly biaxial or radial extensional stress field (maximum principal stress σ_1 vertical; $\sigma_2 \approx \sigma_3$) (Simón, 1989; Arlegui et al., 2005; Liesa et al., 2019). Then, we perform and examine analogue models in order to analyse the factors that control fracture development in contexts comparable to such relay zones.

Although laboratory experiments carried out since the 90's have tried to delve into factors that control the development of extensional fault relay zones, they have been systematically performed under uniaxial extension conditions (e.g., Clifton et al., 2000; Mansfield and Cartwright, 2001; Le Calvez and Vendeville, 2002; Acocella et al., 2005; Hus et al., 2005; Athmer et al., 2010). The present paper is -as far as we know-the first one that describes experiments that simulate a biaxial or radial extensional regime.

In addition to the type of stress field in which relay zones develop,

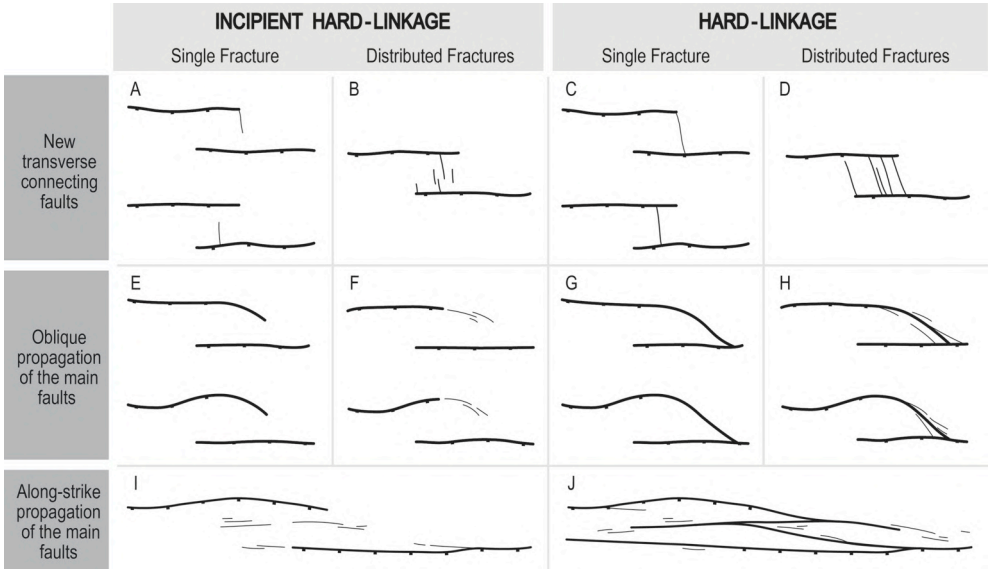

Fig. 1. Classification of fracture patterns within fault relay zones in extensional contexts based on literature reviewing. A, B, C, D: e.g., Ramsay and Huber (1987), p. 533; Peacock and Sanderson (1994), figs. 1, 3d and 12; Ferrill and Morris, 2001, fig. 8d; Peacock (2002), fig. 3c; Fossen and Rotevatn (2016). E, G: e.g., Peacock and Sanderson (1994), fig. 7a and b; Childs et al. (1995), fig. 12; Walsh et al. (1999), fig. 3d; Peacock (2002), fig. 1b; Le Calvez and Vendeville (2002), fig. 15; Moustafa and Khalil (2016), fig. 12. F, H: e.g., Peacock and Sanderson (1994), fig. 2; Gupta and Scholz (2000), fig. 2. I, J: e.g., Peacock and Sanderson (1994), figs. 4a, 9a and 16a; Trudgill and Cartwright (1994), figs. 3b, 5 and 6; Childs et al. (1995); Huggins et al. (1995); Crider and Pollard (1998); Walsh et al. (1999), figs. 3d and 5a; Morley and Wonganan (2000); Mansfield and Cartwright (2001), fig. 7; Nicol et al. (2005), fig. 3; Fossen and Rotevatn (2016), figs. 3a and 6; Moustafa and Khalil (2016); fig. 9.

spatial stress heterogeneity should also be taken into account. Numerical models (e.g., Simón et al., 1988; Kattenhorn et al., 2000) show that, where previous oblique faults do exist, trajectories of the minimum stress axis (σ_3) undergo sharp deflection, veering to become either parallel to the fault (close to the tips) or perpendicular to it (close to the centre). Swapping of σ_2 and σ_3 axes is also a common phenomenon, which result in e.g. orthogonal joint sets (Simón, 1989). Such a dynamic setting makes the results of analogue modelling less predictable and more exciting, open to a wide range of potential deformation patterns.

2. Geological setting

The eastern Iberian Chain (Fig. 2A) shows a large network of Neogene-Quaternary extensional basins that postdate and obliquely cut its compressive structures (Fig. 2B; Álvaro et al., 1979). They represent the onshore deformation linked to rifting of the Valencia Trough, which is accommodated by a listric extensional fault system detached at a depth of 11–14 km (Roca and Guimerá, 1992). Such basins evolved through two main extensional episodes (Simón, 1982, 1983): the first episode, Upper Miocene in age, produced NNE-SSW trending grabens (Teruel and Maestrazgo Grabens, parallel to the Valencia Trough); the second one, Upper Pliocene-Present, gave rise to reactivation of the former basins and created the NNW-SSE trending Jiloca Graben.

The Teruel Basin is a half graben controlled by large N–S striking faults located at the eastern boundary (El Pobo and Javalambre mountain fronts; Fig. 2B and C). It is filled with alternating red clastic materials and carbonates, in which several informal lithological units (Rojo 1, Rojo 2 and Rojo 3, clastic; Páramo 1 and Páramo 2, carbonated) have been used by Godoy et al. (1983a,b), Hernández et al. (1983a,b) and Olivé et al. (1983) for mapping purposes (Fig. 2D). This succession culminates with a thin alluvial cover (Villafranchian pediment) that extends over most of the Neogene basins. Their age, well constrained from numerous mammal fossil localities and magnetostratigraphy, ranges from the beginning of the Upper Miocene (Vallesian, 11.2 Ma) up to Upper Pliocene - earliest Pleistocene (Villafranchian, 1.8 Ma; Ezquerro, 2017).

The Jiloca asymmetric graben shows an overall NNW-SSE trend that results from an en-échelon right-releasing arrangement of NW-SE-striking normal faults, the largest ones being located at the eastern boundary: Calamocha, Sierra Palomera and Concud faults (Fig. 2C). A number of Palaeogene folds are obliquely cut by the graben; nevertheless, they are nearly parallel to the Sierra Palomera and Concud faults, which represent the negative inversion of contractive faults associated to those folds, as explained in Sections 3.2 and 3.3. The basin infill is

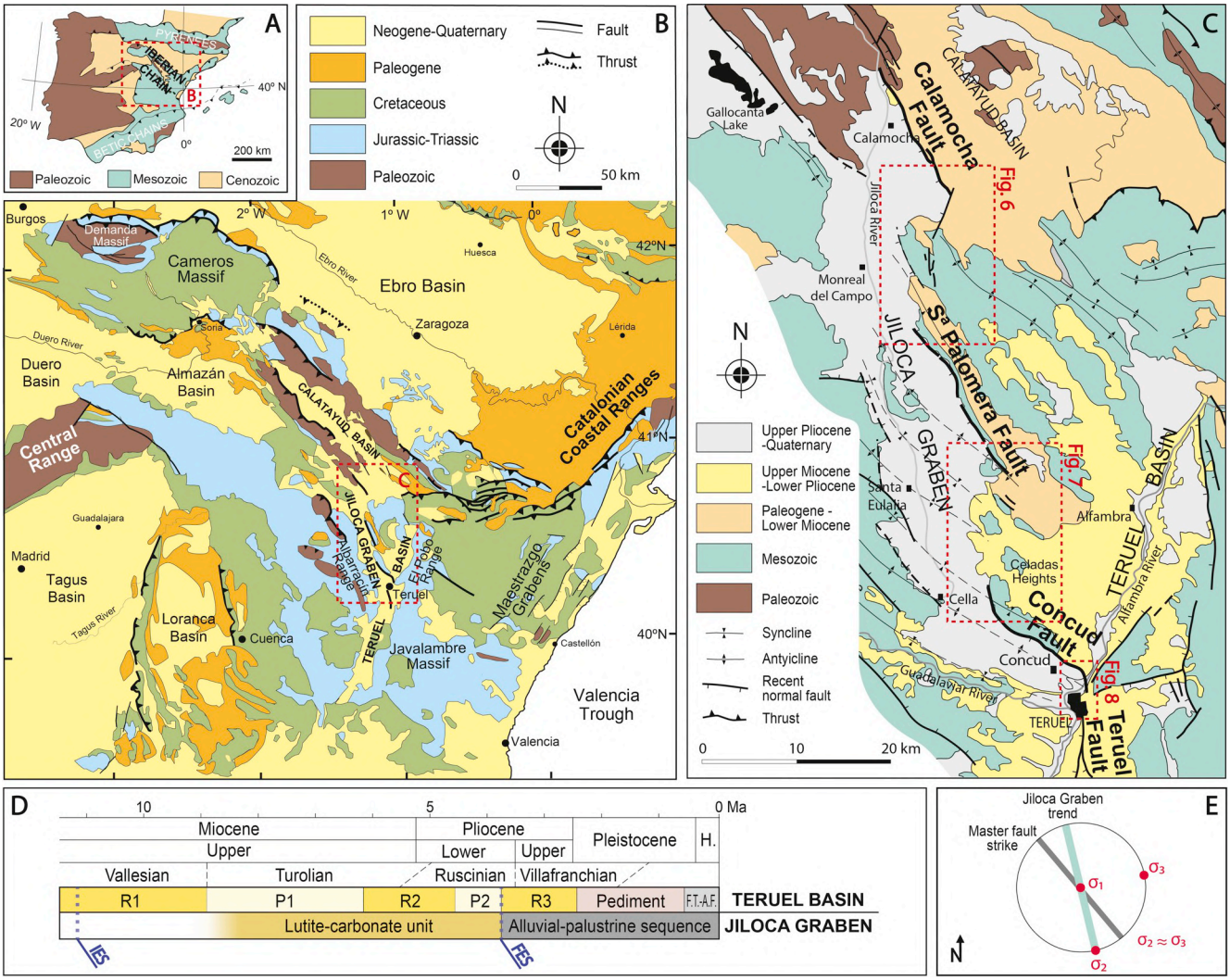

Fig. 2. (A) Location of the Iberian Chain within the Iberian Peninsula. (B) Location of the Teruel graben system within the Iberian Chain. (C) Geological map of the Teruel graben system, with location of Figs. 6–8. (D) Chronostratigraphical diagram of sedimentary units of the Teruel (R1: Rojo 1 unit; P1: Páramo 1; R2: Rojo 2; P2: Páramo 2; R3: Rojo 3; F.T.-A.F. fluvial terraces and alluvial fans) and Jiloca basins, showing the position of the Intramiocene Erosion Surface (IES) and Fundamental Erosion Surface (FES). (E) Sketch of structural trends and their relationship with regional stress directions.

essentially made of an Upper Pliocene-Pleistocene alluvial sequence (with episodic palustrine deposits), underlain at the central sector by an older lutite-carbonate unit attributed to the Upper Miocene-Lower Pliocene (Rubio and Simón, 2007) (Fig. 2D).

The Teruel and Jiloca grabens developed under a tectonic stress field that evolved from (i) uniaxial extension with WNW-ESE trending σ_3 trajectories, prevailing during the first extensional episode (Miocene-Lower Pliocene), to (ii) nearly biaxial or radial extension (σ_1 vertical, $\sigma_2 \approx \sigma_3$) with σ_3 trending nearly WSW-ENE (Fig. 2E), prevailing during the second episode (Upper Pliocene-Quaternary; Simón, 1982, 1989; Arlegui et al., 2005; Liesa et al., 2019). The latter has essentially remained up to the present-day (Herraiz et al., 2000). Nevertheless, both WSW-ENE and WNW-ESE σ_3 directions are recorded all along Pliocene and Quaternary times: the overall biaxial extension stress field has the appearance of being partitioned (in the sense of Simón et al., 2008) into two stress systems with S_{Hmax} axis (maximum horizontal stress) nearly parallel to the Jiloca and Teruel grabens, respectively. Moreover, both directions are linked to the main tectonic stress sources active during Neogene times in eastern Spain: intraplate NNW-SSE compression produced by Africa-Iberia convergence, and WNW-ESE extension induced by rifting at the Valencia Trough (Simón, 1989; Herraiz et al., 2000; Capote et al., 2002; Arlegui et al., 2005).

Mountain massifs all over the region are modelled by two main planation surfaces: Intramiocene Erosion Surface (*IES*; Gutiérrez and Peña, 1976; Peña et al., 1984) and Fundamental Erosion Surface (*FES*, Peña et al., 1984). Within the Teruel Basin, *IES* and *FES* correlate, respectively, with the basal unconformity of the Neogene infill and the top of the youngest lacustrine-palustrine deposits (Páramo 2 unit), with ages 11.2 Ma and 3.7–3.5 Ma (Ezquerro, 2017). Since Upper Pliocene times, the Neogene infill of the Teruel Basin has been deeply excavated by the Alfambra and Turia rivers, giving rise to four main fluvial terrace levels (Peña, 1981; Godoy et al., 1983b) attributed to the Early, Middle, Late Pleistocene and Holocene, respectively (Sánchez Fabre, 1989; Moissenet, 1993; Arlegui et al., 2005; Gutiérrez et al., 2008; Lafuente et al., 2014; Simón et al., 2016, 2017).

Historic and instrumental seismicity of the region is low to moderate. Epicentres are concentrated along N–S striking faults south of Teruel city, the western margin of the Jiloca Graben and its neighbouring Albarracín Range, with a maximum recorded magnitude of Mb = 4.3 (Instituto Geográfico Nacional, 2019). Most of the available focal mechanisms correspond to normal faults and are consistent with the recent stress field (Herraiz et al., 2000).

3. Master faults

3.1. Calamocha fault

The Calamocha Fault is 17.0 km long, strikes NNW-SSE, dips ca. 70°–75°W, and shows pure normal movement. It sinks the northern sector of the Jiloca Graben with respect to the Neogene infill of the neighbouring Calatayud basin (Fig. 2C). Offset of the Lower Pliocene Páramo 2 unit allows calculating the maximum net slip, which at the central segment (where it splits into four synthetic ruptures) has been calculated to be ca. 220 m (Rubio and Simón, 2007; Martín-Bello et al., 2014). Fault movement initiated in Upper Pliocene times, showing an average slip rate of 0,06-0,09 mm/a.

Two outcrops studied close to Calamocha town evince that the fault has undergone recurrent movement during the Late Pleistocene (prior to 53.1 ka BP, and younger than 69.9 ka, 35.3 ka y 11.1 ka BP (Simón et al., 2012; Martín-Bello et al., 2014).

3.2. Sierra Palomera fault

The Sierra Palomera Fault is a 15.6 km long, NNW-SSE striking normal fault that constitutes the central sector of the Jiloca Graben, associated to the eastern limb of a Paleogene E-verging anticline (Fig. 2C). The fault surface dips between 54° and 87°W; the slickenlines observed on it indicate a nearly pure normal movement with transport direction towards WSW (García-Lacosta et al., 2014).

Unfortunately, it is not possible to gain precise knowledge of the displacement on the Sierra Palomera normal fault as neither Neogene nor Quaternary stratigraphic marker can be recognized in both walls. Nevertheless, the morphotectonic setting clearly reveals significant activity since Upper Pliocene time (mainly manifested by tilting and offset of the Fundamental Erosion Surface), which allows estimating a throw in the range of 350–400 m (Rubio and Simón, 2007; García-Lacosta et al., 2014).

A minor antithetic fault, induced by rollover bending associated to the Sierra Palomera Fault, shows evidence of activity during Late Pleistocene time (García-Lacosta et al., 2014).

3.3. Concud fault

The Concud Fault is 14.2 km long, showing an overall NW–SE strike that veers towards NNW–SSE near its northern and southern tips, where it approaches the Teruel Fault (Fig. 2B). The fault surface tipically dips 65-70° SW. The observed slickenlines indicate (i) a nearly pure normal slip in the central sector, and (ii) an oblique slip in the southern, NNW–SSE striking one (striation pith around 75°S), both consistent with average bulk transport direction towards N220°E (Lafuente et al., 2011, 2014).

The Concud Fault follows the vertical to overturned limb of a NW-SE trending, NE-verging anticline, and represents the negative inversion of a previous thrust with an associated propagation anticline (Lafuente et al., 2011, 2014). The extensional fault cross-cuts the previous Upper Miocene-Lower Pliocene infill of the Teruel Basin. The sedimentation was interrupted on its footwall by mid Pliocene time, while a complete syntectonic sequence belonging to the Villafranchian (lacustrine carbonates and red alluvial sediments) and Pleistocene (fluvial terraces and alluvial fans) was deposited on the hanging wall (Simón, 1983; Moissenet, 1985; Ezquerro et al., 2012). The accumulated net displacement since latest Ruscinian time (3.5 Ma; Ezquerro, 2017) is estimated within the range of 255–290 m, resulting in a net slip rate of 0.07–0.08 mm/a (Lafuente et al., 2011, 2014).

Paleoseismological studies indicate that this fault underwent at least eleven events since ca. 74 ka BP, with an average recurrence period of 7.1–8.0 ka. The net accumulated slip during this time lapse has been calculated to 20.5 m, with average coseismic slip of 1.9 m and net slip rate of 0.29 mm/a (Lafuente et al., 2011, 2014; Simón et al., 2016).

3.4. Teruel Fault

The Teruel Fault is a N–S striking, 9.0 km-long, intrabasinal fault that offsets the Neogene infill of the Teruel Basin (Fig. 2B). In detail, it shows a single, N170°E trending trace at the northern sector, while southwards it branches off into several fault traces whose trends range between NNE-SSW and NNW-SSE. The exposed rupture surfaces dip 68° in average, and striations indicate a nearly pure normal movement with transport direction towards N275°E (Simón et al., 2017).

The hanging-wall block shows a roll-over structure revealed by tilting (2° E) of the Páramo 2 unit, which involves a minimum throw of ca. 250 m and a net slip of ca. 270 m. This displacement has been partially accommodated by a bending monocline (dipping up to 17°-30° W), which in combination with the roll-over gives rise to a synform sag parallel to the fault (Lafuente et al., 2011). Taking into account an age of ~3.5 Ma (latest Ruscinian) for the Páramo 2 unit at this area (Ezquerro, 2017), it results in a slip rate of ca. 0.075 mm/a.

The Teruel Fault shows a remarkable Pleistocene activity, but its paleoseismic record is quite limited. Four events occurred between 76.0 and 9.2 ka BP have been recorded from trenching in two distinct fault branches, involving a limited slip rate of ca. 0.04 mm/a (Simón et al., 2017).

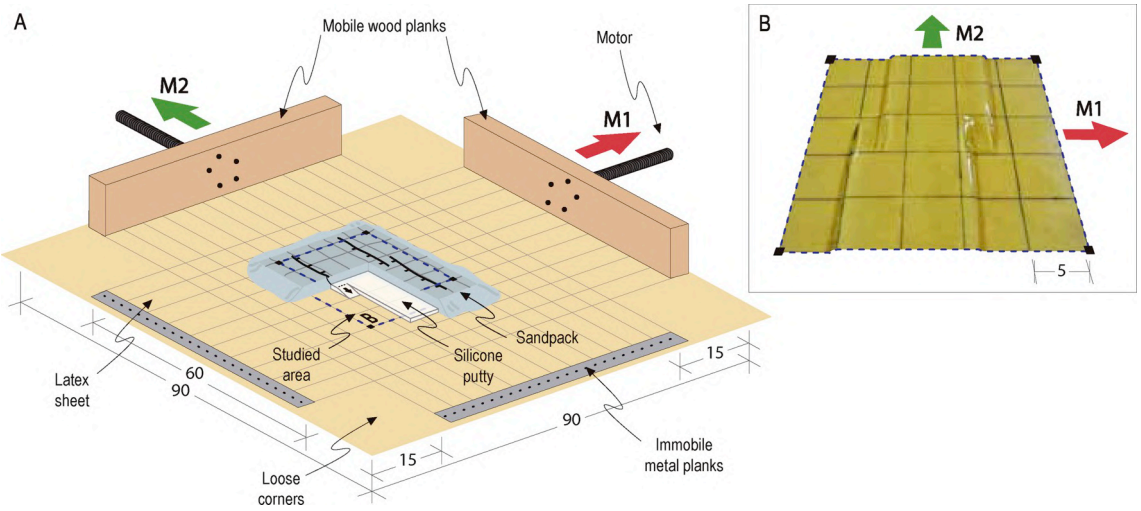

Fig. 3. (A) Experimental set-up. (B) Detail of the studied area and the silicone strip configuration in models B1-1 and B2-1.

4. Methodology

4.1. Structural methods

Minor faults and fractures developed within the three large relay zones at the eastern border of the Jiloca Graben have been mapped with the help of aerial photographs and orthoimages, obtaining geological maps at scales around 1:160.000 and 1:40.000. Published maps (by the Spanish geological survey, IGME) at 1:50000 scale (Martín et al., 1977, 1979; Godoy et al., 1983a, 1983b; Hernández et al., 1983a, 1983b; Olivé et al., 1983; Ramírez et al., 1983) have been used as a start point. Field survey has also been carried out within specific sectors, in order to improve certain map details, to elaborate cross-sections and to characterize deformation structures. To infer the kinematics of these structures at an outcrop scale, data of minor faults and fractures (rupture planes and slickenlines) have been collected when possible, as well as evidence of displacement of stratigraphic markers or the arrangement of reoriented pebbles, among others.

Rose diagrams of faults and fractures have been elaborated using Stereonet software (Allmendinger et al., 2013; Cardozo and Allmendinger, 2013). Rupture orientations have been measured at two different scales: (i) fractures and minor faults at outcrop scale in a total of 22 data sites, all of them located within Neogene and Quaternary materials; (ii) faults at map scale, either those located within relay zones or the master faults themselves, measured considering their orientation changes along their total lengths.

Many of these ruptures are nearly vertical and do not show any evidence of slip. They have been interpreted as tension (Mode 1) fractures, so extension trajectories have been inferred orthogonal to them. In the case of dipping rupture planes, the insufficient number of slickenlines has made impractical the application of classical methods of paleostress inversion based on fault population analysis. Nevertheless, this type of studies has been extensively carried out in the Jiloca Graben and the surrounding region (e.g., Simón, 1989; Arlegui et al., 2005; Liesa et al., 2019). Therefore, our knowledge of the recent regional stress field provides a comprehensive dynamical framework for the investigated fault relay zones.

4.2. Analogue modelling

The analogue models presented in this work are performed in normal gravitational field and are representative of the upper crust, or part of it, in an area subject to biaxial extension. The experimental set-up used for simulating fault relay evolution consists of a basal latex sheet that is fixed by two of its orthogonal ends and, in the other two ends, attached to two mobile walls pushed at constant velocity by stepper motors (Fig. 3A). Models lie centred over the latex sheet and consist of a 0.5-cm-thick silicone strip (~ 25 × 10.8 cm in plan view) overlain by a 1-cm-thick sand pack (25 × 25 cm square in plan view). By moving the two mobile walls away from the two fixed ones, the latex sheet was stretched producing extension in two orthogonal directions of the overlying model. The stepped-shape of the silicone strip in plan view (Fig. 3B) allows generating four main structures and two relay zones in each model, following the configuration proposed by Hus et al. (2005). For this purpose, the function of the silicone strip boundaries is to control nucleation of the main structures. The novelty of our models lies in the application of a biaxial extension regime to study the fracturing evolution of fault relay zones, and to study the influence of two parameters in their development: 1) the regional biaxial extensional regime, and 2) the orientation of the main structures (generated over the silicone strip boundaries).

To represent the brittle behaviour, we used dry sand (Silica Sand L-70/80 S from Sibelco Hispania), with a 99% of SiO_2, grain size between 63 and 400 μm, mean density of 1610 kg m^{-3}, and an internal friction angle of 30°-37° (Román-Berdiel et al., 2019). Sand is a proper material, as it behaves according to the Mohr-Coulomb criterion and shows low cohesion and internal friction angle similar to natural rocks (Mandl et al., 1977; Krantz, 1991; Schellart, 2000; Panien et al., 2006; Klinkmüller et al., 2016). To represent the ductile behaviour, we used

Table 1
Scaling parameters between analogue models and nature.

Parameter	Model value	Nature value	Model/ nature ratio
Length (L)	0.01 m	800 m	1.25×10^{-5}
Density (ρ)	980–1610 kg/m^3	2000–2700 kg/m^3	~ 0.5
Gravity (g)	9.8 m/s^2	9.8 m/s^2	1
Stress (σ = ρgL)	96–158 Pa	16×10^6 – 21×10^6 Pa	6.25×10^{-6}
Viscosity (μ)	7×10^3 Pa s	1×10^{19} Pa s (Koyi, 1988)	7×10^{-16}
Strain rate (ε = σ/μ)	1.37×10^{-2}–2.22×10^{-2} s	1.6×10^{-12}-2.1×10^{-12} s	8.93×10^9
Internal friction angle	30° - 37°	31° - 40° (Bahroudi et al., 2003)	~ 1
Velocity (V= εL)	1.36×10^{-5} – 3.25×10^{-5} m s^{-1}	1.22×10^{-10} - 2.93×10^{-10} m s^{-1}	1.11×10^5
Time (t = 1/ε)	3600 s	3.15×10^{13} s	1.14×10^{-10}

colourless silicone putty (Rhodorsil Gomme FB type from Caldic), which is almost perfectly Newtonian at the strain rates imposed in the experiments, that has a viscosity of 7×10^3 Pa s at 20 °C and a density of 980 kg m^{-3} (Table 1). It allows simulating the plasticity of a possible detachment level of claystones and evaporites (Weijermars y Schmeling, 1986; Rudolf et al., 2016).

A grid of squared passive sand markers drawn over the sand packs allowed analysing superficial deformation during experiments. This grid is drawn parallel to the directions in which the traction is exerted and, therefore, to the primary extension trajectories. Progressive evolution of the surficial structures has been studied thanks to photographs taken at regular time intervals while running experiments.

Models are geometrically, kinematically and dynamically scaled following principles discussed by Hubbert (1937) and Ramberg (1981). We chose a length ratio of 1.25×10^{-5}, so that 1 cm in the models is equivalent to 0.8 km in nature. Gravity field, densities and viscosities are imposed in the models by the experimental conditions and materials used (Table 1). The models are performed in normal gravitational field ($g = 1$), and the ratio of densities between model and natural materials is $\rho \sim 0.5$. Proportionality between tectonic and gravitational forces is $\sigma = \rho\ g\ L \sim 6.25 \times 10^{-6}$ and the scale factor for the viscosity of the ductile level $\mu = 7 \times 10^{-16}$. The temporal relationship is $T = 1.14 \times 10^{-10}$ (1 h of experiment represents 1 Ma in nature), and the ratio of velocity is $V = 1.11 \times 10^5$ (the velocity ranges used in the laboratory, between 4.9 and 11.7 cm/h, represent velocity ranges between 0.38 and 0.92 cm/year in nature).

A total of eight experiments have been carried out, which are divided into two series of three models each (Series 1 and Series 2, Table 2) following a preliminary set of two reference models (R1 and R2, Table 2). The main difference between Series 1 and 2 is the ratio of velocities of both motors: 11.7/4.9 and 10.1/8.0, respectively (Table 2). In this way, Series 2 involves a lower horizontal differential stress ('more biaxial') than Series 1. The three models that make up each series differ in the orientation of the silicone strip to the stretching directions.

In reference models R1 and R2 it was possible to study the deformation fields applied to the latex sheet, which are then transmitted to sand packs of models from Series 1 and 2, respectively. They allowed enclosing a central domain with virtually homogeneous extension where models can be preferably analysed, avoiding possible extension perturbations induced near the fixed boundaries of the latex sheet. These reference models aimed to define the actual deformation field within the latex sheet from a number of circumferences traced on it and then distorted into deformation ellipses under the imposed extension (Fig. 4). Their maximum axes defined extension trajectories that are key elements for subsequent interpretation of structures developed in the sand packs. For detailed analysis of the developed structures, the total length of each single structure has been divided into segments of different orientation. The orientation of each segment is then compared with both the normal to the extension trajectories at that point (γ angle), and the orientation of the silicone strip (θ angle) (Fig. 5). Each individual segment is considered to be controlled by the extensional field when γis less than $\pm 20°$, and controlled by the orientation of the silicone strip (therefore by the orientation of the main structures) when θ is less than $\pm 20°$.

5. Fracture patterns within fault relay zones

5.1. Northern relay zone: Between Calamocha and Sierra Palomera faults

The northern sector of the relay zone between Calamocha and Sierra Palomera faults shows ruptures that mainly affect the Neogene series, as these units dominate within this sector and belong to the Calatayud Basin infill (Fig. 6). On the contrary, its southern sector shows Mesozoic and Palaeogene units affected by folds that trend parallel to the master faults. The whole relay zone exhibits a mixed style, combining features of *soft linkage* (a gentle relay ramp) and incipient *hard linkage* (through short transverse faults) in some sectors.

Jurassic materials in the central part of the relay zone are cut by nearly N–S striking faults that bound narrow grabens infilled with Quaternary sediments (Capote et al., 1981; Gutiérrez et al., 1983). A well-exposed fault within this graben system, the Rubielos de la Cérida Fault (Site 9; Fig. 6), has been studied in an exceptional outcrop where the rupture surface shows average orientation N 175° E and slickenlines indicating a mean transport direction of the hanging-wall block towards WNW (Site 9; fig. 6; Capote et al., 1981). Northwest of that horst-and-graben system, nearly N–S striking fractures (Site 7A; Fig. 6) and faults (Site 7B; Fig. 6) also cut Neogene materials.

Neogene conglomerates at the northern part of this relay zone are affected by a main set of faults and fractures oriented around NE-SW (nearly parallel to the map-scale Bañón Fault), accompanied by a second near-orthogonal set oriented NW-SE (Sites 1, 2, 4, 5 and 6; Fig. 6).

Several Quaternary alluvial fans sourced at the map-scale faults spread out towards the centre of the Jiloca Graben. One of them is cut by scattered fractures with a dominant NW-SE to NNW-SSE direction (Site 8; Fig. 6).

5.2. Central relay zone: Between Sierra Palomera and Concud faults

The geometrical characteristics of this relay zone are similar to those of the former one, with a relay ramp similar in size and several fractured sectors in between. Neogene materials predominate within this relay zone, affected by fractures that have been measured in ten outcrops (Fig. 7). Upper Miocene conglomerates are cut by both primary N–S fractures and secondary E-W fractures that locally abut the former ones (Site 2; Fig. 7). Sets of faults and fractures oriented close to N–S offset Mio-Pliocene limestones at Sites 6, 7, 8, 9, and, with a notable density, in Site 10 (see photograph in Fig. 7). The Upper Pliocene sequence is affected by NNW-SSE to N–S striking fractures at Sites 1A and 3 (Fig. 7), and unconformably overlain by the Villafranchian pediment that is cut by NNW-SSE ones (Site 1B; Fig. 7; Simón, 1983). Two small areas for which Ezquerro (2017) provides detailed mapping of Neogene fractures (Sites 4, 5; Fig. 7) show distinct patterns: while N–S striking fractures

Table 2
Model characteristics and experimental conditions for the different experiments performed. SST = silicone strip thickness; SPT = sand pack thickness; OSS = orientation of the silicone strip; VM1 = velocity of Motor 1; VM2 = velocity of Motor 2; EM1 = total displacement of Motor 1; EM2 = total displacement of Motor 2.

Experiments		SST (cm)	SPT (cm)	OSS (to M1 extension)	VM1 (cm/h)	VM2 (cm/h)	VM1/VM2 (%)	EM1 (cm)	EM2 (cm)
Series 1	R-1	–	–	–	11.7	4.9	~40	20	9
	B1-1	0.5	1	90°	11.7	4.9	~40	20	9
	B1-2	0.5	1	115°	11.7	4.9	~40	20	9
	B1-3	0.5	1	65°	11.7	4.9	~40	20	9
Series 2	R-2	–	–	–	10.1	8	~80	14	12.5
	B2-1	0.5	1	90°	10.1	8	~80	14	12.5
	B2-2	0.5	1	115°	10.1	8	~80	14	12.5
	B2-3	0.5	1	65°	10.1	8	~80	14	12.5

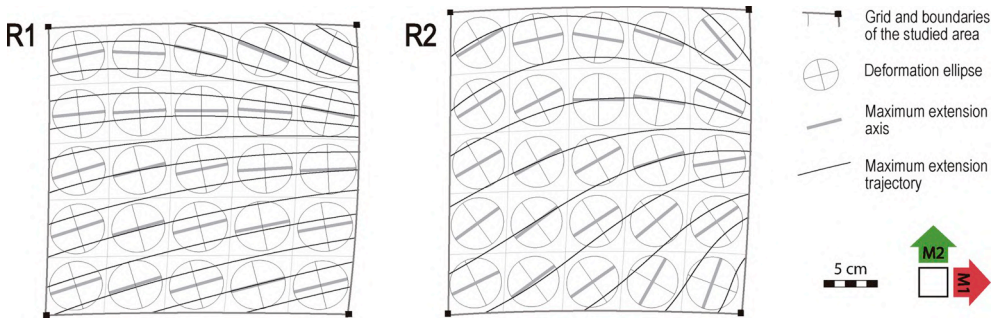

Fig. 4. Reference models R1 and R2 defining the strain field imposed in models of Series 1 and 2, respectively. Extension trajectories inferred from latex sheet deformation, then transferred to the sand pack, are shown.

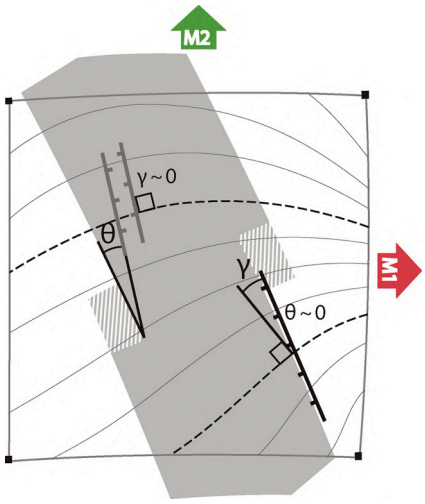

Fig. 5. Angles used for detailed analysis of fractures developed in analogue models; γ: angle between an individual fracture segment and the normal to the extension trajectory; θ: angle between an individual fracture segment and the orientation of the silicone strip.

strongly dominate the middle Miocene of the central sector of the relay zone (Site 4), NW-SE ones prevail at the propagation of Sierra Palomera fault zone, cutting Lower Miocene materials (Site 5).

Larger-scale faults in the northern part of the relay zone mainly affect Paleogene materials, but show Quaternary fans associated to their fault scarps. They are aligned with the possible southern propagation of one branch of the Sierra Palomera Fault, mantaining its NW-SE orientation.

5.3. *Southern relay zone: Between Concud and Teruel faults*

This relay zone is much smaller than the previous ones; the distance between both fault tips is less than 1 km. The displacement is sharply transferred between both faults through a northwards dipping relay ramp, as shown in their displacement-length profiles (Lafuente et al., 2011). Upper Pliocene and Pleistocene materials are affected by faults and fractures oriented NNW-SSE and occasionaly NNE-SSW, which have been studied in three representative outcrops (Fig. 8). Two additional NNW-SSE striking faults, aligned with a hypothetic northern propagation of the Teruel Fault, have also been detected in the northern sector by means of a geophysical survey (magnetometry and georadar, GPR; Peiro et al., 2017).

Data site 1 includes a main fault zone (1B; Fig. 8), striking NNE-SSW and showing a total throw of 18 m, accompanied by NNW-SSE minor faults and NNE-SSW to N–S fracture sets at its footwall and hanging-wall blocks, respectively (1A,C; Fig. 8). The main ruptures are antithetic to the Concud and Teruel faults and show transport directions of the hanging-wall block towards ENE (Peiro et al., 2017).

Three conspicuous faults showing decametre-scale throw crop out at Las Ramblillas area (Fig. 8), two of them synthetic and one antithetic to the Concud and Teruel faults. The western synthetic fault has an average orientation 157, 48 W and striations that pitch 70 S (Simón et al., 2017).

Fractures at Site 2 (Fig. 8) affect both a Middle Pleistocene and a Late Pleistocene fluvial terrace. The former is offset by a fault that shows a minimum throw of 7 m and a roll-over monocline at its hanging-wall block. The latter shows several normal faults and fractures arranged in a conjugate pattern, all of them striking around NW-SE (Peiro et al., 2019).

6. Experimental results

Several analogue models (Series 1 and Series 2), as well as the preliminary reference models (R1 and R2), have been performed and analysed. Velocities of both motors are distinct in Series 1 and similar to each other in Series 2 (Table 2), so that the velocity setting in Series 2 is supposed to simulate more accurately the nearly biaxial or radial extensional stress field at the eastern Iberian Chain.

Boundary fault systems, as well as deformation structures within relay zones, have successfully developed in all the experiments. They consist in either a single fault system, a graben system, or a combination of both (from now these structures will be named as “master faults”; Fig. 9). Models of Series 1 are characterised by pervasive deformation developed not only within the boundary fault systems but also over the central sector of the silicone strip, where a graben system has been generated (models B1-1, B1-2 and B1-3; Fig. 9). In contrast, in Series 2 deformation is concentrated within the boundary fault zones, and therefore within relay zones (models B2-1, B2-2 and B2-3; Fig. 9).

In both series, when the silicone strip is arranged either at 90° (models B1-1 and B2-1; Table 2, Fig. 9) or 115° (models B1-2 and B2-2; Table 2, Fig. 9) to the main extension direction (i.e. M1 in Fig. 9), master faults completely develop along the silicone boundaries. On the contrary, when the silicone strip is arranged at 65° (models B1-3 and B2-3; Table 2, Fig. 9), master faults only develop in half the length of the silicone boundaries.

These results have also been analysed in terms of the main extension trajectories applied in each series (see Fig. 3). On the one hand, when the silicone strip is nearly perpendicular (models B1-1, B1-2) or making a high angle (models B2-1, B2-2) to the main stretching direction (i.e, the silicone boundaries are favorably oriented with respect to the extension trajectories), master faults develop entirely. On the other hand, when the silicone strip makes a low angle to the extension trajectories (models B1-3, B2-3), almost no silicone boundary is favorably oriented and the master faults are hardly developed. These results emphasize the role of the stress/strain trajectories in the resulting fracture pattern, while neglecting the influence of preexisting structures when the latter are not favorably orientated. Such tendency can be recognized even in the case of a nearly biaxial or radial or extensional regime, where a wide range of

fracture orientations would be theoretically able to be activated.

Both in Series 1 and 2, interaction between master faults through relay zones occurs from early stages. Fault traces are usually visible between minutes 30 and 50 of the experiments. In some cases, like model B2-2, the faults start growing at the segments that define the relay zone and then spread to more distant points (Fig. 10A and B). This allows accommodating deformation in a greater extent near the relay zones and, as a result, relay ramps develop (figs. 9, 10C and 11A; Walsh and Watterson, 1991). At intermediate stages, some relay zones evolve through continuous along-strike propagation of one of the master faults, in several cases with a curved geometry (Figs. 10C and 11B), while bending at the relay ramp increases. At advanced stages, propagation of the master faults continues (Fig. 9 models B1-1, B1-2, B2-2, Fig. 10D) and, especially in models of Series 2 transition to *hard linkage* by means of transverse connecting faults initiate (Figs. 9, 10D and 11C).

Nevertheless, it should be noticed that such transverse ruptures are not orthogonal to the master faults, neither oblique in the sense in which they ordinarily arise in models reported in the literature: they make angles $>90^{\circ}$ with the along-strike propagation of the neighbouring master fault (see Figs. 9, 10D and 11C), which constitutes a remarkable anomaly. When compared with the deformation field recorded in the basal latex sheet, it is observed that those connecting faults are almost orthogonal to the extension trajectories. An actual case of such geometry has been described by Nixon et al. (2019), implicitly assuming that the distributed fractures within the relay zone are directly controlled by the remote stress field.

The compatibility analysis of the resulting structures is shown in Fig. 12, where each pie chart represents the total percentage of accumulated length of boundary fault system developed in each experiment, central fractures are not taken into account in this analysis. The percentages of fracture segments controlled by the silicone strip orientation ($\theta < \pm 20^{\circ}$) correspond, almost in its entirety, to the main structures directly developed over the boundaries. The percentages controlled by the extension trajectories ($\gamma < \pm 20^{\circ}$) represent fracture sets developed in relay zones. Thus, both curved propagation of the master faults and fault linkage have been mainly controlled by the extension field.

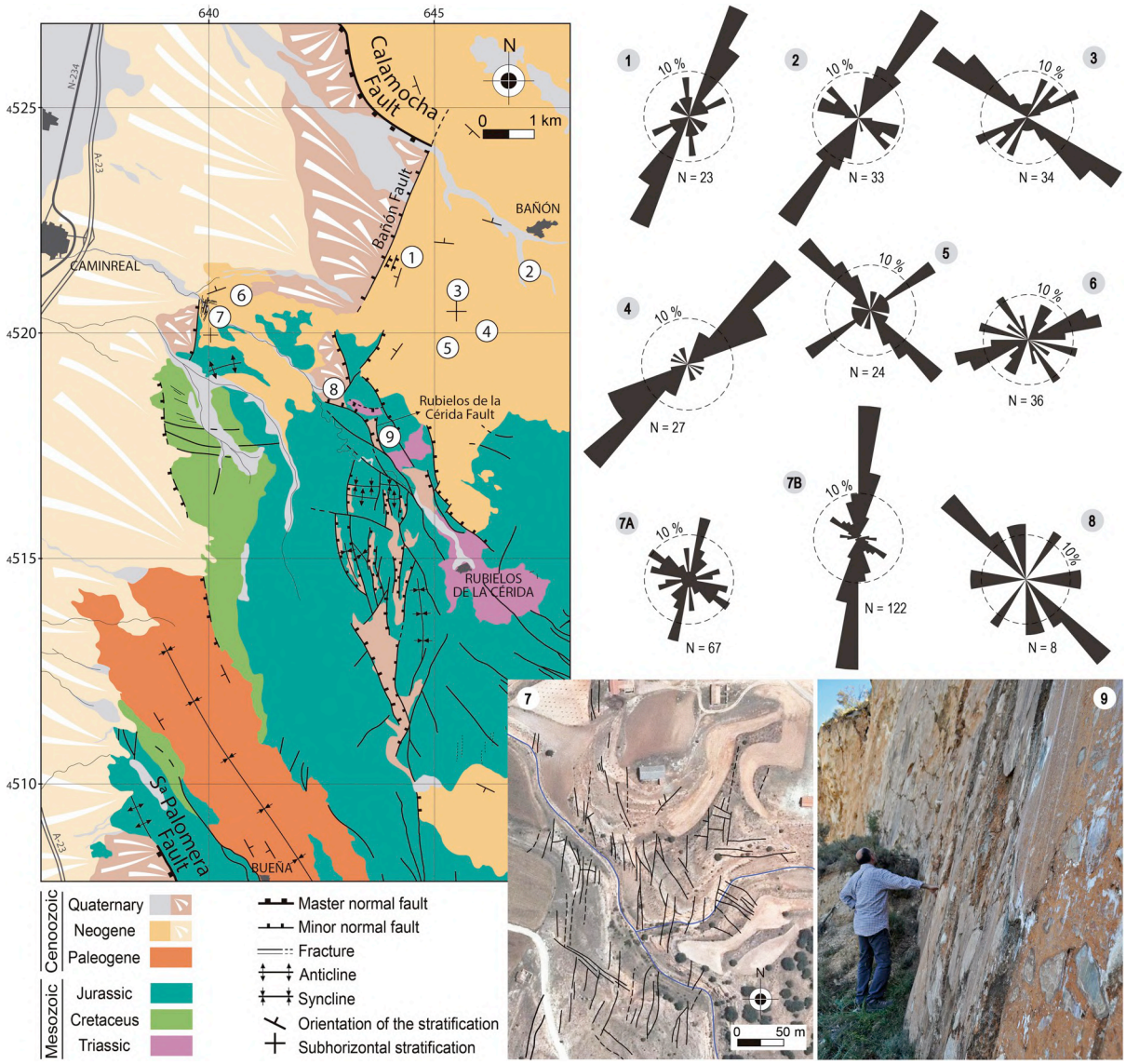

Fig. 6. Geological map and fracture patterns of the northern relay zone, between the Calamocha and Sierra Palomera (see location in Fig. 2B). Rose diagrams show strike distributions of mesostructural fractures measured in sites 1–8; in the case of site 7, fractures and faults are distinguished (7A and 7B, respectively). 7C: detailed fracture map of Site 7.9: Outcrop of the Rubielos de la Cérida Fault.

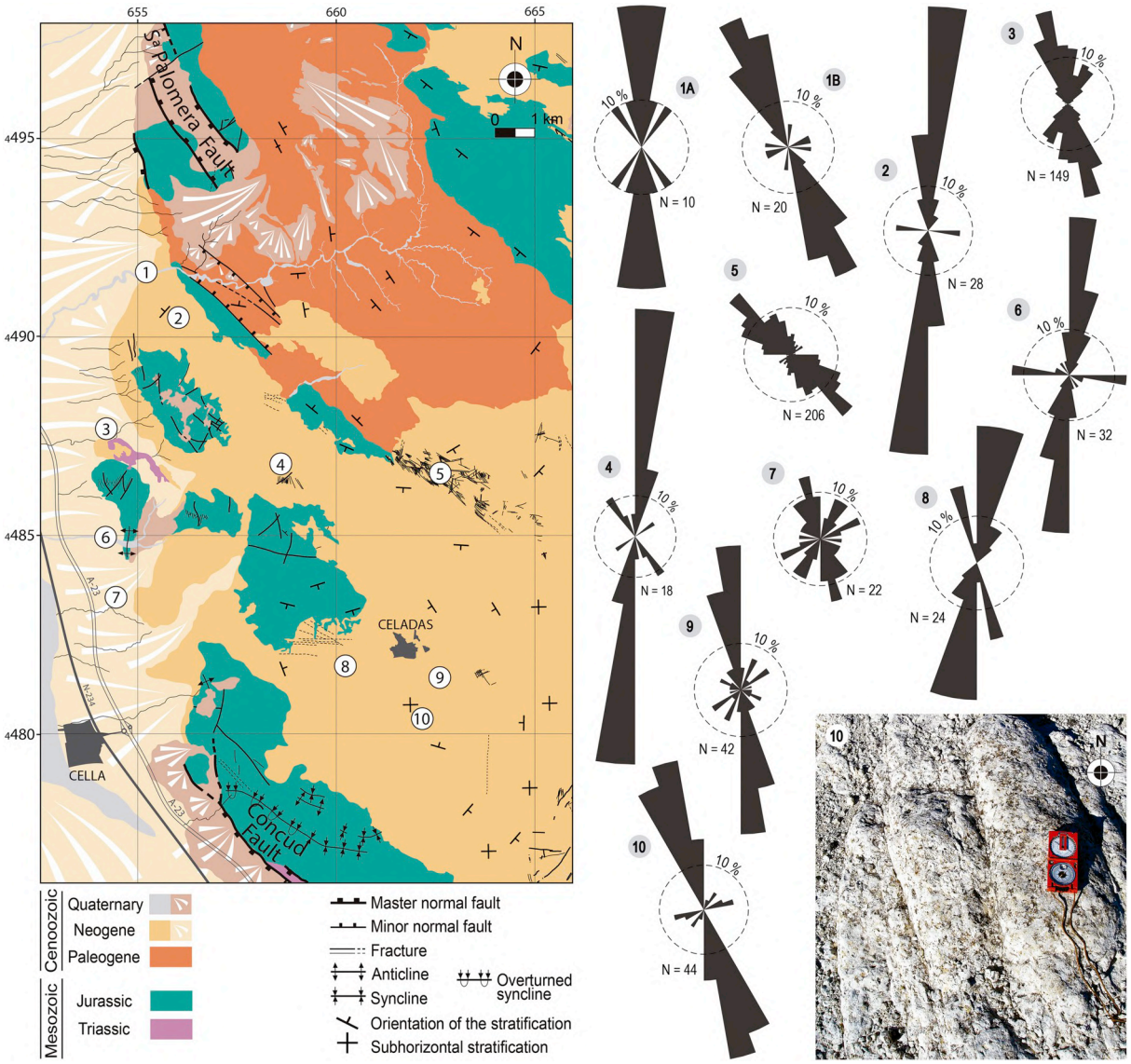

Fig. 7. Geological map and fracture patterns of the central relay zone, between the Sierra Palomera and Concud faults (see location in Fig. 2B). Rose diagrams show strike distributions of mesostructural fractures measured in sites 1–10; for site 1, fractures in units from the Upper Pliocene and the Villafranchian pediment are distinguished (1A and 1B, respectively). Photo 10: field view of systematic NNW-SSE striking fractures cutting Miocene limestones in Site 10.

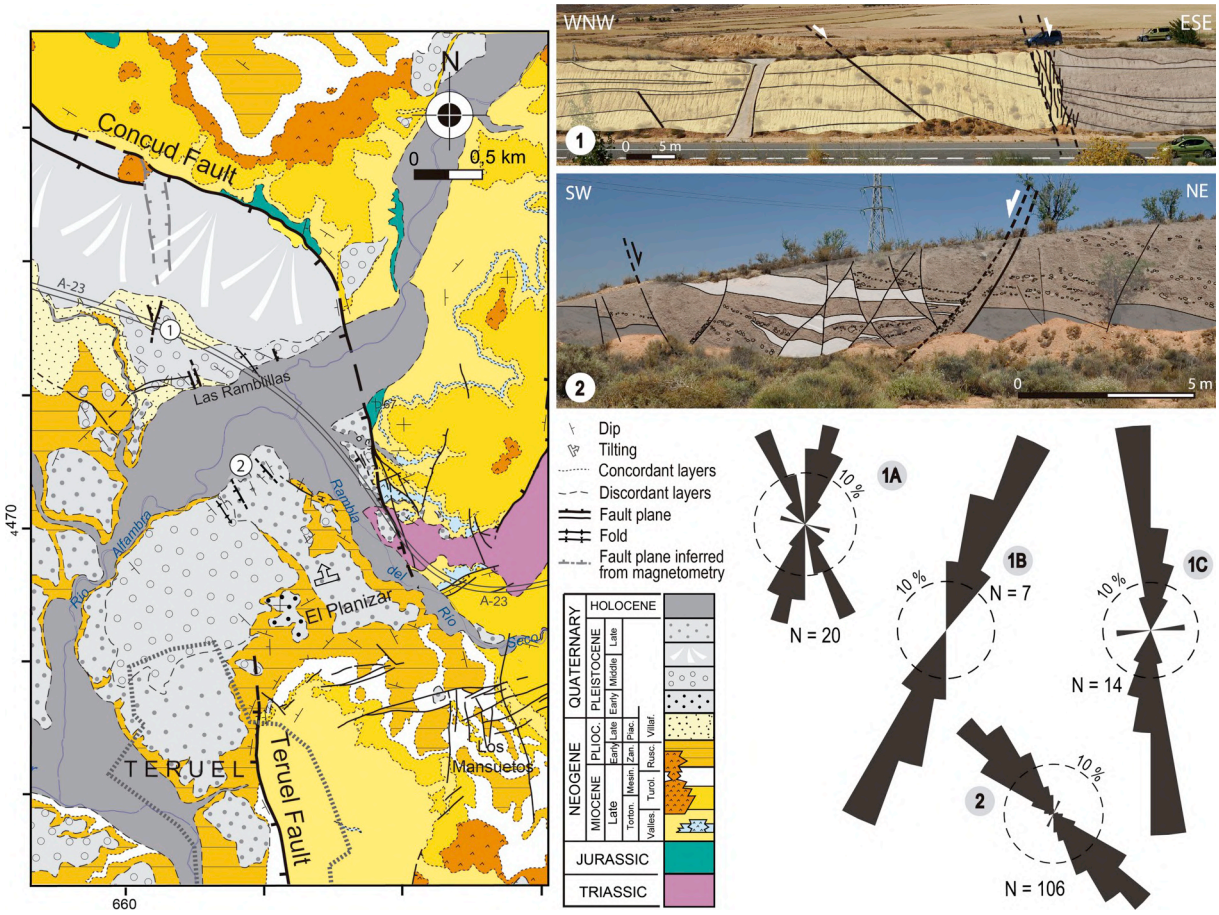

Fig. 8. Geological map and fracture patterns of the southern relay zone, between the Concud and Teruel faults (map modified from Lafuente et al., 2011; see location in Fig. 2B). Rose diagrams show strike distributions of mesostructural fractures measured in sites 1 and 2, whose overall field views are shown in 1A and 2A, respectively. For site 1, fractures in the footwall block, main fault zone and hanging-wall block are distinguished (diagrams 1A, 1B and 1C, respectively).

7. Interpretation and discussion

7.1. Discriminating the influence of external and internal controls over fracture patterns in relay zones

Fracture patterns developed in fault relay zones at the eastern margin of the Jiloca Graben are summarized in rose diagrams of Fig. 13, where strike distributions of (i) fractures and minor faults at outcrop scale, (ii) faults at map scale, and (iii) master faults themselves, have been gathered for each relay zone. In addition, Fig. 14 depicts the interpretation of these rose diagrams in terms of compatibility or incompatibility of the different fracture sets with macrostructure heritage and stress trajectories. Since the general trend of the Jiloca Graben is nearly parallel to S_{Hmax} (Simón, 1989), and its bounding master faults only make a very-low-angle with it, in practice it is not easy to discriminate between 'ruptures controlled by the primary stress field' and 'ruptures controlled by the structural heritage'. Hence a significant percentage of structures are considered as 'controlled by both of them'. All the same, ruptures of any of these origins, overall oriented in the range of 130–200, can be classified as longitudinal or along-strike fractures and grouped into a single genetic category: 'externally controlled' fractures (types I and J in Fig. 1). The latter are conceptually different from transverse fractures 'internally controlled' by the own relay kinematics and the subsequent stress/strain perturbations (types A, B, C and D in Fig. 1). Intermediate cases in which both external controls and internal kinematics occur are represented by types E, F, G and H in Fig. 1.

Most ruptures within the three studied relay zones are along-strike ones (Figs. 13 and 14). They are quite homogeneously distributed and appear at any scale: (a) in the northern relay zone, 61% and 88% of outcrop and map ruptures, respectively; (b) in the central relay zone, 81% and 100%, and (c) in the southern relay zone, 94% and 100%.

The trend controlled by the primary stress field (Fig. 14) can be recognized among the distributed ruptures at map scale of the northern relay zone (making the large N–S graben system; Fig. 6), that involve Neogene and Quaternary deposits. Within the central relay zone, these fractures are homogeneously distributed at outcrop scale and mainly affect Neogene units (Fig. 7). Within the southern relay zone, map-scale faults are also parallel to both the master faults (Teruel and southern segment of Concud; Fig. 8) and the S_{Hmax} trajectories. The incipient northwards propagation of the Teruel Fault, as inferred from surface data and subsoil geophysical exploration (fig. 8; Peiro et al., 2017), also follows the same trend. For this reason, a future junction of the Teruel and Concud faults through along-strike propagation of the former till abutting the latter constitutes a reliable prediction (Peiro et al., 2017).

The trend controlled by the structural heritage (Fig. 14) is clearly recognizable in the central relay zone, where map-scale faults follow the NW-SE orientation of the Sierra Palomera Fault (Fig. 7), as well as in the outcrop-scale fractures from the southern relay zone. Although also present in the northern relay zone, such fracture sets represent a minority with respect to the stress-controlled, N–S trending sets.

Significant transverse ruptures have been found only in the northern relay zone (Figs. 6 and 14). The most noticeable structure is the Bañón Fault, which can be considered as an incipient connecting fault. Within the central and southern relay zones, transverse fractures have been observed only at outcrop scale and barely represent 19% and 6% of the total, respectively (Fig. 14).

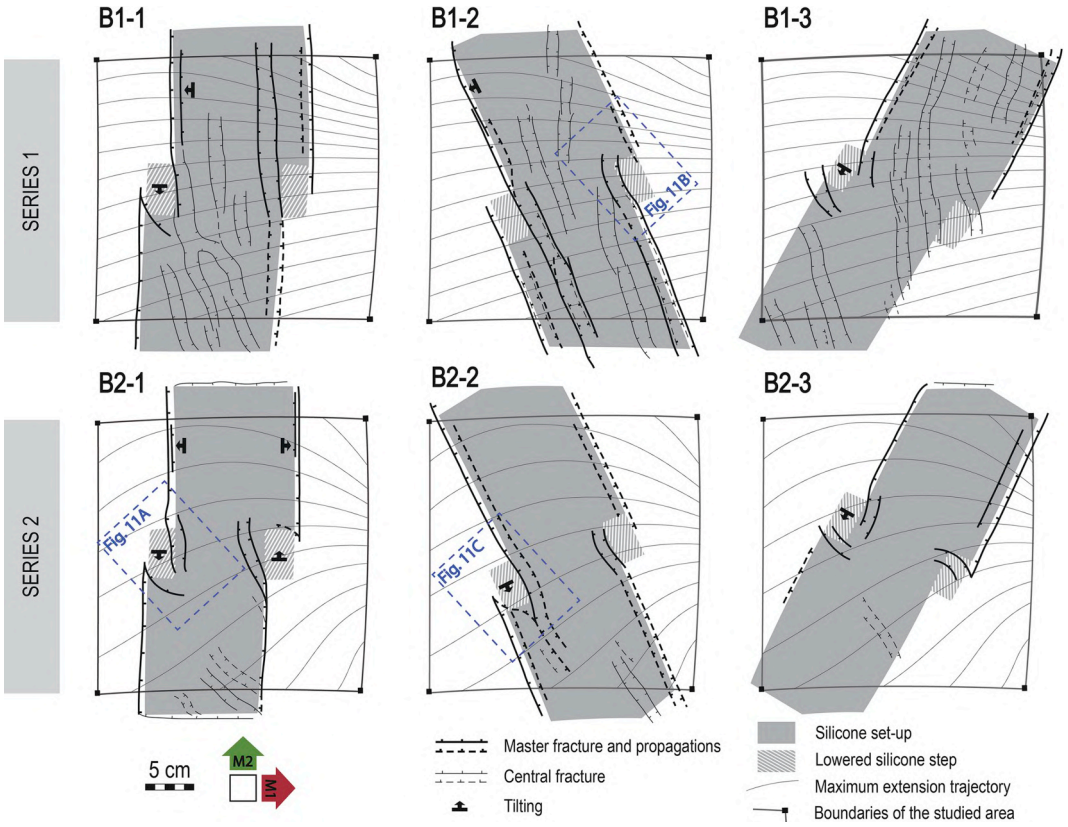

Fig. 9. Line drawing of surface fracture patterns developed in models of Series 1 (B1-1, B1-2 and B1-3) and Series 2 (B2-1, B2-2 and B2-3), with location of Fig. 11A, B and 11C.

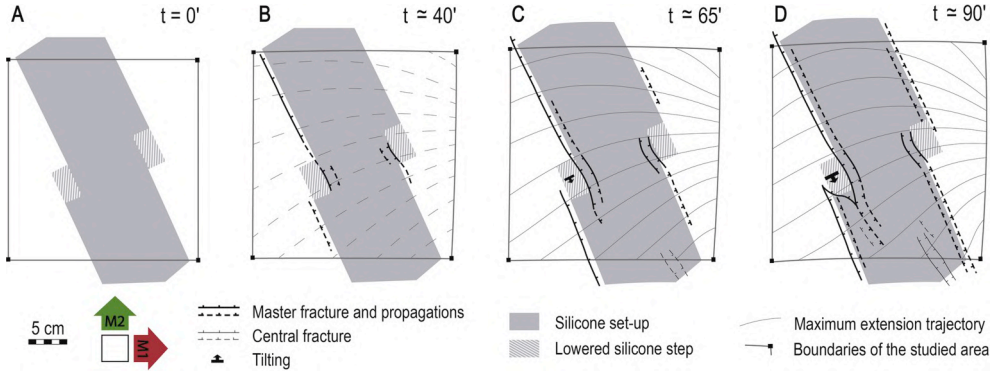

Fig. 10. Line drawing of the surface of model B2-2 showing the evolution of deformation.

It could be expected that transverse, even orthogonal, secondary fractures were more common in relay zones within biaxial extension, owing to the frequent swapping of σ_2 and σ_3 axes occurring under such stress regime, as stated in Section 1. Nevertheless, we should remember that such type of stress perturbation, which commonly results in secondary fractures at right angles to the master faults, typically takes place close to central sectors of the latter. In contrast, in the vicinity of the fault tips, σ_3 trajectories tend to either remain or become orthogonal to those master faults (Simón et al., 1988), hence enabling along-strike rupture propagation.

7.2. *Fault relay zones evolving through distributed longitudinal fractures: contrasting analogue modelling, nature and literature*

The notion of a relay zone evolving through distributed longitudinal fractures, developed under the influence of both inherited faults and the coeval stress regime, and without any significant presence of transverse connecting ruptures, has been corroborated by analogue modelling. When a 'less biaxial' extensional field is applied (Series 1), abundant deformation within both the boundary fault zones and the central sectors develops. Under 'more biaxial' extension (Series 2), deformation is concentrated close to the master faults and within the relay zones (Fig. 9). But, in general, fracture segments controlled by the 'structural inheritance' (silicone strips) or the extension trajectories, i.e. along-strike fractures, clearly dominate in all cases. The structural evolution of the relay zones corresponds to a *soft linkage* by means of relay ramps from early to intermediate stages, and a *hard linkage* by means of connecting faults at advanced stages (Figs. 10 and 11A,C). But the latter do not show the angle commonly observed in analogue and numerical models in the literature ($\leq 90^\circ$ to the along-strike propagation of the master fault). On the contrary, they are nearly orthogonal to the extension trajectories (Figs. 9 and 10D), again revealing the influence of

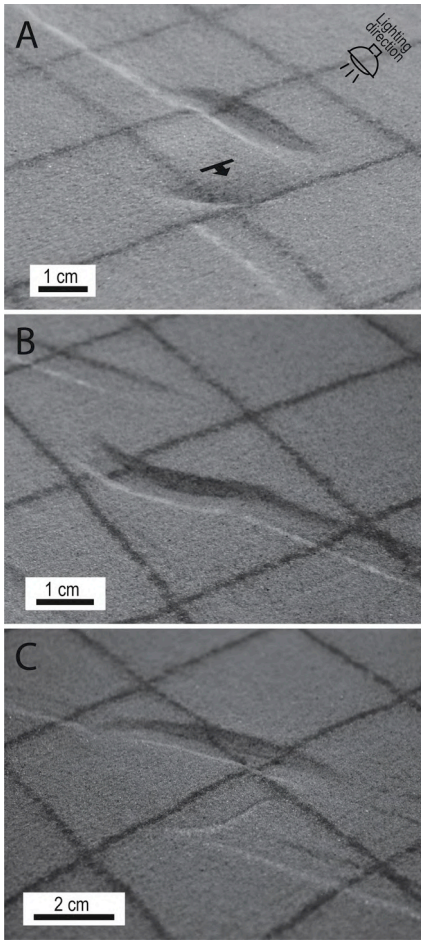

Fig. 11. Photographs of the surface of representative models showing deformation in relay ramps. (A) Relay ramp and incipient transverse connecting fault in model B2-1. (B) Curved propagation of one of the main structures in model B1-2. (C) Transverse connecting fault in model B2-2. Lighting direction is indicated.

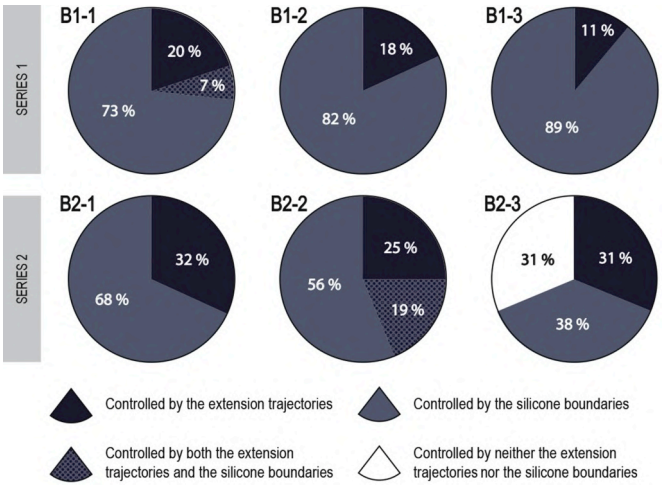

Fig. 12. Percentages of accumulated length of boundary fractures developed in the six analogue models performed, depending on whether their orientations are controlled by the extension trajectories or the silicone boundaries.

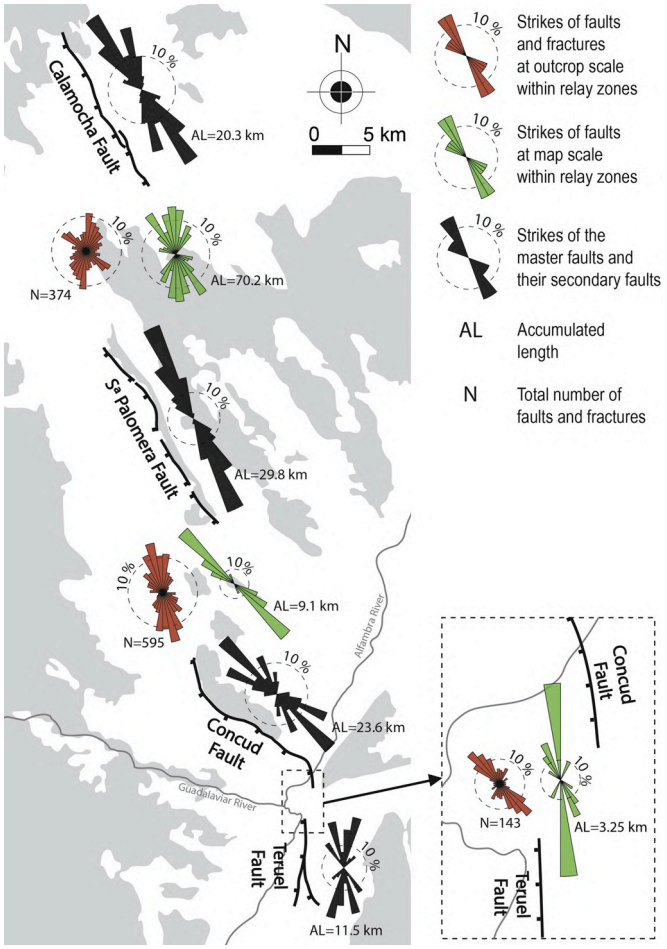

Fig. 13. Fault and fracture patterns, at outcrop and map scale, in the relay zones between the Calamocha, Sierra Palomera, Concud and Teruel faults, and the master fault zones themselves.

the remote stress/strain field beyond the control of relay kinematics.

The described fracture patterns do not fit those classically reported from numerical and analogue models in the literature. It could be argued that the northern and central relay zones are too wide with respect to the fault length, and that their overlapping distances are null, so that they do not constitute representative cases from which useful conclusions could be obtained. But the same attributes have been observed in the southern relay zone, between the closely spaced Concud and Teruel faults, where the classical transverse connecting faults are absent as well.

Therefore, a new conceptual model of relay zone should be defined (Fig. 15), in which fracture sets mimicking the inherited structural trends or responding to the remote stress field (two factors that have been usually disregarded) prevail over internally induced ones. Some of those along-strike or longitudinal ruptures represent propagation of the master faults, but others develop quite homogeneously all over the relay zone.

The resulting fault pattern exhibits features that have been highlighted in two recent papers by Deng et al. (2017), using numerical models of fault reactivation under oblique extension, and Nixon et al. (2019), on the basis of a detailed study of faults and fractures in Lower Jurassic rocks of the Somerset coast (UK). Nixon et al. (2019) describe how within the relay ramp numerous smaller, nearly parallel and quite homogenously distributed faults and veins ('damage-related fractures') develop under increasing stress perturbations, whereas outside of the relay ramp spatial distribution of deformation is more heterogeneous since it is mostly constrained to the master faults. Such distributed longitudinal ruptures play an important role in fault interaction,

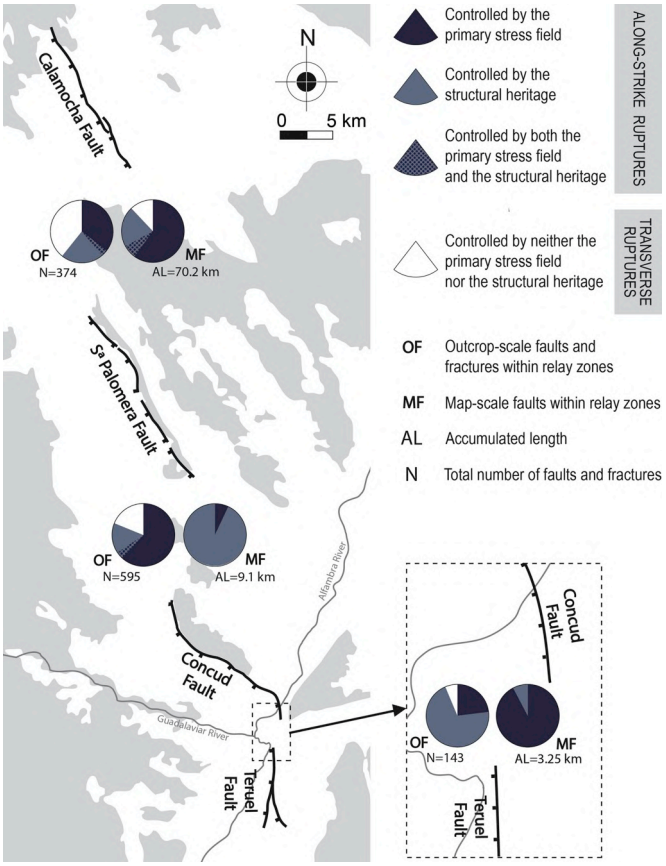

Fig. 14. Comparative balance of structural heritage vs. remote stress field as controls of rupture development within the relay zones between the Calamocha, Sierra Palomera, Concud and Teruel faults at outcrop and map scale.

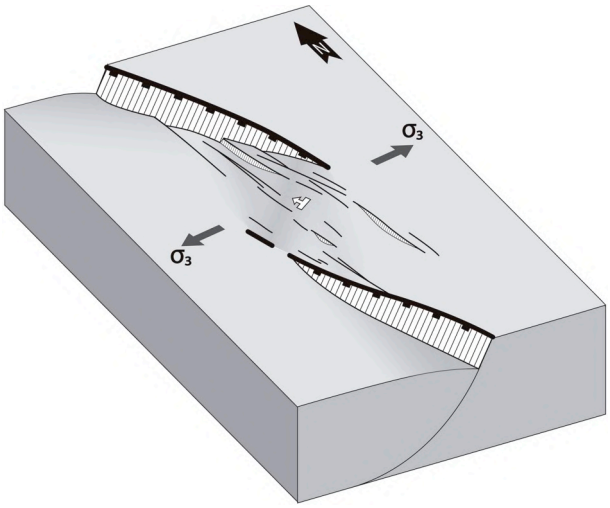

Fig. 15. 3D conceptual model of relay zone with distributed longitudinal, along-strike propagated fractures, developed under the double influence of the structural heritage and remote stress field.

accommodating and transferring part of the displacement between the interacting master faults, also maintaining their kinematic coherency. The influence of pre-existing structures adds geometric complexity to the fault network, resulting in an interfering, partially linked ensemble of reactivated faults and ruptures controlled by the remote stress field (Deng et al., 2017).

It is probable that, at relays of active faults, longitudinal ruptures also contribute to modify their seismic behaviour and hence seismic hazard of the region. They can either enable triggering seismic events on the adjacent master fault (hypothetically resulting in alternating slip on both of them, as it has already been suggested for the Concud and Teruel faults; Simón et al., 2017), or move themselves producing minor seisms that release part of the total energy.

Relay ramps with distributed along-strike fractures represent an interaction stage one step beyond bare *soft linkage*. The relay zones between the Calamocha, Sierra Palomera, Concud and Teruel faults are therefore in an intermediate stage between complete independency and coalescence. Such appraisal was already formulated for the Concud and Teruel faults by Lafuente et al. (2011) based on their displacement-length profiles.

Scenarios of future evolution of the studied relay zones can be envisaged in the light of the analogue models. In spite of these being properly scaled, deformation was not visible after applying the amount of extension undergone by the study region. The latter corresponds to a finite elongation of less than a 1% (estimated from total displacements of the Concud, Teruel and Valdecebro faults; Simón et al., 2012) while in analogue models a finite elongation of 12,5% was reached. Since this extension is higher, the advanced stages of analogue models can be interpreted as tentative predictions of evolution of the regional structures. A future *hard linkage* by means of transverse connecting faults is not expected. Instead, fault coalescence will probably occur in the future by propagation of one of the involved faults, giving rise to a final braided fault pattern (Fig. 1J).

8. Conclusions

The Jiloca Graben is an elongated depression in the eastern Iberian Chain, whose eastern margin consists in a right-relay arrangement of three NW-SE normal faults: Calamocha, Sierra Palomera and Concud. They have been active since Pliocene times under a nearly biaxial or radial extension regime, with σ_3 trending nearly WSW-ENE (Arlegui et al., 2005; Ezquerro, 2017). Together with the Teruel Fault, these faults enclose three relay zones that exhibit fracture networks different from those commonly predicted in fault relay models in the literature.

The three relay zones are characterised by transferring part of the displacement through relay ramps, revealing *soft linkage* interaction. But such relay ramps are further cut by distributed faults and fractures at metre to kilometre scales, affecting both Upper Miocene and Quaternary materials, which also contribute to slip transfer and dynamical interaction. Their structural analysis has allowed to identify three main fracture directions: (i) parallel to the master faults that enclose the relay zones (NW-SE to NNW-SSE), (ii) perpendicular to the σ_3 trendings during Neogene and Quaternary times (NNW-SSE to N–S), and (iii) transverse to the macrostructures (NE-SW). Cases (i) and (ii), classified as along-strike ruptures, dominate within the three relay zones. Their relative weight in each zone depends on the influence of the structural heritage and the stress field. Transverse fractures are more scarce and confined to certain sectors.

Analogue modelling has allowed understanding the controls of such fracture patterns. Fractures are mostly controlled by the inherited anisotropies and the coeval extension trajectories, which results in clear prevalence of along-strike fractures in both 'more biaxial' and 'less biaxial' extension regimes. Although incipient transverse connecting faults occur in advanced stages, they do not show the orientation usually reported in numerical and experimental models, but that controlled (orthogonal to) the remote extension trajectories.

A new conceptual model of fault coalescence through relay zones is defined (Fig. 15), in which externally controlled fracture sets (either parallel to the inherited structural trends, or responding to the remote stress field) prevail over those internally induced by the own relay kinematics.

The Calamocha, Sierra Palomera, Concud and Teruel faults, are interacting and evolving through along-strike fractures distributed

within their relay zones, and constitute good examples of such fault relay type. The overall fault system is at an intermediate stage between complete independence and coalescence. Future linkage will probably occur through along-strike (parallel or at very-low-angle) propagation of the master faults, resulting in a braided geometry.

Authors statements

Alba Peiro: Investigation, Methodology, Formal analysis, Writing - Original Draft, Visualization.

José Luis Simón: Conceptualization, Methodology, Investigation, Writing - Review & Editing, Supervision.

Teresa Román-Berdiel: Methodology, Validation, Investigation, Writing - Review & Editing, Supervision.

Declaration of competing interest

The authors declare that they have no known competing financial interests or personal relationships that could have appeared to influence the work reported in this paper.

Acknowledgements

Financial support was granted by the project Geotransfer-E32_17R of the Gobierno de Aragon and Programa Operativo FEDER Aragón 2014–2020.

References

Acocella, V., Morvillo, P., Funiciello, R., 2005. What controls relay ramps and transfer faults within rift zones? Insights from analogue models. J. Struct. Geol. 27, 397–408.
Allmendinger, R.W., Cardozo, N.C., Fisher, D., 2013. Structural Geology Algorithms: Vectors & Tensors. Cambridge University Press, Cambridge.
Álvaro, M., Capote, R., Vegas, R., 1979. Un modelo de evolución geotectónica para la Cadena Celtibérica. Acta Geol. Hispánica 14, 172–177.
Arlegui, L.E., Simón, J.L., Lisle, R.J., Orife, T., 2005. Late Pliocene-Pleistocene stress field in the Teruel and Jiloca Grabens (eastern Spain): contribution of a new method of stress inversion. J. Struct. Geol. 27, 693–705.
Athmer, W., Groenenberg, R.M., Luthi, S.M., Donselaar, M.E., Sokoutis, D., Willingshofer, E., 2010. Relay ramps as pathways for turbidity currents: a study combining analogue sandbox experiments and numerical flow simulations. Sedimentology 57, 806–823.
Bahroudi, A., Hemin, A.K., Talbot, C.J., 2003. Effect of ductile and frictional dècollements on style of extension. J. Struct. Geol. 25, 1401–1423.
Capote, R., Gutiérrez, M., Hernández, A., Olivé, A., 1981. Movimientos recientes de la fosa del Jiloca (Cordillera Ibérica). V Reunión del Grupo Español de Trabajo del Cuaternario, Sevilla, pp. 245–257.
Capote, R., Muñoz, J.A., Simón, J.L., Liesa, C.L., Arlegui, L.E., 2002. Alpine tectonics I: the alpine system north of the betic cordillera. In: Gibbons, W., Moreno, T. (Eds.), Geology of Spain. The Geological Society, London, pp. 367–400.
Cardozo, N., Allmendinger, R.W., 2013. Spherical projections with OSXStereonet. Comput. Geosci. 51, 193–205.
Cartwrigth, J.A., Trudgill, B.D., Mansfield, C.S., 1995. Fault growth by segment linkage: an explanation for scatter in maximum displacement and trace length data from the Canyonlands Graben of S. E. Utah. J. Struct. Geol. 17, 1319–1326.
Childs, C., Easton, S.J., Vendeville, B.C., Jackson, M.P.A., Lin, S.T., Walsh, J.J., Watterson, J., 1993. Kinematic analysis of faults in a physical model of growth faulting above a viscous salt analogue. Tectonophysics 228, 313–329.
Childs, C., Watterson, J., Walsh, J.J., 1995. Fault overlap zones within developing normal fault systems. J. Geol. Soc. 152, 535–549. London.
Clifton, A.E., Schlische, R.W., Withjack, M.O., Ackermann, R.V., 2000. Influence of rift obliquity on fault-population systematics: results of experimental clay models. J. Struct. Geol. 22, 1491–1509.
Crider, J.G., Pollard, D.D., 1998. Fault linkage: three-dimensional mechanical interaction between echelon normal faults. J. Geophys. Res. 103, 675–692.
Deng, C., Gawthorpe, R.L., Finch, E., Fossen, H., 2017. Influence of a pre-existing basement weakness on normal fault growth during oblique extension: insights from discrete element modeling. J. Struct. Geol. 105, 44–61.
Ezquerro, L., Lafuente, P., Pesquero, M.D., Alcalá, L., Arlegui, L.E., Liesa, C.L., Luque, L., Rodríguez-Pascua, M.A., Simón, J.L., 2012. Una cubeta endorreica residual Plio-pleistocena en la zona de relevo entre las fallas de Concud y Teruel: implicaciones paleogeográficas. Rev. Soc. Geol. Espana 25, 157–175.
Ezquerro, L., 2017. El sector norte de la cuenca neógena de Teruel: tectónica, clima y sedimentación. Ph.D. thesis. Universidad de Zaragoza.
Ferrill, D.A., Morris, A.P., 2001. Displacement gradient and deformation in normal fault systems. J. Struct. Geol. 23, 619–638.
Finzi, Y., Langer, S., 2012. Damage in step-overs may enable large cascading earthquakes. Geophys. Res. Lett. 39, L16303. https://doi.org/10.1029/2012GL052436.
Fossen, H., Rotevatn, A., 2016. Fault linkage and relay structures in extensional settings - a review. Earth Sci. Rev. 154, 14–28.
Fossen, H., Johansen, T.E.S., Hesthammer, J., Rotevatn, A., 2005. Fault interaction in porous sandstone and implications for reservoir management; examples from Southern Utah. Bull. Am. Assoc. Pet. Geol. 89, 1593–1606.
García-Lacosta, A.I., Pueyo, Ó., Arlegui, L.E., Liesa, C.L., Ezquerro, L., Simón, J.L., 2014. La zona de falla reciente de Sierra Palomera (fosa del Jiloca, Cordillera Ibérica): contribución de la geofísica a la caracterización estructural. In: 2ª Reunión Ibérica sobre Fallas Activas y Paleosismología, pp. 51–54. Lorca.
Gawthorpe, R., Hurst, J.M., 1993. Transfer zones in extensional basins: their structural style and influence on drainage development and stratigraphy. J. Geol. Soc. 150, 1137–1152.
Gawthorpe, R., Leeder, M.R., 2000. Tectono-sedimentary evolution of active extensional basins. Basin Res. 12, 195–218.
Gawthorpe, R.L., Jackson, C.A.L., Young, M.J., Sharp, I.R., Moustafa, A.R., Leppard, C. W., 2003. Normal fault growth, displacement localisation and the evolution of normal fault populations: the Hammam Faraun fault block, Suez rift, Egypt. J. Struct. Geol. 25, 883–895.
Gibbs, A.D., 1984. Structural evolution of extensional basin margins. J. Geol. Soc. 141, 609–620.
Gibbs, A.D., 1990. Linked fault families in basin formation. J. Struct. Geol. 12, 795–803.
Godoy, A., Moissenet, E., Ramírez, J.I., Olivé, A., Aznar, J.M., Jerez, L., Aragonés, E., Aguilar, M.J., Ramírez del Pozo, J., Leal, M.C., Adrover, R., Alberdi, M.T., Giner, J., Gutiérrez, M., Portero, J.M., Gabaldón, V., 1983. Mapa Geológico de España 1: 50.000. Instituto Geológico y Minero, Madrid. Hoja 542 (Alfambra).
Godoy, A., Ramírez, J.I., Olivé, A., Moissenet, E., Aznar, J.M., Aragonés, E., Aguilar, M.J., Ramírez del Pozo, J., Leal, M.C., Jerez Mir, L., Adrover, R., Goy, A., Comas, M.J., Alberdi, M.T., Giner, J., Gutiérrez Elorza, M., Portero, J.M., Gabaldón, V., 1983. Mapa Geológico de España 1: 50.000. Instituto Geológico y Minero, Madrid. Hoja 567 (Teruel).
Gutiérrez, F., Gutiérrez, M., Gracia, F.J., McCalpin, J.P., Lucha, P., Guerrero, J., 2008. Plio-Quaternary extensional seismotectonics and drainage network development in the central sector of the Iberian Chain (NE Spain). Geomorphology 102, 21–42.
Gutiérrez, M., Peña, J.L., 1976. Glacis y terrazas en el curso medio del río Alfambra (provincia de Teruel). Bol. Geol. Min. 87, 561–570.
Gutiérrez, M., Peña, J.L., Simón, J.L., 1983. Los valles tectónicos recientes de Rubielos de la Cérida (Teruel). Cuad. do Lab. Xeoloxico Laxe 5, 449–459.
Gupta, A., Scholz, C.H., 2000. A model of normal fault interaction based on observations and theory. J. Struct. Geol. 22, 865–879.
Hernández, A., Olivé, A., Moissenet, E., Pardo, G., Villena, J., Portero, J.M., Gutiérrez, M., Puigdefábregas, C., Giner, J., Aguilar, M.J., Leal, M.C., Gutiérrez, J.C., Gil, M.D., Adrover, R., Gabaldón, V., 1983. Mapa Geológico de España 1: 50.000. Instituto Geológico y Minero, Madrid hoja 491 (Calamocha).
Hernández, A., Ramírez, J.I., Olivé, A., Riba, O., Aragonés, E., Aguilar, M.J., Ramírez del Pozo, J., Leal, M.C., Giner, J., Gutiérrez, M., Goy, A., Comas, M.J., Gutiérrez, J.L., Portero, J.M., Gabaldón, V., 1983. Mapa Geológico de España 1: 50.000. Instituto Geológico y Minero, Madrid hoja 566 (Cella).
Herraiz, M., De Vicente, G., Lindo-Ñaupari, R., Giner, J., Simón, J.L., González-Casado, J. M., Vadillo, O., Rodríguez-Pascua, M.A., Cicuéndez, J.L., Casas, A., Cabañas, L., Rincón, P., Cortés, A.L., Ramírez, M., Lucini, M., 2000. The recent (upper Miocene to Quaternary) and present tectonic stress distributions in the Iberian Peninsula. Tectonics 19, 762–786.
Hubbert, M.K., 1937. Theory of scale models as applied to the study of geologic structures. Bull. Geol. Soc. Am. 48, 1459–1519.
Huggins, P., Watterson, J., Walsh, J.J., Childs, C., 1995. Relay zone geometry and displacement transfer between normal faults recorded in coal-mine plans. J. Struct. Geol. 17, 1741–1755.
Hus, R., Acocella, V., Funiciello, R., De Batist, M., 2005. Sandbox models of relay ramp structure and evolution. J. Struct. Geol. 27, 459–473.
Instituto Geográfico Nacional, 2019. Servicio de Información Sísmica del Instituto Geográfico Nacional. https://www.ign.es/web/ign/portal/sis-catalogo-terremotos.
Kattenhorn, S.A., Aydin, A., Pollard, D.D., 2000. Joints at high angles to normal fault strike: an explanation using 3-D numerical models of fault-perturbed stress fields. J. Struct. Geol. 22, 1–23.
Klinkmüller, M., Schreurs, G., Rosenau, M., Kemnitz, H., 2016. Properties of granular analogue materials: a community wide survey. Tectonophysics 684, 23–38.
Koyi, H., 1988. Experimental modelling of role of gravity and lateral shortening in Zagros mountain Belt. Am. Assoc. Petrol. Geol. Bull. 72, 1381–1394.
Krantz, R.W., 1991. Measurements of friction coefficients and cohesion for faulting and fault reactivation in laboratory models using sand and sand mixtures. Tectonophysics 188, 203–207.
Lafuente, P., Arlegui, L.E., Casado, I., Ezquerro, L., Liesa, C.L., Pueyo, O., Simón, J.L., 2011. Geometría y cinemática de la zona de relevo entre las fallas neógeno-cuaternarias de Concud y Teruel (Cordillera Ibérica). Rev. la Soc. Geol. España 24, 109–125.
Lafuente, P., Arlegui, L.E., Liesa, C.L., Pueyo, O., Simon, J.L., 2014. Spatial and temporal variation of paleoseismic activity at an intraplate, historically quiescent structure: the Concud Fault (Iberian Chain, Spain). Tectonophysics 632, 167–187.
Le Calvez, J.H., Vendeville, B.C., 2002. Experimental designs to model along-strike fault interaction. J. Virtual Explor. 7, 1–17.
Liesa, C.L., Simón, J.L., Ezquerro, L., Arlegui, L.E., Luzón, A., 2019. Stress evolution and structural inheritance controlling an intracontinental extensional basin: the central-northern sector of the Neogene Teruel Basin. J. Struct. Geol. 118, 362–376.

Machette, M.N., Personius, S.F., Nelson, A.R., 1991. The Wasatch fault zone Utah: segmentation and history of Holocene earthquakes. J. Struct. Geol. 13, 137–150.
Mandl, G., De-Jong, L.N.J., Maltha, A., 1977. Shear zones in granular material; an experimental study of their structure and mechanical genesis. Rock Mech. 9, 95–144.
Manighetti, I., Zigone, D., Campillo, M., Cotton, F., 2009. Self-similarity of the largest-scale segmentation of the faults: implications for earthquake behavior. Earth Planet. Sci. Lett. 288, 370–381.
Mansfield, C., Cartwright, J., 2001. Fault growth by linkage: observations and implications from analogue models. J. Struct. Geol. 23, 745–763.
Martín, M., Canerot, J., Del Pan, T., Leyva, F., 1979. Mapa Geológico de España 1: 50.000. Instituto Geológico y Minero, Madrid hoja 517 (Argente).
Martín, M., Canerot, J., Linares-Rivas, A., Grambast, L., Quintero, I., Mansilla, H., De las Heras, A., Fernández, M.C., Leyva, F., Martínez, J.U., 1977. Mapa Geológico de España 1: 50.000. Instituto Geológico y Minero, Madrid hoja 492 (Segura de los Baños).
Martín-Bello, L., Arlegui, L.E., Ezquerro, L., Liesa, C.L., Simón, J.L., 2014. La falla de Calamocha (fosa del Jiloca, Cordillera Ibérica): estructura y actividad pleistocena. In: 2ª Reunión Ibérica sobre Fallas Activas y Paleosismología, pp. 55–58. Lorca.
Moissenet, E., 1985. Les dépressions tarditectoniques des Chaînes Ibériques méridionales: distension, diapirisme et dépôts associés. Compte Rendus de l'Academie du Sciences de Paris 11, 523–528.
Moissenet, E., 1993. L'age et les déformations des terrases alluviales du Fossé de Teruel. In: El. Cuaternario de España y Portugal, vol. I. Instituto Geológico y Minero de España-AEQUA, Madrid, pp. 267–279.
Morley, C.K., Wonganan, N., 2000. Normal fault displacement characteristics, with particular reference to synthetic transfer zones, Mae Moh mine, northern Thailand. Basin Res. 12, 307–327.
Moustafa, A.R., Khalil, S.M., 2016. Control of extensional transfer zones on syntectonic and post-tectonic sedimentation: implications for hydrocarbon exploration. J. Geol. Soc. 174 (2), 318–335.
Nicol, A., Walsh, J., Berryman, K., Nodder, S., 2005. Growth of a normal fault by the accumulation of slip over millions of years. J. Struct. Geol. 27, 327–342.
Nixon, C.W., Vaagan, S., Sanderson, D.J., Gawthorpe, R.L., 2019. Spatial distribution of damage and strain within a normal fault relay at Kilve, UK. J. Struct. Geol. 118, 194–209.
Olivé, A., Hernández, A., Moissenet, E., Pardo, G., Villena, J., Gutiérrez, M., Puigdefábregas, C., Giner, J., Aguilar, M.J., Leal, M.C., Goy, A., Comas, M.J., Adrover, R., Portero, J.M., Gabaldón, V., 1983. Mapa Geológico de España 1: 50.000. Instituto Geológico y Minero, Madrid hoja 516 (Monreal del Campo).
Panien, M., Schreurs, G., Pfiffner, A., 2006. Mechanical behaviour of granular materials used in analogue modelling: insights from grain characterization, ring-shear tests and analogue experiments. J. Struct. Geol. 28, 1710–1724.
Peacock, D.C.P., 2002. Propagation, interaction and linkage in normal fault systems. Earth Sci. Rev. 58, 121–142.
Peacock, D.C.P., Sanderson, D.J., 1991. Displacements, segment linkage and relay ramps in normal fault zones. J. Struct. Geol. 13, 721–733.
Peacock, D.C.P., Sanderson, D.J., 1994. Geometry and development of relay ramps in normal fault systems. Bull. Am. Assoc. Pet. Geol. 78, 147–165.
Peiro, A., Simón, J.L., Liesa, C.L., 2017. New evidence of recent fracturing at the relay zone between the Concud and Teruel faults (eastern Iberian Chain). Geogaceta 62, 31–34.
Peiro, A., Simón, J.L., Román-Berdiel, T., 2019. Zonas de relevo de falla en el margen oriental de la Fosa del Jiloca (Cordillera Ibérica): geometría, cinemática y modelización analógica. Bol. Geol. Min. 3 (in press).
Peña, J.L., 1981. Las acumulaciones cuaternarias de la confluencia de los ríos Alfambra y Guadalaviar, en las cercanías de Teruel. Actas VII Coloquio de Geografía, Pamplona, pp. 255–259.
Peña, J.L., Gutiérrez, M., Ibáñez, M.J., Lozano, M.V., Rodríguez, J., Sánchez, M., Simón, J.L., Soriano, M.A., Yetano, L.M., 1984. Geomorfología de la provincia de Teruel. Instituto de Estudios Turolenses, Teruel.
Ramberg, H., 1981. Gravity, Deformation and the Earth's Crust in Theory, Experiments and Geological Applications. Academic Press, London.
Ramírez, J.I., Olivé, A., Moissenet, E., Aragonés, E., Ramírez, J., Leal, M.C., Aguilar, M.J., Adrover, R., Giner, J., Gutiérrez, J.C., Goy, A., Comas, M.J., Portero, J.M., Gabaldón, V., 1983. Mapa Geológico de España 1: 50.000. Instituto Geológico y Minero, Madrid hoja 541 (Santa Eulalia).
Ramsay, J.G., Huber, M.I., 1987. The Techniques of Modern Structural Geology, Vol. 2: Folds and Fractures. Academic Press, London, pp. 309–700.
Roca, E., Guimerá, J., 1992. The Neogene structure of the eastern Iberian margin: structural constraints on the crustal evolution of the Valencia trough (western Mediterranean). Tectonophysics 203, 203–218.
Román-Berdiel, T., Casas, A.M., Pueyo, E.L., Peiro, A., Soto, R., Pohlenz, A., Warsitzka, M., Rosenau, M., 2019. Ring Shear Test Data of Quartz Sand and Colored Quartz Sand Used for Analogue Experiments in the Analogue Modelling Laboratory of the University of Zaragoza. GFZ Data Services. https://doi.org/10.5880/fidgeo.2019.025. Spain (EPOS TNA call 2017).
Rotevatn, A., Fossen, H., Hesthammer, J., 2007. Are relay ramps conduits for fluid flow? Structural analysis of a relay ramp in Arches National Park, Utah. Geological Society of London 270, 55–71. Special Publications.
Rubio, J.C., Simón, J.L., 2007. Tectonic subsidence vs. Erosional lowering in a controversial intramontane depression: the Jiloca Basin (Iberian Chain, Spain). Geol. Mag. 144, 1–15.
Rudolf, M., Boutelier, D., Rosenau, M., Schreurs, G., Oncken, O., 2016. Rheological benchmark of silicone oils used for analog modeling of short- and long-term lithospheric deformation. Tectonophysics 684, 12–22.
Sánchez Fabre, M., 1989. Estudio geomorfológico de la Depresión de Alfambra-Teruel-Landete y sus rebordes montañosos. Ph.D. thesis. Universidad de Zaragoza.
Schellart, W.P., 2000. Shear test results for cohesion and friction coefficients for different granular materials: scaling implications for their usage in analogue modelling. Tectonophysics 324, 1–16.
Simón, J.L., 1982. Compresión y distensión alpinas en la Cadena Ibérica Oriental. Ph.D. thesis. Universidad de Zaragoza.
Simón, J.L., 1983. Tectónica y neotectónica del sistema de fosas de Teruel. Teruel 69, 21–97.
Simón, J.L., 1989. Late cenozoic stress field and fracturing in the iberian Chain and ebro basin (Spain). J. Struct. Geol. 11, 285–294.
Simón, J.L., Arlegui, L., Liesa, C.L., 2008. Stress partioning: a practical concept for analysing boundary conditions of brittle deformation. Geodin. Acta 53, 1057–1065.
Simón, J.L., Arlegui, L., Lafuente, P., Liesa, C.L., 2012. Active extensional faults in the central-eastern Iberian Chain, Spain. J. Iber. Geol. 38, 127–144.
Simón, J.L., Arlegui, L.E., Ezquerro, L., Lafuente, P., Liesa, C.L., Luzón, A., 2016. Enhaced paleoseismic succession at the Concud Fault (Iberian Chain, Spain): new insights for seismic hazard assessment. Nat. Hazards 80, 1967–1993.
Simón, J.L., Arlegui, L.E., Ezquerro, L., Lafuente, P., Liesa, C.L., Luzón, A., 2017. Structure and paleoseismology of the Teruel fault: dynamic interaction and strain partitioning with the Concud fault (eastern iberian Chain, Spain). J. Struct. Geol. 103, 100–119.
Simón, J.L., Serón, F.J., Casas, A.M., 1988. Stress deflection and fracture development in a multidirectional extension regime. Mathematical and experimental approach with field examples. Ann. Tect. 2, 21–32.
Trudgill, B., Cartwright, J., 1994. Relay-ramp forms and normal-fault linkages, canyonlands national park, Utah. Bull. Geol. Soc. Am. 106, 1143–1157.
Walsh, J.J., Watterson, J., 1991. Geometric and kinematic coherence and scale effects in normal fault systems. In: Roberts, A.M., Yielding, G., Freeman, B. (Eds.), The Geometry of Normal Faults. Geological Society Special Publication, pp. 193–203. No 56.
Walsh, J.J., Watterson, J., Bailey, W.R., Childs, C., 1999. Fault relays, bends and branch-lines. J. Struct. Geol. 21, 1019–1026.
Weijermars, R., Schmeling, H., 1986. Scaling of Newtonian and non-Newtonian fluid dynamics without inertia for quantitative modelling of rock flow due to gravity (including the concept of rheological similarity). Phys. Earth Planet. Inter. 43, 316–330.
Willemse, E.J.M., 1997. Segmented normal faults: correspondence between three-dimensional mechanical models and field data. J. Geophys. Res. 1902, 675–692.
Younes, A.I., McClay, K.R., 2002. Development of accommodation zones in the gulf of suez-red sea rift, Egypt. AAPG (Am. Assoc. Pet. Geol.) Bull. 86, 1007–1010.
Young, M.J., Gawthorpe, R.L., Hardy, S., 2001. Growth and linkage of a segmented normal fault zone; the late jurassic murchison-statfjord north fault, northern north sea. J. Struct. Geol. 23, 1933–1952.

2. Zonas de relevo entre las fallas que limitan la cuenca de Calatayud

Existen zonas de relevo reconocibles entre los segmentos de falla de Río Grío-Lanzuela (RLFS) y Cucalón-Pancrudo (CPFS), en el margen este de la cuenca de Calatayud, así como entre el semigraben de Munébrega y el de Gallocanta o entre la falla de Daroca y la de Calamocha, todas ellas en el margen oeste de la cuenca (Fig. 1.2). Estas zonas de relevo presentan dos características comunes: producen escalonamientos diestros de las fallas que las limitan, y suaves rampas de relevo que basculan los materiales y las superficies de erosión. Los patrones de fracturación reciente de estas áreas, y por tanto de interacción entre las fallas, no han podido ser objeto de estudio debido a la falta de afloramientos de depósitos Neógenos y Cuaternarios. Tampoco se han identificado lineaciones superficiales que pudieran corresponder a rupturas menores.

En el caso de la RLFS y la CPFS, sus gráficos salto vs. distancia (*throw* vs. *Distance* o *T-D*; obtenido a partir del estudio de la deformación del marcador morfotectónico SEF3; Fig 2.15) muestran una geometría irregular. En Su zona de relevo, las curvas individualizadas de ambas fallas muestran una marcada asimetría que indica que ambas están interactuando y transfiriendo desplazamiento a través de dicha zona de relevo (e.g., Peacock y Sanderson, 1994; Gawthorpe y Leeder, 2000). Esta transferencia podría ser a través de la misma rampa de relevo, de la cual se tiene constancia, o de fracturas menores presentes en ella, no identificadas por el momento. El brusco descenso del desplazamiento de la CPFS en las cercanías del pueblo de Barrachina se ha identificado como una zona de relevo ya fracturada que habría llegado a unir dos sectores de la CPFS (e.g., Peacock y Sanderson, 1994; Gawthorpe y Leeder, 2000).

En general, se trata de zonas de relevo de poca extensión: entre la RLFS y CPFS el espaciado es de ≈ 2,5 km, sin apenas solapamiento; en la misma falla de Munébrega, y entre ésta y la de Gallocanta, tanto el espaciado como el solapamiento son de ≈ 1 km; entre las fallas de Daroca y Calamocha hay ≈ 2 km de espaciado y ≈ 4 km de solapamiento. Las zonas de relevo de estas dimensiones no supondrían una barrera para la propagación de las rupturas en el caso de que se produjera un terremoto (Biasi and Wesnousky, 2016). Asimismo, sus rampas de relevo indican cierta interacción de tipo *soft linkage* entre las fallas que las limitan; serían estructuras no completamente independientes pero lejos aún de la coalescencia, de manera similar a las otras zonas de relevo de la fosa del Jiloca y Teruel ya estudiadas (Lafuente *et al*., 2011; Peiro *et al*., 2017; Peiro *et al*., 2020).

3. Present-day evidence of incipient fault propagation from instrumental seismicity: the case of the relay zone between the Concud and Sierra Palomera faults

3.1. Introduction

After structural and modelling approaches, Peiro *et al*. (2020) state that distributed along-strike fracture systems in extensional fault relay zones, like the one between the Concud and Sierra Palomera faults, can reveal that rupture propagation is not chiefly controlled by 'internal' kinematics (elongation along the relay ramp, that would mostly lead to transverse ruptures), but determined by 'external' controls (structural heritage and the remote stress field).

In addition to these approaches, further evidence of distributed longitudinal fractures affecting that fault relay zone comes from seismic data. The latter have been provided by the National Seismic Network of Instituto Geográfico Nacional (IGN) and complemented with those delivered by the new seismometer installed in Celadas (north of the Concud fault). Seismic data have therefore been compiled and analysed in order to test the validity of the proposed evolutionary model and to stablish the fault propagation patterns. These patterns are key for assessing seismogenic potential of fault zones, since they determine the effective area of coseismic rupture for a given fault or fault segment.

3.2. Methodology of seismic analysis

Conventional seismic database (National Seismic Network)

The National Seismic Network of IGN is the organization responsible for seismic monitoring in Spain and neighbouring areas. In the first half of the 20th century, it started to perform this task by compiling the information of its geophysical observatories and the ones belonging to other institutions. In 1985, the germ of the Spanish Seismic Network was created, with eight seismic stations connected to the IGN central office. Since then, the number of stations has been increasing progressively. A qualitative leap was taken in 1999, when digital broadband seismometers were incorporated and the network started to conform to its current configuration. Since 1997, hypocentral locations are performed by LocSAT (Bratt and Naggy, 1991), although its implementation slightly changed in 2016, when SeisComP3 (GFZ and GEMPA GmbH, 2008) was adopted as earthquake monitoring system. The seismic catalogue and bulletins are made using all the available information from the IGN network and the networks of other institutions. The information from other networks has been gathered in the format of seismic arrival parametric data before 2016, and as continuous waveforms since this year. Currently, more than 150 seismic stations in the Iberian Peninsula are used to create the Spanish seismic catalogue. The station density of this whole virtual network is not homogeneous, since it is higher in the areas with higher seismic hazard (i.e., south and south-east of the Iberian Peninsula and Pyrenees). This allows detecting lower magnitude earthquakes with lower location uncertainties in these areas. By introducing LocSAT, in the second half of 1997, location uncertainty in the seismic bulletins is defined by a 90% epicentral confidence ellipse (with a semi-major and a semi-minor axis; sMajAx and sMinAx) and a 90% depth confidence interval (sDepth).

The new seismometer of Celadas

The eastern Iberian Chain has been traditionally considered an area of low seismic hazard, although several of its faults have undergone activity during Late Pleistocene-Holocene times, like the Daroca, Concud or Teruel faults. This was the main motivation to install a new seismic station, that could contribute to increase the low seismic station density of this area. The relay zone between the Concud and Sierra Palomera faults (Fig. 1.2) seemed to gather a high number of events during the years previous to its installation, so it was chosen for this purpose. The new seismic station (E0901) was provisionally installed on 13/07/2017 in a site 2 km far from Celadas village (Teruel; Fig. 7.16a), with coordinates: 40º 28' 50'' N, 1º 07' 41''W. The station lied on the floor of a small hermitage built in solid rough ashlar stone (7.16b,c). This is a low inhabited area (around 400 people) located less than 10 km north of the Concud fault trace (Fig. 1.2), and more than 60 km to the closest seismic station. The station was equipped with a Guralp CMG-6TD three-component digital broadband (0.03 Hz – 100 Hz) seismometer and replaced on 2018-10-18 by a Nanometrics Trillium Compact three-component broadband (0.0083 Hz – 100 Hz) sensor and a Nanometrics Centaur digital recorder. The availability of data from 13/07/2017 to 22/06/2022 is 93.3%.

Data processing – graphical representation

A general characterization of the spatial-temporal evolution of the seismicity has been performed. The region considered for this analysis is restricted between 40.28ºN and 40.68ºN in latitude, and between -1.53ºW and -0.73ºW in longitude, and to temporal period ranging from the 1st of January 2000 to the 25th of May 2022. The total number of events used in this analysis is 171. Calculations have been performed by using the Zmap7 software package (Wiemer, 2001).

On the one hand, the frequency–magnitude earthquake distribution of this catalogue was analysed by means of the Gutenberg–Richter law (Gutenberg and Richter, 1944). To estimate the GR parameters (a, b) the maximum-likelihood approach (Aki, 1965) has been used (Fig. 7.17).

For this kind of seismicity-based studies, assessment of the magnitude of completeness of the seismic record (Mc) is essential. Mc can be defined as the lowest magnitude (Mw) at which 100% of the events in a space-time volume are detected (Rydelek and Sacks, 1989). In this study, Mc value has been estimated with the maximum curvature method (Wiemer and Wyss, 2000), a fast and simple way to calculated Mc that is implemented in the Zmap7

software (Wiemer, 2001). According to this method, Mc corresponds to the point of maximum curvature by computing the maximum value of the first derivative of the frequency-magnitude curve (Mignan and Woessner, 2012). This means that Mc matches the magnitude with the highest frequency of events in the non-cumulative Frequency Magnitude Distribution or FMD. The seismic catalogue is considered to be complete when it considers the events with Mw>Mc. This means that a fraction of events with Mw≤Mc can have occurred and might be missed by the seismic network. For this reason, earthquakes with Mw below or equal to the Mc, estimated at 1.4 for this study (Fig. 7.17), have not been considered.

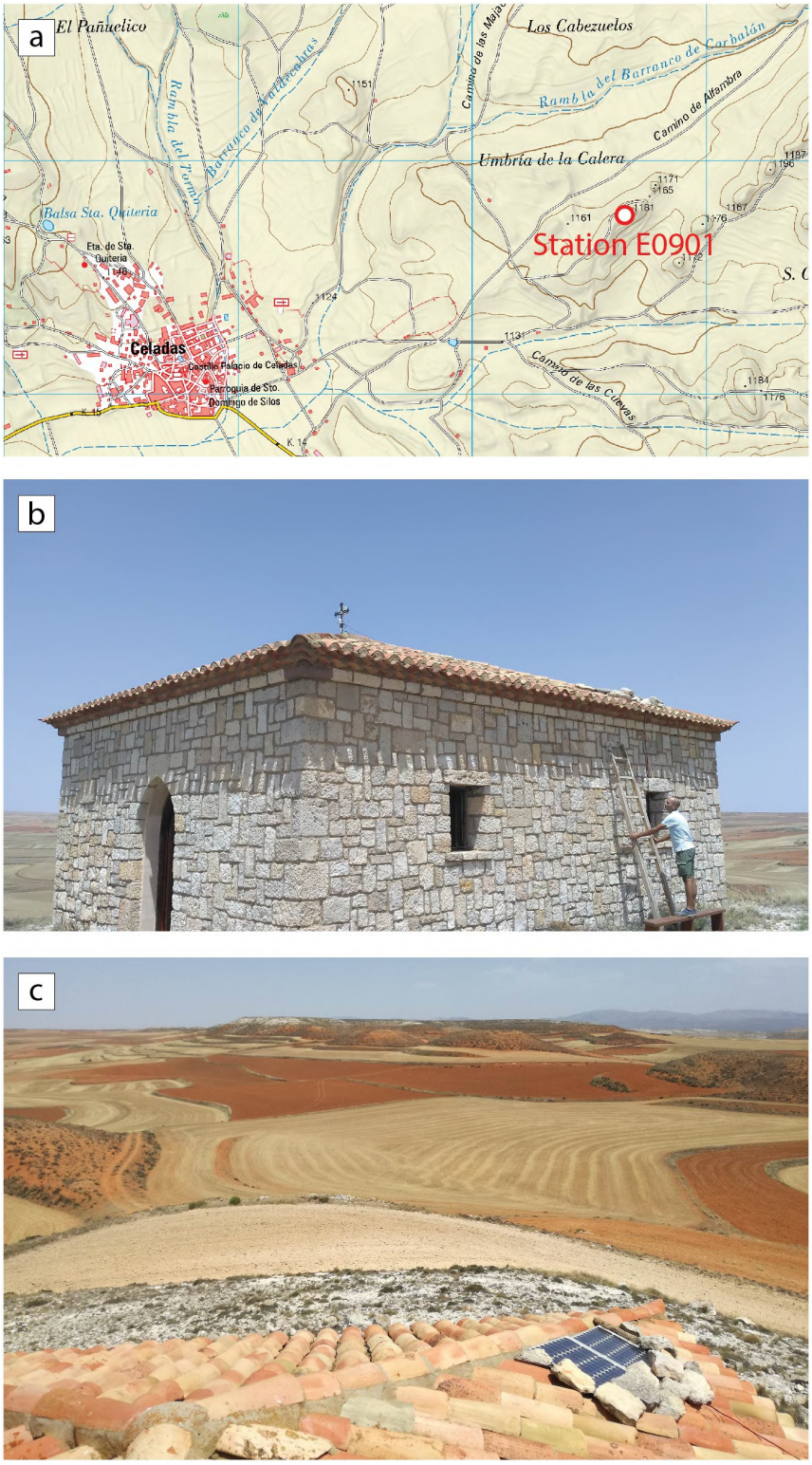

Fig. 7.16.- (a) Geographical location of the station E0901. See location in Figure 1.2. (b) Installation process.
(c) General view of the location; in the foreground: roof of the hermitage with a photovoltaic panel for supplying electricity to the equipment.

On the other hand, once the seismic catalogue has been filtered and considered as complete, the temporal evolution of the seismicity has been presented with the number of events and their magnitudes by date, as well as the cumulative number of events. Moreover, the cumulative seismic moment release has also been computed. The area used for building the cumulative rate and moment release graphics is the same as for the Gutenberg-Richter model.

In order to analyse the spatial distribution of the seismicity, location of hypocentres has been considered, taking into account their uncertainty ellipsoides with a 90% confidence level (represented by the semi major and minor axes, sMajAx, sMinAx, of the epicentral uncertainty elipses, and the depth uncertainty, sDepth). Using Geographic Information Systems (GIS), these hypocentral locations and their associated uncertainties have been translated into both a map based on DEM of the study area, and two profiles (N-S and E-W) that show their depths and associated uncertainties. Within the former, epicentral symbols are colour coded with depth, sized according the registered magnitude, and their associated uncertainty ellipses represented around each epicentre. The study area considered for this spatial analysis is more constrained in order to only encompass the southern sector of the Jiloca graben (latitude between 40.32ºN and 40.64ºN and longitude between -0.99ºW and -1.46ºW), where the relay zone between the Concud and Sierra Palomera is located.

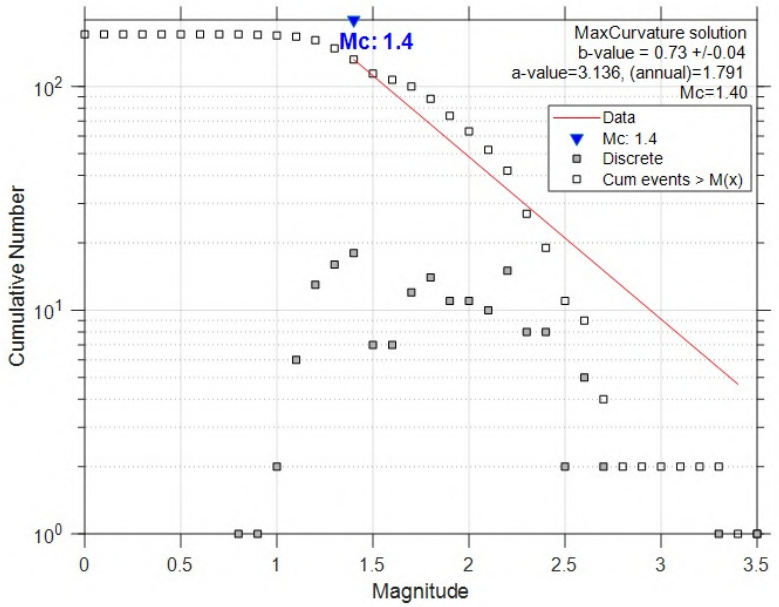

Fig. 7.17.- Gutenberg-Richter law for events from the IGN catalogue for the study area (40.28ºN, 40.68ºN; -0.73ºW, -1.53ºW). Grey squares represent the distribution of non-accumulated events while the white squares are the cumulative events. Mc=1.4 is shown.

Improvement in earthquake detectability due to the new E0901 station

In order to analyse the improvement that the Celadas station entails, two time periods of data from the seismic catalogue have been compared: a first one that ranges from 01/01/2000 to 13/07/2017, and a second one from 13/07/2017 to 30/05/2022. The area that has been firstly considered for this purpose is broader than the Iberian Chain (latitude between 39ºN and 42ºN and longitude between 4ºW and 1ºE), and in these cases the magnitude of completeness (Mc) is around 1.6 for both periods. Within this area, the catalogue has registered 3324 and 1303 events in the first and the second period, respectively, which means 190 and 267 events per year. Regarding the location uncertainty of these events, the average epicentral uncertainties sH (from sMajAx and sMinAx values) and sDepth of events with a Mw ≥ 2.0 have been computed for both periods, their spatial distributions being depicted in Fig. 7.18. When a more constrained area around E0910 station is considered (latitude between 40.28ºN and 40.68ºN and longitude between -1.53ºW and -0.73ºW), we find 125 and 46 events in the first and second periods, which means around 7 and 9 events per year, respectively.

In both cases the seismic network has been capable of locating more events per year since the installation of the E0901 station, and this increase in the number of events in the catalogue should respond to a higher earthquake detectability. Moreover, location of these events is now better constrained because their location uncertainties have clearly decreased in the second period with respect to the first one in the whole area and, more specifically, in the surroundings of the E0901 station (from 4-2.1 km, in the first period, Fig. 7.18a, to ≤3 km, in the second one, Fig. 7.18b). However, there is no visible improvement in their location in depth (Fig. 7.18c,d), probably because of the different implementation of LocSAT before and after 2016.

3.3. Seismological results

Within the period 2000-2022, 109 events with 1.4<Mw≤3.5 have occurred in the study area (40.32ºN, 40.64ºN; -0.99ºW, -1.46ºW) (Fig. 7.19a,b). Although there are 45 events with an unknown depth, the rest are located at depths that vary from ca. 2 to 20 km, being more frequent those located between 6 and 12 km. Almost half of the studied earthquakes, 54 from the total (23 of them with an unknown depth), occurred within the relay zone between the Concud and Sierra Palomera faults, at the footwall block of the Concud fault. Their epicentres define a N-S lineament that starts at the Concud fault trace, ca. 5 km far from its northern tip point, and spreads ca. 10 km to the north. It should be highlighted that the corresponding hypocentres are the deepest in the area, clustering around 4-6 and 8-12 km in depth, but also congregating some events at depths till 20 km.

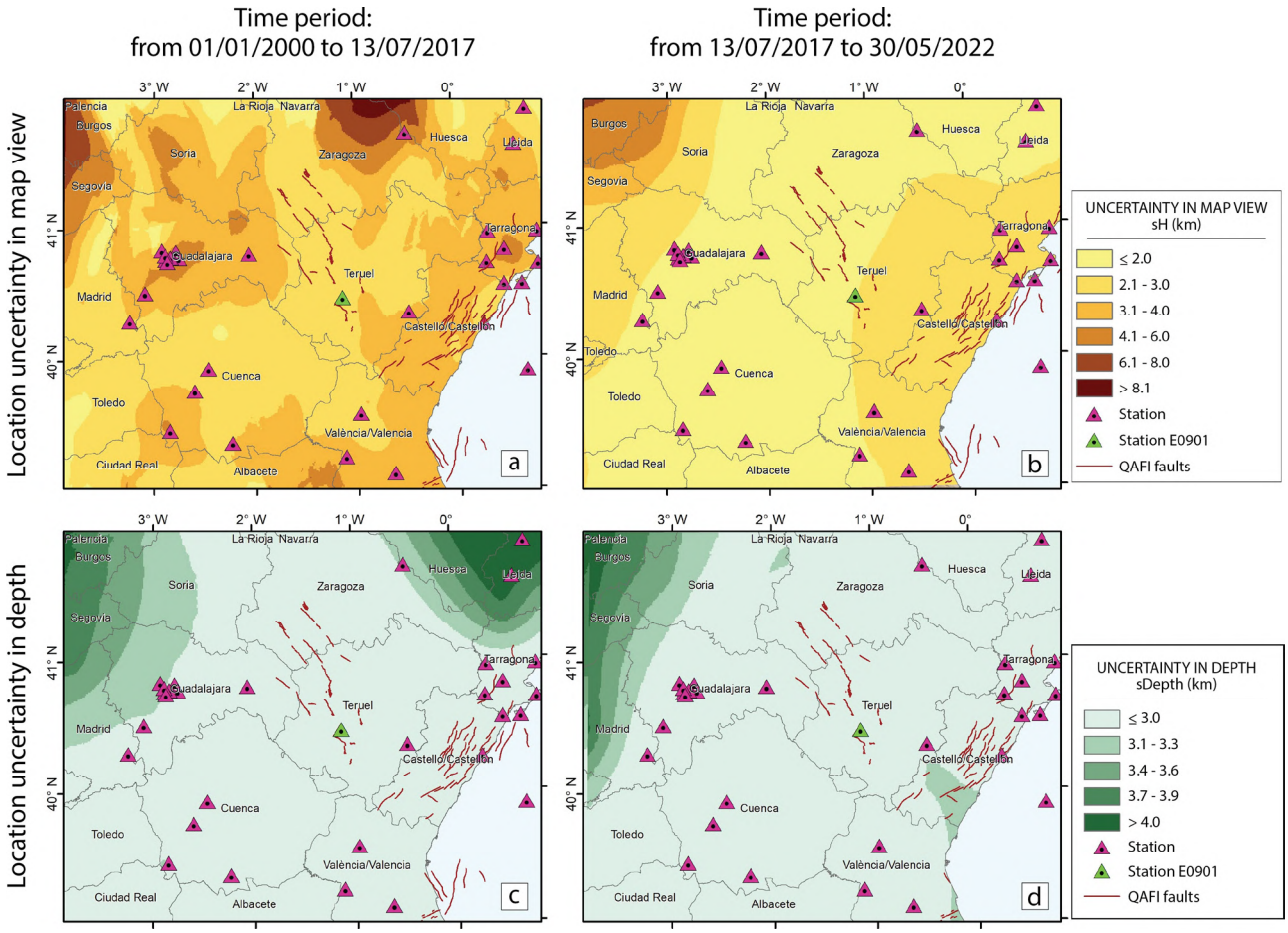

Fig. 7.18.- (a, b) Spatial distribution of location uncertainties in map view (sH) of epicentres of events with Mw ≥ 2.0 computed for the two studied periods. (c, d) Spatial distribution of location uncertainties in depth (sDepth) of epicentres of events with Mw ≥ 2.0 computed for the two studied periods. The main fault systems, the seismic stations network and, more specifically, station E0901, are shown.

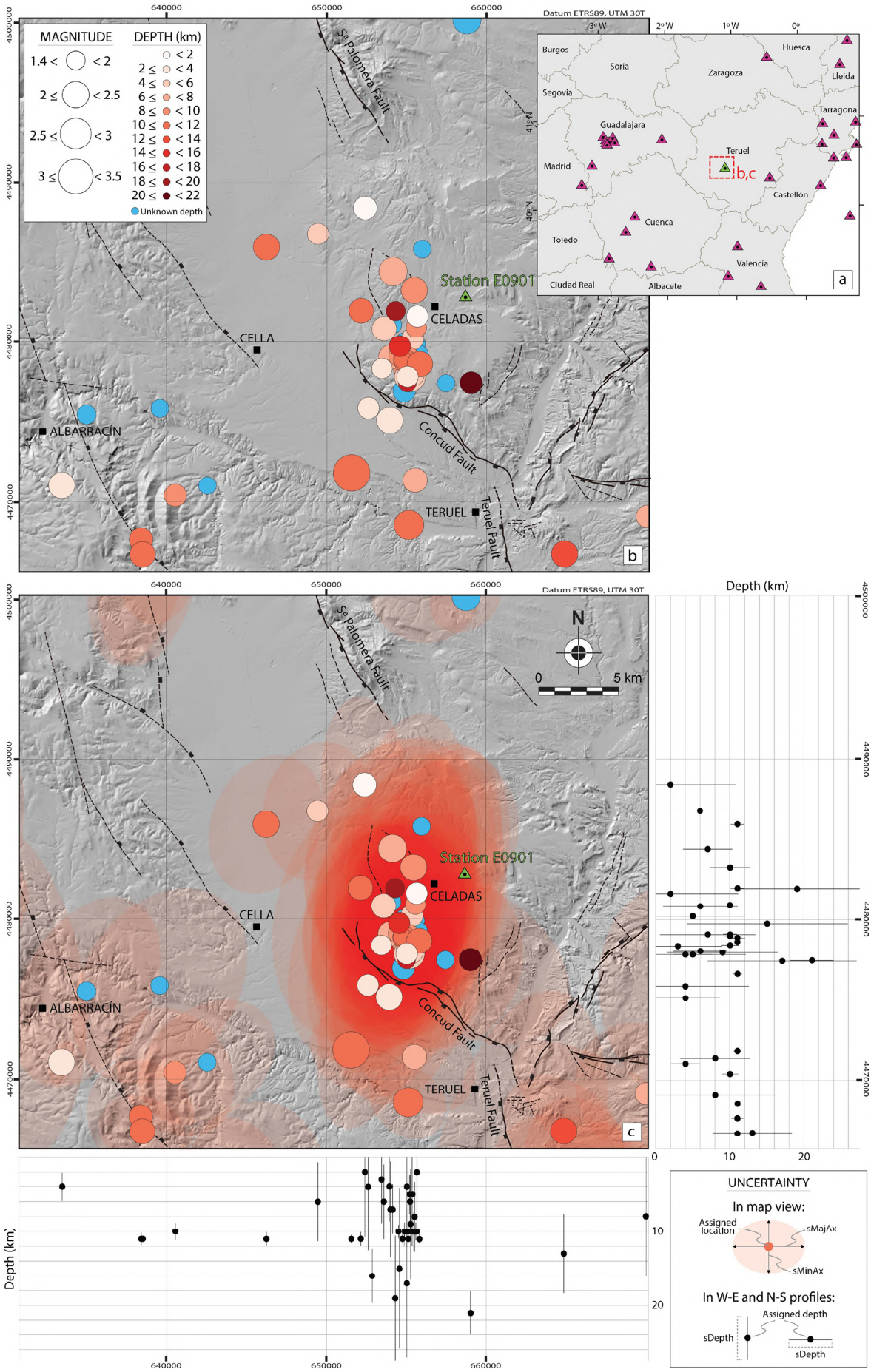

Fig. 7.19.- (a) Location of the seismic station E0901 within the seismic network of the northeastern Iberian Peninsula. (b) Epicentre map of instrumental earthquakes in the southern sector of the Jiloca Basin from the IGN catalogue (IGN, 2022), with different colours indicating the depth of hypocentres. (c) Uncertainties concerning those epicentres in map view and in depth. See location in Fig 1.2.

Location uncertainties within the study area do not detract from the inference of this lineament. Uncertainty ellipses define a striking tendency of sMajAx to be oriented N-S to NNE-SSW in the relay zone between the Concud and Sierra Palomera faults (Fig. 7.19c). Therefore, there is more confidence in locating the epicentres along this lineament, and are better constrained within it because of the striking tendency of sMinAx to trend E-W to WNW-ESE. Uncertainties in depth also corroborate that the deepest events are located in this area.

The assigned focal depths of the events within the relay zone are arranged in a vertical cluster clearly visible in the W-E profile (Fig. 7.19c). In general, they do not define a clear lineament that could be clearly interpreted as a single fault trace, but a subtle alignment can be recognised within this cluster (around coordinate X = 655000 in the W-E profile of Fig. 7.19c), compatible with a nearly vertical fault plane or highly dipping to the W.

Regarding the temporal distribution of the seismic activity, it seems to have had moderate increases in two time periods (Fig. 7.20a): 2005-2008 (segment 2 in Fig. 7.20b) and 2014-2022 (segments 4 and 5 in Fig. 7.20b). Within the latter, two different periods can be distinguished: one up to 2018, when the highest seismic activity occurred within the area of study, with a special increase in year 2016 (Fig. 7.20a; segment 4 in Fig. 7.20b), and another period until now, corresponding with a still increasing but less noticeable activity (segment 5 in Fig. 7.20b). These two main periods of higher amounts of events during time correlate well with two periods of higher seismic energy liberation (segments 2, 4 and 5 in Fig. 7.20c). In this context, two earthquakes are remarkable: one occurred 10 km to the WNW of Teruel city in 2003, with Mw = 3.5 (in 40.38,-1.21; with a depth of 11 km; Fig, 7.20b), and another one occurred 12 km to the E of Teruel city in 2017, with Mw = 3.3 (in 40.36,-0.96; with a depth of 12 km; Fig, 7.20b). Both of them generated the liberation of an especially high amount of energy (Fig, 7.20c).

3.4. Interpretation and discussion

Epicentres located within the relay zone between the Concud and Sierra Palomera faults are visibly gathered in a N-S trending cluster (Fig 7.19b). This arrangement suggests the presence of either a single fault or several distributed longitudinal ruptures, in both cases oriented according to that trend. No surficial rupture has been mapped within this sector of the footwall block of the Concud fault (Godoy *et al*., 1983a,b; Hernández *et al*., 1983c; Ramírez *et al*., 1983; Lafuente, 2011) that could be associated with this activity. Hypocentral distribution neither allows a precise definition of the fracture geometry, but its aspect in a W-E profile (Fig. 7.19c) suggests the occurrence of either a single, nearly vertical fault at depth or, more probably (due to their dispersion), a set of distributed ruptures.

These inferences fit the model of fault coalescence through relay zones defined by Peiro *et al*. (2020). The model shows relay zones transferring part of the displacement through relay ramps mostly cut by along-strike distributed faults and fractures. These ruptures propagate nearly parallel or at small angles to the master faults that enclose the relay zone, being mainly controlled by the current stress field (perpendicular to the σ_3 trajectories). In our case, the ENE-WSW to E-W regional σ_3 trajectories (Arlegui *et al*., 2005) are full compatible with the N–S fractures inferred from the seismic lineament of the Celadas sector. They are externally controlled fracture sets (they respond to the remote stress field), instead of being internally induced by the own relay kinematics, as commonly predicted in fault relay models in the literature (Peiro *et al*., 2020). The latter usually only consider ruptures that are transverse to the macrostructures.

In this way, the present-day seismic activity evidences how the same evolutionary pattern of fracture propagation is nowadays operating along the Concud-Sierra Palomera fault zone. Therefore, only inferences about fracturing geometry can be made; the possible temporal patterns (moderate increases in the seismic activity in 2005-2008 and 2014-2022; Fig. 7.20) imply no relevance for the regional framework, or at least an unknown relevance.

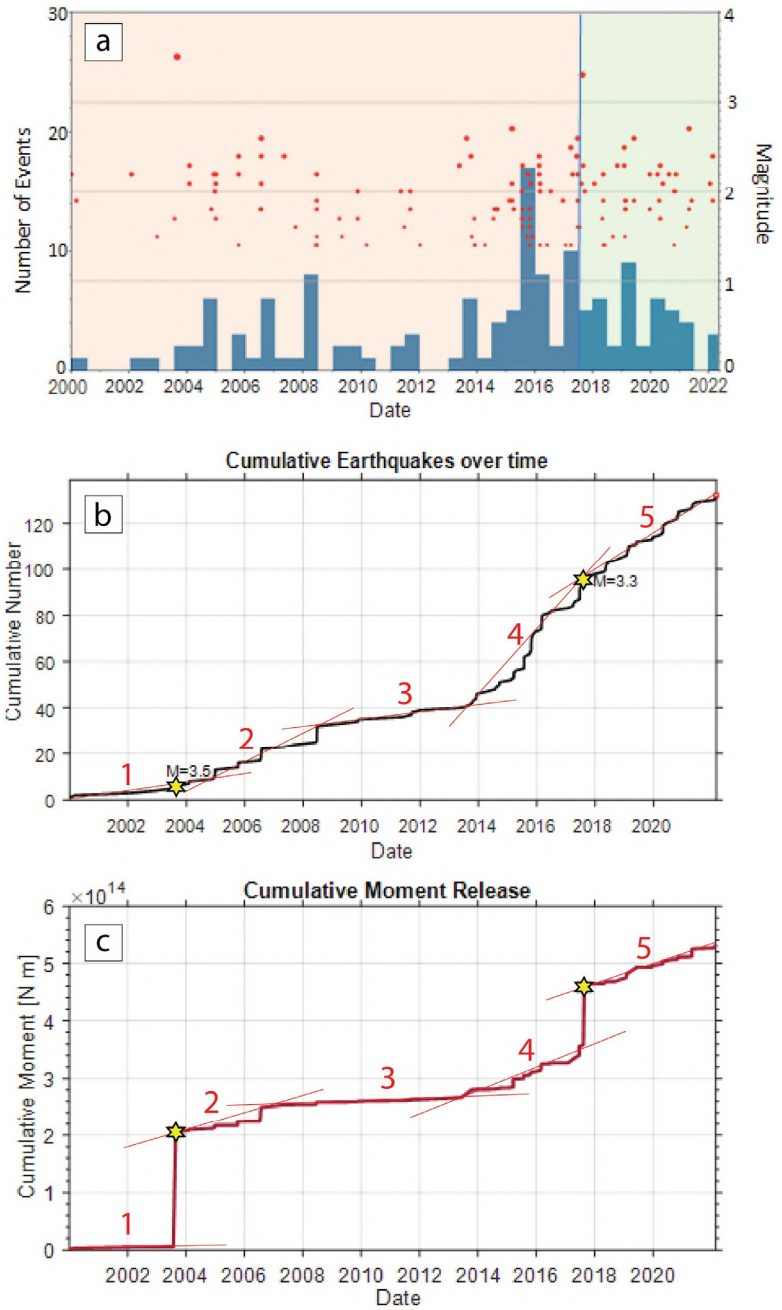

Fig. 7.20.- (a) Histogram of temporal evolution of events for the 2000-2022 time period (number of events (blue bars) and their magnitudes (red dots). Earthquakes recorded before and after the installation of the seismic station E0901 in 2017 are depicted on an orange and green background, respectively. (b) Cumulative number of events with M ≥ Mc. Segments 1-5 correspond to different graphic slopes and, therefore, changes in seismic activity. (c) Cumulative seismic moment release over time for events with M ≥ Mc. Segments 1-5 correspond to different graphic slopes.

VIII

CAPÍTULO VIII.
DISCUSIÓN

1. Evolución de la macroestructura y consideraciones sobre su cinemática

La evolución estructural de la Cordillera Ibérica centro-oriental está principalmente vinculada a la compresión de la Orogenia Alpina durante el Paleógeno, y a la extensión del *rifting* del Surco de Valencia desde el Mioceno hasta la actualidad (e.g. Álvaro *et al*., 1979; Capote *et al*., 2002; Simón, 1982; Roca y Guimerà, 1992; Fig. 1.1b). Con más o menos evidencias que puedan sustentarlo en cada caso, la mayoría de las fallas principales que controlan sus dominios estructurales probablemente representan la inversión tectónica negativa, ocurrida durante el régimen de extensión asociado al *rifting* del Surco de Valencia, principalmente en el Mioceno superior-Cuaternario, de estructuras previas variscas y alpinas tanto compresivas como transpresivas. Supondrían, por tanto, un posible ejemplo del control que ejerce la herencia estructural en la orientación de las estructuras extensionales recientes.

En el caso del primero de los segmentos de la **zona de falla extensional de Río Grío-Pancrudo**, el de Río Grío-Lanzuela, la falla transpresiva ya era fruto, a su vez, de la reactivación de parte del trazado del cabalgamiento de Nigüella-Monforte (Marcén y Román-Berdiel, 2015; Casas *et al*., 2016; Fig. 1.2). Durante este periodo, este segmento de falla presentó una componente de desgarre dextral, pero también con indicios sinestrales (Marcén y Román-Berdiel, 2015). Tras la reactivación como normales de, al menos, los sectores central y sur de este segmento de falla, después también del periodo regional de arrasamiento generalizado del relieve que da lugar a la *Superficie de Erosión Fundamental* (Peña *et al*., 1984), se produjo la deformación y desplazamiento de la SEF3 (Fig. 2.5), el basculamiento de su bloque hundido hacia el plano de falla y la consiguiente inversión del drenaje (Fig. 2.9). De su traza cartográfica se infiere una dirección cercana a N150ºE, corroborada después en el afloramiento de Codos, donde también se infiere un buzamiento de 67ºW (Fig. 2.7a,b) que se considera el buzamiento general de la zona de falla. En los estereogramas de la Figura 2.7d', b", se ven fracturas menores orientadas ca. 160,65W y flancos de pliegues de arrastre en torno a 135,60W, respectivamente, asociados a la falla principal. En todos ellos se han observado estrías con ángulos de cabeceo entre 75 y 90º. Un movimiento normal casi puro, con dirección de transporte media hacia N235ºE, se infiere de esos indicadores cinemáticos.

En el sector norte de la falla de Cucalón-Pancrudo, la falla transpresiva estaría relacionada con el sistema de cabalgamientos de las zonas de Lagueruela y Pelarda, de directriz oblicua en torno a NW-SE (Fig. 1.2). Si bien, la existencia de tal sistema de cabalgamientos no está bien documentada en la literatura previa, la hipótesis parece verosímil, dado el análisis de la cartografía y de afloramientos llevado a cabo en ese sector, y a su directriz acorde con la herencia estructural de toda la cadena (Figs. 2.11, 2.12). En los afloramientos de Lagueruela se ha medido una zona de cizalla con orientación 140,60W y una zona de relevo entre fallas orientadas ca. 170,80W, de las cuales se infieren unas direcciones de transporte de componente inversa hacia N357ºE y N312ºE (Fig. 2.11a,b,c,d). También se encuentran pliegues verticales asociados a la zona de cizalla principal con planos axiales orientados aproximadamente 145,50W (Fig. 2.11a,f,g,h). En la zona de Sierra Pelarda, el plano de cabalgamiento sur se dispone 124,38S. En definitiva, los indicadores cinemáticos analizados de los afloramientos de este sector apuntan hacia una componente sinestral inversa. En el sector sur de la falla de Cucalón-Pancrudo, la falla transpresiva está asociada al anticlinal de Alpeñés-Rillo (Tena y Casas, 1996), presentando estrías que corroboran un sentido de desplazamiento dextral (Guimerà, 1988), hasta su intersección con el cabalgamiento de Portalrubio (Guimerà *et al*., 1990; Simón y Liesa, 2011; Fig. 1.2). El pasado transpresivo del sector central de la falla de Cucalón-Pancrudo, desde aproximadamente el sur del pueblo de Olalla hasta el norte de Alpeñés, es el menos manifiesto ya que no existe una relación clara con estructuras heredadas. Se trata de una sucesión de rupturas alineadas, cuya continuidad en superficie no queda asegurada, posiblemente fruto de neoformación directamente durante el Plio-Cuaternario. Esto se evidencia en la deformación y desplazamiento que producen en la SEF3, y en los abanicos aluviales cuaternarios modelados en glacis que parten de su traza (Figs. 1.2, 2.13). La deformación de la SEF3 también es un rasgo característico de la inversión tectónica negativa de las estructuras alpinas localizadas en los sectores norte y sur de la falla de Cucalón-Pancrudo (Fig. 2.13). En el sector norte, la zona de falla extensional estudiada en la trinchera de Lagueruela está dispuesta en torno a 142,65W, y en el pueblo de Olalla cercana a 147,90 (Figs. 2.20,

2.21, 2.22). En este último también hay fracturas menores orientadas 175,60E y 167,85W. En el sector sur existen posibles evidencias de la continuidad de la falla con direcciones que oscilan entre N150ºE y N010ºE, pero la falta de depósitos recientes impide asegurar que se trate de rupturas asociadas a las últimas etapas (Fig. 2.22). La falta de indicadores cinemáticos en el segmento de falla de Cucalón-Pancrudo no ha permitido inferir una dirección de transporte media de toda la estructura extensional.

La reactivación extensional de la zona de falla de Río Grío-Pancrudo durante el Plio-Cuaternario es menos evidente en unos sectores que en otros, debido a la falta de marcadores de la deformación. Respecto al marcador morfotectónico de la SEF3 y, por lo tanto, a la deformación extensional post-3,5 Ma, está claro su desplazamiento desde Codos hasta Pancrudo. La envolvente que definen la curvas salto vs. distancia (*Throw* vs. *Distance* o *T-D*; obtenidas a partir del estudio de la deformación del marcador morfotectónico SEF3; Fig 2.15) de sus dos segmentos RLFS y CPFS se aproxima al de una media campana. En la zona de relevo de estos dos segmentos, las curvas muestran una marcada asimetría que se interpreta como fruto de la interacción entre ambos segmentos (Gawthorpe y Leeder, 2000; Fig. 8.1). En el RLFS, existen incertidumbres sobre la existencia de retazos de la SEF3 en el sector entre Nigüella y Tobed. Sin embargo, como acabamos de comentar, la geometría que define la curva individualizada de este segmento de falla desde Codos hasta Lanzuela es de una semicampana (Fig 2.15), lo que permite interpretar que, de existir retazos hacia el norte, éstos habrían registrado un desplazamiento tal que haría descender su curva, de manera más o menos progresiva, hacia Nigüella. Esto refuerza la idea de que ese sector también pudo haber sido reactivado extensionalmente post-3,5 Ma. En el CPFS, el desplazamiento de la SEF3 disminuye en los alrededores de Barrachina. Esto podría asociarse, de la manera más conservadora posible, a que directamente no hay desplazamiento de dicho marcador y la falla no se expresa en superficie, o más probablemente, a que existe poco desplazamiento debido a la reciente unión de dos segmentos de falla previos (Fig. 8.1). Respecto a los marcadores del tipo estratigráfico que pudieran registrar deformación extensional más reciente, éstos se encuentran en afloramientos puntuales y dispersos a lo largo de la traza de la zona de falla de Río Grío-Pancrudo. Ya hemos descrito depósitos del Pleistoceno superior afectados por la falla en Codos y en los sectores de Lagueruela-Olalla, así como depósitos holocenos en la trinchera de Lagueruela. De estos últimos se infiere que la rotura responsable de dicha deformación podría ser la equivalente al sector norte de la CPFS, aquel que va desde Cucalón hasta Barrachina. La reactivación extensional de la zona de falla de Río Grío-Pancrudo desde el Pleistoceno superior queda claramente evidenciada, por tanto, en ambos segmentos (RLFS y CPFS).

Respecto a las fallas que conforman el margen SW de la cuenca de Calatayud y su límite con la fosa del Jiloca, las **fallas de Munébrega, Daroca y Calamocha**, éstas también provendrían de la inversión negativa de un sistema de cabalgamientos alpinos durante la tercera etapa del régimen de extensión actual. En la primera de ellas hay evidencias en su sector sur, donde discurre paralelamente a una falla inversa que buza hacia el SW y que afecta a materiales paleozoicos y triásicos (Del Olmo *et al*., 1983a; Gutiérrez, 1998; Gutiérrez *et al*., 2008). De su plano de falla normal principal, el situado al W, sólo se conoce su dirección media (ca. N155ºE) pero es seguro que buza hacia el SW, mientras que el plano situado al E del anterior sí que se ha podido medir en un afloramiento y se orienta 155,70E (Gutiérrez *et al*., 2009; Fig. 5.1). Similar evolución se infiere para la zona de falla extensional de Daroca-Calamocha, la cual es resultado de la reactivación del cabalgamiento de Daroca (Colomer, 1987; Gracia, 1990, 1992; Gutiérrez *et al*., 2008, 2020a; Fig. 5.3) y de otras posibles estructuras contractivas previas que afloran en el sector NW de la falla de Calamocha (Corral, 2014; Liesa *et al*., 2021). En la literatura no se constata la presencia de indicadores cinemáticos que permitan obtener una dirección de transporte media de las fallas de Munébrega y Daroca. Para la falla de Calamocha, en cambio, sí que se describe en esta tesis la orientación de sus dos ramas de falla principales situadas más al oeste, la rama A y la B, en dos afloramientos en los que se orienta 160,70W (Fig. 3.11c) y 178,75W (Fig. 3.12d), respectivamente. Las estrías medidas en la primera de estas ramas indican un predominio del movimiento normal, con una dirección de transporte media hacia N234ºE (Fig. 3.11c).

Las evidencias de inversión tectónica negativa también son claras en la **falla de Sierra Palomera** (Rubio y Simón, 2007), ya que se observa que la falla discurre por el flanco casi vertical de un anticlinal vergente al este

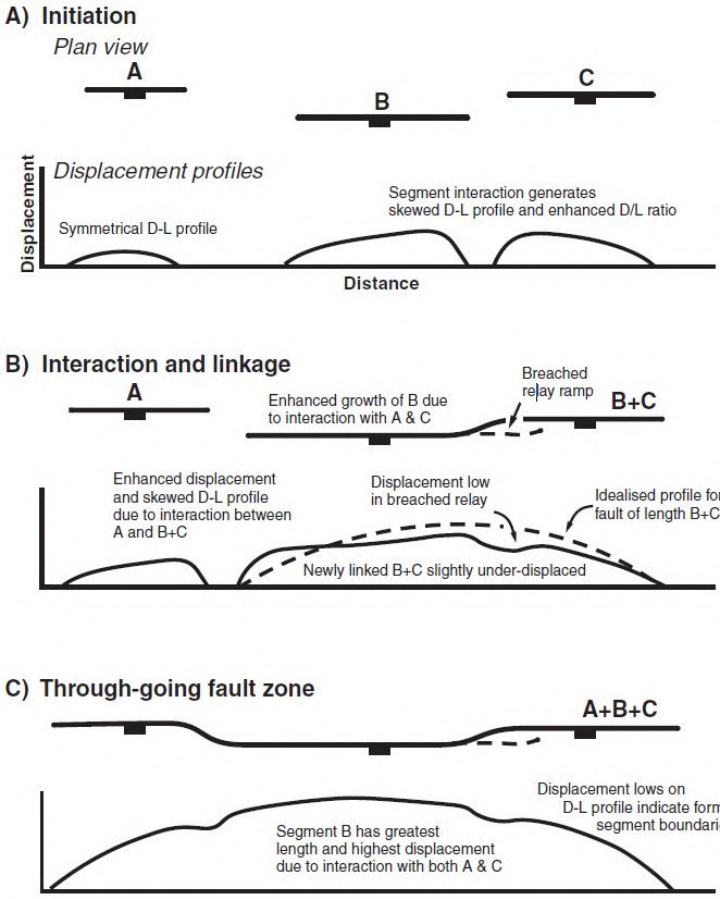

Fig. 8.1.- Modelo esquemático de evolución de tres segmentos de falla que coalescen para producir una zona de falla única. (A) Estadio inicial, en el que ya hay cierta interacción entre los segmentos más cercanos, tal y como se infiere de la diferencia entre la curva simétrica del segmento aislado y las asimétricas de los otros dos. (B) Estadio de interacción y enlace, que da lugar a curvas irregulares, y (C) estadio de desarrollo de la zona de falla continua. Tomada de Gawthorpe y Leeder (2000).

(Fig. 4.3). Su núcleo está representado por rocas triásicas, y presenta un cierre periclinal que coincide con la terminación de la misma falla (Fig. 4.2). El plano de falla principal se orienta en torno a 155,70W, como muestra el estereograma de la Figura 4.4a. Bajo la extensión plio-cuaternaria, el movimiento normal de sus bloques ha quedado registrado con estrías cuyos cabeceos oscilan entre 54º y 87ºW (Fig. 4.4a), indicando un movimiento normal casi puro y una dirección de transporte media hacia Nº230E.

La **falla de Concud** sigue el trazado NW-SE de un anticlinal vergente al norte, con su flanco frontal invertido. Esto sugiere que la falla normal actual también representa la inversión tectónica negativa durante el Plio-Cuaternario de un cabalgamiento asociado a dicho pliegue (Lafuente, 2011; Lafuente *et al*., 2011a,b; Fig. 5.16). Lafuente (2011) describe una superficie mecánica en rocas jurásicas orientada 152,32W, con marcas de fricción groseras con cabeceo 85ºS que permiten inferir una cinemática inversa casi pura. Los buzamientos medios de la superficie principal de la falla normal reactivada oscilan entre 65º y 70º SW, y en los casos en los que se han observado estrías sus ángulos de cabeceo son cercanos a 75ºS (Lafuente, 2011). La dirección de transporte tectónico calculada a partir de estos datos es cercana a N220ºE en todos sus tramos, lo que indica que aunque estos tramos tengan directrices diferentes (como ocurre en la zona de relevo con la falla de Teruel; Fig. 5.16) son compatibles cinemáticamente entre sí (Lafuente, 2011). La falla de Concud muestra actualmente actividad sísmica en su bloque levantado, en la zona de relevo con la falla de Sierra Palomera. Se trata de una alineación N-S de epicentros que parte desde el segmento más norte de la falla de Concud, y que no puede asociarse a rupturas superficiales reconocidas. Se interpreta como una posible prolongación septentrional de la falla de Concud por medio de un sistema de fracturas dispersas que alcanzaría aproximadamente 15 km de profundidad, aunque tampoco puede descartarse la existencia de un plano de falla único. La cinemática de esta fracturación reciente se desconoce ya que no se ha determinado ningún mecanismo focal de estos sismos.

Las **fallas de Teruel, Valdecebro, El Pobo, Peralejos-Tortajada-Cabigordo** y **La Hita** también representan probablemente la reactivación de estructuras heredadas de anteriores etapas (Ezquerro, 2017; Fig. 5.21). Lo sugiere la geometría de estas fallas, ya que la mayoría está formada por un conjunto de superficies de rotura paralelas o subparalelas, en ocasiones dispuestas con un cierto escalonamiento o relevo. Asimismo, también es clave la directriz NNE-SSW general de esta zona de falla, que sigue la dirección del borde del sector norte de la fosa de Teruel y de algunas familias de fracturación mesozoica (Liesa, 2011; Ezquerro, 2017). La estructura en su conjunto podría corresponder a la propagación superficial de un accidente de mayores dimensiones localizado en profundidad. Las diferencias entre las directrices de la deformación heredada al oeste de la cuenca de Teruel (NW-SE, como en el caso ya mencionado de la falla de Concud), y al este (NNW-SSE y N-S, como por ejemplo en la Sierra del Pobo; Liesa, 2011), sugieren que durante la etapa compresiva alpina existió una gran estructura de orientación NNE-SSW, posiblemente heredada de la etapa extensional mesozoica o de la deformación varisca o tardivarisca, que controló dicho cambio estructural y marcó la distinción de estos dos grandes dominios de deformación (Liesa, 2000; Liesa y Simón, 2009; Ezquerro, 2017). Respecto a la cinemática correspondiente al periodo extensional, los indicadores estudiados en la literatura implican un movimiento normal casi puro de toda la estructura. En varios afloramientos de los sectores central y sur de la falla de Teruel (Fig. 5.16) se infiere una dirección de transporte hacia N275ºE. En algunos planos de falla menores del sector de El Pobo, su movimiento normal puro se evidencia en una de sus dos familias de estrías, indicando una dirección de transporte hacia N260ºE (Ezquerro, 2017; Ezquerro *et al*., 2020). La dirección de transporte para la falla de Peralejos es hacia N295ºE, y para Tortajada hacia N315ºE (Ezquerro, 2017). En estas tres últimas fallas principales, hay constancia puntual de una segunda familia de estrías que presenta cabeceos bajos e indicaría un movimiento dextral-normal. Por último, las estrías medidas en un plano de falla representativo de la falla de Valdecebro indican una dirección de transporte media hacia N202°E (Fig. 5.19c; Simón *et al*., 2019). Esta dirección de transporte, junto con la directriz WNW-ESE de la falla de Valdecebro, son excepcionales respecto a las demás del sector norte de la cuenca de Teruel.

Las zonas de relevo diestro entre las fallas de Calamocha, Sierra Palomera, Concud y Teruel evolucionan por medio de fracturación longitudinal distribuida. Recordemos el modelo propuesto en ese sentido por Peiro *et al*. (2020). En el caso de la zona de relevo entre las fallas de Sierra Palomera y Concud este tipo de fracturación queda corroborada por el estudio de la sismicidad reciente. Estas dos fallas están en un estadio intermedio entre la independencia completa y la coalescencia (Lafuente, 2011; Lafuente *et al*., 2011; Peiro *et al*., 2017), al igual que todo el sistema de fallas del sector norte de la cuenca de Teruel (Ezquerro *et al*., 2020). En este contexto, la fracturación controlada por factores externos a la misma (como la herencia estructural o el campo de esfuerzos regional) prevalece respecto a aquella inducida por la cinemática de la misma zona de relevo.

En cuanto al **sistema de fosas del Maestrat**, su evolución también podría estar tentativamente relacionada con la reactivación de estructuras previas, como podría ser la gran estructura antiforme mesozoica orientada ESE que se interpreta en este sector (Simón, 1982). Sin embargo, la penetración de la fracturación distensiva posterior es tal que no deja entrever con claridad dicha estructura ni su cinemática. Las fallas que limitan estos grábenes han sido reactivadas en sucesivas ocasiones durante el Mioceno Superior, Plioceno y Pleistoceno (Simón 1982, Simón *et al*., 1983), así como modeladas por la erosión y enmascaradas por los últimos depósitos aluviales. Esto dificulta el análisis de sus planos de falla, y sólo se han registrado estrías en los planos de la falla de La Rambla de la Viuda y Talaies, que indican direcciones de transporte hacia N252ºE y N088ºE, respectivamente (Fig. 5.22c), y movimientos normales casi puros en ellas.

2. Dinámica: síntesis bibliográfica de paleoesfuerzos

Ya hemos visto que la actividad extensional de la Cordillera Ibérica centro-oriental está influenciada por la herencia estructural de su pasado contractivo. Por ello, es importante tener en cuenta, en primer lugar, el comportamiento dinámico de esta región durante la compresión cenozoica. Tres campos de esfuerzos compresivos intraplaca controlaron la evolución tectónica de la Cordillera Ibérica centro-oriental desde el Eoceno,

con tres direcciones de compresión preferentes (Liesa, 2000; Liesa y Simón, 2009; Simón, 2019): NE-SW (compresión *Pirenaica-Ibérica*), ESE-WNW a SSE-NNW (que incluye las compresiones *Bética* y *Guadarrama*), y NNE–SSW (compresión *Pirenaica tardía*). En general, las dos primeras compresiones estuvieron activas en la región desde el Eoceno hasta el Mioceno inferior, aunque con fluctuaciones de intensidad, y todas las compresiones se sucedieron en una secuencia alternante (Liesa y Simón, 2009; Simón, 2019): WNW-ESE (Eoceno s.l.); NE-SW (del Eoceno medio al Oligoceno superior); NW-SE (del Oligoceno superior al Mioceno inferior); NNW-SSE (desde el Oligoceno final-Mioceno inferior), y NNE-SSW (desde el Oligoceno superior-Mioceno inferior). Todas estas compresiones estuvieron, por tanto, parcialmente superpuestas, están conducidas por fuerzas tectónicas independientes relacionadas con los márgenes de placa activos de Iberia, y pueden mostrar perturbaciones de las trayectorias de esfuerzo tanto a escala local como regional (Liesa y Simón, 2009). El esfuerzo máximo horizontal (S_{Hmax}) NNW-SSE es el propio del Sistema Bético, y el NNE-SSW lo es del dominio pirenaico y Cuenca del Ebro, ambos activos en la actualidad.

A partir del Mioceno inferior-medio, el régimen de esfuerzos compresivos de esta región pasa progresivamente a una tectónica de tipo distensivo (Fig. 8.2). Simón (1982, 1983) unifica la bibliografía regional de la que se disponía hasta el momento sobre los procesos extensionales y la completa con información de toda la Cordillera Ibérica centro-oriental. Con todo ello, termina caracterizando el campo de esfuerzos reciente con un σ_3 orientado en torno a E-W, siendo de tipo triaxial mayoritariamente durante el Mioceno-Plioceno inferior, y radial o multidireccional (σ_1 vertical, $\sigma_2 \approx \sigma_3$) durante el Plioceno superior - Cuaternario. Simón (1982, 1983, 1989) ya

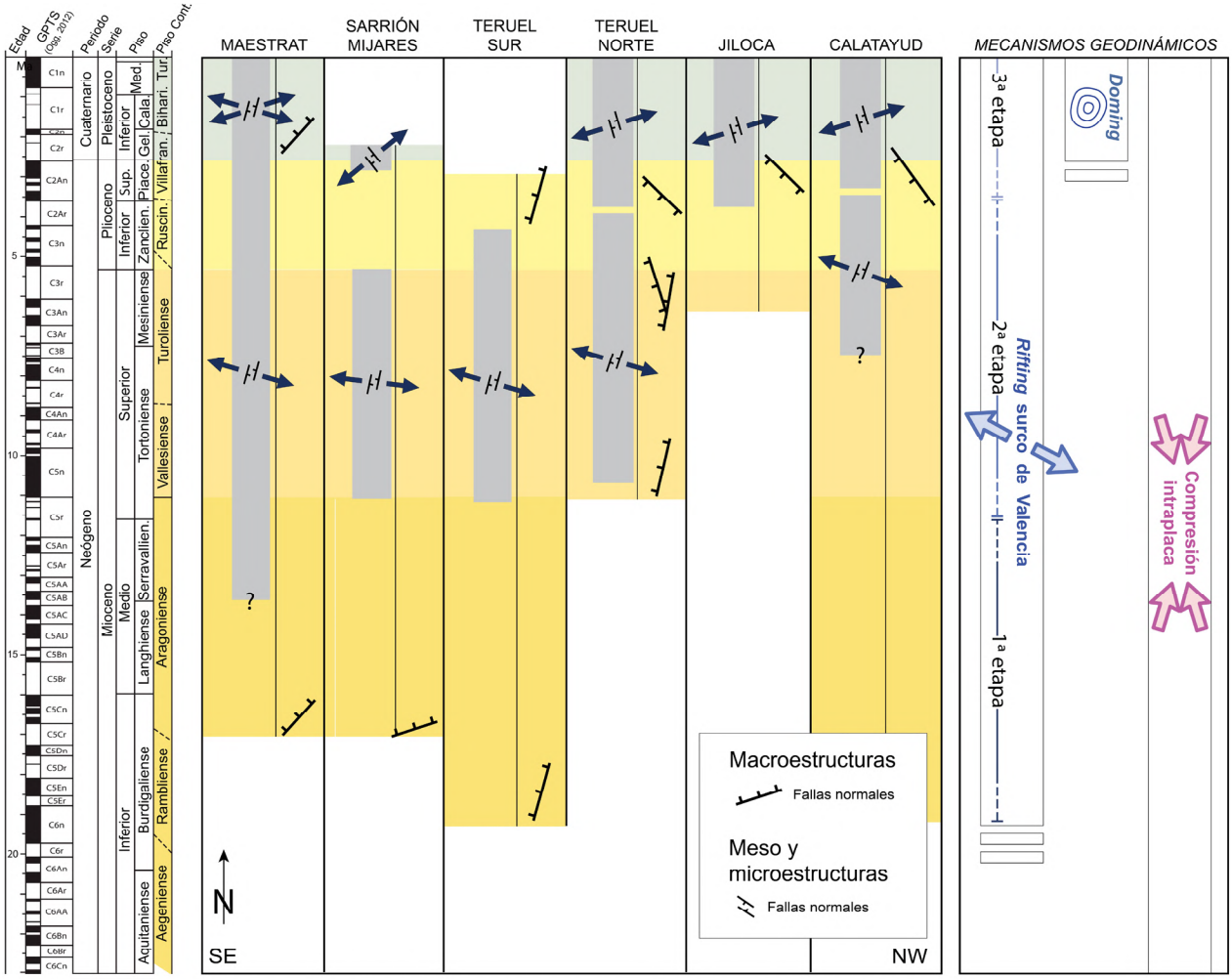

Fig. 8.2.- Cuadro cronológico modificado de Ezquerro y Simón (2017) para sintetizar el registro de la extensión neógeno-cuaternaria en las cuencas principales de la Cordillera Ibérica centro-oriental. Las flechas oscuras ilustran los sistemas de esfuerzos extensionales (dirección promedio del eje σ_3 horizontal). Los fondos amarillentos indican la amplitud temporal aproximada del registro sedimentario en cada cuenca, y los recuadros grises la de cada sistema de esfuerzos. En cada cuenca, la columna de la derecha sintetiza las macroestructuras extensionales presentes y su orientación promedio. La escala cronológica se basa en la de Hilgen *et al.* (2012).

planteó que existe una dirección de extensión neta de orientación WNW-ESE inducida por el *rifting* del Surco de Valencia, y que la extensión radial reciente podría ser consecuencia del proceso de *doming*, que levanta asimétricamente gran parte de la región desde el sector de Javalambre y Gúdar. Posteriormente, se afianza esa dirección de extensión neta con σ_3 cercano a WNW-ESE para el campo de esfuerzos triaxial, y se determina otra dirección preferente de extensión más próxima a WSW-ENE para el campo de esfuerzos radial (Simón, 1986, 1989; Cortés y Simón, 1997; Cortés-Gracia, 1999; Capote *et al*., 2002). Arlegui *et al*. (2005, 2006) consolidan estas trayectorias primarias extensionales, al igual que Lafuente (2011). Posteriormente, Liesa *et al*. (2019) sugieren de esa extensión dominante WSW-ENE en la región de Teruel se consolida realmente en el Pleistoceno, mientras que en el Mio-Plioceno todavía prevalece una extensión E-W a WNW-ESE. Por otra parte, Arlegui *et al*. (2006), Lafuente (2011), Ezquerro (2017) y Liesa *et al*. (2019) evidencian la existencia de perturbaciones relacionadas con grandes fallas, como por ejemplo la de Concud en su zona de relevo con la de Teruel, con frecuentes intercambios locales de los ejes σ_2 y σ_3, que representan un rasgo intrínseco del régimen de extensión radial. Los tensores de esfuerzos de mecanismos focales de sismos analizados por Herraiz *et al*. (2000) establecen que, en la actualidad, existe una dirección de extensión máxima ENE-WSW en la Cordillera Ibérica centro-oriental. Es muy similar a la dirección del campo de esfuerzos radial o multidireccional plio-cuaternario, por lo que se puede afirmar que dicho régimen permanece vigente en la actualidad.

3. Modelo cinemático y dinámico global en el contexto tectónico

Existe coherencia entre la geometría-cinemática de la fracturación inferidas en nuestra investigación y los modelos de campo de esfuerzos inferidos en los estudios previos. Esto hace viable su integración en un modelo global que represente el estado tectónico actual de la región dentro del contexto geodinámico de la Península Ibérica. En la sección II.2.2 ya hemos hecho una aproximación a la comparación con las estructuras contractivas. El sistema de cabalgamientos NW-SE de las zonas de Lagueruela y Pelarda, así como la misma zona de falla inicialmente transpresiva de Río Grío-Pancrudo, podrían representar tanto la compresión *Pirenaica-Ibérica* (NE-SW) como la *Pirenaica tardía* (NNE-SSW), con evidencias asimismo de actuación puntual de la compresión *Bética temprana* (ESE-WNW; movimiento de desgarre sinestral en la falla de Cucalón-Pancrudo en la zona de Lagueruela).

Poniendo el foco en la deformación extensional reciente en la Cordillera Ibérica centro-oriental, ésta muestra una zonificación desde el interior hacia la costa mediterránea. Las fallas que enmarcan o cortan las cuencas de Calatayud y Jiloca tienen dirección dominante NW-SE, longitudinal a la misma cadena, con direcciones de transporte bastante homogéneas hacia el SW. En el caso de la cuenca de Calatayud como tal, ésta también presenta dirección NW-SE, y en la fosa del Jiloca, dado que las fallas se disponen oblicuas y en relevo diestro en su margen oriental, el eje del graben es NNW-SSE. En el sector norte de la cuenca de Teruel confluyen y coexisten varios sistemas de fallas que en general son próximos a N-S o NNE-SSW. Muestran una cinemática variable con direcciones de transporte tanto hacia el WSW como hacia WNW. También de manera excepcional, existen estructuras transversas, como la falla de Valdecebro con dirección de transporte hacia el SSW. La fracturación de las zonas de relevo entre las fallas que limitan las fosas del Jiloca y Teruel se dispone NW-SE, paralelamente a las estructuras heredadas y, en mayor medida, NNW-SSE. Finalmente, las fallas que limitan el sistema de fosas del Maestrat se orientan uniformemente NNE-SSW y tienen direcciones de transporte contenidas en un plano de movimiento E-W.

Esa heterogeneidad espacial de la deformación, aunque está condicionada por la herencia estructural, parece relacionarse sobre todo con variaciones espaciales y temporales del campo de esfuerzos regional, debidas a la combinación de varios mecanismos geodinámicos que se solapan en la región. El más obvio es el proceso de *rifting* del vecino Surco de Valencia, al cual se le asocia un proceso de abombamiento o *doming* cortical, con centro en la región de Gúdar, y ambos son compatibles, a su vez, con el campo de extensión radial o multidireccional (Figs. 8.2, 8.3). Todo ello actuaría conjuntamente con la compresión que se transmite al interior de la Placa Ibérica desde los márgenes bético y pirenaico, que es la que acabaría estableciendo la dirección preferente del S_{Hmax} (ortogonal a la dirección de extensión) del campo de esfuerzos radial actual.

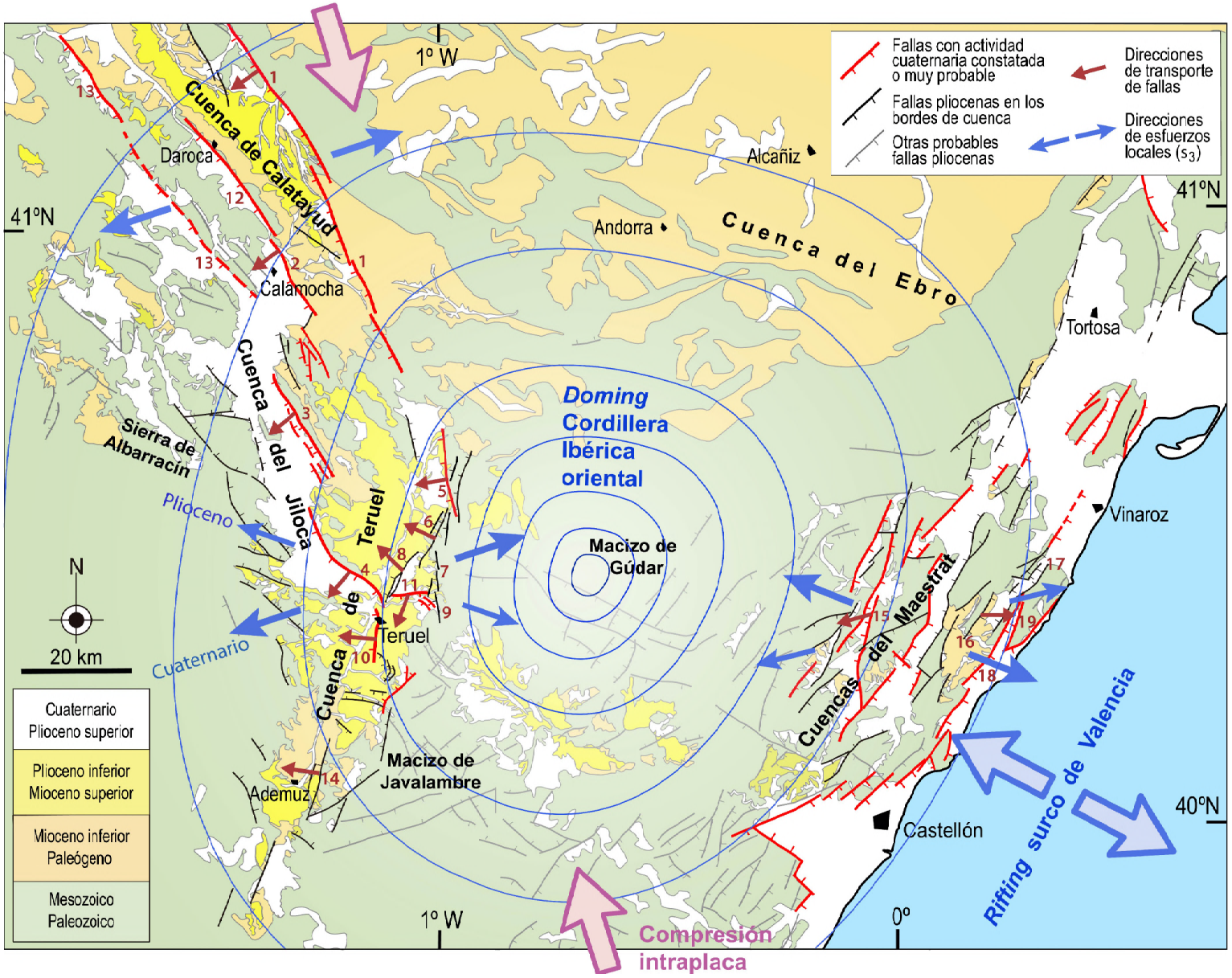

Fig. 8.3.- Síntesis interpretativa de la estructura y cinemática del sistema extensional plio-cuaternario Teruel-Jiloca-Calatayud en el contexto geodinámico de la Cordillera Ibérica centro-oriental. Los números señalan a las fallas: 1) Río Grío-Pancrudo, 2) Calamocha, 3) Sierra Palomera, 4) Concud, 5) El Pobo, 6) Peralejos, 7) Cabigordo, 8) Tortajada, 9) La Hita, 10) Teruel, 11) Valdecebro, 12) Daroca, 13) Munébrega, 14) Ademuz, 15) R. de la Viuda, 16) Talaies, 17), Xivert, 18) Torreblanca, 19) Irta. Tomada de Simón *et al.*, 2022.

Los datos recogidos en esta tesis y en los trabajos previos permiten determinar que la extensión asociada a la apertura del Surco de Valencia (WNW-ESE, ortogonal al eje del mismo) persiste en el Maestrat más allá de las primeras etapas extensionales, y se atenúa hacia las cuencas interiores. En ellas, concretamente en las cuencas del Jiloca y Calatayud, la directriz general refleja en gran medida la influencia de la herencia estructural, que a su vez es la más propicia a activarse bajo el *doming* y el consiguiente campo de extensión radial. La multiplicidad de geometrías y cinemáticas de las estructuras del sector norte de la cuenca de Teruel y su confluencia con la del Jiloca, estudiadas mayoritariamente en trabajos previos a éste, refleja una situación intermedia entre todas las cuencas anteriores. Coexisten fallas con direcciones más dispersas (NNW-SSE, N-S, NNE-SSW e incluso WNW-ESE), así como de transporte y extensión. Todo ello, y siendo especialmente importantes las estructuras transversales, refleja mayoritariamente la influencia del campo de extensión radial de esta región. Estas estructuras transversales no sólo se limitan al sector norte de la cuenca de Teruel, como la ya mencionada falla de Valdecebro o la estructura de Los Mansuetos (al E de la zona de relevo entre Concud y Teruel), sino que aparecen también en el sector sur de la cuenca de Teruel, como en Cascante del Río, y en la Sierra de Albarracín, en el área de Almohaja (Simón, 1989).

Debido a esa heterogeneidad, no es viable elaborar un modelo simple de la deformación cortical de toda la región. Sin embargo, sí puede ensayarse un modelo semicuantitativo 2D para el entorno inmediato de Teruel, donde cuatro fallas bien conocidas (Concud, Teruel, Valdecebro y Tortajada) confluyen y acomodan casi la totalidad de la deformación (Fig. 8.4). Integrando los vectores de estiramiento horizontal obtenidos a partir del salto neto y la dirección de transporte de cada una de ellas, puede construirse una elipse de deformación horizontal virtual (Fig. 8.4, sin escala). Se trata de un ejercicio geométrico similar al clásico problema de la obtención de la elipse de deformación a partir de al menos tres líneas elongadas, resuelto por Ramsay (1967). El eje X resultante se dispone N080ºE, curiosamente muy próximo al eje σ_3 promedio, en torno a N070ºE, inferido por Arlegui *et al.* (2005) y Liesa *et al.* (2019).

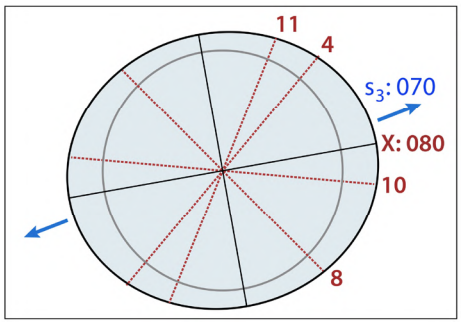

Fig. 8.4.- Elipse de deformación horizontal virtual. Integra los vectores de estiramiento del salto neto y la dirección de transporte de las fallas: 4, 8, 10 y 11 de la Figura 8.3. Se indican las direcciones de su eje X de máximo estiramiento y del eje σ_3 del campo de esfuerzos actual. Tomada de Simón *et al.*, 2022.

Este sistema evoluciona en el tiempo como un corredor extensional heterogéneo, propagándose desde el eje del *rift* del Surco de Valencia hacia el interior de la Península. Las edades en que se inicia el desarrollo o la reactivación de las fosas son progresivamente más recientes de E a W: Mioceno inferior en el Maestrat, Mioceno superior en Teruel, Plioceno en el Jiloca y Calatayud. Por otro lado, partiendo de tasas de movimiento similares en toda la región en el Plioceno, la actividad tiende a disminuir durante el Cuaternario en el sistema extensional del Maestrat (también en las Catalánides; Masana, 1995; Masana *et al.*, 2001; Perea *et al.*, 2006; Simón *et al.*, 2012, 2013) mientras aumenta en el sistema Teruel-Calatayud.

Todo ello cabe interpretarlo como consecuencia de factores externos al sistema extensional, como son las variaciones en la forma de operar y combinarse los mecanismos geodinámicos ya mencionados, y de factores internos del sistema extensional. Algunos de ellos ya fueron propuestos por Ezquerro *et al.* (2020), y en esta tesis los corroboramos y ampliamos. En primer lugar, podría deberse a la propagación de la deformación extensional desde el Surco de Valencia hacia el interior de la Península. Las fallas del Maestrat ya habrían acomodado la mayor

parte del estiramiento cortical desde su formación en el Mioceno inferior, y ésta habría empezado a migrar hacia las cuencas de Teruel-Calatayud a partir del Mioceno superior, haciendo que disminuya en el Maestrat progresivamente a partir de este momento. En segundo lugar, el *doming* cortical podría haber estado progresando hacia el W desde sus comienzos en el Plioceno superior y, sumado a la compresión intraplaca, producir esa persistente dirección de extensión WSW-ENE del campo de esfuerzos radial. Cabe destacar que, en estos dos escenarios geodinámicos, las directrices predominantes de las macroestructuras NW-SE, NNW-SSE, así como la N-S, son favorables a su activación bajo la extensión generada en cada caso (Liesa *et al*., 2019). En un segundo plano, esta extensión actúa conjuntamente con la compresión intraplaca, la cual podría estar experimentando cambios. A mayor intensidad de la misma y, por tanto, mayor valor de S_{Hmax}, la deformación se hace más anisótropa con un S_{Hmin} más acentuado, bajo el que es más probable que se activen macroestructuras como las estudiadas. Finalmente, el aumento de las tasas de desplazamiento de las fallas estudiadas también responde a cambios en los factores internos del sistema, como son las coalescencias graduales entre segmentos de falla. Existen evidencias que ponen de manifiesto estas uniones, las cuales permitirían aumentar el desplazamiento máximo de la falla como respuesta al reajuste de sus perfiles salto vs. distancia (*T-D*), bien después de su unión o en estadios inminentes previos en los que ya hay una interacción mecánica (Cowie y Roberts, 2001). En estos contextos, y aun sin variar el campo de esfuerzos, las tasas máximas en el centro de las nuevas estructuras también se incrementarían (e.g. Peacock y Sanderson, 1991; Cowie y Scholz, 1992; Dawers y Anders, 1995; Cartwright *et al*., 1995; Cowie y Roberts, 2001).

No se tiene constancia de dicho aumento de la tasa de desplazamiento en el segmento de falla de Cucalón-Pancrudo (CPFS). Como se discute en la sección II.2.4, no haberla registrado podría deberse a:

(1) La poca representatividad de los datos de tasas recogidos para el Pleistoceno superior (a partir de la excavación de una única trinchera).

(2) La partición del desplazamiento entre varias ramas de fallas no identificadas u otras estructuras de deformación, ya que se tiene constancia de que el monoclinal asociado al bloque hundido de la CPFS, junto con la falla de Valverde, están acomodando gran parte de la deformación de toda la estructura.

(3) Un proceso de coalescencia reciente entre el sector norte y sur de la CPFS. Las uniones entre segmentos de falla ya hemos visto que pueden acabar aumentando la tasa de desplazamiento. Sin embargo, la coalescencia entre los dos sectores de la CPFS podría ser reciente, ya que sus curvas T-D todavía no se han reajustado y uniformizado a una geometría de campana conjunta. Por ello, la CPFS habría empezado a aumentar su tasa de desplazamiento desde época reciente y no quedaría reflejado en los datos.

La explicación en nuestro caso podría encontrarse en la acción combinada de estos tres escenarios, quedando excluido un cuarto relacionado con un posible límite de la extensión propagada hacia el interior desde el *rifting* del Surco de Valencia y el *doming*. El hecho de que su vecino segmento norte, el de Río Grío-Lanzuela (RLFS) sí que experimente este aumento en sus tasas permitiría de alguna forma descartar este cuarto escenario, ya que es un sector todavía más alejado de las fuentes que el de la CPFS.

En definitiva, a grandes rasgos el proceso geodinámico de *doming* y el consiguiente régimen de extensión radial, sumado a la compresión intraplaca, podrían estar derivando en que el corredor extensional del sector Calatayud-Teruel pasase a experimentar un proceso de *rifting* con características diferentes a las del Surco de Valencia. Éste se habría estado propagando hacia el interior de la Península Ibérica durante la tercera etapa de extensión (Plioceno superior-Cuaternario), favorecido por la herencia estructural. El proceso de *doming* habría estado levantando la región al noreste de este corredor extensional respecto a los fondos de las depresiones principales. Sin embargo, al igual que en el trabajo de Ezquerro *et al*. (2020), en esta tesis también se ha estudiado únicamente la geometría, cinemática y dinámica de estructuras someras, por lo que no se pueden determinar con seguridad las dimensiones de este proceso.

4. Implicaciones en el cálculo de peligrosidad sísmica y contribución al QAFI

La peligrosidad sísmica evalúa el nivel de movimiento del suelo que pueden producir los terremotos futuros que ocurran en una región, y para ello han de definirse y caracterizarse correctamente las fuentes sísmicas presentes en ella. Se trata de un concepto probabilista en el que se debe especificar qué nivel de movimiento del suelo se considera constitutivo de peligro potencial, y durante qué periodo de tiempo se espera que ocurra un sismo que produzca tal movimiento (IGN-UPM, 2013). Normalmente se expresa como la aceleración sísmica esperable en un periodo determinado que, a efectos de normativa sismorresistente en España, sería de 475 años.

Las fallas tectónicas son una fuente sísmica si se identifica actividad reciente en ellas. Para ello, se precisa de información geológica, sismológica y, en especial, paleosismológica, que puede proporcionar datos sobre las tasas de desplazamiento y de recurrencia de las fallas, sus magnitudes máximas, profundidades de sismos, la posible segmentación, etc. Esta tesis reúne los datos de este tipo recogidos en el sistema de fallas extensionales de la Cordillera Ibérica centro-oriental, y aporta evidencias de actividad durante el Plio-Cuaternario de la mayor parte de ellas. Pretende incrementar el conocimiento actual de las fallas activas de la Península Ibérica, empezando por ampliar la información recogida en la base de datos de fallas activas durante el Cuaternario de Iberia (*Quaternary Active Faults Database of Iberia* o *QAFI*; García-Mayordomo *et al.*, 2012; IGME, 2022). Se trata de una iniciativa que pone a disposición de todos el mapa de las fallas que han estado activas los últimos ca. 2,6 Ma (límite del Cuaternario según Cohen *et al.*, 2022), indicando sus parámetros geométricos, sísmicos y de otra índole asociados a ellas. Asimismo, clasifica las estructuras según el periodo temporal de su actividad, la fiabilidad de su traza cartográfica y su tasa de desplazamiento (Fig. 8.5).

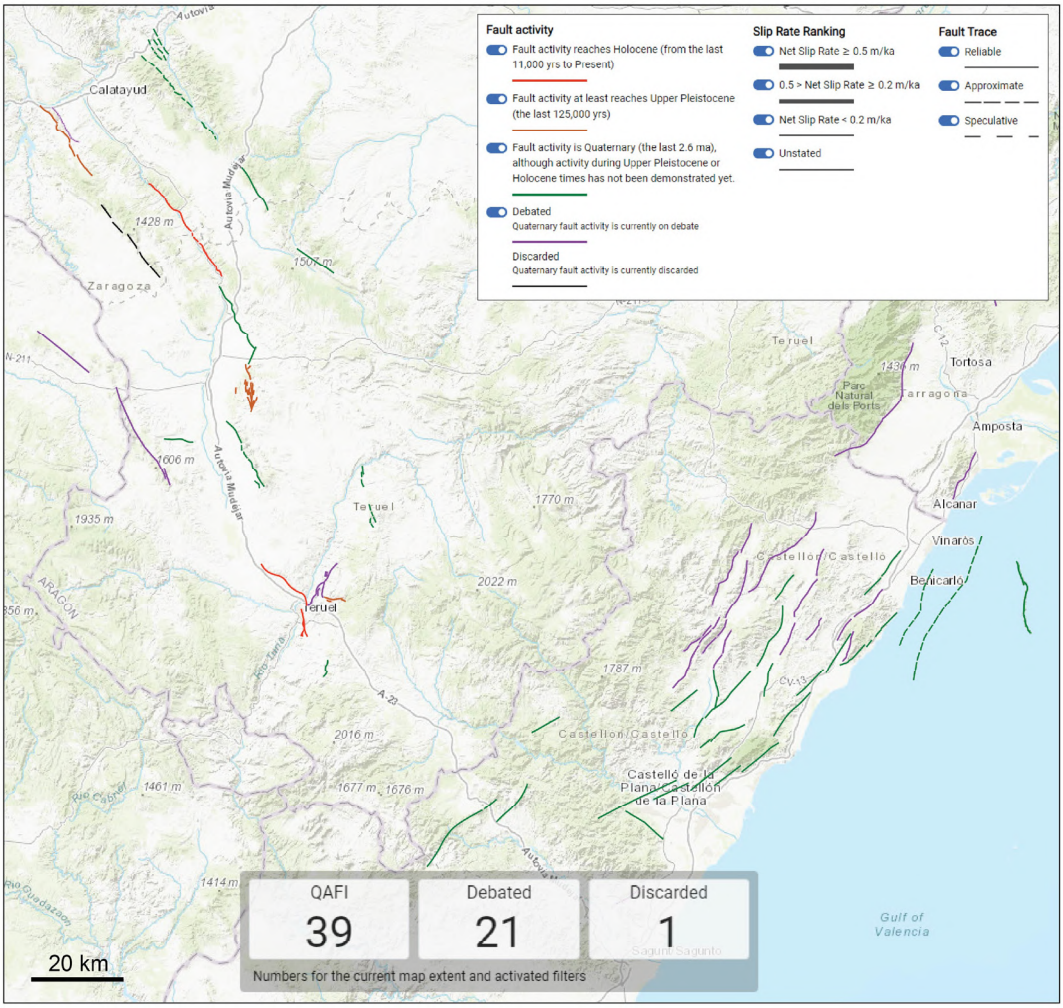

Fig. 8.5.- Representación combinando las fallas de la QAFI v.4 (García-Mayordomo *et al.*, 2012; IGME, 2022) y del Mapa Neotectónico de España (IGME y ENRESA, 1998) para el sector estudiado de la Cordillera Ibérica centro-oriental. Se trata de un volcado de pantalla modificado de la versión online de QAFI, señalando la leyenda original y el recuento de estructuras que abarca el volcado.

En esta tesis se revalida mucha de la información geológica que se muestra en los detalles de cada falla de la QAFI, y se propone que se valore la inclusión de otra adicional derivada de los estudios estructurales, geomorfológicos y paleosismológicos llevados a cabo en esta tesis, en gran medida ya recogida en la Tabla 6.1. La propuesta consiste en:

- Ampliar la información del segmento de falla de Río Grío-Lanzuela, cartografiando su traza desde Nigüella, siguiendo la margen este del río Grío y pasando por Codos, y por el frente montañoso linear de las sierras de Algairén y Peco hasta Lanzuela (Figs. 1.2, 2.5) Se pueden diferenciar dos tramos en su traza para una mejor adaptación a la clasificación de la QAFI. Un primer tramo abarcaría desde Nigüella hasta las cercanías de Tobed, y entraría dentro de las categorías de *Falla con evidencia de actividad en el Cuaternario, aunque su actividad durante el Pleistoceno superior o el Holoceno todavía no se ha demostrado*, y de traza de falla aproximada. El segundo tramo llegaría hasta Lanzuela y pertenecería a las categorías de *Falla con evidencia de actividad en el Pleistoceno superior*, y de traza de falla fiable. La información de este último sector podría anexionarse con la de las denominadas como "falla de Modorra" y "falla de Badules", ya presentes en la base de datos (IGME y ENRESA, 1998; García-Mayordomo *et al*., 2012; Gutiérrez *et al*., 2013; IGME, 2022). Por último, también podría ampliarse la información sobre su geometría y cinemática, actividad cuaternaria, tasa de desplazamiento y parámetros sismológicos, con los datos recogidos en la literatura y en la Tabla 6.1.
- Añadir la información del segmento de falla de Cucalón-Pancrudo, cartografiando su traza desde Cucalón por el frente montañoso de las sierras de Cucalón y Pelarda, pasando por las proximidades de Nueros, Torre los Negros y Alpeñés hasta Pancurdo (Figs. 1.2, 2.10). De nuevo, se pueden diferenciar varios tramos en su traza. Un primer tramo abarcaría desde Cucalón hasta Barrachina y entraría dentro de las categorías de *Falla con evidencia de actividad en el Holoceno* y de traza de falla fiable. Un segundo tramo en el sector Barrachina-Torre los Negros, que podría pertenecer tanto a la categoría *Falla con evidencia de actividad en el Cuaternario, aunque su actividad durante el Pleistoceno superior o el Holoceno todavía no se ha demostrado* como, siendo más conservadores, a la de *Falla cuya evidencia de actividad en el Cuaternario está en debate*, y su traza sería aproximada. Por último, un tercer tramo hasta Pancrudo considerado como *Falla con evidencia de actividad en el Cuaternario, aunque su actividad durante el Pleistoceno superior o el Holoceno todavía no se ha demostrado*, y traza fiable o aproximada. Por último, también debería incluirse la información sobre su geometría y cinemática, actividad cuaternaria, tasa de desplazamiento, paleoterremotos y parámetros sismológicos recogidos en la literatura y en la Tabla 6.1.
- Completar la información de la ya incluida falla de Calamocha, cambiando su categoría a *Falla con evidencia de actividad en el Pleistoceno superior*, y ampliando la información sobre su geometría y cinemática, actividad cuaternaria, tasa de desplazamiento, paleoterremotos y parámetros sismológicos, con los datos recogidos en la literatura y en la Tabla 6.1.
- Ampliar la información de la ya incluida falla de Sierra Palomera, en primer lugar, sopesando si cambiar su categoría a *Falla con evidencia de actividad en el Pleistoceno superior* dadas las evidencias recogidas que lo sugieren. En segundo lugar, añadiendo información sobre su geometría y cinemática, actividad cuaternaria y parámetros sismológicos de la literatura y en la Tabla 6.1.
- Revisar los parámetros sismológicos del resto de fallas estudiadas pertenecientes a la Cordillera Ibérica centro-oriental, y valorar si añadir los valores de magnitud máxima de sus máximos terremotos esperables obtenidos mediante la regresión empírica de Wesnousky (2008), incluidos en la Tabla 6.1, ya que es la recomendada en contextos de fallas intraplaca lentas después del análisis hecho por Stirling *et al*. (2013) para el *Global Earthquake Model* (*GEM*).

Existen varias metodologías para estimar la peligrosidad sísmica de una región, de entre las que destaca la conocida como PSHA (*Probabilistic Seismic Hazard Assessment*). Este método aplicado a una región termina proporcionando una estimación de los valores de aceleración horizontal máxima o pico de referencia (*Peack Ground Acceletarion* o *PGA*, en unidades de medida *g*) para un periodo de retorno establecido. Requiere asumir

ciertas hipótesis sobre la influencia de la fuente sísmica y del medio por el que se propagan las ondas, por lo que el cálculo lleva asociado numerosas incertidumbres. Acaba generando, por tanto, unos resultados con un alto grado de dispersión, que tiende a ser mayor en las zonas de menor sismicidad (IGN-UPM, 2013). La PSHA es la metodología más ampliamente adoptada en los cálculos de peligrosidad sísmica, y es la seguida para la realización de los Mapas de Peligrosidad Sísmica de España del Instituto Geográfico Nacional. Para ello, considera que el territorio se divide en distintas zonas sismogenéticas, cada una de las cuales tiene un potencial sísmico uniforme. En sus últimas versiones (IGN-UPM, 2013; IGN, 2015), el mapa de peligrosidad sísmica muestra para las fosas del Jiloca y Teruel una *PGA* media, esperada para un periodo de retorno de 475 años, entre 0,040 y 0,047 g, con un descenso hasta alrededor de 0,039 g en el sector centro-sur de la cuenca de Calatayud, y un nuevo incremento hasta superar 0,040 g en su sector norte (Fig. 8.6). En las fosas del Maestrat los valores también oscilan entre 0,040 y 0,050 g.

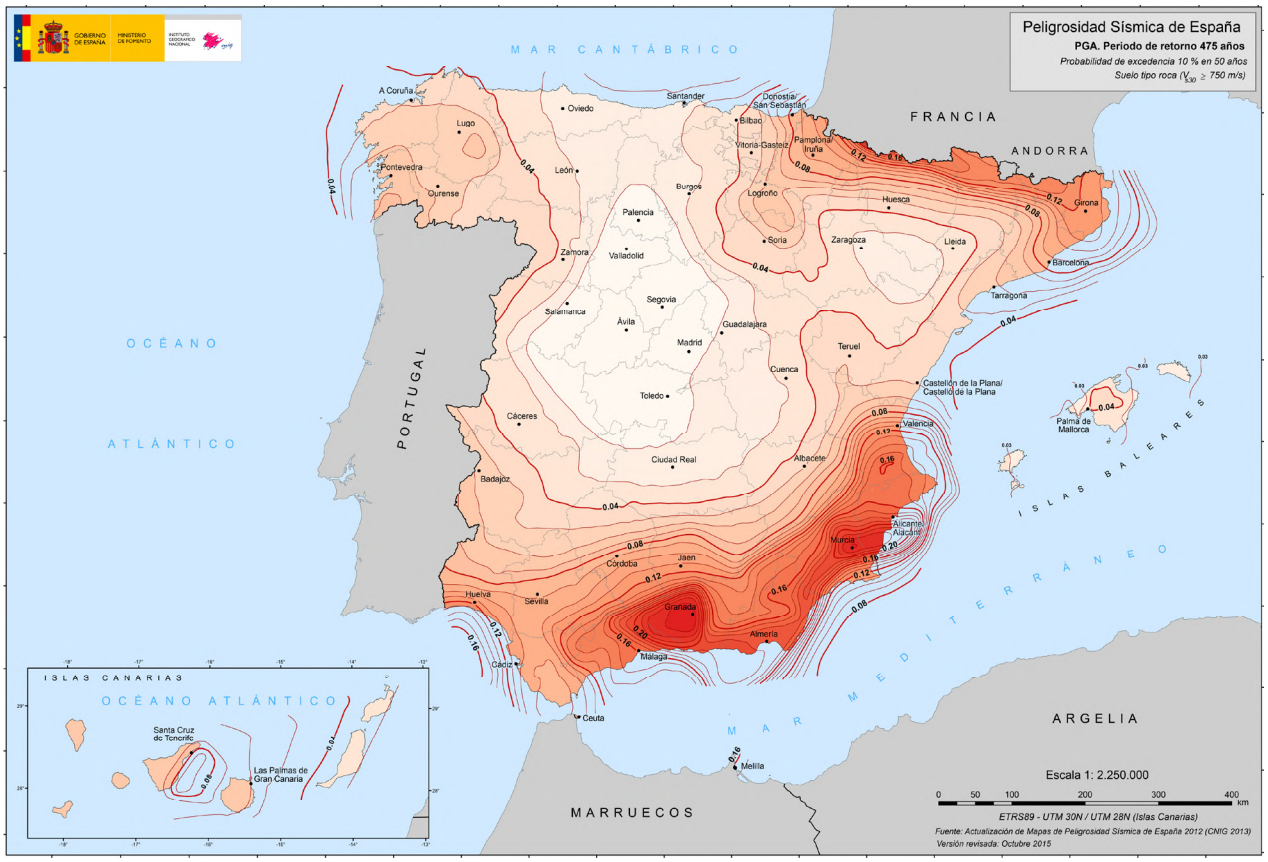

Fig. 8.6.- Mapa de Peligrosidad Sísmica de España a escala 1: 2.250.000, que representa la aceleración espectral del suelo, de periodo 0,2 segundos, para un periodo de retorno de 475 años. Tomada de IGN (2015).

Las únicas aproximaciones al cálculo de peligrosidad sísmica específicas de una falla activa de la Cordillera Ibérica centro-oriental realizadas hasta la fecha corresponden a la falla de Concud y tuvieron relación con el proyecto de construcción del nuevo hospital de la ciudad de Teruel (Martínez y Cabañas, 2013; Simón *et al*., 2014). Mediante aproximaciones basadas en el modelo del terremoto característico, Simón *et al.* (2014) calculaban una *PGA* de 0,105 g. Este estudio estima también que el mayor seísmo que puede generar la falla de Concud alcanzaría una magnitud aproximada de 6.8, con un periodo de retorno medio de 7,3 ± 2,7 ka, y una probabilidad de ocurrencia en un plazo de 500 años de entre 2,3 y 26,1 % (dependiendo del tiempo transcurrido desde su último evento, todavía no bien acotado). En el informe de Martínez y Cabañas (2013) sobre la peligrosidad sísmica de la ciudad de Teruel realizado por el IGN para el Servicio Aragonés de Salud, basado en la metodología de PSHA, se obtuvo una *PGA* para un periodo de retorno de 475 años de 0,050 g, y un valor de aceleración sísmica de cálculo de 0,092 g.

El borrador de la nueva norma sismorresistente NCSR-22 (en trámite de aprobación) establece como necesaria su aplicación en la construcción de edificaciones de nueva planta cuando la *PGA* sea igual o mayor a 0,040 g. Asimismo, también muestra un mapa de peligrosidad sísmica obtenido a partir de la *PGA*, para un periodo de retorno de 475 años, pero cuyos resultados son muy similares al mapa ya mencionado del IGN (2015; Fig. 8.6). Ya hemos visto cómo los análisis de peligrosidad sísmica realizados para la revisión del plan urbanístico de Teruel por el nuevo hospital público (Martínez y Cabañas, 2013; Simón *et al*., 2014) cuestionaban los valores de *PGA* atribuidos en los mapas de peligrosidad sísmica al sector de Concud-Teruel, y establecían un valor mayor después de haber abordado en profundidad su estudio geológico y de PSHA. Se trata de una *PGA* más alta que la especificada en el borrador de la nueva norma sismorresistente, por lo que el hospital público de Teruel ya ha sido construido contemplando medidas antisísmicas específicas y cumpliendo con dicha norma (que sigue las directrices de la que estaba en vigor en aquel momento, la NCSE-02; RD 997/2002, de 27 de septiembre). En la actualidad, cada vez es más habitual que la Administración de Teruel contemple la implementación de medidas sismorresistentes en los proyectos de creación de nuevos edificios públicos, como también es el caso del nuevo centro cultural del barrio de San Julián.

Esta tesis implica una ampliación de la información geológica de las fallas de la Cordillera Ibérica centro-oriental que puede repercutir en futuras actualizaciones de la base de datos QAFI, sobre la que se apoya, a su vez, la zonificación empleada en PSHA para generar mapas de peligrosidad sísmica. Podrá suponer, por tanto, una mejora en la precisión de los próximos mapas en la región de estudio, y un avance en la delimitación de las zonas con una peligrosidad sísmica tal que deba tenerse en cuenta para implementar medidas antisísmicas. Las aportaciones más significativas corresponden al sector centro-sur de la cuenca de Calatayud, hasta ahora infravalorado en el resultado final de los mapas de peligrosidad sísmica. Los resultados de esta tesis también servirán de base para nuevos estudios paleosismológicos y futuros análisis mediante PSHA en la región, que permitan terminar de afinar la evaluación del potencial sismogénico de cada falla, obteniendo registros paleosismológicos más completos, valores de magnitud máxima esperable y periodos de recurrencia más realistas, o llevando a cabo modelizaciones de sus rupturas.


CONCLU
SIONES

Sobre la geometría y cinemática de las fallas de Río Grío-Pancrudo, Calamocha y Sierra Palomera

Los dos grandes dominios tectónicos recientes de la Cordillera Ibérica son: el sector oriental, donde destacan las fallas extensionales de dirección N-S a NNE-SSW, paralelas al Surco de Valencia, y el sector central, de dirección NW-SE a NNW-SSE, con influencia de la herencia estructural ibérica. Las fallas más estudiadas en esta tesis (Río Grío-Pancrudo, Calamocha y Sierra Palomera) se encuentran en este último corredor extensional.

La falla de Río Grío-Pancrudo es una macroestructura extensional que forma parcialmente el borde noreste de la cuenca de Calatayud, rehundiendo su relleno mio-plioceno. Su dirección media es NNW-SSE y se extiende hasta los 95 km de longitud, dividida en dos segmentos (Río Grío-Lanzuela y Cucalón-Pancrudo).

El segmento de falla de Río Grío-Lanzuela desplaza la Superficie de Erosión Fundamental o SEF (3,8–3,5 Ma) produciendo un salto neto de 260 m en 3,5 Ma, con una tasa neta a largo plazo de 0,07 mm/a. Se trata del salto máximo absoluto de este marcador conocido para el sector sur de la falla (desde aproximadamente Codos hasta Lanzuela), desconociendo si en su sector norte (desde Nigüella hasta Codos) este salto podría ser mayor. El estudio geológico en superficie revela que se ha producido la inversión del drenaje del río Güeimil por acción de esta falla, y permite inferir un salto neto de 155-235 m en 2 Ma, con una tasa neta de 0,07-0,11 mm/a. También desplaza un marcador estratigráfico hasta ca. 22 m en 66 ka, implicando una tasa neta de 0,30-0,36 mm/a. Se mueve con una dirección de transporte media hacia N235ºE.

El segmento de falla de Cucalón-Pancrudo también desplaza la SEF, pero muestra una distribución irregular del salto neto a lo largo de la traza: un máximo en su sector norte (desde Cucalón hasta Barrachina), con 205 m y una tasa neta a largo plazo de 0,06 mm/a en 3,5 Ma; otro máximo en su sector sur (desde Barrachina hasta Pancrudo) de 110 m, y un mínimo marcado entre ellos donde el salto disminuye hasta cerca de 30 m (en los alrededores de Barrachina). El salto máximo absoluto de esta falla (205 m) asciende hasta los 305-325 m, con una tasa neta a largo plazo de 0,09 mm/a, si se tiene en cuenta la importante componente de *bending* en su bloque superior, sumada a la acción de la falla intracuenca de Valverde.

La falla de Calamocha es una falla normal de 18 km de longitud que forma el límite suroeste de la cuenca de Calatayud y el límite noreste de la fosa del Jiloca, con una dirección media NNW-SSE y un buzamiento de 70-75ºE. En superficie, su sector central se ramifica en tres planos de falla sintéticos y casi paralelos. La dirección de transporte media de toda la estructura es hacia N234ºE, con un movimiento normal casi puro. Su salto neto máximo lo registra asimismo la SEF y oscila entre 180 y 210 m, con una tasa neta a largo plazo de 0,05-0,06 mm/a en 3,8 Ma.

La falla de Sierra Palomera también limita la fosa del Jiloca por el este, con dirección NNW-SSE uniforme a lo largo de sus 26 km de longitud. Se mueve de manera normal casi pura con una dirección de transporte media hacia N230ºE. Desplaza la SEF hasta ca. 330, y hasta aprox. 480 m cuando se incluye la componente de *bending* de su bloque superior, con unas tasas a largo plazo de 0,09-0,10 y 0,13-0,15 mm/a, respectivamente. Su bloque superior está cortado por la falla de Las Vallejadas, sintética a la principal, y por la falla de La Peñuela, antitética a la misma.

Estas tres fallas normales son el resultado de la inversión negativa de estructuras variscas previas, reactivadas durante la compresión alpina en el Paleógeno y finalmente invertidas en la extensión Neógeno-Cuaternaria. En la actualidad, esta extensión está representada por un campo de esfuerzos radial con una dirección de extensión preferente ENE-WSW, y las direcciones de transporte de las fallas estudiadas son coherentes con ella.

Sobre su paleosismología y potencial sismogénico

En el segmento de falla de Río Grío-Lanzuela se han estimado sus parámetros sísmicos usando diferentes regresiones empíricas. De entre ellas, la de Wesnousky (2008) es la más apropiada para contextos tectónicos como el estudiado. La máxima magnitud (Mw) inferida para este segmento de falla es 6.9 ± 0.3, con un desplazamiento cosísmico medio de 1,7 m y un periodo de recurrencia de 5-6 ka.

El estudio paleosismológico de una trinchera excavada en el segmento de falla de Cucalón-Pancrudo ha permitido interpretar dos eventos, y un posible tercer evento adicional incierto, comprendidos entre 18 y 3 ka, que se asocian al sector norte de la falla (desde Cucalón hasta Barrachina). Su periodo de recurrencia medio está en el rango entre 8,2 y 4,2 ka, y la media de sus saltos cosísmicos es de 0,5 m. El salto neto total registrado en la trinchera es de 1,1 m, e implica una tasa neta en este sector de la falla de 0,07-0,08 mm/a para los últimos 18 ka. Usando la regresión empírica, la magnitud que se infiere para el sector norte es 6.8 ± 0.3, y para todo el segmento de falla de Cucalón-

Pancrudo sería de 6.9 ± 0.3. De la misma forma, en el hipotético caso de una ruptura conjunta de toda la zona de falla de Río Grío-Pancrudo, su magnitud sería de 7.0 ± 0.3.

La interpretación paleosismológica de dos taludes artificiales que cortan a una de las ramas de la falla de Calamocha apunta hacia cuatro eventos comprendidos entre 125 y 70 ka, uno de los cuales se correlaciona tentativamente entre dos de los taludes. Se infiere un posible evento adicional incierto, que sería anterior a esos cuatro y estaría datado en 140 ka. El estudio de un tercer talud que corta a otra rama de la falla principal muestra una cronología de eventos limitada, que únicamente acota su último evento a una edad de 14 ka. De todo ello se infiere una tasa neta a corto plazo de 0,10 mm/a para los últimos 70 ka, saltos cosísmicos medios de 0,5-1,3 m y un periodo de recurrencia medio inferior a 15 ka. Se ha obtenido una magnitud de 6.3-6.9 para su máximo terremoto esperable, y de 6.9 ± 0.3 en el hipotético caso de una ruptura conjunta de toda la zona de falla de Daroca-Calamocha.

En el caso de la falla de Sierra Palomera, su aproximación paleosismológica se ha llevado a cabo en una trinchera excavada en la falla antitética de La Peñuela, en la que se han interpretado hasta siete eventos. Su modelo de edad es muy limitado y prácticamente sólo acota el último evento a una edad de 50 ka. Tampoco se ha podido obtener una tasa neta a corto plazo ni otras características sismogénicas. Éstas se han calculado usando las correlaciones empíricas, estimando una magnitud (Mw) entre 6.1 y 6.8, con un desplazamiento cosísmico medio variable entre 0,3 y 2 m.

Sobre el resto de fallas activas de la Cordillera Ibérica centro-oriental

En el sector central de la Cordillera Ibérica existen otras fallas principales de dirección NW-SE a NNW-SSE que se encuentran en los márgenes de la cuenca de Calatayud (Munébrega-Gallocanta, Daroca) y la fosa del Jiloca (Concud), así como en la cuenca de Teruel (fallas de la Sierra de El Pobo, Peralejos, Cabigordo, Tortajada, Teruel, La Hita). Con carácter más local, aparecen otras fallas de dirección próxima a E-W (Valdecebro, Cascante). El sector oriental corresponde al sistema de fosas del Maestrat, de dirección N-S a NNE-SSW.

Son fallas con longitudes del orden de 10^1 km y buzamientos en superficie en torno a 70º. El movimiento es siempre próximo a normal puro, con direcciones de transporte del bloque superior hacia SW y WSW, en el caso de las vinculadas a las cuencas de Calatayud y Jiloca, o hacia W y WNW, en la cuenca de Teruel.

Desplazan la SEF con saltos máximos del orden de 10^2 m durante el Plioceno superior-Cuaternario, arrojando tasas netas de movimiento a largo plazo de entre 0,05 y 0,15 mm/a (media: 0,08 mm/a). La mayoría de las fallas también evidencian actividad recurrente durante el Cuaternario. En el sector central, a excepción de las fallas de Daroca y Munébrega-Gallocanta, las tasas a corto plazo (0,05–0,36 mm/a; media: 0,21 mm/a; Pleistoceno superior) son superiores a las promediadas a largo plazo. Esto contrasta con lo que ocurre en el sector oriental, donde trabajos previos muestran cómo su actividad tiende a disminuir durante el Cuaternario.

Sobre el modelo geodinámico

La actividad conjunta de las fallas extensionales plio-cuaternarias en la Cordillera Ibérica centro-oriental revela un régimen de deformación general de la corteza caracterizado como un estiramiento radial. Dicho estiramiento es heterogéneo en el espacio y en el tiempo, reflejando combinaciones variables de tres componentes del campo de esfuerzos regional originados por sendos mecanismos geodinámicos:

(i) La extensión WNW-ESE ligada al *rifting* en el surco de Valencia, que es dominante en el sector más oriental de la cadena, sobre todo durante el Mio-Plioceno.

(ii) El proceso de abombamiento o *doming* cortical que afecta a la Cordillera Ibérica centro-oriental desde el Plio-Cuaternario, que induce el campo de extensión radial y probablemente intensifica la actividad de las fallas durante el Cuaternario en el sector central.

(iii) La compresión intraplaca NNW-SSE relacionada con el empuje de la Placa Africana, que determina la orientación dominante de las trayectorias de S_{Hmax} y S_{Hmin} en ese sector central y favorece la activación de las fallas longitudinales.

A lo largo del Plioceno-Cuaternario, la propagación del *rifting* hacia el interior de Iberia y el influjo creciente del *doming* pueden explicar la aceleración registrada en el movimiento en las fallas principales de Teruel, y su atenuación en las fallas del margen del Surco de Valencia.


BIBLIOGRAFIA

Abdul-Aziz, H., Hilgen, F., Krijgsman, W., Sanz-Rubio, E. y Calvo, J. P. (2000). Astronomical forcing of sedimentary cycles in the Miocene continental Calatayud Basin (NE Spain). *Earth Planet. Sci. Letters* 177, 9-22.

Adrover, R. (1975). Principales yacimientos paleomastológicos de la provincia de Teruel y su posición estratigráfica relativa. En: *Actas I Coloq. Intern. Bioestratigrafía Continental del Neógeno Superior-Cuaternario Inferior*. M.T. Alberdi y E. Aguirre (eds.), 31-48.

Adrover, R., Mein, P. y Moissenet, E. (1976). Mise en évidence du Pliocène moyen continental Dans le nord du fossé de Teruel (Espagne). Le gisement de Villalba Alta. *Nouv. Arch. Mus. Hist. Nat. Lyon* 14, 11-14.

Adrover, R., Feist, M., Hugueney, M., Mein, P. y Moissenet, E. (1982). L' âge et la mise en relief de la formation détritique culminante de la Sierra Pelarda (prov. de Teruel, Espagne). *Comptes Rendus de l'Academie des Sciences Paris* 295 (Série II), 231-236.

Agosta, F., Mulch, A., Camberline, P. y Aydin, A. (2008). Geochemical traces of CO2 rich fluid flow along normal faults in central Italy. *Geophysical Journal International* 174, 758-770. doi: 10.1111/j.1365-46X.2008.03792.x

Agustí, J., Cabrera, L., Garcés, M., Krijgsman, W., Oms, O. y Parés, J.M. (2001). A calibrated mammal scale for the Neogene of western Europe; state of the art. *Earth Sci. Rev*. 52, 247-260.

Aitken, M.J. (1998). *An introduction to optical dating: The dating of Quaternary sediments by the use of photon-stimulated luminescence*. Oxford Science Publications, University Press, 267 pp.

Aki, K. (1965). Maximum likelihood estimate of b in the formula logN = a-bM and its confidence limits. *Bull. Earthq. Res. Inst.* 43, 237–239.

Alcalá, L., Alonso-Zarza, A.M., Álvarez, M.A., Azanza, B., Calvo, J.P., Cañaveras. J.C., van Dam, J.A., Garcés, M., Krijgsman, W., van der Meulen, A.J., Morales, J., Peláez, P., Pérez-González, A., Sánchez, S., Sancho, R. y Sanz, E. (2000). El registro sedimentario y faunístico de las cuencas de Calatayud-Daroca y Teruel. Evolución paleoambiental y paleoclimática durante el Neógeno. *Rev. Soc. Geo. Esp.* 13, 323-343.

Allen, C.R., Amand, P., Richter, C.F. y Nordquist, J.M. (1965). Relationship between seismicity and geologic structures in the southern California region. *Bulletin of the Seismological Society of America* 55, 753-797.

Allmendinger, R. W., Cardozo, N. C. y Fisher, D. (2012). *Structural Geology Algorithms: Vectors & Tensors*. Cambridge University Press, England, 289 pp.

Alonso-Zarza, A.M. y Calvo, J.P. (2000). Palustrine sedimentation in an episodically subsiding basin: the Miocene of the Northern Teruel Graben (Spain). *Palaeogeography, Palaeoclimatology, Palaeoecology* 160, 1-21.

Alonso-Zarza, A.M., Meléndez, A., Martín-García, R., Herrero, M.J. y Martín-Pérez, A. (2012). Discriminating between tectonism and climate signatures in palustrine deposits: Lessons from the Miocene of the Teruel Graben, NE Spain. *Earth-Science Reviews* 113 (3), 141-160.

Álvaro, M., Capote, R. y Vegas, R. (1979). Un modelo de evolución geotectónica para la Cadena Celtibérica. *Acta Geol. Hispánica* 14, 172-177.

Anadón, P. y Moissenet, E. (1996). Neogene basins in the Eastern Iberian Range. En: *Tertiary basins of Spain*. P.F. Friend y C.J. Dabrio (eds.). The stratigraphic record of crustal kinematics. Cambridge Univ. Press, Cambridge, 68-76.

Anadón, P., Alcalá, L., Alonso-Zarza, A.M., Calvo, J.P., Ortí, F., Rosell, L. y Sanz-Rubio, E. (2004). Cuencas de la Cordillera Ibérica. En: *Geología de España*. J.A. Vera (ed.). SGE-IGME, Madrid, 562-569.

Anderson, E. (1951). *The dynamics of faulting and dyke formation with application to Britain*. Oliver & Boyd, Edimburgh, 206 pp.

Antoine, P., Lautridou, J.P. y Laurent, M. (2000). Long-term fluvial archives in NW France: response of the Seine and Somme rivers to tectonic movements, climate variations and sea-level changes. *Geomorphology* 33, 183-207.

Aragonés, E., Hernández, A., Aguilar, M.J., Ramírez, J., García-Alcalde, G.L. y Arbizu, M. (1981). *Mapa Geológico de España 1: 50.000, hoja nº 409 (Calatayud)*. IGME, Madrid.

Arlegui, L.E., Simón, J.L., Lisle, R.J. y Orife, T. (2004). El campo de esfuerzos extensional plioceno-cuaternario en el entorno de la falla de Concud (fosa de Jiloca, Teruel). *Geo-Temas* 6 (3), 131-134.

Arlegui, L.E., Simón, J.L., Lisle, R.J. y Orife, T. (2005): Late Pliocene-Pleistocene stress field in the Teruel and Jiloca grabens (eastern Spain): contribution of a new method of stress inversion. *Journal of Structural Geology*, 27(4), 693-705.

Arlegui, L.E., Simón, J.L., Lisle, R.J. y Orife, T. (2006). Analysis of non-striated faults in a recent extensional setting: the Plio-Pleistocene Concud fault (Jiloca graben, eastern Spain). *Journal of Structural Geology* 28(6), 1019-1027.

Arthaud, F. y Matte, P. (1975). Les décrochements tardi-hercyniens du Sud-Ouest de l'Europe. Géométrie et essai de reconstitution des conditions de la déformation. *Tectonophysics* 25(1-2), 139-171.

Banda, E. y Channel, J.E.T. (1979). Evidencia geofísica para un modelo de evolución de las cuencas del Mediterráneo Occidental. *Estud. Geol.* 35, 5–14.

Banda, E. y Santanach, P. (1992). The Valencia Trough (western Mediterranean): an overview. *Tectonophysics* 208, 183–202.

Biasi, G. P. y Wesnousky, S. G. (2016). Steps and gaps in ground ruptures: Empirical bounds on rupture propagation. *Bulletin of the Seismological Society of America* 106(3), 1110-1124.

Bonilla, M.G. (1967). *Historic surface faulting in continental United States and adjacent parts of Mexico*. National Center for Earthquake Research, U.S. Geological Survey and the U.S. Atomic Energy Commission, 36 pp. (comunicado TID-24124).

Bonilla, M.G. (1970). Surface faulting and related effects. En: *Earthquake Engineering*. R.L. Wiegel (ed.). Prentice-Hall, Englewood Cliffs, J.J., 47-74.

Boschi, L., Faccenna, C. y Becker, T.W. (2010). Mantle structure and dynamic topography in the Mediterranean Basin. *Geophys. Res. Lett.* 37(20). doi: 10.1029/ 2010GL045001.

Bott, M.H.P. (1959). The mechanism of oblique-slip faulting. *Geological Magazine* 96, 109-117.

Bratt, S. y Naggy, W. (1991). The LocSAT Program, Science Applications International Corporation (SAIC), San Diego, California.

Cabañas, L., Rivas-Medina, A., Martínez-Solares, J. M., Gaspar-Escribano, J. M., Benito, B., Antón, R. y Ruiz-Barajas, S. (2015). Relationships between Mw and other earthquake size parameters in the Spanish IGN seismic catalog. *Pure and Applied Geophysics* 172(9), 2397-2410.

Calvín-Ballester, P. y Casas, A. (2014). Folded Variscan thrusts in the Herrera unit of the Iberian Range (NE Spain). *Geological Society, London, Special Publications* 394(1): 39-52.

Cande, S.C. y Kent, D.V. (1995). Revised calibration of the geomagnetic polarity timescale for the Late Cretaceous and Cenozoic. *Journal of Geophysical Research* 100, 6093-6095.

Capote, R., Gutiérrez, M., Hernández, A. y Olivé, A. (1981). Movimientos recientes en la fosa del Jiloca (Cordillera Ibérica). *V Reunión Grupo Español de Trabajo del Cuaternario*, Sevilla, 245-257.

Capote, R., Muñoz, J.A., Simón, J.L., Liesa, C.L. y Arlegui, L.E. (2002). Alpine tectonics I: The Alpine system north of the Betic Cordillera. En: *Geology of Spain*. W. Gibbons y T. Moreno (eds.). The Geological Society, London, 367-400.

Cardozo, N. y Allmendinger, R.W. (2013). Spherical projections with OSXStereonet. *Computers & Geosciences* 51, 193-205.

Cartwrigth, J.A., Trudgill, B.D. y Mansfield, C.S. (1995). Fault growth by segment linkage: an explanation for scatter in maximum displacement and trace length data from the Canyonlands Graben of SE Utah. *J. Struct. Geol.* 17, 1319–1326.

Casas A.M., Marcén, M., Calvín, P., Gil, A., Román-Berdiel, T. y Pocoví, A. (2016). Deformación varisca, tardivarisca y alpina en la Rama Aragonesa de la Cordillera Ibérica: propuesta para diferenciación y denominación de estructuras. *Geo-Temas* 16, 495-8.

Casas-Sainz, A.M. y Cortés-Gracia, A. L. (2002). Cenozoic landscape development within the central Iberian Chain, Spain. *Geomorphology* 44(1-2), 19-46.

Casas-Sainz, A.M., Gil-Imaz, A., Simón, J.L., Izquierdo-Llavall, E., Aldega, L., Román-Berdiel, T., Osácar, M.C., Pueyo-Anchuela, Ansón, M., García-Lasanta, C., Corrado, S., Invernizzi, C. y Caricchi, C. (2018). Strain indicators and magnetic fabric in intraplate fault zones: Case study of Daroca thrust, Iberian Chain, Spain. *Tectonophysics* 730, 29-47. doi: 10.1016/j.tecto.2018.02.013

Cesca, S., Grigoli, F., Heimann, S., González, A., Buforn, E., Maghsoudi, S., Blanch, E. y Dahm, T. (2014). The 2013 September–October seismic sequence offshore Spain: a case of seismicity triggered by gas injection? *Geophysical Journal International* 198(2), 941-953.

Chen, R. F., Lin, C. W., Chen, Y. H., He, T. C. y Fei, L. Y. (2015). Detecting and characterizing active thrust fault and deep-seated landslides in dense forest areas of southern Taiwan using airborne LiDAR DEM. *Remote Sensing* 7(11), 15443-15466.

Cohen, K.M., Harper, D.A.T. y Gibbard, P.L. (2022). ICS International Chronostratigraphic Chart. International Commission on Stratigraphy, IUGS. www.stratigraphy.org (visitada el 12/07/2022)

Colomer, M. (1987). *Estudi geològic de la vora Sudoest de la Fossa de Calatayud-Daroca, entre Villafeliche i Calamocha*. Tesis de Licenciatura, Universidad de Barcelona, 99 pp.

Colomer, M. y Santanach, P. (1988). Estructura y evolución del borde sur-occidental de la Fosa de Calatayud-Daroca. *Geogaceta* 4, 29-31.

Cowie, P.A. y Roberts, G.P. (2001). Constraining slip rates and spacings for active normal faults. *J. Struct. Geol.* 23, 1901–1915.

Cowie, P.A. y Scholz, C.H. (1992). Physical explanation for the displacement-length relationship of faults using a post-yield fracture mechanics model. *J. Struct. Geol.* 14, 1133–1148.

Corral, M.B. (2014). Estructura y relaciones tectónica-sedimentación en el contacto del Paleozoico de Villafeliche-Calamocha y la cuenca neógena de Calatayud. Trabajo Fin de Grado, Universidad de Zaragoza, 30 pp.

Cortés, A.L. y Simón, J.L. (1997). Campo de esfuerzos recientes en la fosa de Alfambra-Teruel-Mira. *Actas III Congreso del Grupo Español del Terciario*, Cuenca. En: *Avances en el conocimiento del Terciario Ibérico*. J.P. Calvo y J. Morales (eds.). ECM-CSIC, 65-68.

Cortés, A.L., Casas, A.M. y Simón, J.L. (2000). Coexistencia de varias direcciones de esfuerzos recientes (Mioceno superior-Cuaternario) en la Cordillera Ibérica. *Geo-Temas* 1 (1), 53-56.

Cortés-Gracia, A. L. (1999). *Evolución tectónica reciente de la Cordillera Ibérica, cuenca del Ebro y Pirineo centro-occidental*. Tesis Doctoral, Universidad de Zaragoza, 406 pp.

Cortés-Gracia, A. L. y Casas-Sainz, A.M. (1996). Deformación alpina de zócalo y cobertera en el borde norte de la Cordillera Ibérica (Cubeta de Azuara-Sierra de Herrera). *Revista de la Sociedad Geológica de España* 9(1-2), 51-66.

Cortés-Gracia, A.L. y Casas-Sainz, A.M. (2000). ¿Tiene el sistema de fosas de Teruel origen extensional? *Rev. Soc. Geol. España* 13 (3-4), 445-470.

Cunningham, D., Grebby, S., Tansey, K., Gosar, A. y Kastelic, V. (2006). Application of airborne Lidar to mapping seismogenic faults in forested mountainous terrain, southeastern Alps, Slovenia. *Geophys. Res. Lett.* 33, L20308. doi: 10.10297/ 2006GL027014).

Dawers, N.H. y Anders, M.H. (1995). Displacement-length scaling and fault linkage. *J. Struct. Geol.* 17, 607–614.

De Bruijn, H. (1967). Gliridae, Sciridae, y Eomyidae (Rodentia, Mammalia) miocenos de Calatayud (Zaragoza, España) y su relación con la biostratigrafía del área. *Bol. Geol. Min.* 78, 189-373.

del Olmo, P., Hernández, A., Aragonés, E., Gutiérrez, M., Puigdefábregas, C., Giner, J., Aguilar, M.J., Leal, M.C., Gutiérrez, J.C., Gil, M., Adrover, R., Portero, J.M. y Gabaldón, V. (1983a). *Mapa Geológico de España 1: 50.000, hoja nº 437 (Ateca).* IGME, Madrid.

del Olmo, P., Portero, J.M., Gutiérrez, M., Puigdefábregas, C., Giner, J., Aguilar, M.J., Leal, M.C., Goy, A., Comas, M.J. y Gabaldón, V. (1983b). *Mapa Geológico de España 1: 50.000, hoja nº 464 (Used).* IGME, Madrid.

del Olmo, P., Portero, J.M., Villena, J., Pardo, G., Gutiérrez, M., Puigdefábregas, C., Giner, J., Aguilar, M.J., Leal, M.C., Goy, A., Comas, M.J. y Gabaldón, V. (1983c). *Mapa Geológico de España 1: 50.000, hoja nº 490 (Odón).* IGME, Madrid

Doglioni, C., Gueguen, E., Sabat, F. y Fernández, M. (1997). The western Mediterranean extensional basins and the Alpine orogen. *Terra Nova* 9 (3), 109–112.

Echeverría, M.T. (1988). *Geomorfología de la rama aragonesa de la Cordillera Ibérica entre las depresiones de Calatayud y Almazán y su reborde soriano*. Tesis Doctoral, Universidad de Zaragoza, 969 pp.

Etchecopar, A., Vasseur, G. y Daignières, M. (1981). An inverse problem in microtectonics for the determination of stress tensors from fault striation analysis. *Journal of Structural Geology* 3, 51-65.

Ezquerro, L. (2017). *El sector norte de la cuenca neógena de Teruel: tectónica, clima y sedimentación*. Tesis Doctoral, Universidad de Zaragoza, 452 pp.

Ezquerro, L. y Simón, J.L. (2017). El tránsito compresión-extensión en las cuencas cenozoicas de la Cordillera Ibérica oriental: registro mediante lineaciones de disolución en el norte de la Cuenca de Teruel. *Rev. Soc. Geol. España* 30(2), 9-26.

Ezquerro, L., Moretti, M., Liesa, C. L., Luzón, A., & Simón, J. L. (2015). Seismites from a well core of palustrine deposits as a tool for reconstructing the palaeoseismic history of a fault. *Tectonophysics*, 655, 191-205.

Ezquerro, L., Lafuente, P., Pesquero, MD., Alcalá, L., Arlegui, LE., Liesa, CL., Luque, L., Rodríguez-Pascua, MA. y Simón, JL. (2012). Una cubeta endorreica residual Plio-Pleistocena en la zona de relevo entre las fallas de Concud y Teruel: implicaciones paleogeográficas. *Revista de la Sociedad Geológica de España* 25, 157-75.

Ezquerro, L., Simón, J.L., Luzón, A. y Liesa, C.L. (2020). Segmentation and increasing activity in the Neogene-Quaternary Teruel Basin rift (Spain) revealed by morphotectonic approach. *Journal of Structural Geology* 135 (publicación online). doi: 10.1016/j.jsg.2020.104043

Faccenna, C., Becker, T.W., Lallemand, S., Lagabrielle, Y., Funiciello, F. y Piromallo, C. (2010). Subduction-triggered magmatic pulses: a new class of plumes? *Earth Planet. Sci. Lett.* 299, 54-68. doi: 10.1016/j.epsl.2010.08.012.

Gabaldón, V., Lendínez, A., Ruiz, V., Carls, P., Alvaro, M., Guitérrez, M., Hernández, A., Gómez, J.J., Meléndez, A., Perez, A., Pardo, G., Villena, J., Aguilar, M., Leal, M.C., Comas, M.J., Goy, A., Lago, M., y Conte, J.C. (1989a). *Mapa Geológico de España 1: 50.000, hoja nº 466 (Moyuela).* IGME, Madrid.

Gabaldón, V., Lendínez, A., Ruiz, V., Carls, P., Alvaro, M., Guitérrez, M., Soriano, M.A., Hernández, A., Gómez, J.J., Meléndez, A., Aurell, M., Pérez, A., Pardo, G., Villena, J., Aguilar, M., Leal, M.C., Comas, M.J., Goy, A., Lago, M. y Conte, J.C. (1989b). *Mapa Geológico de España 1: 50.000, hoja nº 439 (Azuara).* IGME, Madrid.

Gabaldón, V., Lendinez, A., Ferreiro, E., Ruiz, V., López de Alda, F., Valverde, M., Lago San José, M., Meléndez, A., Pardo, G., Ardevol, L., Villena, J., González, A., Hernández, A., Alvaro, M., Leal, M. C., Aguilar Tomás, M., Gómez, J. J. y Carls, P. (1991). *Mapa Geológico de España 1: 200.000, hoja nº 40 (Daroca).* IGME, Madrid.

Garcia-Mayordomo, J., Insua-Arevalo, J.M., Martinez-Diaz, J.J., Jimenez-Diaz, A., Martin-Banda, R., Martin-Alfageme, S., Alvarez-Gomez, J.A., Rodriguez-Peces, M., Perez-Lopez, R., Rodriguez-Pascua, M.A., Masana, E., Perea, H., Martin-Gonzalez, F., Giner-Robles, J., Nemser, E.S., Cabral, J., the QAFI Compilers Working Group (2012). The quaternary faults database of iberia (QAFI v.2.0). *Journal of Iberian Geology*, 38 (1), 285– 302.

Gawthorpe, R. y Leeder, M.R. (2000). Tectono-sedimentary evolution of active extensional basins. *Basin Research* 12, 195–218.

GFZ, German Research Centre for Geosciences, y GEMPA GmbH (2008). The SeisComP seismological software package. *GFZ Data Services*. doi: 10.5880/GFZ.2.4.2020.003

Giachetta, E., Molin, P., Scotti, V. N. y Faccenna, C. (2015). Plio-Quaternary uplift of the Iberian Chain (central-eastern Spain) from landscape evolution experiments and river profile modeling. *Geomorphology* 246, 48-67.

Giner-Robles, J.L., Silva, P.G., Elez, J., Rodríguez-Pascua, M.A., Bardaji, T., Perucha, M.A., Pérez-López, R., Roquero, E., Huerta, P. y Rodríguez-Escudero, E. (2017). Análisis preliminar de los efectos ambientales del terremoto de Ademuz de junio de 1656 (Valencia, España). *IX Reunião do Quaternário Ibérico*, Faro, 133-136.

Giner-Robles, J.L., Elez, J., Silva, P.G., Pérez-López, R., Bardaji, T., Rodríguez-Pascua, M.A., Sánchez-Sánchez, Y. y Roquero, E. (2022). Los terremotos de Ademuz del 7 de junio de 1656 y del 10 de marzo de 2006: ¿una fuente sísmica común? *Resúmenes IV Reunión Ibérica sobre Fallas Activas y Paleosismología*, Teruel, Universidad de Zaragoza, 85-88.

Godoy, A., Ramírez, J.I., Olivé, A., Moissenet, E., Aznar, J.M., Aragonés, E., Aguilar, M.J., Ramírez del Pozo, J., Leal, M.C., Jerez Mir, L., Adrover, R., Goy, A., Comas, M.J., Alberdi, M.T., Giner, J., Gutiérrez Elorza, M., Portero, J.M. y Gabaldón, V. (1983a). *Mapa Geológico de España 1: 50.000, hoja nº 567 (Teruel).* IGME, Madrid.

Godoy, A., Moissenet, E., Ramírez, J.I., Olivé, A., Aznar, J.M., Jerez, L., Aragonés, E., Aguilar, M.J., Ramírez del Pozo, J., Leal, M.C., Adrover, R., Alberdi, M.T., Giner, J., Gutiérrez, M., Portero, J.M. y Gabaldón, V. (1983b). *Mapa Geológico de España 1: 50.000, hoja nº 542 (Alfambra).* IGME, Madrid.

Gracia, F.J. (1990). *Geomorfología de la Región de Gallocanta (Cordillera Ibérica Central).* Tesis Doctoral, Universidad de Zaragoza, 660 pp.

Gracia, F.J. (1992). Tectónica pliocena de la Fosa de Daroca (prov. de Zaragoza). *Geogaceta* 11, 127-129.

Gracia, F.J. (2014). Gallocanta Saline Lake, Iberian Chain. En: *Landscapes and Landforms of Spain*. F. Gutiérrez y M. Gutiérrez (eds.). Springer Science, Business Media, Dordrecht, 137-144.

Gracia, F.J. (2020). Relief Evolution of the Iberian Chain. En: *The Geology of Iberia: A Geodynamic Approach*, Vol. 5: Active Processes: Seismicity, Active Faulting and Relief. C. Quesada y J. T. Oliveira (eds.). Springer, Switzerland, 97-102.

Gracia, F.J., Gutiérrez, M. y Leránoz, B. (1988). Las superficies de erosión neógenas en el sector central de la Cordillera Ibérica. *Revista de la Sociedad Geológica de España* 1, 135–42.

Gracia, F.J., Gutiérrez, M. y Simón, J.L. (1989). *Memoria y Mapa Neotectónico y Sismotectónico de España 1: 200.000, hoja nº 40 (Daroca)*. IGME-IGN, Madrid, 37 p.

Gracia, F.J., Gutiérrez, F. y Gutiérrez, M. (2002). Origin and evolution of Gallocanta polje. *Zeitschrift für Geomorph.* 46, 245-262.

Gracia, FJ., Gutiérrez, F. y Gutiérrez, M. (2003). The Jiloca karst polje-tectonic graben (Iberian Range, NE Spain). *Geomorphology* 52, 215-231

Gray, H.J., Mahan, S.A., Rittenour, T. y Nelson, M.S. (2015). Guide to luminescence dating techniques and their application for paleoseismic research in Western States Seismic Policy Council: Basin and Range Province. *Seismic Hazards Summit III, Utah Geological Survey Miscellaneous Publication*, Proceeding Volume, 15-5.

Green, A., Gross, R., Holliger, K., Horstmeyer, H. y Baldwin, J. (2003). Results of 3-D georadar surveying and trenching the San Andreas fault near its northern landward limit. *Tectonophysics* 368(1-4), 7-23.

Guimerà, J. (1988). *Estudi structural de l'enllaç entre la Serralada Iberica y la Serralada Costanera Catalana*. Tesis Doctoral, Universidad de Barcelona, 600 pp.

Guimerà, J. (2013). El cabalgamiento de Daroca. En: *XLVII Curso de Geología Práctica, La Orogenia Alpina en la Cordillera Ibérica*. J.L. Simón y C.L. Liesa (eds.). Universidad de Verano de Teruel, Teruel, 38-42.

Guimerà, J., González, A. y Pérez García, A. (1990). Evolución del cabalgamiento de la Muela de Montalbán (Cordillera Ibérica, Teruel). *Geogaceta* 8, 47-49.

Gutenberg, B. y Richter, C. F. (1944). Frequency of earthquakes in California. *Bull. Seismol. Soc. Am.* 34, 185–188.

Gutiérrez, F. (1996). Gypsum karstification induced subsidence: effects on alluvial systems and derived geohazards (Calatayud Graben, Iberian Range, Spain). *Geomorphology* 16, 277–293.

Gutiérrez, F. (1998). *Fenómenos de subsidencia por disolución de formaciones evaporíticas en las fosas neógenas de Teruel y Calatayud*. Tesis Doctoral, Universidad de Zaragoza, 569 pp.

Gutiérrez, F., Gracia, F.J. y Gutiérrez, M. (1996). Consideraciones sobre el final del relleno endorreico de las fosas de Calatayud y Teruel y su paso al exorreismo: implicaciones morfoestratigráficas y estructurales. *IV Reunión de Geomorfología*. A. Grandal y J. Pagés (eds.). Sociedad Española de Geomorfología, O Castro, A Coruña, 23-43

Gutiérrez, F., Gutiérrez, M., Gracia, F. J., McCalpin, J. P., Lucha, P. y Guerrero, J. (2008). Plio-Quaternary extensional seismotectonics and drainage network development in the central sector of the Iberian Chain (NE Spain). *Geomorphology* 102(1), 21-42.

Gutiérrez, F., Masana, E., González, A., Guerrero, J., Lucha, P. y McCalpin, J.P. (2009). Late Quaternary paleoseismic evidence on the Munébrega Half-graben fault (Iberian Range, Spain). *International Journal of Earth Sciences* 98, 1691-1703. doi: 10.1007/s00531-008-0319-y.

Gutiérrez, F., Gracia, F.J., Gutiérrez, M., Lucha, P., Guerrero, J., Carbonel, D. y Galve, J.P. (2012). A review on Quaternary tectonic and nontectonic faults in the central sector of the Iberian Chain, NE Spain. *J. Iber. Geol.* 38 (1), 145.

Gutiérrez, F., Lucha, P. y Jordá, L. (2013). The Río Grío depression (Iberian Chain, NE Spain). Neotectonic graben vs. Fluvial valley. *Cuaternario y Geomorfología* 27 (3-4), 5-32.

Gutiérrez, F., Carbonel, D., Sevil, J., Moreno, D., Linares, R., Comas, X., Zarroca, M., Roqué, C. y McCalpin, J.P. (2020a). Neotectonics and late Holocene paleoseismic evidence in the Plio-Quaternary Daroca half-graben, Iberian Chain, NE Spain. Implications for fault source characterization. *J. Struct. Geol.* 131, 103933. doi: 10.1016/j.jsg.2019.103933

Gutiérrez, F., Moreno, D., López, G. I., Jiménez, F., del Val, M., Alonso, M. J., Martínez-Pillado, V., Guzmán, O., Martínez, D. y Carbonel, D. (2020b). Revisiting the slip rate of Quaternary faults in the Iberian Chain, NE Spain. Geomorphic and seismic-hazard implications. *Geomorphology* 363, 107233.

Gutiérrez, M. y Peña-Monné, J.L. (1976). Glacis y terrazas en el curso medio del río Alfambra (Provincia de Teruel). *Boletín Geológico y Minero* 87-6, 561-570.

Gutiérrez, M., Peña, J.L. y Simón, J.L. (1989). *Memoria y Mapa Neotectónico y Sismotectónico de España 1: 200.000, hoja nº 47 (Teruel)*. IGME-IGN, Madrid, 54 p.

Gutiérrez, M., Peña, J.L., Rodríguez, J. y Simón, J.L. (1983a). Criterios geomorfológicos aplicados al estudio de la neotectónica en áreas continentales (ejemplos en la Cadena Ibérica, Depresión del Ebro y Pirineos). *Primeras jornadas sobre neotectónica y su aplicación al análisis de riesgos de emplazamientos energéticos e industriales*. J.E.N., Madrid, 158–213.

Gutiérrez, M., Peña, J.L. y Simón, J.L. (1983b). Los valles tectónicos recientes de Rubielos de la Cérida (Teruel). *Actas VI Reunión Nacional Grupo Español de Trabajo del Cuaternario*, Vigo-Santiago de Compostela, 449–459.

Gutiérrez-Elorza, M. y Gracia, FJ. (1997). Environmental interpretation and evolution of the Tertiary erosion surfaces in the Iberian Range (Spain). En: *Palaeosurfaces: Recognition, Reconstruction and Palaeoenvironmental Interpretation*. M. Widdowson (ed.). Geological Society Special Publication 120, 147-158

Hanks, T.C. y Kanamori, H. (1979). A moment magnitude scale. *J. Geophys. Res.* 84, 2348–2350.

Hernández, A., Olivé, A., Moissenet, E., Carls, P., Sdzuy, K., Kolb, S., Gutiérrez, M., Portero, J.M., Puigdefábregas, C., Giner, J., Aguilar, M.J., Leal, M.C., Liñán, E., Gutiérrez, J.C., Gil., M.D., Adrover, R. y Gabaldón, V. (1983a). *Mapa Geológico de España 1: 50.000, hoja nº 465 (Daroca)*. IGME, Madrid.

Hernández, A., Olivé, A., Moissenet, E., Pardo, G., Villena, J., Portero, J.M., Gutiérrez, M., Puigdefábregas, C., Giner, J., Aguilar, M.J., Leal, M.C., Gutiérrez, J.C., Gil., M.D., Adrover, R. y Gabaldón, V. (1983b). *Mapa Geológico de España 1: 50.000, hoja nº 491 (Calamocha)*. IGME, Madrid.

Hernández, A., Ramírez, J.I., Olivé, A., Riba, O., Aragonés, E., Aguilar, M.J., Ramírez del Pozo, J., Leal, M.C., Giner, J., Gutiérrez, M., Goy, A., Comas, M.J., Gutiérrez, J.L., Portero, J.M. y Gabaldón, V. (1983c). *Mapa Geológico de España 1: 50.000, hoja 566 (Cella)*. IGME, Madrid.

Hernández, A., Ramírez, J.I., Navarro, J.J., Cortes, A.L., Rodríguez, R., Babiano, F., Gómez, D., Ramírez, J., Cuenca, G., Pozo, M. y Casas, J. (2005). *Mapa Geológico de España 1: 50.000, hoja nº 411 (Longares)*. IGME, Madrid.

Herraiz, M., De Vicente, G., Lindo-Ñaupari, R., Giner, J., Simón, J.L., González-Casado, J.M., Vadillo, O., Rodríguez-Pascua, M.A., Cicuéndez, J.L., Casas, A., Cabañas, L., Rincón, P., Cortés, A.L., Ramírez, M. y Lucini M. (2000). The recent (upper Miocene to Quaternary) nd present tectonic stress distributions in the Iberian Peninsula. *Tectonics* 19, 762-786.

Hilgen, F.J., Lourens, L.J., Van Dam, J.A., 2012. *The Neogene Period en The Geologic Time Scale*. F.M. Gradstein, J.G. Ogg., M.D. Schimtz y G.M. Ogg (eds.). Elsevier, Amsterdam, 923-978.

Huntley, D. J., Godfrey-Smith, D.I. y Thewalt, M.L.W. (1985). Optical dating of sediments. *Nature* 313, 105-107.

IGME, Instituto Geológico y Minero de España (2022). QAFI v.4, Quaternary Active Faults Database of Iberia: https:// info.igme.es/QAFI (visitada en julio del 2022).

IGME y ENRESA (1998). *Mapa Neotectónico de España 1: 1.000.000*. Madrid, 99 p.

IGN, Instituto Geográfico Nacional (2022). Servicio de Información Sísmica del Instituto Geográfico Nacional. https:// www.ign.es/web/ign/portal/sis-catalogo-terremotos (visitada en julio del 2022).

IGN (2015). *Mapa de Peligrosidad Sísmica de España 1: 2.250.000*. https://www.ign.es/web/mapas-sismicidad (visitada en septiembre del 2022).

IGN-UPM (2013). *Actualización de Mapas de Peligrosidad Sísmica de España 2012*. Centro Nacional de Información Geográfica, Madrid, 267 pp.

Julivert, M. (1954). Observaciones sobre la tectónica de la Depresión de Calatayud. Arrahona, Museo de Sabadell, 3-18.

Lafuente, P. (2011). *Tectónica activa y paleosismicidad de la falla de Concud (Cordillera Ibérica central)*. Tesis Doctoral, Universidad de Zaragoza, 272 pp.

Lafuente, P., Rodríguez-Pascua, M.A., Simón, J.L., Arlegui, L.E. y Liesa, C.L. (2008). Sismitas en depósitos pliocenos y pleistocenos de la fosa de Teruel. *Revista de la Sociedad Geológica de España* 21, 133-149.

Lafuente, P., Arlegui, L.E., Liesa, C.L. y Simón, J.L. (2011a). Paleoseismological analysis of an intraplate extensional structure: the Concud fault (Iberian Chain, Eastern Spain). *International Journal of Earth Sciences* 100 (7), 1713-1732.

Lafuente, P., Arlegui, L.E., Casado, I., Ezquerro, L., Liesa, C.L., Pueyo, Ó. y Simón, J.L. (2011b). Geometría y cinemática de la zona de relevo entre las fallas neógeno-cuaternarias de Concud y Teruel (Cordillera Ibérica). *Rev. Soc. Geol. Esp.* 24,117-132.

Lafuente, P., Arlegui, L. E., Liesa, C. L., Pueyo, Ó. y Simón, J. L. (2014). Spatial and temporal variation of palaeoseismic activity at an intraplate, historically quiescent structure: The Concud fault (Iberian Chain, Spain). *Tectonophysics* 632, 167-187.

Lensen, G. J. (1976). *Earth deformation in relation to town planning in New Zealand*. New Zealand Geological Survey, 17 pp. (comunicado).

Leonard, M. (2010). Earthquake fault scaling: Self-consistent relating of rupture length, width, average displacement, and moment release. *Bulletin of the Seismological Society of America* 100 (5A), 1971-1988. doi: 10.1785/0120090189

Liesa, C.L. (2000). *Fracturación y campos de esfuerzos compresivos alpinos en la Cordillera Ibérica y el NE peninsular*. Tesis Doctoral, Universidad de Zaragoza, 760 pp.

Liesa, C.L. (2011). Evolución de campos de esfuerzos en la Sierra del Pobo (Cordillera Ibérica, España). *Rev. Soc. Geol. España* 24, 49-68.

Liesa, C.L. y Simón, J.L. (2009). Evolution of intraplate stress fields under multiple compressions: The case of the Iberian Chain (NE Spain). *Tectonophysics* 474, 144-159.

Liesa, C.L., Simón, J. L., Ezquerro, L., Arlegui, L. E. y Luzón, A. (2019). Stress evolution and structural inheritance controlling an intracontinental extensional basin: The central-northern sector of the Neogene Teruel Basin. *Journal of Structural Geology* 118, 362-376.

Liesa, C.L., Corral, M.B., Arlegui, L.E., Peiro, A. y Simón, J.L. (2021). Inversión tectónica negativa y estructuración de la zona de relevo entre las fallas normales plio-cuaternarias de Calamocha y Daroca. *X Congreso de Geología de España*, Sociedad Geológica de España, Vitoria, Spain.

Lozano, M.V. (1988). *Estudio geomorfológico de las Sierras de Gúdar (Provincia de Teruel)*. Tesis Doctoral, Universidad de Zaragoza, 804 pp.

Maillard, A. y Mauffret, A. (1999). Crustal structure and riftogenesis of the Valencia Trough (north-western Mediterranean Sea). *Basin Research* 11(4), 357-379.

Machette, M. N. (2000). Active, capable, and potentially active faults—a paleoseismic perspective. *Journal of Geodynamics* 29(3-5), 387-392.

Manzocchi, T., Childs, C. y Walsh, J. (2010). Faults and fault properties in hydrocarbon flow models. *Geofluids* 10, 94-113. doi: 10.1111/j.1468-8123.2010.00283.x

Marcén, M. (2020). *Fábricas Magnéticas aplicadas al estudio de Zonas de Falla: Ejemplos de la Península Ibérica*. Tesis Doctoral, Universidad de Zaragoza, 301 pp.

Marcén, M. y Román-Berdiel, M.T. (2015). Geometría y cinemática de la zona de falla de Río Grío: evidencias de transpresión alpina en la Cadena Ibérica. *Geogaceta* 58, 180-3.

Marín, A. (1932). Sondeos de Investigación de sales potásicas. Boletín de Sondeos. Tomo III. IGME, 115.

Martín, M., Canerot, J., Del Pan, T. y Leyva, F. (1979). *Mapa Geológico de España 1: 50.000, hoja nº 517 (Argente)*. IGME, Madrid.

Martín, M., Canerot, J., Linares-Rivas, A., Grambast, L., Quintero, I., Mansilla, H., De las Heras, A., Fernández, M.C., Leyva, F. y Martínez, J.U. (1977). *Mapa Geológico de España 1: 50.000, hoja nº 492 (Segura de los Baños)*. IGME, Madrid.

Martín-Bello, L., Arlegui, L.E., Ezquerro, L., Liesa, C.L. y Simón, J.L. (2014). La falla de Calamocha (fosa del Jiloca, Cordillera Ibérica): estructura y actividad pleistocena. *Resúmenes II Reunión Ibérica sobre Fallas Activas y Paleosismología*, Lorca (en prensa).

Martínez, J.M. y Cabañas, L. (2013). *Peligrosidad sísmica en el emplazamiento del nuevo hospital general de Teruel*. IGN, informe inédito al Gobierno de Aragón, 15 p.

Masana, E. (1995). *L'activitat neotectonica ales Cadenes Costarenes Catalanes*. Tesis Doctoral, Universidad de Barcelona.

Masana, E., Villamarín A., J., Sanchez-Caban~ero, J., Plaza, J. y Santanach, P. (2001). Seismogenic faulting in an area of lowseismic activity: Paleoseismicity of the El Camp fault (northeast Spain). *Geol. Mijnbouw/Netherlands J. Geosciences* 80, 29–41.

McCalpin, J.P. (2009). *Paleoseismology*, 2ª Edición. Academic Press. International Geophysics Series, 613 pp.

McCalpin, J.P. y Nelson, A.R. (2009). Introduction to Paleoseismology. En: *Paleoseismology*, 2ª Edición (J.P. McCalpin ed.), Academic Press, International Geophysics Series, 1-27.

Meghraoui, M. y Crone, A. J. (2001). Earthquakes and their preservation in the geological record. *Journal of Seismology* 5(3), 281-285.

Mignan, A., Woessner, J. (2012). Estimating the magnitude of completeness for earthquake catalogs. CORSSA (Community Online Resource for Statistical Seismicity Analysis), 1–45.

Moissenet, E., Adrover, R. y Aguirre, E. (1974). Fosa de Teruel. *Col. Int. Bioestrat. Cont. Neog. Sup. Cuat. Inf*. Libro Guía, 49-68.

Moissenet, E. (1980). Relief et déformations récentes: trois transversales dans les fossés internes des chaînes ibériques orientales. *Revue géographique des Pyrénées et du Sud-Ouest, Sud-Ouest Européen* 51(3), 315-44.

Moissenet, E. (1982). Le Villafranchien de la région de Teruel (Espagne), Stratigraphie, Déformations, Milieux. *Collòque "Le Villafranchien Méditerranéen"*, Lille.

Moissenet, E. (1983). Aspectos de la neotectónica en la fosa de Teruel. En: *Libro Jubilar*, J.M. Ríos. *Geología de España*, Tomo 2. Comba J.A. (ed.). IGME, Madrid, 427-446.

Moissenet, E. (1985). Le Quaternaire moyen alluvial du fossé de Teruel (Espagne). *Physio-Géo*. 14/15, 61-78.

Moissenet, E. (1993). L'age et les déformations des terrases alluviales du Fossé de Teruel. En: *El Cuaternario de España y Portugal*, IGME-AEQUA, Madrid, 1, 267-279.

Moissenet, E., Adrover, R. y Aguirre, E. (1974). Fosa de Teruel. *Col. Int. Bioestrat. Cont. Neog. Sup. Cuat. Inf*. Libro Guía, 49-68.

Moreno, D., Gutiérrez, F., del Val, M., Carbonel, D., Jiménez, F., Alonso, M. J., Martínez-Pillado, V., Guzmán, O., López, G.I. y Martínez, D. (2021). A multi-method dating approach to reassess the geochronology of faulted Quaternary deposits in the central sector of the Iberian Chain (NE Spain). *Quaternary Geochronology*, 65, 101185.

Nichols, D.R. y Buchanan-Banks, J.M. (1974). *Seismic hazards and land-use planning*. U.S. Geo. Survey, 33 pp. (comunicado 690).

NRC, Nuclear Regulatory Commission (1997). *Identification and Characterization of Seismic Sources and Determination of Safe Shutdown Earthquake Ground Motions*. Regulatory Guide nº 1.165, U.S. Office of Nuclear Regulatory Research, Washington.

Ogg, J.G. (2012). Chapter 5: geomagnetic polarity time scale. En: *The Geologic Time Scale*. F.M.Gradstein, J.G. Ogg, M.D. Schmitz y G.M. Ogg (eds.). Elsevier, Amsterdam.

Olivé, A., del Olmo, P., Portero, J.M., Carls, P., Sdzuy, K., Collande, C.V., Kolb, S., Teyssen, T., Gutiérrez, M., Puigdefábregas, C., Giner, J., Aguilar, M.J., Leal, M.C., Goy, A., Comas, M.J., Adrover, R. y Gabaldón, V. (1983a). *Mapa Geológico de España 1: 50.000, hoja nº 438 (Paniza)*. IGME, Madrid.

Olivé, A., Hernández, A., Moissenet, E., Pardo, G., Villena, J., Gutiérrez, M., Puigdefábregas, C., Giner, J., Aguilar, M.J., Leal, M.C., Goy, A., Comas, M.J., Adrover, R., Portero, J.M. y Gabaldón, V. (1983b). *Mapa Geológico de España 1: 50.000, hoja nº 516 (Monreal del Campo)*. IGME, Madrid.

Pailhé, P. (1984). *La Chaîne Ibérique Orientale. Étude géomorphologique*. Tesis Doctoral, Universidad de Bordeaux, 682 pp.

Pantosti, D., Schwartz, D. P. y Valensise, G. (1993). Paleoseismology along the 1980 surface rupture of the Irpina fault; implications for earthquake recurrence in the southern Apennines, Italy. *Journal of Geophysical Research* 98, 6561–6577.

Pavlides, S. y Caputo, R. (2004). Magnitude versus faults' surface parameters: quantitative relationships from the Aegean Region. *Tectonophysics* 380, 159–188.

Peacock, D.C.P. y Sanderson, D.J. (1991). Displacements, segment linkage and relay ramps in normal fault zones. *J. Struct. Geol*. 13, 721–733.

Peacock, D.C.P. y Sanderson, D.J. (1994). Geometry and development of relay ramps in normal fault systems. *Bull. Am. Ass. Petrol. Geol.* 78, 147-165.

Peiro, A. y Simón, J.L. (2021). The Río Grío-Pancrudo Fault Zone (central Iberian Chain, Spain): recent extensional activity revealed by drainage reversal. *Geo. Magazine* 159(1), 21-36. doi:10.1017/S0016756821000790

Peiro, A., Simón, J.L. y Liesa, C.L. (2017). New evidence of recent fracturing at the relay zone between the Concud and Teruel faults (eastern Iberian Chain). *Geogaceta* 62, 31–34.

Peña, J.L. (1981). Las acumulaciones cuaternarias de la confluencia de los ríos Alfambra y Guadalaviar en las cercanías de Teruel. En: *Actas VII Col. Geografía*. Pamplona, 1-13.

Peña, J.L., Sánchez, M. y Simón, J.L. (1981). Algunos aspectos de la tectónica cuaternaria en el margen oriental de la fosa del Alfambra-Teruel. *Teruel* 66, 31-48.

Peña, J.L., Gutiérrez, M., Ibáñez, M.J., Lozano, M.V., Rodríguez, J., Sánchez-Fabre, M., Simón, J.L., Soriano, M.A. y Yetano, L.M. (1984). *Geomorfología de la provincia de Teruel*. Instituto de Estudios Turolenses, 149 pp.

Peña-Monné, J. L., Cunha, P. P., Sampietro-Vattuone, M. M., Bridgland, D. R., Murray, A. S. y Buylaert, J. P. (2022). The connections between river terraces and slope deposits as paleoclimate proxies: the Guadalaviar-Turia sequence (Eastern, Iberia Chain, Spain). *Global and Planetary Change*, 103728. doi: 10.1016/ j.gloplacha.2021.103728

Perea, H. (2006). *Falles actives i perillositat sísmica al marge nord-occidental del solc de València*. Tesis Doctoral, Universidad de Barcelona, 317 pp.

Perea, H., Masana, E. y Santanach, P. (2006). A pragmatic approach to seismic parameters in a region with low Seismicity: the case of eastern Iberia. *Nat. Hazards* 39, 451–477.

Perea, H., Masana, E. y Santanach, P. (2012). An active zone characterized by slow normal faults, the northwestern margin of the València trough (NE Iberia): a review. *Journal of Iberian Geology* 38 (1), 31-52.

Pérez, A., Azanza, B, Cuenca, G., Pardo, G. y Villena, J. (1985). Nuevos datos estratigráficos y paleontológicos sobre el Terciario del borde meridional de la Depresión del Ebro (Provincia de Zaragoza). Estudios Geológicos 41, 405-411

Piromallo, C. y Morelli, A. (2003). P-wave tomography of the mantle under the Alpine- Mediterranean area. *J. Geophys. Res*. 108. doi: 10.1029/2002JB001757.

Pueyo, Ó., Lafuente, P., Arlegui, L., Liesa, C. L. y Simón, J. L. (2016). Geophysical characterization of buried active faults: the Concud Fault (Iberian Chain, NE Spain). *International Journal of Earth Sciences* 105(8), 2221-2239.

Ramírez, J.I., Olivé, A., Moissenet, E., Aragonés, E., Ramírez, J., Leal, M.C., Aguilar, M.J., Adrover, R., Giner, J., Gutiérrez, J.C., Goy, A., Comas, M.J., Portero, J.M. y Gabaldón, V. (1983). *Mapa Geológico de España 1: 50.000, hoja nº 541 (Santa Eulalia)*. IGME, Madrid.

Ramsay, J.G. (1967). *Folding and fracturing of rocks*. McGraw-Hill, Nueva York, 588 pp.

Roca, E. (1992). *L'estructura de la conca Catalano-Balear: paper de la compressió i de la distensió en la seva gènesi*. Tesis Doctoral, Universidad de Barcelona, 330 pp.

Roca, E. y Guimerà, J. (1992). The Neogene structure of the eastern Iberian margin: structural constraints on the crustal evolution of the Valencia trough (western Mediterranean). *Tectonophysics* 203, 203-218.

Rubio, J.C. y Simón, JL. (2007). Tectonic subsidence vs. erosional lowering in a controversial intramontane depression: the Jiloca basin (Iberian Chain, Spain). *Geological Magazine* 144, 1-15.

Rubio, J.C., Simón, J.L. y Soriano, M.A. (2007). Interacting tectonics, hydrogeology and karst processes in an intramontane basin: the Jiloca graben (NE Spain). *Hydrogeology Journal* 15(8), 1565-1576.

Rydelek, P. A., y Sacks, I. S. (1989). Testing the completeness of earthquake catalogs and the hypothesis of self-similarity. *Nature* 337(6204), 251–253. doi: 10.1038/337251a0

Salas, R. y Casas, A. (1993). Mesozoic extensional tectonics, stratigraphy and crustal evolution during the Alpine cycle of the eastern Iberian Chain. *Tectonophysics* 228, 33-55.

Santonja, M., Pérez-González, A., Domínguez-Rodrigo, M., Panera, J., Rubio-Jara, S., Sesé, C., Soto, E., Arnold, L.J., Duval, M., Demuro, M., Ortiz, J.E., de Torres, T., Mercier, N., Barba, R. y Yravedra, J. (2014). The Middle Paleolithic site of Cuesta de la Bajada (Teruel, Spain): a perspective on the Acheulean and Middle Paleolithic technocomplexes in Europe. *Journal of Archaeological Science* 49, 556-571.

Sanz-Rubio, E. (1999). *Análisis de los sistemas deposicionales carbonáticos y evaporíticos del Neógeno de la Cuenca de Calatayud (provincia de Zaragoza)*. Tesis Doctoral, Universidad Complutense de Madrid, 579 pp.

Sanz-Rubio, E., Sánchez-Moral, S., Cañaveras, J. C., Abdul-Aziz, H., Calvo Sorando, J. P., Cuezva, S., Mazo, A. V., Rouchy, J. M., Sesé, C., y Van Dam, J. (2003). Síntesis de la cronoestratigrafía y evolución sedimentaria de los sistemas lacustres evaporíticos y carbonatados neógenos de la Cuenca de Calatayud-Montalbán. *Estudios Geológicos* 59(1-4), 83-105.

Schorlemmer, D., Wiemer, S. y Wyss, M. (2005). Variations in earthquake-size distribution across different stress regimes. *Nature* 437(7058), 539–542.

Scotti, V.N., Molin, P., Faccenna, C., Soligo, M. y Casas-Sainz, A.M. (2014). The influence of surface and tectonic processes on landscape evolution of the Iberian Chain (Spain): Quantitative geomorphological analysis and geochronology. *Geomorphology* 206, 37-57. doi: 10.1016/j.geomorph.2013.09.017.

Sesé, C. (2003). Paleontología y bioestratigrafía del Mioceno continental de la Cuenca de Calatayud (Zaragoza): Nuevos yacimientos de micromamíferos. *Estudios Geológicos* 59(1-4), 249-264.

Slemmons, D.B. y dePolo, C. M. (1986). Evaluation of active faulting and associated hazards. En: *Active Tectonics*. R.E. Wallace (ed.). Washington D.C., National Academy Press, 45-62.

Slemmons, D.B. y McKinney, R. (1977). *Definition of "Active Fault"*. U.S. Army Engineer Waterways Experiment Station Soil and Pavements Laboratory, Mississippi, 22 pp. (comunicado)

Sieh, K.E. (1981). A review of geological evidence for recurrence times for large earthquakes. En: *Earthquakes Prediction, An International Review*. D. W. Simpson y P.G. Richards (eds.). Am. Geophys. Union, Washington, DC. Maurice Ewing Ser. 4, 181-207.

Simón, J.L. (1982). *Compresión y distensión alpinas en la Cadena Ibérica Oriental.* Tesis Doctoral, Universidad de Zaragoza, 255 pp.

Simón, J.L. (1983). Tectónica y neotectónica del sistema de fosas de Teruel. *Teruel* 69, 21-97.

Simón, J.L. (1986). Analysis of a gradual change in stress regime (example from the Eastern Iberian Chain, Spain). *Tectonophysics* 124, 37-53.

Simón, J.L. (1989). Late Cenozoic stress field and fracturing in the Iberian Chain and Ebro Basin (Spain). *Journal of Structural. Geology* 11, 285-294.

Simón, J. L. (2019). Evolución de paleoesfuerzos registrada en la cuenca cenozoica de Montalbán (Teruel, Cordillera Ibérica). *Geogaceta* 66, 111-114.

Simón, J.L. y Liesa, C.L. (2011). Incremental slip story of a thrust: diverse transport directions and internal folding of the Utrillas thrust sheet (NE Iberian Chain, Spain). *Geological Society of London*, Special Publications 349, 77-97.

Simón, J.L. y Soriano, M.A. (1993). La falla de Concud (Teruel): actividad cuaternaria y régimen de esfuerzos asociado. En: *El Cuaternario en España y Portugal, Actas 2ª Reunión del Cuaternario Ibérico*, 2, 729-737.

Simón, J.L., Pérez, A. y Calvo, A. (1983). Morfogénesis y neotectónica en el sistema de fosas del Maestrat (Provincia de Castellón). *Estudios Geológicos* 39, 167-177.

Simón, J.L., Peña, J.L. y Lozano, M.V. (1989). *Memoria y Mapa Neotectónico y Sismotectónico de España 1: 200.000, hoja nº 48 (Vinaroz)*. IGME-IGN, Madrid, 45 p.

Simón, J.L., Lafuente, P., Arlegui, L.E., Liesa, C.L. y Soriano, M.A. (2005). Caracterización paleosísmica preliminar de la falla de Concud (fosa del Jiloca, Teruel). *Geogaceta* 38, 63-66.

Simón, J.L., Arlegui, L.E., Lafuente, P. y Liesa, C.L. (2012). Active extensional faults in the central-eastern Iberian Chain, Spain. *Journal of Iberian Geology* 38 (1), 127-144.

Simón, J.L., Pérez-Cueva, A.J. y Calvo-Cases, A. (2013). Tectonic beheading of fluvial valleys in the Maestrat grabens (eastern Spain): Insights into slip rates of Pleistocene extensional faults. *Tectonophysics* 593, 73-84.

Simón, J.L., Arlegui, L.E., Ezquerro, L., Lafuente, P. y Liesa, C.L. (2014). Aproximación a la peligrosidad sísmica en la ciudad de Teruel asociada a la falla de Concud (NE España). *Geogaceta* 5, 7–10.

Simón, J. L., Arlegui, L. E., Ezquerro, L., Lafuente, P., Liesa, C. L. y Luzón, A. (2016). Enhanced palaeoseismic succession at the Concud Fault (Iberian Chain, Spain): new insights for seismic hazard assessment. *Natural Ha*zards 80(3), 1967-1993.

Simón, J. L., Arlegui, L. E., Ezquerro, L., Lafuente, P., Liesa, C. L. y Luzón, A. (2017). Assessing interaction of active extensional faults from structural and paleoseismological analysis: The Teruel and Concud faults (eastern Spain). *Journal of Structural Geology* 103, 100-119.

Simón, J. L., Ezquerro, L., Arlegui, L. E., Liesa, C. L., Luzón, A., Medialdea, A., García, A. y Zarazaga, D. (2019). Role of transverse structures in paleoseismicity and drainage rearrangement in rift systems: the case of the Valdecebro fault zone (Teruel graben, eastern Spain). *International Journal of Earth Sciences* 108(5), 1429-1449.

Simón, J.L., Casas-Sainz, A.M. y Gil-Imaz, A. (2021). Controversial epiglyptic thrust sheets: The case of the Daroca Thrust (Iberian Chain, Spain). *Journal of Structural Geology* 145, 104298. doi: 10.1016/j.jsg.2021.104298

Simón, J.L., Peiro, A., Arlegui, L.E., Ezquerro, L., García-Lacosta, A.I., Lafuente, P., Liesa, C.L., Luzón, A., Martín-Bello, L., Pueyo, O. y Soriano, M.A. (2022). Actividad plio-cuaternaria de fallas en el sistema extensional Teruel-Jiloca-Calatayud (Cordillera Ibérica central). *Resúmenes IV Reunión Ibérica sobre Fallas Activas y Paleosismología*, Teruel, Universidad de Zaragoza, pp. 27-30.

Simón-Porcar, G., Simón, J.L. y Liesa, C.L. (2019). La cuenca neógena extensional de El Pobo (Teruel, Cordillera Ibérica): sedimentología, estructura y relación con la evolución del relieve. *Rev. Soc. Geol. Esp.* 32, 17–42.

Sinusía, C., Pueyo, E.L., Azanza, B. y Pocoví, A. (2004). Datación magnetoestratigráfica del yacimiento paleontológico de La Puebla de Valverde (Teruel). *Geo-Temas* 6(4), 339-342.

Stephenson, W.J., McBride, J.H. (2003). Preface to Special Issue, "Contributions to neotectonics and seismic Hazard from shallow geophysical imaging". *Tectonophysics* 1(368), 1–5.

Stirling, M., Rhoades, D. y Berryman, K. (2002). Comparison of Earthquake Scaling Relations Derived from Data of the Instrumental and Preinstrumental Era. *Bull. Seism. Soc. America* 92(2), 812-830. doi: 10.1785/0120000221

Stirling, M., Goded, T., Berryman, K. y Litchfield, N. (2013). Selection of Earthquake Scaling Relationships for Seismic-Hazard Analysis. *Bull. Seism. Soc. America* 103(6), 2993-3011. doi: 10.1785/0120130052

Strom, A. (2017). Active faults at structure's foundations: Definition and its influence on hazard assessment. *Proceedings 16th World Conference on Earthquake Engineering*, Santiago de Chile.

Tena, S. y Casas, A.M. (1996). Estructura y cinemática de la falla de Alpeñés (Cordillera Ibérica). *Geogaceta* 20(4), 789-791.

Vacherat, A., Bonnet, S. y Mouthereau, F. (2018). Drainage reorganization and divide migration induced by the excavation of the Ebro basin (NE Spain). *Earth Surface Dynamics* 6, 369-387.

Vanneste, K., Verbeeck, K. y Petermans, T. (2008). Pseudo-3D imaging of a low-slip-rate, active normal fault using shallow geophysical methods: the Geleen fault in the Belgian Maas River valley. *Geophysics* 73(1), B1–B9. doi: 10.1190/1.2816428

Vegas, R., Fontboté, J.M. y Banda, E. (1979). Widespread Neogene rifting superimposed on alpine regions of the Iberian Peninsula. *Proceedings Symposium Evolution and Tectonics of the Western Mediterranean and Surrounding Areas*, EGS, Viena, Instituto Geográfico Nacional, Madrid, Special Publ. 201, 109-128.

Villamor, P. y Berryman, K.R. (1999). La tasa de desplazamiento de una falla como aproximación de primer orden en las estimaciones de peligrosidad sísmica. *1er Congreso Nacional de Ingeniería Sísmica*, Murcia, 153-163.

Villena, J. (1969). Mapa geológico de la Laguna de Gallocanta (Teruel-Zaragoza) y sus alrededores. *Guía Excursión V Reun. Grupo Esp. Sedimentología*, Pamplona.

Wallace, R.E. (1970). Earthquake recurrence intervals on the San Andreas fault. *Geol. Soc. Am. Bull.* 88, 1267-1281.

Weerd, A. van de (1976). Rodent faunas of the Mio-Pliocene continental sediments of the Teruel-Alfambra region, Spain. *Utrecht Micropaleontology Bulletin*, Special Publication 2, 217 pp.

Wells, D. L. y Coppersmith K. J. (1994). New empirical relationships among magnitude, rupture length, rupture width, rupture area, and surface displacement. *Bulletin of the Seismological Society of America* 84 (4), 974-1002.

Wesnousky, S.G. (2008). Displacement and geometrical characteristics of earthquake surface ruptures: Issues and implications for seismic-hazard analysis and the process of earthquake rupture. *Bull. Seism. Soc. America* 98(4), 1609-1632.

Wesson, R. L, Helley, E. J., Lajoie, K.R. y Wentworth, C.M. (1975). *Faults and future earthquakes, in studies for seismic zonation of the San Francisco Bay Region*. U.S. Geological Survey, 5-30 (comunicado 941-A).

Westaway, R., Maddy, D. y Bridgland, D. (2002). Flow in the lower continental crust as a mechanism for the Quaternary uplift of south-East England: constraints from the Thames terrace record. *Quat. Sci. Rev.* 21, 559-603. doi: 10.1016/ S0277-3791(01)00040-3.

Western States Seismic Policy Council (1997). *Active fault definition for the Basin and Range Province*. Western States Seismic Policy Council, San Francisco, 3 pp. (comunicado).

Wiemer, S. (2001). A software package to analyze seismicity: ZMAP. *Seismol. Res. Lett.* 72(3), 373–382. doi: 10.1785/gssrl.72.3.373.

Wiemer, S. y Wyss, M. (2000). Minimum magnitude of completeness in earthquake catalogs: Examples from Alaska, the western US and Japan. *Bull. Seism. Soc. Am.* 90, 859-869.

Willis, B. (1923). A fault map of California. *Bulletin of the Seismological Society of America* 13, 1-12.

Wood, H. O. (1916). The earthquake problem in the western United States. *Bulletin of the Seismological Society of America* 6, 181-217.

Wortel, M.J.R. y Spakman, W. (2000). Subduction and slab detachment in the Mediterranean-Carpathian region. *Science* 290, 1910-1917. doi: 10.1126/science.290.5498.1910.

Ziegler, P.A. (1992). European Cenozoic rift system. *Tectonophysics* 208, 91–111.


ANEXOS

ANEXO I:

Reflexiones preliminares sobre las incertidumbres de las dataciones

Durante el periodo de tiempo en que ha estado elaborándose esta tesis, han surgido polémicas en torno a las edades de las muestras analizadas mediante Luminiscencia Ópticamente Estimulada (*Optically stimulated luminiscence*, OSL) en el Laboratorio de Datación y Radioquímica de la Universidad Autónoma de Madrid (UAM). Gutiérrez *et al*. (2020a) y Moreno *et al*. (2021) indagan en el protocolo seguido en dicho laboratorio, señalando incongruencias y falta de información metodológica, con lo que aseguran que se obtienen edades demasiado recientes. A pesar de que el debate se debería abrir para todas las muestras analizadas en España por la UAM (años 2000-2015, aproximadamente), los autores ponen el foco en las edades de los depósitos cuaternarios desplazados por algunas fallas de la Cordillera Ibérica centro-oriental. Para ello, se basan en una comparación con edades de muestras nuevas tomadas en dichos depósitos, obtenidas mediante protocolos más modernos y tratadas en los laboratorios del Centro Nacional de Investigación sobre la Evolución Humana (CENIEH, Burgos). Analizan las muestras con cuatro métodos de datación diferentes: OSL, U/Th, espín electrónico (*Electro Spin Resonance*, ESR) y espectrometría de masas con acelerador para la datación del radiocarbono (*Accelerator Mass Spectrometry*, AMS). Con todo ello, los autores concluyen que en general los resultados obtenidos son sistemáticamente entre 3 y 6 veces más antiguos que los resultados previos y cuestionan seriamente la fiabilidad de todas las edades obtenidas en la UAM.

Parece realista considerar que la metodología seguida por la UAM se limitaba al estado del conocimiento sobre OSL del que se disponía durante los años de actividad del laboratorio, y que hoy en día se siguen procedimientos más complejos y seguramente más precisos, como los empleados en el CENIEH. Por lo tanto, en esta tesis consideramos adecuada la idea base de Gutiérrez *et al.* (2020a) de poner a prueba la cronología del modelo evolutivo de actividad de algunas de las fallas de la Cordillera Ibérica centro-oriental propuesto previamente en la literatura (e.g., Gutiérrez *et al*., 2008, Lafuente, 2011, Simón *et al.*, 2017).

Cabe destacar que esta problemática no afecta a las edades con las que se ha trabajado en los resultados principales de esta tesis (de la zona de falla de Río Grío-Pancrudo, así como de las fallas de Calamocha y Sierra Palomera), ya que éstas se han obtenido en el Laboratorio de Datación por Luminiscencia del CENIEH y en el de la Universidad de Georgia. Sin embargo, creemos conveniente reflexionar de manera preliminar sobre todo ello, dado que las incertidumbres que haya sobre las edades de otras fallas pueden afectar al modelo evolutivo general.

Dadas nuestras limitaciones a la hora de abordar uno de los pilares fundamentales de esta problemática, el referente a la metodología del análisis en el laboratorio, la manera de seguir poniéndola a prueba ha sido recoger muestras nuevas de algunos de los afloramientos mencionados en estos trabajos y comparar sus resultados. Con esa idea, en esta tesis hemos tomado 9 muestras adicionales para analizarlas de nuevo, mediante OSL, en el CENIEH. De ese total, 4 muestras están tomadas en afloramientos datados tanto en la literatura previa como por Gutiérrez *et al*. (2020a). Esto nos posibilita comparar las edades resultantes en cada caso, y debería haber permitido sacar algunas conclusiones y extrapolarlas a las demás edades. Sin embargo, tal y como exponemos más adelante, esto no ha sido posible.

Se ha visto que la problemática de las dataciones cuaternarias de la Cordillera Ibérica centro-oriental es de una gran complejidad y sigue presentando incertidumbres importantes en todas sus partes. Por ello creemos que, con la información de la que se dispone hoy en día, es excesivamente precipitado tanto confirmar como refutar la hipótesis de que la edad de todas las muestras analizadas en la UAM debería ser mayor. En esta sección sólo se pretende hacer un esbozo con algunas consideraciones, apoyándonos en las dataciones adicionales que aportamos aquí. Abordarla concienzudamente implica realizar más campañas de dataciones, y una revisión exhaustiva de los resultados del análisis de cada muestra. Esta tarea la dejamos para trabajos futuros del grupo de investigación, para los cuales esta sección servirá de base. Mientras tanto, en esta tesis decidimos mantener, en cierta medida, el modelo evolutivo clásico con las aportaciones de las dataciones nuevas, hasta que se pueda concretar más.

A continuación, en relación con todos los resultados de dataciones involucradas en la literatura y en esta tesis, exponemos las consideraciones preliminares que, como decíamos, no permiten todavía poner fin a la polémica (véase la Tabla comparativa incluida en este Anexo):

(1) La localización de muchas de las muestras analizadas en los trabajos recientes no corresponde a la original de trabajos previos (pueden llegar a encontrarse a distancias de entre 80 y más de 400 m). Es algo lógico, dado que

muchas corresponden a trincheras que ya fueron restauradas, pero consideramos que es un factor a tener en cuenta en la valoración final, ya que en cuestión de pocos metros pueden producirse cambios laterales de unidades que harían variar la estratigrafía.

(2) El método de datación no es el mismo en muchas de ellas (se emplean hasta cuatro métodos de datación). Ya Moreno *et al*. (2021) señalan que el uso de múltiples métodos de datación podría impedir esclarecer qué edades son las más veraces si los resultados obtenidos muestran inconsistencias importantes, como es el caso. Para poder poner en cuestión correctamente las dataciones de la UAM, que están obtenidas siguiendo la metodología de OSL, deberíamos compararlas con otras analizadas con ese mismo método. De las 16 muestras recogidas por Gutiérrez *et al*. (2020a) que comparan con dataciones previas de la UAM, sólo 3 están datadas siguiendo la metodología de OSL.

(3) No todas las edades nuevas son más antiguas que las edades previas de la literatura, sino que las tres edades obtenidas con AMS para el radiocarbono (Gutiérrez *et al*., 2020a) son mucho más recientes que las originales. Los autores lo justifican por las características sedimentológicas de los depósitos en los que se tomaron. Al menos una de nuestras tres dataciones OSL análogas a las anteriormente mencionadas (la LM21171-08 y, aún con posible blanqueo parcial*, la LM21171-09) podría confirmar que se trata de un error. Sin embargo, la tercera de nuestras dataciones OSL (LM21171-03) confirma la de AMS de Gutiérrez *et al*. (2020a), dando una edad incluso más reciente que la publicada anteriormente. Cabe destacar, además, que las dos primeras suponen la diferencia de edad más grande de todas las cuestionadas y corresponden a dos rellenos fisurales en la trinchera de Los Baños (Concud).

(4) Parte de la sucesión de edades inferida de las dataciones nuevas no es estratigráficamente coherente entre sí. Las cuatro dataciones de Gutiérrez *et al*. (2020a) del subnivel alto de la Terraza Media o T2 en Los Baños deberían solaparse en cierta medida. En este mismo sector, el relleno fisural de la Unidad 12 se generó en un evento anterior al que dio lugar al relleno fisural de la Unidad 13 (Lafuente, 2011; Lafuente *et al*., 2011), por lo que sus edades deberían reflejar esa relación cronológica. El glacis muestreado cerca de la trinchera de La Mataueta cubre el subnivel medio de la T1 por lo que, tanto en los resultados de Gutiérrez *et al*. (2020a) como en los de las dataciones adicionales de esta tesis, su edad debería ser menor o no diferir demasiado de la del subnivel en cuestión. Este último está datado en Masada Cociero y en un nivel correlacionable en Gea (Peña-Monné *et al*., 2022). Sin embargo, hay que tener en cuenta que, en este caso de las muestras de La Mataueta, no están tomadas en el punto original de muestreo, sino a cierta distancia.

(5) Aunque se trate de dataciones realizadas a cierta distancia de los sectores estudiados (en Gea y San Blas), las realizadas por Peña-Monné *et al*. (2022) en el *Nordic Laboratory for Luminescence Dating* (Universidad de Aarhus, Dinamarca) también pueden entrar en la comparación. Muestran la tendencia de edades de niveles de terraza correlacionables con los subniveles alto y medio de la Terraza Inferior o T1, y les atribuyen unas edades que en el caso del subnivel alto se asemejan a la datación nueva de esta tesis del Puente Minero, y en el caso del subnivel medio se acerca más a las dataciones previas de la UAM.

(6) Las muestras obtenidas de la trinchera de Sierra Palomera podrían haber arrojado cierta claridad a la problemática de la que es objeto esta sección, ya que fueron analizadas en el Laboratorio de Datación por Luminiscencia de la Universidad de Georgia (EE. UU.; Tabla 4.1 del texto principal de esta tesis). Sin embargo, esas muestras tienen limitaciones que lo han impedido. Cinco de las siete muestras resultaron estar saturadas, y las indicaciones del laboratorio fueron que sus edades deben de ser mayores que el rango 193-378 ka y no pueden entrar, por tanto, en la comparación con las demás dataciones. Las dos muestras restantes tienen unas edades algo mayores que las obtenidas en la UAM en un afloramiento análogo, pero de nuevo sin una diferencia excesiva.

(7) Para la correlación de eventos inferida para la falla de Calamocha (Fig. 3.13 del texto principal) se han tenido en cuenta tanto muestras nuevas analizadas en el mismo CENIEH como originales de la UAM (Tabla 3.1 del texto principal), y dicha correlación muestra coherencia, sin diferencias importantes entre las edades.

* Desde el punto de vista de la luminiscencia, la edad de la muestra LM21171-01 no es fiable porque existe blanqueo afectándole claramente, por lo que su edad debería ser menor. Esta muestra se ha tomado en un depósito de terraza que ha de ser de época histórica porque muy cerca se han encontrado varios fragmentos de teja árabe que corresponderían a los últimos siglos. La edad de la muestra LM21171-09 tampoco es del todo fiable porque presenta blanqueo parcial. El resto tienen distribuciones de dosis con dispersiones muy bajas, por lo que no hay ningún indicio de que el blanqueamiento de las muestras haya tenido efecto en las dataciones.

Resultados de las nuevas dataciones con OSL

(Laboratorio de Datación con Luminiscencia del CENIEH, Burgos)

Muestra	Referencia del laboratorio	Profundidad (m)	*Dose rate* (Gy/ka)	*Burial dose* (Gy)	Edad (ka)
VLobos21	**LM21171-01**	1,5	2,64 ± 0,12	19,1 ± 1,7	7,2 ± 0,7
PM21-1	**LM21171-02**	4,8	2,08 ± 0,09	238,4 ± 8,5	114,8 ± 6,3
CO21-1	**LM21171-03**	2,5	1,85 ± 0,08	13,2 ± 0,2	7,1 ± 0,3
CO21-2	**LM21171-04**	4,1	2,00 ± 0,09	70,4 ± 1,1	35,1 ± 1,6
MOSQ-1	**LM21171-05**	4,5	2,28 ± 0,11	165,7 ± 2,5	72,6 ± 3,6
MOSQ-2	**LM21171-06**	1,2	2,29 ± 0,10	150,0 ± 3,2	65,5 ± 3,3
HO21-1	**LM21171-07**	2,3	2,23 ± 0,10	344,6 ± 11,3	154,5 ± 8,6
Baños_FF2	**LM21171-08**	0,3	1,52 ± 0,07	331.1 ± 11,7	218,0 ± 12,3
Baños_FF3	**LM21171-09**	0,3	1,67 ± 0,07	293,1 ± 10,6	175,5 ± 10,0

Comparativa entre las dataciones previas y las nuevas

			DATACIONES PREVIAS				OTRAS DATACIONES NUEVAS					DATACIONES NUEVAS DE ESTA TESIS				
			Localización de la muestra	Método	Referencia del laboratorio	Edad (ka)	Referencia bibliográfica	Localización de la muestra	Método	Referencia del laboratorio	Edad (ka)	Referencia bibliográfica	Localización de la muestra	Método	Referencia del laboratorio	Edad (ka)	Referencia bibliográfica
RLFS													Afloramiento de depósitos aluviales en contacto con la falla	OSL	LM20132-09 LM20132-08 (CENIEH)	40,2 ± 4,4 66,6 ± 6,5	Esta tesis
CPFS													Trinchera excavada en un abanico aluvial cortando a la falla	OSL	Varias, ver Tabla 2.2 (CENIEH)	Desde 34,6 ± 3,0 hasta 3,2 ± 0,2	Esta tesis
MUNÉBREGA			Unidad A1 de trinchera excavada en glacis cortando a la falla	OSL	MAD-4801 (UAM)	71,8 ± 5,6	Gutiérrez *et al.* (2009)	Afloramiento de la misma unidad morfoestratigráfica a más de 400 m de distancia	ESR	SR17105-07 (CENIEH)	241 ± 50 235 ± 54	Gutiérrez *et al.* (2020a)					
DAROCA			Afloramiento de glacis (P4; Unidad 2) en contacto con la falla	OSL	No encontradas (UAM)	112,9 ± 9,2 118,7 ± 16,2	Gutiérrez *et al.* (2008)	Mismo afloramiento de glacis (P4; Unidad 2) en contacto con la falla	ESR	SR17105-06 (CENIEH)	329 ± 43	Gutiérrez *et al.* (2020a,b)					
CALAMOCHA			Taludes/Trincheras en depósitos detríticos en contacto con la falla		Varias, ver Tabla 3.1 (UAM)	Desde 69,9 ± 5,5 hasta 13,8 ± 0,9	Esta tesis						Trinchera en depósitos detríticos cortando a la falla	OSL	Varias, ver Tabla 3.1 (CENIEH)	Desde 145,9±9,1 hasta 68,9±5,2	Esta tesis
Sª PALOMERA			Afloramiento del techo de abanico aluvial (La Sima) a 250 m de distancia de la trinchera	OSL	MAD-6327BIN (UAM)	19,2 ± 1,1	Esta tesis						Trinchera excavada en el mismo abanico aluvial (La Sima) cortando a falla antitética a la principal	OSL	Varias, ver Tabla 4.1 (Univ. Georgia)	49,2 ± 5,4 97,4 ± 10,2 (Y desde más de 378-193)	Esta tesis
CONCUD	Los Baños		Afloramiento de terraza (subnivel alto de la Terraza Media o T2)	U/Th	No encontradas (UAM)	169 ± 10 116 ± 4 ka	Arlegui *et al.* (2004) Lafuente (2011)	Mismo afloramiento de terraza (subnivel alto de la Terraza Media o T2)	ESR	SR17105–02 (CENIEH)	327 ± 31	Gutiérrez *et al.* (2020a)					
					No encontradas (Univ. McMaster)	250+32/−25 213+33/−26	Gutiérrez *et al.* (2008)		U/Th	SU17105–04 SU17105–05 (CENIEH)	≥ 285,2 ± 14 ≥ 228,4 ± 11,4						
		Trinchera en depósitos detríticos cortando a la falla	Unidad 1 - terraza (equivalente aL subnivel alto de la T2)	OSL (U/Th)	MAD-5316SDA (UAM)	113,6 ± 7,3, y entre 169 y 116	Arlegui *et al.* (2004) Lafuente (2011)	Misma trinchera en depósitos detríticos cortando a la falla	Unidad 1 - terraza (equivalente al subnivel alto de la T2)	ESR	SR17105–01 (CENIEH)	480 ± 44					
			Unidad 2 - terraza (equivalente al subnivel alto de la T2)	U/Th	No encontradas (UAM)	Entre 169 y 116			Unidad 2 - terraza (equivalente al subnivel alto de la T2)	U/Th	SU17105–06 (CENIEH)	387,7 ± 9,5					
			Unidad 3	OSL	No encontradas (UAM)	71,7 ± 5,2	Gutiérrez *et al.* (2008)		Unidad 3	OSL	LM17105–01 (CENIEH)	> 276,9 ± 34,6					
			Unidad 6		No encontradas (UAM)	64,2 ± 4,4			Unidad 6	ESR	LM17105–02 (CENIEH)	372 ± 29					
			Unidad 9		MAD-5330SDA (UAM)	62,4 ± 6,6 63,7 ± 4,0	Gutiérrez *et al.* (2008) Lafuente (2011)		Unidad 9		LM17105–03 (CENIEH)	198 ± 16					
			Unidad 12 - relleno fisural		MAD-5317SDA (UAM)	38,6 ± 2,3	Lafuente (2011)		Unidad 12 - relleno fisural	AMS	Beta-471,194 (CENIEH)	2344–2155 cal. yr BP		Misma trinchera	Unidad 12 - relleno fisural	OSL	LM21171-08 (CENIEH)	218,0 ± 12,3	Esta tesis
			Unidad 13 - relleno fisural		MAD-4680SDA (UAM)	32,1 ± 2,4			Unidad 13 - relleno fisural		Beta-471,193 (CENIEH)	7972–7851 cal. yr BP			Unidad 13 - relleno fisural		LM21171-09 (CENIEH)	175,5 ± 10,0	
	El Hocino		Trincheras excavadas en glacis cortando la falla	OSL	Varias, ver Tabla 1 de Lafuente *et al.* (2014) (UAM)	Desde 77,3 ± 4,3 hasta 19,4 ± 2,1	Lafuente *et al.* (2014)						Afloramiento del mismo glacis a más de 150 m de distancia de la trinchera		LM21171-07 (CENIEH)	154,5 ± 8,6	
	Masada Cociero		Afloramiento de depósito coluvial fosilizando la falla		MAD-4681SDA (UAM)	15,0 ± 1,0	Lafuente (2011)	Mismo afloramiento de depósito coluvial fosilizando la falla	AMS	B-512900 (CENIEH)	7589–7486 cal. yr BP	Gutiérrez *et al.* (2020a)	Mismo afloramiento de depósito coluvial fosilizando la falla		LM21171-03 (CENIEH)	7,1 ± 0,3	
			Afloramiento de terraza (subnivel medio de la Terraza Inferior o T1) afectado por la falla		No encontrada, MAD-4681SDA (UAM)	15,0 ± 0,9 15,6 ± 1,3	Gutiérrez *et al.* (2008) Lafuente (2011)	Mismo afloramiento de terraza (subnivel medio de la T1) afectado por la falla		OSL	LM-17105-04 (CENIEH)	60,0 ± 2,5		Mismo afloramiento de terraza (subnivel medio de la T1) afectado por la falla		LM21171-04 (CENIEH)	35,1 ± 1,6	
								Afloramiento de terraza (equivalente al subnivel medio de la T1; ver Tabla 1 de Peña-Monné *et al.*, 2022) en Gea			ALBAR-3 (NLLD)	22 ± 7	Peña-Monné *et al.* (2022)					
	Matagueta		Trinchera excavada en glacis (cubre el subnivel medio de la T1) cortando a la falla		Varias, ver Tabla 1 de Simón *et al.* (2016) (UAM)	Desde 27,6 hasta 12,8	Simón *et al.* (2016)	Afloramiento del mismo glacis (cubre el subnivel medio de la T1) a 90 m de distancia de la trinchera			LM-17105-05 (CENIEH)	87,1 ± 3,0	Gutiérrez *et al.* (2020a)	Afloramiento del mismo glacis (cubre el subnivel medio de la T1) a 55 m de distancia de la trinchera		LM21171-05 LM21171-06 (CENIEH)	65,5 ± 3,3 (techo) 72,6 ± 3,6 (base)	
TERUEL	Pitraque		Trincheras excavadas en terraza (subnivel bajo de la T2) cortando a la falla	OSL	Varias, ver Tabla 3 de Simón *et al.* (2017) (UAM)	Desde 78,3 ± 5,2 hasta 46,5 ± 3,1	Simón *et al.* (2017)	Afloramiento de la misma terraza (subnivel bajo de la T2) a 80 m de distancia de la tricnhera	ESR	SR17105–03 (CENIEH)	307 ± 25	Gutiérrez *et al.* (2020a)					
	Rambla Valdelobos		Trinchera excavada en terraza (Terraza Subactual o T0) cortando a la falla		MAD-6073SDA MAD-6074SDA (UAM)	26,7 ± 1,9 9,9 ± 0,7							Afloramiento de la misma terraza (T0) a unos 30 m de distancia de la trinchera	OSL	LM21171-01 (CENIEH)	7,2 ± 0,7	Esta tesis
Otros	Puente Minero		Afloramiento de terraza (subnivel alto de la T1)	OSL	MAD-5778rpSDA (UAM)	22,0 ± 1,6	Lafuente (2011)	Afloramiento de terraza (equivalente al subnivel alto de T1; ver Tabla 1 de Peña-Monné *et al.*, 2022) en San Blas	OSL	SBLAS-3 SBLAS-1 SBLAS-2 (NLLD)	136 ± 20 111 ± 6 81 ± 5	Peña-Monné *et al.* (2022)	Mismo afloramiento de terraza (subnivel alto de la T1)	OSL	LM21171-02 (CENIEH)	114,8 ± 6,3	Esta tesis

Localización de muestras nuevas:

1) Los Baños

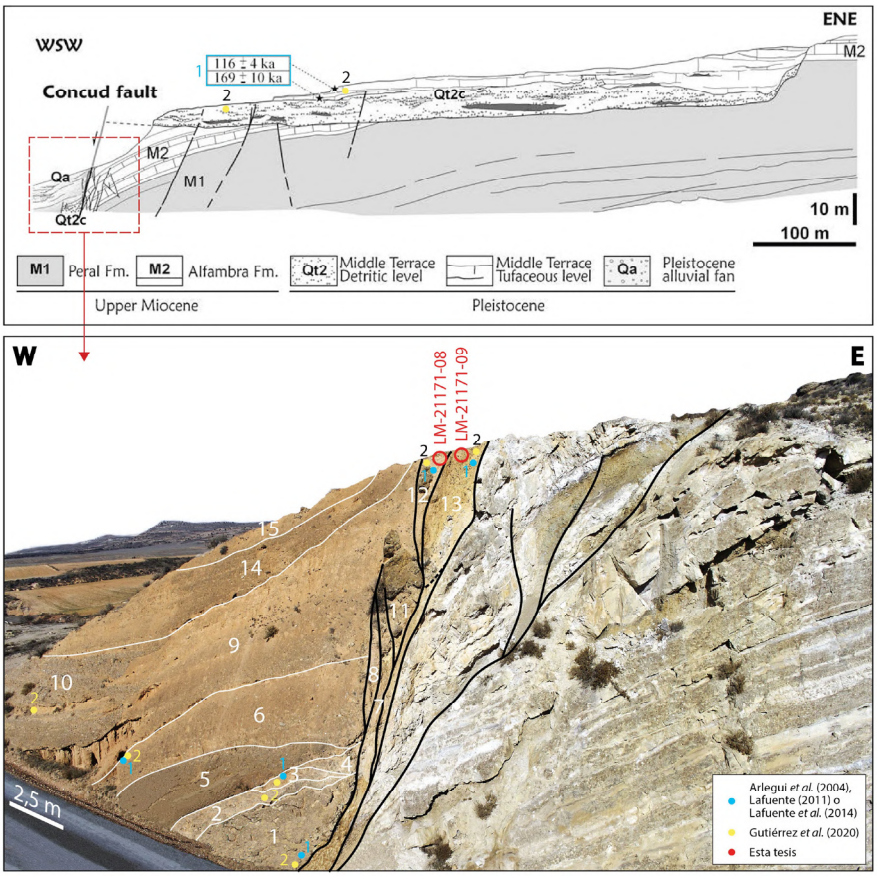

Localización de muestras nuevas:

2) El Hocino

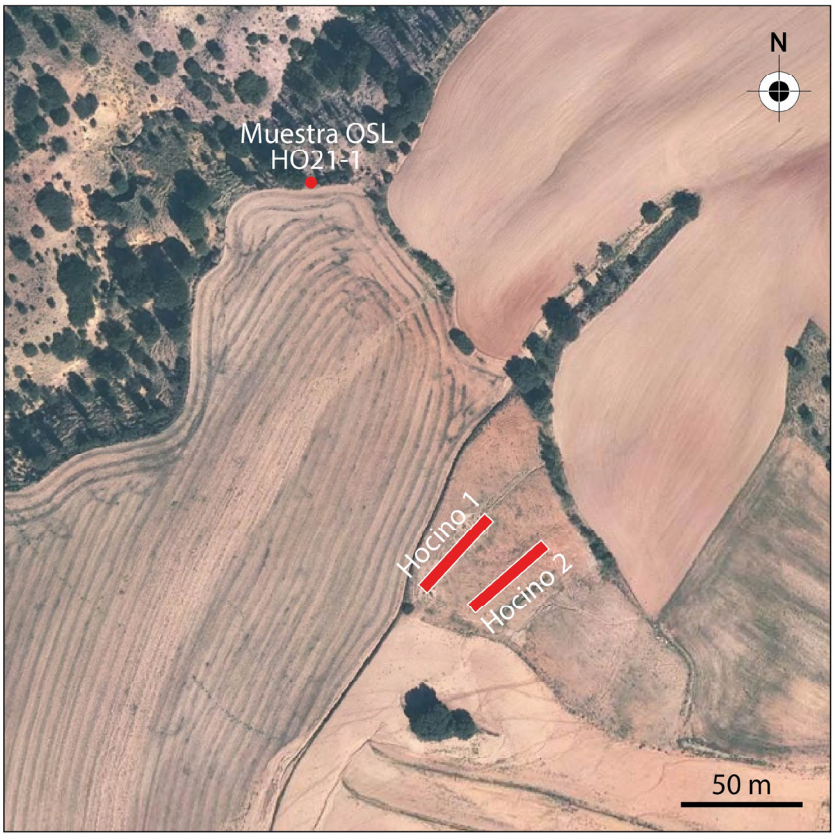

Localización de muestras nuevas:

3) Masada Cociero, Matausta y Puente Minero

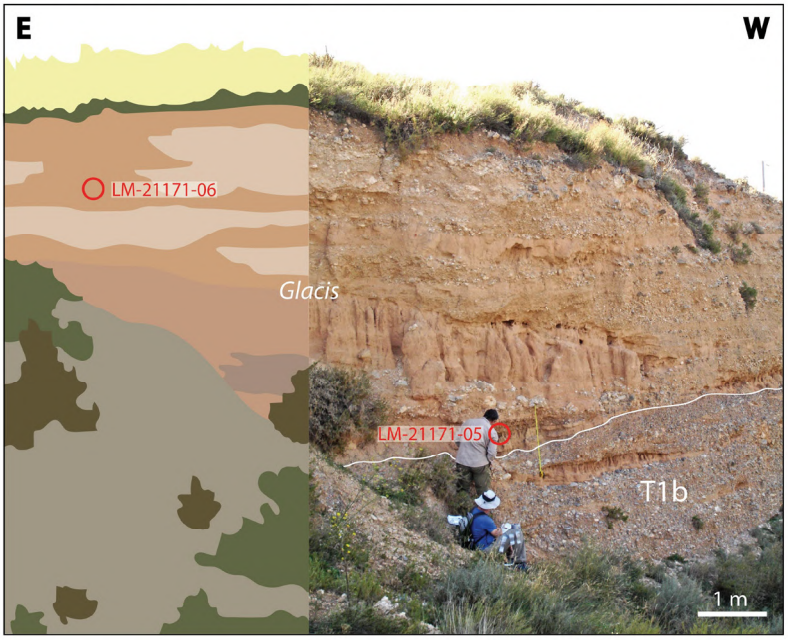

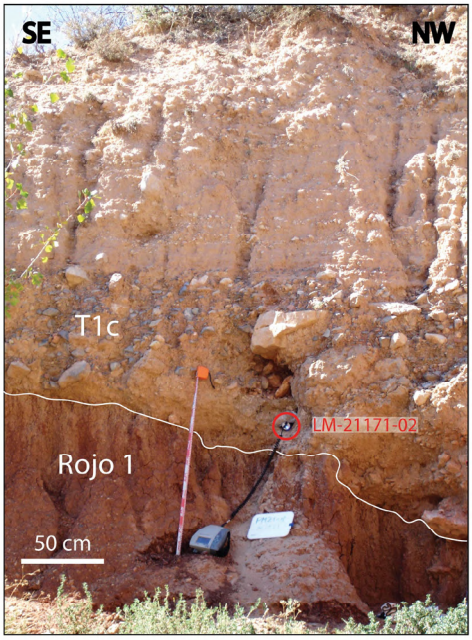

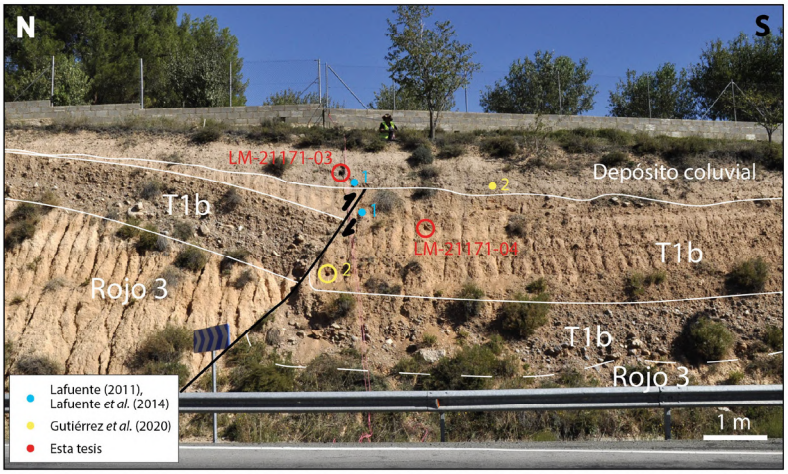

Localización de muestras nuevas:

4) Rambla de Valdelobos

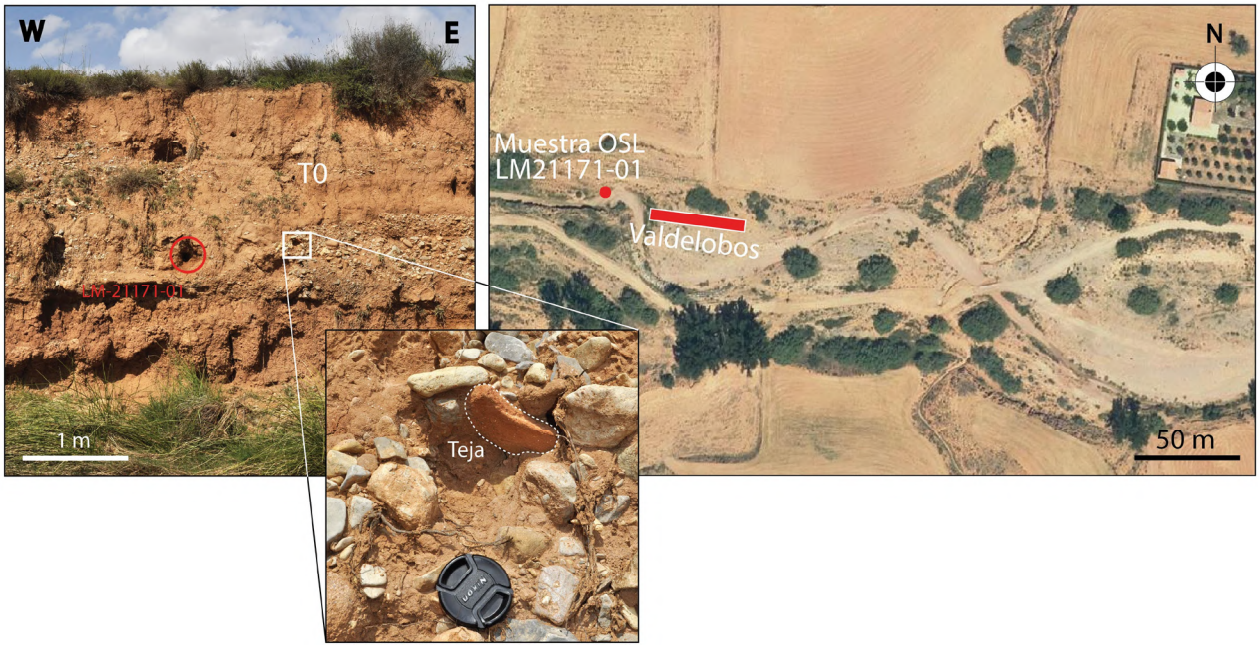

ANEXO II:

Datos de longitud y pendiente de los glacis villafranquienses regionales

Material suplementario de la publicación de Peiro y Simón (2021)

	Pediment name or location	Length (km)	Slope (º)	Reference
1	Around Cervera de la Cañada village	2.6	1.5	Aragonés *et al.* (1981)
2	Around the San Quintín site	1.6	1.5	
3		2.9	1.4	
4		1.8	3.1	
5		1.6	3.6	
6		1.1	3.2	
7	Las Planas site	3.5	0.6	Hernández *et al.* (2005)
8	Around Belmonte de Gracián village	1.7	2.5	del Olmo *et al.* (1983a)
9	Around Castejón de Alarba village	1.5	2.4	
10	Las Artigas site	2.3	1.2	Olivé *et al.* (1983a)
11	Los Guijares site	4.1	3.8	
12	Paridera Orilla del Pinar site	2.4	2.9	Gabaldón *et al.* (1989b)
13	Around Tortuera village	1.9	1.0	del Olmo *et al.* (1983c)
14		2.6	1.2	
15		2.2	1.8	
16		2.5	1.2	
17	Around Campillo de Dueñas village	2.2	0.7	
18		4.1	2.0	
19		1.3	3.2	
20		4.6	1.2	
21		3.5	1.9	
22		5.2	0.8	
23		3.5	1.2	
24		2.4	1.2	
25	Around La Yunta village	2.0	2.1	
26		3.6	1.6	
27	Around Machacón site	5.2	0.6	
28		5.4	0.5	
29	Around Villalba de los Morales village	3.0	2.1	Hernández *et al.* (1983b)
30		1.6	2.2	
31		3.3	0.6	
32		2.4	0.6	
33	Around Calamocha village	3.3	1.6	
34		2.7	1.7	
35	Along the Jiloca River, between Torrijo del Campo and Villafranca del Campo villages	4.7	0.7	Olivé *et al.* (1983b)
36		5.1	0.8	
37		3.3	0.5	
38		5.2	0.7	
39		4.0	0.7	
40		3.5	0.8	
41		4.0	0.8	
42		4.7	0.6	
43		6.0	1.3	
44		4.6	1.3	
45		3.9	1.3	
46		3.8	1.6	
47		3.3	1.8	

ANEXO III:

Información para el compendio de publicaciones

Peiro, A., Simón, J.L., Román-Berdiel, M.T. (2020). Fault relay zones evolving through distributed longitudinal fractures: the case of the Teruel graben system (Iberian Chain, Spain). *Journal of Structural Geology* 131, 103942. doi: 10.1016/j.jsg.2019.103942

Área temática: *GEOSCIENCES, MULTIDISCIPLINARY*

Factor de Impacto (JCR) en 2020: 3,571

Cuartil en 2020: Q2

Contribución (CRediT author statement): *Investigation*, *Methodology*, *Formal analysis*, *Writing - Original Draft*, *Visualization*.

Peiro, A., Simón, J.L. (2021). The Río Grío-Pancrudo Fault Zone (central Iberian Chain, Spain): recent extensional activity revealed by drainage reversal. *Geological Magazine* 159(1), 21-36. doi: 10.1017/S0016756821000790

Área temática: *GEOSCIENCES, MULTIDISCIPLINARY*

Factor de Impacto (JCR) en 2021: 2,656

Cuartil en 2021: Q3

Contribución (CRediT author statement): *Conceptualization*, *Investigation, Methodology*, *Formal analysis*, *Writing – original draft*, *Visualization*.

Peiro, A., Simón, J.L., Arlegui, L.E., Ezquerro, L., García-Lacosta, A.I., Lamelas, T., Liesa, C.L., Luzón, A., Martín-Bello, L., Pueyo-Anchuela, O., Russo, N. (2022). Hanging-wall deformation at the active Sierra Palomera extensional fault (Jiloca basin, Spain) from structural, morphotectonic, geophysical and trench analysis. *Tectonophysics* 828, 229274. doi: 10.1016/j.tecto.2022.229274

Área temática: *GEOCHEMISTRY & GEOPHYSICS*

Factor de Impacto (JCR) en 2021: 3,660

Cuartil en 2021: Q2

Contribución (CRediT author statement): *Investigation*, *Methodology*, *Formal analysis*, *Writing – original draft*, *Visualization*.

Peiro, A., Simón, J.L., Martín-Bello, L., Arlegui, L.E., Ezquerro, L., Luzón, A., Medialdea, A., Corral, B., Liesa, C.L. (2022). Recent activity and paleoseismicity of an intraplate extensional fault: the Calamocha fault (Jiloca graben, central Iberian Chain). *International Journal of Earth Sciences*, online. doi: 10.1007/s00531-022-02265-3

Área temática: *GEOSCIENCES, MULTIDISCIPLINARY*

Factor de Impacto (JCR) en 2021: 2,698

Cuartil en 2021: Q3

Contribución (CRediT author statement): *Conceptualization*, *Investigation*, *Methodology*, *Formal analysis*, *Writing – original draft*, *Visualization*.

Simón, J.L., Simón-Porcar, G., **Peiro, A.**, (2022). *Memory of the Earth* and human memory on natural disasters: the 1953 earthquake in western Aragón (Spain). *Geoheritage*, online. doi: 10.1007/s12371-022-00758-w

Área temática: *GEOSCIENCES, MULTIDISCIPLINARY*

Factor de Impacto (JCR) en 2021: 2,786

Cuartil en 2021: Q3

Contribución (CRediT author statement): *Investigation, Writing – Review & Editing, Visualization*.

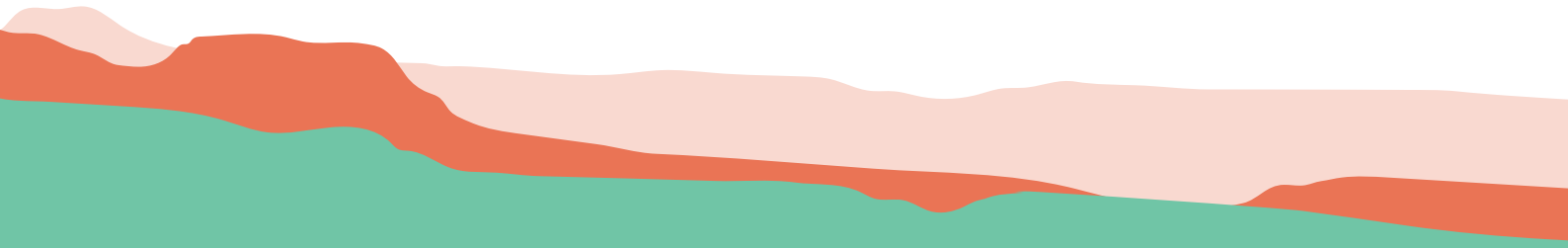

GOBIERNO DE ESPAÑA
MINISTERIO DE EDUCACIÓN, CULTURA Y DEPORTE

GEOtransfer
Grupo de Investigación
Geología para la Ciencia y la Sociedad
Universidad Zaragoza

juca
Instituto Universitario de Investigación en Ciencias Ambientales de Aragón
Universidad Zaragoza